STUDIA UNIVERSITATIS
BABEŞ-BOLYAI

UNIVERSITATEA BABEŞ-BOLYAI
BABEŞ-BOLYAI TUDOMÁNYEGYETEM
BABEŞ-BOLYAI UNIVERSITÄT
BABEŞ-BOLYAI UNIVERSITY
TRADITIO ET EXCELLENTIA

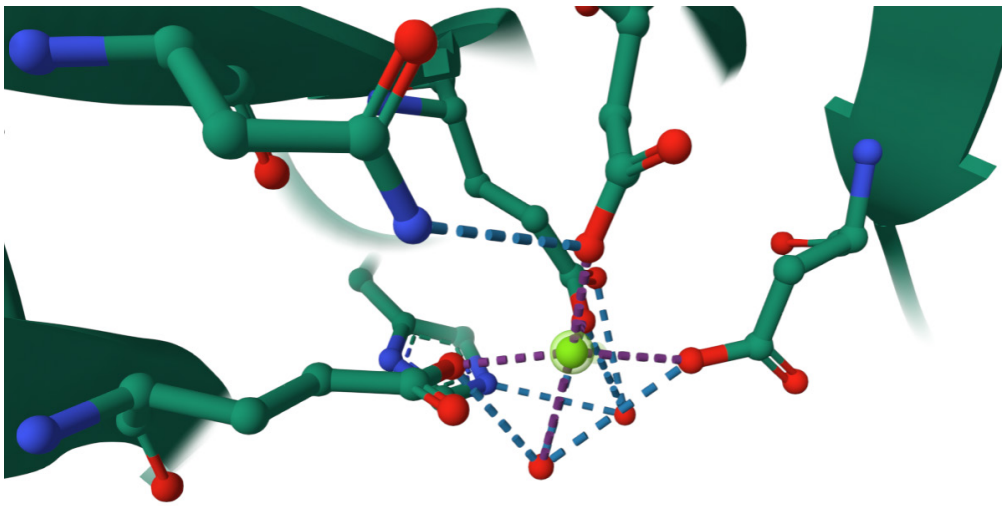

CHEMIA

2/2026

STUDIA
UNIVERSITATIS BABEŞ-BOLYAI
CHEMIA

2/2026

ISSN (print): 1224-7154
ISSN (online): 2065-9520; ISSN-L: 1224-7154

Published by Babeş-Bolyai University

https://studia.reviste.ubbcluj.ro/index.php/chemia/
studiachemia@ubbcluj.onmicrosoft.com

YEAR **Volume 71 (LXXI) 2026**
MONTH **June**
ISSUE **2**

PUBLISHED ONLINE: 2026-06-23
PUBLISHED PRINT: 2026-06-30
ISSUE DOI: 10.24193/subbchem.2026.2

S T U D I A
UNIVERSITATIS BABEŞ–BOLYAI
CHEMIA

2

CONTENT/ SOMMAIRE/ INHALT/ CUPRINS

Studia Universitatis Babes-Bolyai Chemia has been selected for coverage in Thomson Reuters products and custom information services. Beginning with V. 53 (1) 2008, this publication is indexed and abstracted in the following:

- Science Citation Index Expanded (also known as SciSearch®)
- Chemistry Citation Index®
- Journal Citation Reports/Science Edition

STUDIA UBB CHEMIA, LXXI, 2, 2026 (p. 7-20)
(RECOMMENDED CITATION)
DOI:10.24193/subbchem.2026.2.01

PARAMETRIC STUDY AND OPTIMIZATION OF D-GLUCOSE ISOMERIZATION USING SWEETZYME IT: A FACTORIAL DESIGN APPROACH

Souad-Diana TORK[a]*, Mălina Ioana POP[a], Alina FILIP[a], Judith-Hajnal BARTHA-VARI[a]

ABSTRACT. High-fructose corn syrup (HFCS) is produced industrially by the immobilized glucose isomerase Sweetzyme IT (from *Streptomyces murinus*), one of the most widely used biocatalysts in the food industry. Although its individual operating parameters are well established, simultaneous interactions between operational variables over time have rarely been systematically quantified. In this study, a two-level full factorial design modeled the combined effects of initial glucose concentration, temperature and Mg^{2+} cofactor concentration on the process. Reaction progress was followed polarimetrically through a dedicated glucose-fructose calibration; concurrent refractometric monitoring proved insensitive due to total dissolved solids conservation. The regression models ($R^2 > 0.99$) identified temperature as the dominant operational factor. Incorporating reaction time as a factor revealed a significant temperature × time interaction and a shift of rate control from initial substrate concentration to temperature near equilibrium. A maximum conversion of 45.98 % (close to the thermodynamic equilibrium of the reaction) was obtained at 0.2 M glucose, 60 °C and 1.5 mM Mg^{2+} after 24 h. A comparative screening of divalent cations confirmed $MgSO_4 \cdot 7H_2O$ as the superior chemical activator, over Ni^{2+}, Mn^{2+}, Cu^{2+} and Ca^{2+} with Ca^{2+} among the poorest, consistent with its known inhibitory role. This study establishes a reliable mathematical approach that can be extended to predict and optimize other complex bioprocesses.

Keywords: *enzymatic isomerisation; HFCS; Sweetzyme IT; glucose isomerase; design of experiments / factorial design; polarimetry; optical rotation; D-glucose*

[a] *Babeş-Bolyai University, Faculty of Chemistry and Chemical Engineering, 11 Arany Janos str., RO-400028, Cluj-Napoca, Romania*
* *Corresponding author: souad.tork@ubbcluj.ro*

INTRODUCTION

High-fructose corn syrup (HFCS) has become an essential component in the food and beverage industry, representing an economical alternative to traditional sucrose. [1, 2] The major industrial interest in this product is based on the superior properties of fructose, which is the sweetest naturally available carbohydrate (being approximately 1.7 times sweeter than glucose) making it particularly valuable for dietary products and processed foods. [3] The large-scale production of HFCS is achieved through the interconversion of D-glucose to D-fructose, a process that can be approached both chemically and biocatalytically. [4-6]

Although the isomerization reaction can be chemically catalysed in alkaline or acidic media, chemo-catalytic processes present major technological disadvantages: they require high temperatures and pH values, have low selectivity (typically yielding 20-30%), and generate non-metabolizable by-products (e.g., psicose) or degradation compounds that alter the colour and flavour of the final product. [3, 7] For these reasons, enzymatic processes mediated by glucose isomerase (GI) (D-xylose ketol-isomerase, EC 5.3.1.5) have become the undisputed industrial standard, offering exceptional reaction specificity, operation under mild ambient conditions, and generating no unwanted by-products. [6, 8]

Glucose isomerase is a metalloenzyme whose catalytic activity and structural stability depend strictly on the presence of divalent metal cations, such as Mg^{2+}, Co^{2+}, or Mn^{2+}. Advanced structural studies, including X-ray and neutron diffraction, have demonstrated that the enzyme possesses two distinct metal sites (M1 and M2) that orchestrate the catalytic mechanism (Figure 1A). [9-10] The generally accepted reaction mechanism proceeds in three fundamental steps: the opening of the sugar ring, an isomerization step mediated by metal ions via a hydride transfer (from C2 to C1), and finally, ring closure to release the fructose (Figure 1B). [9, 11]

Despite its high efficiency, GI is predominantly an intracellular enzyme, and its use in a free, soluble form involves major losses and prohibitive costs for continuous industrial processes. [3] To overcome these limitations, the established approach has consisted of immobilizing the enzyme on solid supports, an approach that facilitates the recovery and repeated reuse of the biocatalyst while simultaneously solving issues of thermal and operational stability. [12] In particular, commercial preparations such as Sweetzyme IT (Novozymes) are widely used due to their robustness in continuous-flow packed-bed reactors. Derived from a selected strain of *Streptomyces murinus*, this specific biocatalyst is obtained through the glutaraldehyde cross-linking of whole-cell homogenates combined with an inorganic carrier. Engineered

into dense, cylindrical particles (0.2–0.4 mm in diameter) with a high specific activity (e.g. 450 IGIU/g), Sweetzyme IT exhibits exceptional mechanical and catalytic stability, making it highly effective for the large-scale industrial conversion of glucose to fructose. [13-15]

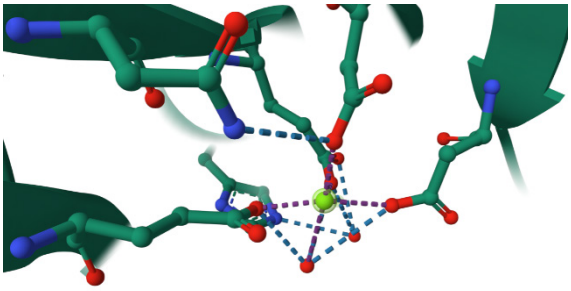

A

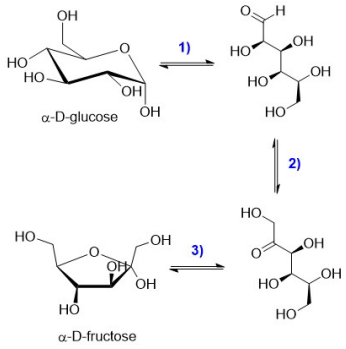

B

Figure 1. A) M2 catalytic site of *Streptomyces murinus* glucose isomerase (PDB ID: 1DXI). The catalytic magnesium ion (Mg^{2+}) is tightly coordinated by conserved residues His220, Glu217, Asp257, and Asp255 (bidentate binding). Purple dashed lines represent direct metal-ligand coordination, while blue dashed lines indicate hydrogen-bonding networks; **B)** Reaction mechanism of D-glucose to D-fructose interconversion. The process proceeds through three fundamental steps: 1) ring opening of α-D-glucose, 2) metal-mediated isomerization via hydride transfer, and 3) ring closure to yield α-D-fructose.

The aim of this study is to evaluate and optimize the kinetics and efficiency of the enzymatic isomerization of D-glucose to D-fructose using the commercial immobilized biocatalyst Sweetzyme IT. To understand the impact of the reaction parameters, a factorial design was employed to investigate key operational conditions (initial glucose concentration, temperature and magnesium cofactor concentration) and the activating or inhibiting effects of alternative metal cations on the enzyme's specific activity were evaluated.

Glucose isomerase is among the most thoroughly studied industrial enzymes, and the behaviour of commercial preparations such as Sweetzyme IT is well documented at the level of individual operating parameters. The contribution of the present study therefore lies not in the enzyme or the reaction themselves, but in how their operational space is modelled and monitored. First, in contrast to the prevailing one-factor-at-a-time practice, a two-level full factorial design quantifies the interactions among substrate concentration, temperature and cofactor concentration for this specific

commercial biocatalyst, yielding a predictive regression model ($R^2 > 0.99$) rather than a set of isolated optimal values [16-18]. Second, by treating reaction time as an explicit factor, the analysis reveals that the rate-controlling variable changes during the reaction (substrate-controlled at short times and temperature-controlled near equilibrium, with a statistically significant temperature × time interaction) a kinetic feature that conventional single-time-point optimisation cannot capture. Third, the work provides a validated, low-cost polarimetric assay that converts a single optical-rotation reading into conversion, and shows that refractometry, although standard for sugar syrups, is intrinsically blind to this mass-conserving isomerisation. Together, these establish a compact, reproducible design-and-monitor methodology that is readily transferable to other immobilised glucose isomerases and to process-scale decisions [19, 20].

RESULTS AND DISCUSSION

The conversion of D-glucose into D-fructose catalysed by Sweetzyme IT was first quantified by a dedicated polarimetric calibration (Section 1) and then optimised through a two-level full factorial design (Section 2). The three operational variables - glucose concentration, temperature and Mg^{2+} concentration - were modelled as a 2^3 design (Section 2.1), while the role of reaction time was resolved by treating it as a fourth factor in a 2^4 analysis (Section 2.2). Finally, the activating/inhibiting effect of alternative divalent cations was screened (Section 3).

1. Polarimetric calibration and determination of conversion

D-glucose and D-fructose are both optically active but rotate plane-polarised light in opposite directions and the optical rotation of a reaction mixture is a direct, non-destructive proxy for its composition. Eleven standard glucose-fructose mixtures (total 1 M, 0.01 M $MgSO_4 \cdot 7H_2O$, 100 mm cell, 589 nm, 25 °C) were measured to construct the calibration curve (Figure 2). Pure glucose is strongly dextrorotatory ($\alpha_G = +51.22°$) and pure fructose strongly levorotatory ($\alpha_F = -80.69°$); the response is linear over the whole composition range:

$$\alpha = 50.44 - 131.15 \times X_F \quad (R^2 = 0.9999) \quad \text{(Eq. 1)}$$

Since optical rotation is additive, the residual glucose concentration in any sample of total monosaccharide concentration (C_{total}) is obtained from

$$C_G = (\alpha - C_{total} \times \alpha_F) / (\alpha_G - \alpha_F);\ C_F = C_{total} - C_G \quad \text{(Eq. 2)}$$

and the molar conversion of glucose into fructose is

$$\text{Conversion (\%)} = C_F / C_{total} \times 100 \quad \text{(Eq. 3)}$$

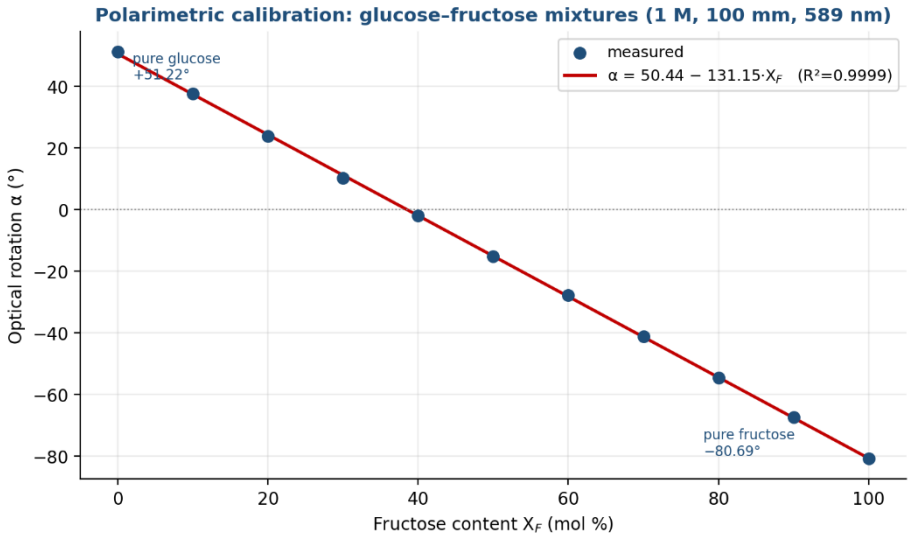

Figure 2. Polarimetric calibration of glucose-fructose mixtures. The linear fit (Eq. 1) is used with Eqs. 2–3 to convert every measured optical rotation into a conversion value.

2. Factorial-design optimization of the isomerization

The optimization of reaction conditions is a critical step in any bioprocess, aiming to maximise conversion while minimising time, energy and material costs. Traditional one-factor-at-a-time (OFAT) optimization is laborious and fails to capture the interactions between variables. Design of Experiments (DoE) offers a more powerful, systematic alternative: a two-level full factorial design allows the simultaneous investigation of several variables, quantifying both their main effects and their interaction effects, and fits the data to a mathematical model that defines the input–response relationship over the experimental region [16, 18].

2.1 Operational factors: a 2^3 full factorial design (response: conversion %)

Three operational variables were selected as the factors most likely to govern the isomerization: initial glucose concentration (z_1), temperature (z_2) and Mg^{2+} concentration (z_3). Each was studied at two coded levels, −1 (low) and +1 (high), about a central point (z_{10} = 0.4 M, z_{20} = 50 °C, z_{30} = 1.0 mM), giving a 2^3 = 8-run design (Table 1). The reaction was monitored polarimetrically and the optical rotation converted to conversion via Eq. 1–3; the full 16-point data set (eight conditions sampled at 4 h and 24 h) is given in Table 2**.**

Table 1. Experimental factors and their coded levels utilized in the factorial design matrix.

Factor	Symbol	Units	Low (−1)	Centre (0)	High (+1)
[glucose]	Z_1 (A)	M	0.2	0.4	0.6
Temperature	Z_2 (B)	°C	40	50	60
$[Mg^{2+}]$	Z_3 (C)	mM	0.5	1.0	1.5

Table 2. Experimental matrix, measured optical rotation and derived conversion.

Run	[G] (M)	T (°C)	$[Mg^{2+}]$ (mM)	Time (h)	α (°)	C (%)
1	0.6	60	1.5	4	3.120	34.88
2	0.2	60	1.5	4	1.833	31.88
3	0.6	40	1.5	4	4.176	33.55
4	0.2	40	1.5	4	4.194	22.93
5	0.6	60	0.5	4	2.657	35.47
6	0.2	60	0.5	4	2.167	30.61
7	0.6	40	0.5	4	4.380	33.29
8	0.2	40	0.5	4	4.333	22.40
9	0.6	60	1.5	24	-1.528	40.76
10	0.2	60	1.5	24	-1.889	45.99
11	0.6	40	1.5	24	2.148	36.11
12	0.2	40	1.5	24	0.944	35.25
13	0.6	60	0.5	24	-1.454	40.66
14	0.2	60	0.5	24	-1.556	44.72
15	0.6	40	0.5	24	2.231	36.01
16	0.2	40	0.5	24	2.028	31.14

Considering the 24 h end-point, temperature is by far the dominant operational factor: it accounts for 78 % of the variance in conversion, raising it on average by +8.4 percentage points between 40 °C and 60 °C. The glucose concentration × temperature interaction (AB) is the next largest contribution, while the main effects of Mg^{2+} (+1.4 pp) and glucose concentration (-0.9 pp) are minor. The first-order model in coded factors is:

$$C\ (\%) = 17.33 - 2.22\times [G] + 0.420\times T + 1.39\times [Mg^{2+}] \quad \text{(Eq. 4)}$$

The positive temperature coefficient confirms that, within the 40-60 °C interval, raising the temperature accelerates the approach to the fructose-rich equilibrium. The minor positive Mg2+ term indicates that even the low level (0.5 mM) nearly saturates the enzyme's metal sites, so additional cofactor yields little extra conversion. Interestingly, at the early (4 h) sampling point the ranking is reversed: glucose concentration dominates (+7.3 pp) ahead of temperature (+5.2 pp), reflecting a substrate-driven initial rate before the system approaches equilibrium. This time-dependent shift in factor importance motivates the time-resolved analysis. The highest experimental conversion, 45.98 %, was obtained at 0.2 M glucose, 60 °C, 1.5 mM Mg^{2+} after 24 h (Run 10, Table 2), close to the ~45 % thermodynamic ceiling of the reversible isomerization.

2.2 Resolving reaction time: a 2^4 analysis (response: conversion %)

To quantify the role of reaction time and its coupling with the operational factors, the two sampling times (4 h and 24 h) were incorporated as a fourth two-level factor (D), expanding the design to a 2^4 = 16-run experiment. A first-order model with two-way interactions was fitted; the third- and fourth-order interactions (5 degrees of freedom) provided the error estimate. The ANOVA (Table 3) shows a highly significant model, and the model summary (Table 4) confirms an excellent and well-balanced fit.

Table 3. ANOVA for the 2^4 design (response = conversion %). Terms with P ≤ 0.05 are significant; the dominant terms are highlighted.

Source	DF	Adj SS	Adj MS	F	P
Model	10	632.68	63.27	126.93	0.000
D (Time)	1	269.12	269.12	539.92	0.000
B (Temp.)	1	184.24	184.24	369.62	0.000
AD	1	67.78	67.78	135.98	0.000
AB	1	51.38	51.38	103.07	0.000
A ([G])	1	41.65	41.65	83.56	0.000
BD	1	10.49	10.49	21.04	0.006
AC	1	3.32	3.32	6.67	0.049
C ([Mg^{2+}])	1	3.09	3.09	6.21	0.055
CD	1	1.05	1.05	2.11	0.206
BC	1	0.55	0.55	1.10	0.342
Error	5	2.49	0.498		
Total	15	635.17			

Table 4. Model summary statistics for the 2^4 model.

S	R^2	R^2 (adj)	R^2 (pred)
0.706	99.61 %	98.82 %	95.98 %

Reaction time (D) emerges as the single most influential variable (F = 540, P < 0.001), narrowly ahead of temperature (B; F = 370, P < 0.001). The two factors that couple with time and substrate concentration (the glucose concentration × time (AD) and glucose concentration × temperature (AB) interactions) are also highly significant, as is the temperature × time interaction (BD; F = 21.0, P = 0.006). The reduced model in coded factors is:

$$C\ (\%) = 34.73 + 1.61 \times A + 3.39 \times B + 0.44 \times C + 4.10 \times D - 1.79 \times AB - 0.46 \times AC - 2.06 \times AD + 0.81 \times BD \quad \text{(Eq. 5)}$$

The Pareto chart (Figure 3) confirms this ranking: the bars for D, B, AD, AB, A, BD and (marginally) AC extend beyond the t = 2.571 significance reference line, whereas the Mg^{2+} main effect (C) sits just below it (P = 0.055). The temperature × time interaction is best appreciated in the response surface (Figure 4) and the interaction plot (Figure 5): the two temperature lines are not parallel, the benefit of operating at 60 °C is modest at 4 h (+5.2 pp over 40 °C), but widens markedly by 24 h (+8.4 pp). Mechanistically, the isomerization is kinetically controlled within this window: temperature sets the rate, while time determines how far the system has travelled toward the fructose-rich equilibrium, so the two effects reinforce each other. An equivalent analysis on the directly measured optical rotation yields the same dominant factors (time, temperature and their interaction; R^2 = 99.15 %), confirming that the conclusions are robust to the choice of response variable.

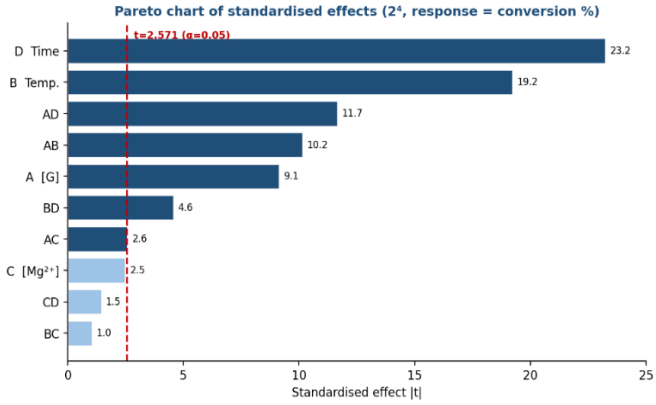

Figure 3. Pareto chart of the standardised effects (2^4, conversion %). Dark bars are significant (|t| ≥ 2.571); light bars are not.

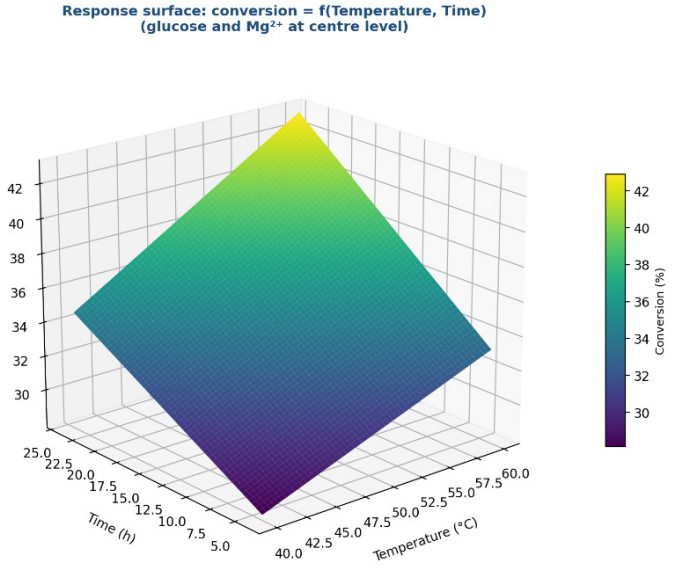

Figure 4. Response surface of conversion as a function of temperature and time (glucose concentration and Mg^{2+} concentration held at their centre levels). The twist of the surface is the visual signature of the temperature × time interaction.

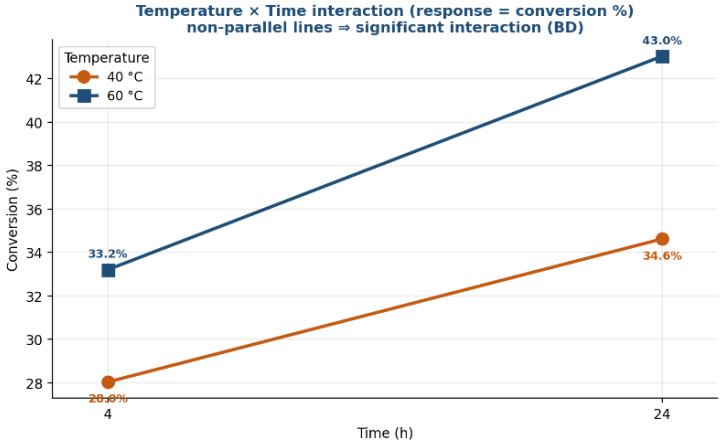

Figure 5. Temperature × time interaction plot (conversion %). Non-parallel lines confirm the significant BD interaction: temperature matters more at long reaction times.

3. Effect of divalent metal cations

Glucose isomerase is a metalloenzyme whose two metal sites (M1, structural; M2, catalytic) require divalent cations. To map the catalyst's activation/inhibition profile, the standard Mg^{2+} activator was compared with Ni^{2+}, Mn^{2+}, Cu^{2+} and Ca^{2+} (0.5 mM salt, 0.6 M glucose, 60 °C, 24 h; Table 5). $MgSO_4 \cdot 7H_2O$ gave the lowest optical rotation and therefore the highest conversion (38.2 %), clearly outperforming all alternatives. Ca^{2+} and Ni^{2+} were the poorest (34.9 % and 34.2 %); the weak performance of Ca^{2+} is consistent with its well-documented role as a competitive inhibitor that displaces Mg^{2+} from the active centre. Ca^{2+} has a significantly larger ionic radius (100 pm) compared to Mg^{2+} (72 pm). When calcium enters the active center, its bulky ionic volume coordinates poorly with the conserved carboxylic residues (such as Asp and Glu) in the M1/M2 pockets. [10, 21] This creates severe steric strain, distorting the precise geometry required for the hydride transfer step and effectively locking the enzyme in an inactive conformation. While Ni^{2+} has a matching ionic radius (69 pm), it forms overly rigid coordination complexes. This locks the carbohydrate intermediate too tightly in the active center, slowing down the product release rate and lowering overall turnover. [22]

These results confirm $MgSO_4 \cdot 7H_2O$ as the superior chemical activator for Sweetzyme IT under the studied conditions.

Table 5. Divalent-cation screening (0.6 M glucose, 60 °C, 24 h). Mg^{2+} (highlighted) is the most effective activator.

Salt	Cation	α (°)	Conversion (%)
$MgSO_4 \cdot 7H_2O$	Mg^{2+}	0.528	38.2
$CuSO_4$	Cu^{2+}	1.685	36.7
$MnCl_2 \cdot 4H_2O$	Mn^{2+}	2.380	35.8
$CaCl_2$	Ca^{2+}	3.102	34.9
$NiCl_2 \cdot 6H_2O$	Ni^{2+}	3.667	34.2

4. Complementary refractometric analysis

In parallel with the polarimetric measurements, every kinetic aliquot was analysed with a digital handheld refractometer, recording three quantities on three scales: °Brix, refractive index (RI) and the instrument's built-in "Fructose % w/w" scale. Measurements were performed for all three temperatures series (40, 50 and 60 °C) on the same 1:10-diluted samples used for polarimetry. The ranges obtained are summarised in Table 6.

Table 6. Range of refractometric readings across all kinetic samples.

Sample series	Total sugar (after 1:10 dilution)	°Brix	Refractive index	Fructose % (w/w)
0.2 M glucose	≈ 0.02 M	0.1 - 0.5	1.3324 - 1.3336	0.1 - 0.5
0.6 M glucose	≈ 0.06 M	0.5 - 0.6	1.3328 - 1.339	0.5 - 0.6
Water baseline	0	0	≈ 1.3330	0

The isomerization process cannot be monitored by refractometric analysis for these particular mixtures. Over each reaction, where polarimetry showed the conversion rising from ~0 % to a maximum of 45.98 % (0.2 M glucose, 60 °C, 24 h), the °Brix, refractive-index and “Fructose % w/w” readings remained essentially flat, changing negligibly between the 0-minute and 24-hour samples. The few elevated points (e.g. RI = 1.339 at 40 °C/0.25 h, °Brix = 0.9 at 60 °C/4 h) are isolated outliers rather than genuine trends. The 1:10 dilution lowered the samples to 0.02–0.06 M (~0.4–1 % w/w sugar), placing the readings at the resolution limit of a handheld refractometer, where they are dominated by noise. What refractometry did capture correctly is the total sugar loading: the 0.6 M series read consistently higher (Brix ≈ 0.5–0.6, RI up to ≈ 1.339) than the 0.2 M series (Brix ≈ 0.2–0.3), reflecting the 3-fold concentration difference.

All quantitative conversion data were obtained by polarimetry [23], which is effective precisely because the two isomers possess large, opposite specific rotations (α_G = +51.22°, α_F = −80.69°), the single property that distinguishes them. Reporting refractometry as a tested but insensitive method strengthens the justification for the polarimetric protocol used throughout this work.

CONCLUSIONS

This work shows that a two-level factorial design provides an efficient, interaction-aware alternative to one-factor-at-a-time optimization of the Sweetzyme IT–catalyzed isomerization of D-glucose to D-fructose. The validated regression models ($R^2 > 0.99$) identify temperature as the dominant operational factor within the 40–60 °C range studied: higher temperature accelerated the approach to equilibrium, the maximum conversion of 45.98 % being reached at 60 °C after 24 h, a value close to the thermodynamic ceiling of the reaction (~45 % fructose) rather than a limit of catalyst efficiency. Operation above ~60 °C is not advisable owing to the well-documented thermal inactivation of the enzyme. Incorporating reaction time as an explicit

factor uncovered a feature inaccessible to single-time-point studies: the rate-controlling variable shifts from substrate concentration at short reaction times to temperature near equilibrium, accompanied by a statistically significant temperature × time interaction. Within the tested range the Mg^{2+} concentration had only a minor effect, indicating that even 0.5 mM nearly saturates the enzyme's metal sites; nevertheless, the comparative cation screening confirmed $MgSO_4 \cdot 7H_2O$ as the most effective activator, clearly outperforming Mn^{2+}, Cu^{2+}, Ni^{2+} and the inhibitory Ca^{2+}. Finally, the dedicated polarimetric calibration offered a rapid, non-destructive route to conversion, whereas refractometry proved intrinsically insensitive to this mass-conserving isomerization.

EXPERIMENTAL SECTION

Materials

D-glucose and D-fructose (Fluka AG), magnesium sulfate heptahydrate (Reactivul Bucuresti), and the commercial immobilized glucose isomerase Sweetzyme IT (Novozymes) were used for the isomerization experiments. Stock solutions of various metal salts, specifically $NiCl_2 \cdot 6H_2O$, $MnCl_2 \cdot 4H_2O$, $CuSO_4$, and $CaCl_2$, were prepared in-house to test cofactor effects.

Equipment

Optical rotation was measured using an ADP220 automatic digital polarimeter (Bellingham & Stanley Ltd) equipped with a 589 nm LED light source. Refractive index and Brix values were determined using a digital handheld refractometer.

Methods

Polarimetric calibration: Standard mixtures with varying molar ratios of glucose to fructose were prepared by diluting 1 M stock solutions in 0.01 M $MgSO_4 \cdot 7H_2O$. The optical rotation of 11 distinct calibration samples was measured at 25 °C using a 100 mm cell length and a wavelength of 589 nm to establish the calibration curves. A 0.01 M $MgSO_4 \cdot 7H_2O$ solution was used as the blank.

Enzymatic isomerization and Factorial design: To optimize the enzymatic conversion of glucose to fructose, a factorial experiment was designed varying three key parameters: temperature (40 and 60 °C), initial glucose concentration (0.2 M and 0.6 M), and Mg^{2+} concentration (0.5 mM

and 1.5 mM). Reactions were performed in 50 mL volumes containing 0.125 g of immobilized Sweetzyme IT. The reaction mixtures were incubated under continuous magnetic stirring at 250 rpm, and the temperature was strictly maintained using a thermostatic water bath. Samples were collected at predetermined intervals: 0, 5, 15, and 30 minutes, followed by 1, 2, 4, and 24 hours. Each collected aliquot was diluted 1:10 with distilled water prior to polarimetric and refractometric measurements to determine the reaction conversion rate.

Effect of metal cations: To investigate the activating or inhibiting effects of different metal ions on the enzyme's specific activity, 50 µL of 0.5 M metal salt solutions (Ni^{2+}, Mn^{2+}, Cu^{2+}, Ca^{2+} and Mg^{2+} as standard) were added to 50 mL of 0.6 M glucose solution. The mixtures, each containing 0.125 g of immobilized enzyme, were incubated at 60 °C. After 24 h the samples were diluted 1:10 and their optical rotation measured against the corresponding 0.01 M salt-solution blanks.

Data analysis: Optical rotations were converted to conversion via the calibration (Eq. 1–3). Factorial effects, ANOVA, regression coefficients and model-quality statistics (R^2, R^2adj, R^2pred) were computed for the two-level designs using Minitab Statistical Software.

ACKNOWLEDGMENTS

This research was supported by the project “Renewable Enzyme Immo bilization - RENZI” funded by European Union – NextGenerationEU and the Romanian Government, under National Recovery and Resilience Plan for Romania, contract no 760241/28.12.2023, cod PNRR-C9-I8-CF 87/31.07.2023 through the Romanian Ministry of Research, Innovation and Digitalization, within Component 9, Investment I8.

REFERENCES

1. K. Parker; M. Salas; V.C. Nwosu, V; *Biotechnol. Mol. Biol. Rev.*, **2010**, *5*, 71-78.
2. J.S. White; *Am. J. Clin. Nutr.*, **2008**, *88*, 1716S-1721S.
3. S.S. Desai; D.B. Gachhi; B.S. Hungund; Glucose Isomerising Enzymes in *Microbial Enzyme Technology in Food Applications,* 1st ed, CRC Press, Boca Raton, Florida, **2016**, 69-84.
4. S. Souzanchi; L. Nazari; K.T.V. Rao; Z.S. Yuan; Z.C. Tan; C.B. Xu; *Catal. Today*, **2019**, *319*, 76-83.

5. A.L.M. Kognou; S. Shrestha; Z. Jiang; C. Xu; F. Sun; W. Qin; *J. Bioresour. Bioprod.,* **2022**, *7*,148-160.
6. H. Li; S. Yang; S. Saravanamurugan; A. Riisager; *ACS Catal.*, **2017**, *7*, 3010-3024.
7. J.M. Carraher; C.N. Fleitman; J.P. Tessonnier; *ACS Catal.*, **2015**, *5*, 3162-3173.
8. S.H. Bhosale; M.B. Rao; V.V. Deshpande; *Microbiol. Rev.*, **1996**, *60*, 280-300.
9. H. Taberman; C.S. Bury; M.J. van der Woerd; E.H. Snell; E.F. Garman; *J. Synchrotron Radiat.*, **2019**, *26*, 931-944.
10. A.Y. Kovalevsky; L. Hanson; S.Z. Fisher; M. Mustyakimov; S.A. Mason; V.T. Forsyth; M.P Blakeley; D.A Keen; T. Wagner, H.L. Carrell, A.K. Katz, J.P. Glusker; P. Langan; *Structure*, **2010**, *18*, 688-699.
11. B. Asbóth; G. Náray-Szabó; *Curr. Protein Pept. Sc.*, **2000**, *1*, 237-254.
12. S.S. Tükel; D. Alagöz; (2008). *Food Chem.*, **2008**, *111*, 658-662.
13. R. DiCosimo; J. McAuliffe; A.J., Poulose; G. Bohlmann; *Chem. Soc. Rev.*, **2013**, *42*, 6437-6474.
14. L. Zittan; P.B. Poulsen; S.H. Hemmingsen; *Starch - Stärke*, **1975**, *27*, 236–241.
15. EFSA Panel on Food Contact Materials, Enzymes and Processing Aids (CEP). *EFSA J.*, **2019**, *17*, e05969.
16. D.C. Montgomery; *Design and Analysis of Experiments*, 10th ed., Wiley, Hoboken, NJ, **2019**.
17. G.E.P. Box; J.S. Hunter; W.G. Hunter; *Statistics for Experimenters: Design, Innovation, and Discovery*, 2nd ed., Wiley-Interscience, Hoboken, NJ, **2005**.
18. R. Leardi; *Anal. Chim. Acta*, **2009**, *652*, 161-172.
19. S.A. Weissman; N.G. Anderson; *Org. Process Res. Dev.,* **2015**, *19*, 1605-1633.
20. C.F. Mandenius; A. Brundin; *Biotechnol. Prog.,* **2008**, *24*, 1191-1203.
21. K.H. Nam; *Appl. Sci.*, **2022**, *12*, 428.
22. R. Bogumil; R. Kappl; J. Hüttermann, *Eur. J. Biochem.*, **1997**, *36*, 12844-12853.
23. S.A Jaywant; H. Singh; K.M. Arif; *Sensors*, **2022**, *22*, 2290.

STUDIA UBB CHEMIA, LXXI, 2, 2026 (p. 21-40)
(RECOMMENDED CITATION)
DOI:10.24193/subbchem.2026.2.02

PHYSICO-CHEMICAL PROPERTIES, RHEOLOGICAL BEHAVIOR AND MINERAL CONTENTS OF HONEY VARIETIES FROM OLTENIA REGION

Mirabela PĂDURE[a], Andra TĂMAȘ[a*], Sabina NIȚU[a], Gerlinde RUSU[a], Adina NEGREA[a], Bogdan PASCU[b]

ABSTRACT. The honey samples analysed in this study were obtained from a private producer located in Olt County who requested a qualitative characterization of his products depending on honey sources. The first stage of the investigation involved key physicochemical parameters: moisture content, free and total acidity, initial and total invert sugars, sucrose levels, and the presence of hydroxymethylfurfural (HMF) and metallic elements. Differential Scanning Calorimetry (DSC) was additionally used to characterize the thermal properties of the samples. The final part of the study examines the rheological behavior of four honey varieties under different temperature conditions, providing insights into their flow characteristics and structural stability. All the obtained values fall within the ranges established by European regulations, except for Pb; the exceedances reflect the influence of anthropogenic factors in the mentioned region.

Keywords: *acidity, differential scanning calorimetry, heavy metals, honey, invert sugar, hydroxymethylfurfural, moisture, sucrose, viscosity*

INTRODUCTION

The use and production of honey have a long and complex historical trajectory. After more than six thousand years of written history, honey is still widely recognized for its nutritional and medicinal properties. Honey was the first sweetener used by humans and has a high nutritional value, providing

[a] *Faculty of Chemical Engineering, Biotechnologies and Environmental Protection, Politehnica University, Timișoara, Romania*
[b] *Renewable Energy Research Institute—ICER, Politehnica University, Timișoara, Romania*
* *Corresponding author: andra.tamas@upt.ro*

simple sugars, organic acids, amino acids, macro- and microelements, as well as biologically active compounds beneficial to human health [1,2]. It is consumed directly, used as an ingredient in various food products, or applied in preventive medicine [2].

The physical, chemical, and sensory characteristics of honey are strongly influenced by its botanical and geographical origin. Carbohydrates, particularly the reducing sugars-collectively known as “invert sugar”-represent the most important constituents of honey. Small amounts of sucrose are also present. The determination of invert sugar and sucrose content is a key criterion for the authenticity of bee products and relies on the reducing properties of sugars [3,4].

Despite its high nutritional and therapeutic value, honey is also among the food products most susceptible to adulteration. Evaluating the quality and authenticity of honey is a significant research area with implications for industry, consumer protection, and regulatory compliance. Honey authenticity is defined by the Codex Alimentarius Committee, the EU Honey Directive, and national legislation. The concept of “authenticity” concerns two main aspects: production authenticity (prevention of adulteration) and authenticity related to geographic or botanical origin (prevention of mislabelling) [5].

The measurement of 5-hydroxymethylfurfural (HMF) is widely used to assess honey quality, as its concentration increases during processing and improper storage. Heating honey to reduce viscosity or prevent crystallization can also increase HMF levels, depending on the type of honey [6]. HMF is produced through the acid-catalyzed dehydration of hexoses [7] and its accumulation is influenced by the chemical properties of the honey [8]. Codex Alimentarius [9,10] sets a maximum HMF content of 40 mg/kg after processing and/or blending. The European Union [11] has also set the maximum limit of 40 mg/kg, with exceptions of 80 mg/kg for honeys from tropical regions and 15 mg/kg for honeys with low enzymatic activity [12].

Some of metals (K, Ca, Na, Fe, Cu, Zn) are commonly present in honey attending the route: soil-plants-bees-honey and may increase its nutritional value. Metals as Pb, Cd, Ni, Cr, Al are contaminants from industrial and logistics activities, agrochemicals (cadmium-based fertilizers, organic mercury compounds, and arsenic-containing pesticides), polluted soil and water [13,14]. From these points of view, honey is an effective biomarker reflecting environmental quality over large areas, due the foraging activity of honeybees [15-17].

Floral honeys typically contain 0.1–0.2% minerals, while honeydew honeys can reach 1% or more [18]. Recent research has quantified metal concentrations in honey from several European countries [19].

This study also examines the rheological behaviour of honey as a function of temperature and presents results from DSC analyses. Viscosity, an important physical parameter of honey, is correlated with its other physicochemical properties [20,21]. Understanding honey rheology is necessary for its production, processing, and storage. Most honey varieties exhibit Newtonian behaviour [22,23]; however, some studies report non-Newtonian behaviour associated with the presence of high molecular weight compounds, such as proteins or polysaccharides [24].

The viscosity of honey depends primarily on water content, temperature and chemical composition. Honey typically contains between 13 g and 29 g of water per 100 g. Higher water content results in lower viscosity [25]. Temperature is another determining factor: as temperature increases, viscosity decreases due to reduced molecular friction and hydrodynamic forces [26,27]. The temperature-viscosity relationship can be described using the Arrhenius model [22,26].

The thermal behaviour of authentic honeys has been investigated using Differential Scanning Calorimetry (DSC), with glass transition temperatures (Tg) reported between -46°C and -32°C, depending on honey variety [28]. Understanding the properties of honey at low temperatures is essential for proper storage. The present study aims to characterize the rheological properties of Romanian honey varieties and to describe the influence of temperature on their viscosity.

RESULTS AND DISCUSSION

Moisture

Moisture content, along with storage temperature and any heat treatments, are parameters that influence the quality of honey.

Table 1. The moisture content of the honey samples

Honey	n_1	n_2	n_3	Refractive index (mean ± SD, n = 3)	Moisture %
Robinia pseudoacacia	1.4925	1.4924	1.4923	1.4924±0.0001	17.6
Linden	1.5008	1.5006	1.5004	1.5006±0.0002	14.4
Polyfloral	1.4990	1.4994	1.4992	1.4992±0.0002	15.0
Fir honeydew	1.4915	1.4911	1.4913	1.4913±0.0002	18.1
Rapeseed + Robinia pseudoacacia	1.4972	1.4972	1.4972	1.4972±0.0000	15.8

The moisture content of honey is directly associated with its botanical origin, harvesting and processing conditions and, implicitly, varies from year to year. Low moisture content prevents fermentation, the development of microorganisms and inhibits the formation of HMF, increasing shelf life and maintaining the quality of honey unaltered.

The results are expressed as mean ± standard deviation (n = 3). Each sample was analysed in triplicate and results are expressed as mean ± standard deviation (n = 3)

As shown in Table 1, the moisture content of the analysed honey samples ranges from 14.4% to 18.1%, with all values remaining below the 20% limit established by Codex Alimentarius [9], confirming their good quality and stability against fermentation.

Determination of pH, free and total acidities and lactone content

The lactone content of honey reflects the contribution of esterified organic acids to its overall acidity profile, serving as an indicator of both botanical origin and the degree of freshness or chemical stability of the product.

Table 2. pH values, acidity and lactone content

Honey	pH (mean ± SD, n = 3)	Free acids, meq/kg (mean ± SD, n = 3)	Lactone, meq/kg (mean ± SD, n = 3)	Total acidity, meq/kg (mean ± SD, n = 3)
Robinia pseudoacacia	4.72±0.01	20.20±0.01	14.41±0.02	34.61±0.02
Linden	4.28±0.02	22.62±0.01	14.60±0.02	37.22±0.02
Polyfloral	5.08±0.01	28.51±0.02	12.52±0.01	41.03±0.02
Fir honeydew	3.92±0.01	27.50±0.01	19.49±0.03	46.99±0.03
Rapeseed + Robinia pseudoacacia	4.92±0.02	23.41±0.01	20.51±0.01	43.92±0.01

Data from the literature shows that good quality honey has an acceptable pH range between 3.5 and 4.5 [29,30]. The lower value of pH in honey inhibits the growth of microorganisms. An increase in pH above the typical range could indicate adulteration or the beginning of a fermentation process. From Table 2, it can be observed that Robinia pseudoacacia honey, polyfloral honey and the rapeseed-Robinia pseudoacacia mixture have slightly higher, but insignificant, pH values. The pH values, ranging from 3.92 to 5.08, remain within acceptable quality limits, confirming the stability of the samples and the absence of fermentation-related alterations.

The data in Table 2 show that all honey samples fall within the expected acidity range for authentic honeys, according with UE regulation [31], with total acidity varying between 34.6 and 47.0 meq/kg. Also, the experimental values are in accordance with other studies [32]. Polyfloral, fir honeydew and the rapeseed-Robinia pseudoacacia mixture exhibit the highest acidity values, consistent with their botanical origin. The lactone content follows a similar pattern, indicating a balanced contribution of free and lactonic acids to the overall acidity profile.

Determination of proline

Based on the calibration curve it was established the equation that characterized the variation of the absorbance (A) with the concentration of proline solution (c, gx10^{-4}/g sample): $A=0.013 + 89.851 \cdot c$, $R^2= 0.9924$.

The results in Table 3 show that, among the analysed honey samples, the proline content varies significantly, reflecting their botanical origin. Fir honeydew has the highest percentage of proline (0.06%), consistent with its generally richer nitrogen profile.

Table 3. The proline (Pro) content in honey samples

Honey	Absorbance (520 nm) (mean ± SD, n = 3)	g Pro x 10^{-4} / g sample (mean ± SD, n = 3)	Pro, % (mean ± SD, n = 3)
Robinia pseudoacacia	0.1270±0.0002	4.388±0.002	0.01±0.0002
Linden	0.0765±0.0003	4.658±0.003	0.02±0.0003
Polyfloral	0.0765±0.0003	4.658±0.003	0.02±0.0003
Fir honeydew	0.1065±0.0004	9.524±0.004	0.06±0.0004
Rapeseed + Robinia pseudoacacia	0.0720±0.0003	7.763±0.003	0.03±0.0003

Linden honey and polyfloral honey have intermediate levels of proline (0.02%), while Robinia pseudoacacia honey has the lowest value (0.01%), in agreement with literature data indicating naturally lower amino acid concentrations in acacia varieties [33]. The rapeseed-Robinia pseudoacacia mixture shows a moderate proline content (0.03%), suggesting contributions from both floral sources. Overall, all samples fall within the expected ranges for authentic honey, which supports their natural origin.

Determination of HMF content

The HMF content of honey samples is presented in Table 4.

Table 4. HMF content in honey samples

Honey	Absorbance (550 nm) (mean ± SD, n = 3)	HMF, mg/kg (mean ± SD, n = 3)
Robinia pseudoacacia	0.070±0.0012	13.5±0.2
Linden	0.067±0.0013	12.8±0.2
Polyfloral	0.089±0.0017	17.2±0.3
Fir honeydew	0.157±0.003	30.2±0.6
Rapeseed + Robinia pseudoacacia	0.080±0.0015	15.4±0.3

The HMF values presented in Table 4 are low for all analysed honey samples, remaining well below the maximum limits established by Codex Alimentarius and EU legislation. Fir honeydew exhibits the highest HMF content (3.02 mg/100g), which is still characteristic of minimally processed and properly stored honey. The slightly elevated values from the polyfloral and rapeseed-Robinia pseudoacacia samples probably reflect natural variability associated with floral origin. Overall, the low HMF concentrations confirm that all honeys were fresh, unheated, and stored under appropriate conditions [34].

Invert sugar and sucrose determination

The content of invert sugar and sucrose is an essential indicator of the authenticity and maturity of honey, as high levels of invert sugar reflect the enzymatic activity of bees, while low values of sucrose confirm the absence of adulteration and minimal processing [34,35].

The values of reducing sugar direct before inverting (RSDBI), reducing sugar direct after inverting (RSDAI) and sucrose content are presented in Table 5.

Table 5. Invert sugar and sucrose content of honey samples

Honey	RSDBI		RSDAI		Sucrose %[a)]
	Invert sugar (mg)*, [a)]	Initial invert sugar, %[a)]	Invert sugar (mg)*, [a)]	Total invert sugar, %[a)]	
Robinia pseudoacacia	45.9±0.8	75.25±0.8	48.5±0.9	79.5±0.9	4.25±1.2
Linden	43.7±0.7	72.69±0.7	46.1±0.8	76.77±0.8	4.08±1.06
Polyfloral	45.5±0.8	75.70±0.8	43.4±0.7	80.51±0.7	4.81±1.13
Fir honeydew	41.4±0.8	68.95±0.8	45.5±0.8	75.73±0.8	6.78±1.13
Rapeseed + Robinia pseudoacacia	45.9±0.8	75.25±0.8	48.5±0.9	79.5±0.9	4.25±1.2

* in accordance with [4,36]

a) the results are expressed as mean ± standard deviation (n = 3). Each sample was analysed in triplicate and the results are expressed as mean ± standard deviation (n = 3).

The data in Table 5 show that all honey samples contain levels of invert sugar characteristic of authentic, unadulterated honey. Total invert sugar values exceed 75% in all samples, well above the minimum of 60% required for floral honey, confirming their natural origin. Fir honeydew has the lowest percentage of invert sugar, as expected for honeydew varieties, that typically contain higher amounts of oligosaccharides. Sucrose levels remain low in most samples, except the fir honeydew sample, whose higher sucrose content (6.78%) remains within acceptable limits and reflects botanical specificity rather than adulteration. Overall, the carbohydrate profiles support the authenticity and good quality of the analysed honeys.

Ash content

Ash content is a direct measure of the inorganic mineral content in honey. The ash content of honey is generally low and influenced by the chemical composition of the nectar, which varies depending on the different botanical sources involved in the formation of the honey. It can vary between 0.02% and 1.0%, and the maximum limit allowed by legislation for honey from floral sources is 0.6%. Normally, however, ash contents between 0.1% and 0.3% are found for these honeys. The very high mineral content (around 1.0%) is only found in honeydew, and the ash content is often used to identify this type of honey [37].

Table 6 presents the ash content of honey samples.

Table 6. Ash content of honey samples

Honey	**Ash content, % (mean ± SD, n = 3)**
Robinia pseudoacacia	0.20±0.004
Linden	0.14±0.003
Polyfloral	0.51±0.01
Fir honeydew	0.30±0.006
Rapeseed + Robinia pseudoacacia	0.24±0.005

In all samples, the ash content is low, indicating that the organic fraction (primarily sugars) is predominant, while the levels of microminerals, macrominerals and heavy metals are minimal.

Determination of metal content

The content of macrominerals and microminerals in the five honey samples is presented in Tables 7a and 7b.

Table 7a. Macrominerals content in honey samples

Honey	Ca^{2+}	Mg^{2+}	Na^{+}	K^{+}	Al^{3+}	Mn^{2+}
	mg/kg					
Robinia pseudoacacia	0.46	1.86	0.17	0.25	0.02	< 0.01
Linden	1.40	2.49	0.45	2.28	0.01	< 0.01
Polyfloral	0.36	1.54	0.25	3.85	1.17	10.00
Fir honeydew	1.18	3.31	0.27	1.71	0.21	0.84
Rapeseed + Robinia pseudoacacia	0.25	0.46	0.24	13.72	15.25	155.59

*the detection limit of the method (LOD) was 0.01

Variations in the content of microminerals and macrominerals (not considered contaminants) do not negatively influence the quality of honey, giving it a therapeutic effect specific to its content and implicitly, to the honey variety.

Table 7b. Microminerals content in honey samples

Honey	Ag^{+}	Co^{2+}	Cr^{n+}	Li^{+}	Ni^{2+}	Sr^{2+}	Ti^{2+}	Se^{2+}	V^{3+}
	mg/kg								
Robinia pseudoacacia	<0.01	0.11	0.19	0.10	0.36	29.14	0.99	1.69	<0.01
Linden	0.08	0.04	0.17	1.38	0.32	42.75	0.25	0.68	0.14
Polyfloral	0.04	<0.01	0.34	0.89	1.12	14.96	0.24	<0.01	0.05
Fir honeydew	0.11	0.01	0.14	5.20	0.32	55.22	0.74	<0.01	<0.01
Rapeseed + Robinia pseudoacacia	0.04	<0.01	0.10	0.88	0.23	16.66	<0.01	<0.01	<0.01

*the detection limit of the method (LOD) was 0.01

Table 8 contains the heavy metal content in honey samples.

Table 8. Heavy metal content in honey samples

Honey	Cd^{2+}	Cu^{2+}	Fe^{n+}	Pb^{2+}	Zn^{2+}
	mg/kg				
Robinia pseudoacacia	0.046	1.03	0.07	0.183	< 0.01
Linden	0.16	2.68	0.09	0.17	0.01
Polyfloral	0.28	5.30	0.09	0.198	0.01
Fir honeydew	0.027	3.24	0.11	0.213	0.00
Rapeseed + Robinia pseudoacacia	0.084	0.64	0.04	0.29	0.01
MPC* according to [31]	**0.2**	**-**	**1.00**	**0.20**	**1.0-3.0**

*MPC-Maximum Permitted Concentration; the detection limit of the method (LOD) was 0.01

The values for Cu^{2+}, Fe^{n+}, and Zn^{2+} are within the permitted limits or close to the detection limit [9,11].

The analysis of heavy metal content shows variations depending on the botanical origin of the honey. Pb^{2+} concentrations slightly exceed the maximum allowed values in some samples, especially in the mixture (rapeseed + Robinia pseudoacacia) and in fir honeydew, suggesting the influence of anthropogenic factors (industrial pollution, road traffic, soil contamination) [31,38,39]. Due to its high mobility in the environment and plant affinity, lead is sequestered from the soil by melliferous flora and translocated into nectar [40,41]. Through the maturation process, the honeybee acts as a secondary concentrator, ensuring that the final matrix provides an accurate spatial reflection of geogenic and anthropogenic contamination in the foraging area. These elevated levels have also been reported in other scientific studies [42].

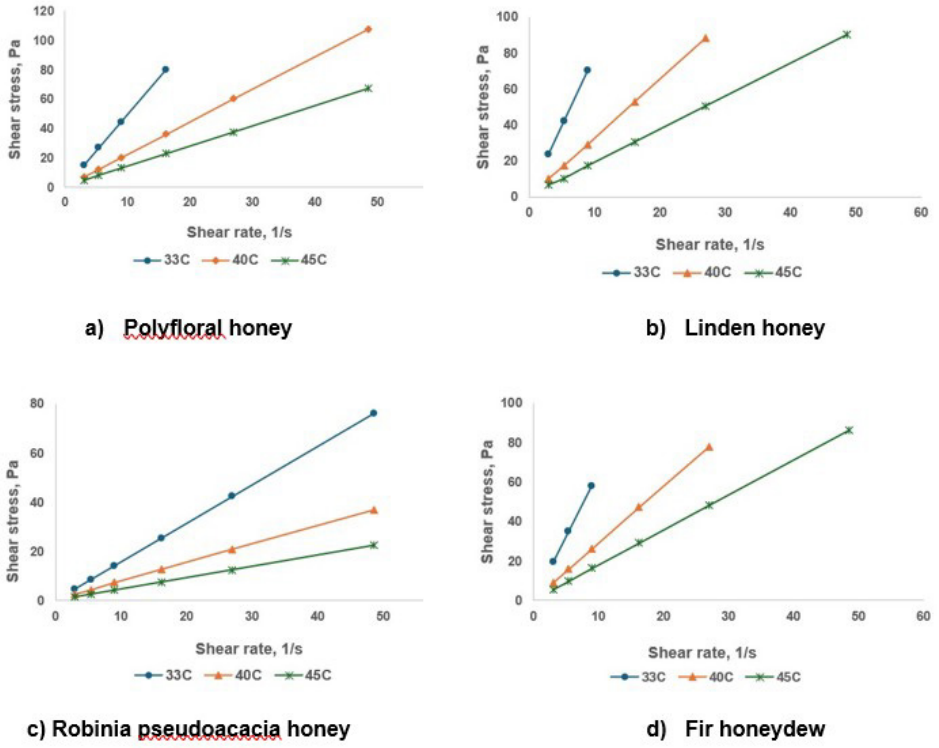

Figure 1. Shear stress vs. shear rate

The results confirm that honey can be used as a bioindicator of environmental pollution, and periodic monitoring of heavy metals is necessary to ensure food safety [43].

Rheological behavior

The dependence between shear stress (t=) and shear rate ($\dot{\gamma}$), at three temperature values, is presented in Figures 1 (a-d). It is observed that, regardless of temperature values, these dependences are linear, which suggests a Newtonian behavior. Also, the values of dynamic viscosity decrease with increasing temperature.

The experimental data were fitted using the software package Table Curve 2D. Thus, the model used to describe the rheological properties of honey samples is defined by Newton's equation (1):

$$\tau = \eta \cdot \dot{\gamma} \quad (1)$$

where η is the dynamic viscosity of the fluid [22, 44-46].

The values of dynamic viscosity are presented in Table 9.

Table 9. The values of dynamic viscosity of the honey samples

Honey	Dynamic viscosity, Pa.s		
	33°C	40°C	45°C
Polyfloral	4.94	2.23	1.38
Linden	7.79	3.26	1.84
Robinia pseudoacacia	1.57	0.75	0.46
Fir honeydew	6.46	2.89	1.78

The Arrhenius model (eq. (2)) has been that most often used to adequately describe the dependence of viscosity on temperature [22,44].

$$\eta = A \cdot e^{\frac{E_a}{R \cdot T}} \quad (2)$$

where E_a is the activation energy reflecting the sensitivity of viscosity to temperature variation and the pre-exponential factor (A) represents viscosity at a temperature close to infinity.

The particular form of equation (2) for the honey samples is presented in Table 10, together with the percentage of decrease in dynamic viscosity with increasing temperature from 33°C to 45°C.

Table 10. Particular forms of Arrhenius type equation

Honey	Eq. (2)	E_a, kJ/mol	Viscosity decrease, %
Polyfloral	$\eta = 7.2 \cdot 10^{-15} \cdot exp(^{10454}/_{T})$	86.9	72.1
Linden	$\eta = 2.3 \cdot 10^{-16} \cdot exp(^{11647}/_{T})$	96.8	76.4
Robinia Pseudoacacia	$\eta = 1.4 \cdot 10^{-14} \cdot exp(^{9888.3}/_{T})$	82.2	70.7
Fir honeydew	$\eta = 6.5 \cdot 10^{-15} \cdot exp(^{10567}/_{T})$	87.8	72.5

The values of the activation energy of the viscous flow are relatively close. However, from these values and the percentage of viscosity decrease, it is confirmed that the linden honey with the highest activation energy value exhibits the greatest change (decrease) in viscosity with temperature.

It is also confirmed that for linden, polyflora and Robinia pseudoacacia honeys, increasing the moisture content leads to a decrease in viscosity, regardless of the temperature value, according to [25].

DSC analysis

For honey, DSC analysis can be used to study the melting point or crystallization phenomena and to determine the glass transition temperature (T_g) [46-49]. Because honey is normally used below its melting point, it is a supercooled liquid and, although it appears liquid, it is in a metastable state in which sugar crystals can spontaneously form. Generally, honey has glass transition temperature values between -30°C and -50°C. Below these values, it is in a vitreous state, becoming an amorphous, non-crystalline solid [50].

DSC thermograms are presented in Figures 2 (a-e) and the values of glass transition temperature (T_g) in Table 11.

It is observed that all the glass transition temperatures have negative values from -32°C to -46°C, what is typical for natural honeys with normal moisture content (15÷20%). The values show that Robinia pseudoacacia honey has the lowest T_g value and the highest water content (Table 1), which denotes a high fructose content, and therefore, the honey has a low tendency to crystallize.

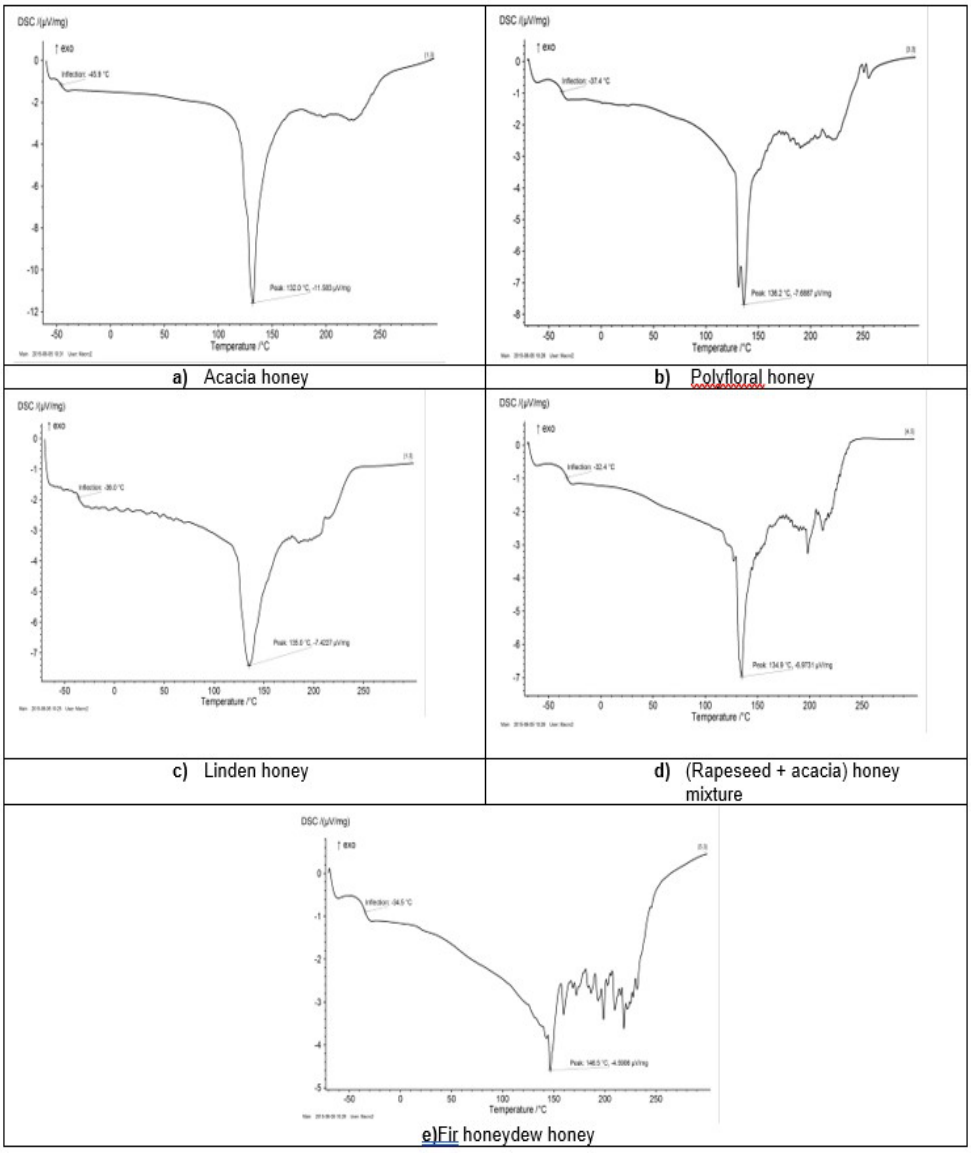

Figure 2. DSC thermograms of honey samples

Table 11. The values of glass transition temperatures

Honey	**T_g, °C**
Robinia pseudoacacia	- 45.9
Linden	- 36.0
Polyfloral	- 37.4
Fir honeydew	- 34.5
Rapeseed + Robinia pseudoacacia	- 32.4

In contrast, the honey mixture (rapeseed + Robinia pseudoacacia) has the highest T_g value (-32.4°C), suggesting a more rigid amorphous structure. Rapeseed honey is typically glucose-rich and prone to rapid crystallization, which is consistent with a higher T_g value and reduced molecular mobility of the supercooled sugar phase. The increased T_g value observed in the blended sample indicates that the presence of rapeseed honey significantly influences the thermal behavior of the blend, despite the contribution of Robinia pseudoacacia honey. Linden, polyfloral and fir honeys exhibited intermediate T_g values (-36°C to -34°C), reflecting more balanced fructose-glucose ratios and heterogeneous botanical composition.

In addition, in all cases, an endothermic peak appears in the range (130÷145)°C, corresponding to thermal decomposition (in fact, rather the decomposition of sugars which are the major constituents, honey being a supersaturated sugar solution).

CONCLUSIONS

Five honey samples from the Oltenia region were studied in terms of physico-chemical parameters.

The obtained results indicated the following:

· The Newtonian behavior observed across all samples indicates a predictable and consistent flow, enhancing consumer experience through uniform texture, ease of pouring, and stable sensory attributes. This rheological linearity also serves as a physical marker of product homogeneity and purity, confirming the absence of advanced crystallization or structural additives

· The carbohydrate composition, characterized by high invert sugar levels and low sucrose contents, demonstrates the authenticity, proper maturation, and overall quality of the analysed honey samples.

· In all samples, the ash content is low, demonstrating the preponderance of the organic phase.

· The content of micro- and macrominerals does not negatively influence the quality of honey. However, a slightly higher lead content indicates a high degree of pollution, due to the natural background of the soil, industrial areas or other factors.

· The DSC data classify the studied honeys in the value ranges mentioned in the literature.

EXPERIMENTAL SECTION

Materials

The five honey samples produced from different floral origins were purchased from beekeepers in the Oltenia region, Romania, in 2023. The honeys were stored at 16÷18°C throughout the entire period of the experimental determinations.

Determination of moisture content

The moisture content of honey samples was obtained by measuring the refractive index (Method 969.383) according to [51] with a Carl Zeiss 16531 refractometer at 20°C, using refractive index of distilled water as a reference. The refractive index was converted to moisture content (%) based on a Chataway Table [3,52].

Determination of pH, free and total acidities and lactone content

pH measurements were performed potentiometrically at 20°C, using a MultiMeter MM 41 in a solution prepared by dissolving 10 g of honey in 75 mL of CO_2-free distilled water. All measurements were performed in triplicate after a preliminary calibration at pH 3.0, 7.0 and 9.0 [3]. The content of free acids and lactone was determined by a titrimetric method. The previously prepared solution was titrated with 0.05 M NaOH solution to pH 8.3 (free acidity). Immediately, 10 mL of 0.05 M NaOH solution was added and the mixture was titrated again with 0.05 M HCl solution to pH 8.3 (lactone acidity) [53]. Total acidity was obtained by adding the two values.

Determination of proline

Proline content was determined using ninhydrin spectrophotometric method (Method 979.20) according to [51]. This method is based on the reaction of proline (a proteinogenic amino acid) with ninhydrin, with the formation of a colored complex with a characteristic maximum at 520 nm [3].

a) Calibration curve for proline: 0.0, 0.1, 0.2, … 0.9 mL of proline standard solution (0.05 mg/mL) are introduced into 10 test tubes to which distilled water is added up to 5.5 mL. To each test tube is added 1 mL of 3% ninhydrin solution in ethylene glycol and 0.25 mL of formic acid. The samples were kept in a boiling water bath for 15 minutes, then cooled for 5 minutes in a water bath at 22°C. 5 mL of solvent (2-propanol and water, ratio 1:1) was added to each sample under stirring. After 35 minutes, the absorbance is determined at 520 nm with a blank containing 0.5 mL of distilled water.

b) Proline determination: 2.5 g honey are transferred to a 50 mL volumetric flask with distilled water to obtain working solutions. 0.5 mL of sample, 5 mL of distilled water, 0.25 mL of formic acid and 1 mL of 3% ninhydrine solution in ethylene glycol are placed in a test tube (triplicate for each honey sample). Each sample is treated according to the instructions above, and the results are calculated as an average value.

Determination of hydroxymethylfurfural - HMF (Winkler method)

HMF forms with barbituric acid, in the presence of p-toluidine, a red compound that exhibits a characteristic absorption maximum at 550 nm.

5 g of honey were weighted and transferred to a 25 mL volumetric flask. The appropriate volume of distilled water was added and homogenized. 2 mL of the honey solution prepared above were transferred to 2 test tubes. 5 mL of p-toluidine solution (10% in 2-propanol) was added to each test tube. 1 mL of distilled water was added to the control tube, and 1 mL of 0.5% aqueous solution of barbituric acid was added to the other tube and homogenized. After 4 minutes, the absorbance was determinated at 550 nm [3, 54].

Determination of invert sugar and sucrose (Elser method)

The method is based on the fact that the reducing sugars (glucose and others) in honey can reduce Cu (II) at Cu (I) in the presence of heat. The amount of red precipitate of copper (I) oxide (Cu_2O) is proportional to the invert sugar content in the sample [36].

a) *Reducing sugar direct before inverting (RSDBI)*: 20 mL Fehling I solution, 20 mL Fehling II solution and 20 mL water are added in a 250 mL Erlenmeyer. The mixture is brought to boiling. The honey stock solution was prepared by diluting about 3 g honey with distilled water in a 200 mL volumetric flask. 20 mL of honey work solution (prepared by diluting 20 mL of stock solution in a 100 mL volumetric flask with distilled water) is added to the previously boiling mixture and boiled for another 5 minutes. To dissolve the red precipitate (Cu_2O), 35 mL of saturated acidified NaCl solution and 2-3 g of $NaHCO_3$ were used to alkalinize the mixture (finally, the mixture becomes clear blue with $NaHCO_3$ crystals). The solution is finally titrated with 0.05 N iodine solution. Since the chemical reaction occurs slowly and the equivalence point is difficult to observe, a small excess of iodine is used and back-titrated with 0.05 N $Na_2S_2O_3$ solution in the presence of a 1% starch solution until the colour turns light blue (the change is green – dark blue – light blue). The effective volume of iodine solution is the difference between the initial and final volumes used in the titration.

$$RSDBI(\%) = \frac{m \cdot 10 \cdot 5}{m_1 \cdot 1000} \cdot 100 \quad (3)$$

where: m – the amount of sugar corresponding to the volume of iodine, mg [4,55]; 10 – volumetric ratio between stock solution and working solution (200/20); 5 – volumetric ratio between working solution and sample solution (100/20); m_1 – the amount of honey sample, g.

b) *Sucrose determination*: in a 100 mL volumetric flask, 20 mL of working solution, 30 mL of distilled water and 1.0 mL of HCl solution were added and maintained for 30 minutes in a boiling water bath for sucrose hydrolysis. To the cooled mixture was added 1.0 mL of 1 N NaOH solution and the volume was adjusted with distilled water. The reducing sugar direct after inverting (RSDAI) was determined as before, using the final mixture as a working solution.

$$Sucrose(\%) = [RSDAI(\%) - RSDBI(\%)] \cdot 0.95 \quad (4)$$

0.95 represents the ratio between the molar mass of sucrose and the molar mass of glucose and fructose.

Determination of ash content

The ash content was determined according to the method of incineration of honey samples (Method 920.181) according to [51].

To remove moisture and prevent foaming, about 5 g of honey was preheated with an infrared lamp, after which the sample was incinerated in a muffle furnace at 600°C, until constant weight. The sample was weighed again after cooling to room temperature [29].

Determination of metal content

For sample preparation, 5 g of honey was weighed and incinerated at a temperature of 450°C for 13 hours. The resulting ash was dissolved in 10 mL of 0.5 M HNO_3, quantitatively filtered through filter paper and brought to a final volume of 100 mL. The content of macrominerals, microminerals, and heavy metals in honey was determined by inductively coupled plasma mass spectrometry (ICP-MS), using a BRUKER Aurora M90 inductively coupled plasma spectrometer equipped with a mass detector.

Rheological behavior

Viscosity measurements were performed on honey samples at different temperature values (33°C, 40°C and 45°C), with a Rheotest-2 rotational viscometer equipped with a thermostatic control bath and a coaxial cylinder system (S/S1). Experimental determinations were performed at the shear rate ramp-up (from 3 s^{-1} to 81 s^{-1}) and ramp-down (from 81 s^{-1} to 3 s^{-1}). Each measurement was taken in duplicate.

DSC analysis

DSC analysis were performed using a DSC 204F1 Phoenix differential scanning calorimeter produced by Netzsch. Honey samples were placed in aluminum crucibles and heated from -50°C to 300°C with a heating rate of 10 K/min. Thermograms were interpreted using Netzsch Proteus Thermal Analysis software version 6.1.0.

REFERENCES

1. L. Juszczak; T. Fortuna; *J. Food Eng.,* **2006**, *75(1),* 43-49
2. I. Dobre; L.A. Georgescu; P. Alexe; O. Escuredo; M.C. Seijo; *Food Res. Int.*, **2012**, *49(1),* 126-132

3. S. Bogdanov; *Harmonised Methods of the International Honey Commission*, **2009**, pp. 1-63
4. N. Popescu; S. Meica; *Produsele apicole și analiza lor chimică,* Ed. Diacon Coresi, București, **1997**, pp.149-155
5. S. Bogdanov; C. Lullmann; P. Martin; W. von der Ohe; H. Russmann; G. Vorwohl; L. Persano Oddo *et.al.*, *Mitt. Lebensm. Hyg.*, **1999**, *90*, 108-125
6. M. Zappala; B. Fallico; E. Arena; A. Verzera; *Food Control,* **2005**, *16(3),* 273-277
7. H.-D. Belitz; W. Grosch; P. Schieberle; *Food Chemistry,* Springer Berlin, Heidelberg, **2009**, pp.862-891
8. P.K. Bath; N. Singh; *Food Chem.*, **1999**, *67(4)*, 389-397
9. Codex, A.C. Codex Alimentarius Commission: Revised Codex Standard for Honey Codex Stan 12-1981, Rev. 1 (1987), Rev. 2 (2001). *Codex Stand.* **2001**, *12*, 1–7
10. Alinorm 01/25 – *Report of the 17th Session of the Codex Committee on Sugars*, London, 9-11 February **2000**
11. Directiva 2001/110/CE/20-dec-2001 privind mierea, https://eur-lex.europa.eu/eli/dir/2001/110/oj
12. A. Ojha; R. Parveen; B. Parveen; S. Ahmad; *Food Chem.*, **2025**, *493(1)*, 145677
13. A. Rashid; B.J. Schutte; A. Ulery; M.K. Deyholos; S. Sanogo; E.A. Lehnhoff; L. Beck; *Agronomy*, **2023**, *13(6)*, 1521
14. A. Alengebawy; S.T. Abdelkhalek; S.R. Qureshi; M-Q.Wang; *Toxics*, **2021**, *9(3)*, 42
15. P. M. da Silva; C. Gauche; L. V. Gonzaga; A. C. Oliveira Costa; R. Fett; *Food Chem.*, **2016**, *196*, 309-323
16. S. Bogdanov; M. Haldimann; W. Luginbuhl; P. Gallmann; *J. Apic. Res. And Bee World*, **2007**, *46(4),* 269-275
17. M.N. Rashed; M.T.A. El-Haty; S.M. Mohamed; *Toxicol. Environ. Chem.*, **2009**, *91(3), 389-403*
18. A. Pavlin; D. Kocar; J. Imperl; M. Kolar; G. Marolt; P. Petrova; *Foods*, **2023**, *12(15)*, 2826
19. N. Bilandzic; M. Dokic; M. Sedak; B.S. Kolanovic; I.Varenina; A. Koncurat; N. Rudan; *Food Chem.*, **2011**, *128(4)*, 1160-1164
20. J. Gasparoux; D. Laux; J.Y. Ferrandis; J. Attal; P. Tordjeman; *J. Non-Newtonian Fluid Mech.,* **2008**, *153(1)*, 46-52
21. M. Oroian; S. Ropciuc; S. Paduret; *J. Food Sci. Technol.*, **2018**, *55(12),* 4711-4718
22. C. Faustino; L. Pinheiro; *Foods,* **2021**, *10*, 1709
23. K. Polatidou; C. Nouska; C. Tananaki; C.G. Billiaderis; A. Lazaridou; *Foods*, **2025**, *14(10),* 1835

24. M. Witczak; L. Juszczak; D. Galkovska; *J. Food Eng.,* **2011**, *104(4)*, 532-537
25. S. Yanniotis; S. Skaltsi; S. Karaburnioti; *J. Food Eng.*, **2006**, *72*, 372-377
26. D. Gomez-Diaz; J.M. Navaza; L.C. Quintas-Riveiro; *Int. J. Food Prop.*, **2009**, *12(2),* 396-404
27. M.P. Recondo; B.E. Elizalde; *J. Food Eng.*, **2006**, *77(1),* 126-134
28. J. Tomaszewska-Gras; S. Bakier; K. Goderska; K. Mansfeld; *J. Apic. Sci.*, **2015**, *59(1)*, 109-118
29. E. Majewska; B. Druzynska; R. Wolosiak; *Food Sci. Biotechnol.*, **2019**, *28(5)*, 1307-1314
30. A. Albu; G. Frunza; R. Zaharia; I.M. Pop; *Scientific Papers – Animal Science Series,* UASMV Iasi, **2021**, *75*, 237-243
31. https://eur-lex.europa.eu/eli/reg/2023/915/oj?locale=ro, Regulamentul (UE) 2023/915 al Comisiei din 25 aprilie 2023 privind nivelurile maxime pentru anumiți contaminanți din produsele alimentare și de abrogare a Regulamentului (CE) nr.1881/2006
32. A.C. Șarba; Al.L. Mărghitaș; A. Timar; *Agriculture-Science and Practice*, **2015**, *1-2(93-94)*, 73-77
33. N. Czipa; M. Borbely; Z. Gyori; *Acta Alimentaria*, **2011**, *41(1)*, 26-32
34. V.H. Sedlackova; K.F. Sramkova; Z. Harutyunyan; K. Pylypco; L. Adamchuk; *Agrobiodivers. Improv. Nutr. Health Life Qual.,* **2022**, *6,* 280-291
35. I. Smetanska; S.S. Alharthi; K.A. Selim; *J. King Saud Univ. Sci.*, **2021**, *33(5)*, 101447
36. R. Iancu; L. Oprean; M.A. Tița; E. Lengyel; V. Codoi; A.G. Boicean; A.O. Schneider; *Bull. UASVM Animal Sci. and Biotech.*, **2012**, *69(1-2)*, 255-260
37. M.L. Felsner; C.B. Cano; J.R. Matos; L.B. de Almeida-Muradian; R.E. Bruns; *J. Braz. Chem. Soc.*, **2004**, *15(6),* 797-802
38. S. Bogdanov; *Apidologie*, **2005**, *37*, 1-18
39. Codex Alimentarius – General Standard for Contaminants and Toxins in Food and Feed (CXS 193-1995), *https://www.fao.org/fao-who-codexalimentarius/codex-texts/list-standards/en/#CXS%20193-1995*
40. S. Bartha; I. Taut; G. Goji; I.A. Vlad; F. Dinulică; *Int. J. Environ. Res. Public Health*, **2020**, *17(5)*, 1507
41. C. Naccari; V. Ferrantelli; G. Cammilleri; C. Barbaccia; P. Riolo; M.C. Ferrante; A. Procopio; E. Palma; *Foods*, **2025**, *14*, 1986
42. P. Pohl; *Trends Anal. Chem.,* **2009**, *28(1),* 117-128
43. C. Porrini; A.G. Sabatini; S. Girotti; S. Ghini; P.Medrzycki; F. Grillenzoni; L. Bortolotti; E. Gattavecchia; G. Celli; *Apiacta*, **2003**, *38*, 63-70

44. A. Miclăuș; V. Pode; *Cazuri particulare de curgere a fluidelor ideale și reale. Elemente de reologie,* Ed. Casa Cărții de Știință, Cluj-Napoca, **2018**, pp.49-50
45. I. Stanciu; *Orient. J. Chem.,* **2021**, *37(2),* 440-443
46. K.D. Tafa; V.P. Sundramurthy; N. Subramanian; *Int. J. Food Prop.*, **2021**, *24(1),* 1117-1131
47. F. Dranca; S. Ropciuc; D. Pauliuc; M. Oroian; *LWT*, **2022**, *168,* 113910
48. C. Cordella; J.-F. Antinelli; C. Aurieres; J.-P. Faucon; D. Cabrol-Bass; N. Sbirrazzuoli; *J. Agric. Food. Chem.*, **2002**, *50*, 203-208
49. C. Cordella; J.-P. Faucon; D. Cabrol-Bass; N. Sbirrazzuoli; *J. Therm. Anal. Calorim.*, **2003**, *71*, 279-290
50. Z. Kantor; G. Pitsi; J. Thoen; *J. Agric. Food. Chem.*, **1999**, *47(6)*, 2327-2330
51. *Official Methods of Analysis of AOAC International*, edited by P. Cunniff, 16th ed., AOAC International, Arlington, **1995**, Methods 969.383, 920.181, 979.20
52. A. Belay; W.K.Solomon; G. Bultossa; N. Adgaba; S. Melaku; *Food Chem.*, **2013**, *141*, 3386-3392
53. A. Boussaid; M. Chouaibi; L. Rezig; R. Hellal; F. Donsi; G. Ferrari; S.Hamdi; *Arabian J. Chem.,* **2018**, *11(2)*, 265-274
54. I.C.Maeda; A.N.C.E Sampaio; E.F. Flores Caron; J.F.Nardy; S.C. Oliveira; J.G. Pereira; O.A. Martins; *Braz. J. Food Technol.,* **2023**, *26(3)*, e2022133
55. A.X. Lupea; D. Ardelean; M. Pădure; *Chimia și controlul alimentelor de origine animală,* Ed. Politehnica, Timișoara, **2001**, pp.214.

STUDIA UBB CHEMIA, LXXI, 2, 2026 (p. 41-64)
(RECOMMENDED CITATION)
DOI:10.24193/subbchem.2026.2.03

COMPARISON OF QUALITY PARAMETERS OF EDIBLE FILMS WITH RHUBARB ADDITION PRODUCED BY TWO DIFFERENT METHODS

Esra PEKDOĞAN ÇAKAL[a,b], Ebru AKKEMİK[b,*], Bülent HALLAÇ[b]

ABSTRACT. In edible films with added plant extracts, the effects of the polymer matrix used and the production method on film performance have not yet been sufficiently clarified. Therefore, in this study, the quality parameters of starch-gelatin and chitosan-based edible films with added rhubarb (*Rheum ribes* L.), produced by two different methods, were comparatively examined. The films were characterized in terms of thickness, water solubility, mechanical properties, water vapor permeability, optical properties, color parameters, antioxidant capacity, biodegradability, and structural properties. The results showed that the film properties changed significantly depending on both the polymer matrix used and the rhubarb extract concentration. Starch-gelatin-based films exhibited higher water solubility and flexibility, while chitosan-based films showed higher mechanical strength and better water vapor barrier properties. Rhubarb addition significantly increased the antioxidant potential of the film-forming mixtures in both methods. Color analyses revealed that the films darkened with increasing rhubarb concentration. SEM and FT-IR analyses showed that rhubarb addition caused physical changes in the film structure but did not alter the chemical structure. Chitosan-based films with rhubarb addition may be considered as a potential alternative for active and sustainable food packaging applications.

Keywords: *Edible film, rhubarb (Rheum ribes L.), chitosan, starch-gelatin, antioxidant activity, biodegradability*

[a] *Atatürk University, Faculty of Agriculture, Department of Food Engineering, Erzurum, Türkiye.*
[b] *Siirt University, Faculty of Engineering, Department of Food Engineering, Siirt, Türkiye.*
[*] *Corresponding author: eakkemik@siirt.edu.tr*

INTRODUCTION

Increased packaging use stands out as one of the most significant problems causing environmental pollution today. One of the main reasons for this is that consumers cannot properly classify and dispose of packaging waste for recycling. It was reported that approximately 40% of the packaging put on the market in Türkiye cannot be recycled [1]. The use of traditional food packaging materials such as plastic, paper, glass, metal and composite in edible packaging applications is limited. Petroleum-based plastics such as polyethylene and polypropylene pose serious ecological threats due to their non-environmentally friendly structure [2, 3]. Most of them are single-use plastics and are released directly into nature, especially oceans or soil, after use. In addition, burning these materials causes greenhouse gas emissions, triggering global warming [3-5].

To mitigate these environmental threats, the use of recyclable or biodegradable packaging materials is encouraged, and public awareness campaigns are being conducted. In this context, edible films and coatings, offering environmentally sustainable and functional properties, have attracted significant attention, particularly in recent years [3, 6-9]. Edible packaging extends the shelf life of food products, prevents microbial spoilage, and reduces waste. Thanks to developing technologies, these types of biopolymers can be transformed into edible films and coatings, and they can be applied directly to food as packaging or bags in film form, or as coatings. One of the most important advantages of edible packaging is that it is consumed as an integral part of the product, eliminating the need to open the packaging [3, 10]. Furthermore, the biodegradability of edible packaging provides environmental benefits in terms of reducing plastic waste and decreasing dependence on fossil fuels [3, 11-14]. Edible films and coatings can be produced based on lipids, polysaccharides, and proteins, or their combinations [15, 16]. Today, the most preferred edible film polymers are polysaccharides. Edible films and coatings of polysaccharide structure are hydrophilic, and have low moisture barriers and high gas barriers. They are produced from polysaccharide-structured substances such as starch, chitin, chitosan, cellulose, gums and pectin [17].

Chitosan is the polymer material most commonly preferred in the production of edible packaging. It has non-toxic, biocompatible, biodegradable, and biologically functional properties. Thanks to these properties, it is widely used in the production of edible films [6]. Among various biopolymers, chitosan is a good candidate for food packaging material due to its film-forming ability and biodegradability. However, pure chitosan film does not have the ideal antioxidant capacity for antioxidant-active food packaging materials. This situation creates a disadvantage in terms of long-term storage

of foods with high fat content [18]. To overcome these shortcomings, it is necessary to improve the antioxidant capacity of pure chitosan film to expand its application in food packaging [19]. In addition, improvements are made in the formulation of these films by adding functionality-enhancing additives such as plasticizers, antimicrobials, colorants, flavorings, probiotics, and live microorganisms for biocontrol purposes [3, 12-14, 20-24]. In these improvements, the use of purees, pulps and extracts of fruit and vegetable origin is carried out in order to improve the sensory and nutritional properties and suitable mechanical performance of these films [11].

Starch, another preferred material in the production of edible packaging, is a natural storage carbohydrate produced in plants. Starch is composed of two types of structures called amylose and amylopectin, which are classes of α-D-glucose [25]. Not all starch is digested by amylase enzymes and is absorbed in the small intestine. Due to this structure, it controls blood sugar levels, has positive effects on cholesterol, diabetes, colon cancer prevention, and gastrointestinal health [26]. Also, starch, which contains a high amount of dietary fiber, can be used as a fiber source in healthy eating [27].

Starch granules are insoluble in water, and they swell by absorbing water. The ability of starch to absorb water stems from the numerous hydroxyl groups it contains. When starch is added to water, hydrogen bonds weaken above 56 °C, and the granule size increases several times its original size in a phenomenon called gelatinization. As the granules absorb moisture, the solution becomes clear and the viscosity increases [28]. Starch is widely used in many sectors such as textiles, paper, pharmaceuticals, paints, cosmetics, and the food industry. Its widespread use is due to its tasteless and odorless nature, natural origin, minimally altering of the product's structure, and viscosity, flow properties, gel resistance, and yield properties [27, 28]. In this study, we aimed to compare the characterization parameters of chitosan and starch-based films by adding rhubarb to them.

Rhubarb (*Rheum ribes* L.), a perennial herbaceous plant of the Polygonaceae family, grows in Iran, Iraq, Lebanon, Palestine, and Turkey [29]. Rhubarb is also known in the region by names such as wild rhubarb and mountain banana [30]. Reaching up to 150 cm in height, rhubarb is a green, leafless plant. It has a sour taste due to its low pH of 3.56 [31]. It was reported that 100 g of rhubarb contains 20.4 mg ascorbic acid, 2.25 g protein, 0.24 g fat, 1.15 g ash, 25.1 mg phosphorus, 114.4 mg potassium, 60.3 mg calcium, and 24.6 mg sodium [32, 33]. However, research has shown that rhubarb contains chrysophanol, physcion, and emodol anthraquinones, as well as quercetin, 5-deoxyquercetin, quercetin 3-O-rhamnoside, quercetin 3-O-galactoside, and quercetin 3-O-rutinoside flavonoids [34]. The results of the studies indicated that rhubarb has a high amount of phenolic compounds [31, 35]. It was also reported to have an antibacterial effect [36, 37].

The present study aimed to determine the extent to which the addition of rhubarb (*Rheum ribes* L.) improves the antioxidant capacity, and functional physicochemical properties (mechanical strength, barrier properties, color, and thickness) of chitosan and starch-based edible film matrices, and to identify the relationship between this improvement and the film matrix.

The present study primarily focuses on evaluating the effect of different polymer matrices on the physicochemical, mechanical, and functional properties of rhubarb-enriched edible films. Although two different preparation methods were employed, these methods were selected based on the specific processing requirements of each polymer system rather than as independent variables for comparison. Starch–gelatin and chitosan matrices differ significantly in terms of solubility, film-forming mechanisms, and structural behavior, which necessitates the use of matrix-specific preparation conditions.

In addition, different forms of rhubarb (puree and lyophilized powder) were used to ensure compatibility with each polymer system. The use of rhubarb puree in starch–gelatin films is suitable due to its aqueous and gelatinization-based structure, whereas lyophilized rhubarb powder provides better dispersion and stability in chitosan-based systems. Therefore, the primary comparison in this study is based on the polymer matrix type, while preparation methods and rhubarb forms were adapted to achieve optimal film formation within each system.

RESULTS AND DISCUSSION

A total of 12 edible films were produced using two different methods (Figure 1). Characterization studies were performed on all film samples.

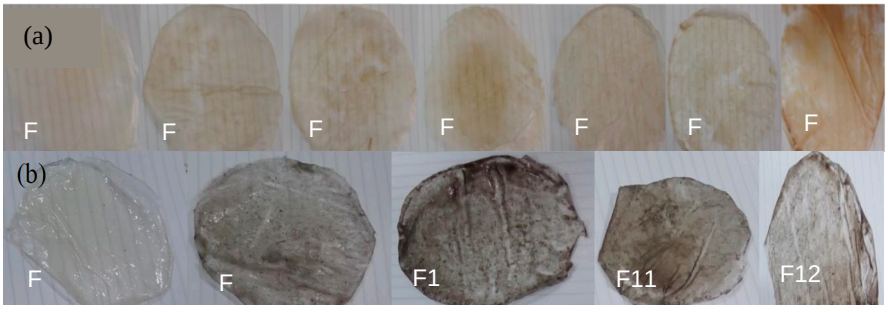

Figure 1. Film samples produced by both methods

The statistically analyzed film thickness (FT) values of the film samples revealed significant differences among the samples ($p \leq 0.05$) (Table 1). F1, F2, F3, F4, and F5 samples were classified within the same statistical group ("a"), and no significant difference was determined among the thickness values of these samples. In contrast, when the F6 and F7 films were examined, the effect of increasing gelatin concentration on film thickness in the presence of lecithin was found to be statistically significant ($p \leq 0.05$). When the film thickness values of the F8–F12 samples were statistically evaluated, the addition of rhubarb extract was found to have a significant effect on film thickness ($p \leq 0.05$) (Table 1).The fact that the control group F8, which does not contain rhubarb, showed the lowest thickness value revealed that the addition of the extract volumetrically strengthened the polymer matrix. The continuously increasing thickness in formulations F9, F10, F11, and F12 where the rhubarb ratio was gradually increased, showed that the extract interacts with the chitosan structure, expanding the net structure of the film and increasing its water-holding capacity. These results revealed that rhubarb extract concentration is one of the determining factors of film thickness in chitosan-based films. While the thickness increased regularly with increasing rhubarb extract in chitosan-based films, the thickness in starch-gelatin based films varied more widely, especially depending on the amount of gelatin and lecithin.

When the water solubility (WS) values of the F1–F7 samples were statistically evaluated, the formulations were found to have a significant effect on solubility ($p \leq 0.05$) (Table 1). While the F1 sample was classified in group "b", all other samples containing rhubarb were included in the same statistical group ("a") and did not show significant differences among themselves. This result indicated that the addition of rhubarb reduced the solubility of the films. The fibrous structure of rhubarb and the phenolic compounds present in its composition may have contributed to the formation of a denser and more compact film matrix, thereby limiting the penetration of water molecules into the film structure. In contrast, the addition of lecithin and gelatin did not produce a statistically significant effect on water solubility. When the water solubility (WS) values of the chitosan-based films belonging to the F8–F12 samples were statistically evaluated, significant differences were determined among the formulations ($p \leq 0.05$) (Table 1). In general, a decrease in water solubility values was observed with increasing rhubarb extract incorporation. This result may be attributed to the fibrous structure, phenolic compounds, and solid matter content of *Rheum ribes*, which likely contributed to the formation of a more compact film matrix. In addition, the incorporation of *Rheum ribes* may have enhanced the interactions between chitosan chains, thereby limiting the penetration of water molecules into the film structure and consequently increasing the water resistance of the films.

When the water vapor permeability (WVP) values of the F1–F7 samples were statistically evaluated, the formulations were found to have significant effects on WVP ($p \leq 0.05$) (Table 1). F2, F3, and F7 samples were classified within the same statistical group ("abc"), while the F5 sample was included in group "a" and the F4 sample in group "c", showing statistically significant differences compared to some other samples. The results indicated that the presence of lecithin at low concentrations contributed to a reduction in water vapor permeability, whereas increasing amounts of gelatin and lecithin resulted in higher WVP values. In addition, the incorporation of *Rheum ribes* was considered to contribute to the reduction of water vapor permeability, particularly in the presence of low gelatin and lecithin concentrations, by promoting the formation of a more compact film matrix. When the water vapor permeability (WVP) values of the F8–F12 samples were statistically evaluated, all samples were found to be included in the same statistical group ("a"), and no significant differences were determined among the samples ($p > 0.05$). This result indicated that the formulation modifications and the incorporation of rhubarb extract did not produce a statistically significant effect on the water vapor permeability of the chitosan-based films. The findings suggested that the barrier properties of the chitosan matrix were largely preserved and that the applied additive concentrations did not substantially alter water vapor transfer.

Table 1. Results of film thickness (FT), water solubility (WS), elongation at break (EB), tensile strength (TS), and water vapor permeability (WVP) analyses of the film samples

Film samples	FT (mm)	WS (%)	WVP (g mm $h^{-1}cm^{-2}$ $Pa^{-1}x10^{-6}$) 24h	EB (%)	TS (MPa)
F1	0.164 ± 0.0048^{a}	95.47 ± 0.50^{b}	0.35 ± 0.05^{bc}	66.78 ± 2.77^{a}	0.53 ± 0.002^{c}
F2	0.163 ± 0.0050^{a}	93.50 ± 0.50^{a}	0.32 ± 0.01^{abc}	59.94 ± 1.90^{a}	0.34 ± 0.009^{a}
F3	0.165 ± 0.0056^{a}	93.08 ± 0.50^{a}	0.30 ± 0.01^{abc}	59.14 ± 2.35^{a}	0.60 ± 0.024^{d}
F4	0.258 ± 0.011^{a}	93.38 ± 0.50^{a}	0.37 ± 0.02^{c}	65.17 ± 2.31^{a}	0.64 ± 0.009^{d}
F5	0.172 ± 0.007^{a}	92.49 ± 0.50^{a}	0.26 ± 0.05^{a}	66.39 ± 14.3^{a}	0.41 ± 0.025^{b}
F6	0.185 ± 0.006^{b}	93.54 ± 0.50^{a}	0.28 ± 0.01^{ab}	66.58 ± 1.46^{a}	0.51 ± 0.014^{c}
F7	0.277 ± 0.016^{c}	91.78 ± 0.50^{a}	0.30 ± 0.06^{abc}	67.94 ± 0.29^{a}	0.51 ± 0.041^{c}
F8	0.162 ± 0.0019^{a}	88.96 ± 0.50^{d}	0.2 ± 0.01^{a}	88.33 ± 11.8^{b}	2.17 ± 0.189^{b}
F9	0.210 ± 0.0044^{b}	84.92 ± 0.50^{c}	0.4 ± 0.09^{a}	63.85 ± 2.71^{a}	1.20 ± 0.013^{a}
F10	0.213 ± 0.0088^{b}	83.75 ± 0.50^{bc}	0.2 ± 0.03^{a}	57.60 ± 3.09^{a}	1.17 ± 0.096^{a}
F11	0.218 ± 0.0011^{bc}	81.60 ± 0.50^{ab}	0.3 ± 0.02^{a}	54.93 ± 1.27^{a}	1.21 ± 0.005^{a}
F12	0.225 ± 0.0044^{c}	81.08 ± 0.50^{a}	0.3 ± 0.1^{a}	52.07 ± 0.84^{a}	1.16 ± 0.011^{a}

*Different letters (a–e) in the table indicate a statistically significant difference between samples within each polymer group/method ($p < 0.05$). Data are presented as mean ± standard deviation, and statistical analysis was performed using one-way analysis of variance (ANOVA) and the Duncan multiple comparison test. Both methods were subjected to independent statistical evaluation within their respective groups.

When the elongation at break (%EB) and tensile strength (TS) values of F1–F7 samples were statistically evaluated, it was determined that the formulations did not have a significant effect on %EB values ($p>0.05$), whereas significant differences were observed in TS values ($p\leq0.05$) (Table 1). The fact that all samples were grouped within the same statistical category ("a") in terms of %EB indicated that gelatine, lecithin, and *Rheum ribes* incorporation did not significantly affect the elasticity of the films ($p>0.05$). In contrast, the presence of different statistical groups in TS values demonstrated that formulation changes had a considerable effect on film strength. In particular, lecithin addition was thought to reduce tensile strength in some samples, whereas increasing gelatine concentration strengthened the film matrix and contributed to higher TS values. When the elongation at break (%EB) and tensile strength (TS) values of F8–F12 samples were statistically evaluated, significant differences were determined among the samples ($p\leq0.05$) (Table 1). The F8 sample was found to be statistically different from all other samples in terms of both TS and %EB values and was classified in group "b". In contrast, the F9–F12 samples were included in the same statistical group ("a") and did not exhibit significant differences among themselves. The results indicated that increasing rhubarb extract incorporation led to a reduction in the mechanical strength and flexibility of the film structure. In particular, the decrease in TS values may be associated with the weakening effect of the plant-based additive on the integrity of the chitosan matrix and the partial disruption of the regular interactions between polymer chains. Similarly, the reduction in %EB values may be attributed to the development of a more brittle and less elastic film structure. Nevertheless, the inclusion of the F9–F12 samples within the same statistical group suggested that, beyond a certain incorporation level, further increases in rhubarb extract concentration did not produce an additional significant effect on the mechanical properties of the films. TS values in the chitosan group ranged from 1.16 to 2.17 MPa, approximately 2-4 times higher than those of starch-based films. These results indicated that the polymer structure of chitosan-based films exhibited a stronger network compared to the starch–gelatin-based films, and that increasing the proportion of rhubarb concentration reduced elasticity in chitosan films while maintaining strength within a certain range. In general, chitosan-based films offered higher mechanical strength, while starch–gelatin-based films exhibited a more flexible but lower-strength structure.

When the FRAP and DPPH antioxidant activity values of F1–F7 samples were statistically evaluated, significant differences were determined among the samples ($p\leq0.05$) (Table 2). According to the FRAP results, the F1 sample exhibited the lowest antioxidant capacity and was classified in group "a".

A marked increase in FRAP values was observed in all film samples containing *Rheum ribes*, with the F4 sample showing the highest value and being classified in group “d”. While F3, F5, and F6 samples were included in the same statistical group (“c”), F2 and F7 samples were classified in group “b”. A similar trend was observed in the DPPH results, where the F4 sample exhibited the highest radical scavenging capacity and was classified in group “c”. F2 and F3 samples were included in group “b”, whereas F5, F6, and F7 samples were grouped together with F1 in group “ab”, with no statistically significant differences determined among them. Overall, the results indicated that the incorporation of *Rheum ribes* enhanced the antioxidant capacity of the film-forming mixtures. However, higher gelatin and lecithin concentrations may have influenced the distribution or interactions of antioxidant compounds within the film matrix, thereby leading to a reduction in antioxidant activity in some samples.

Table 2. FRAP and DPPH results of film-forming mixtures and color parameters of dried film samples

Film samples	FRAP (µg BHA eq /mL)	DPPH (µg ascorbic acid eq/mL)	*L**	*a**	*b**
F1	25.10±1.78^{a}	229.48±51.06^{a}	86.31±3.33^{c}	-4.21±1.69^{a}	11.70±5.00^{a}
F2	72.79±9.16^{b}	431.37±108.94^{b}	80.68±2.06^{bc}	-4.63±0.27^{a}	13.17±1.34^{a}
F3	101.66±1.73^{c}	489.96±83.64^{b}	79.07±3.77^{abc}	-4.31±1.44^{a}	12.66±4.14^{a}
F4	135.84±13.09^{d}	637.50±99.51^{c}	74.91±4.79^{ab}	-5.16±0.92^{a}	15.83±3.49^{a}
F5	105.02±1.58^{c}	359.97±76.89^{ab}	81.63±2.34^{bc}	-6.29±1.07^{a}	18.44±4.25^{a}
F6	98.86±9.80^{c}	368.42±71.77^{ab}	79.07±3.77^{abc}	-4.31±1.44^{a}	13.00±4.71^{a}
F7	72.56±7.78^{b}	360.86±41.29^{ab}	69.66±10.84^{a}	-6.21±1.32^{a}	20.20±6.35^{a}
F8	19.52±0.98^{a}	221.64±46.92^{a}	93.40±5.53^{d}	-3.70±0.29^{ab}	10.56±1.55^{a}
F9	85.20±3.70^{b}	466.27±53.70^{b}	57.73±7.00^{c}	-6.23±0.88^{a}	33.93±2.05^{d}
F10	91.40±31.25^{b}	787.85± 70.93^{c}	57.53±5.90^{c}	-4.44±0.92^{ab}	36.57±0.04^{d}
F11	154.88±15.55^{d}	853.667±113.04^{c}	19.94±5.59^{a}	-0.79±0.98^{c}	24.03±5.28^{c}
F12	187.26±16^{e}	893.63±23.92^{c}	31.00±8.01^{b}	-2.86±0.06^{bc}	16.76±8.54^{b}

*Different letters (a–e) in the table indicate a statistically significant difference between samples within each polymer group/method ($p<0.05$). Data are presented as mean ± standard deviation, and statistical analysis was performed using one-way analysis of variance (ANOVA) and the Duncan multiple comparison test. Both methods were subjected to independent statistical evaluation within their respective groups.

When the FRAP and DPPH antioxidant activity values of F8–F12 samples were statistically evaluated, significant differences were determined among the samples ($p\leq0.05$) (Table 2). According to the FRAP results, the F8 sample exhibited the lowest antioxidant capacity and was classified in

group “a”. A significant increase in FRAP values was observed with the incorporation of rhubarb extract, while the F11 and F12 samples exhibited the highest antioxidant capacities and were classified in groups “d” and “e”, respectively. In contrast, the F9 and F10 samples were included in the same statistical group (“b”) and did not show significant differences between each other. Evaluation of the DPPH results revealed that the F8 sample had the lowest radical scavenging capacity and was classified in group “a”. While the F9 sample was classified in group “b”, the F10, F11, and F12 samples were included in the same statistical group (“c”) and no significant differences were determined among them. Overall, the obtained results indicated that the incorporation of rhubarb extract significantly enhanced the antioxidant capacity of the film-forming mixtures. This increase may be attributed to the phenolic compounds, and other bioactive components present in the structure of *Rheum ribes*. Furthermore, increasing rhubarb extract concentration was considered to enrich the film matrix with greater amounts of antioxidant compounds, thereby enhancing both reducing power and free radical scavenging capacity. It should also be noted that the antioxidant activity analyses were performed on the film-forming mixtures before the drying process. Therefore, the FRAP and DPPH values obtained in this study should be interpreted as indicators of the antioxidant potential of the precursor film-forming systems rather than as direct measurements of the antioxidant performance of the final dried films. Drying conditions, polymer–phenolic interactions, and possible changes in phenolic stability and availability within the dried film matrix may influence the actual functional performance of the films.

A reduction in antioxidant activity was observed following the addition of soy lecithin. Although rhubarb addition significantly enhanced antioxidant activity, the incorporation of soy lecithin slightly decreased the antioxidant performance in starch–gelatin-based films. This reduction may be attributed to the entrapment of antioxidant compounds within the emulsion matrix formed by soy lecithin, thereby limiting their accessibility. Furthermore, the aggregation of phenolic compounds at high concentrations or their non-homogeneous distribution within the film matrix may also explain the decrease in antioxidant activity. In a study conducted on polyvinyl alcohol/starch-based films enriched with rosemary extract, antioxidant activity analyses similarly reported that rosemary extract enhanced antioxidant activity, whereas the subsequent addition of kaolin reduced this activity. The decrease was attributed to synergistic interactions arising from the simultaneous presence of additives, negatively affecting antioxidant performance [38]. Moreover, Laguerre et al. (2007), in their study investigating the relationship between antioxidants and lipids, reported that various synergistic effects may occur

between antioxidants and lipids, including interactions of antioxidants distributed in multiphase environments with different polarities, phases, or solvents. Despite this decrease, the antioxidant activity of rhubarb- and soy lecithin-containing samples remained higher than that of the control sample [39]. Similarly, studies conducted on films produced using gelatin, soy polysaccharides, and tea polyphenols, as well as another study on chitosan–starch-based films enriched with thyme extract, reported that the incorporation of phenolic compounds significantly enhanced antioxidant activity [40, 41]. Overall, the FRAP and DPPH values obtained in the present study indicate a higher antioxidant capacity compared with many edible film systems reported in the literature. This may be explained by the high phenolic compound content of rhubarb extract, its strong interactions with the chitosan matrix, and the enhanced stability of antioxidant compounds resulting from these interactions. The results represent the antioxidant capacity imparted by rhubarb extracts obtained through two different methods within the respective film matrices. In another study, DPPH analyses performed on chitosan–gelatin-based films enriched with ferulic acid, caffeic acid, and tyrosol revealed that although radical scavenging capacity reached up to 90%, the release rate decreased [42]. These findings suggest that rhubarb extract possesses a richer phenolic composition and a stronger redox potential.

When the color parameters (*L*, a*,* and *b**) of F1–F7 samples were statistically evaluated, significant differences were determined among the samples, particularly in terms of *L** values ($p \leq 0.05$) (Table 2). According to the *L** results, the F1 sample exhibited the highest brightness value and was classified in group “c”, whereas the F7 sample showed the lowest *L** value and was classified in group “a”. The F2 and F5 samples were included in group “bc”, the F3 and F6 samples in group “abc”, and the F4 sample in group “ab”. The results indicated that the incorporation of *Rheum ribes* led to a decrease in film brightness, resulting in a darker film appearance. In particular, the combined effect of higher gelatin and lecithin concentrations together with *Rheum ribes* incorporation may have increased color intensity within the film matrix, thereby reducing light transmission. In contrast, evaluation of the *a** and *b** values revealed that all samples were included in the same statistical group (“a”), and no significant differences were determined among the samples ($p > 0.05$). Nevertheless, numerical evaluation indicated that increasing *Rheum ribes* incorporation caused the *a** values to shift toward more negative values, while the *b** values increased. This effect may be attributed to the natural pigments and phenolic compounds present in *Rheum ribes*, which likely imparted more greenish-yellow tones to the films.

When the color parameters (*L*, a*,* and *b**) of the F8–F12 film samples were statistically evaluated, the formulations were found to exert significant effects on all color parameters ($p \leq 0.05$) (Table 2). Evaluation of the *L** values revealed that the F8 sample exhibited the highest brightness value and was classified in group “d”. In contrast, the F11 sample showed the lowest *L** value and was classified in group “a”. The F12 sample was included in group “b”, whereas the F9 and F10 samples were classified within the same statistical group (“c”). These results indicated that increasing Rheum ribes incorporation decreased the brightness of the films, resulting in a darker appearance. This effect may be attributed to the high phenolic compound and natural pigment contents of *Rheum ribes*, which likely increased color intensity within the film matrix. In terms of *a** values, the F11 sample exhibited the highest value and was classified in group “c”, whereas the F9 sample showed the lowest value and was classified in group “a”. The F8 and F10 samples were included in the same statistical group (“ab”), while the F12 sample was classified in group “bc”. The results suggested that Rheum ribes incorporation altered the green color tones of the films. In particular, more negative *a** values indicated the development of more pronounced greenish tones in the film structure. Evaluation of the *b** values demonstrated significant differences among all samples ($p \leq 0.05$). The F9 and F10 samples exhibited the highest *b** values and were classified within the same statistical group (“d”). The F11 sample was included in group “c”, the F12 sample in group “b”, and the F8 sample in group “a”. These findings indicated that the incorporation of rhubarb extract increased the yellowness values of the films and particularly contributed to the development of more intense yellow tones at moderate incorporation levels.

The SEM images (Figure 2) revealed that the F1 control film (a) in the starch-gelatin based films exhibited a smoother and more homogeneous surface structure, with a limited number of small particles observed in the matrix. This indicated that the base formulation without rhubarb extract forms a more compact structure. With the addition of rhubarb extract, the F2 film (b) featured significant irregularities, aggregates, and larger particles on the surface, indicating that the extract components are not fully dispersed within the polymer matrix. Although sample F3 (c) showed a more uniform structure compared to F2, irregular particles attached to the extract were still present on the surface. It could be said that the matrix integrity was partially improved with increasing gelatin content. Formulation F4 (d) exhibited the most pronounced surface roughness and heterogeneous distribution. It was observed that increasing amounts of gelatin and rhubarb led to denser aggregations and a more irregular morphology. In general, the addition of

rhubarb extract disrupted the surface morphology and increased surface unevenness, while the amount of gelatin partially moderated this effect but increased heterogeneous formations at high rates.

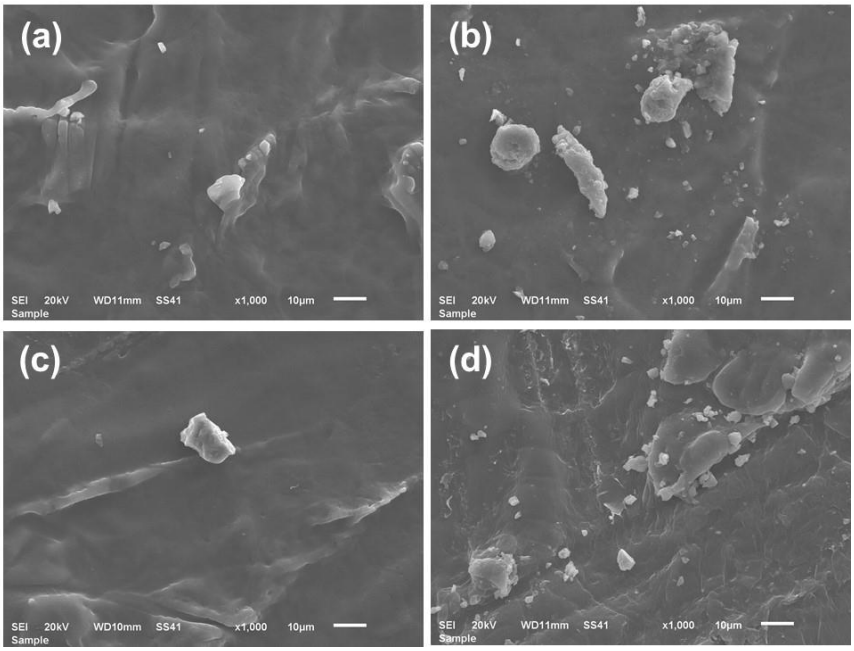

Figure 2. SEM images of (a) F1, (b) F2, (c) F3, and (d) F4 samples

SEM images in Figure 3 revealed that starch-containing gelatin-added rhubarb mixtures exhibited similar behavior. As the gelatin addition ratio increased with the addition of lecithin, a homogeneous distribution of particles on the surface was observed. The SEM images of chitosan-based films (Figure 4) showed that in the control sample (Figure 4a), particles of different sizes and shapes were formed on a homogeneous film, whereas in the rhubarb-added films (Figure 4 b-e), the chitosan-derived particles covered the surface more homogeneously. Furthermore, as the level of rhubarb addition increased, the size of the chitosan particles increased. This can be explained by the presence of a physical interaction in chitosan-rhubarb gel mixtures.

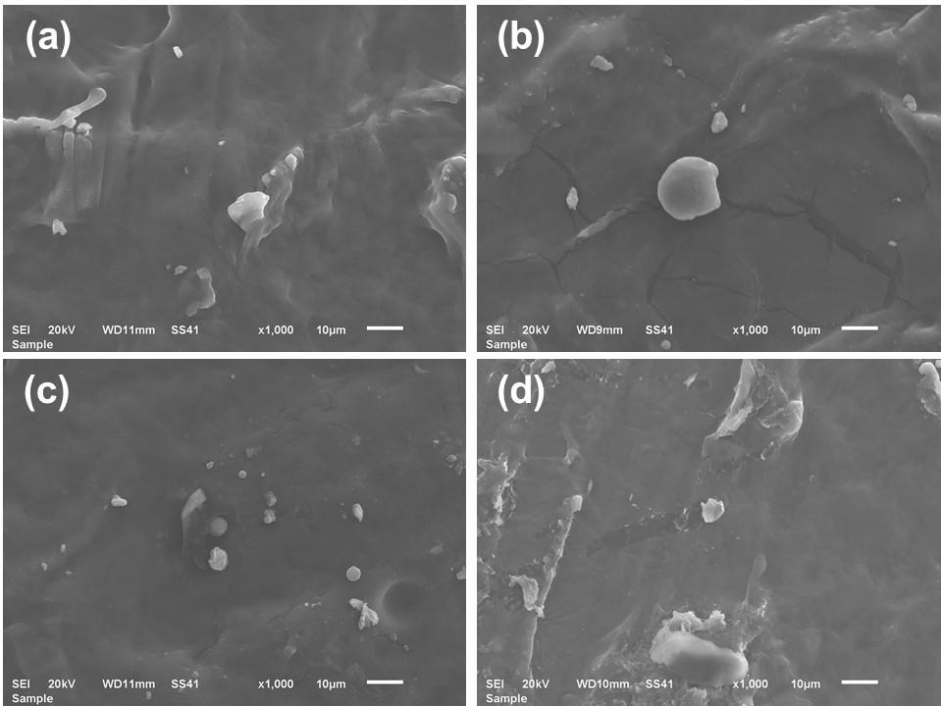

Figure 3. SEM images of a) F1, b) F5 c) F6, and d) F7 samples

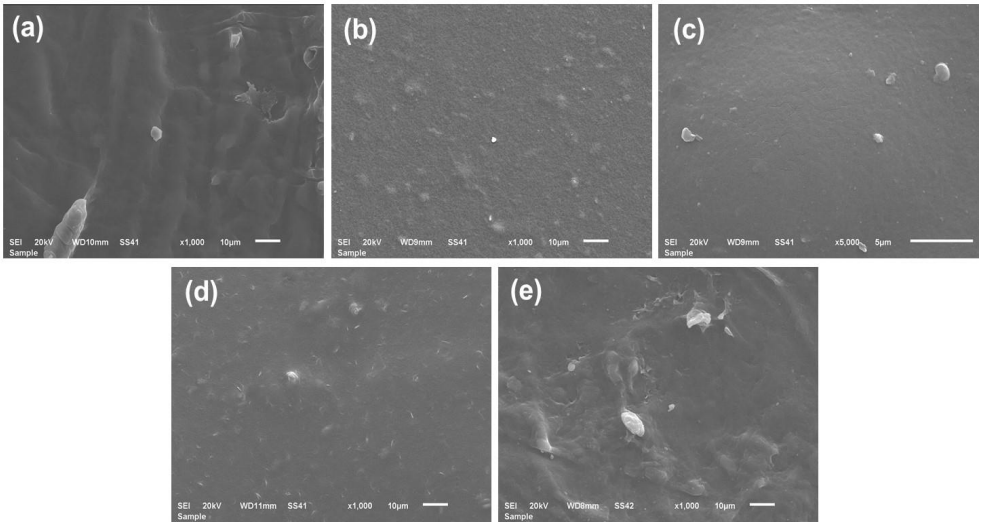

Figure 4. SEM images of a) F8, b) F9 c) F10 d) F11 and e) F12 samples

A comparison of the SEM films made with both methods showed that rhubarb addition increased surface roughness, but lecithin addition provided a more homogeneous image in starch-gelatin based films. It was determined that the amount of particles on the surface increased as the amount of gelatin increased. Overall, surface roughness increased slightly from the control samples to the other samples.

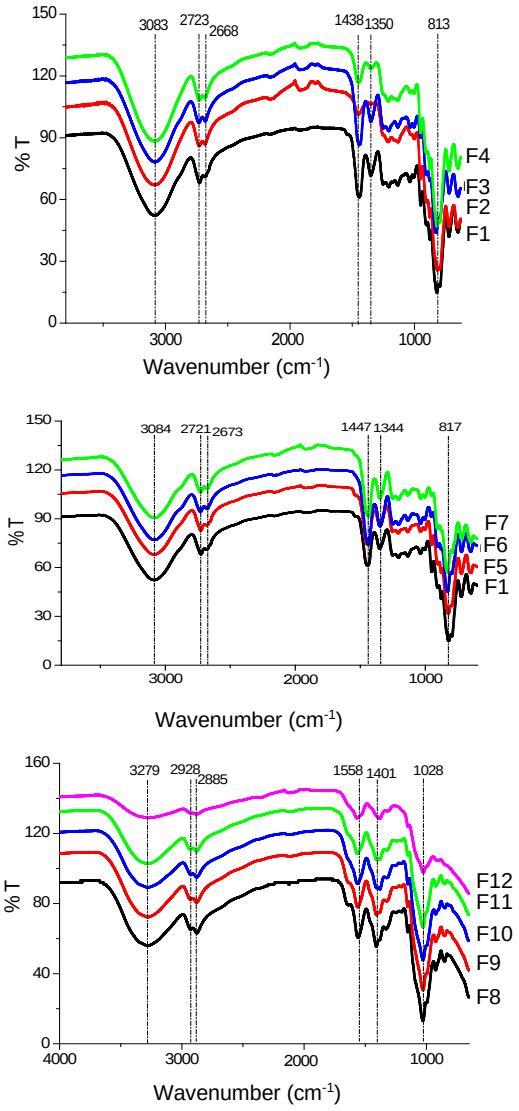

Figure 5. FT-IR spectra of the film samples

FT-IR spectra of samples produced by both methods are shown in Figure 5. In starch-gelatin based films, the band observed at the peak value of 3083 cm^{-1} in the spectra corresponds to the -O-H- bond strain in the -OH- structure. The bands observed at wavenumber values of 1152 and 1079 cm^{-1} belong to natural starch and correspond to the -C-O-- bond strain in the -C-O-H structure of starch. Furthermore, the peaks at 1160 and 1100 cm^{-1} belong to the -C-O-C- bond strain. The peaks at 1000-800 cm^{-1} originate from -C-H- bond strains [38]. In addition, the absorption band observed at approximately 2721 cm^{-1} can be attributed to the symmetric stretching vibration of CH_2 groups, while the band at 2668 cm^{-1} is associated with the vibration of $CH_3NH_3^+$ groups. In films prepared with starch-gelatin mixtures, it was observed that starch and gelatin had their own peaks in their spectra. Since there was no change in peaking or peak intensity, the structure did not deviate from the natural starch-gelatin structure and no chemical deformation occurred.

In the FT-IR spectra of chitosan-based films, characteristic bands of chitosan were present, and there was no change in band positions. These findings may indicate that no major chemical interaction or structural deformation occurred during film preparation. It was observed that there was no interaction between the functional groups of chitosan and the active groups of the added substance, and the bond structure of the films remained unchanged [43].

A comparison of the film samples produced by both methods showed that the spectra of film mixtures prepared with starch showed characteristic peaks of starch and gelatin. This indicated that the structure did not deviate from the natural mixture and that no chemical deformation occurred. A similar situation was observed in film mixtures prepared with chitosan.

The absorbance and transmittance values of the 12 films produced are given in Figure 6. Since the values were not within the 0-1 range when the samples were used undiluted, the samples were diluted 10-fold with distilled water before analysis. In the samples created with starch-gelatin based films, a decrease in absorbance values was observed among the samples with added rhubarb, except for sample F7. The transmittance values of the samples indicated that an increase was observed among the samples with added rhubarb, except for sample F7. In chitosan-based films, the absorbance values of the samples showed a regular increase towards the control sample F8 and the rhubarb-added samples (F9-F12). Transmittance values showed a regular decrease towards the control sample F8 and the rhubarb-added samples (F9-F12).

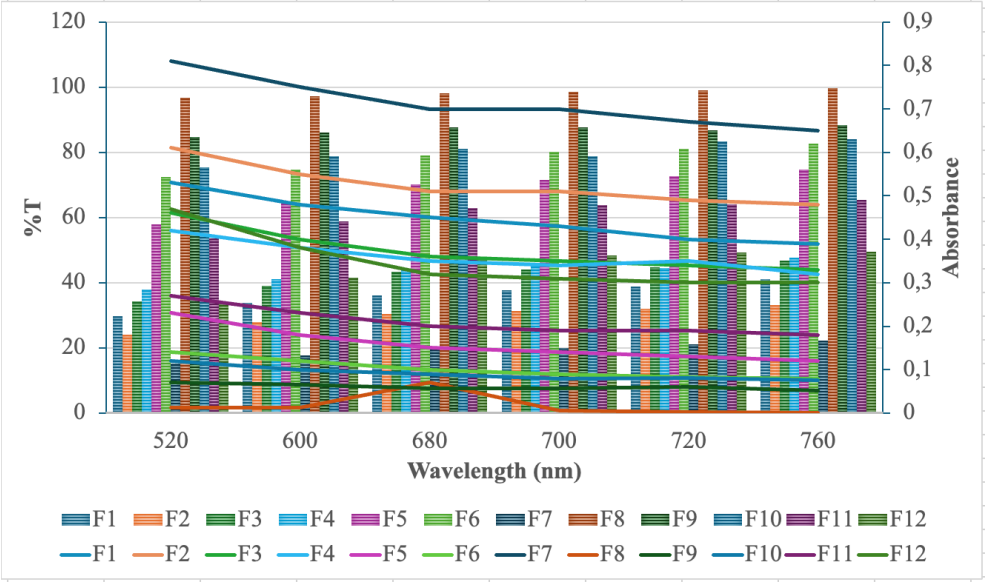

Figure 6. Absorbance–%Transmittance (%T) results of the film samples
*single-line absorbance, triple-line transmittance.

Figure 6 indicates that the absorbance and transmittance behavior of the 12 film samples produced showed significant differences depending on both wavelength and film matrix type. Performing measurements on samples diluted 10 times allowed for the analytical evaluation of absorbance values within a reliable range. In starch-gelatin based films, with the addition of rhubarb, absorbance curves generally remained lower across all wavelengths except for sample F7, while transmittance values increased. This can be attributed to the more homogeneous distribution of rhubarb within the starch-gelatin matrix and the resulting effect of reduced light scattering in the film structure. The exception of sample F7 to this general trend suggested the presence of a denser structure or components that absorbed light more in the film matrix. In chitosan-based films, on the other hand, absorbance values increased regularly across all wavelengths from the control sample F8 to the rhubarb-added samples (F9-F12), while transmittance values decreased significantly. This trend indicated that rhubarb-induced phenolic and colored components in the chitosan matrix increased the optical density of the film, thus limiting light transmittance. The consistent change in absorbance and transmittance curves, particularly across increasing wavelengths, revealed that rhubarb addition was structurally integrated into the film matrix and enhanced its optical barrier properties. Overall, the results demonstrated that rhubarb

addition had a matrix-specific effect on film optical properties and can provide advantages for packaging applications, especially in chitosan-based films, by reducing light transmittance.

The biodegradation behavior of the films was evaluated separately for each polymer system. Starch–gelatin-based films (F1–F7) exhibited biodegradability values ranging from 32.09% to 66.99% after 24 h of incubation. (24-hour; F1: 66.99±6.21, F2: 64.45±0.07%, F3: 56.96±4.42%, F4: 59.43±4.86%, F5: 61.37±12.01%, F6: 37.35±1.44% and, F7: 32.09±4.45%) At 72 hours of incubation, the biodegradability values of starch–gelatin-based films were determined as follows: F1: 90.44±1.58%, F2: 86.69±2.74%, F3: 87.20±2.48%, F4: 89.85±2.15%, F5: 89.74±3.25%, F6: 82.37±0.71% and F7: 84.26±0.94% indicating a high level of degradation within a relatively short time period. At 120 hours, F1–F7 exhibited complete biodegradation (100%), demonstrating that the degradation process was rapid and nearly completed within five days. These results highlight the fast degradation behavior of starch–gelatin matrices, which can be attributed to their hydrophilic nature and relatively loose polymer network. This can be explained by the hydrophilic structure of these biopolymers and the presence of glycosidic and peptidic bonds that are easily broken down by microorganisms. The film sample showing 90.44% biodegradability, in particular, revealed that the polymer matrix has a looser network structure and is susceptible to rapid degradation under environmental conditions. Chitosan-based films (F8–F12) showed a gradual increase in biodegradation over the incubation period. At day 5, the biodegradability values were determined as F8: 35.77%, F9: 29.00%, F10: 35.53%, F11: 40.88%, and F12: 37.43%. As the incubation period progressed, these values increased, and at day 15, biodegradability values were recorded as F8: 57.96%, F9: 62.17%, F10: 53.61%, F11: 59.89%, and F12: 53.36%. F8-F12 films, on the other hand, featured biodegradability values ranging from 78.33% to 97.79% after a 30-day incubation period (F8: 91.08±1.92%, F9: 97.79±3.13%, F10: 88.20±0.45%, F11: 83.40±0.04% and F12: 78.33±0.96%). The highest biodegradability rate of 97.79% can be attributed to the gradual hydrolysis of chitosan chains during long-term incubation and the decrease in the initially present antimicrobial effect over time. On the other hand, the film sample showing 78.33% biodegradability exhibited a denser and partially crystalline polymer network structure, displaying a relatively more resistant structure against microorganisms. It should be noted that the biodegradation behavior of starch–gelatin-based and chitosan-based films was evaluated over different incubation periods. Therefore, the results were interpreted separately within each polymer system rather than through direct quantitative comparison between the two film groups. This methodological difference should be considered when evaluating the biodegradation performance of the films.

Although the present study provides useful comparative information on rhubarb-enriched edible films prepared using starch–gelatin and chitosan matrices, it should be noted that the two experimental systems differed not only in polymer matrix type but also in rhubarb form, preparation procedure, and processing conditions. Therefore, the differences observed in physicochemical, mechanical, and functional properties cannot be attributed exclusively to the polymer matrix. Instead, these results should be interpreted as the combined effect of the matrix characteristics and the matrix-specific formulation and processing conditions required for successful film formation.

CONCLUSIONS

In the present study, the physicochemical, mechanical, optical, antioxidant, biodegradability, and structural properties of starch-gelatin and chitosan-based edible films with rhubarb (*Rheum ribes* L.) addition, produced by two different methods, were comparatively evaluated. The results revealed that film performance varied significantly depending on the production method and the polymer matrix used. Starch-gelatin-based films exhibited higher water solubility and flexibility, while chitosan-based films showed higher tensile strength and better water vapor barrier properties.

Rhubarb addition significantly increased the antioxidant potential of the film-forming mixtures in both systems. This increase was more pronounced in the chitosan-based film-forming mixtures. Color and optical analyses showed that increasing rhubarb concentration led to darkening of the film matrix and a decrease in light transmittance. SEM and FT-IR analyses revealed that rhubarb addition caused physical changes in the film structure but did not result in any degradation in the chemical structure of the polymers. Biodegradability results revealed distinct degradation patterns within each polymer system. Starch–gelatin-based films and chitosan-based films were evaluated over different incubation periods; therefore, the biodegradation findings were considered separately within each polymer matrix, and no direct quantitative comparison was made between the two systems. Overall, chitosan-based films with rhubarb addition appeared to exhibit improved functional and mechanical properties and may represent a promising alternative for active and sustainable food packaging applications. Under the experimental conditions of this study, chitosan-based films appeared to show relatively favorable mechanical and functional properties; however, these findings should be interpreted with caution because the two systems differed in rhubarb form, preparation conditions, and polymer matrix composition.

EXPERIMENTAL SECTION

Production of Edible Films

Method 1: The method described by Tulamandi et al. was revised and used [44]. The method and steps used are summarized in Table 3. In this context, first, the peel of the rhubarb stored at -18°C was removed, cut into small pieces, and pureed in distilled water (1/0.5-w/v) using a homogenizer (OVS-VELP Scientifical). A starch (BCCB9290, Sigma Aldrich) film solution was prepared at the concentrations given in Table 4. The solution was incubated at 75°C for 30 min on a magnetic stirrer (Heildolph MR Hei Standard-505-20000-00-2). Then, glycerol (SZBE030EV, Sigma Aldrich) was added. The mixture was cooled to 55-60°C while stirring continued for 30 min. Finally, gelatin (PE 19-00723-1, Sigma Aldrich) and soy lecithin (SIL29018-1, Sigma Aldrich) were added in the specified proportions. It was observed that soy lecithin did not achieve sufficient dissolution when added directly to the film solution. The best dissolution was achieved by heating 1 mL of glycerol and 1 mL of distilled water to 55°C and slowly adding soy lecithin. The produced film samples were spread in glass petri dishes. The samples spread in the petri dishes were left to dry in an oven at 40°C (POL-EKO-APARATURE-SLN-53-std) for 18 hours.

Table 3. Film formulation used in the first method

Film Samples	Rhubarb	**Starch**	**Gelatin**	**Glycerol**	**Lecithin**
F1	-	2%	2%	3%	0.5%
F2	8**%**	2%	1%	3%	-
F3	8**%**	2%	2%	3%	-
F4	8**%**	2%	3%	3%	-
F5	8**%**	2%	1%	3%	0.5%
F6	8**%**	2%	2%	3%	0.5%
F7	8**%**	2%	3%	3%	0.5%

Method 2: The method described by Ponce et al. was used with some modifications [45]. The method and its steps are summarized in Table 4. Firstly; the rhubarb (*Rheum ribes* L.) plant, which was kept at -18°C, was taken, after removing the peel it was powdered by evaporating the water by keeping it in a lyophilizer (LABCONCO-7670530) at -44°C for 48 hours. Solutions within the concentration range shown in Table 4 were stirred on a magnetic stirrer (Heildolph MR Hei Standard-505-20000-00-2) for 6-12 hours before the addition of rhubarb. The rhubarb concentrations specified in Table 4 were added to the mixtures after incubation and homogenized for 15 minutes using a homogenizer (OVS-VELP Scientifical). The resulting mixtures were spread into glass petri dishes and dried at 30°C for 18 hours to evaporate the water.

Table 4. Film formulation used in the second method

Film Samples	Rhubarb	Chitosan	Glycerol
F8	0%	2%	1%
F9	0.5%	2%	1%
F10	1%	2%	1%
F11	1.5%	2%	1%
F12	2%	2%	1%

Characterization Studies of Films

Film Thickness

Film thickness was determined using a digital micrometer. At least six measurements were taken from different points of the film, in at least three parallels, and the average thickness was determined [46].

Water Solubility

The method described by Tunç et al. was revised and used [47]. The sample, dried at 103°C for 24 hours, was weighed and the initial weight was determined. Ten times the weight of the weighed sample was added to distilled water. It was stirred with a magnetic stirrer at 100 RPM at room temperature for six hours. Then, the part that did not dissolve in water was passed through filter paper. The part remaining on the filter paper was dried at 103°C for 24 hours until it reached a constant weight and weighed at the end of the period.

Color Measurements of Films

Each film sample was measured on a white standard surface using a color analyzer (PenColorArt USB Model, 1L) for *L** (lightness), *a** (red-green), and *b** (yellow-blue) color parameters. The analysis was performed in three parallels for each film [44].

Determination of Tensile Strength and Elongation at Break (TS, %EB) of Films

The tensile strength (TS, tensile strength) and elongation at break (EB, elongation at break) values of the films were determined using the standard method of ASTM standard method 882 [48]. Results were obtained using a texture analyzer (TA. HD Plus Stable Micro Systems Texture Analyser, UK). Films (6 cm x 1 cm) were cut and attached to the ends of the tensile probe. The initial distance between the probe ends was determined as 25 mm, and the films were stretched at a speed of 10 mm/s. Tensile measurements were performed

using a 5 kg load cell. Measurements were performed at room temperature as two replicates [49]. Tensile strength (TS, MPa) and elongation at break (E, %) were calculated using Equations (1) and (2), respectively:

$$TS\ (MPa) = (RE \times g) / (W \times T \times 10^{-6}) \quad (1)$$

$$E\ (\%) = (L / L_0) \times 100 \quad (2)$$

where T is the average thickness of the film samples (m), W is the width (m), RE is the resistance to elongation (kg), g is the gravitational acceleration (9.81 m/s²), L is the final length of the film (m), and L_0 is the initial length of the film (m).

Absorbance and Transmittance Values

The absorbance and transmittance values of the film solutions were read using a UV spectrophotometer (Shimadzu, UV–1280, Kyoto, Japan) at wavelengths of 520 nm, 600 nm, 680 nm, 700 nm, 720 nm, and 760 nm [50].

Fourier Transform Infrared Spectroscopy (FT-IR)

The films were analyzed with an FT-IR instrument (Thermo/Nicolet iseon 912A0607) at a resolution of 4 cm^{-1}, each with ratios between 4000-400 cm^{-1} [44].

Scanning Electron Microscopy (SEM)

SEM experiments were carried out with a JEOL JSM 6510 SEM. Prior to analysis, the samples were coated with a thin layer of gold (Au) to enhance conductivity. The SEM observations were performed at an accelerating voltage of 20 kV, and a magnification of 1000x was used for cross-sectional imaging [51].

Antioxidant Activity Analyses

Reducing power of ferric ions (Fe^{3+}) to ferrous ions (Fe^{2+}) (FRAP method) was measured according to the method of Benzie and Strain [52]. DPPH (2,2-diphenyl-1-picrylhydrazyl) radical scavenging activity was performed according to the method of Blois [53]. Antioxidant activity analyses of the samples used in the study were performed by taking samples directly from the mixtures before drying the gels. All analyses were performed in triplicate.

Biodegradability

The method applied by Jaramillo et al. was revised and applied [54]. Soil samples taken from the same conditions were filled into pots as 1 kg each. The samples, dried in Petri dishes, were divided into six different parts.

The samples were weighed (G1). Six different wells were opened in the pots containing the soil, and the samples were buried and covered with soil. The pots were watered with 50 mL of water daily. Every five days, the samples were removed, cleaned, and weighed (G2). The analysis was conducted at room temperature for 30 days. All studies were performed as two parallel processes.

Biodegradability (%) = $((G1-G2)/G1)\times 100$.

Water Vapor Permeability

The water vapor permeability of the films was determined using the ASTM (2003) method [55]. Silica gel (1 g) was placed in tubes. To prevent moisture from remaining in the tubes and silica gel, they were kept at 103°C for 24 hours. Film samples were cut into 2.5 cm x 2.5 cm pieces and placed at the mouth of the tubes. The tubes were coated with paraffin to prevent moisture absorption. The bottom of the desiccator was filled with distilled water. The tubes were placed in the desiccator and kept at 25°C for 24 hours. Samples were weighed at 0, 3, 6, 9, 24, 27, 30 and 33 hours.

x = Film thickness (mm), w/t (Slope) = Calibration slope (g/hour),

A = Surface area of the film in contact with water vapor (cm^2),

ΔP = Applied pressure difference (Pa)

Water vapor permeability = (w/t) × [x / (ΔP × A)].

Statistical Analysis

All data obtained are expressed as mean ± standard deviation. Statistical differences between samples were evaluated using one-way analysis of variance (ANOVA), and the Duncan multiple comparison test was applied to determine the differences between groups. A p-value of ≤ 0.05 was considered statistically significant. Statistical analyses were performed using the IBM SPSS Statistics 20 software package.

ACKNOWLEDGMENTS

This study was derived from Esra PEKDOĞAN ÇAKAL's master's thesis, which was conducted in 2021 under the supervision of Assist. Prof. Dr. Bülent HALLAÇ and Assoc. Prof. Dr. Ebru AKKEMİK. The research was supported by Siirt University, Scientific Research Projects Coordination Office (Project No: 2019-SİÜFEB-026). The authors are thankful for this support. The authors would like to sincerely thank Yıldız Technical University, Faculty of Chemical and Metallurgical Engineering, Department of Food Engineering, Graduate Research Laboratory for their support in the mechanical analyses of the films, including tensile strength and elongation at break measurements. We also gratefully acknowledge Siirt University Scientific and Technological Research and Application Center for providing FT-IR analysis services, and Bingöl University Central

Research Laboratory Application and Research Center for SEM analysis support. The authors would also like to thank Dr. Züleyha KUDAŞ for her support and contributions to the study. Their valuable technical contributions are greatly appreciated. The authors would like to thank Dr. Şule Azime YENİÇERİ for her valuable contributions to the editing of the manuscript.

REFERENCES

[1] Pekdoğan, E.; Akkemik, E.; Hallaç, B., *Journal of the Institute of Science and Technology*, (2024) **14**, 271.
[2] Sundqvist-Andberg, H.; Åkerman, M., *Journal of Cleaner Production*, (2021) **306**, 127111.
[3] Kumar, L.; Ramakanth, D.; Akhila, K.; Gaikwad, K. K., *Environ Chem Lett*, (2022) **20**, 875.
[4] Ramakanth, D.; Singh, S.; Maji, P. K.; Lee, Y. S.; Gaikwad, K. K., *Environ Chem Lett*, (2021) **19**, 3597.
[5] Meys, R.; Frick, F.; Westhues, S.; Sternberg, A.; Klankermayer, J.; Bardow, A., *Resour Conserv Recy*, (2020) **162**.
[6] Mohamed, S. A. A.; El-Sakhawy, M.; El-Sakhawy, M. A. M., *Carbohyd Polym*, (2020) **238**.
[7] de Oliveira, S. J. r.; de Araújo, J. S.; de Asevedo, E. A.; de Medeiros, F. G. M.; dos Santos, V. S.; de Sousa, F. J. r.; de Araújo, N. K.; dos Santos, E. S., *Biomass Convers Bior*, (2023) **13**, 1565.
[8] Kurt, A. S.; Cekmecelioglu, D., *Biomass Convers Bior*, (2023) **13**, 6981.
[9] Oloye, M. T.; Jabar, J. M.; Adetuyi, A. O.; Lajide, L., *Biomass Convers Bior*, (2023) **13**, 2125.
[10] Saklani, P.; Siddhnath; Das, S. K.; Singh, S. M., *International Journal of Current Microbiology and Applied Sciences*, (2019) **8**, 2885.
[11] Otoni, C. G.; Avena-Bustillos, R. J.; Azeredo, H. M. C.; Lorevice, M. V.; Moura, M. R.; Mattoso, L. H. C.; McHugh, T. H., *Compr Rev Food Sci F*, (2017) **16**, 1151.
[12] Díaz-Montes, E.; Castro-Muñoz, R., *Foods*, (2021) **10**.
[13] Hassan, B.; Chatha, S. A. S.; Hussain, A. I.; Zia, K. M.; Akhtar, N., *Int J Biol Macromol*, (2018) **109**, 1095.
[14] Falguera, V.; Quintero, J. P.; Jiménez, A.; Muñoz, J. A.; Ibarz, A., *Trends Food Sci Tech*, (2011) **22**, 292.
[15] Debeaufort, F.; Quezada-Gallo, J. A.; Voilley, A., *Crit Rev Food Sci*, (1998) **38**, 299.
[16] Oğuzhan Yıldız, P.; Yangılar, F., *BEU Journal of Science*, (2016) **5**, 27.
[17] Yüksel, Ç.; Atalay, D.; Erge, H. S., *Gıda*, (2020) **45**.
[18] Yong, H. M.; Wang, X. C.; Bai, R. Y.; Miao, Z. Q.; Zhang, X.; Liu, J., *Food Hydrocolloid*, (2019) **90**, 216.
[19] Wang, X. C.; Yong, H. M.; Gao, L.; Li, L. L.; Jin, M. J.; Liu, J., *Food Hydrocolloid*, (2019) **89**, 56.
[20] Aydogdu, A.; Radke, C. J.; Bezci, S.; Kirtil, E., *Int J Biol Macromol*, (2020) **148**, 110.
[21] Guimaraes, A.; Abrunhosa, L.; Pastrana, L. M.; Cerqueira, M. A., *Compr Rev Food Sci F*, (2018) **17**, 594.
[22] Jeevahan, J. J.; Chandrasekaran, M.; Venkatesan, S. P.; Sriram, V.; Joseph, G. B.; Mageshwaran, G.; Durairaj, R. B., *Trends Food Sci Tech*, (2020) **100**, 210.

[23] Ribeiro, A. M.; Estevinho, B. N.; Rocha, F., *Food Bioprocess Tech*, (2021) **14**, 209.
[24] Suhag, R.; Kumar, N.; Petkoska, A. T.; Upadhyay, A., *Food Res Int*, (2020) **136**.
[25] Özdemir, F.; Ramazanoğlu, D., *Journal of Bartin Faculty of Forestry*, (2019) **19**, 377.
[26] Zhu, F.; Wang, S. N.; Wang, Y. J., *J Sci Food Agr*, (2013) **93**, 3100.
[27] Demirekin, A.; Gül, H., *Journal of Agricultural Faculty of Uludag University*, (2016) **30**, 71.
[28] Gönül, M., *Gıda*, (1978) **3**.
[29] Fazli-Bazaz, B. S.; Khajehkaramadin, M.; Shokouhizadeh, H. R., *Iranian Journal of Pharmaceutical Research*, (2005) **4**, 87.
[30] Taşkın, T.; Bulut, G., *Istanbul J Pharm*, (2019) **49**, 7.
[31] Meral, R., *Yuzuncu Yıl University Journal of Agricultural Sciences*, (2017) **27**, 88.
[32] Alan, R.; Padem, H., *Gıda*, (1989) **14**.
[33] Tuncer, B.; Günsan, B., *Turkish Journal of Agricultural Research*, (2017) **4**, 296.
[34] Tosun, F.; Akyüz Kızılay, Ç., *Ankara Eczacılık Fakültesi Dergisi*, (2003) **32**, 31.
[35] Naemi, F.; Asghari, G.; Yousofi, H.; Yousefi, H. A., *Avicenna J Phytomedi*, (2014) **4**, 191.
[36] Alan, Y.; Erbil, N.; Dıgrak, M., *Journal of Selçuk University Natural and Applied Science*, (2013) **1**, 23.
[37] Alaadin, A. M.; Al-Khateeb, E. H.; Jäger, A. K., *Pharmaceutical Biology*, (2007) **45**, 688.
[38] Kavas E; Terzioğlu P; Taş M; Parın FN; Kuş Ç; Küçükaydın S; ME, D., *Eurasian Journal of Biological and Chemical Sciences*, (2020) **3**, 121.
[39] Laguerre, M.; Lecomte, J.; Villeneuve, P., *Progress in lipid research*, (2007) **46**, 244.
[40] Liu, J.; Song, Z.; Wang, Y.; Pei, Y.; Tang, K., *Polymers*, (2025) **17**, 2174.
[41] Talón, E.; Trifkovic, K. T.; Nedovic, V. A.; Bugarski, B. M.; Vargas, M.; Chiralt, A.; González-Martínez, C., *Carbohyd Polym*, (2017) **157**, 1153.
[42] Benbettaïeb, N.; Tanner, C.; Cayot, P.; Karbowiak, T.; Debeaufort, F., *Food chemistry*, (2018) **242**, 369.
[43] Xiao, C. B.; Zhang, J. H.; Zhang, Z. J.; Zhang, L. N., *J Appl Polym Sci*, (2003) **90**, 1991.
[44] Tulamandi, S.; Rangarajan, V.; Rizvi, S. S. H.; Singhal, R. S.; Chattopadhyay, S. K.; Saha, N. C., *Food Packaging Shelf*, (2016) **10**, 60.
[45] Ponce, A. G.; Roura, S. I.; del Valle, C. E.; Moreira, M. R., *Postharvest Biol Tec*, (2008) **49**, 294.
[46] Atarés, L.; De Jesús, C.; Talens, P.; Chiralt, A., *J Food Eng*, (2010) **99**, 384.
[47] Tunc, S.; Angellier, H.; Cahyana, Y.; Chalier, P.; Gontard, N.; Gastaldi, E., *J Membrane Sci*, (2007) **289**, 159.
[48] ASTM, D., *ASTM International: West Conshohocken, PA, USA*, (2002).
[49] Kurt, A.; Kahyaoglu, T., *Carbohyd Polym*, (2014) **104**, 50.
[50] Akşehir, K. Ondokuz Mayıs University (2013).
[51] Kocakulak, S. Middle East Technical University (2019).
[52] Benzie, I. F. F.; Strain, J. J., *Anal Biochem*, (1996) **239**, 70.
[53] Blois, M. S., *Nature*, (1958) **181**, 1199.
[54] Jaramillo, C. M.; Gutiérrez, T. J.; Goyanes, S.; Bernal, C.; Famá, L., *Carbohyd Polym*, (2016) **151**, 150.
[55] Testing, A. S. f.; Materials, *Annual Book of ASTM Standards 2003: Metals test methods and analytical procedures. Nondestructive testing*, University: (2003).

STUDIA UBB CHEMIA, LXXI, 2, 2026 (p. 65-85)
(RECOMMENDED CITATION)
DOI:10.24193/subbchem.2026.2.04

GREEN SYNTHESIS AND STRUCTURAL CHARACTERIZATION OF IRON OXIDE NANOPARTICLES FROM *ROBINIA PSEUDOACACIA* L. FRUITS FOR DYE REMOVAL FROM AQUEOUS SOLUTIONS

Semra DEMIR[a], Bülent AKAR[b,*], Cemalettin BALTACI[b]

ABSTRACT. In this study, iron oxide nanoparticles were produced and characterized using a green synthesis method with *Robinia pseudoacacia* fruits. The structural and functional properties of the nanoparticles were investigated using XRD, TEM/EDX, and FTIR analyses. The results indicated that the produced iron oxide nanoparticles had nanoscale particle sizes and exhibited a poorly crystalline (predominantly amorphous) structure according to XRD analysis. The comparative adsorption performance of the synthesized FeONPs and fruit powder in the removal of malachite green (MG), phenol red (PR) and methylene blue (MB) from aqueous solutions was evaluated. According to the results, the adsorption capacity followed the order MB> MG > PR. FeONPs exhibited consistently higher Q_e values across all dye systems compared to the fruit powder. High removal efficiencies were obtained at low and moderate initial concentrations, while increasing the adsorbent dose enhanced the overall removal but resulted in a reduction in the adsorption capacity per unit mass. The obtained findings indicate that biosynthesized iron oxide nanoparticles can be used as an efficient and environmentally friendly adsorbent for eliminating environmental pollutants.

Keywords: *green synthesis, fruit extract, iron oxide nanoparticles, Robinia pseudoacacia, dye removal*

[a] *Gümüşhane University, Graduate Education Institute, Department of Biotechnology, 29000, Gümüşhane, Türkiye*
[b] *Gümüşhane University, Faculty of Engineering and Natural Sciences, Department of Food Engineering, 29000, Gümüşhane, Türkiye*
* *Corresponding author: akarblnt@gmail.com*

INTRODUCTION

When it comes to the management of environmentally polluted areas, since the pollutant removal of from contaminated environments is generally a process that involves high costs due to technical requirements, preventive strategies aimed at avoiding the environmental contamination and natural resources from the outset are much more sustainable and effective. However, pollutants originating largely from intensive human activities enter the air, water, and soil and accumulate, creating stress on ecosystems, reducing biodiversity, decreasing soil fertility, and leading to crop losses. In addition, the transfer of these pollutants across the food chain poses various threats to other organisms and humans [1]. The increase in environmental pollution has required the development of appropriate methods for remediation of pollution sources from affected environments. The elimination of contaminants from the environment through organisms is referred to as bioremediation. The primary aim of this technology is to reduce or remove pollution [2]. Phytoremediation, defined as the elimination of pollutants from contaminated soil, air, and water using plants, is a type of bioremediation. This approach involves the use of plants together with rhizosphere microorganisms to eliminate, transform, or accumulate chemical compounds present in groundwater, surface water, soil, sediment, and the atmosphere [3-4]. Recently, studies using innovative approaches have increasingly targeted the reduction of pollution levels. Nanotechnology, with applications in a wide range of scientific and industrial fields, is also attracting growing attention in environmental remediation [5]. Notably, the production of nanosized particles using chemical and physical methods has long been recognized as a conventional approach [6-7]. However, due to these disadvantages, biological synthesis (green synthesis) has emerged in recent years as a simpler, lower-cost, and environmentally friendly alternative [8]. Indeed, research on biologically synthesized nanoparticles using yeasts, bacteria, algae and plants, have seen a significant increase in the last decade compared to chemical and physical methods [9-10]. Biosynthesis studies often include metal and metal oxide nanoparticles. Owing to their unique biological, physicochemical, magnetic, and optical characteristics, these nanoparticles have attracted considerable scientific interest [11]. In this context, the ability of plants to reduce metal ions is one of the key features of biological (green) synthesis processes. Plant extracts are among the most widely used natural reducing agents due to their lower cost, easier availability and high biocompatibility. In particular, the polyphenols, terpenoids, glutathione, carotenoids, and glucosinolates found in these extracts are environmentally

friendly biomolecules that contribute to the reduction of metal ions and the stabilization of nanoparticles [12]. One significant application area for environmentally friendly approaches is the remediation of water pollution. As water pollution is a serious global environmental problem, research into effective treatment strategies is intensifying. Bioremediation processes are therefore receiving increasing attention as a means of removing organic pollutants and heavy metals from aqueous solutions [13]. Bioremediation of dyes in wastewater is an effective method of treating textile waste, offering advantages over traditional techniques. Dyes are classified as hazardous pollutants by various international environmental agencies, including the US Environmental Protection Agency (EPA). Due to their carcinogenic properties, even low concentrations of dyes in water can have serious negative environmental and ecological impacts [14].

In bioremediation studies, plant-derived materials are commonly used as effective, sustainable and economical absorbents for removing synthetic dyes from water [15]. In this study, the fruits of *Robinia pseudoacacia* L., belonging to the Fabaceae family, and iron oxide nanoparticles obtained from these extracts, were characterized and their capacity to remove polluting dyes from water was determined. The *R. pseudoacacia* tree is adaptable to environmental stress and has high ecological and economic value. It is therefore widely used as an ornamental plant and for landscaping purposes in Türkiye and many others around the world [16]. The chemical composition and biological activities of *R. pseudoacacia* have been studied [17-19]. These studies have revealed that the species exhibits significant biological activity. Although other plant species and metal oxides may possess the potential for high dye-removal efficiency, many of these alternatives are not practical for dye remediation applications because of their high cost and limited availability. Therefore, the use of *R. pseudoacacia* fruit as an economical and readily accessible biomass, together with iron as a low-cost and environmentally benign metal, forms the main basis for their selection in this study. This study aims to synthesize iron oxide nanoparticles through a green approach using fruit extracts of *R. pseudoacacia* and to examine their structural and chemical characteristics. In addition, the study aims to evaluate the effectiveness of both the fruit-derived material and the synthesized iron oxide nanoparticles from fruit extract in removing synthetic dyes from aqueous solutions. Accordingly, this work aims to facilitate the development of a sustainable, environmentally friendly, and economically efficient remediation strategy.

RESULTS AND DISCUSSION

1. Characterization of Iron Oxide Nanoparticles

The formation of FeONPs was evaluated to determine whether the process had occurred as intended. During this assessment, the appearance of a dark, nearly black coloration was noted, and this change is generally regarded as a qualitative indication of FeONP formation [20]. Following the observation of the characteristic dark color formation, the reaction mixture was further examined by UV–Vis spectroscopy to verify nanoparticle synthesis. The most significant finding in the spectral analysis presented in Figure 1 is the substantial decrease in absorbance observed upon completion of the reaction, in comparison with the high absorption values recorded at the beginning of the experiment. This change is indicative of the fundamental chemical transformations that occur during the synthesis process. The absorbance decreased as free organic compounds bound to iron ions during FeONP formation. In particular, the absorbance variation observed in the 400–500 nm region reflects the characteristic features of FeONPs.

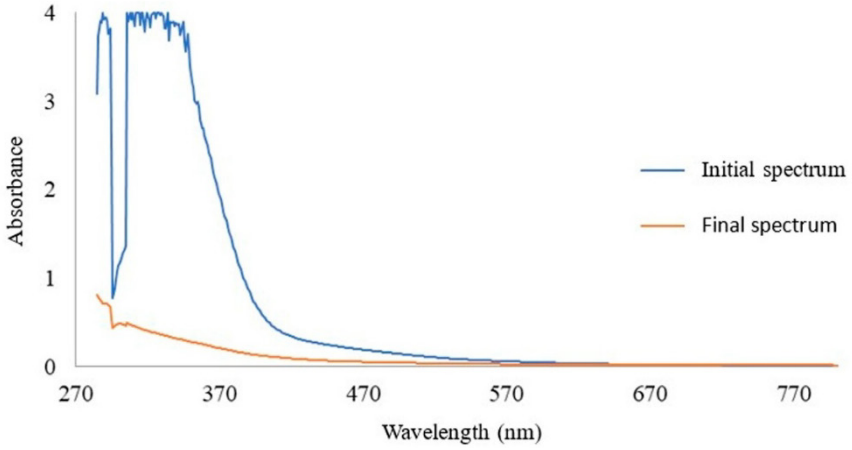

Figure 1. UV–Vis spectral variations observed during FeONP biosynthesis

The functional groups in the plant extract and the produced iron nanoparticles were determined using FTIR analysis (Figure 2). In the of 3200–3500 cm^{-1} range, a broad band was observed particularly in the extract, which is mainly attributed to O–H stretching vibrations arising from phenolic-

derived compounds; however, this band may also overlap with N–H stretching and other O–H bands in complex plant matrices [21]. In the iron nanoparticles, a slight shift and weakening the band were detected, indicating that the O–H groups interacted with iron ions and became bound to the nanoparticle surface. In the 1580–1650 cm^{-1} interval, the extract exhibited a characteristic band (≈1588 cm^{-1}) that may arise from overlapping C=C stretching, C=O stretching, or aromatic ring deformation vibrations [22]. In the present study, this band was noticeably weakened and shifted to approximately 1610 cm^{-1} following the formation of iron nanoparticles, indicating that these functional groups, particularly carbonyl and aromatic-based moieties, participated in the reduction of Fe^{3+} and the subsequent coordination of both Fe^{2+} and Fe^{3+} ions with oxygen-containing groups such as OH and conjugated C=O moieties on the nanoparticle surface [22]. In the 1000–1400 cm^{-1} interval, the extract exhibited bands mainly associated with C–N and C–O stretching vibrations, together with overlapping contributions from phenolic O–H -related modes, C–H deformation, and amine- or amide-associated NH_2 vibrations. This interpretation is consistent with previous FTIR assessments for plant-derived green synthesis [21]. In both the extract and the FeONP sample, characteristic bands were observed within the 500–800 cm^{-1} range. In the extract, two notable bands appeared at approximately 530 and 620 cm^{-1}, which fall within the typical Fe–O vibration region. In the FeONPs, this region showed additional minor features and a broader, more complex spectral profile. Similar observations reported in earlier studies suggest that the 800–400 cm^{-1} range is characteristic of Fe–O bonding, with magnetite generally exhibiting a strong Fe–O band near 573 cm^{-1} and additional shoulders attributed to surface oxidation [22]. Accordingly, the plant extract acted not only as a reducing agent, facilitating the conversion of Fe^{3+} to Fe^{2+} during nanoparticle formation, but also as a stabilizing agent through the coordination of its functional groups with the nanoparticle surface.

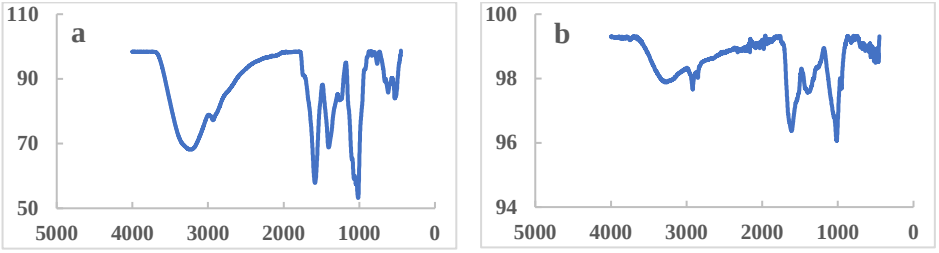

Figure 2. FT-IR spectra of the fruit extract (a) and the synthesized FeONPs (b)

The TEM images of FeNOPs synthesized from fruit extracts are presented in Figure 3. The images indicate the formation of nanoscale iron oxide particulate structures. However, due to the very small particle size and slight agglomeration, individual particle boundaries are not sharply defined. Particle size is one of the key factors influencing surface properties. Smaller particles exhibit a higher surface-to-volume ratio, enhances mass transport [23] and provides a clear advantage in the adsorption of pollutant adsorption [24]. In the present study, the high dye removal efficiencies are consistent with the formation of these very small iron oxide nanoparticles, whose large surface area supports efficient adsorption.

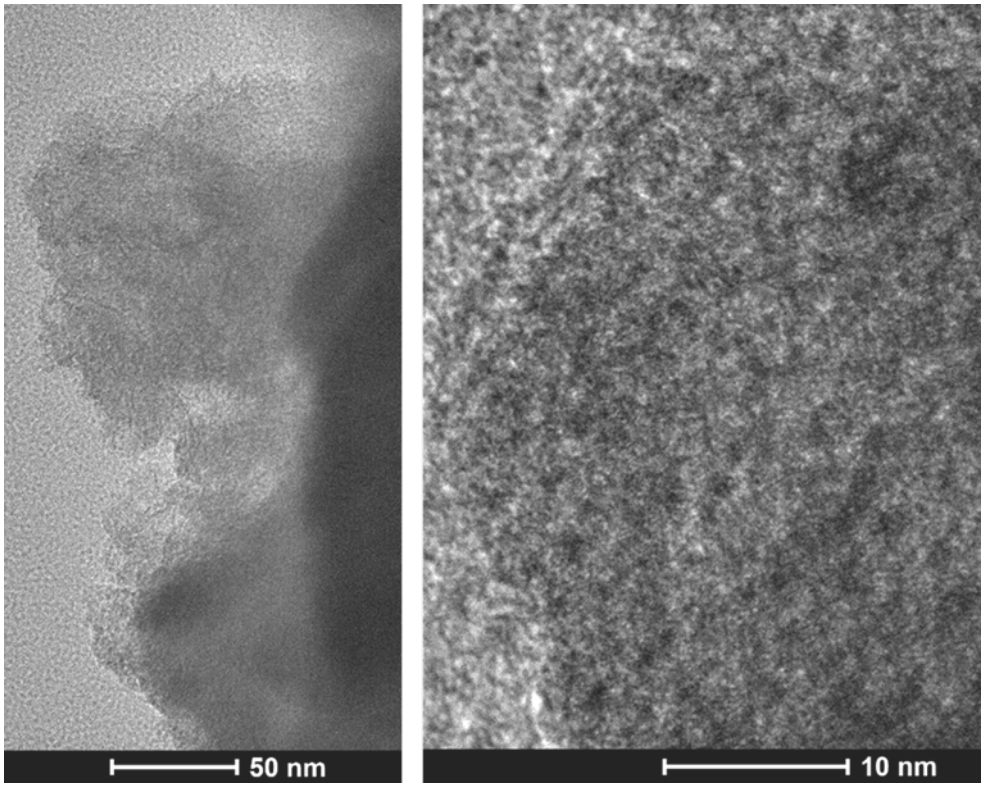

Figure 3. TEM images of FeONPs taken at different magnifications

EDX analysis confirmed the elemental composition of the produced FeONPs and their successful formation [25-26]. The EDX results for the FeONPs are presented in Figure 4 and Table 1. According to the EDX analysis, oxygen (O), carbon (C), and iron (Fe) were identified as the major elemental

constituents of the FeONPs, accounting for the highest percentage contributions. Based on the atomic percentage data, oxygen was measured at 39.32%, carbon at 25.38%, and iron at 26.34%. In the weight percentage profile, iron appeared as the dominant element with 48.81%, followed by oxygen (23.50%), copper (14.68%), and carbon (11.18%). Magnesium, silicon, and sulfur were detected only in trace quantities, with atomic percentages of 0.64%, 0.26%, and 0.94%, and corresponding weight percentages of 0.54%, 0.25%, and 1.04%, respectively. The high amounts of iron and oxygen detected in the nanoparticle samples support the presence of iron oxide in their structure [27]. Similar findings have also been reported in the literature. For example, in iron oxide nanoparticles synthesized from plant materials, the atomic percentages of iron and oxygen have been reported as follows: 33.29% Fe and 66.71% O in neem plant (*Azadirachta indica* A. Juss) leaf extract [28]; 14.21% Fe and 47.33% O in firethorn (*Pyracantha coccinea* Roem.) fruit extract [29]; 8.65% Fe and 50.55% O in algal biofilm–derived nanoparticles [30]; and 77.08% Fe and 22.97% O in nanoparticles synthesized using *Eichhornia crassipes* (Mart.) Solms leaf extract [31].

Table 1. EDX elemental composition of the FeONPs

Atom No	Element	Atomic %	Weight %
6	Carbon	25.38	11.18
8	Oxygen	39.32	23.50
12	Magnesium	0.64	0.54
14	Silicon	0.26	0.25
16	Sulfur	0.94	1.04
26	Iron	26.34	48.81
29	Copper	7.13	14.68

The identification of carbon as the third most abundant element after oxygen and iron, in both atomic and mass percentages, indicates the presence of residual organic compounds associated with the nanoparticle surface rather than being a structural component of the FeONPs. Green synthesis studies indicate that the carbon content of iron nanoparticles may vary depending on the plant species, the plant part used, and the synthesis conditions. For example, in FeONPs synthesized from mango peel extracts, carbon was reported as 14.95%, following iron (48.5%) and oxygen (34.06%) [32]; 40.79% in those produced from algal biofilms [30]; 38.46% in iron nanoparticles synthesized from *Pyracantha coccinea* Roem. fruit extract [29]; and 16.22% in nanoparticles obtained from waste tea extracts [33]. The copper signal detected in the EDX spectrum originates from the TEM copper grid used during sample preparation and does not indicate the incorporation of copper

into the nanoparticle structure [34]. The small amount of sulfur detected in the EDX analysis originates from the $FeSO_4$ precursor used in the synthesis. Similarly, Da'na [35] reported that the sulfur peak corresponds to the sulfate group derived from $FeSO_4$. The trace levels of silicon and magnesium are considered to arise from the plant extract, laboratory glassware, or minor environmental contamination during synthesis or sample preparation. These findings indicate that the FeNOPs were successfully synthesized and possess an oxidized structure.

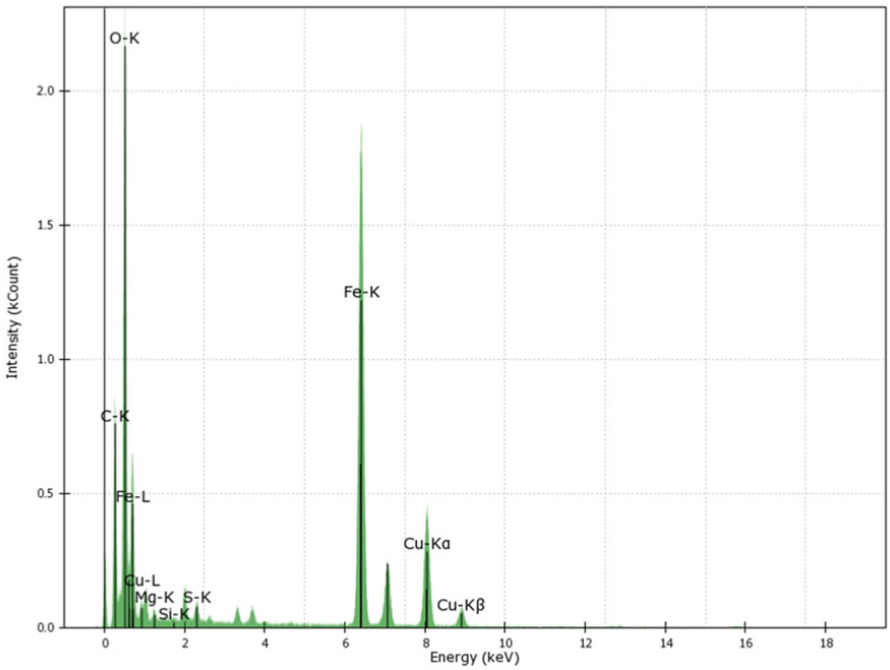

Figure 4. EDX spectra of the FeONPs

In this study, the crystal structure of iron oxide (FeOx) nanoparticles produced using *R. pseudoacacia* fruit extracts was analyzed by X-ray diffraction (XRD). The theoretical XRD peak positions reported for JCPDS Card No. 19-0629 were used as a reference for comparison, with characteristic peaks at 2θ values of 30.1° (220), 35.5° (311), 43.1° (400), 53.4° (422), 57.0° (511), and 62.6° (440). In the XRD analysis conducted in the present study, the diffraction pattern obtained is presented in Figure 5. In the 2θ regions corresponding to the theoretical peaks of JCPDS 19-0629, broad and suppressed signals were observed instead of distinct and sharp diffraction peaks. This XRD pattern

indicates a predominantly amorphous structure, with only a few weak signals that may correspond to trace crystallinity associated with iron oxide phases. In addition, the presence of broad features in the diffraction pattern, particularly at $2\theta \approx 22°$ and 36°, may also indicate the possible presence of iron oxyhydroxide phases, such as goethite (FeOOH). However, due to the absence of distinct peaks, it does not appear possible to distinguish Fe_3O_4 from other iron oxide phases such as Fe_2O_3 based on the amorphous diffraction pattern in Figure 5. For this reason, the synthesized material is described more appropriately and conservatively as iron oxide nanoparticles (FeOx) rather than being attributed to a specific crystalline phase such as Fe_3O_4. It has been reported that X-ray diffraction patterns of FeNOPs synthesized using fruit extracts tend to exhibit amorphous characteristics. For instance, in the XRD pattern of iron nanoparticles obtained from *Pyracantha coccinea* fruits, broad bands belonging to the amorphous structure were observed instead of the characteristic peaks specific to iron oxide nanoparticles [29].

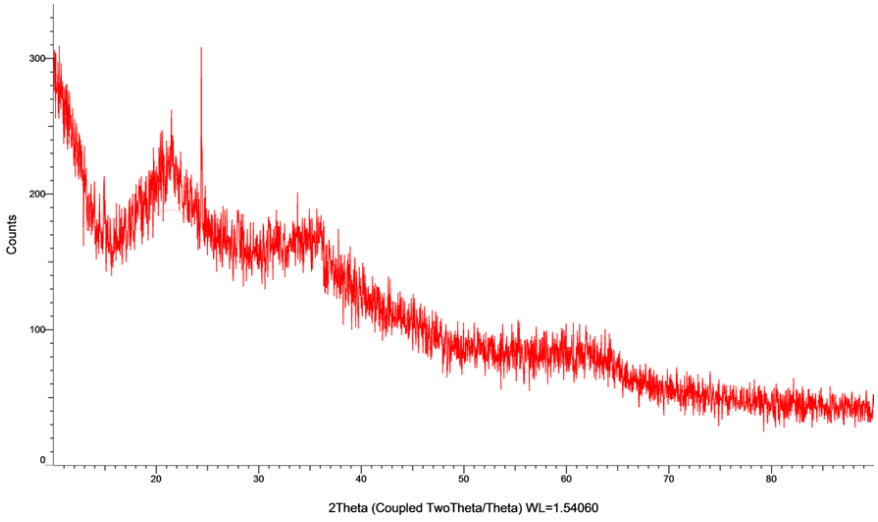

Figure 5. XRD diffraction pattern of the FeONPs

Similarly, the XRD patterns of iron nanoparticles synthesized using mango leaves, neem leaves, clove buds and rose leaves showed well-defined characteristic peaks of Fe_3O_4 together with α-Fe. However, in the nanoparticles produced using ajwain (carom) seeds, which served as the only fruit-derived source in that study, only a single weak peak was observed. This indicated a very low degree of crystallinity and the formation of a typical biosynthesized

amorphous structure due to the capping effect of biopolymers [36]. In the literature, there is evidence that iron nanoparticles synthesized not only from plant extracts derived from leaves, seeds or flowers [37-38], but also from fruit extracts, may exhibit an amorphous structure. For example, the XRD pattern of iron nanoparticles synthesized using an extract obtained from the fruit of *Dipteryx alata* Vogel displayed an amorphous character [39]. The findings suggest that crystal nucleation may be restricted due to the presence of rich biopolymer structures in the fruit extracts, which could have a negative impact on crystallization.

The amorphous structure detected in this study may be related to the presence of various biologically active components in fruit extracts, including flavonoids, phenolic acids, carbohydrates, proteins and organic acids. These compounds may participate in the reduction of iron ions and simultaneously function as surface-stabilizing agents, potentially limiting nucleus growth and hindering the complete development of a crystalline structure.

2. Dye Adsorption Studies

The residual dye concentrations in solutions at different initial methylene blue (MB) concentrations were quantified, and the percentage adsorption values were calculated for both the nanoparticle and the fruit-powder adsorbents (Figure 6A, B).

In the methylene blue (MB) adsorption experiments, the percentage adsorption values of FeONPs (1.25, 2.5, and 5.0 g/L) and fruit powder (FrP) (5.0, 10.0, and 20.0 g/L) exhibited a similar trend at low dye concentrations (2.5–40 mg/L), despite differences in adsorbent dosage. In both adsorbent substances, high adsorption efficiencies were obtained within this concentration range; adsorption reached over 97% for the FeONP, while the FrP showed values ranging from 96.4% to 99.82%. The FrP achieved almost complete removal at high adsorbent concentrations, such as 10 and 20 g/L, whereas similarly high efficiencies were obtained with the FeONPs at much lower concentrations (particularly 2.5 and 5.0 g/L). This observation is related to the higher active surface area per unit mass of the nanoparticles. At low initial concentrations, the equilibrium concentrations measured for both the FeONPs and the FrP were close to zero. The results shows that the available active surface area in the system was sufficient to completely retain the dye molecules. It also shows that increasing the amount of adsorbent provided only a limited improvement within this range. Similarly, Padmavathy et al. [40] reported that the adsorption efficiency showed only very limited variation at low initial concentrations, and that this was due to the active surface sites being

already used effectively. This result is also similar to the limited variation observed at different adsorbent concentrations in the present study; since the system did not reach surface saturation within the low concentration range, increasing the adsorbent concentration did not produce a noticeable difference in the adsorption efficiency. At moderate initial methylene blue concentrations of 100 and 250 mg/L, the lowest adsorption efficiency in the FeONP system was observed at the 1.25 g/L adsorbent concentration. At this concentration, the %Ads value was 96.61% at the 100 mg/L initial level, decreasing to 90.67% at 250 mg/L. In contrast, increasing the adsorbent concentration to 5 g/L enhanced the removal performance, yielding 94.73% adsorption at 250 mg/L. In the FrP system, at the same initial dye concentrations, the lowest value at 100 mg/L was 98.65% at 5 g/L adsorbent concentration, while the highest removal rate at 250 mg/L reached 99.63%.

The obtained results showed that by increasing the adsorbent concentration in both the FeONP and FrP systems, it is possible to maintain the adsorption capacity at moderate initial concentrations. This may be due to the increased availability of active surface sites. The result conforms with observations reported in the literature [41]. The correlation between the number of active sites and the progression of adsorption is supported by kinetic models [42]. At high initial dye concentrations (500–1000 mg/L), the amount of adsorbent used becomes the main factor affecting the adsorption performance of both the FeONP and FrP systems. In the nanoparticles, the adsorption efficiency remained at 60.68% at 500 mg/L and 55.91% at 1000 mg/L when an adsorbent amount of 1.25 g/L was used; however, increasing the amount to 5.0 g/L enhanced the efficiency to 90.26% and 93.00%, respectively. Similarly, in the FrP, the efficiency was measured as 87.47% at 500 mg/L and 67.00% at 1000 mg/L with an adsorbent amount of 5 g/L, and increasing the amount to 20 g/L improved these values to 91.08% and 75.43%, respectively. These findings indicate that, at high initial concentrations, where the amount of dye in the solution is high relative to the active surface regions, the adsorbent surface approaches saturation, and that this effect can be partially balanced by the wide surface area provided by the increased adsorbent amount. This mechanism is also consistent with the Langmuir [43] isotherm approach, which describes the tendency toward saturation in the presence of a limited number of active sites. The situation is also supported by the Q_e values. At the lowest adsorbent amounts, the Q_e values for the FeONPs reached quite high capacities, with 77.29 mg/g at an initial concentration of 100 mg/L, 181.34 mg/g at 250 mg/L, 242.74 mg/g at 500 mg/L, and 447.27 mg/g at 1000 mg/L. In contrast, in the fruit powder, the Q_e values at the lowest adsorbent amounts were lower at the same initial concentrations, occurring at 19.73 mg/g, 49.40 mg/g, 87.47 mg/g, and 134.00 mg/g, respectively. This difference arises from

the fact that the nanoparticles, due to their high specific surface area and fine morphology containing more active sites, can bind far more dye molecules per unit adsorbent [44]. When the Q_e values are taken as the basis, they provide a clear superiority compared to the fruit powder, offering 3–4 times higher adsorption capacity particularly at moderate and high initial concentrations such as 250–1000 mg/L. Comparable proportional differences were also obtained at the other adsorbent amounts.

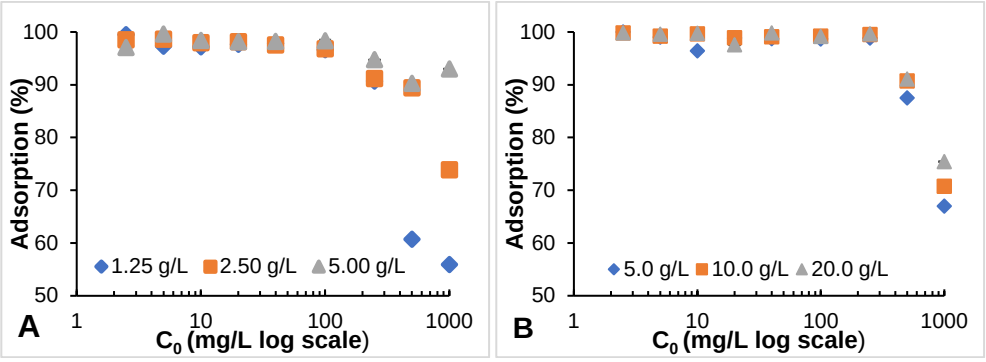

Figure 6. MB adsorption at different concentrations: (A) FeONPs, (B) FrP.

Malachite green (MG) aqueous dye solutions with various initial concentrations (2.5, 5.0, 10.0, 50.0, 100.0, and 250.0 mg/L) were exposed to three different amounts of FeONPs (1.25, 2.5, and 5 g/L) and FrP of *R. pseudoacacia* (5.0, 10.0, and 20.0 g/L) used as adsorbents for a period of 12 hours. After completion of the process, the residual dye concentration (C_e) and adsorption efficiency (% Ads.) in the solution were calculated (Figure 7A, B). In the adsorption of malachite green (MG), both FeONPs and FrP exhibited high removal efficiencies at low initial dye concentrations (2.5–10 mg/L), ranging from 94.70% to 99.99%. In this concentration range, a distinct concentration-dependent difference in performance was observed for the FrP, and the adsorption efficiency remained consistently above 99% at an adsorbent concentration of 20 g/L. These results indicate that, at low dye concentrations, both systems possess sufficient active surface sites, allowing adsorption to proceed without reaching surface saturation. As the initial concentration increased, differences in removal efficiency among the adsorbent concentrations became more noticeable. For example, at 250 mg/L MG, FeONPs achieved 90.30% removal at an adsorbent concentration of 1.25 g/L, whereas increasing the adsorbent concentration to 5 g/L enhanced the removal efficiency to 98.93%. Similarly, for the FrP, 5 g/L adsorbent provided 95.06% removal at

250 mg/L MG, while 20 g/L resulted in a markedly higher efficiency of 99.66%. These point to the fact that increasing the adsorbent concentration significantly improves the adsorption performance under high pollutant loads by increasing the overall surface area and the availability of active binding sites [42,45]. Malachite green (MG) exhibited adsorption performance similar to methylene blue (MB). The Q_e values calculated for the iron nanoparticles were higher than those of the fruit powder at all adsorbent concentrations. Furthermore, as observed for MB, the Q_e values decreased with increasing adsorbent concentration. For instance, at an initial MG concentration of 250 mg/L, the Q_e values for the iron nanoparticles were determined to be 180.60, 96.65, and 49.47 at adsorbent concentrations of 1.25, 2.50, and 5.00 g/L, respectively. In contrast, under the same conditions, the corresponding Q_e values for the fruit powder were calculated as 47.53, 24.34, and 12.46, respectively. At low adsorbent concentrations, the dye molecules present in the solution are required to bind to a limited density of active surface sites. Therefore, a larger amount of dye is adsorbed per unit mass of the adsorbent. As the adsorbent concentration increases, the dye molecules have access to a larger surface area; however, since the total amount of dye in the solution remains constant, some of the available active sites remain unused. Consequently, less dye is adsorbed per unit mass of the adsorbent, resulting in lower Q_e values.

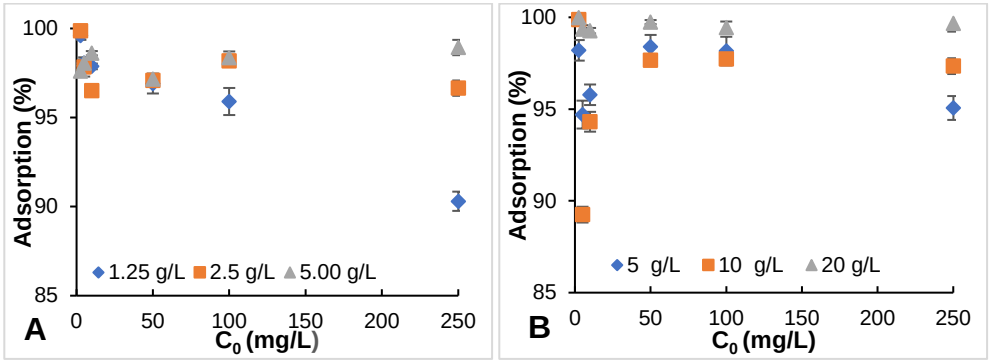

Figure 7. MG adsorption at different concentrations: (A) FeONPs, (B) FrP.

In the removal of another dye, phenol red (PR), adsorption tests were carried out with solutions at initial concentrations ranging from C_0 = 2.50 to 250.00 mg/L and FeONP adsorbent concentrations of 1.50, 2.00, and 5.00 g/L. The adsorption performance was evaluated in terms of equilibrium concentrations (C_e) and % adsorption (Figure 8A, B).

At an initial dye concentration of 2.5 mg/L, methylene blue (MB) and malachite green (MG) exhibited high removal efficiencies in the range of 95–99% using fruit-derived FeONPs at an adsorbent dose of 1.25 g/L, whereas phenol red (PR) showed a comparatively limited adsorption performance of 89.38% even at a higher FeONP dose of 1.50 g/L at the same initial concentration. However, while holding the initial dye concentration (2.5 mg/L) constant, increasing the adsorbent amount to 2.00 and 5.00 g/L resulted in a substantial enhancement of PR removal, with efficiencies reaching 98.81% and 98.87%, respectively. These findings suggest that PR adsorption is more sensitive to the amount of adsorbent at low levels than the other dyes, and that high removal efficiencies are attainable only when an adequate surface area is available. When the dye concentration ranged between 5 and 250 mg/L, a gradual decrease in PR removal efficiency was observed at an adsorbent amount of 1.50 g/L. At an adsorbent amount of 1.50 g/L, the adsorption efficiency was 86.93% at 5 mg/L and progressively declined with increasing concentration, reaching 68.81% at 250 mg/L. Similarly, at an adsorbent amount of 2.00 g/L, PR removal efficiency generally decreased with increasing initial dye concentration, declining from 89.24% at 5 mg/L to 82.46% at 250 mg/L. In contrast, at an adsorbent amount of 5.00 g/L, the system exhibited enhanced stability against increasing dye concentration, maintaining efficiencies above 91.50% up to 100 mg/L before decreasing to 83.67% at 250 mg/L. These results indicate that, particularly at lower adsorbent amounts, increasing the initial dye concentration facilitates surface saturation, whereas at higher adsorbent amounts this effect is partially offset by the increased availability of active surface area. By contrast, at a low initial PR dye concentration (C_0 = 2.5 mg/L), removal efficiencies above 95% were achieved nearly at all adsorbent amounts, except for the lowest FeONP dose (1.50 g/L), indicating that surface saturation was not reached under low adsorbate-to-adsorbent ratio conditions. It was observed that increasing the initial concentration generally led to a decrease in removal efficiency. In particular, for the FrP, at an adsorbent amount of 10 g/L, the lower removal values observed at initial concentrations of 5 and 10 mg/L (35.64% and 18.94%, respectively) deviated from the general concentration–efficiency relationship. However, the systematic decreasing trend was preserved in the other dose and concentration combinations. For example, at an initial concentration of 100 mg/L, the removal efficiencies at 5, 10, and 20 g/L were determined as 57.87%, 76.94%, and 58.94%, respectively; when the initial concentration was increased to 250 mg/L, these values decreased to 20.25%, 35.02%, and 51.53%. These results indicate that increasing dye concentration limits removal performance at all doses, and that although increasing the adsorbent dose at higher concentrations provides a partial improvement, the efficiency levels observed at lower concentrations could not be achieved.

The Q_e values calculated for phenol red were higher for the FeONP adsorbent than for the FrP, similar to the results obtained for the other two dyes examined in this study. Furthermore, a systematic decrease in Q_e values was observed with increasing adsorbent dosage. The Q_e values calculated for an initial dye concentration of 250 mg/L and FeONP adsorbent concentrations of 1.5, 2.0 and 5.0 g/L were found to be 114.69, 103.07 and 41.83 mg/g respectively. At the same initial dye concentration, the Q_e values for the FrP at adsorbent dosages of 5.0, 10.0, and 20.0 g/L were 10.13, 8.75, and 6.44 mg/g. The decrease in Q_e values observed with increasing adsorbent concentration, as noted for the other dyes, can be explained by reduction in adsorption capacity per unit mass resulting from the increase in adsorbent amount at a fixed initial concentration.

When the adsorption capacities (Q_e) are considered, the overall performance of the dyes followed the order MB> MG > PR. These results can be partly explained by the chemical structures of the dye molecules and the possible influence of solution pH on the adsorption process. The natural pH values of the dye solutions used in the study were measured and determined as 4.88 for MB, 3.02 for MG, and 3.76 for PR. The relatively less acidic pH of the MB solution could be one of the factors influencing its higher observed adsorption efficiency. However, no pH-controlled experiments were performed. Under such pH conditions, the adsorbent surface may become more negatively charged, which may enhance electrostatic attraction toward cationic dyes. Similarly, higher pH values increase the negative charge on the adsorbent surface and favor the adsorption of positively charged molecules [46]. In addition, the pH-dependent protonation of nitrogen and sulfur groups may modulate dye–surface interactions; under acidic conditions, their protonated forms can also contribute to adsorption through electrostatic attraction and hydrogen bonding [47]. The relatively lower adsorption performance of MG and PR may be associated with differences in their molecular structures and their behavior under the studied solution conditions.

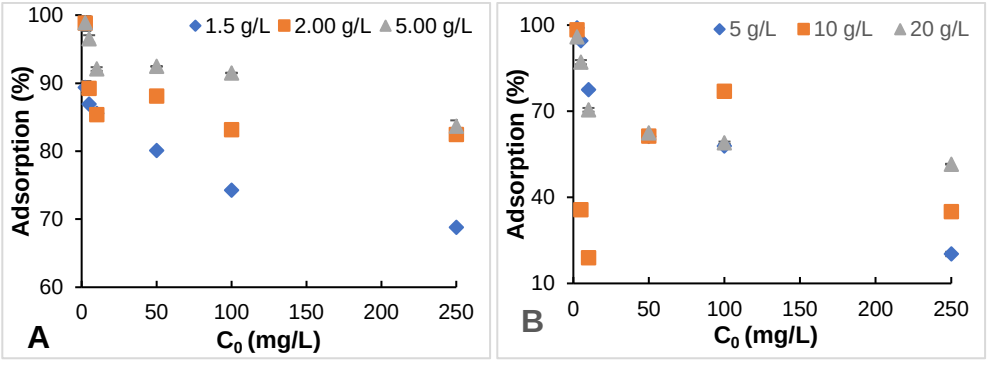

Figure 8. PR adsorption at different concentrations: (A) FeONPs, (B) FrP.

CONCLUSION

Iron oxide nanoparticles (FeONPs) were produced through green synthesis using *R. pseudoacacia* fruit extract and investigated by UV–Vis, XRD, FTIR, TEM, and EDX techniques. The obtained data indicated the successful synthesis of amorphous FeONPs with particle sizes in the nanoscale range. The adsorption performance of synthesized FeONPs and FrP was comparatively investigated for malachite green (MG), phenol red (PR), and methylene blue (MB). The results of the study showed that the adsorption capacity ranking was MB > MG > PR. FeONPs exhibited higher Q_e values in all dye systems in comparison to fruit powder. Efficient removal of the dye was observed at low and medium initial concentrations, with an increase in the amount of adsorbent resulting in an enhancement of the total removal process. However, this was associated with a reduction in the adsorption capacity per unit mass. Biosynthesized FeONP may serve as a sustainable, economical, and efficient adsorbent for dye removal, thereby representing a significant alternative in advanced environmental treatment technologies.

EXPERIMENTAL SECTION

1. Sampling

The fruits of *R. pseudoacacia* trees cultivated for landscaping purposes in the Eskibağlar Neighborhood of Gümüşhane Province, Türkiye, were collected in September 2023.

2. Preparation of Fruit Extracts

The fruits of the plant were dried at room temperature in an environment protected from sunlight and subsequently pulverized into a fine powder with a blender. The entire fruit (legume pod), including both the pericarp and the enclosed seeds, was used without any prior separation. A total of 1.1 kg of this powder was transferred into a 20-L container along with 10 L of distilled water. The mixture was boiled in a closed vessel for 2.5 hours and then allowed to cool to room temperature. After the formation of the extract, the mixture was separated using sieves with pore sizes of 1.00, 0.50, and 0.25 mm. The dry matter content of the resulting extract was then determined to be 4.00% ± 0.25 using a digital refractometer (Hanna HI96801). The extract was concentrated in a vacuum evaporator at 60 °C and 150 mbar to obtain a dry matter content of 10% [29].

3. Synthesis of Iron Oxide Nanoparticles (FeONPs)

For the green synthesis of FeONPs from *R. pseudoacacia* fruit samples, solutions containing iron(III) and iron(II) ions were prepared. For this purpose, 125 mL of a 0.2 M Fe^{3+} solution was prepared using $FeCl_3 \cdot 6H_2O$ salt. Additionally, 3.8 g of $FeSO_4$ was weighed to obtain 125 mL of a 0.1 M Fe^{2+} solution, and both substances were dissolved separately in beakers and then combined in a volumetric flask and made up to 250 mL. Then, 250 mL of *R. pseudoacacia* fruit extract (FE) with a 10% dry matter content was added to a 600-mL beaker. Using a pH meter (OHAUS Starter 3000), The pH value was then adjusted to 10 by gradually dropping 1.0 M NaOH into the solution. Following this, the solution was stirred on a magnetic stirrer (750 rpm), and the Fe^{2+}/Fe^{3+} solution was added dropwise at a rate of one drop per second using a separatory funnel. This dropwise addition was completed in 60 minutes for the total volume of 250 mL. Then, the beaker was covered with a glass lid and stirred at 750 rpm for 2.5 hours [48-49]. The synthesis of FeONP was accompanied by a visible change in color of the reaction mixture, giving it a completely black appearance. The resulting FeONP solution was pipetted into eight 50 mL falcon centrifuge tubes and centrifuged at 4000 rpm using a NÜVE NF 800R centrifuge and this process was repeated three times. The precipitates were placed in pre-weighed glass Petri dishes and air-dried in a vacuum dryer at 60 °C for three hours, thereby completing the synthesis process [48-49].

4. Characterization of Iron Oxide Nanoparticles

UV–Vis spectroscopy was used to confirm the formation of FeONPs using a Shimadzu UV-1800 spectrophotometer (Kyoto, Japan) within the wavelength range of 200–800 nm. To evaluate the chemical structure of the nanoparticles obtained from the *R. pseudoacacia* fruit extract (FE), Fourier Transform Infrared Spectroscopy (FTIR) analysis was performed on both the nanoparticles and the plant extract used in the synthesis. The analyses were performed using a PerkinElmer FT-IR spectrophotometer (model: UATR Two) at the Gümüşhane University Central Research Laboratory Application and Research Center, within the wavenumber range of 4000–450 cm^{-1}.

Structural characterization of the FeONPs was performed using X-ray diffraction (XRD). The measurements were performed using a Bruker D8 DISCOVER instrument at the Bayburt University Central Research Laboratory. A copper (Cu) anode served as the X-ray source, operated at 40 kV and 40 mA. Diffraction patterns were recorded over the 2θ range of 10°–80°.

The morphological and elemental characteristics of the synthesized FeONPs were examined using a transmission electron microscope (TEM) at

the Bayburt University Central Research Laboratory. The analyses were carried out with a Thermo Fisher Scientific Talos F200S TEM operated at 200 kV. Elemental composition was determined using an energy-dispersive X-ray spectroscopy (EDX) system attached to the TEM. The scale bars in the TEM images were generated by the instrument software.

5. Adsorption of Dyes

Green-synthesized FeONPs and *R. pseudoacacia* fruit powder (FrP) were used, and stock solutions of each dye (malachite green, MG; methylene blue, MB and phenol red, PR) were prepared at a concentration of 2500.0 mg/L. From these stock solutions, defined volumes were taken and diluted with deionized water to obtain seven different dye solutions at concentrations of 2.5, 5.0, 10.0, 20.0, 40.0, 100.0 and 250.0 mg/L for MG and PR, and nine solutions for MB by additionally preparing 500.0 and 1000.0 mg/L concentrations. The original pH values of each prepared dye solution (MB at pH 4.88, MG at pH 3.02, and PR at pH 3.76) were measured. To perform the adsorption tests, 0.0125, 0.025 and 0.050 g of FeONPs were placed into polypropylene (PP) tubes, to which 10 mL of the dye solutions were added. Accordingly, the concentrations of the adsorbent suspensions were set to 1.25, 2.50 and 5.00 g/L. Then, blank sampling was carried out by adding 10 mL of deionized water to 0.050 g and 0.100 g of FeONPs. For phenol red (PR), preliminary trials showed that the lowest FeONP suspension concentration (1.25 g/L) resulted in insufficient dye removal; therefore, slightly higher doses (1.50 and 2.00 g/L), in addition to 5.00 g/L, were adopted to ensure measurable adsorption. For FrP, higher adsorbent doses (5, 10 and 20 g/L) were employed because the powdered *R. pseudoacacia* fruits exhibited noticeably lower adsorption capacity compared with the FeONPs. The samples were shaken on an orbital shaker at 50 rpm for 12 h and then centrifuged at 5000 rpm for 15 min to separate the solid and liquid phases. The residual dye concentrations in the supernatants obtained after centrifugation were analyzed using a UV–Vis spectrophotometer [30,50]. The spectral profile of methylene blue was evaluated by scanning a 5.0 mg/L solution between 200 and 1000 nm using the spectrophotometer, which clearly showed a distinct absorption maximum at 664 nm. For quantitative calibration, standard solutions prepared at 1.0, 2.5, 5.0, 10.0 and 25.0 mg/L were analyzed, and the resulting measurements were used to generate a linear calibration curve described by $y = 0.1477x + 0.0422$, with an R^2 value of 0.999. In addition to the measurements reported for methylene blue, the same wavelength-scanning and calibration procedure was applied to malachite green and phenol red. Malachite green displayed its absorption maximum at 617 nm, and the calibration curve obtained from its standard solutions was described by $y = 0.353x - 0.0114$

(R^2 = 0.998). Phenol red exhibited a maximum absorbance at 430 nm, with a corresponding calibration relationship expressed as y = 0.0248x − 0.0038. In this study, the residual dye concentration in the solution (C_e) was determined from the UV–Vis absorbance data for the calculation of dye adsorption onto FeONPs. Adsorption efficiency (%) and adsorption capacity per unit mass of adsorbent (Q_e, mg/g) were calculated. All tests were repeated at least three times, and the results are reported as mean ± standard deviation. All necessary calculations were carried out using the formulas presented below (Equations 1–3) [30,50].

$$Remaining\ dye\ \left(\frac{mg}{L}\right) = (A - B)/E \quad (1)$$

Equation 1 defines A as the recorded signal intensity, with B serving as the intercept and E representing the slope of the calibration graph. The % adsorption was determined using Equation 2.

$$Adsorption\ Percentage = ((C_0 - C_e)/C_0)\ x\ 100 \quad (2)$$

According to Equation 2, C_0 (mg/L) refers to the initial dye level, while Ce (mg/L) indicates the residual concentration in the equilibrium phase. Using the dye concentration remaining in the solution phase (C_e), the amount of dye taken up by 1 g of FeONP (mg/g) was determined according to Equation 3.

$$Q_e = ((C_0 - C_e)\ x\ V)/m \quad (3)$$

In Equation 3, V represents the volume of the adsorbate solution (L), m indicates the mass of the adsorbent (g), Q_e denotes the amount of adsorbate adsorbed per gram of FeONPs (mg/g), C_0 refers to the initial dye concentration (mg/L), and C_e represents the equilibrium dye concentration (mg/L).

REFERENCES

1. Alengebawy, A.; Abdelkhalek, S. T.; Qureshi, S. R.; Wang, M. Q. *Toxics* **2021**, 9 (3), 42.
2. Kumar, A.; Bisht, B. S.; Joshi, V. D.; Dhewa, T. *Int. J. Environ. Sci.* **2011**, 1 (6), 1079–1093.
3. Çınar Acar, B.; Yüksekdağ, Z. *OKU J. Inst. Sci. Technol.* **2023**, 6 (1), 1006–1029.
4. Tziourrou, P.; Golia, E. E. Soil Syst. 2025, 9 (4), 137.
5. Beni, A. A.; Jabbari, H. Results Eng. 2022, 15, 100467.
6. Kulkarni, A. G.; De Britto, S.; Jogaiah, S. Economic considerations and limitations of green synthesis vs chemical synthesis of nanomaterials. In *Advances in Nano-fertilizers and Nano-pesticides in Agriculture*; Woodhead Publishing: Cambridge, UK, **2021**; pp. 459–468.

7. Mutaf, T.; Çalışkan, G.; Öncel, S. Ş.; Elibol, M. *Ege J. Fish. Aquat. Sci.* **2023**, 40 (1), 81–89.
8. Ying, S.; Guan, Z.; Ofoegbu, P. C.; Clubb, P.; Rico, C.; He, F.; Hong, J. *Environ. Technol. Innov.* **2022**, 26, 102336.
9. Hussain, A.; Lakhan, M. N.; Hanan, A.; Soomro, I. A.; Ahmed, M.; Bibi, F.; Zehra, I. *Mater. Today Sustain.* **2023**, 100420.
10. Akar, B.; Baltacı, C.; Düzgün, A. Ö.; Karpuz, O.; Karakullukcu, V.; Erdoğdu, E. G. *Environ. Eng. Manag. J.* **2025**, 24 (5), 1013–1025.
11. Yakut, Ş. M.; Karataş, M. *Duzce Univ. J. Sci. Technol.* **2021**, 9, 1267–1281.
12. Bukhari, A.; Ijaz, I.; Gilani, E.; Nazir, A.; Zain, H.; Saeed, R.; Naseer, Y. Coatings 2021, 11 (11), 1374.
13. Coelho, L. M.; Rezende, H. C.; Coelho, L. M.; de Sousa, P. A.; Melo, D. F.; Coelho, M. N. Bioremediation of polluted waters using microorganisms. In *Advances in Bioremediation of Wastewater and Polluted Soil*; IntechOpen: Rijeka, Croatia, **2015**; Vol. 10, pp. 2–15.
14. Ihsanullah, I.; Jamal, A.; Ilyas, M.; Zubair, M.; Khan, G.; Atieh, M. A. *J. Water Process Eng.* **2020**, 38, 101680.
15. Mihai, S.; Bondarev, A.; Necula, M. *Processes* **2025**, 13 (2), 589.
16. Arslan, E. S. *Turk. J. For.* **2019**, 20 (2), 142–148.
17. Marinas, I. C.; Oprea, E.; Geana, E. I.; Chifiriuc, C.; Lazar, V. *J. Serb. Chem. Soc.* **2014**, 79 (11), 1363–1378.
18. Hosseinihashemi, S. K.; HosseinAshrafi, S. K.; Goldeh, A. J.; Salem, M. Z. *BioResources* **2016**, 11 (1), 1634–1646.
19. Aktürk, B. K.; Arslan Burnaz, N. *Chem. Biodivers.* **2025**, e00547.
20. Aydogan, T.; Dumanlı, F. T. Ş.; Derun, E. M. *J. Polytech.* **2022**, 25 (4), 1423–1427.
21. Pasieczna-Patkowska, S.; Cichy, M.; Flieger, J. *Molecules* **2025**, 30 (3), 684.
22. Abdullah, J. A. A.; Eddine, L. S.; Abderrhmane, B.; Alonso-González, M.; Guerrero, A.; Romero, A. *Sustain. Chem. Pharm.* **2020**, 17, 100280.
23. Losito, D. W.; Souza, N. I.; Martins, T. S.; Britos, T. N.; Schumacher, M. L.; Haddad, P. S. *J. Mater. Sci.* **2024**, 59 (34), 16038–16068.
24. Doan, L. *ChemEngineering* **2023**, 7 (5), 77.
25. Hussain, M.; Ceccarelli, R.; Marchisio, D. L.; Fino, D.; Russo, N.; Geobaldo, F. *Chem. Eng. J.* **2010**, 157 (1), 45–51.
26. Titus, D.; Samuel, E. J. J.; Roopan, S. M. Nanoparticle characterization techniques. In *Green Synthesis, Characterization and Applications of Nanoparticles*; Shukla, A. K.; Iravani, S., Eds.; Elsevier: Amsterdam, Netherlands, **2019**; pp. 303–319.
27. Winsett, J.; Moilanen, A.; Paudel, K.; Kamali, S.; Ding, K.; Cribb, W.; Neupane, S. *SN Appl. Sci.* **2019**, 1, 1–8.
28. Zambri, N. D. S.; Taib, N. I.; Abdul Latif, F.; Mohamed, Z. *Molecules* **2019**, 24 (20), 3803.
29. Karakullukçu, V.; Akar, B.; Baltacı, C.; Düzgün, A. Ö.; Karpuz, Ö. *Karaelmas Sci. Eng. J.* **2023**, 13 (2), 255–265.

30. Demirel, İ. T.; Akar, B.; Baltacı, C.; Karpuz, Ö.; Gülbahar, E. *J. Anatolian Environ. Anim. Sci.* **2024**, 9 (2), 174–183.
31. Jagathesan, G.; Rajiv, P. *Biocatal. Agric. Biotechnol.* **2018**, 13, 90–94.
32. Desalegn, B.; Megharaj, M.; Chen, Z.; Naidu, R. *Heliyon* **2019**, 5 (5).
33. Gautam, A.; Rawat, S.; Verma, L.; Singh, J.; Sikarwar, S.; Yadav, B. C.; Kalamdhad, A. S. *Environ. Nanotechnol. Monit. Manag.* **2018**, 10, 377–387.
34. Król-Gracz, A.; Michalak, E.; Nowak, P.; Dyonizy, A. *Open Chem.* **2011**, 9 (6), 982–989.
35. Da'na, E.; Taha, A.; Afkar, E. *Appl. Sci.* **2018**, 8 (10), 1922.
36. Afsheen, S.; Tahir, M. B.; Iqbal, T.; Liaqat, A.; Abrar, M. *J. Alloys Compd.* **2018**, 732, 935–944.
37. Kouhbanani, M. A. J.; Beheshtkhoo, N.; Taghizadeh, S.; Amani, A. M.; Alimardani, V. *Adv. Nat. Sci.: Nanosci. Nanotechnol.* **2019**, 10 (1), 015007.
38. Góral-Kowalczyk, M.; Grządka, E.; Orzeł, J.; Góral, D.; Skrzypek, T.; Kobus, Z.; Nawrocka, A. *Materials* **2024**, 17 (11), 2515.
39. Corrêa, C. R. R.; de Siqueira, A. B.; Matos Lopes, P. R.; Ambrosio, J. A. R.; Simioni, A. R.; de Vasconcelos, L. G.; Morais, E. B. *AQUA—Water Infrastruct. Ecosyst. Soc.* **2024**, 73 (4), 771–789.
40. Padmavathy, K. S.; Madhu, G.; Haseena, P. V. *Procedia Technol.* **2016**, 24, 585–594.
41. Vargas, A. M. M.; Cazetta, A. L.; Kunita, M. H.; Silva, T. L.; Almeida, V. C. *Chem. Eng. J.* **2011**, 168 (2), 722–730.
42. Ho, Y. S.; McKay, G. *Process Biochem.* **1999**, 34 (5), 451–465.
43. Langmuir, I. *J. Am. Chem. Soc.* **1918**, 40 (9), 1361–1403.
44. Mansour, A. T.; Alprol, A. E.; Ashour, M.; Ramadan, K. M.; Alhajji, A. H.; Abualnaja, K. M. *Gels* **2022**, 8 (5), 310.
45. Foo, K. Y.; Hameed, B. H. *Chem. Eng. J.* **2010**, 156 (1), 2–10.
46. Galloni, M. G.; Bortolotto, V.; Falletta, E.; Bianchi, C. L. *Polymers* **2022**, 14 (22), 4897.
47. Aziz, D. M.; Hassan, S. A.; Aziz, S. B.; Kader, D. A. *Next Mater.* **2025**, 9, 101015.
48. Yusefi, M.; Shameli, K.; Ali, R. R.; Pang, S. W.; Teow, S. Y. *J. Mol. Struct.* **2020**, 1204, 127539.
49. Gedikli, H.; Akdogan, A.; Karpuz, O.; Akmese, O.; Kobya, H. N.; Baltaci, C. *BioResources* **2024**, 19 (1), 380.
50. Bozbeyoglu, P.; Duran, C.; Baltaci, C.; Gundogdu, A. *Hittite J. Sci. Eng.* **2020**, 7 (3), 239–256.

STUDIA UBB CHEMIA, LXXI, 2, 2026 (p. 87-103)
(RECOMMENDED CITATION)
DOI:10.24193/subbchem.2026.2.05

APPARENT BIOACCESSIBILITY OF PHENOLIC COMPOUNDS AND LYCOPENE FROM TOMATO POMACE DURING STATIC *IN VITRO* DIGESTION

Vanda Liliana BĂBĂLĂU FUSS[a], Oana CADAR[a], Ancuța IVAN[a], Cristina BĂLGĂRĂDEAN[a], Lucian CUIBUS[b], Anca BECZE[a,*]

ABSTRACT. Tomato pomace, a major by-product of industrial tomato processing composed mainly of peels and seeds, represents a valuable source of bioactive compounds with potential nutraceutical applications. This study comparatively evaluated the apparent bioaccessibility of phenolic compounds and lycopene from tomato pomace using two distinct *in vitro* gastrointestinal digestion approaches: sequential phase sampling (R1) and cumulative digestion sampling (R2). A static digestion model including oral, gastric, and intestinal phases was applied to assess the release of bioactive compounds into digestive fluids. Total phenolic content was determined using the Folin–Ciocalteu method and expressed as gallic acid equivalents (GAE), while lycopene was quantified by UHPLC-DAD. Phenolic compounds showed the highest concentration in the oral phase (332.65±29.67 mg GAE L^{-1}), followed by the intestinal phase ((234.73±21.45 mg GAE L^{-1}), with the lowest value observed in the gastric phase (171.78±14.73 mg GAE L^{-1}). Lycopene bioaccessibility increased progressively during digestion, reaching 8.61% in the oral phase, 16.47% in the gastric phase, and 29.07% in the intestinal phase. The cumulative digestion fraction was lower (22.1%), suggesting partial degradation of lycopene and retention of carotenoids within the insoluble fiber fraction of the tomato pomace matrix. These results indicate that digestion conditions and matrix interactions significantly influence the release and apparent bioaccessibility of tomato-derived bioactive compounds.

Keywords: *Tomato pomace; phenolic compounds; lycopene; in vitro gastrointestinal digestion; bioaccessibility; food by-products.*

[a] *National Institute for Research and Development for Optoelectronics INOE 2000, Research Institute for Analytical Instrumentation, 67 Donath Str., RO-400293 Cluj-Napoca, Romania*
[b] *Faculty of Food Science and Technology, University of Agricultural Sciences and Veterinary Medicine, 400372, Cluj-Napoca, Romania*
* *Corresponding author: anca.naghiu@icia.ro*

INTRODUCTION

The tomato processing industry generates millions of tons of waste each year. Tomato pomace, the peels and seeds left after processing, makes up about 3–7% of the raw tomato weight. Typically discarded or used as low-value animal feed, this waste is now attracting growing interest as a promising source of valuable bioactive compounds. [1,2].

Tomato pomace contains two main types of health-promoting substances: phenolic compounds and lycopene. Phenolics, such as quercetin and rutin, have antioxidant and anti-inflammatory effects [3]. Lycopene, the pigment that gives tomatoes their distinctive red colour, has been associated with reduced risks of prostate cancer and cardiovascular disease [4]. Tomato peels are especially rich in lycopene, up to five times more than the pulp [5]. However, a critical limitation exists: simply having these bioactive compounds in food matrices does not ensure their physiological efficacy. Phenolic compounds and lycopene present fundamentally distinct physicochemical properties, phenolics are hydrophilic and readily soluble in aqueous environments, while lycopene is highly lipophilic and remains locked in the cellular structures of plants [6]. The determinant factor for health benefits is bioaccessibility, defined as the fraction of compounds released from the food matrix during digestion and made available for intestinal absorption [7,8]. The structural complexity of the food matrix has a profound influence: dietary fiber and proteins can form insoluble complexes with phenolics, while lycopene absorption requires the presence of lipids and emulsification by bile salts to facilitate micelle formation and subsequent uptake [9].

To study these processes without conducting clinical trials on humans, researchers use static *in vitro* digestion models. These systems replicate the physiological conditions of the human gastrointestinal tract, including appropriate pH gradients, enzymatic activities, and temporal dynamics, within a controlled and reproducible experimental setting [10,11]. The standardized INFOGEST protocol, originally developed by Minekus et al. [12] and later refined by Brodkorb et al. [13], has established itself as the internationally recognized gold standard methodology for such studies. Static *in vitro* digestion models, such as the INFOGEST protocol used in the present study, simulate gastrointestinal conditions using fixed experimental parameters including pH, enzyme activity, digestion time, and fluid composition. In contrast, dynamic digestion models continuously adjust these parameters during digestion and more closely reproduce physiological processes such as gradual gastric emptying, variable secretion rates, and peristaltic mixing. In the present work, only a static digestion model was applied, while dynamic digestion studies are discussed solely for comparative interpretation of the obtained results. Previous studies have shown distinct kinetic patterns for these bioactive

compounds. Phenolic compounds typically show high concentrations in the oral phase, decrease significantly under conditions of gastric acidity, and increase again during intestinal digestion [14,15]. In contrast, lycopene follows an inverse trajectory: initial concentrations remain low, followed by a progressive accumulation that reaches peak levels in the intestinal phase, where bile-mediated solubilization facilitates micelle formation and the release of the compound [16,17]. Although several studies have investigated either phenolic compounds or carotenoids individually during *in vitro* digestion, relatively few studies have simultaneously monitored hydrophilic and lipophilic bioactive compounds within the same tomato pomace matrix under standardized gastrointestinal conditions. Moreover, the methodological impact of sequential versus cumulative sampling strategies on apparent bioaccessibility estimates remains insufficiently explored. Since digestion sampling design may significantly influence the recovery and interpretation of matrix-bound compounds, a systematic comparison of these approaches is necessary for improving the reliability and comparability of *in vitro* digestion studies.

Therefore, this study aimed not only to evaluate the release kinetics of phenolic compounds and lycopene from tomato pomace during simulated gastrointestinal digestion, but also to systematically compare sequential (R1) and cumulative (R2) digestion protocols as methodological approaches for estimating apparent bioaccessibility.Using both sequential and cumulative sampling protocols, we monitored the apparent bioaccessibility profiles of these bioactive compounds, with distinct structures, throughout each digestive phase. The results contribute to a mechanistic understanding of the effects of the food matrix on nutrient availability and provide a scientific basis for the strategic utilization of byproducts resulting from tomato processing in functional food applications.

RESULTS AND DISCUSSION

Distribution of phenolic compounds during simulated gastrointestinal digestion

The initial total phenolic content of the undigested tomato pomace was 950 mg GAE/100g DW, while the initial lycopene content was 6.58 µg/g DW. These values were used as reference concentrations for calculating apparent bioaccessibility.

The release of phenolic compounds from tomato pomace during simulated gastrointestinal digestion was evaluated using two experimental protocols. In protocol R1, the supernatant was collected after each digestive phase, allowing the evaluation of phenolic compound distribution in the oral,

gastric, and intestinal fluids. In protocol R2, the digestion process was performed continuously without intermediate separation, and phenolic compounds were determined only in the final supernatant after complete digestion. This two-protocol approach remedies an important methodological gap identified in recent studies [18], as the choice between serial and cumulative sampling significantly influences estimates of apparent bioaccessibility and their biological relevance [19]. For protocol R1, the concentration of total phenolic compounds measured in the digestive fluids showed significant variation between phases. The highest concentration was observed in the oral phase (332.65±29.67 mg GAE/L), followed by the intestinal phase (234.73±21.45 mg GAE/L), while the gastric phase showed the lowest value (171.78±14.73 mg GAE/L) (Figure 1).

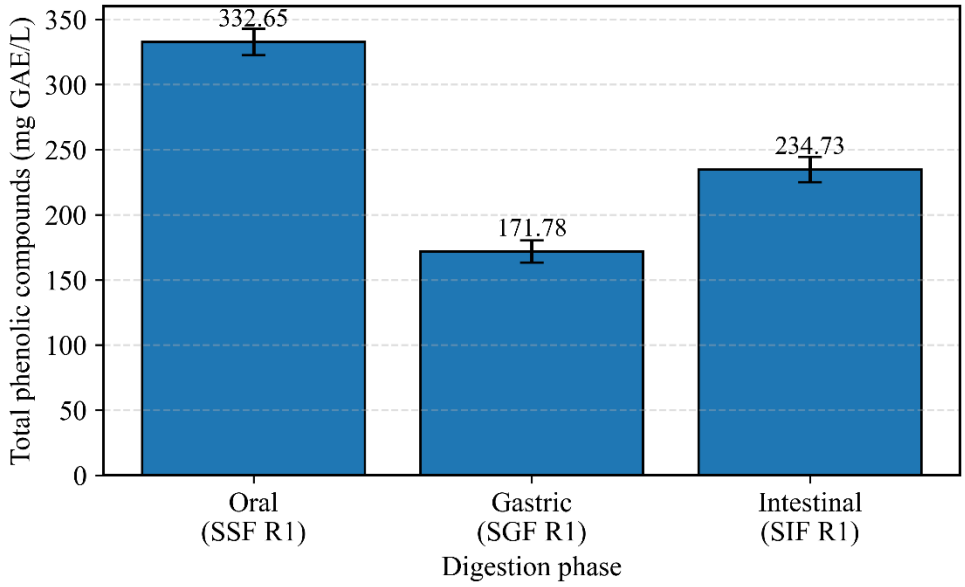

Figure 1. Concentration of total phenolic compounds released into the digestive supernatant during sequential *in vitro* digestion protocol R1. SSF, simulated salivary fluid; SGF, simulated gastric fluid; SIF, simulated intestinal fluid. Results are expressed as mg GAE/L. Error bars represent standard deviation of triplicate analyses.

One-way ANOVA indicated significant differences between digestion phases for total phenolic compounds ($p < 0.05$). The oral phase showed significantly higher phenolic release than the gastric phase, while the intestinal phase showed an intermediate recovery.

The peak observed during the oral phase is consistent with recent findings that surface phenolic compounds are rapidly released upon contact with saliva, before enzymes or acids break down the matrix [20, 21]. Similar patterns have been reported for anthocyanins in black carrots by Kamiloglu et al. [22] and for polyphenols in grapes by Tagliazucchi et al. [7], who also noted an initial rapid release followed by reassociation with the matrix. However, this early availability is short-lived, as phenolic compounds may be re-bound to fibers or degrade during longer incubation, a point that cumulative protocols often overlook [23], as demonstrated by Wang et al. [24] in studies on tomato waste.

The difference between our R1 and R2 results highlights the current debate regarding standards for digestion protocols. Recent studies conducted in multiple laboratories by Egger et al. [25] show that the timing of sample collection alone can alter apparent bioaccessibility estimates by 30–60% for matrix-bound polyphenols, confirming the concerns expressed by Carbonell-Capella et al. [26] regarding the choice of analytical methods. Our data suggest that the phenolic compounds in tomato pomace may behave as three functional fractions during digestion: a rapidly released fraction observed in the oral phase, a potentially reversibly bound fraction influenced by gastrointestinal conditions, and a fraction retained within the insoluble matrix residues. However, this interpretation should be considered a mechanistic hypothesis inferred from the digestion profiles and supported by literature describing polyphenol–fiber and polyphenol–protein interactions in plant-based matrices.

The distribution of phenolic compounds between the digestive phases was 45.0% in the oral phase, 23.2% in the gastric phase, and 31.8% in the intestinal phase. These results indicate that a considerable fraction of the phenolic compounds present in tomato pomace is rapidly released during the oral stage of digestion. This pattern mirrors findings by Kamiloglu et al. [27] for black carrot anthocyanins who similarly reported early-phase dominance due to rapid solubilization of surface-localized compounds. The high concentration observed in the oral phase suggests that a significant proportion of these compounds are present in a soluble form or are weakly bound to the plant cell structures consistent with the “labile fraction” concept described by Pérez-Jiménez and Saura-Calixto [28] for non-extractable polyphenols in fruits and vegetables.

Under neutral pH conditions and short incubation time, these compounds are readily transferred into the aqueous phase [29]. In contrast, the decrease in phenolic concentration observed during the gastric phase can be attributed to the acidic environment and potential interactions between phenolic compounds and structural components of the tomato pomace matrix. Similar gastric-phase drops were reported by Bouayed et al. [30] for apple

varieties. Tomato pomace contains considerable amounts of dietary fiber and residual proteins, which can bind phenolic compounds through hydrogen bonding or hydrophobic interactions. These interactions may limit the transfer of phenolic compounds into the liquid phase under gastric conditions, as demonstrated by Le Bourvellec and Renard [31] in their comprehensive review of polyphenol-macromolecule binding.

During the intestinal phase, the concentration of phenolic compounds increased again compared to the gastric phase. This increase may be explained by the higher pH and the presence of bile salts and pancreatic enzymes, which can destabilize interactions between phenolic compounds and the plant matrix. Consequently, phenolic compounds previously retained within the solid structure may be partially released into the digestive fluid, consistent with the “re-release” mechanism described by Jakobek [32] for polyphenol interactions with food matrices.

Phenolic Compounds after Complete Digestion

In protocol R2, phenolic compounds were determined only in the final supernatant after completion of the entire digestion process. The measured concentration was 63.92 mg GAE/L, considerably lower than the values obtained in individual digestive phases in protocol R1. This significant difference is similar to the findings of Pellegrini et al. [33], who reported similar differences between dynamic and static digestion of tomato waste, as well as to those of Fernández-Jalao et al. [34] in their meta-analysis of protocol variations. This difference can be explained primarily by the larger total volume of digestive fluids used in the cumulative digestion protocol, leading to dilution of phenolic compounds. Additionally, prolonged interaction between the liquid phase and the solid tomato pomace matrix may promote adsorption and retention of phenolic compounds within the fibrous structure as demonstrated by Elleuch et al. [35] for dietary fiber matrices. Tomato pomace is characterized by high contents of insoluble fiber and porous plant structures that can retain both digestive fluids and dissolved compounds. This retention effect, described by Saura-Calixto [36] as a key factor limiting polyphenol bioaccessibility from fiber-rich foods, can reduce the amount of phenolic compounds recovered in the supernatant after centrifugation, resulting in lower measured concentrations.

These results highlight the importance of the digestion protocol when evaluating the apparent bioaccessibility of phenolic compounds. However, R1 and R2 should not be interpreted as directly equivalent digestion outputs. The sequential protocol R1 describes the amount of phenolic compounds released into the supernatant after each individual digestive phase, while the cumulative protocol R2 represents the final soluble fraction recovered after

the complete digestion sequence without intermediate separation. Therefore, the comparison between R1 and R2 is used here to illustrate the methodological impact of sampling strategy on phenolic recovery, rather than to compare identical analytical endpoints. The lower value obtained for R2 may reflect dilution, prolonged contact with the insoluble matrix, re-adsorption of released phenolics, degradation, or incomplete recovery from the final supernatant. (Figure 2)

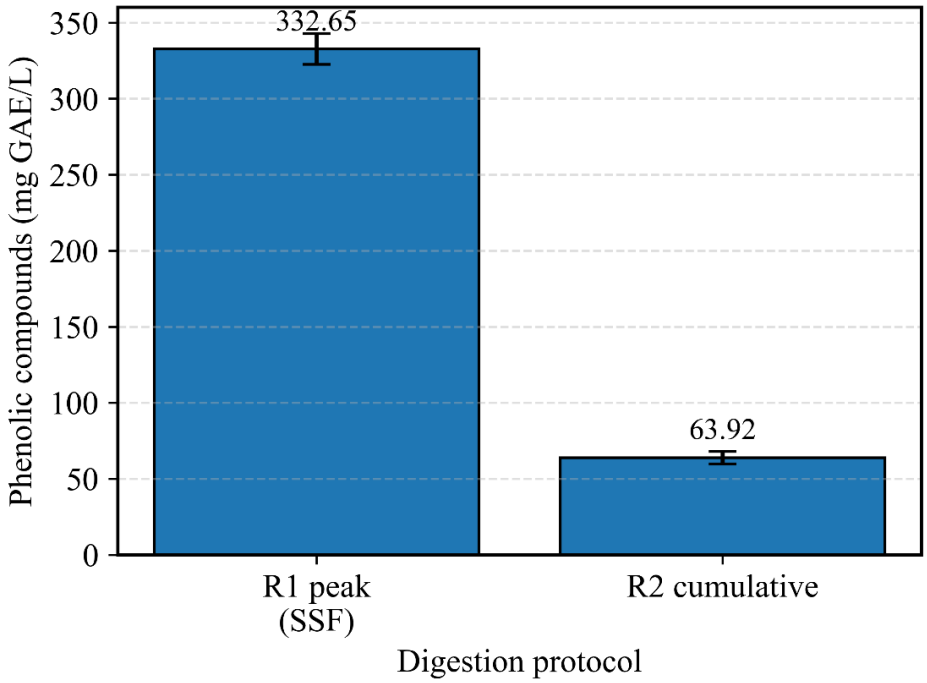

Figure 2. Comparison between sequential digestion protocol R1 and cumulative digestion protocol R2 for the release of total phenolic compounds from tomato pomace. Results are expressed as mg GAE/L in the recovered digestive supernatants. Error bars represent standard deviation of triplicate analyses.

The initial total phenolic content of the tomato pomace was 950 mg GAE/100 g DW. Based on this value, the apparent bioaccessibility of phenolic compounds released during simulated gastrointestinal digestion was calculated relative to the initial amount present in the undigested sample. (Tabel 1)

Table 1. Apparent bioaccessibility of phenolic compounds from tomato pomace during simulated gastrointestinal digestion

Digestion phase	Concentration in supernatant (mg GAE/L)	Digestion volume (mL)	Released phenolics (mg GAE)	Apparent bioaccessibility (%)
Oral phase (SSF R1)	332.65	2.5	0.832	17.5
Gastric phase (SGF R1)	171.78	2.5	0.429	9.0
Intestinal phase (SIF R1)	234.73	2.5	0.587	12.4
Cumulative digestion (R2)	63.92	17.5	1.119	23.6

The oral phase exhibited the highest apparent bioaccessibility (17.5%), followed by the intestinal phase (12.4%), while the gastric phase showed the lowest value (9.0%). In contrast, the cumulative digestion protocol (R2) resulted in a total apparent bioaccessibility of 23.6%, reflecting the overall soluble phenolic fraction remaining after prolonged interaction with the digestive matrix. These results indicate that the digestion protocol and sampling strategy significantly influence the estimation of phenolic compound release and apparent bioaccessibility from tomato pomace.

In vitro bioaccessibility of lycopene

The *in vitro* gastrointestinal digestion experiment revealed a gradual increase in lycopene release across the simulated digestion phases. The initial oral phase resulted in relatively low bioaccessibility of 8.61%, corresponding to approximately 0.57 μg g^{-1} released lycopene based on the average concentration determined in the samples (6.58 μg g^{-1} DW). This limited release aligns with findings by Reboul and Borel [37] who demonstrated that carotenoids remain largely sequestered within chromoplast structures and are poorly solubilized under neutral aqueous conditions of the oral environment. During the gastric phase, lycopene bioaccessibility increased to 16.47% (approximately 1.08 μg g^{-1}). The acidic conditions and mechanical agitation promote partial disruption of cellular structures and protein–carotenoid complexes, facilitating the release of lipophilic compounds from the tomato matrix (Figure 3), consistent with mechanisms described by Fernández-García et al. [38] for carotenoid apparent bioaccessibility from plant foods. Notably, this gastric-phase increment remains modest compared to intestinal values, reflecting the inherent limitation of aqueous acidic environments for solubilizing highly lipophilic compounds without lipid co-components or bile-mediated emulsification [39].

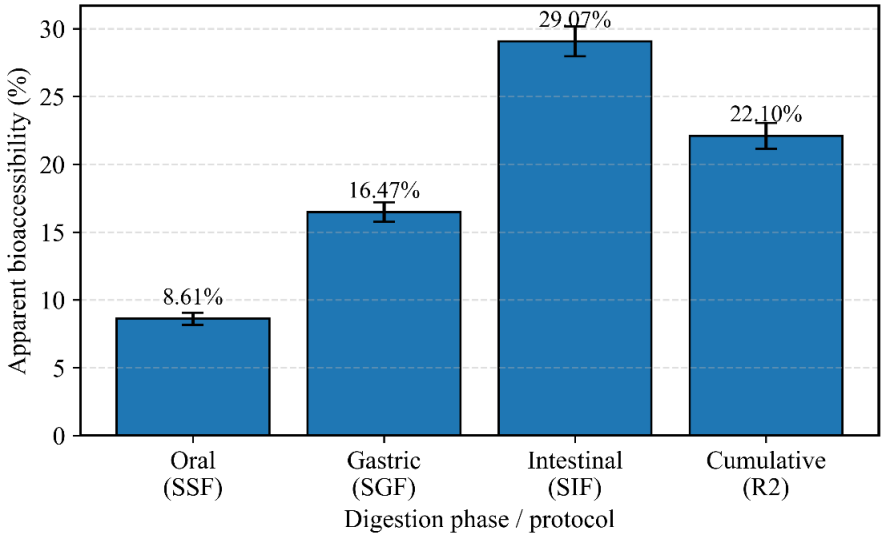

Figure 3. Apparent bioaccessibility of lycopene from tomato pomace during simulated *in vitro* gastrointestinal digestion. Values are expressed as percentage of the initial lycopene content in the undigested tomato pomace. Error bars represent standard deviation of triplicate analyses.

The highest bioaccessibility was observed during the intestinal phase, reaching 29.07%, equivalent to approximately 1.91 μg g^{-1} lycopene released from the tomato pomace matrix. In addition to micellar solubilization, digestive conditions may also induce structural changes in lycopene. Lycopene occurs predominantly as the all-trans isomer in raw tomato matrices, but thermal processing, acidic pH, bile salts, digestive enzymes, and prolonged incubation may promote partial trans-to-cis isomerization. This aspect is relevant because cis-isomers generally present higher solubility in lipid phases and may be more efficiently incorporated into mixed micelles than the all-trans form [6, 8]. Therefore, the increase observed during the intestinal phase may reflect not only the release of lycopene from the tomato pomace matrix, but also changes in isomeric profile that favor micellar incorporation. At the same time, lycopene is highly susceptible to oxidative degradation due to its conjugated double-bond structure. Exposure to oxygen, light, acidic conditions, and digestive incubation may contribute to partial degradation or loss of recoverable lycopene [38]. These processes may partly explain why the cumulative bioaccessibility value was lower than the maximum intestinal-phase value. One-way ANOVA also indicated significant differences in lycopene apparent bioaccessibility between digestion phases ($p < 0.05$), with the intestinal phase showing the highest bioaccessibility.

This increase is consistent with the presence of bile salts and digestive enzymes in the intestinal environment, which promote the formation of mixed micelles necessary for the solubilization and potential absorption of carotenoids. Interestingly, the overall cumulative bioaccessibility calculated across the digestion process was lower (22.1%) than the maximum value observed during the intestinal phase. This apparent decrease may be attributed to several factors, including oxidative degradation of lycopene during digestion, possible trans-to-cis isomerization followed by differential recovery of isomers, adsorption of carotenoids onto insoluble dietary fiber fractions, or losses during sample processing and phase separation [39,]. Similar discrepancies between phase-specific and cumulative recovery were reported by Corte-Real et al. [40]. Tomato pomace contains significant levels of dietary fiber and insoluble polysaccharides, which can retain lipophilic compounds within the solid fraction and limit their transfer to the micellar phase, as demonstrated by Saura-Calixto [36]. These findings are consistent with previously reported values for tomato matrices, where lycopene bioaccessibility typically ranges between 10 and 35%, depending on processing conditions, matrix structure, and lipid content. The presence of endogenous lipids from tomato seeds, particularly unsaturated fatty acids such as linoleic and oleic acids, may contribute to micelle formation and thus enhance carotenoid solubilization during the intestinal phase, consistent with the lipid effect described by Brown et al. [41] and Roodenburg et al. [42] for carotenoid absorption.

CONCLUSIONS

This study evaluated the apparent bioaccessibility of phenolic compounds and lycopene from tomato pomace during simulated *in vitro* gastrointestinal digestion. The results demonstrated that these bioactive substances follow significantly different release patterns during the digestive phases. Phenolic compounds exhibited the highest concentration in the oral phase, decreased in the gastric phase, and then partially recovered in the intestinal phase. This fluctuating profile may indicate the presence of phenolic compounds with different interaction strengths within the tomato pomace matrix, including readily soluble compounds and fractions more strongly associated with insoluble structural components. In contrast, lycopene showed a progressive release, confirming that bile-mediated emulsification is essential for the solubilization of carotenoids.

The cumulative digestion protocol (R2) yielded considerably lower values than sequential sampling (R1) for both classes of compounds. One of the most significant findings of this study is that the choice of digestion

protocol substantially affects apparent bioaccessibility estimations for both hydrophilic and lipophilic compounds. Sequential phase analysis (R1) provided a dynamic representation of compound release throughout digestion, whereas cumulative digestion (R2) reflected the final soluble fraction remaining after prolonged matrix interaction. The large discrepancies observed between the two approaches demonstrate that sampling strategy is not merely a procedural detail, but a critical methodological factor influencing the interpretation and comparability of *in vitro* digestion studies.

These findings demonstrate that the properties of the food matrix and digestive conditions influence the release of phytochemicals in a combined manner, but in ways specific to each compound. Phenolic compounds respond primarily to pH changes and the action of surfactants, while lycopene depends on lipid availability and micelle formation. Tomato pomace represents a promising dual source of hydrophilic and lipophilic bioactive compounds for nutraceutical applications. However, realizing this potential may require tailored processing strategies, like breaking down cell walls to boost the release of phenolic compounds or mixing in lipids to make lycopene more bioavailable. Therefore, the comparative evaluation of R1 and R2 protocols represents an important methodological contribution for future bioaccessibility studies involving complex plant-based matrices and food by-products.

EXPERIMENTAL SECTION

Chemicals and Reagents

All solvents used were of analytical or HPLC grade. Methanol, acetone, hexane, sodium carbonate, sodium chloride (NaCl), potassium chloride (KCl), potassium dihydrogen phosphate (KH_2PO_4), sodium hydrogen carbonate ($NaHCO_3$), calcium chloride dihydrate ($CaCl_2 \cdot 2H_2O$), magnesium chloride hexahydrate ($MgCl_2 \cdot 6H_2O$), and hydrochloric acid (HCl) were purchased from Merck (Darmstadt, Germany). Folin–Ciocalteu reagent and gallic acid standard were obtained from Sigma-Aldrich (Saint Louis, MO, USA). Digestive enzymes including α-amylase from porcine pancreas (≥5 U/mg), pepsin from porcine gastric mucosa (≥2500 U/mg protein), pancreatin from porcine pancreas (4× USP), and bile extract were also purchased from Sigma-Aldrich (Steinheim, Germany). Ultra-pure water was obtained using an ULTRACLEAR UV UF EVOQUA purification system (Pittsburgh, PA, USA).

Sample Preparation

Tomato pomace consisting of peels and seeds obtained as by-products from industrial tomato processing was used as raw material.The tomato pomace samples were dried in a laboratory oven (MEMMERT UN55, Schwabach, Germany) at 50 °C until constant weight, in order to reduce moisture while limiting thermal degradation of phenolic compounds and lycopene. The dried material was subsequently ground to obtain a homogeneous powder and stored in airtight containers at 4 °C until further analysis.

For digestion experiments, approximately 0.5 g of dried tomato pomace was used. For phenolic compound extraction, approximately 2.5 g of sample was extracted with 10 mL of methanol for 20 min in an ultrasonic bath (Sonorex RK 512H, BANDELIN electronic GmbH & Co. KG, Berlin, Germany) at room temperature. The extracts were subsequently centrifuged at 11,000 rpm for 2 min using a MicroCL 17 centrifuge (Thermo Fisher Scientific, Waltham, MA, USA), and the supernatant was filtered through a 0.45 µm cellulose membrane filter (Whatman, Sigma-Aldrich, St. Louis, MO, USA) prior to analysis.

Determination of Total Phenolic Compounds

Total phenolic compounds were determined using the Folin–Ciocalteu method. Briefly, 0.5 mL of sample extract was mixed with 5 mL of distilled water and 0.5 mL of commercial Folin–Ciocalteu reagent. After 3 min, 1.5 mL of sodium carbonate solution (10%, w/v) was added and the mixture was incubated for 45 min at room temperature in the dark. The absorbance was measured at 765 nm using a UV-Vis spectrophotometer (Lambda 25, Perkin Elmer, Waltham, MA, USA). Gallic acid was used for calibration, and the results were expressed as gallic acid equivalents (GAE).

Determination of lycopene by UHPLC–DAD

Lycopene was extracted from dried tomato pomace samples according to a modified solvent extraction procedure [43]. Approximately 0.5 g of homogenized dried sample was mixed with 10 mL of hexane: acetone: ethanol (2:1:1, v/v/v). The mixture was vortexed and allowed to stand for 10 min at room temperature to facilitate carotenoid solubilization. The samples were then centrifuged at 11,000 rpm for 2 min and the supernatant was filtered through a 0.45 µm cellulose membrane filter. Ultrasound-assisted extraction was not applied for lycopene in order to limit possible oxidative degradation and isomerization of this highly unsaturated carotenoid. All extraction steps were carried out under reduced light conditions to minimize carotenoid degradation.

Lycopene determination was performed using a UHPLC system (Vanquish, Thermo Fisher Scientific, Germany) equipped with a diode array detector. Chromatographic separation was achieved on an Acclaim™ C30 column (3 µm, 3.0 × 150 mm) maintained at 40 °C. The mobile phase consisted of methanol containing 3.2 g L^{-1} ammonium acetate (70%) and acetonitrile (30%) delivered at a flow rate of 1.7 mL min^{-1}. The injection volume was 8 µL. Detection was performed at 460 nm and quantification was achieved using external calibration curves prepared with certified lycopene standards in the concentration range 1–20 µg mL^{-1} with a coefficient of determination (R^2) of 0.9994. Results were expressed as µg g^{-1} dry weight. All analyses were carried out in triplicate. (Figure 4)

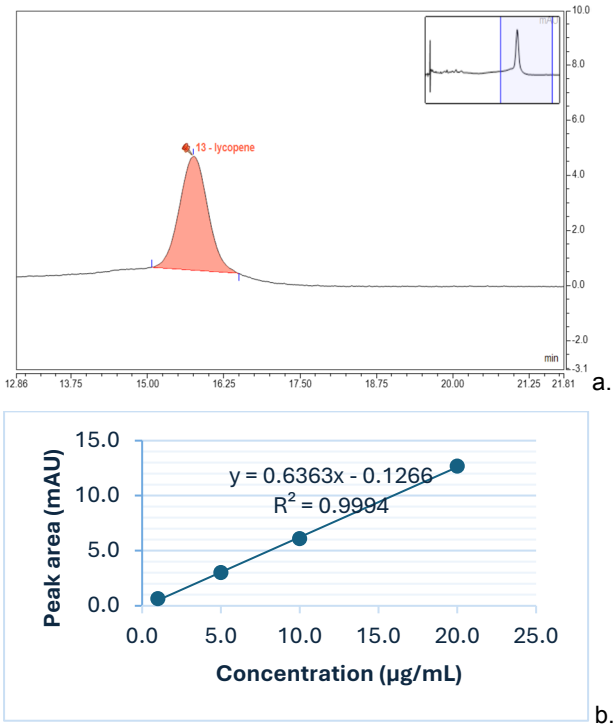

Figure 4. (a) Representative UHPLC-DAD chromatogram of lycopene standard; (b) External calibration curve used for lycopene quantification, showing excellent linearity within the investigated concentration range, y = 0.6363x - 0.1266, R^2 = 0.9994.

Apparent bioaccessibility (%) was calculated as follows: Bioaccessibility (%) = (amount of compound recovered in the digestive supernatant / initial amount of compound in the undigested tomato pomace) × 100.

In Vitro Gastrointestinal Digestion

A static *in vitro* gastrointestinal digestion model was applied to simulate the digestive conditions of the human gastrointestinal tract. The digestion protocol was adapted from the standardized method described by Minekus et al. and Brodkorb et al., which has been widely used for evaluating nutrient bioaccessibility in food matrices [12, 13]. The digestion process consisted of three sequential phases: oral, gastric, and intestinal.

The simulated digestive fluids were prepared using the electrolyte compositions recommended by the INFOGEST protocol, including sodium chloride (NaCl), potassium chloride (KCl), potassium dihydrogen phosphate (KH_2PO_4), sodium hydrogen carbonate ($NaHCO_3$), magnesium chloride hexahydrate ($MgCl_2{\cdot}6H2O$), calcium chloride dihydrate ($CaCl_2{\cdot}2H_2O$), ammonium carbonate ($(NH_4)2CO_3$), sodium hydroxide (NaOH), and hydrochloric acid (HCl).

For the digestion experiments, 0.5 g of dried tomato pomace sample was used. During the oral phase, the sample was mixed with 2.5 mL simulated salivary fluid (SSF) containing α-amylase (75 U/mL). The mixture was adjusted to pH 7.0 and incubated for 2 min at 37 °C under continuous agitation (100 rpm). For the gastric phase, the remaining solid fraction or oral bolus was mixed with 2.5 mL simulated gastric fluid (SGF) containing pepsin (2000 U/mL) and gastric lipase (60 U/mL). The pH was adjusted to 3.0 using 1 M HCl, under continuous monitoring with a calibrated pH meter, and the samples were incubated for 2 h at 37 °C under continuous agitation. or the intestinal phase, the gastric chyme was mixed with 2.5 mL simulated intestinal fluid (SIF) prepared using the electrolyte components recommended by the INFOGEST protocol, including NaCl, KCl, KH_2PO_4, $NaHCO_3$, $MgCl_2{\cdot}6H_2O$, and $CaCl_2{\cdot}2H_2O$. The SIF contained pancreatin corresponding to trypsin activity of 100 U/mL and bile salts at a final concentration of 10 mM. The pH was adjusted to 7.0 using NaOH solution under continuous monitoring with a calibrated pH meter, and the digestion continued for 2 h at 37 °C under continuous agitation at 100 rpm. Two digestion approaches were applied. In protocol R1, the supernatant was separated after each digestion phase by centrifugation and analyzed individually. In protocol R2, the digestion process was performed continuously without intermediate separation, with cumulative addition of digestive fluids throughout the digestion sequence.

At the end of digestion, enzyme activity was stopped by placing the samples in an ice bath for 10 min. The digested samples were centrifuged at 4500 rpm for 30 min using a Universal 320 centrifuge (Hettich, Tuttlingen, Germany). The supernatants were collected, filtered through 0.45 µm membrane filters, and stored at 4 °C until analysis.

Blank digestion samples containing the same digestive fluids and enzymes without tomato pomace were processed under identical conditions to correct possible interferences originating from enzymes and digestion buffers. All analyses were performed in triplicate.

Statistical Analysis

All analyses were performed in triplicate, and the results are expressed as mean ± standard deviation (SD). Statistical analysis was performed using one-way ANOVA to evaluate significant differences between digestion phases. Differences were considered statistically significant at $p < 0.05$.

ACKNOWLEDGMENTS

This paper was co-financed by the European Regional Development Fund (ERDF) through the Smart Growth, Digitization and Financial Instruments Program (PoCIDIF), call PCIDIF/144/PCIDIF_P1/OP1/RSO1.1/PCIDIF_A3, Project SMIS number 309287, acronym METROFOOD-RO Evolve.

REFERENCES

1. M. Knoblich; B. Anderson; D. Latshaw; *J. Food Sci.*, **2005**, 70, C495–C500
2. N. Mirabella; V. Castellani; S. Sala; J. *Clean. Prod*., **2014**, 65, 28–41
3. A. Raiola; M. M. Rigano; R. Calafiore; L. Frusciante; A. Barone; *Mediators Inflamm*., **2014**, 139873.
4. E. Giovannucci; *Exp. Biol. Med*., **2002**, 227, 852–859
5. I. F. Strati; V. Oreopoulou; *Int. J. Food Eng*., **2011**, 7, 1–16
6. E. Reboul; *Nutrients*, **2013**, 5, 3563–3581
7. D. Tagliazucchi; E. Verzelloni; D. Bertolini; A. Conte; *Food Chem*., **2010**, *120*, 599–606
8. E. Fernández-García; I. Carvajal-Lérida; M. Jarén-Galán; J. Garrido-Fernández; A. Pérez-Gálvez; D. Hornero-Méndez; *Food Res. Int*., **2012**, *46*, 438–450
9. F. Saura-Calixto; J. Agric. *Food Chem*., **2011**, *59*, 43–49
10. C. H. M. Versantvoort; A. G. Oomen; E. Van de Kamp; C. J. M. Rompelberg; A. J. A. M. Sips; *Food Chem. Toxicol*., **2005**, *43*, 31–40
11. M. S. Brewer; Compr. Rev. *Food Sci. Food Saf*., **2011**, *10*, 221–247
12. M. Minekus; M. Alminger; P. Alvito; S. Ballance; T. Bohn; C. Bourlieu; F. Carrière; R. Boutrou; M. Corredig; D. Dupont; C. Dufour; L. Egger; M. Golding; S. Karakaya; B. Kirkhus; S. Le Feunteun; U. Lesmes; A. Maclerzanka; A. MacKie; et al.; *Food Funct*., **2014**, *5*, 1113–1124

13. A. Brodkorb; L. Egger; M. Alminger; P. Alvito; R. Assunção; S. Ballance; T. Bohn; C. Bourlieu-Lacanal; R. Boutrou; F. Carrière; A. Clemente; M. Corredig; D. Dupont; C. Dufour; C. Edwards; M. Golding; S. Karakaya; B. Kirkhus; S. Le Feunteun; U. Lesmes; A. Macierzanka; A. R. Mackie; C. Martins; S. Marze; D. J. McClements; O. Ménard; M. Minekus; R. Portmann; C. N. Santos; I. Souchon; R. P. Singh; G. E. Vegarud; M. S. J. Wickham; W. Weitschies; I. Recio; *Nat. Protoc.*, **2019**, *14*, 991–1014
14. J. Bouayed; L. Hoffmann; T. Bohn; *Food Chem.*, **2011**, *128*, 14–21
15. J. Pérez-Jiménez; F. Saura-Calixto; *Food Res. Int.*, **2015**, *74*, 315–323
16. G. C. Carvalho; B. A. F. de Camargo; J. T. C. de Araújo; M. Chorilli; *Trends Food Sci. Technol.*, **2021**, *118*, 447–458
17. G. Knockaert; S. K. Pulissery; I. Colle; S. Van Buggenhout; M. Hendrickx; A. V. Loey; *Food Chem.*, **2012**, *135*, 1290–1297
18. D. Dupont; M. Alric; S. Blanquet-Diot; et al.; Crit. Rev. *Food Sci. Nutr.*, **2019**, *59*, 1546–1562
19. L. Egger; O. Ménard; C. Delgado-Andrade; et al.; *Food Res. Int.*, **2022**, 154, 110962
20. V. Athanasiadis; T. Chatzimitakos; K. Kotsou; D. Kalompatsios; E. Bozinou; S. I. Lalas; *Int. J. Mol. Sci.*, **2023**, *24*, 15914
21. M. Morzel; F. Canon; S. Guyot; J. Agric. Food Chem., **2022**, *70*, 6317–6327
22. S. Kamiloglu; A. A. Pasli; B. Ozcelik; J. Van Camp; E. Capanoglu; *Food Chem.*, 2015, *186*, 74–82
23. F. Saura-Calixto; J. Pérez-Jiménez; Curr. Opin. Food Sci., **2021**, 42, 168–175
24. C. Wang; H. Wu; Z. Liu; C. J. Barrow; F. Dunshea; H. A. R. Suleria; *Food Funct.*, **2022**, *13*, 4954-4966
25. L. Egger; O. Ménard; C. Delgado-Andrade; P. Alvito; R. Assunção; et al.; *Food Res. Int.*, **2016**, *88*, 217–225
26. J. M. Carbonell-Capella; M. Buniowska; F. J. Barba; M. J. Esteve; A. Frígola; Compr. Rev. *Food Sci. Food Saf.*, **2014**, *13*, 155–171
27. S. Kamiloglu; A. A. Pasli; B. Ozcelik; et al.; *LWT-Food Sci. Technol.*, **2015**, *64*, 1305–1312
28. J. Pérez-Jiménez; F. Saura-Calixto; *Food Res. Int.*, **2015**, *74*, 315–323
29. A. Sridhar; M. Ponnuchamy; P. S. Kumar; A. Kapoor; D. N. Vo; S. Prabhakar; *Environ. Chem. Lett.*, **2021**, *19*, 3409–3443
30. J. Bouayed; L. Hoffmann; T. Bohn; *Food Chem.*, **2011**, *128*, 14–21
31. C. Le Bourvellec; C. M. G. C. Renard; Crit. Rev. *Food Sci. Nutr.*, **2012**, *52*, 213–248
32. L. Jakobek; M. Matošić; *Foods*, **2019**, *8*, 633
33. M. Pellegrini; R. Lucas-Gonzalez; E. Sayas-Barberá; et al.; *Food Res. Int.*, **2021**, *147*, 110546
34. I. Fernández-Jalao; C. Sánchez-Moreno; B. De Ancos; Crit. Rev. *Food Sci. Nutr.*, **2022**, *62*, 4892–4908
35. M. Elleuch; D. Bedigian; O. Roiseux; et al.; *Food Chem.*, **2011**, *124*, 411–421
36. F. Saura-Calixto; *J. Agric. Food Chem.*, **2011**, *59*, 43–49
37. E. Reboul; P. Borel; Prog. *Lipid Res.*, **2011**, *50*, 388–402

38. E. Fernández-García; I. Carvajal-Lérida; M. Jaren-Galan; et al.; *Food Res. Int*., **2012**, *46*, 438–450
39. P. Borel; C. Desmarchelier; U. Dumont; et al.; Br. J. Nutr., **2016**, *115*, 1701–1711
40. J. Corte-Real; E. Richling; L. Hoffmann; *Food Funct*., **2016**, *7*, 3235–3244
41. M. J. Brown; M. G. Ferruzzi; M. L. Nguyen; et al.; *Am. J. Clin. Nutr*., **2004**, *80*, 396–403
42. A. J. Roodenburg; R. Leenen; H. van Berg; et al.; *Am. J. Clin. Nutr.,* **2000**, *71*, 1187–1193
43. W. W. Fish; P. Perkins-Veazie; J. K. Collins; J*. Food Compos. Anal.*, **2002,** *15*, 309-317

STUDIA UBB CHEMIA, LXXI, 2, 2026 (p. 105-123)
(RECOMMENDED CITATION)
DOI:10.24193/subbchem.2026.2.06

COMPARATIVE APPLICATION OF RAW-ANN AND PCA-ANN FOR THE SPECTROPHOTOMETRIC DETERMINATION OF CAFFEINE, PROPYPHENAZONE, AND PARACETAMOL IN TABLETS

Asiye ÜÇER[a,b], Nazangül ÜNAL[c], Erdal DİNÇ[a,*]

ABSTRACT. Comparative chemometric approaches based on raw artificial neural networks (RAW-ANN) and principal component analysis-artificial neural networks (PCA-ANN) were developed and applied to the simultaneous spectrophotometric determination of caffeine (CFN), propyphenazone (PRPN), and paracetamol (PRC) in a commercial ternary pharmaceutical formulation. The spectral overlap of the three components within the 220-300 nm region renders conventional spectrophotometric methods inadequate without prior separation. The proposed ANN-based models enabled direct analysis of raw UV spectral data without requiring any separation procedure over concentration ranges of 2.5-12.0 µg/mL (CFN), 3.0-12.0 µg/mL (PRPN), and 3.0-16.0 µg/mL (PRC).

Both training approaches demonstrated satisfactory analytical performance, with mean recoveries ranging between 97% and 105%. In particular, PCA-ANN yielded relative standard deviations below 2.5%, indicating enhanced precision and predictive stability compared to RAW-ANN. Statistical evaluation confirmed the robustness and reliability of the developed models. The methods were successfully applied to the quantitative analysis of pharmaceutical tablets, demonstrating their suitability for routine quality control of complex multicomponent formulations.

Keywords: *Spectrophotometric determination, artificial neural networks, principal component analysis, caffeine, propyphenazone, paracetamol*

[a] *Department of Analytical Chemistry, Faculty of Pharmacy, Ankara University, 06560 Yenimahalle, Ankara, Türkiye.*
[b] *Department of Analytical Chemistry, Faculty of Pharmacy, Ankara Yıldırım Beyazıt University, 06010 Etlik, Keçiören, Ankara, Türkiye.*
[c] *Department of Pharmacy Services, Eşme Vocational School, Uşak University, 64600, Uşak, Turkey.*
[*] *Corresponding author: dinc@ankara.edu.tr*

INTRODUCTION

In modern medical practice, multi-component pharmaceutical formulations are increasingly preferred over single-agent therapies due to their enhanced therapeutic efficacy and improved clinical outcomes. In particular, triple-component analgesic combinations are widely used in over-the-counter preparations to achieve synergistic effects and improved patient compliance. Among these, the combination of paracetamol, propyphenazone, and caffeine is frequently incorporated into commercial pharmaceutical products.

Paracetamol (acetaminophen; IUPAC: N-(4-hydroxyphenyl) acetamide) is a widely used analgesic and antipyretic agent administered alone or in combination with other drugs in various dosage forms [1]. Propyphenazone (IUPAC: 1,5-dimethyl-2-phenyl-4-propan-2-yl-pyrazol-3-one) is a pyrazolone-derived nonsteroidal anti-inflammatory drug (NSAID) possessing analgesic and antipyretic properties and is commonly included in combination analgesics [2-3]. Caffeine (IUPAC: 1,3,7-trimethyl-3,7-dihydro-1H-purine-2,6-dione), a methylxanthine derivative, enhances analgesic efficacy through central nervous system stimulation and adenosine receptor antagonism [4-5]. Owing to its pharmacological effects, caffeine is frequently incorporated into multicomponent formulations [6-7].

The accurate and reliable quantification of these active ingredients in ternary pharmaceutical formulations is essential for quality control, regulatory compliance, and routine industrial analysis. However, the simultaneous determination of paracetamol, propyphenazone, and caffeine represents a considerable analytical challenge due to their strongly overlapping absorption spectra and the complexity of multicomponent systems.

Numerous chromatographic methods, including RP-HPLC [8–9], gradient HPLC [10], TLC and HPTLC [10–14], gas chromatography [15], pressurized planar electrochromatography [13], micellar electrokinetic capillary chromatography [16], and voltammetric techniques [17], have been reported for the analysis of these compounds in pharmaceutical preparations and biological matrices. Although these approaches offer high selectivity and sensitivity, they often require sophisticated instrumentation, extensive sample preparation, long analysis times, and increased operational costs.

UV spectrophotometry offers a rapid and cost-effective alternative for routine pharmaceutical analysis. Nevertheless, the pronounced spectral overlap of paracetamol, propyphenazone, and caffeine within the 220-300 nm region severely limits the applicability of classical univariate spectrophotometric approaches. To address this limitation, several mathematical and multivariate techniques have been proposed, including derivative spectrophotometric methods [18,22], absorption ratio approaches [19], principal component regression [20], net analyte signal-based strategies [21], and flow-through UV

systems [23]. Although these methods improve selectivity, they may suffer from sensitivity to noise amplification, complex data preprocessing steps, or limited predictive robustness when applied to highly collinear spectral datasets.

Artificial neural networks (ANNs) have emerged as powerful chemometric tools capable of modeling complex and nonlinear relationships in multivariate analytical data. Raw artificial neural networks (RAW-ANNs) directly utilize original spectral data, enabling the resolution of severely overlapping signals without prior mathematical manipulation. Furthermore, the integration of principal component analysis with ANN (PCA-ANN) reduces data dimensionality, alleviates collinearity, and enhances model stability and convergence performance [24-27]. In comparison with conventional chromatographic and classical spectrophotometric approaches, ANN-based training methods provide several practical and computational advantages for multicomponent pharmaceutical analysis. These methods enable direct quantitative analysis of highly overlapping spectral data without requiring prior separation procedures, thereby reducing analysis time, instrumental complexity, and sample preparation steps. Furthermore, ANN architectures are capable of modeling complex and nonlinear relationships within highly collinear datasets, while PCA-assisted dimensional reduction improves numerical stability, accelerates convergence, and enhances predictive robustness. Despite their proven effectiveness in various multicomponent pharmaceutical systems, a systematic comparative evaluation of RAW-ANN and PCA-ANN for the direct spectrophotometric determination of the paracetamol-propyphenazone-caffeine ternary system has not yet been reported.

In the present study, RAW-ANN and PCA-ANN models were comparatively developed and applied for the first time to the simultaneous spectrophotometric determination of caffeine (CFN), propyphenazone (PRPN), and paracetamol (PRC) in a commercial ternary pharmaceutical formulation without any prior separation step. The predictive performance, precision, and convergence characteristics of both chemometric strategies were systematically evaluated, and their applicability to routine pharmaceutical quality control was demonstrated.

THEORETICAL BACKGROUND

Artificial Neural Networks (ANN)

Artificial neural networks (ANNs) are data-driven modeling tools inspired by biological neural systems and are widely used for nonlinear multivariate training in analytical chemistry. In feedforward neural networks, the relationship between input variables and output responses is established through interconnected processing units (neurons) organized in layers.

For a typical two-layer feedforward ANN, the output Y_k can be expressed as:

$$Y_k = f_o\left(\sum_{j=1}^{m} \omega_{jk}^{(2)} f_h\left(\sum_{i=1}^{n} \omega_{ij}^{(1)} x_i + b_j^{(1)}\right) + b_k^{(2)}\right) \quad (1)$$

where x_i represents the input spectral variables, $\omega_{ij}^{(1)}$ and $\omega_{jk}^{(2)}$ are weight coefficients, $b_j^{(1)}$ and $b_k^{(2)}$ are bias terms, f_h and f_o denote hidden and output layer activation functions, respectively.

In chemometric training, ANN models are particularly advantageous for handling collinear spectral data and nonlinear relationships between absorbance and concentration values. RAW-ANN utilizes the original spectral absorbance matrix directly as the input dataset.

Principal Component Analysis (PCA)

Principal component analysis (PCA) is a multivariate projection method used to reduce the dimensionality of highly correlated datasets while preserving the maximum variance. The original spectral matrix X can be decomposed as:

$$X = TP^T + E \quad (2)$$

where T is the score matrix, P is the loading matrix, and E is the residual matrix. Principal components are orthogonal linear combinations of the original variables and therefore eliminate multicollinearity inherent in spectral data. The removal of multicollinearity improves numerical stability by reducing the condition number of the data matrix, minimizes variance inflation of model parameters, and enhances predictive robustness. Furthermore, by compressing redundant spectral information and filtering low-variance noise components, PCA preprocessing reduces the risk of overfitting and improves convergence behavior when applied before ANN modeling.

In the PCA-ANN approach, the reduced score matrix obtained from PCA is used as the input dataset for ANN modeling instead of the original absorbance matrix. This preprocessing step reduces dimensionality, improves computational efficiency, enhances convergence speed, and minimizes the risk of overfitting.

Therefore, while RAW-ANN directly models the original spectral data, PCA-ANN operates on decorrelated and compressed input variables, potentially leading to improved prediction performance and model robustness.

RESULTS AND DISCUSSION

RAW-ANN and PCA-ANN Modeling Strategy and Advanced Comparative Evaluation

To achieve reliable simultaneous quantification of PRC (Figure 1a), CFN (Figure 1b), and PRPN (Figure 1c), in the presence of severe spectral overlap in the 220-300 nm region, two nonlinear multivariate training strategies, RAW-ANN and PCA-ANN, were systematically developed and compared.

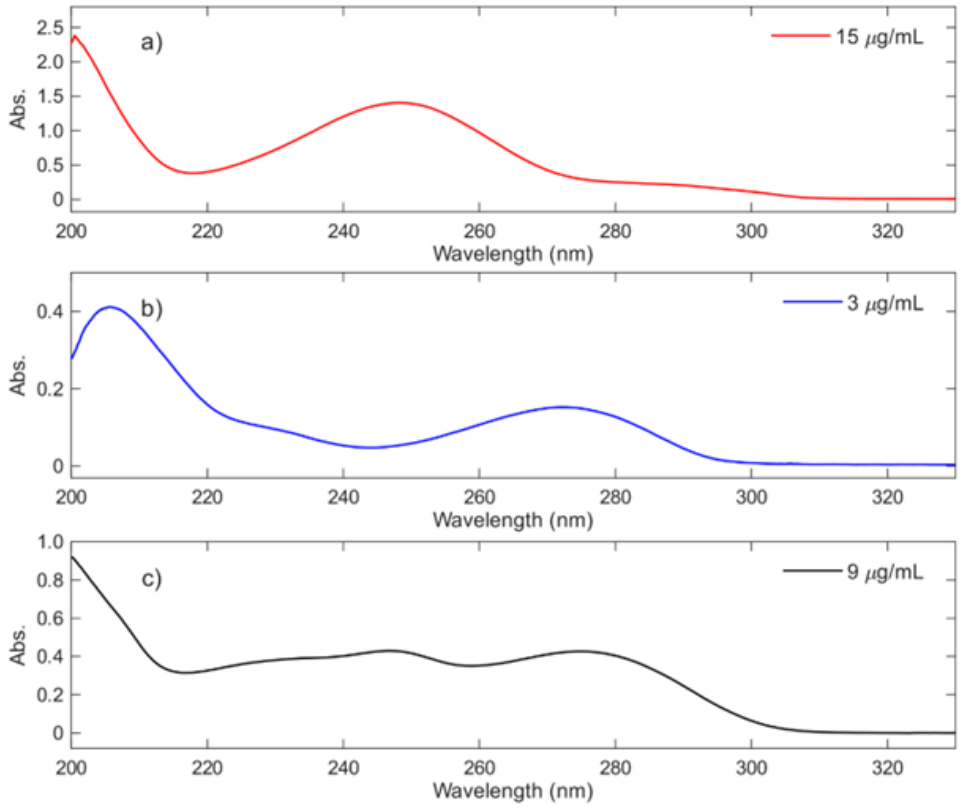

Figure 1. UV absorption spectra of a) 15.0 µg/mL PRC, b) 3.0 µg/mL CFN, and c) 9.0 µg/mL PRPN

The training dataset consisted of 35 synthetic ternary mixtures prepared using a structured concentration design to ensure adequate and balanced coverage of the working ranges of CFN, PRPN, and PRC (Table 1).

For each mixture, UV absorption spectra were recorded over 220-300 nm, generating 700 absorbance variables per sample. This resulted in an initial spectral matrix of 700 × 35 (wavelength × sample), which was subsequently rearranged to 35 × 700 before ANN modeling.

Table 1. A concentration set that includes mixtures of analyzed drugs

Sample No.	Actual CFN (µg/mL)	Actual PRPN (µg/mL)	Actual PRC (µg/mL)	Sample No.	Actual CFN (µg/mL)	Actual PRPN (µg/mL)	Actual PRC (µg/mL)
1	2.5	3	3	19	2.5	6	12
2	2.5	3	8	20	2.5	6	16
3	2.5	3	12	21	4	3	3
4	2.5	3	16	22	4	3	8
5	4	6	3	23	4	3	12
6	4	6	8	24	4	3	16
7	4	6	12	25	8	12	3
8	4	6	16	26	8	12	8
9	8	9	3	27	8	12	12
10	8	9	8	28	8	12	16
11	8	9	12	29	12	9	3
12	8	9	16	30	12	9	8
13	12	12	3	31	12	9	12
14	12	12	8	32	12	9	16
15	12	12	12	33	0	0	15
16	12	12	16	34	0	9	0
17	2.5	6	3	35	3	0	0
18	2.5	6	8				

The same spectral acquisition and preprocessing procedures were applied to independent datasets, including 13 external validation mixtures, 18 intra-day and inter-day precision samples, 12 standard addition samples, and 10 commercial tablet solution samples prepared from the marketed formulation. The latter dataset was used to evaluate the practical applicability of the proposed models to real pharmaceutical samples. The three-dimensional UV absorption spectra of 35 training sets, 43 validation sets (13 external validation mixtures, 18 intra-day and inter-day sensitivity samples, 12 standard additive samples), and 10 commercial triple tablet formulation samples are shown in Figures 2a-c.

Training of both RAW-ANN and PCA-ANN models was performed using the Levenberg–Marquardt backpropagation algorithm (trainlm). The weights and biases between layers were iteratively optimized by minimizing the mean squared prediction error. A maximum of 1000 epochs and a performance goal of 1×10^{-8} were employed, together with validation monitoring to improve generalization and reduce overfitting.

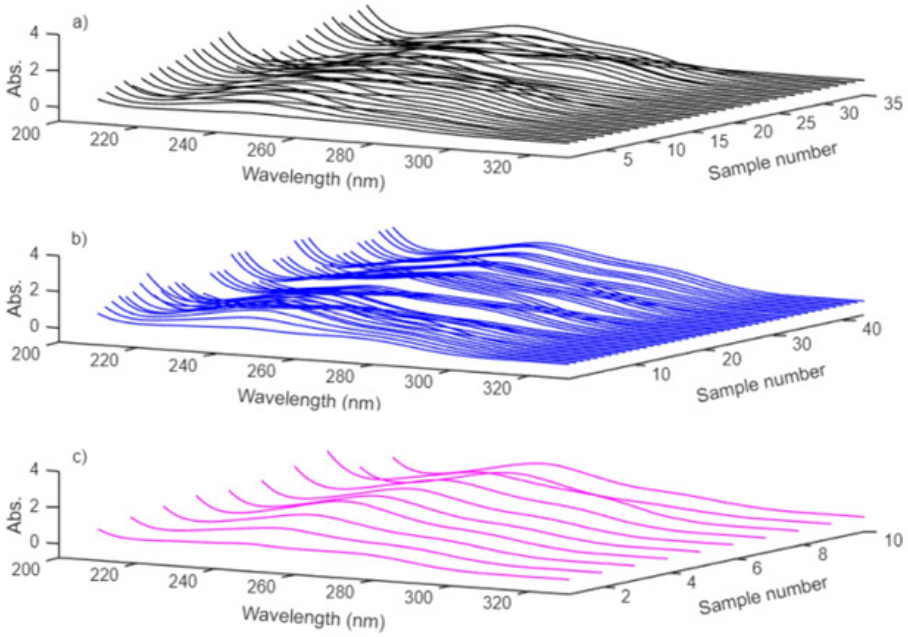

Figure 2. 3D-UV Absorption spectra of a) 35 training sets, b) 43 validation sets (13 external validation mixtures, 18 intra-day and inter-day precision samples, 12 standard addition samples), and c) 10 commercial ternary tablet formulation samples

RAW-ANN Modeling

To reduce spectral redundancy and computational burden, consecutive wavelength variables were averaged, compressing the original 700 absorbance variables into 100 representative inputs. This preprocessing step transformed the original 35 × 700 training matrix into a reduced 35 × 100 dataset used as the ANN input. These 100 correlated inputs were introduced into a multilayer feedforward ANN with architecture:

- Input layer: 100 neurons
- First hidden layer: 50 neurons (logsig transfer function)
- Second hidden layer: 25 neurons (purelin transfer function)
- Output layer: 3 neurons corresponding to CFN, PRPN, and PRC
- Training was performed using the Levenberg–Marquardt backpropagation algorithm (trainlm), with a maximum of 1000 epochs and a performance goal of 1×10^{-8}.

The optimized network topology was presented in Table 2.

Table 2. ANN topologies for the applied training methods

	RAW-ANN	**PCA-ANN**
Input sizes	100	10
Hidden transfer functions	logsig, purelin	logsig, purelin
Output transfer functions	purelin	purelin
epochs	61	9
train time (min.)	5.06	1.06

This 100-50-25-3 configuration resulted in more than 6,600 adjustable parameters (weights and biases), reflecting substantial model complexity relative to the training sample size (n = 35). Although such parameterization enhances nonlinear approximation capability, it increases sensitivity to multicollinearity inherent in highly correlated spectral datasets.

The trained RAW-ANN model was subsequently applied to independent datasets processed using identical preprocessing steps:

- External validation mixtures (13 × 100)
- Intra-day and inter-day precision samples (18 × 100)
- Standard addition samples (12 × 100)
- Commercial tablet solutions (10 × 100)

The corresponding quantitative results are summarized in Tables 4, 5, 6, and 7. Training required 303.90 s (≈5.06 min), with a total processing time of 307.09 s. The training performance curve is presented in Figure 3a, demonstrating slower convergence relative to PCA-ANN (Figure 3b), primarily due to the higher-dimensional and correlated input structure.

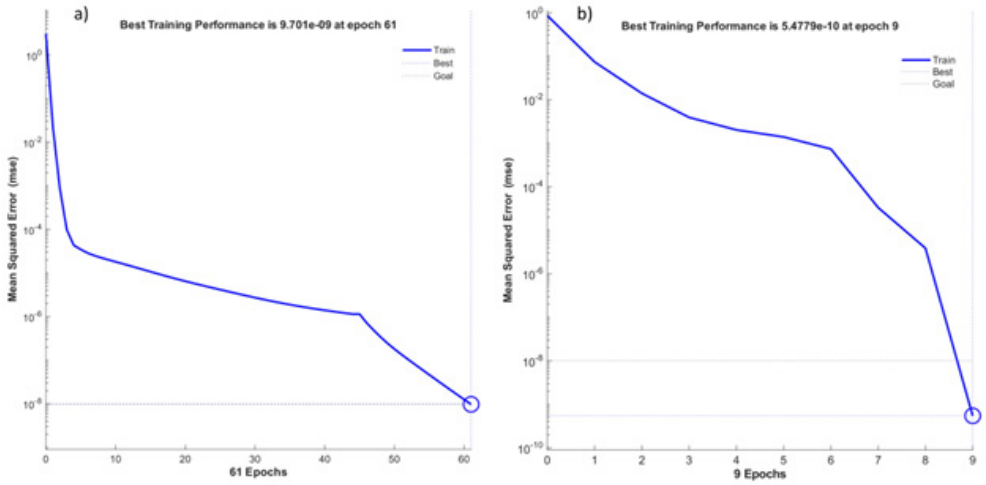

Figure 3. a) Mean Squared Error performance for training of ANN with RAW Data Inputs, b) Mean Squared Error performance for training of ANN with PCA Applied Inputs

Statistical parameters summarized in Table 3 indicate satisfactory training performance; however, higher RMSEP and SEP values compared to PCA-ANN suggest limited predictive stability under high-dimensional correlated input conditions.

PCA-ANN Modeling

To overcome multicollinearity and reduce spectral dimensionality, principal component analysis (PCA) was applied to the original 35 × 700 training matrix prior to ANN modeling. The PCA decomposition generated loading vectors, score matrices, and eigenvalues of the covariance matrix.

Although the first five principal components explained 99.6% of the total spectral variance, ten principal components were retained to ensure preservation of minor spectral contributions and to enhance numerical stability. Consequently, the training dataset was reduced to a 35 × 10 score matrix.

Prior to ANN modeling, the input datasets were normalized to improve numerical stability and network convergence. In the PCA-ANN approach, PCA scores derived from the spectral matrix were used as orthogonalized inputs for ANN training.

The optimized network structure of the PCA-ANN architecture consisted of:

- Input layer: 10 neurons (principal component scores)
- First hidden layer: 10 neurons (logsig transfer function)
- Second hidden layer: 5 neurons (purelin transfer function)
- Output layer: 3 neurons corresponding to CFN, PRPN, and PRC concentrations.
- Training was performed using the Levenberg–Marquardt backpropagation algorithm (trainlm), with a maximum of 1000 epochs and a performance goal of 1×10^{-8}.

Compared to the RAW-ANN (100 input neurons), the PCA-ANN structure significantly reduced the number of adjustable parameters, thereby improving the training sample-to-parameter ratio and enhancing model generalization capability.

Validation datasets (13 × 10), intra/inter-day samples (18 × 10), standard addition samples (12 × 10), and commercial tablet solutions (10 × 10) were projected onto the PCA loading space prior to ANN prediction to ensure methodological consistency.

The evolution of training performance is shown in Figure 3b. PCA-ANN exhibited faster convergence and earlier stabilization compared to RAW-ANN (Figure 3a), requiring approximately 1.06 minutes for training.

Statistical parameters summarized in Table 3 further confirm the superiority of PCA-ANN. RMSEP values decreased notably for CFN (0.2523 → 0.1319) and PRC (0.4353 → 0.2491), while SEP values were consistently lower for all analytes, demonstrating improved predictive robustness.

Comparative Computational and Predictive Performance

The tenfold reduction in input dimensionality (100 RAW variables vs. 10 orthogonal principal components) substantially influenced the bias-variance balance of the ANN models. By eliminating multicollinearity and redundant spectral information, PCA preprocessing improved numerical conditioning, reduced parameter variance, and minimized overfitting risk.

As summarized in Table 2, the PCA-ANN architecture employed a significantly reduced effective input space while maintaining identical training parameters. This dimensional compression translated directly into computational efficiency: training time decreased from 5.06 min (RAW-ANN) to approximately 1.06 min for PCA-ANN, corresponding to nearly a fivefold acceleration.

The training performance curves (Figures 3a and 3b) clearly demonstrate faster convergence and earlier stabilization for PCA-ANN. In contrast, RAW-ANN required longer iterative refinement due to the higher-dimensional and correlated input structure.

Overall, PCA-ANN exhibited improved predictive stability and lower validation errors compared to RAW-ANN, confirming the beneficial effect of dimensional reduction on ANN-based spectrophotometric calibration.

The improved performance of PCA-ANN was primarily associated with the reduced and orthogonalized input space rather than network complexity alone. While RAW-ANN utilized 100 correlated spectral variables, PCA-ANN used 10 principal component scores, resulting in improved numerical stability, faster convergence, and enhanced predictive robustness.

Table 3. Statistical parameters in the training and prediction steps

	RAW-ANN			PCA-ANN		
Analyte	SEC	RMSEP	SEP	SEC	RMSEP	SEP
CFN	0.0017	0.2523	0.2247	0.1071	0.1319	0.1280
PRPN	0.0008	0.3341	0.2990	0.1057	0.3236	0.1797
PRC	0.0012	0.4353	0.3955	0.1054	0.2491	0.2312

The standard error of training (SEC)
The standard error of prediction (SEP)
The root mean squared error of prediction (RMSEP)

Validation of RAW-ANN and PCA-ANN Methods

The predictive reliability of the developed models was evaluated using independent ternary validation mixtures containing CFN, PRPN, and PRC. The mean recovery values and relative standard deviations (RSD%) are summarized in Table 4.

For all analytes, recovery values were close to 100%, and RSD values were generally below 3%, demonstrating satisfactory trueness and precision. PCA-ANN exhibited slightly lower variability, particularly for CFN and PRC, indicating improved stability in prediction.

Further assessment using standard error of calibration (SEC), standard error of prediction (SEP), and root mean square error of prediction (RMSEP) (Table 3) confirmed the enhanced predictive performance of PCA-ANN. The consistently lower SEP values obtained with PCA-ANN indicate improved external prediction capability. Linear regression analysis between actual and predicted concentrations yielded slopes close to unity and high correlation coefficients, confirming the absence of systematic bias.

Table 4. Recovery results obtained by the application of RAW-ANN and PCA-ANN to the validation set consisting of CFN, PRPN, and PRC

Validation set			RAW-ANN			PCA-ANN			RAW-ANN			PCA-ANN		
Added (µg/mL)			Found (µg/mL)			Found (µg/mL)			Recovery (%)			Recovery (%)		
CFN	PRPN	PRC	CFN	PRPN	PRC	CFN	PRPN	PRC	CFN	PRPN	PRC	CFN	PRPN	PRC
3	9	3	2.98	9.01	2.83	3.05	9.03	2.83	99.4	100.1	97.3	101.6	100.3	94.5
3	9	8	2.90	9.44	8.06	2.93	9.25	8.06	96.8	104.9	102.2	97.8	102.8	100.8
3	9	12	2.92	9.17	11.87	2.98	9.24	11.87	97.3	101.9	96.9	99.2	102.7	98.9
3	9	16	2.96	9.12	15.86	2.99	9.43	15.86	98.6	101.4	97.0	99.6	104.7	99.1
2.5	9	15	2.48	8.82	14.99	2.45	9.44	14.99	99.1	98.0	99.3	97.9	104.9	100.0
4	9	15	4.19	8.94	14.95	4.08	9.3	14.95	104.7	99.3	99.4	102.1	103.4	99.7
8	9	15	7.64	9.24	15.49	7.55	9.34	15.49	95.5	102.7	102.3	94.4	103.8	103.2
12	9	15	12.53	8.59	15.58	12.02	9.20	15.58	104.4	95.4	105.6	100.1	102.2	103.8
3	3	15	3.06	2.92	15.31	3.04	2.98	15.31	101.9	97.2	103.3	101.3	99.5	102.1
3	6	15	2.96	5.76	15.2	3.00	5.91	15.20	98.6	95.9	99	99.9	98.4	101.3
3	9	15	3.03	9.17	15.13	3.03	9.40	15.13	100.9	101.9	103.6	100.9	104.5	100.9
3	12	15	2.89	12.50	14.89	2.93	12.24	14.89	96.4	104.2	96.6	97.8	102.0	99.3
3	9	15	3.17	8.72	15.02	3.04	9.21	15.02	105.7	96.8	103.2	101.5	102.3	100.1
								Mean	100	100	100.4	99.5	102.4	100.3
								SD	3.35	3.14	3.07	2.14	2.00	2.32
								RSD	3.35	3.14	3.06	2.15	1.95	2.31

SD: Standard Deviation, RSD: Relative Standard Deviation

As a result, the obtained SEC, SEP, RMSEP, recovery, and precision results confirmed the analytical reliability of both ANN-based training strategies, with PCA-ANN exhibiting superior predictive robustness and lower validation error.

Precision and Reproducibility

Intra-day and inter-day precision studies were conducted at three concentration levels for each analyte. The corresponding recovery, RSD, and relative standard error (RSE) values are presented in Table 5.

Table 5. The recovery results obtained in the intra-day and inter-day samples by the proposed RAW-ANN and PCA-ANN methods (n=3 for every concentration level)

				Found (µg/mL)					
	Added (µg/mL)			RAW-ANN			PCA-ANN		
	CFN	PRPN	PRC	CFN	PRPN	PRC	CFN	PRPN	PRC
Inter-day	3	4	5	3.02	3.96	4.98	2.93	4.08	4.98
	6	12	10	5.83	12.08	9.65	5.98	12.31	9.76
	9	16	15	8.77	16.35	14.93	9.02	16.04	14.84
Intra-day	3	4	5	3.00	3.97	4.97	2.95	4.04	4.96
	6	12	10	5.88	12.54	9.71	5.98	12.33	9.72
	9	16	15	8.93	16.31	14.28	9.04	16.12	14.82
				Recovery (%)					
				CFN	PRPN	PRC	CFN	PRPN	PRC
Inter-day				100.7	98.9	99.5	97.8	101.9	99.5
				97.2	100.7	96.5	99.7	102.6	97.6
				97.5	102.2	99.6	100.3	100.3	98.9
Intra-day				100.0	99.2	99.5	98.2	101.0	99.3
				97.9	104.5	97.1	99.6	102.7	97.2
				99.3	101.9	95.2	100.5	100.7	98.8
				RSD (%)					
				CFN	PRPN	PRC	CFN	PRPN	PRC
Inter-day				4.15	3.54	2.35	0.52	1.44	1.18
				0.45	2.82	1.04	0.59	0.49	1.65
				1.6	1.43	1.44	1.14	0.2	1.34
Intra-day				4.18	3.66	0.81	0.78	3.43	1.23
				0.71	2.47	3.42	1.19	0.33	0.98
				2.19	2.34	2.42	0.61	0.19	0.58
				RE (%)					
				CFN	PRPN	PRC	CFN	PRPN	PRC
Inter-day				0.67	-1.08	-0.47	-2.22	1.92	-2.22
				-2.83	0.69	-3.47	-0.28	2.58	-0.28
				-2.52	2.19	-0.44	0.26	0.27	0.26
Intra-day				0	-0.83	-0.53	-1.78	1	-1.78
				-2.06	4.53	-2.93	-0.39	2.72	-0.39
				-0.74	1.94	-4.78	0.48	0.73	0.48

RSD: Relative Standard Deviation, RE: Relative Error

RSD values remained consistently low for both models, demonstrating good repeatability and intermediate precision. Notably, PCA-ANN exhibited reduced inter-day variability, suggesting greater robustness against minor instrumental fluctuations and environmental variations.

Selectivity and Standard Addition Studies

Selectivity and potential matrix effects were evaluated using the standard addition method applied to commercial tablet solutions. Known amounts of CFN, PRPN, and PRC (0-6 µg/mL) were added and analyzed in triplicate. The recovery values summarized in Table 6 confirm that common excipients present in the pharmaceutical formulation did not interfere with the quantitative determination of the analytes. Low RSD values further demonstrate predictive stability in complex matrices. PCA-ANN again showed slightly improved consistency, reinforcing the beneficial impact of dimensional reduction on model conditioning.

Table 6. The recovery results obtained in the standard addition samples by the proposed RAW-ANN and PCA-ANN methods

	Added (µg/mL)			**Found (µg/mL)**					
				RAW-ANN			**PCA-ANN**		
	CFN	**PRPN**	**PRC**	**CFN**	**PRPN**	**PRC**	**CFN**	**PRPN**	**PRC**
Formulation	2	2	2	1.99	2.03	2.00	1.93	2.04	2.00
Formulation	4	4	4	3.94	4.02	3.91	3.96	4.02	3.89
Formulation	6	6	6	5.88	5.96	5.89	6.10	5.98	5.94
				Recovery (%)					
				RAW-ANN			PCA-ANN		
				CFN	PRPN	PRC	CFN	PRPN	PRC
				99.3	101.3	100.2	96.3	102.0	100.2
				98.5	100.6	97.8	98.9	100.5	97.3
				98.0	99.4	98.2	101.7	99.7	99.1
				RSD (%)					
				RAW-ANN			PCA-ANN		
				CFN	PRPN	PRC	CFN	PRPN	PRC
				1.04	3.79	1.04	2.52	1.80	2.02
				2.29	2.32	2.04	1.42	1.39	0.50
				2.85	3.03	2.61	0.35	2.41	1.95

RSD: Relative Standard Deviation

Analysis of Commercial Ternary Tablet Formulation

The developed models were applied to the simultaneous determination of CFN, PRPN, and PRC in commercial tablet formulations. The predicted content values (Table 7) were in close agreement with labeled amounts. Statistical parameters, including standard deviation and percent RSD, confirmed the analytical reliability of both methods. Despite strong spectral overlap and the presence of pharmaceutical excipients, accurate and precise quantification was achieved without any separation step.

Table 7. Analysis results obtained by applying RAW-ANN and PCA-ANN to tablets

			mg/tablet			
		RAW-ANN			PCA-ANN	
Exp No.	**CFN**	**PRPN**	**PRC**	**CFN**	**PRPN**	**PRC**
1	50.0	148.7	249.3	49.5	149.4	248.3
2	50.8	147.9	256.2	53.3	144.9	251.2
3	50.3	144.2	240.4	50.8	143.2	243.8
4	48.7	140.8	262.6	48.7	142.3	256.2
5	47.7	144.5	259.7	49.7	148.8	255.7
6	50.0	149.3	249.3	49.5	149.5	248.3
7	50.7	144.3	249.8	50.0	151.7	251.0
8	47.0	147.5	255.3	51.0	150.8	256.0
9	51.2	149.0	255.2	50.2	153.2	252.8
10	48.2	154.7	261.6	50.2	154.2	255.3
Mean	49.5	147.1	253.9	50.3	148.5	251.9
SD	1.46	3.84	6.81	1.27	3.06	4.13
RSD	2.95	2.61	2.68	2.52	2.06	1.64

SD: Standard Deviation, RSD: Relative Standard Deviation,
Label claim: 50 mg CFN/150 mg PRPN/250 mg PRC per tablet)

CONCLUSIONS

This study demonstrates that nonlinear ANN-based training strategies can successfully resolve highly collinear and severely overlapping UV spectral data without requiring prior chromatographic separation. By comparatively evaluating RAW-ANN and PCA-ANN architectures, the present work systematically illustrates how input dimensional organization directly influences predictive stability, computational efficiency, and model generalization in multicomponent spectrophotometric analysis.

Although both ANN strategies provided accurate and precise quantification of CFN, PRPN, and PRC in ternary pharmaceutical formulations, the incorporation of principal component compression prior to ANN modeling fundamentally improved the balance between model complexity and predictive robustness. Transforming correlated spectral variables into orthogonal principal components enhanced numerical conditioning, reduced overparameterization risk, accelerated convergence, and improved validation performance, while maintaining analytical accuracy.

Beyond the specific formulation investigated, the findings underscore a broader chemometric principle: in high-dimensional analytical systems, structured dimensional reduction can be as critical as the nonlinear modeling algorithm itself. The PCA-ANN framework presented herein offers a computationally efficient, scalable, and transferable strategy for addressing multicollinearity in spectroscopic datasets and provides a practical alternative for routine quality control analysis of complex multicomponent pharmaceutical preparations.

EXPERIMENTAL SECTION

Instruments and software

A Shimadzu UV-2550 UV-VIS spectrophotometer (Kyoto, Japan), equipped with Shimadzu UVPC software, was used to record absorption spectra in the wavelength range of 200-300 nm ($\Delta\lambda$ = 0.1 nm). Although the spectra were recorded over the 200-300 nm range, only the 220-300 nm region was used for RAW-ANN and PCA-ANN modeling in order to minimize potential interference from the solvent and pharmaceutical matrix components at lower wavelengths. Data acquisition and statistical analyses were performed using MATLAB 7.0 (MathWorks, USA) and Microsoft Excel. Custom-written m-files were developed within the MATLAB environment for the implementation of the RAW-ANN and PCA-ANN training models.

Chemicals and reagents

Reference standards of caffeine (CFN, 99.7% purity), propyphenazone (PRPN, ≥99% purity), and paracetamol (PRC, 99.6% purity) were obtained from Sigma-Aldrich (Steinheim, Germany). Analytical-grade methanol suitable for gradient applications was also purchased from Sigma-Aldrich (USA) and used as the solvent throughout the study. All working solutions were freshly prepared on a daily basis and protected from light during analysis to maintain chemical stability.

The commercial tablet formulation Minoset® Plus 30 (Bayer Türk Chemical Industry Ltd., Ümraniye, Istanbul, Turkey) was selected for pharmaceutical analysis. Each tablet is labeled to contain 50 mg CFN, 150 mg PRPN, and 250 mg PRC, along with common pharmaceutical excipients such as microcrystalline cellulose, hydroxypropyl methylcellulose, formaldehyde casein (Esma spreng), corn starch, talc, magnesium stearate, and colloidal anhydrous silica.

Preparation of stock standard, calibration, and validation solutions

Individual stock standard solutions of caffeine (CFN), propyphenazone (PRPN), and paracetamol (PRC) were prepared by accurately weighing 10.0 mg of each compound and dissolving them separately in methanol using 100 mL volumetric flasks. These primary stock solutions were subsequently diluted with methanol to obtain working solutions required for calibration, validation, and precision studies.

For the construction of the RAW-ANN and PCA-ANN training models, a total of 35 calibration mixtures were prepared within the concentration ranges of 2.5-12.0 µg/mL for CFN, 3.0-12.0 µg/mL for PRPN, and 3.0-16.0 µg/mL for PRC (Table 1).

Additionally, thirteen synthetic ternary mixtures covering different concentration combinations within the working range were prepared to evaluate model performance (Table 2). Precision studies were carried out by preparing intra-day and inter-day samples at three concentration levels for each analyte. The selected concentration levels were 3.0, 6.0, and 9.0 µg/mL for CFN; 4.0, 12.0, and 16.0 µg/mL for PRPN; and 5.0, 10.0, and 15.0 µg/mL for PRC (Table 4).

For accuracy assessment via the standard addition method, known amounts of CFN, PRPN, and PRC standard solutions (0, 2.0, 4.0, and 6.0 µg/mL) were spiked into aliquots of the commercial tablet solution. Each level was prepared in triplicate.

Preparation of Tablet Samples

Ten tablets of Minoset® Plus (Bayer Türk Chemical Industry Ltd.) were accurately weighed, thoroughly crushed in a mortar until a homogeneous mixture, and the quantity corresponding to one-twentieth of a tablet was transferred to a 100 mL volumetric flask after thorough pulverization of the tablets in a mortar. The flask was filled with methanol, and the powdered sample was mixed with a mechanical stirrer for one hour. Filtration was conducted through a 0.45 µm pore size nylon filter (ISOLAB, Wertheim,

Germany). The resulting solution was diluted with methanol to reach a concentration of 3.0 µg/ mL CFN, 9.0 µg/ mL PRPN, and 15 µg/ mL PRC. The diluted tablet solution was subjected to UV-VIS analysis for the application of the RAW-ANN and PCA-ANN methods.

ACKNOWLEDGMENTS

This work was carried out at the Chemometric Laboratory of Ankara University, Faculty of Pharmacy funded by the scientific research project number 10A3336001.

REFERENCES

1. K. Palur; S. C. Archakam; B. Koganti; *Spectrochim. Acta A Mol. Biomol. Spectrosc.*, **2020**, *243*, 118801.
2. V. Boerlin; B. Maeglin; W. Hägler; M. Kuhn; E. Nüesch; *Eur. J. Clin. Pharmacol.*, **1986**, *31*, 127-131.
3. J. K. Aronson; Meyler's Side Effects of Drugs: The International Encyclopedia of Adverse Drug Reactions and Interactions (Fifteenth Edition), Elsevier Science, Amsterdam, **2006**, pp. 2954-2955.
4. V. S. Reddy; S. Shiva; S. Manikantan; S. Ramakrishna; "Pharmacology of caffeine and its effects on the human body". *European Journal of Medicinal Chemistry Reports*. 2 March **2024**, *10,* 100138.
5. G. Faudone; S. Arifi; D. Merk; *Journal of Medicinal Chemistry*, **2021**, *64 (11),* 7156-7178.
6. A. Rajput; R. Sharma; R. Bharti; *Materials Today: Proceedings,* **2022**, *48,* 1407-1415.
7. L. C. Adam; D. Repantis; N. Boris; B. N. Konrad; M. Dresler; S. Kühn; *Brain and Cognition,* **2021***, 154*, 105802.
8. K. Delvadiya; P. Kabra; R. Kimbahune; N. Patel; L. V. G. Nargund; *Indian J Pharm Educ Res*, **2013***, 47(4)*, 65-72.
9. F. Soponar; D. Staniloae; G. Moise; B. Szaniszlo; V. David; *Rev. Roum. Chim*, **2013**, *58(4-5)*, 433-440.
10. H. Ibrahim; A. M. Hamdy; H. A. Merey; A. S. Saad; *J. Chromatogr. Sci.*, **2021**, *59(2)*, 140-147.
11. H. Tománková; M. Vasatova; *Pharmazie*, **1989**, *44(3)*, 197-198.
12. N. Kosmeas; J. T. Clerc; *Pharm. Acta Helv.*, **1989**, *64(1)*, 2-7.
13. A. Hałka-Grysińska; P. Ślązak; G. Zaręba; W. Markowski; A. Klimek-Turek; T. H. Dzido; *Anal. Methods*, **2012**, *4(4)*, 973-982.
14. K. Bober-Majnusz; A. Pyka-Pająk; *Processes*, **2024**, *12(6)*, 1153.
15. S. Markovic; Z. Kusec; *Pharmazie*, **1990**, *45(12)*, 935-936.
16. R. Injac; B. Srdjenovic; M. Prijatelj; M. Boskovic; K. Karljikovic-Rajic; B. Strukelj; *J. Chromatogr. Sci.*, **2008**, *46(2)*, 137-143.

17. W.P. Silva; L.A.J. Silva; C.H. França; R.M.F. Sousa; R.A.A. Muñoz; E.M. Richter; *Electroanalysis*, **2017**, *29*, 1860-1866.
18. E. Dinç; G. Kökdil; F. Onur; *J. Pharm. Biomed. Anal.*, **2001**, *26(5-6)*, 769-778.
19. A. F. Pulungan; D. L. P. Effendy; M. S. Siti; *AJPRD*, **2018**, *6(5)*, 5-8.
20. H. Rosaldi; A. F. Pulungan; R. Ridwanto; A. S. Daulay; *IJSP*, **2023**, *1(2)*, 74-79.
21. G. Gergov; A. Alin; P. Katsarov; V. Simeonov; D. Yankov; Y. Al-Degs; *Bulg. Chem. Commun*., **2018**, *50*, 265-273.
22. M. Ü. Özgür; G. Alpdoğan; B. Aşçi; *Monatsh. Chem.*, **2002**, *133(2)*, 219-223.
23. A. Domínguez Vidal; P. Ortega Barrales; A. Molina Díaz; *Microchim. Acta*, **2003**, *141(3)*, 157-163.
24. J. M. Xia; X. J. Wu; Y. J. Yuan; *Metabolomics*, **2007**, *3(4)*, 531-537.
25. G. Absalan; M. Soleimani; *Anal. Sci.*, **2004**, *20(5)*, 879-882.
26. G. Ioele; M. De Luca; E. Dinç; F. Oliverio; G. Ragno; *Chem. Pharm. Bull.*, **2011**, *59(1)*, 35-40.
27. E. Dinç; D. Baleanu; N. Ş. Köktaş; *Rev. Anal. Chem.,* **2011**, 30 (1), 11-15.

STUDIA UBB CHEMIA, LXXI, 2, 2026 (p. 125-145)
(RECOMMENDED CITATION)
DOI:10.24193/subbchem.2026.2.07

PHOTOCHEMICAL SELF-PURIFICATION OF AQUATIC SYSTEMS IN THE PRESENCE OF VITAMIN B_6

Viorica GLADCHI[a], Vladislav BLONSCHI[a], Gheorghe DUCA[b], Angela LIS[a,*], Radu SILAGHI-DUMITRESCU[c]

ABSTRACT. Vitamin B_6 (pyridoxine, PN) released from anthropogenic and biogenic activities can influence the chemical self-purification of surface waters through its photochemical transformations. The present study aimed to investigate the kinetics and mechanisms of pyridoxine photodegradation under conditions that partially simulate the natural environment (pH ~7, aerated medium) using simulated solar irradiation. Three model systems were investigated: (1) *PN–hv*; (2) *PN–H_2O_2–hv*; (3) *PN–H_2O_2–Cu(II)–hv*, using direct spectrophotometry (λ = 328 nm). The kinetic parameters determined included partial reaction orders (using the van't Hoff method), effective rate constants, and half-lives ($\tau_{1/2}$). Direct photolysis of PN follows a partial reaction order of 0.2 with respect to [PN], with $k = (5.38\pm0.26)\cdot10^{-4}$ s^{-1} and $\tau_{1/2}$ = 21±0.5 min. However, the low quantum yields $(7.31–10.70)\cdot10^{-3}$ indicate that direct photolysis of vitamin B_6 is negligible under natural aquatic conditions. In the presence of H_2O_2, the partial reaction orders are 0.3 (PN) and 0.7 (H_2O_2), with $W = k\cdot[PN]^{0.3}\cdot[H_2O_2]^{0.7}$, $k = (3.69\pm0.11)\cdot10^{-4}$ s^{-1} and $\tau_{1/2}$ = 31.1±0.30 min. For *PN–H_2O_2–Cu(II)*, the partial reaction orders are 0.2 (PN), 0.4 (H_2O_2), and 0.3 (Cu^{2+}) with $k = (3.91\pm0.17)\cdot10^{-4}$ s^{-1}, and $\tau_{1/2}$ = 29.2±0.53 min. In conclusion, PN undergoes measurable photodegradation under simulated natural conditions.

Keywords: *Vitamin B_6, pyridoxine, photolysis, H_2O_2, Cu(II), water self-purification, reaction kinetics.*

[a] *Moldova State University, Faculty of Chemistry and Chemical Technology, 60 Mateevici str., MD-2009, Chisinau, Republic of Moldova*
[b] *Moldova State University, Institute of Chemistry, 3 Academiei str., MD-2028, Chisinau, Republic of Moldova*
[c] *Department of Chemistry and Chemical Engineering, Babes-Bolyai University, 11 A. Janos Street, RO-400028, Cluj-Napoca, Romania*
* *Corresponding author: angela.lis@usm.md*

INTRODUCTION

The increasing anthropogenic impact on aquatic ecosystems leads to the deterioration of their physicochemical characteristics. The problem is compounded by the fact that the self-purification capacity of these water systems is significantly lower (and continues to make it smaller) with respect to the quantity and quality of pollutants entering them.

Water self-purification can occur through multiple physical, biological and chemical processes. Among these, chemical self-purification in the upper layers of water under sunlight is particularly important, as it can be achieved through photochemical degradation of pollutants.

Water pollution with organic matter is a pressing problem that requires continuous evaluation and investigation. Therefore, it is important to study the role of various pollutants with reducing properties in the photochemical processes of water self-purification. Vitamins, including vitamin B_6, are among these substances. Vitamin B_6 in natural waters is present as a result of metabolic processes of aquatic organisms, discharges from the pharmaceutical industry producing food additives, and municipal wastewater. Vitamin B_6 concentrations in natural waters are generally very low and depend on several natural and anthropogenic factors [1, 2]. In the neutral or weakly alkaline environment characteristic of natural waters, pyridoxine (PN) is the most stable form of vitamin B_6 [3-8].

In the surface layers of water, photolysis is a predominant pathway of chemical self-purification. Photolytic transformations in nature occur under the influence of ultraviolet radiation. For most organic pollutants, maximum spectral activity occurs within the wavelength range of 310–350 nm [9-10]. Photochemical transformations of pollutants may proceed via direct, induced, or sensitized photolysis.

Direct photolysis occurs when a pollutant (P) undergoes chemical transformation under the influence of sunlight, according to the equation [9-10]:

$$\mathrm{P} + h\nu \rightarrow \mathrm{P}^{*} + Products \quad (1)$$

Induced photolysis is characterized by the oxidation of P by free radicals formed during the decomposition of photoinitiator molecules under the influence of sunlight. In aqueous media, the most common photoinitiator is hydrogen peroxide (H_2O_2), so the reaction process can be represented as follows [9-10]:

$$\mathrm{H_2O_2} + h\nu \rightarrow 2\bullet\mathrm{OH} \quad (2)$$

$$2\bullet\mathrm{OH} + \mathrm{P} \rightarrow Products \quad (3)$$

Another pathway of photochemical transformation of pollutants in aquatic environments is sensitized photolysis, which involves the participation of sensitizing species (S):

$$S + hv \rightarrow S^* \quad (4)$$

$$S^* + \mathrm{P} \rightarrow Products \quad (5)$$

The behavior of vitamin B_6 in aquatic systems has been poorly studied. Therefore, understanding its role in the photochemical self-purification processes of natural waters is of considerable importance.

RESULTS AND DISCUSSION

Direct photolysis

For the direct photolysis of vitamin B_6 (pyridoxine, PN) under the established conditions, the kinetic parameters of the process were determined, including the partial reaction order with respect to the substrate concentration (Figure 1).

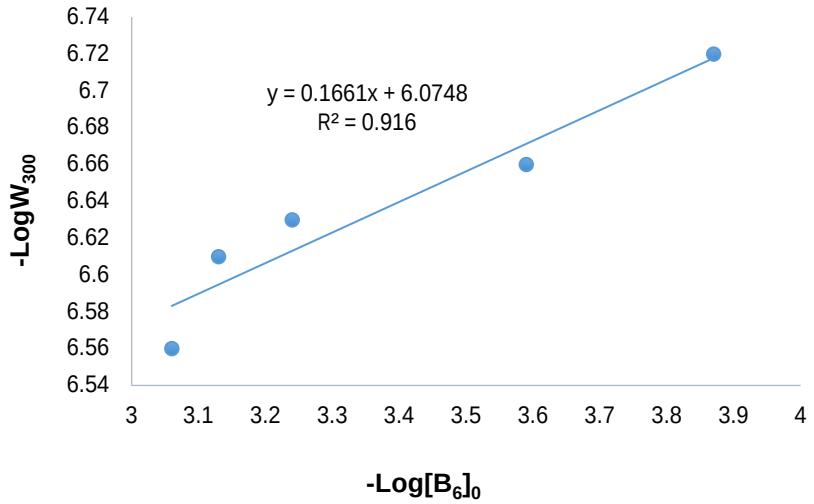

Figure 1. Determination of the partial reaction order (log-log plot of rate vs. [B_6]) for the photochemical oxidation of vitamin B_6 (20^0C, pH = *const.* = 7). Radiation source: Oriel Solar Simulator, AM1.5D filter [own data]

The data used to determine the reaction order with respect to the concentration of vitamin B_6 during direct photolysis are presented in Table S.1. The partial reaction order for the direct photolysis of vitamin B_6 was found to be 0.2. Therefore, the mathematical expression describing the reaction rate can be written as follows:

$$W = \kappa \cdot [B_6]^{0.2} \quad (6)$$

The effective rate constant (at different concentrations of components in the systems) depends on several factors, including temperature, dissolved oxygen concentration, and pH.

Under the experimental conditions employed in this study, the effective rate constant for the direct photolysis of vitamin B_6 was calculated to be $k = (5.38 \pm 0.26) \cdot 10^{-4}$ s^{-1}. Based on this value, the half-life of the process was determined to be $\tau_{1/2} = 21.0 \pm 0.5$ min.

Previous studies have investigated the photochemical transformations of vitamin B_6 under similar conditions and identified the products formed during direct photolysis [11-13] (Table 1).

Table 1. Vitamin B_6 (pyridoxine) photoproducts under various conditions

Conditions	Radiation sources	The main products of photolysis	Comments/ mechanisms	Bibliographic source
pH 7.0, O_2 present	UV (254–300 nm)	4-Pyridoxic acid (4-PA), traces of pyridoxal	The quantum yield is low; quinone-methide formation as intermediates	[11]
pH 7.0, O_2 present	UV (313–365 nm)	4-PA, lactone derivatives, dehydropyridoxine	The main pathway is hydrolysis of the quinone-methide intermediates	[12]
pH 5–9	UV (290–350 nm)	Traces of pyridoxal-5-phosphate (due to hydrolysis), 4-PA	The quantum yield is very low; the protonation configuration is important	[13, 14]
pH 7.0, O_2 present	UVC (254 nm)	Chain termination with the formation of low molecular weight organic acids	Direct photolysis with radical products (C–N and C–C cleavages)	[11]

Therefore, the existing literature indicates several possible products of vitamin photodegradation that may be confirmed or ruled out in future research.

The determination of the light intensity emitted by the solar simulator is essential for the quantitative evaluation of photochemical transformations of vitamin B_6 in aqueous solution. The efficiency of light energy utilization in photochemical reactions is characterized by the quantum yield, which is defined as the ratio between the amount of product formed and the amount of absorbed light during irradiation. Therefore, accurate determination of the photon flux emitted by the irradiation source is necessary for the calculation of the quantum yield of direct photolysis.

For this purpose, the photon flux of the Solar Simulator was determined using the potassium ferrioxalate(III) chemical actinometer, $K_3[Fe(C_2O_4)_3]\cdot 3H_2O$ (Table 2). The use of this actinometer was appropriate because potassium ferrioxalate(III) is sensitive in the spectral range of 250–480 nm, while vitamin B_6 exhibits a maximum absorption at 328 nm, which falls within this interval. The synthesized chemical actinometer was irradiated under the same experimental conditions as the studied system, and the photon flux was subsequently calculated. Simultaneously, a control sample of identical composition that was not exposed to irradiation was monitored. No formation of Fe(II) ions was observed in the control sample, confirming that the photochemical transformation occurred only under irradiation.

Table 2. Luminous flux and energy flux of Solar Simulator Oriel 9119X, AM1.5D filter

$[K_3[Fe(C_2O_4)_3]]$	ϕ	$\Delta n\ (Fe^{2+})/\Delta t \cdot 10^8$, mol·s^{-1}	$I_{avg.}$ (photon flux)·10^8, Einstein·s^{-1}	$I_{avg.}$ (photon flux)·10^6, Einstein·L^{-1}·s^{-1}	Luminous flux·10^8, Einstein·cm^{-2}·min^{-1}	Energy flux·10^2, Joules·cm^{-2}·min^{-1}
0.006 M	1.26	32.90	26.10	26.10	124.00	58.00
0.012 M	1.26	32.80	26.00	26.00	124.00	58.00
0.015 M	1.26	32.80	26.00	26.00	124.00	58.00

The obtained results indicate that the photon flux emitted by the Solar Simulator equipped with the AM 1.5D filter was $(26.10\pm0.06)\cdot 10^{-6}$ Einstein·L^{-1}·s^{-1}. Based on the irradiated surface area, it was also possible to calculate the average light intensity, luminous flux, and energy flux of the irradiation source (Table 2). The obtained data confirmed that the emitted radiation intensity does not depend on the initial concentration of the chemical actinometer or on traces of impurities, since very close results were obtained for three different concentrations of potassium ferrioxalate(III).

To evaluate the probability and efficiency of direct photolysis of vitamin B_6 in aqueous systems, the quantum yields of the process were determined for all investigated concentrations (Table 3).

Table 3. Kinetic parameters of the vitamin B_6 direct photolysis

$[B_6]_0 \cdot 10^4$, M	$W_{300} \cdot 10^7$, $M \cdot s^{-1}$	$\phi \cdot 10^3$	$k \cdot 10^4$, s^{-1}	$\tau_{1/2}$, min
1.34	1.90	7.31	5.38±0.26	21.0±0.5
2.56	2.20	8.46		
5.73	2.33	8.96		
7.34	2.47	9.50		
8.64	2.78	10.70		

The obtained results showed that the quantum yield of vitamin B_6 direct photolysis is significantly lower than unity and decreases with decreasing substrate concentration in solution. This behavior may be explained by the fact that the process occurs in dilute aqueous solutions (10^{-4} M), where photoexcited molecules are efficiently deactivated through collisions with solvent molecules, resulting in non-radiative energy dissipation.

The determined quantum yield values, ranging from $7.31 \cdot 10^{-3}$ to $10.70 \cdot 10^{-3}$, indicate a relatively low probability of direct photochemical transformation of vitamin B_6 under the studied conditions. Although the calculated half-life values demonstrate that the substrate undergoes measurable degradation under irradiation, the low quantum yield suggests that only a small fraction of absorbed photons effectively initiates photochemical conversion. Extrapolating the results obtained under laboratory conditions to real environmental conditions, it can be concluded that the direct photolysis of vitamin B_6 in natural waters is relatively limited, especially considering that the concentration of vitamin B_6 in aquatic environments is usually very low, typically ranging from pM to nM levels. Moreover, the efficiency of this process is influenced by environmental factors such as cloudiness, time of day, season, solar radiation intensity etc. Therefore, under natural aquatic conditions, the contribution of direct photolysis to the degradation of vitamin B_6 may be considered negligible.

Photolysis of vitamin B_6 in the presence of hydrogen peroxide

It is known that the chemical composition of natural waters also includes hydrogen peroxide, which ensures their dynamic redox balance and the content of which varies in the range of 10^{-5}-10^{-7} M. When exposed to UV radiation in the range of 300-310 nm, photolytic decomposition of hydrogen peroxide occurs with the formation of $OH^{\cdot}$ radicals:

$$H_2O_2 + h\nu \rightarrow 2HO^{\bullet} \quad (7)$$

$$H_2O_2 + HO^{\bullet} \rightarrow HO_2^{\bullet} + H_2O \quad (8)$$

Therefore, it is of interest to investigate the influence of hydrogen peroxide on the photodegradation of vitamin B_6 under conditions inspired by the composition of natural waters. This was achieved by modeling the system consisting of a solution of vitamin B_6 and hydrogen peroxide at pH 7.0, which was subjected to irradiation with a Solar Simulator with a filter which simulates the amount of solar energy and the wavelength of UV rays reaching the soil surface. The concentration of vitamin B_6 was varied in the range of 10^{-4} M, and of hydrogen peroxide in the range of 10^{-5} M.

To determine the partial reaction order of the induced photolysis with respect to the concentration of vitamin B_6, the required data were calculated, as presented in Table S.2. The partial reaction order was determined graphically from the dependence of ($-\log W_{300}$) on ($-\log C_{B6}$). The slope of the resulting linear plot with respect to the x-axis corresponds to the partial reaction order and was found to be 0.3 (Figure 2).

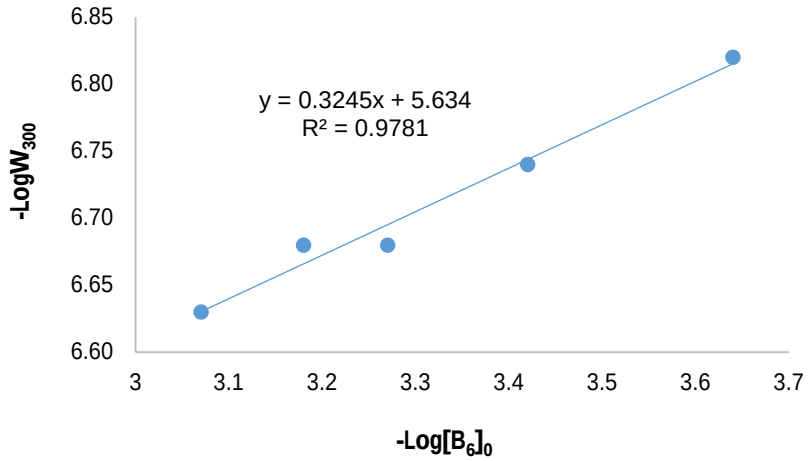

Figure 2. Determination of the partial reaction order (log-log plot of rate vs. [B_6]) for the photodegradation of vitamin B_6 in the presence of hydrogen peroxide ([H_2O_2] = *const.* = $3 \cdot 10^{-5}$ M, 20^0C, pH = *const.* = 7). Radiation source: Oriel Solar Simulator, AM1.5D filter [own data]

Similarly, the data required to determine the partial reaction order of induced photolysis with respect to the concentration of hydrogen peroxide were obtained and are presented in Table S.3. The partial reaction order with respect to hydrogen peroxide was determined to be 0.7 (Figure 3).

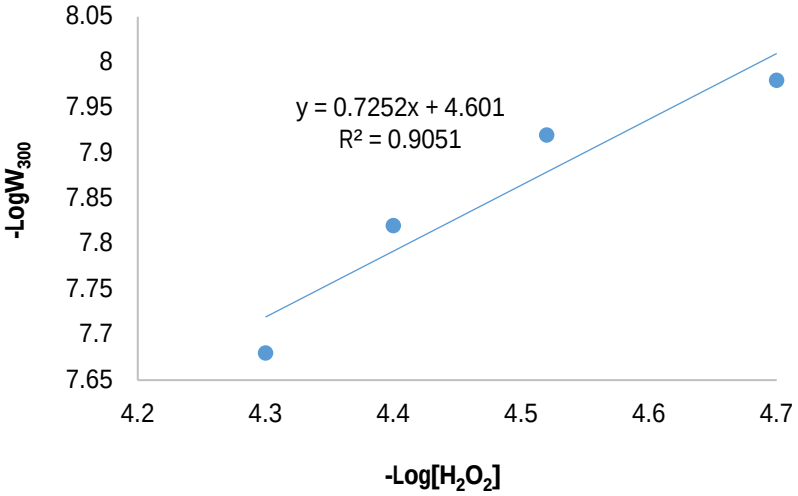

Figure 3. Determination of the partial reaction order (log-log plot of rate vs. $[H_2O_2]$) for the photodegradation of vitamin B_6 in the presence of hydrogen peroxide ($[B_6]$ = *const*. = $3 \cdot 10^{-4}$ M, 20^0C, pH = *const*. = 7). Radiation source: Oriel Solar Simulator, AM1.5D filter [own data]

Consequently, the following kinetic equation describing the dependence of the reaction rate on the concentrations of the system components was derived:

$$W = \kappa \cdot [B_6]^{0.3} \cdot [H_2O_2]^{0.7} \quad (9)$$

where: k – the rate constant (s^{-1}), which is influenced by temperature, dissolved oxygen concentration in water, and pH value.

For the photooxidation of vitamin B_6 in the presence of hydrogen peroxide, the effective rate constant was calculated to be $(3.69 \pm 0.11) \cdot 10^{-4}$ s^{-1} at various concentrations of the system components. Based on this value, the half-life was determined to be 31.1±0.3 min.

Upon irradiation of a mixture of pyridoxine and hydrogen peroxide, the initial stage involves the photolysis of hydrogen peroxide with the formation of hydroxyl radicals [15]. These radicals subsequently interact with the substrate and promote its degradation. Data reported by several authors who investigated the photolysis of vitamin B_6 in the presence of hydrogen peroxide [13, 16–20] indicate the formation of several products, including pyridoxal, 4-pyridoxic acid, and other low-molecular-weight compounds (Table 4).

Table 4. Possible products of photolysis of pyridoxine (vitamin B_6) in the presence of H_2O_2

Product	Formation mechanism	Bibliographic source
Pyridoxal (PL)	•OH attack on the $–CH_2OH$ group → formation of an aldehyde	[20-28]
4-Pyridoxic acid (4-PA)	Oxidation of the aldehyde group → carboxylic acid	[13, 17]
6-Hydroxy-pyridoxine (6-OH-PN)	Hydroxylation of the aromatic ring •OH	[18]
Pyridoxyquinone-type products	Oxidation of the aromatic ring → quinone-like products	[19]
Peroxide adducts (hydroperoxide, endoperoxide)	Adduct formation with $^1O_2$ or •OH; unstable intermediates	[19]
Small acids (formic, oxalic), CO_2	Mineralization in excess of •OH	[20]
Fragmentation (isopyridoxal etc.)	C–N and C–C bond cleavage	[28]

Analysis of the effective rate constants and half-lives for the direct photolysis of pyridoxine and its photolysis in the presence of hydrogen peroxide shows that the second process proceeds less efficiently (Table 5).

Table 5. Effective constant and half-life of pyridoxine (vitamin B_6) photolysis under various conditions [own data]

System	Effective constant (k), s^{-1}	Half-life ($\tau_{½}$), min
Pyridoxine-hv	$(5.38±0.25)\cdot10^{-4}$	21.0±0.5
Pyridoxine-H_2O_2-hv	$(3.69±0.11)\cdot10^{-4}$	31.1±0.3

The obtained results can be theoretically explained on the basis of previous studies conducted in this field [4, 13, 14, 19-21]. In aqueous solution, pyridoxine (PN, vitamin B_6) undergoes direct photolysis mainly through photoexcitation of the pyridine chromophore, leading to oxidation to pyridoxal (PL) and subsequently to products such as pyridoxic acid (4-PA). However, when hydrogen peroxide (H_2O_2) is present, the observed rate of PN photodegradation decreases.

Several photophysical and photochemical factors may account for this inhibitory effect. One possible explanation is the UV-screening effect of H_2O_2. Hydrogen peroxide absorbs UV radiation below 300 nm, partially overlapping with the absorption spectrum of PN. As a result, the intensity of

UV radiation available to excite PN molecules is reduced, thereby decreasing the rate of direct photolysis. However, since PN is present in the reaction mixtures at concentrations approximately one order of magnitude higher than those of hydrogen peroxide and exhibits significantly higher molar extinction coefficients owing to its aromatic structure, the shielding effect is expected to contribute only marginally to the observed inhibition.

The reduced efficiency of vitamin photooxidation may also be associated with limited radical generation and radical recombination processes. Although H_2O_2 can generate hydroxyl radicals (•OH) upon photolysis, this process proceeds relatively slowly in neutral aqueous media in the absence of a catalyst. Furthermore, radical recombination (•OH + •OH → H_2O_2) decreases the concentration of reactive species available for PN oxidation [22–24].

Finally, in the absence of metal catalysts, the distribution of reactive oxygen species (ROS) may differ, further reducing the efficiency of substrate photooxidation. Without Cu^{2+} or Fe^{3+} ions, H_2O_2 remains relatively stable under irradiation. Thus, although it acts as an oxidant in catalytic (Fenton-like) systems, in a simple *PN–H_2O_2* photolysis system hydrogen peroxide may instead suppress the direct photochemical degradation of PN [19].

Taken together, these considerations explain why the direct photolysis of pyridoxine proceeds more efficiently than photolysis in the presence of hydrogen peroxide. Nevertheless, these hypotheses require further verification and should be confirmed by additional experimental evidence obtained using modern analytical techniques.

Photolysis of vitamin B_6 in the presence of H_2O_2 and Cu^{2+} ions

An important component of the chemical composition of natural waters is Cu^{2+} ions, which act as effective catalysts in pollutant transformation reactions occurring during chemical self-purification processes. The Cu^{2+}/Cu^{+} redox couple exhibits a catalytic effect in numerous oxidation–reduction systems. It is also known that Cu(II) complexes, upon irradiation, can form excited species capable of promoting substrate oxidation, according to the following reaction [25]:

$$Cu(II)\text{-}L + h\nu \rightarrow Cu(II)\text{-}L^{\cdot} \rightarrow Cu(I) + L^{+} + e \qquad (10)$$

At the same time, Cu(I) ions promote the generation of additional hydroxyl radicals (•OH), according to the following equation [25]:

$$Cu(I) + H_2O_2 \rightarrow Cu(II) + HO^{\bullet} + OH^{-} \qquad (11)$$

Therefore, to more realistically simulate natural water conditions, a model system was designed in which the kinetic behavior of pyridoxine photodegradation was investigated in the presence of hydrogen peroxide and Cu^{2+} ions. Under neutral conditions (pH ≈ 7.0), the concentration of pyridoxine was 10^{-4} M, while the concentrations of hydrogen peroxide and Cu^{2+} ions varied within the range of $1.0 \cdot 10^{-6}$ - $5.0 \cdot 10^{-6}$ M.

Similarly to the previous systems, the initial rates of the modeled photochemical processes were determined (Tables S.4–S.6). The differential Van't Hoff method was used to calculate the partial reaction orders. Based on the experimental data, plots of lgW_{300} the logarithm of concentration were constructed for each varying system component. The partial reaction order was determined from the slope of the resulting linear plot with respect to the x-axis (Figures 4–6).

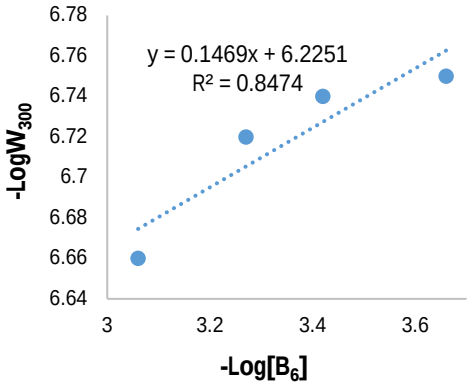

Figure 4. Dependence of the negative logarithm of the reaction rate of vitamin B_6 photooxidation on the negative logarithm of its concentration in the system under the influence of UV radiation. $[H_2O_2]$ = *const.* = $3 \cdot 10^{-5}$ M; $[Cu^{2+}]$ = *const*. = $3 \cdot 10^{-6}$ M. Radiation source: Oriel Solar Simulator, AM1.5D filter [own data]

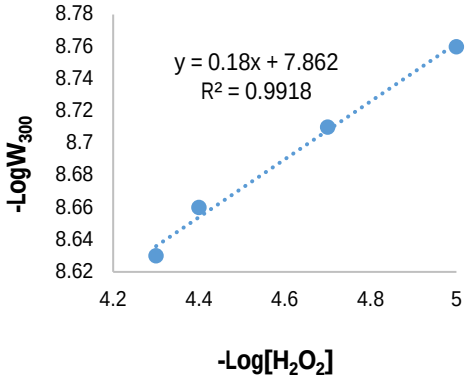

Figure 5. Dependence of the negative logarithm of the photooxidation reaction rate of vitamin B_6 on the negative logarithm of the hydrogen peroxide concentration in the system under the influence of UV radiation. $[B_6]$ = *const*. = $3 \cdot 10^{-4}$ M; $[Cu^{2+}]$ = *const*. = $3 \cdot 10^{-6}$ M. Radiation source: Oriel Solar Simulator, AM1.5D filter [own data]

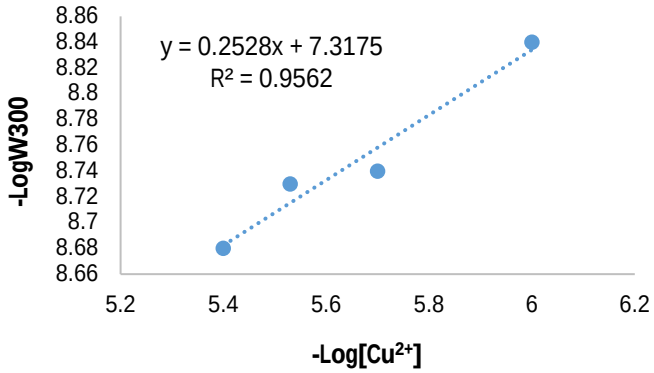

Figure 6. Dependence of the negative logarithm of the reaction rate of vitamin B_6 photooxidation on the negative logarithm of the concentration of copper ions in the system under the influence of UV radiation. [B_6] = *const.* = $3 \cdot 10^{-4}$ M; [H_2O_2] = *const.* = $3 \cdot 10^{-5}$ M. Radiation source: Oriel Solar Simulator, AM1.5D filter [own data]

As a result of the calculations, the partial reaction orders with respect to the concentrations of the system components were determined to be 0.2 for vitamin B_6, 0.4 for hydrogen peroxide, and 0.3 for Cu^{2+} ions. Accordingly, the rate equation describing the photolysis of vitamin B_6 in the studied system can be expressed as follows:

$$W = \kappa \cdot [B_6]^{0.2} \cdot [H_2O_2]^{0.4} \cdot [Cu(II)]^{0.3} \quad (12)$$

The effective rate constant of the process was determined to be k = $(3.91 \pm 0.17) \cdot 10^{-4}$ s^{-1} and is influenced by the temperature and pH of the medium. Based on this value, the half-life of the process was calculated to be 29.2±0.5 min.

Comparison of the kinetic parameters obtained for vitamin B_6 photolysis in the B_6-H_2O_2-Cu^{2+} system with those determined for the B_6-H_2O_2 system, for which the half-life was 31 min, reveals only a slight decrease in the substrate half-life of approximately 2 min (Table 6). This finding indicates that the process is largely governed by the photochemical behavior of pyridoxine, which is present at a concentration of 10^{-4} M, approximately two orders of magnitude higher than that of copper ions. Under these conditions, Cu^{2+} does not appear to exhibit significant catalytic activity.

Table 6. Effective constant and half-life of pyridoxine (vitamin B_6) photolysis under various conditions [own data]

System	Effective constant (k), s^{-1}	Half-life ($\tau_{½}$), min
Pyridoxine-hv	$(5.38\pm0.25)\cdot10^{-4}$	21.0±0.5
Pyridoxine-H_2O_2-hv	$(3.69\pm0.11)\cdot10^{-4}$	31.1±0.3
Pyridoxine-H_2O_2-Cu(II)-hv	$(3.91\pm0.17)\cdot10^{-4}$	29.2±0.5

Analysis of the literature data indicates that several products may be formed during the photodegradation of vitamin B_6 in the presence of hydrogen peroxide and Cu^{2+} ions under neutral conditions (Table 7).

Table 7. Possible products of photolysis of pyridoxine in the presence of H_2O_2 and ions of Cu^{2+}

Product	Main mechanism	Role of H_2O_2 / Cu^{2+} / light	Bibliographic source
Pyridoxal (4'-aldehyde)	Oxidation of the primary hydroxymethyl group (–CH_2OH) to an aldehyde via •OH attack or one-electron oxidation of radical intermediates	•OH produced by Cu(II)/H_2O_2 (Fenton-like system) or photogenerated ROS oxidize the side chain; irradiation can photoreduce Cu(II) to Cu(I), enhancing ROS generation	[4, 11, 26]
Isopyridoxal / isomeric aldehydes	Radical-induced isomerization and intramolecular hydrogen transfer following excitation or radical attack	The radical pool (•OH, O_2•$^-$) generated from H_2O_2/Cu promotes molecular rearrangements; photochemical excitation increases excited-state species	[11, 26]
Pyridoxi-quinone (oxidized pyridine ring, 3,6-quinone derivatives)	Sequential electron/ proton abstractions from ring followed by O_2 addition and dehydrogenation to give quinone-like structures	Strong oxidants (•OH and photogenerated ROS) promote aromatic ring oxidation; Cu/H_2O_2 systems accelerate deeper oxidative transformation	[11, 28, 29]
Hydroxylated derivatives (6-OH-pyridoxine etc.)	•OH addition to the aromatic ring producing mono- and polyhydroxylated product	•OH generated in Fenton-like Cu/H_2O_2 systems are the main oxidizing agents; these processes increase the •OH flux under near-neutral pH when Cu redox cycling occurs	[30-37]
Demethylated / dealkylated fragments	Homolytic cleavage of C–C or C–O bonds in excited states or via radical attack, leading to loss of	Radical-induced bond scission is enhanced by high ROS concentrations; Cu-catalyzed peroxygenation may produce	[27, 31]

Product	**Main mechanism**	**Role of H_2O_2 / Cu^{2+} / light**	**Bibliographic source**
	methyl or hydroxymethyl fragments	selective C–H hydroxylation followed by bond cleavage	
Pyridoxic acid and other carboxylic fragments	Oxidation of aldehyde intermediates to carboxylic acids; further oxidation and ring cleavage produce small organic acids	High oxidative load (sustained •OH flux) promotes deeper oxidation and partial mineralization; photo-assisted Cu redox cycling increases the extent of transformation	[11, 26]
Low-molecular-weight carbonyls, short-chain acids, CO_2	Progressive oxidative fragmentation and ring opening produce small carbonyl compounds and acids, eventually leading to mineralization to CO_2	Enhanced by sustained ROS generation in Cu/H_2O_2 systems and photo-Fenton-like processes; the extent depends on irradiation time and reagent concentrations	[30]

To confirm the formation and identity of these products, future investigations should be carried out using modern methods and analytical techniques.

CONCLUSIONS

Although vitamin B_6 undergoes measurable direct photolysis under simulated solar irradiation, its highly subunitary quantum yield indicates that direct photolysis is likely negligible under natural aquatic conditions. The presence of hydrogen peroxide and Cu(II) ions decreases the photodegradation rate of pyridoxine, possibly due to competition for UV photons and quenching of the excited states of PN, without efficient generation of reactive radicals in neutral solution. This phenomenon requires further investigation to identify the degradation products formed and to elucidate the underlying mechanisms of the process.

These results demonstrate the involvement of vitamin B_6 in the photochemical self-purification processes occurring in the surface layers of aquatic systems. Such participation may contribute to the restoration of the original properties of aquatic environments when vitamin B_6 enters these systems as a pollutant. Nevertheless, further comprehensive studies are required to fully clarify its environmental fate and role in aquatic photochemical processes.

EXPERIMENTAL SECTION

To investigate the behavior of vitamin B_6 (pyridoxine) in water under irradiation, model systems were constructed according to the 'simple-to-complex' principle. The simplest system consisted of a vitamin B_6 aqueous solution representative of that encountered in natural surface waters. The substrate concentration studied was of the order of 10^{-4} M, and the pH was maintained at 7.0. To ensure constant pH values, a buffer solution of pH 7.0 (25°C in H_2O) consisting of disodium hydrogen phosphate/potassium dihydrogen phosphate, produced by Sigma-Aldrich, was used.

These conditions were simulated in the laboratory using a Solar Simulator Oriel Model 9119X equipped with an Air Mass 1.5 Direct (AM1.5D) filter, which reproduces the solar energy flux and the spectral distribution of UV radiation reaching the Earth's surface when the Sun is positioned at approximately 48.2° from the zenith.

To study the kinetics of vitamin B_6 phototransformations in aqueous solution, a direct spectrophotometric method was employed using a phosphate buffer at pH 7. The absorbance of the solution was measured at 328 nm in order to determine the substrate concentration. Under laboratory conditions, the following photochemical systems were modeled: vitamin B_6-$H_2O_{dist.}$-O_2-hv (1); vitamin B_6-$H_2O_{dist.}$-O_2-H_2O_2-hv (2); *vitamin* B_6-$H_2O_{dist.}$-O_2-H_2O_2-*Cu(II)*-hv (3). All systems were investigated under aerobic conditions.

Hydrogen peroxide (H_2O_2), a naturally occurring oxidant in surface waters, was added in system (2). The inclusion of copper(II) compounds in system (3) was justified by their environmental relevance and by the catalytic role of Cu(II) ions in redox transformations of pollutants.

Kinetic relationships were studied for each modeled system by varying the concentration of a single component while keeping the others constant. All experiments were performed in triplicate, and the results are presented as the arithmetic means. In the kinetic studies, the initial reaction rates were determined within the first 300 s (W_{300}). This time interval was selected due to the relatively rapid degradation of the substrate and to highlight the characteristics of the initial stage of the process, which corresponds to the maximum reaction rate. Based on these data, partial reaction orders were determined, rate equations were derived, and effective rate constants together with substrate half-lives were calculated. The effective rate constant is presented in the form (k±Δk), where Δk represents the absolute measurement error, calculated according to the following relationship:

$$\frac{\Delta k}{k} = \frac{\Delta t}{t} + \frac{\Delta A}{A_0 \cdot 2.3 \cdot log\frac{A_0}{A}} + \frac{\Delta A}{A \cdot 2.3 \cdot log\frac{A_0}{A}} \quad (13)$$

where: Δk – the absolute measurement error (s^{-1}); k – the effective rate constant (s^{-1}); Δt – the absolute error in time measurement (s); t – time (s); ΔA – the absolute error in absorbance measurement; A_0 – the absorbance at time 0; and A – the absorbance at time t.

The concentrations of the components in the model systems were chosen to approximate natural conditions, except for vitamin B_6: hydrogen peroxide at approximately 10^{-5} M, Cu(II) ions at approximately 10^{-6} M, and vitamin B_6 at 10^{-4} M, ensuring appropriate optical density values for spectrophotometric measurements. The numerical data obtained from these experiments are presented in Supporting Information Tables S.1–S.6.

Determination of the quantum yield

To determine the light intensity of the radiation sources used in this study, the potassium ferrioxalate(III) chemical actinometer method ($K_3[Fe(C_2O_4)_3]$) was employed [38, 39].

Synthesis of the potassium ferrioxalate(III) chemical actinometer

The preparation of the potassium ferrioxalate(III) chemical actinometer involves the synthesis of the complex $K_3[Fe(C_2O_4)_3]\cdot 3H_2O$. Potassium ferrioxalate crystals were obtained by mixing three volumes of 1.5 M $K_2C_2O_4$ solution with one volume of 1 M $FeCl_3$ solution. The resulting crystals were recrystallized three times at 45°C using warm double-distilled water and subsequently stored in the dark (Eq. 14) [38, 39]:

$$3K_2C_2O_4 + FeCl_3 \rightarrow K_3[Fe(C_2O_4)_3] + 3KCl \quad (14)$$

Green crystals were obtained as a result of the synthesis. For the actinometric measurements, potassium ferrioxalate(III) solutions of 0.006 M, 0.012 M, and 0.015 M were prepared.

Determination of photon flux

The photon flux of the Solar Simulator Oriel 9119X equipped with AM0 and AM1.5D filters was determined using the potassium ferrioxalate(III) chemical actinometer. The actinometer solution consisted of $K_3[Fe(C_2O_4)_3]\cdot 3H_2O$ dissolved in 0.01 N sulfuric acid. Upon irradiation, the following photochemical reactions occur (Eqs. 15 and 16) [38, 39]:

$$Fe(C_2O_4)_3^{3-} \xrightarrow{h\vartheta} Fe^{2+} + C_2O_4^- + 2C_2O_4^{2-} \quad (15)$$

$$Fe(C_2O_4)_3^{3-} + C_2O_4^- \rightarrow Fe^{2+} + 2CO_2 + 3C_2O_4^{2-} \quad (16)$$

A volume V_1 of the actinometer solution was irradiated for a time interval t. Subsequently, a volume V_2 of the irradiated solution (usually 1 mL) was transferred into a 25 mL volumetric flask (V_3). Then, (10 – V_2) mL of 0.1 N sulfuric acid, 2 mL of 0.1% aqueous 1,10-phenanthroline solution, and 5 mL of acetate buffer solution were added.

The volume was adjusted to the mark with double-distilled water, mixed thoroughly, and kept in the dark for 30 min to establish equilibrium. The absorbance of the Fe(II)-1,10-phenanthroline complex was measured at 510 nm. The amount of formed Fe^{2+} ions (υ) was calculated according to Eq. 17 [38, 39]:

$$\nu_{Fe^{2+}} = 10^{-3} \frac{V_1 \cdot V_3 \cdot A}{V_2 \cdot \varepsilon \cdot l} \quad (17)$$

where: V_2 – the volume of irradiated actinometer solution (mL); V_3 – the final dilution volume (mL); A – the absorbance at 510 nm; ε – the molar extinction coefficient at 510 nm ($1.11 \cdot 10^4$ $M^{-1} \cdot cm^{-1}$); l – the optical path length of the cuvette (cm).

The photon flux was calculated according to Eq. 18 [38, 39]:

$$I = 10^{-3} \frac{V_1 \cdot V_3 \cdot A}{V_2 \cdot \varepsilon \cdot l \cdot \Phi \cdot t} \quad (18)$$

where: I – the light intensity (photon flux) emitted by the irradiation source, Einstein$\cdot s^{-1}$; Φ – the quantum yield of potassium ferrioxalate(III).

The irradiation interval (t) was selected to ensure absorbance changes within the range of 0.1 – 0.6 units. For improved accuracy, a blank experiment using a non-irradiated sample was also performed.

Calculation of Quantum Yield and Light Parameters

The light intensity allows the calculation of the quantum yield for photochemical reactions. The quantum yield of product formation (Φ) was determined as the ratio between the amount of product formed (Δv) and the amount of absorbed light (ΔI_a), during the irradiation time (t) [38, 39]:

$$\Phi = \frac{\Delta \nu}{\Delta I_a \cdot t} \quad (19)$$

The average light intensity (photon flux) emitted by the irradiation source ($I_{avg.}$) was calculated according to Eqs. 20 and 21 [38, 39]:

$$I_{avg.} = \frac{\Delta\nu(Fe^{2+})}{\Delta t \cdot \Phi} \quad (20)$$

where: $I_{avg.}$ – the average light intensity emitted by the irradiation source, (Einstein·s^{-1}); $\Delta\nu$ (Fe^{2+}) – the amount of Fe^{2+} formed after irradiation (mol); Δt – the irradiation time (s); and Φ is the quantum yield.

$$I_{avg.} = \frac{\Delta\nu(Fe^{2+})\cdot 1000}{\Delta t \cdot \Phi \cdot V_s} \quad (21)$$

where: V_s – the irradiated sample volume (mL), and 1000 – the conversion factor from mL to L.

The luminous flux (Einstein·cm^{-2} ·min^{-1}) was calculated according to Eq. 22 [38, 39]:

$$Luminous\ flux = \frac{I_{avg.}\cdot 60}{S} \quad (22)$$

where: S – the irradiated surface area (cm^2); and 60 – the conversion factor from seconds to minutes.

The energy flux (J·cm^{-2}·min^{-1}) was determined according to Eq. 23 [38, 39]:

$$Energy\ flux = \frac{Luminous\ flux \cdot j \cdot h \cdot c \cdot 10^9 \cdot 100}{\lambda} \quad (23)$$

where: j – the number of photons per Einstein ($6{,}02\cdot10^{23}$); h – Planck's constant ($6{,}626\cdot10^{-34}$ J·s); c – the speed of light ($3\cdot10^8$ m·s^{-1}); and λ – the wavelength of light (nm).

ACKNOWLEDGMENTS

The results have been obtained in the framework of the projects funding from the Ministry of Education and Research of the Republic of Moldova (project 010603 – Advanced research in computational and ecological chemistry: identification of technological procedures for water treatment and formation of water quality and quantity, and project 25.80013.5107.20ROMD – New redox and coordination chemistry with cobalamin and related systems (REDOXCOB)) and from the Ministry of Education and Research of Romania (joint funding for project REDOXCOB – PN-IV-PCB-RO-MD-2024-0515, contract no. 52PCBROMD/2025).

The authors thank Dr. Cezara Zagrean-Tuza and Nicoleta Andrian (UBB) for helpful discussions.

REFERENCES

1. L. P. Barada; L. Cutter; J. P. Montoya; E. A. Webb; D. G. Capone; S. A. Sañudo-Wilhelmy, *Front. Microbiol.*, 2013, 4, 25, DOI: 10.3389/fmicb.2013.00025.
2. M. A. Sneineh, *Nutr. Res. Food Sci. J.*, 2021, 4(1), 1–9, DOI: 10.31038/NRFSJ.2021411.
3. P. Bilski; M. Y. Li; M. Ehrenshaft; M. E. Daub; C. F. Chignell, Vitamin B6 (Pyridoxine) and Its Derivatives Are Efficient Singlet Oxygen Quenchers and Potential Fungal Antioxidants. *Photochemistry and Photobiology*, 2007, DOI: 10.1562/0031-8655(2000)0710129SIPVBP2.0.CO2.
4. J. Natera; W. Massad; N. A. García, The role of vitamin B6 as an antioxidant in the presence of vitamin B2-photogenerated reactive oxygen species. A kinetic and mechanistic study. *Photochem. Photobiol. Sci.*, 2012, 11(6), 938–945, DOI: 10.1039/c2pp05318g.
5. A. H. Merrill Jr; J. M. Henderson, Vitamin B6 metabolism by human liver. *Ann. N. Y. Acad. Sci.*, 1990, 585, 110–117, DOI: 10.1111/j.1749-6632.1990.tb28047.x.
6. R. Percudani; A. Peracchi, A genomic overview of pyridoxal-phosphate-dependent enzymes. *EMBO Rep.*, 2003, 4(9), 850–854, DOI: 10.1038/sj.embor.embor914.
7. R. G. Wilson; R. E. Davis, Clinical chemistry of vitamin B6. *Adv. Clin. Chem.*, 1983, 23, 1–68, DOI: 10.1016/s0065-2423(08)60397-2.
8. A. C. Eliot; J. F. Kirsch, Pyridoxal phosphate enzymes: mechanistic, structural, and evolutionary considerations. *Annu. Rev. Biochem.*, 2004, 73, 383–415, DOI: 10.1146/annurev.biochem.73.011303.074021.
9. Gh. Duca; Iu. Scurlatov, *Ecological Chemistry*, Publishing Center M.S.U., Chisinau, 2002, 279 pp., ISBN: 9947-70-172-8.
10. M. S. Aleksevnina; I. V. Pozdnev, *Sanitary Hydrobiology with Fundamentals of Aquatic Toxicology: Textbook*, Perm State National Research University, Perm, 2016, 205 pp., ISBN: 978-5-7944-2769-1.
11. H. Reiber, Photochemical reactions of vitamin B6 compounds, isolation and properties of products. *Biochim. Biophys. Acta*, 1972, 279(2), 310–315, DOI: 10.1016/0304-4165(72)90148-1.
12. D. W. Brousmiche, et al., Photogeneration of quinone methide-type intermediates from vitamin B6. *J. Org. Chem.*, 2002, 67(2), 559–566, DOI: 10.1016/S1010-6030(01)00654-2.
13. M. Wu; Q. Xu; A. Strid; J. M. Martell; L. A. Eriksson, Theoretical study of pyridoxine (vitamin B6) photolysis. *J. Phys. Chem. A*, 2011, 115(46), 13556–13563, DOI: 10.1021/jp205724k.
14. P. Bilski; M. Y. Li; M. Ehrenshaft; M. E. Daub; C. F. Chignell, Vitamin B6 (pyridoxine) and its derivatives are efficient singlet oxygen quenchers and potential fungal antioxidants. *Photochem. Photobiol.*, 2000, 71(2), 129–134, DOI: 10.1562/0031-8655(2000)071<0129:SIPVBP>2.0.CO;2.

15. H. Ikai; K. Nakamura; M. Shirato; T. Kanno; A. Iwasawa; K. Sasaki; Y. Niwano; M. Kohno, Photolysis of hydrogen peroxide, an effective disinfection system via hydroxyl radical formation. *Antimicrob. Agents Chemother.*, 2010, 54(12), 5086–5091, DOI: 10.1128/AAC.00751-10.
16. R. Joshi; S. Adhikari; T. Mukherjee, Pulse radiolysis studies on pyridoxine. *Res. Chem. Intermed.*, 2002, 28(8), 703–713, DOI: 10.1163/15685670260373272.
17. R. J. Yang, et al., Vitamin B6 metabolism and biomarkers. *Animals*, 2023, 13(8), 1333, DOI: 10.3390/ani13081333.
18. J. M. Matxain, et al., Reactivity of vitamin B6 towards hydroxyl radicals. *J. Phys. Chem. A*, 2009, 113(28), 8010–8017, DOI: 10.1021/jp903023c.
19. B. K. Ohta; C. S. Foote, Characterization of pyridoxine endoperoxides and peroxides. *J. Am. Chem. Soc.*, 2002, 124(46), 12064–12065, DOI: 10.1021/ja0205481.
20. W. H. Glaze; J. W. Kang; D. H. Chapin, The chemistry of water treatment processes involving ozone, hydrogen peroxide and UV-radiation. *Ind. Eng. Chem. Res.*, 1995, 34(7), 2314–2323, DOI: 10.1021/ie00046a013.
21. S. L. Murov; I. Carmichael; G. L. Hug, *Handbook of Photochemistry*, 2nd ed.; CRC Press, 1993.
22. G. V. Buxton; C. L. Greenstock; W. P. Helman; A. B. Ross, *J. Phys. Chem. Ref. Data*, 1988, 17(2), 513–886.
23. J. J. Pignatello; E. Oliveros; A. MacKay, Advanced oxidation processes for organic contaminant destruction. *Crit. Rev. Environ. Sci. Technol.*, 2006, 36(1), 1–84.
24. I. Mansilla-Rivera; J. O. Nriagu, Copper Chemistry in Freshwater Ecosystems: An Overview. *J. Great Lakes Res.*, 1999, 25(4), 599–610, DOI: 10.1016/S0380-1330(99)70765-3.
25. G. Albarrán; F. Ramírez-Cahero; R. Aliev, Radiolysis of pyridoxine (vitamin B6) in aqueous solution under different conditions. *Radiat. Phys. Chem.*, 2008, DOI: 10.1016/j.radphyschem.2007.09.013.
26. P. N. Moorthy; E. Hayon, One-electron redox reactions of water-soluble vitamins. III. Pyridoxine and pyridoxal phosphate (vitamin B6). *J. Am. Chem. Soc.*, 1975, DOI: 10.1021/ja00841a009.
27. R. Joshi; S. Kapoor; T. Mukherjee, Free radical reactions of pyridoxal (vitamin B6): A pulse radiolysis study. *Res. Chem. Intermed.*, 2002, DOI: 10.1163/15685670260373272.
28. K. Aoki, et al., Crystal structure of a photolysis product of vitamin B6: A pyridodihydrofuran-condensed skeleton compound of pyridoxal 5'-phosphate. *J. Mol. Struct.*, 2017, DOI: 10.1016/j.molstruc.2017.06.068.
29. M. Pérez-Moya; T. Kaisto; M. Navarro; L. J. del Valle, Study of the degradation performance (TOC, BOD, and toxicity) of bisphenol A by the photo-Fenton process. *Environ. Sci. Pollut. Res.*, 2016, DOI: 10.1007/s11356-016-7386-6.
30. I. Garcia-Bosch, et al., Copper-catalyzed oxidation of alkanes with H2O2 under mild conditions. *Angew. Chem. Int. Ed.*, 2016, DOI: 10.1002/anie.201607216.
31. J. W. Moffett; R. G. Zika, Reaction kinetics of hydrogen peroxide with copper and iron in seawater. *Environ. Sci. Technol.*, 1987, DOI: 10.1021/es00162a012.

32. B. Kim, et al., Fenton-like Chemistry by a Copper(I) Complex and H2O2 Relevant to Enzyme Peroxygenase C–H Hydroxylation. *J. Am. Chem. Soc.*, 2023, DOI: 10.1021/jacs.3c02273.
33. L. Wang, et al., A review on advanced oxidation processes: mechanisms, catalysts and optimizations. *Chem. Eng. J.*, 2022, DOI: 10.1016/j.cej.2021.132108.
34. S. Hussain, et al., A review of copper-based Fenton reactions for the removal of organic pollutants from wastewater over the last decade. *Environ. Sci. Pollut. Res.*, 2021, DOI: 10.1007/s11356-021-16097-0.
35. D. Kahoun, et al., Development and validation of an LC-MS/MS method for quantification of vitamin B6 vitamers in seafood. *J. Food Compos. Anal.*, 2022, DOI: 10.1016/j.jfca.2022.104518.
36. R. J. Yang, et al., Phosphate, 4-pyridoxine acid and pyridoxal in animal tissues: LC/MS identification. *J. Chromatogr. B*, 2023, DOI: 10.1016/j.jchromb.2015.07.008.
37. S. A. Walling, Fenton and Fenton-like wet oxidation for degradation of organic wastes: a critical review. *npj Mater. Degrad.*, 2021, DOI: 10.1038/s41529-021-00192-3.
38. A. Lis. Direct photolysis of cysteine and thiourea in aqueous solutions. Studia Universitatis Moldaviae, 2016, 6(96), 133–141. ISSN 1814-3237.
39. A. Lis; V. Gladchi; S. Travin. Direct photolysis of some thiol substances in the aquatic environment and their role in ecochemical processes in natural waters. Chisinau: CEP USM, 2022, pp. 200–219. ISBN 978-9975-159-05-0.

STUDIA UBB CHEMIA, LXXI, 2, 2026 (p. 147-170)
(RECOMMENDED CITATION)
DOI:10.24193/subbchem.2026.2.08

ADSORPTION OF METHYLENE BLUE ONTO RAW SECONDARY SEWAGE SLUDGE: ISOTHERM, KINETIC, AND CHARACTERIZATION STUDIES

Ilhaam KHATRI[a], Ashish TAMBI[b,*], Deepak Singh RAJAWAT[c]

ABSTRACT. The increased discharge of synthetic dyes into aquatic ecosystems has caused significant environmental concerns, prompting the search for sustainable adsorbents. Sewage sludge, an abundant by-product of wastewater treatment facilities, offers the opportunity for dye removal within a circular economy paradigm. This study investigates the potential of raw dried secondary treated sewage sludge as an effective adsorbent for the removal of methylene blue, a cationic dye, from aqueous solutions. The adsorbent was characterized by Fourier transform infrared spectroscopy, field emission scanning electron microscopy, and Brunauer–Emmett–Teller surface analysis to evaluate its morphology, functional groups and textural properties. Batch adsorption experiments examined the effects of pH, initial dye concentration, adsorbent dosage, particle size, and contact time on the removal efficiency. Optimal conditions were observed at pH 9, with 0.5 g of sewage sludge (particle size 0.5 mm) in 50 mL of 10 mg/L dye solution and a contact time of 30 minutes. The adsorption equilibrium data conformed best to the Langmuir isotherm model, with a maximum monolayer adsorption capacity of 14.08 mg/g. Kinetic studies indicated that the adsorption process followed the pseudo-second-order model (R^2=0.999), suggesting chemisorption as the predominant mechanism. The adsorbent also exhibited a pH-stabilizing behaviour, wherein the solution pH after adsorption shifted toward neutrality regardless of the initial pH, highlighting its suitability for practical wastewater treatment applications. The study demonstrates the potential of raw secondary treated sewage sludge as an eco-friendly adsorbent, aligning with sustainable wastewater treatment strategies.

Keywords: *Adsorption, dye removal, methylene blue, sewage sludge, wastewater treatment*

[a] *Department of Environmental Science, IIS (Deemed to be University), Jaipur, Rajasthan, India*
[b] *Amity School of Earth and Environmental Sciences, Amity University Punjab, Mohali, Punjab, India*
[c] *Department of Chemistry, IIS (Deemed to be University), Jaipur, Rajasthan, India*
* *Corresponding author: ashishtambi006@gmail.com*

1. INTRODUCTION

The textile industry makes a huge contribution to the global economy, but it is also a major source of environmental pollution due to the discharge of dye-laden wastewater. Textile processing makes considerable use of synthetic dyes to produce bright and diversified colours in fabrics. These dyes are usually highly stable and resistant to degradation, allowing them to persist in aquatic environments. Furthermore, textile businesses rely on considerable amounts of water, resulting in significant amounts of wastewater. For dyeing about a kg of fabric, 70-150 litres of freshwater are required [1].

During manufacturing operations, synthetic dyes like methylene blue (MB), a common cationic dye, are frequently released into water bodies because they are not completely bonded to textile fibres [2]. Studies show that around 50% of dyes used end up being released into the water bodies [3]. These colours disturb food chains, increase biochemical oxygen demand (BOD), and reduce dissolved oxygen (DO) in aquatic environments by restricting sunlight penetration, which hinders photosynthesis. Furthermore, their toxicity, carcinogenicity, and mutagenicity characteristics provide serious health risks [2].

Methylene blue (MB), in particular, is an aromatic heterocyclic compound known for its environmental persistence and potential toxicity. At high concentrations, it can cause adverse health effects in humans such as chest pain, headaches, abdominal discomfort, and methemoglobinemia [3]. Therefore, the removal of methylene blue from wastewater has garnered considerable attention. Various physicochemical techniques have been developed for dye removal, including coagulation, filtration, oxidation, and membrane separation. However, adsorption has emerged as one of the most effective and economical techniques due to its increased efficiency, simplicity, and broad applicability [4]. Activated carbon is a conventional adsorbent known for its excellent performance, but its high production and regeneration costs have driven the search for low-cost alternatives [5]. Global production of Sewage Sludge (SS), a by-product of municipal wastewater treatment, is enormous. 3.96 million tons of dry sludge are produced annually in India alone from the roughly 62,000 million litres of sewage per day (MLD) that are created, of which only around 20,120 MLD are treated [6]. The most popular methods for managing and disposing of sewage sludge are landfilling, land application, and incineration. All of these methods have serious disadvantages, including land degradation, soil contamination, and air pollution [7].

Despite the abundance of sewage sludge, its capacity as a low-cost adsorbent for colour removal has garnered limited attention. While prior research has investigated the conversion of sludge into biochar for dye

adsorption, such procedures typically require considerable energy inputs and operating expenditures, which may reduce the overall sustainability and economic viability of the process, especially for large-scale applications [8]. The potential of using raw sludge directly as a low-cost, readily available material has not been adequately assessed. Therefore, the current work is focused on the use of raw, dried sewage sludge with no chemical or thermal modification as an effective and affordable adsorbent for methylene blue removal from aqueous solutions. The main objectives of this research were to characterise and assess the adsorption capacity of raw sewage sludge for MB removal under various experimental factors. Adsorption isotherms and kinetic models were applied to assess the adsorption mechanism.

Unlike most studies that rely on thermally or chemically modified sludge, this work eliminates the need for energy-intensive or chemical pre-treatment, thereby significantly reducing operational costs and environmental impact. By directly repurposing sludge, the study aligns with circular economy principles, promoting a waste-to-resource approach that addresses both waste management and water pollution challenges.

2. MATERIALS AND METHODS

2.1. Dye Solution Preparation

Analytical grade methylene blue (MB) dye ($C_{16}H_{18}ClN_3S$) was obtained from Molychem India LLP, Mumbai (India). A stock solution of 500 mg/L was prepared using deionised water and diluted to obtain six initial working concentrations, i.e., 10, 20, 40, 50, 75 and 100 mg/L. The pH of the system was adjusted using 0.1 M NaOH (Merck Life Science Private Limited, Mumbai) and HCl (Thermo Fisher Scientific India Pvt. Ltd., Mumbai). All the reagents used were of analytical grade.

2.2. Collection and Preparation of Adsorbent

Dewatered secondary treated sewage sludge (SS) was collected from a nearby municipal wastewater treatment plant based on the Sequential Batch Reactor process located at Devri, Mansarovar, Jaipur, Rajasthan, India. The sludge was dried for 2-3 days, followed by oven drying at 105°C for 24 hours to ensure complete removal of moisture. The dried sludge was then crushed using a mortar and pestle and sieved to obtain a uniform particle size. The prepared sludge powder was stored in an airtight container for further use in batch adsorption studies.

2.3. Characterisation of Adsorbent

2.3.1. Fourier Transform Infrared Spectroscopy (FTIR)

FTIR analysis was performed using the Bruker FTIR Alpha 2 spectrometer to identify the functional groups present on the surface of the adsorbent before and after adsorption. The samples were analysed in the range of 4000–400 cm^{-1} with 4 cm^{-1} resolution using the KBr pellet method. Changes in peak intensities and positions were used to determine the interaction of functional groups with methylene blue dye molecules.

2.3.2. Scanning Electron Microscopy

The surface morphology and elemental composition of the dried sewage sludge were analysed using field emission scanning electron microscopy (FESEM). FESEM provided insights into the surface texture, porosity, and structural features of the sludge that might be helpful in adsorption.

2.3.3. Brunauer–Emmett–Teller (BET) Surface Area Analysis

Using nitrogen adsorption-desorption isotherms via BET analysis, the adsorbent's (before and after adsorption) specific surface area, pore volume, and pore size distribution were determined. To perform the measurements, a Quantachrome NOVA TouchWin v1.24 analyser was used. The SS sample for both before and after adsorption was degassed for approximately two hours at 150°C. The specific surface area was estimated using the produced isotherms, and the total pore volume was computed using the BET technique.

2.3.4. Determination of Point of Zero Charge (pH_{pzc})

The point of zero charge (pH_{pzc}) of the sewage sludge was determined by the pH drift method [9]. A series of 50 mL of 0.01 M NaCl solutions was adjusted to initial pH values ranging from 2 to 12 using 0.1 M HCl or NaOH. To each solution, 0.2 g of the dried adsorbent was added. The suspensions were then shaken at room temperature for 24 hours. The final pH values were recorded, and the difference between final and initial pH (ΔpH) was plotted against the initial pH. The point at which ΔpH = 0 was identified as the pH_{pzc} of the adsorbent.

2.4. UV–Vis Spectrophotometric Analysis of Methylene Blue

The concentration of methylene blue in aqueous solution was determined using a UV–Vis spectrophotometer (Shimadzu UV 1900i) by measuring the absorbance at the maximum wavelength (λmax) of 664 nm. A calibration curve was constructed using standard methylene blue solutions with concentrations

ranging from 0.5–10 mg/L. The absorbance values measured at 664 nm were plotted against the corresponding concentrations to obtain the calibration curve, which was subsequently used to determine the residual dye concentration in all adsorption experiments. The UV–Vis spectra of the standard solutions used for calibration are presented in Figure 1.

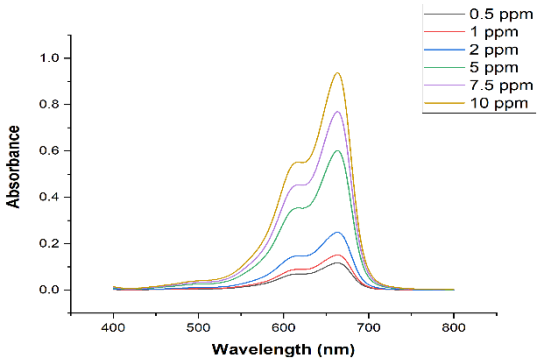

Figure 1. UV–Vis spectra of methylene blue standard solutions

3. BATCH ADSORPTION STUDY

Batch experiments were performed by adding 0.5 g of sewage sludge (SS) to 50 mL of methylene blue (MB) solution in 250 mL Erlenmeyer flasks. The flasks were agitated at 180 rpm in a rotary flask shaker (Icon Instruments Company, New Delhi) for 30 minutes and subsequently centrifuged at 3000 rpm for 10 minutes. For each adsorption experiment, the supernatant solution was analyzed using UV–Vis spectroscopy in the range of 400–800 nm, and the absorbance at 664 nm was used to determine the residual dye concentration. The effects of pH, initial dye concentration, particle size, adsorbent dosage, and contact time were analysed in the range of 3-11, 10-100 mg/L, 0.25-1 mm, 0.25-1 g, and 5-120 mins, respectively. The adsorption efficiency of sewage sludge and the amount of MB dye adsorbed were computed using equations (1) and (2) as mentioned below:

$$\% \text{ dye removal} = \left(\frac{C_o - C_f}{C_o}\right) * 100 \quad (1)$$

$$q_e = \left(\frac{C_o - C_f}{m}\right) * V \quad (2)$$

where C_o and C_f are the initial and final dye concentration (mg/L), q_e is the MB dye equilibrium concentration (mg/g), V is the volume of the dye solution, and m is the mass of adsorbent (g).

3.1. Adsorption Isotherm Models

The adsorption isotherms help in evaluating the correlation between q_e, i.e., the amount of adsorbed dye on the adsorbent (mg/g) and C_e, i.e., the concentration of dye adsorbed in the equilibrium phase (mg/L) in the liquid phase [10].

In the present study, adsorption mechanisms and the parameters involved in dye adsorption were investigated using two-parameter isotherms, including the Freundlich, Langmuir, Harkin-Jura, and Temkin isotherm models, to determine a specific relationship between dye in the liquid and solid phases—these models' experimental results over a broad range of concentrations and temperatures. The equations and their respective description to obtain the graphs are shown in Table 1.

Table 1. Adsorption isotherm models applied to the experimental data

Isotherm Model	Equation	Description	Parameters
Langmuir [10, 11]	$\frac{1}{q_e} = \frac{1}{K_L}.q_{max}.C_e + \frac{1}{q_{max}}$	q_e- amount of dye adsorbed at equilibrium q_{max}- maximum adsorption capacity K_L-adsorption energy C_e- concentration at equilibrium R_L- separation factor	K_L=intercept/slope q_{max}=1/intercept $R_L = 1/(1+K_LC_o)$
Freundlich [11]	$logq_e = logK_F + \frac{1}{n}logC_e$	q_e- adsorbent capacity at equilibrium C_e- concentration at equilibrium K_F- Freundlich constant *1/n*- relative adsorption capacity of the adsorbent	*1/n*= slope
Temkin [12, 13]	$q_e = B_T lnA_T + B_T lnC_e$	*T*- absolute temperature *R*- universal gas constant (8.314 J/mol·K) A_T- equilibrium binding constant b_T- heat of adsorption constant	$B_T = RT/b_T$
Harkin-Jura [11]	$\frac{1}{{q_e}^2} = \frac{B}{A} - \frac{1}{A}logC_e$	*B* and *A*- Harkin-Jura constants	

The Langmuir adsorption isotherm assumes that adsorption occurs on a homogeneous surface of the adsorbent and that the sites possess equal energy for adsorption. Further, it was assumed that adsorption proceeds until a monolayer is completed [5,10]. In contrast to the Langmuir isotherm, the Freundlich isotherm explains adsorption on heterogeneous surfaces and has different affinities. The Temkin isotherm determines whether the adsorption process is chemisorption or physisorption [13]. The model assumes the heat of adsorption decreases evenly as more pollutants are added to the surface [12]. The Harkin-Jura model is suitable for rough adsorbent surfaces where adsorption forms heterogeneous multi-layers and has different pore distributions [11].

3.2. Adsorption Kinetics

Experiments regarding adsorption kinetics were performed to determine the rate of adsorption. To investigate the kinetics of MB dye adsorption onto sewage sludge, Pseudo First-Order (PFO), Pseudo Second-Order (PSO), Elovich, and Intraparticle Diffusion (IPD) models were utilised, as shown in Table 2.

The Lagergren model (1898), also known as the Pseudo-first order (PFO) model, assumes that the mechanism involved in adsorption is physisorption, which is controlled by diffusion and mass transfer, while the Pseudo-second order (PSO) model assumes that the mechanism involved for adsorption is chemisorption (chemical sorption), which is a rate-limiting step [14]. The Elovich model is applied where the adsorbent's surface is heterogeneous, implying that adsorption occurs through chemisorption. The Weber-Morris model (1963) or Intra-particle diffusion (IPD**)** was applied to investigate the diffusion mechanism. This model helps in finding whether diffusion is the rate-limiting step for adsorption. The mathematical expressions for all the above-described models are provided in Table 2.

Table 2. Adsorption kinetic models applied to the experimental data [15]

Kinetic Model	Equation	Description
PFO	$ln\ (q_e - q_t) = ln\ q_e - k_1 t$	q_e- amount of dye adsorbed at equilibrium q_t- amount of dye adsorbed at time 't' k_1, k_2 and k_{id}- rate constants t- time α- initial adsorption coefficient β- desorption coefficient C_i- Intercept (boundary layer effect)
PSO	$t/q_t = (1/k_2 q_e^2) + t/q_e$	
Elovich	$q_t = \frac{1}{\beta} ln\ (\alpha\beta) + \frac{1}{\beta} ln\ t$	
IPD	$q_t = k_{id}\ .t^{1/2} + C_i$	

3.3. Thermodynamics study

To determine the thermodynamic parameters controlling the adsorption process, studies were carried out at 298, 308, and 318 K. As equilibrium was achieved, the dye solutions were centrifuged, and absorbance was taken at 664 nm using a UV-visible spectrophotometer. The thermodynamic parameters included are the change in Gibbs free energy (ΔG), change in enthalpy (ΔH), and change in entropy (ΔS), which were calculated by the Clausius-Clapeyron equation (3) and the Gibbs free energy equation (4)

$$\ln K_d = \frac{\Delta S}{R} - \frac{\Delta H}{RT} \quad (3)$$

$$\Delta G = \Delta H - T\Delta S \quad (4)$$

where K_d represents the constant associated with the Langmuir isotherm, R denotes the universal gas constant valued at 8.314 $J \cdot mol^{-1} K^{-1}$, and T indicates temperature (K). The expression used to determine the distribution coefficient (K_d) is given by equation (5).

$$K_d = q_e/C_e \quad (5)$$

4. RESULTS AND DISCUSSIONS

4.1. Adsorbent Characterization

4.1.1. FTIR

The FTIR spectra of sewage sludge (SS) before and after adsorption of methylene blue (MB) are shown in Figure 2(a) and (b), while the corresponding peak assignments are summarized in Table 3. The spectra indicate the presence of several functional groups on the sludge surface, including C–O, C=O, C–H, and O–H groups, which may participate in the adsorption process. After MB adsorption, noticeable changes in peak intensity and slight shifts in peak positions were observed, particularly for the C–O, C–H, and O–H stretching bands, indicating possible interactions between dye molecules and functional groups on the adsorbent surface. The shift of the O–H stretching band and changes in the C=O region suggest that hydrogen bonding and other surface interactions may contribute to the adsorption mechanism. These results indicate that oxygen-containing functional groups on the sewage sludge surface play an important role in MB dye adsorption.

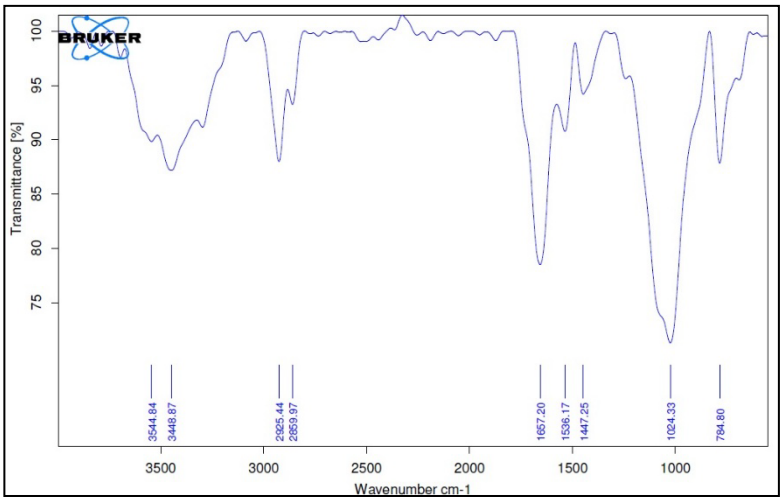

(a)

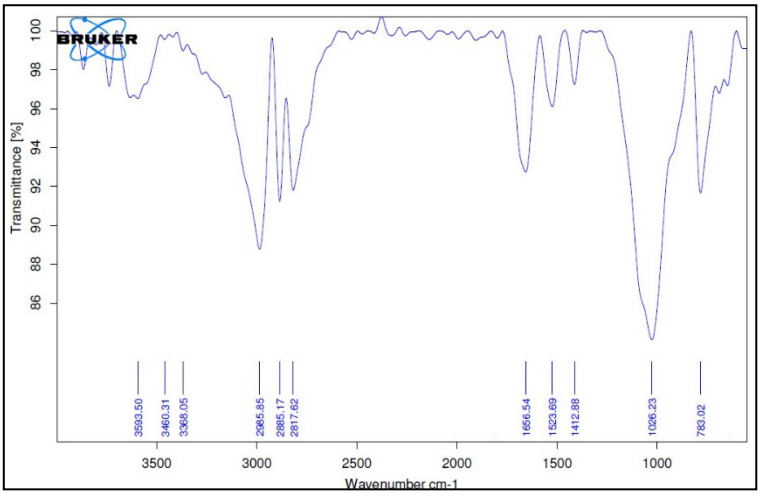

(b)

Figure 2. FTIR analysis (a) before and (b) after adsorption of methylene blue dye

Table 3. FTIR spectral analysis before and after the adsorption of the MB dye

Wavenumber (cm^{-1}) before adsorption	Wavenumber (cm^{-1}) after adsorption	Functional group	Band description	Reference
784.8	783.02	CH_2 scissoring deformation	Aliphatic moieties	[16]
1024.33	1026.23	C-O stretching	Alcohol	[5,17]
1447.25	1412.88	CH_2 rocking	Methylene group	[16]
1536.17 1657.20	1523.69 1656.34	C=O stretching vibrations	Amide group	[17,18]
2859.97 2925.44	2817.62 2885.17 2985.85	C-H stretching	Aliphatic chain	[17]
3448.87 3544.84	3368.05 3460.31 3593.50	-OH stretching vibration	Alcohol	[19]

4.1.2. Field Emission Scanning Electron Microscopy (FESEM)

The surface morphology of the sewage sludge (SS) adsorbent before and after MB adsorption was examined using FESEM at a magnification of 500 nm, as shown in Figure 2. Before adsorption (Figure 3a), the SS surface exhibited a porous and irregular structure with pores of varying shapes and sizes, providing numerous active sites for dye adsorption.

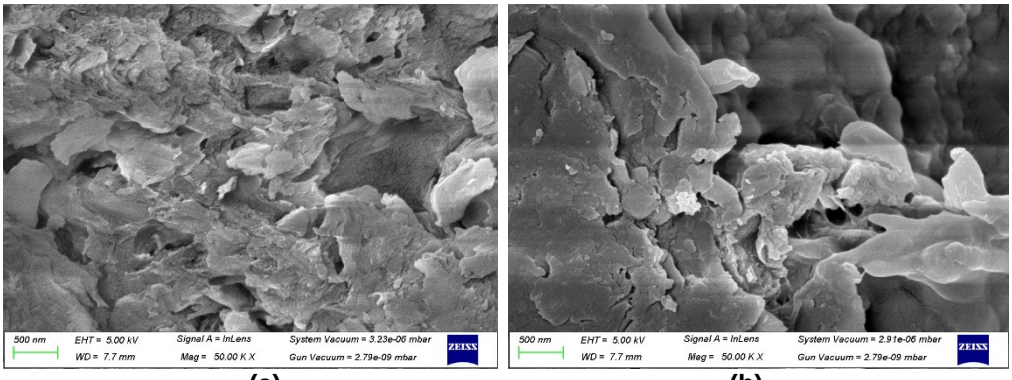

(a) **(b)**

Figure 3. FESEM results for SS (a) before adsorption, (b) after adsorption

After adsorption of MB molecules (Figure 3b), the surface appeared comparatively smoother, and several pores were partially covered or filled, indicating the deposition of dye molecules on the adsorbent surface. These morphological changes suggest that MB adsorption occurred through surface interaction and pore filling within the sludge matrix.

4.1.3. Brunauer–Emmett–Teller (BET)

The textural properties of the sewage sludge adsorbent were characterized using nitrogen adsorption–desorption analysis at 77 K. The adsorption isotherm exhibited a Type II profile, indicating multilayer adsorption behaviour typically associated with materials possessing macroporous structures or limited porosity (Figure 4a and 4b). The BET surface area of the sewage sludge was 1.669 m^2/g, with a total pore volume of 0.00437 cm^3/g and an average pore diameter of 10.47 nm (Table 4). The relatively low surface area is characteristic of untreated sludge materials and may be attributed to the presence of organic matter and mineral components that partially block internal pores.

After adsorption, the BET surface area decreased to 1.131 m^2/g, while the total pore volume decreased to 0.00353 cm^3/g, as shown in Table 4. In contrast, the average pore diameter increased slightly to 12.47 nm. The reduction in surface area and pore volume suggests that adsorbate molecules occupied and partially blocked the available pores of the sewage sludge adsorbent during the adsorption process, indicating effective interaction between the adsorbate molecules and the adsorbent surface.

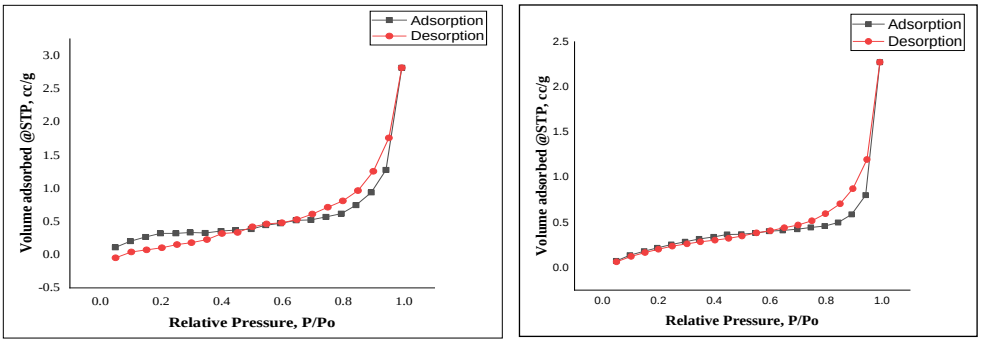

(a) **(b)**

Figure 4. Nitrogen adsorption/desorption isotherm plot of Sewage Sludge before (a) and after adsorption (b)

Table 4. Textural properties of the Sewage Sludge adsorbent before and after adsorption

Sample (Sewage Sludge)	BET Surface Area (m^2/g)	Total pore volume (cm^3/g)	Average Pore diameter (nm)
Before adsorption	1.669	0.00437	10.47
After adsorption	1.131	0.00353	12.47

4.2. Batch adsorption studies

Batch adsorption experiments were carried out to investigate the influence of key operational parameters on the removal of methylene blue using sewage sludge as an adsorbent. The effects of solution pH, adsorbent particle size and dosage, initial dye concentration, and contact time were examined to determine the optimal conditions for adsorption.

4.2.1. Effect of pH

The adsorption capacity and dye solubility are significantly influenced by the pH of the dye solution. This study assessed the MB dye adsorption capacity on sewage sludge across a pH range of 3-11. As depicted in Figure 5(a), the amount of dye removed decreased with rising pH from 3 to 5. From pH 3 to pH 5, the amount of dye eliminated is reduced. The dye removal decreases further when the pH rises from 5 to 7. However, an impressive increase in the sorption capacity with increasing pH was noted, between pH 9 and pH 11. While the highest adsorption was observed at pH 11, the increase in adsorption capacity compared to pH 9 was marginal. Considering the minimal performance disparity and the operational and environmental benefits of functioning at a reduced pH, pH 9 was considered appropriate. Maintaining a pH of 9 aligns with standard wastewater treatment pH ranges, hence reducing the necessity for post-treatment neutralization. To verify the adsorption process spectroscopically, UV–Vis spectra of methylene blue solution at different contact times (for an initial concentration of 10 mg/L) were recorded. As shown in Figure 5(b), the absorbance at 664 nm decreases progressively with increasing contact time, confirming dye uptake by the adsorbent.

The pH-dependent behaviour of MB adsorption can be explained in terms of the point of zero charge (pH_{pzc}). The point of zero charge (pH_{pzc}) of the sewage sludge (adsorbent) was determined using the pH drift method, as shown in Figure 5(c) and found to be 7.6. At pH values higher than 7.6, the sludge surface becomes negatively charged, which enhances attraction toward the positively charged MB dye molecules. Conversely, at pH values lower than pH_pzc, the surface becomes positively charged, resulting in reduced adsorption due to electrostatic repulsion. This explains the observed increase in dye removal efficiency under alkaline conditions, which is similar to several other studies reported for the adsorption of methylene blue [5].

In the present study, a significant shift in solution pH was also observed after the adsorption of methylene blue onto sewage sludge. Regardless of the initial pH, whether acidic (pH 3–5) or alkaline (pH 9–11), the final pH consistently stabilized in the near-neutral range of 6.6 to 7.1. For instance, an initial pH of 3.0 increased to 6.6, while a starting pH of 9.0 decreased to 7.1 after the adsorption process. This convergence toward neutrality reflects a pH-stabilising or

neutralizing effect. Such behaviour is likely due to the acid–base interactions and ion-exchange properties of surface functional groups present in sewage sludge, particularly hydroxyl, carboxylic, and amine moieties, which can either release or absorb protons depending on the solution environment. A similar phenomenon was reported by another study, where sludge-derived biochar exhibited a stabilising effect on pH following the adsorption of both phosphate and methylene blue [18]. This is attributed to residual mineral components and functional groups retained or modified during sludge treatment, which facilitate proton exchange and mitigate extreme pH variations. This pH-regulating property of sewage sludge enhances its practical applicability in real-world wastewater treatment scenarios, ensuring that treated effluents maintain acceptable pH levels for safe discharge or further processing.

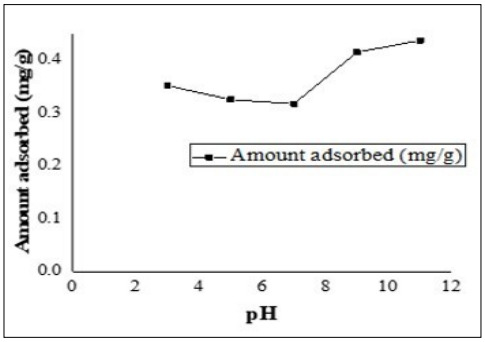

Figure 5(a) Effect of dye solution's pH (0.5 g of SS, $[MB]_i$ = 10 mg /L, V = 50 mL, particle size = 0.5 mm, T = 25°C and shaking speed = 180 rpm)

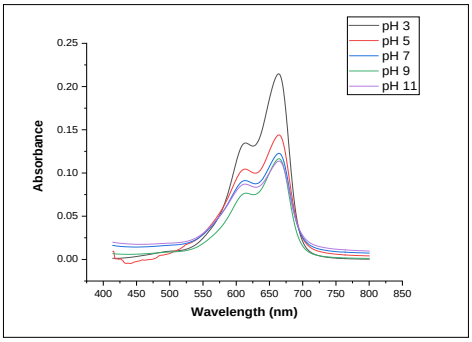

Figure 5(b) UV–Vis spectra of methylene blue solutions after adsorption at different pH using sewage sludge adsorbent.

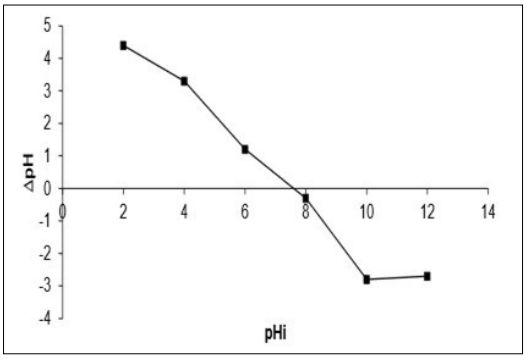

Figure 5(c) Determination of point of zero charge (pH_pzc) of sewage sludge by pH drift method.

4.2.2. Effect of Initial Dye Concentration and Contact Time

The dye solutions were prepared at varying concentrations ranging from 10 to 100 mg/L. The impact of initial dye concentration along with the contact time on dye removal is depicted in Figure 6(a). The results concerning the effect of contact time indicate that the absorbance of MB dye increased significantly as the contact time was extended from 5 minutes to 30 minutes. After 45 minutes, the system reached equilibrium for every concentration. Also, an increase in adsorption capacity was seen with increasing dye concentration, which may be due to increased mass transfer. To verify the adsorption process spectroscopically, UV–Vis spectra of methylene blue solution at different contact times (for an initial concentration of 10 mg/L) were recorded. As shown in Figure 6(b), the absorbance at 664 nm decreases progressively with increasing contact time, confirming dye uptake by the adsorbent.

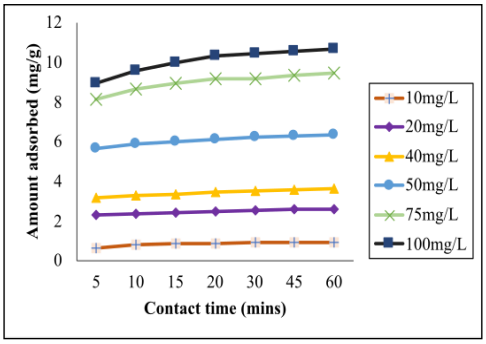

Figure 6(a). Effect of dye concentration and contact time (0.5 g of SS, particle size = 0.5 mm, V = 50 mL, pH =9, T = 25°C and shaking speed = 180 rpm)

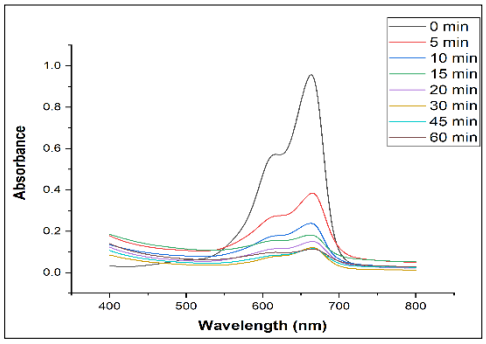

Figure 6(b). Time-dependent UV–Vis spectra of methylene blue solution (10 mg/L) during adsorption onto sewage sludge.

4.2.3. Effect of Particle Size

The sorption capacity of MB was studied at three particle sizes, i.e., 0.25, 0.5, and 1 mm, for which the amount of adsorbed dye was observed. As shown in Figure 7(a), the dye removal capacity increased with lower particle size (0.25 mm) due to increased surface area. However, the difference was not significant, but the MB dye removal capacity increased with increasing contact time and decreasing particle size of the adsorbent. The UV–Vis spectra of the residual dye solutions obtained for different adsorbent particle sizes are shown in Figure 7(b), where the decrease in absorbance at 664 nm indicates enhanced adsorption with decreasing particle size.

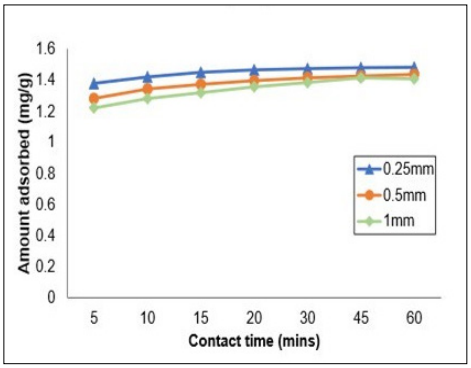

Figure 7(a). Effect of adsorbent particle size and rate of adsorption (0.5 g of SS, $[MB]_i$ = 10 mg /L, V = 50 mL, pH = 9, T = 25°C and shaking speed = 180 rpm)

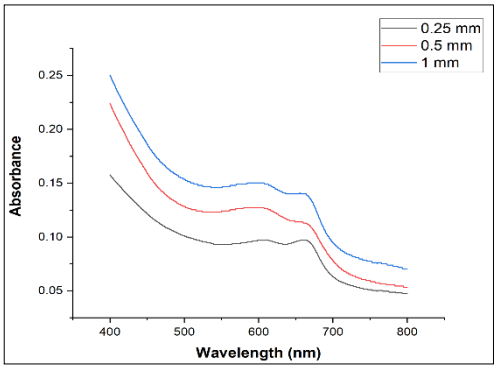

Figure 7(b). UV–Vis spectra of methylene blue solutions after adsorption using different particle sizes of sewage sludge (contact time 30 min)

4.2.4. Effect of Adsorbent Amount

The effect of the adsorbent amount for MB dye was studied by varying the adsorbent amount, ranging from 0.25 g to 1 g of SS in 50 mL of dye solution (10 mg/L).

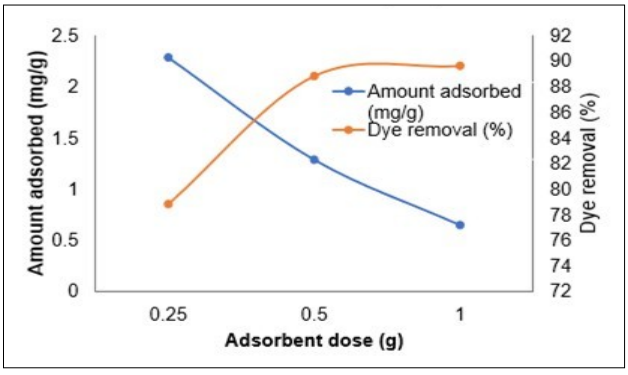

Figure 8. Effect of adsorbent dosage on the adsorption of methylene blue onto sewage sludge. ($[MB]_i$ = 10 mg/L, particle size = 0.5 mm, V = 50 mL, pH =9, T = 25°C and shaking speed = 180 rpm)

As the overall concentration of dye in the solution remains constant, the addition of adsorbent mass reduces the ratio of dye to adsorbent, which suggests a lower dye adsorption per gram of adsorbent, as shown in Figure 8. As a result, while the overall dye removal percentage increases due to the increased number of available active sites, specific adsorption capacity reduces.

4.3. Adsorption Isotherm Models

Adsorption isotherms were studied in batch experiments by varying the dye concentrations at 10 and 20. 30, 50, 75, 100, 150, and 200 mg/L. Contact time, adsorbent dose, pH, and temperature were fixed at 45 min, 0.5 g, 9, and 25 ±5 °C, respectively, in the experimental study.

The equilibrium adsorption data were analyzed using Langmuir, Freundlich, Temkin, and Harkin-Jura isotherm models. The corresponding linear plots are presented in Figure 9 (a-d). The fitting parameters of the isotherm models were determined from these linear plots, and the results are summarized in Table 5.

The Langmuir adsorption parameters were determined using equations mentioned in Table 1. MB dye showed a maximum adsorption efficiency of 14.08 mg/g. The favorability of adsorption was further evaluated using the dimensionless separation factor (R_L). The R_L values calculated using the Langmuir constant (K_L = 0.26 L mg^{-1}) were found to be 0.039 for the studied concentration range (10 to 200 mg/L), indicating favourable adsorption of methylene blue onto sewage sludge. The value of the separation factor (R_L) ranges from 0.03 to 0.3. The decrease in R_L with increasing initial concentration indicates favourable adsorption at higher concentrations. The higher K_L value compared with other studies indicates a stronger adsorption affinity [11]. Additionally, a lower R_L value of 0.039 for this study compared to the value reported by Kaya (2025) confirms the adsorption to be more favourable [11]. The R^2 value of 0.991 indicates the Langmuir isotherm to be the best fit for explaining the adsorption process.

The parameters for the Freundlich isotherm were also evaluated using the equations mentioned in Table 1. The value of the Freundlich constant (K_F) was 2.53 L/mg, the heterogeneity factor (n) was found to be in the range 1-10 (1.314), and a lower value of $1/n$ (0.76) indicates that the adsorption is favourable and moderate and the surface is heterogeneous compared to the value reported by Hayfron et al. (2025), n = 0.89 for zeolite prepared from mixing kaolinite clay and rice husk ash [4]. The current results indicate higher adsorption intensity (n>1). The R^2 value of MB dye for the Freundlich isotherm was 0.965, which is lower than that of the Langmuir isotherm (0.991), suggesting that this model does not fit the equilibrium data well.

For the Temkin isotherm model, the values of the parameters mentioned in Table 1 were calculated. The equilibrium binding constant (A_T) value was 2.31 L/mg, and the heat of adsorption constant (b_T) was 0.843 KJ/mol. A higher A_T value implies that there was a strong interaction between the dye and the adsorbent. According to Nandiyanto et al. (2023), if the value of b_T is below 8 kJ, the adsorption process would be governed by physisorption, while if the value is above 8 kJ, then by chemisorption [12]. Therefore, according to this study, the adsorption of MB onto SS was controlled by physisorption due to the lower b_T value of 3.04. Having higher b_T and A_T values suggests that the adsorption process might have occurred through a combination of physical and chemical sorption. The correlation coefficient value of MB dye for the Temkin isotherm is 0.981.

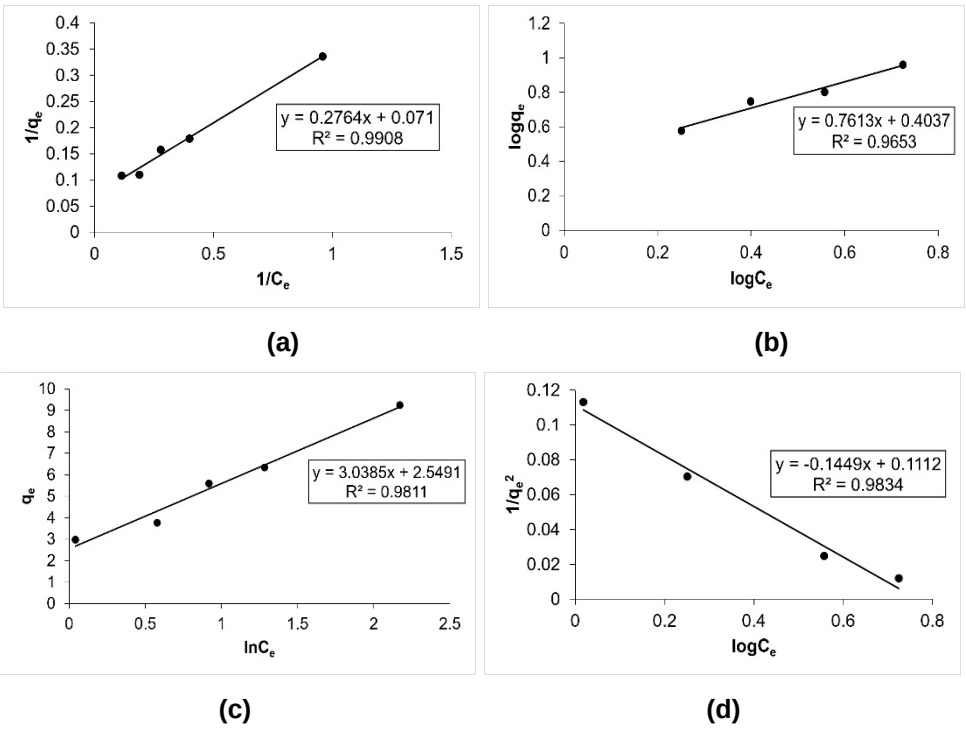

Figure 9. Experimental adsorption isotherm showing the relationship between equilibrium adsorption capacity (q_e) and equilibrium dye concentration (C_e) for methylene blue adsorption onto sewage sludge using (a) Langmuir, (b) Freundlich, (c) Temkin, and (d) Harkin-Jura

The Harkin-Jura isotherm parameters were calculated using equations given in Table 1. The values of Harkin-Jura constants *A* (6.901 mg/g) suggested a moderate adsorption capacity of the adsorbent, and constant *B* (0.767) suggested the presence of multilayer adsorption and that the adsorbent does not possess uniform energy distribution. The value of the correlation coefficient (0.983) for the model indicated an effective multilayer adsorption due to a heterogeneous surface.

Table 5. Isotherm parameters for MB dye adsorption on sewage sludge

Isotherm Models	Langmuir	Freundlich	Temkin	Harkin-Jura
Parameters and their values	q_{max}-14.08 mg/g	*n*- 1.314	A_T-2.31 L/mg	*A*- 6.901 mg/g
	K_L- 0.26 L/mg	*1/n*- 0.761	B_T-3.04	*B*- 0.767
	R_L- 0.039	K_F- 2.53 L/mg	b_T- 0.843 kJ/mol	R^2- 0.983
	R^2 - 0.991	R^2 - 0.965	R^2 - 0.981	

The maximum adsorption capacity (q_{max}) of different non-conventional low-cost adsorbents utilised for dye adsorption was compared, and the comparative data with sewage sludge are summarised in Table 6. The adsorption capacity achieved by the adsorbent was determined by the Langmuir isotherm, yielding a value of 14.08 mg/g. This performance stands out, giving strong competition to other listed adsorbents (Table 6). A comparison of the adsorption capacity of SS used in the present study for MB removal from aqueous solution with other low-cost adsorbents reported by various researchers is shown in Table 6. It can be concluded that even in its natural state, without any modification, SS was found to be a better alternative for the efficient removal of MB dye from aqueous solutions as compared to other adsorbents reported for the removal of MB.

Table 6. Comparison between the adsorption capacities of different adsorbents for dye removal

Adsorbent	Dye	Maximum adsorption capacity (mg/g)	Reference
Coconut dreg	Methylene Blue	5.72	[20]
	Brilliant Red Remazol	3.76	
Lemon peel	Eosin	8.24	[21]
Coconut husk	Crystal Violet	0.73	[22]
Nanobentonite	Malachite Green	13.8	[23]
Graphite and nano-bentonite clay	Basic Blue 5	2.33	[24]
Sewage sludge	Methylene Blue	**14.08**	**This work**

4.4. Adsorption Kinetics

Adsorption kinetics experiments were performed by adding 0.5 g of sewage sludge (SS) to 50 mL of methylene blue (MB) aqueous solution with an initial concentration of 25 mg/L at temperatures ranging from 25–45 ± 5°C. Samples were withdrawn at predetermined contact times (5, 10, 15, 20, 30, 45, 60, 90, and 120 min), and the absorbance was measured to determine the residual dye concentration.

The predicted theoretical kinetics and the data for the experimental equilibrium of MB on SS are shown in Figure 10. An attempt was made to plot ln (q_e-q_t) against time (t) as seen in Figure 10(a), resulting in undefined negative values, rendering the first-order kinetic model unfeasible and suggesting that the first-order linearised equation is unsuitable to describe the sorption process (Table 7).

According to the experimental data shown in Table 7 and Figure 10(b), the pseudo-second-order model was found to be the best fit to the adsorption equilibrium data with a correlation coefficient value of 0.999, which is greater than that of the pseudo-first-order (0.982), Intra-particle diffusion (0.8087) and Elovich models (0.931), which signifies possibility of chemisorption involved in sorption process. The pseudo-second-order model provided the best description of the adsorption kinetics with a higher correlation coefficient (R^2 = 0.999). In addition, the calculated adsorption capacity (3.08 mg/g) obtained from the pseudo-second-order model was in good agreement with the experimentally determined q_e value (3.14 mg/g), further confirming that this model adequately describes the adsorption process. The pseudo-second order model predicted an adsorption capacity of 3.08 mg/g, which was closest to the experimental value of 3.14 mg/g.

A greater value of the intra-particle diffusion rate constant (k_{id}) suggested that the adsorbent quickly diffuses into the pores, and as the intercept denoting the boundary layer effect (C_i) is not equal to 0, it can be concluded that intra-particle diffusion is not the sole rate-limiting mechanism (Table 7, Figure 10(c)).

Table 7. Kinetic parameters for MB dye adsorption under optimised conditions

Kinetic Models	PFO	PSO	Elovich	IPD
Parameters and their values	q_e (mg/g) = -0.456	q_e (mg/g) = 3.14	α (mg/g.min) = 141800	K_{id} (mg/g.min$^{1/2}$) = 2.5711
	k_1 (min^{-1}) = -0.051	k_2 (g/mg.min) = 0.2011	β (g/mg) = 5.83	C_i = 0.0569
	R^2 = 0.982	R^2 = 0.999	R^2 = 0.931	R^2 = 0.8087

The results of the Elovich model indicated a higher *α* value (141,800 mg/g.min), as shown in Table 7 and Figure 10(d), which suggests that the adsorption was rapid, indicative of adsorption following chemisorption.

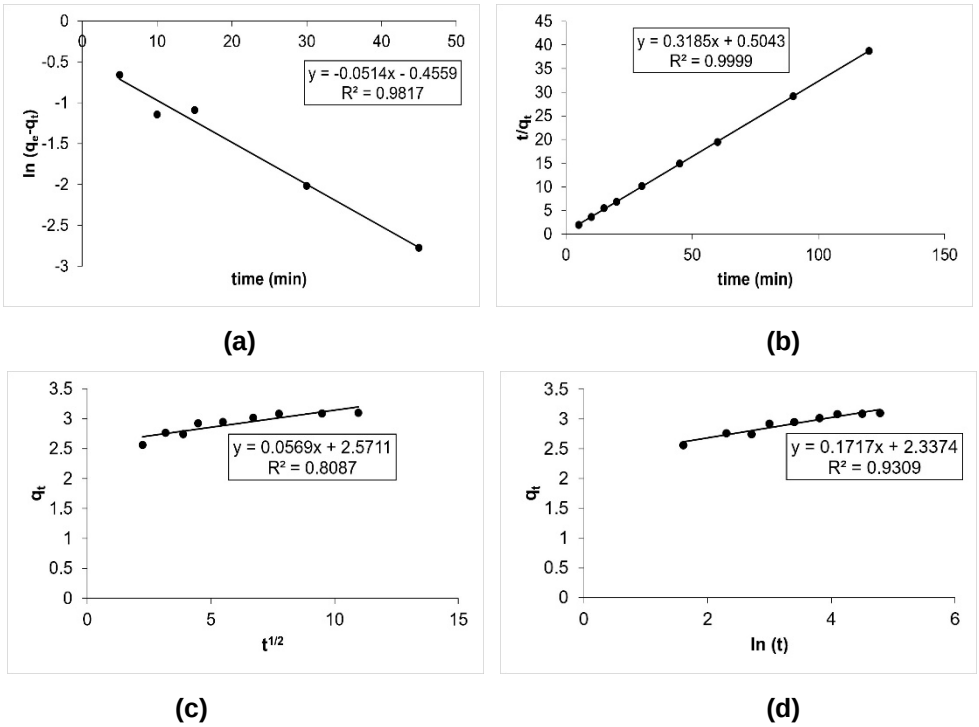

Figure 10. Kinetic study for MB dye adsorption using (a) PFO, (b) PSO, (c) IPD, and (d) Elovich models

4.5. Thermodynamics study

To evaluate the thermodynamic feasibility and nature of methylene blue adsorption onto sewage sludge, adsorption experiments were conducted at different temperatures (298–318 K). The thermodynamic parameters were calculated from the equilibrium distribution coefficient (K_d) using the Van't Hoff relationship, and the results are presented in Table 8. The values of K_d decreased with increasing temperature, indicating a reduction in adsorption capacity at higher temperatures and suggesting that the adsorption process is

exothermic in nature. This trend is also reflected in the decrease in adsorption capacity (q_e) from 3.080 to 2.227 mg/g as the temperature increased from 298 to 318 K.

The negative values of Gibbs free energy change ($\Delta G°$) obtained at all studied temperatures indicate that the adsorption of methylene blue onto sewage sludge is a spontaneous process. Furthermore, the negative value of the enthalpy change ($\Delta H°$) confirms the exothermic nature of the adsorption process, indicating that lower temperatures favour dye uptake. The magnitude of the enthalpy change ($\Delta H° = -46.48$ kJ/mol) suggests relatively strong interactions between methylene blue molecules and the functional groups present on the sewage sludge surface, indicating that the adsorption process may involve strong physical interactions and possible surface complexation. The entropy change ($\Delta S°$) was found to be negative, suggesting a decrease in randomness at the solid–solution interface during adsorption. This decrease in randomness may be attributed to the orderly arrangement of dye molecules on the surface of the adsorbent during the adsorption process. Similar thermodynamic behaviour for methylene blue adsorption has been reported in previous studies using various low-cost adsorbents [25, 26]. Overall, the thermodynamic parameters indicate that the adsorption of methylene blue onto sewage sludge is spontaneous and exothermic, with adsorption being more favourable at lower temperatures.

Table 8. Thermodynamic parameters for methylene blue adsorption onto sewage sludge at different temperatures

Temperature (K)	C_e (mg/L)	q_e (mg/g)	K_d	$\Delta G°$ (kJ/mol)	$\Delta H°$ (kJ/mol)	$\Delta S°$ (J/mol.K)
298	0.707	3.080	4.36	-3.49	-46.48	-144.23
308	1.154	2.277	1.97	-2.05	-	-
318	1.657	2.227	1.34	-0.60	-	-

The thermodynamic parameters were further analyzed using the Van't Hoff plot by plotting ln K_d against 1/T, as shown in Figure 11. The slope and intercept of the linear plot were used to determine the enthalpy change ($\Delta H°$) and entropy change ($\Delta S°$), respectively. The linear relationship obtained confirms the applicability of the thermodynamic model for describing the adsorption behaviour of methylene blue onto sewage sludge.

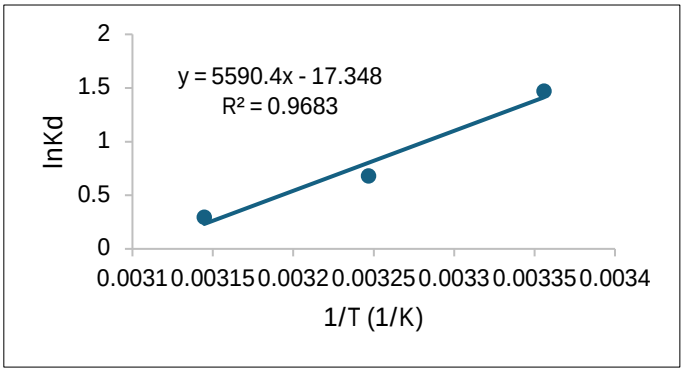

Figure 11. Van't Hoff plot (ln K_d versus 1/T) for methylene blue adsorption onto sewage sludge.

5. CONCLUSIONS

The present study investigated the potential use of secondary treated sewage sludge as a low-cost adsorbent for the removal of methylene blue from aqueous solutions. Characterization of the material using FTIR, SEM, and BET analyses revealed the presence of surface functional groups, porous morphology, and adequate surface area that provide suitable adsorption sites for dye molecules. The adsorbent exhibited a point of zero charge (pH_{pzc}) of 7.6, which explains the enhanced adsorption of the cationic dye under alkaline conditions due to the development of negatively charged surface sites.

Batch adsorption experiments demonstrated that operational parameters such as pH, adsorbent dosage, contact time, particle size, and initial dye concentration significantly influence the adsorption process. Optimal conditions were observed at pH 9, with 0.5 g of sewage sludge in 50 mL of 10 mg/L dye solution and a contact time of 30 minutes. Although the highest dye removal efficiency was observed at pH 11, pH 9 was considered the optimum pH due to the minimal difference in removal performance and its practical advantage of producing a near-neutral final pH, thereby reducing post-treatment adjustment requirements. The adsorption equilibrium data showed good agreement with the Langmuir isotherm model, with a maximum adsorption capacity of 14.08 mg/g, while the adsorption kinetics followed the pseudo-second-order model, indicating that the adsorption process is governed by interactions between dye molecules and active sites on the sludge surface.

Thermodynamic analysis based on temperature-dependent equilibrium data and the Van't Hoff plot indicated that the adsorption process is spontaneous and exothermic. The negative values of ΔG° confirmed the feasibility of the process, while the negative values of ΔH° and ΔS° suggested an exothermic adsorption process accompanied by decreased randomness at the solid–solution interface.

An additional observation was the pH-stabilizing behaviour of the adsorbent, where the final solution pH tended to converge toward near-neutral values regardless of the initial pH. This buffering-like effect is likely associated with the presence of surface functional groups and mineral constituents in the sludge and further enhances its practical applicability for wastewater treatment.

Overall, the results demonstrate that untreated sewage sludge can serve as an effective and environmentally sustainable adsorbent for methylene blue removal from contaminated water. The utilization of sewage sludge not only contributes to wastewater treatment but also promotes waste valorization and resource recovery. Future studies may focus on environmentally benign modification strategies to further enhance the adsorption performance of the material.

ACKNOWLEDGEMENTS

The infrastructural financial support under the CURIE programme from the WISE-KIRAN division of the Department of Science and Technology, New Delhi, India, to IIS (deemed to be University), Jaipur, India (File No. DST/CURIE-02/2023/IISU) is gratefully acknowledged.

REFERENCES

1. V. K. Parida; N. Singh; M. Priyadarshini; P. Kumari; D. Datta; A. Tambi; *J. Ind. Eng. Chem.,* **2025**, *150*, 247–264.
2. R. Al-Tohamy; S. S. Ali; F. Li; K. M. Okasha; Y. A. Mahmoud; T. Elsamahy; H. Jiao; Y. Fu; J. Sun; *Ecotoxicol. Environ. Saf.,* **2022**, *231*, 113160.
3. I. Susanti; H. B. N. Sajidah; S. R. Rosdiana*;* IOP Conf. Ser.: Earth Environ. Sci., **2024**, *1425*, 012009.
4. J. Hayfron; S. Jääskeläinen; S. Tetteh; *Heliyon,* **2024**, *11*, 41325.
5. M. A. Ibrahim; A. Salama; F. Zahran; M. S. Abdelfattah; A. Alsalme; M. Bechelany; A. Barhoum; *Front. Chem.*, **2024***; 12*, 1330810.
6. S. Moosavi; C. W. Lai; S. Gan; G. Zamiri; P. O. Akbarzadeh; M. R. Johan; *ACS Omega*, **2020**, *5*, 20684–20697.

7. M. Dhamsaniya; D. Christian; M.A. Shabiimam; Issues of Sustainable Sludge Handling and Management in the Wastewater Sector: A Review. In *Innovation in Smart and Sustainable Infrastructure*, Volume 2. ISSI **2022**. Lecture Notes in Civil Engineering, vol 485; D. Patel; B. Kim; D. Han Eds.; Springer, Singapore, 2024, pp. 55–68.
8. V. Singh; H. C. Phuleria; M. K. Chandel; *J. Clean. Prod.*, **2020**, *276*, 122538.
9. A. Raj; A. Yadav; A. P. Rawat; A. K. Singh; S. Kumar; A. K. Pandey; R. Sirohi; A. Pandey; *Environ. Technol. Innov.,* **2021**, *23*, 101556.
10. M. Keshawy; R. S. Kamal; A. E. Abdelhamid; A. Labena; A. Amin; A. M. Hasan; M. E. Abdel-Raouf; *Int. J. Environ. Sci. Technol.,* **2025**, *22*, 8895-8918.
11. H. Kaya; *Cellulose. Chem. Technol.*, **2025**, *59*, 441-450.
12. A. B. D. Nandiyanto; M. Fiandini; D. A. Fadiah; P. A. Muktakin; R. Ragadhita; W. C. Nugraha; T. Kurniawan; M. R. Bilad; J. Yunas; A. S. M. Al Obaidi; *J. Adv. Res. Fluid Mech. Therm. Sci.,* **2023**, *105*, 41-58.
13. F. Mohamed; M. Shaban; S. K. Zaki; M. S. Abd-Elsamie; R. Sayed; M. Zayed; N. Khalid; S. Saad; S. Omar; A. M. Ahmed; A. Gerges; H. R. Abd El-Mageed; N. K. Soliman; *Scientific Reports*, **2022,** *12*, 18031.
14. O. A. Abdel Moamen; A. A. Mohammed; H. A. Ibrahim, A. M. El-Kamash; *Geoenviron. Disasters.,* **2025***, 12*, 29.
15. N. Jawad; T. M. Naife; *Iraqi J. Chem. Pet. Eng.*, **2022**, *23*, 59-69.
16. J. de Oliveira Silva; G. Rodrigues Filho; C. da Silva Meireles; S. D. Ribeiro; J. G. Vieira; C. V. da Silva; D. A. Cerqueira; *Thermochim. Acta*, **2012,** *528*, 72-75.
17. H. Messaoudi; A. Koukouch; I. Bakhattar; M. Asbik; S. Bonnamy; E. G. Bennouna; T. Boushaki; B. Sarh; A. Rouboa; *Energies*, **2024**, *17*, 582.
18. L. Romero; T. Joglar; P. Oulego; S. Collado; M. Díaz; *J. Environ. Man.*, **2025**, *391*, 126380.
19. Y. N. Teixeira; J. M. Menezes; R. N. Teixeira; F. J. Paula Filho; T. M. Oliveira; *Textiles*, **2023**, *3*, 52-65.
20. H. Shukor; A. Z. Yaser; N. F. Shoparwe; M. MohdZainiMakhtar; N. Mokhtar; *Int. J. Chem. Eng.*, **2022**, *2022*, 1–11.
21. A. Bukhari; I. Ijaz; H. Zain; E. Gilani; A. Nazir; A. Bukhari; S. Raza; S. Hussain; S. S. Alarfaji; Y. Naseer; *Arab. J. Chem*., **2022**, 15, 103873.
22. M. S. Imran; T. Javed; I. Areej; M. N. Haider; *Water Sci. Technol.*, **2022**, *85*, 2295-2317.
23. M. T. Moustafa; *Scientific Reports,* **2023**, *13*, 4493.
24. N. Elshemy; H. Mashaly; S. Elhadad; *Pigment Resin Technol.,* **2023**, *53*, 900–910.
25. L. Ykhlef; H. Ghania; H. Salah; *Cellul. Chem. Technol.*, **2024**, *58*, 1135.
26. M. F. M. Yusop; A. Aziz; M. A. Ahmad; *Arab. J. Chem.*, **2022**, *15,* 104081.

STUDIA UBB CHEMIA, LXXI, 2, 2026 (p. 171-187)
(RECOMMENDED CITATION)
DOI:10.24193/subbchem.2026.2.09

EFFECT OF TRACE SILICON ON THE PROPERTIES OF IRON-BASED HETEROGENEOUS FENTON CATALYSTS

Jianjun ZHAO[a,*], Yan SHU[a], Leifeng JIA[b], Xianfeng ZHANG[a], Muxin LIU[a], Xu LI[a], Anping XU[a], Xiaoxuan ZHANG[a], Jing YE[a], Ran RONG[a], Jiatong HAN[a], Shenghao LIAO[a]

ABSTRACT. It is an important task for modifying heterogeneous Fenton catalysts to effectively degrade organic pollutants in water. Most studies have modified heterogeneous Fenton catalysts through addition of other metal active species. Here, a series of Si-Fe/γ-Al_2O_3 (x, x = Si/Fe mass ratio per gram of support) catalysts were prepared via wet impregnation method, and the characterization results show that the addition of trace Si (x < 0.10) facilitated the dispersion of Fe species, thereby leading to an increase in the specific surface area, average pore size and pore volume of the catalysts. At the same time, trace Si addition can effectively improve the acid-base properties of the catalyst surface. All these changes may be beneficial to the catalytic degradation of the phenol simulated wastewater.

Keywords: *heterogeneous Fenton catalyst, trace Si modification, highly dispersed active components, acid-base properties of catalyst.*

INTRODUCTION

In recent decades, the intensification of human activities has led to the increase in the accumulation of organic pollutants in water bodies. Organic pollutants in water are not only harmful to the health of humans and aquatic organisms, but also pose significant environmental risks. These organic pollutants must be treated before they are discharged into natural water bodies [1-4].

[a] *Bengbu University, School of Materials and Chemical Engineering, Bengbu, 233030 China.*
[b] *General Water of China (Bengbu) Co., LTD, Bengbu, 233000 China.*
* *Corresponding author: zjj@bbc.edu.cn*

For treating organic wastewater, advanced oxidation processes (AOPs) are considered a promising method because they can convert a variety of organic pollutants into harmless or biodegradable substances [5-8]. In the AOPs, the Fenton reagent, which is composed of iron (or other transition metals) ions and hydrogen peroxide (H_2O_2), has attracted a great deal of researchers' interest [6, 9-11]. The Fenton oxidation process involves the activation of H_2O_2 by Fe^{2+} to generate various reactive oxygen species, such as hydroxyl radicals (•OH), hydrogen peroxide radicals (HO_2•) (equations 1 and 2) [12-15].

$$S\text{-}Fe^{3+} + H_2O_2 \rightarrow S\text{-}Fe^{2+} + HO_2\bullet + H^+ \quad (1)$$

$$S\text{-}Fe^{2+} + H_2O_2 + H^+ \rightarrow S\text{-}Fe^{3+} + H_2O + \bullet OH \quad (2)$$

where S represents the catalyst surface.

With a high redox potential of 2.8 V, the •OH can effectively degrade most organic pollutants into small molecules (such as CO_2 and H_2O) or biodegradable compounds in a non-selective manner. The HO_2• with a slightly weaker oxidation ability (redox potential of 1.50 V) can also participate in the degradation of pollutants (equations 3 and 4) [14].

$$\bullet OH + \text{organics} \rightarrow \ldots\ldots \rightarrow CO_2 + H_2O \quad (3)$$

$$HO_2\bullet + \text{organics} \rightarrow \text{by products} \quad (4)$$

The degradation of organic wastewater using the Fenton reagent includes the homogeneous Fenton process and the heterogeneous Fenton process. Compared with the homogeneous Fenton process, the heterogeneous Fenton process has attracted much attention because of its easy separation of catalyst and avoiding secondary pollution to water bodies [11, 16-18].

Improving the activity of heterogeneous Fenton catalysts is a critical technology in the field of organic wastewater degradation. In order to improve the efficiency of heterogeneous Fenton catalysts, external energies such as ultraviolet lights, ultrasonic waves and microwaves are often used in the catalytic system. Although these methods effectively improve catalyst activity, the high cost of external energy hinders the practical application of these methods [19]. Therefore, fabricating a catalyst with higher activity that requires no external energy supply is one of the goals of researchers devoted to heterogeneous Fenton catalysts.

The modification of heterogeneous Fenton catalysts remains a key focus in contemporary catalysis research. Dopants such as graphene, activated carbon (AC), boron (B), nitrogen (N), sulfur (S), and phosphorus (P) can effectively modulate electron transfer during the catalytic process, thereby enhancing catalytic activity [20-22]. However, an undeniable fact is that the highly dispersed active components can not only improve the microstructure

of the catalyst, but also optimize its surface properties, thereby further enhancing the catalyst activity. Thus, the development of catalysts with highly dispersed active components is an important aspect of research on heterogeneous Fenton catalytic system [19, 23, 24].

Currently, silicon (Si) has been employed in iron-based Fenton catalysts primarily as a high-content support material (e.g., silica or mesoporous silica) [25, 26] or a physical coating shell to suppress metal leaching [27-29], rather than as a trace dopant for interface regulation. Recent studies involving Si-Fe systems, such as Fe on silica support or core-shell structured SiO_2 coating, focus on bulk structural effects rather than atomic-scale control of the Fe–support interface [25-27, 29]. To date, no literature has documented the influence of trace Si on the performance of Fe-based heterogeneous Fenton catalysts (with Si/Fe mass ratio < 0.1) and the corresponding mechanism.

In this work, a series of Si-Fe/γ-Al_2O_3 (x, x = Si/Fe mass ratio per gram of support) catalysts were prepared and used for the degradation of phenol simulated wastewater. The innovation of this study is reflected in the following aspects: In the Si-Fe/γ-Al_2O_3 (x < 0.10), the introduction of Si elements can effectively enhance the dispersion of the active component Fe, increase the specific surface area of the catalyst, optimize its pore structure, and regulate the acid-base properties of the catalyst surface. Consequently, the catalytic activity of the catalyst is significantly improved. The main objectives include: (1) Structure, morphology and chemical properties of Si-Fe/γ-Al_2O_3 (x) catalysts were analyzed by various characterization methods; (2) Catalytic activity of Si-Fe/γ-Al_2O_3 (x) catalysts for the degradation of phenol simulated wastewater was investigated; (3) Hypothetical catalytic mechanism of Si-Fe/γ-Al_2O_3 (x) catalysts for the degradation of organic wastewater was deduced.

RESULTS AND DISCUSSION

Catalyst Characterization

The XRD patterns of the as prepared Si-Fe/γ-Al_2O_3 (x) catalysts are presented in Figure 1a. For all the samples, there are no strong diffraction peaks which indicate that the prepared catalysts show high dispersion states or amorphous structure. However, there are clear diffraction peaks at 37.4°, 45.8° and 67.3° which are assigned to the (311), (400) and (440) crystallographic faces of γ-Al_2O_3 respectively [PDF no. 10-0425]. Meanwhile, for all the Si-Fe/γ-Al_2O_3 (x) samples, there are weak diffraction peaks (α and b peaks) at 33.2°, 35.6° which are assigned to the (104) and (110) crystallographic faces of α-Fe_2O_3 (PDF no. 33-0664).

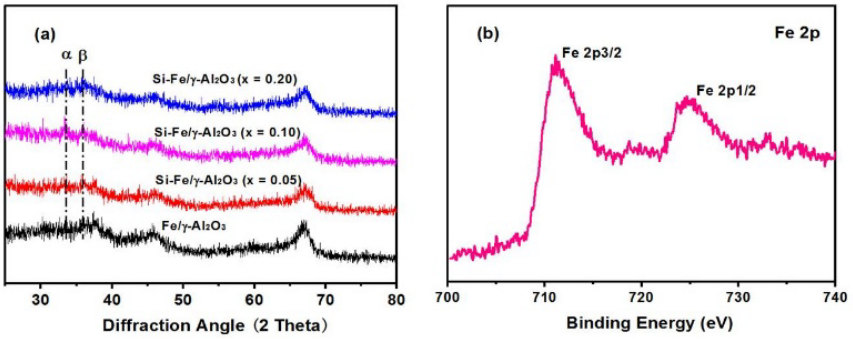

Figure 1. (a) XRD patterns of Si-Fe/γ-Al_2O_3 (x) catalysts and (b) Fe 2p XPS spectra of a Si-Fe/γ-Al_2O_3 (x = 0.10) sample.

In order to further verify the valence state of Fe element in the catalysts, XPS measurement is employed to determine the valence state of Fe on the surface of the Si-Fe/γ-Al_2O_3 (x = 0.10) sample, and the results are shown in Figure 1b. Two distinct peaks at binding energies of 711.1 eV for Fe 2p3/2 and 724.4 eV for Fe 2p1/2 with a weak satellite peak at 718.8 eV are observed, which further indicates that Fe in the Si-Fe/γ-Al_2O_3 (x = 0.10) sample is mainly in the +3 valence [30, 31].

The crystallite size of α-Fe_2O_3 in the Si-Fe/γ-Al_2O_3 (x) catalysts is calculated using the Scherrer equation 5:

$$D = k\lambda/\beta\cos\theta \quad (5)$$

where D represents the crystallite size, k denotes the shape factor (taken as 0.89), λ is the X ray wavelength (Cu Kα radiation, λ = 0.1542 nm), β is the full width at half maximum (FWHM) of the diffraction peak, and θ corresponds to the angular position of the peak maximum. The calculation is applied to the (110) diffraction peak of α-Fe_2O_3, and the results are shown in Table 1.

Table 1. Crystallite size of α-Fe_2O_3 in the Si-Fe/γ-Al_2O_3 (x) catalysts.

Catalyst	FWHM	crystallite size (nm)
Fe/γ-Al_2O_3 (x = 0)	0.168	0.8581
Si-Fe/γ-Al_2O_3 (x = 0.05)	0.187	0.7709
Si-Fe/γ-Al_2O_3 (x = 0.10)	0.273	0.5280
Si-Fe/γ-Al_2O_3 (x = 0.20)	0.148	0.9740

Table 1 shows that adding a small amount of Si doping to the Fe/γ-Al_2O_3 catalyst (x < 0.10) leads to a gradual reduction in the crystallite size of α-Fe_2O_3, which decreases from 0.8581 nm to 0.5280 nm. However, at x = 0.2, the α-Fe_2O_3 crystallite size increases, reaching 0.9740 nm.

N_2 adsorption-desorption measurements are carried out to evaluate the specific surface area (BET surface area) and pore size distribution of the prepared catalysts. The BET surface areas of the Fe/γ-Al_2O_3 (x = 0), Si-Fe/γ-Al_2O_3 (x = 0.05), Si-Fe/γ-Al_2O_3 (x = 0.10) and Si-Fe/γ-Al_2O_3 (x = 0.20) samples are determined to be 255.96, 249.72, 275.82, and 257.84 $m^2 \bullet g^{-1}$, respectively (Table 2). It can be inferred that the addition of a small amount of Si (x < 0.10) is conducive to the increase of specific surface area of the Fe/γ-Al_2O_3 catalyst, and the increase of the catalyst's specific surface area in a certain range is helpful to improve the catalyst's activity. It can also be seen from Table 2 that the pore volume and average pore diameter of the Si-Fe/γ-Al_2O_3 (x = 0.10) catalyst are larger than those of the other catalysts. The larger pore volume and average pore diameter help to reduce the steric hindrance in the reaction, thereby improving the catalyst's activity.

Table 2. BET surface area, average pore diameters and pore volume for the Si-Fe/γ-Al_2O_3 (x) catalysts.

Catalyst	BET surface area ($m^2 \cdot g^{-1}$)	verage pore diameter (nm)	Pore volume ($mL \cdot g^{-1}$)
Si-Fe/γ-Al_2O_3 (x = 0)	255.96	4.56	0.389
Si-Fe/γ-Al_2O_3 (x=0.05)	249.72	4.60	0.375
Si-Fe/γ-Al_2O_3 (x=0.10)	275.82	4.68	0.391
Si-Fe/γ-Al_2O_3 (x=0.20)	257.84	4.63	0.376

Figure 2 shows the N_2 adsorption-desorption isotherms of the Si-Fe/γ-Al_2O_3 (x) catalysts as well as the corresponding pore size distribution. All samples exhibit type IV adsorption-desorption isotherms, which indicates the existence of mesopores in the catalysts (Figure 2a) [31]. Interestingly, Figure 2b shows that the Si-Fe/γ-Al_2O_3 (x = 0.10) sample has a more concentrated pore size distribution than the other samples, although this catalyst has the largest specific surface area. It is reasonable to infer that the Si-Fe/γ-Al_2O_3 (x = 0.10) catalyst with larger specific surface area, pore volume and pore size has better catalytic activity than the other catalysts.

The surface morphology and the corresponding Fe dispersion of the Si-Fe/γ-Al_2O_3 (x) catalyst samples were observed via SEM and EDS. As shown in Figure 3, the surface morphology of the Fe/γ-Al_2O_3 (x = 0) catalyst was relatively smooth, and a few crystal particles were present on its surface. With the increase of Si in the catalyst, more dispersed particles appeared on the catalyst surface (x = 0.05 and 0.1). Meanwhile, the Si-Fe/γ-Al_2O_3 (x = 0.1) catalyst exhibited relatively uniform particle dispersion on its surface. While the mass ratio of Si to Fe was 0.2 in the catalyst, the particles on the catalyst surface began to grow larger. This phenomenon shows that the addition of a

small amount of Si (x < 0.1) in the catalyst contributes to the dispersion of particles on the catalyst surface. Notably, agglomeration of surface particles occurs when the Si content exceeds 0.1. This observation correlates well with the increase in crystallite size estimated by the Scherrer equation.

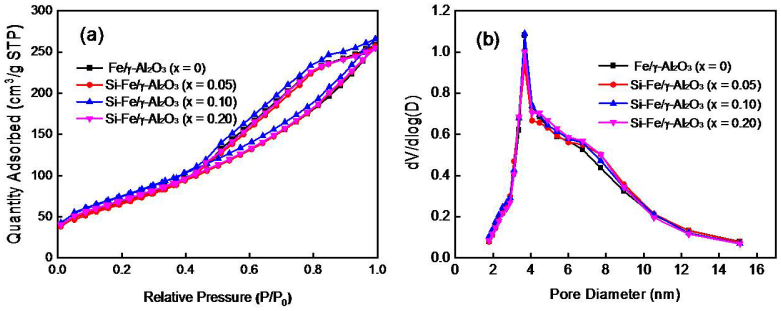

Figure 2. (a) N_2 adsorption-desorption curves and (b) pore diameter distribution of the Si-Fe/γ-Al_2O_3 (x) catalysts.

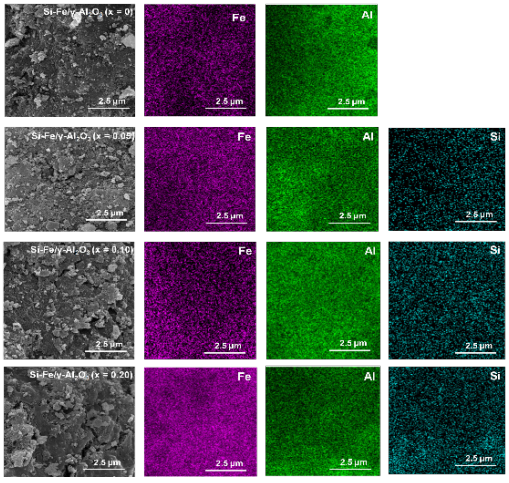

Figure 3. SEM images of Si-Fe/γ-Al_2O_3 (x) catalysts and corresponding Fe, Al, Si elemental mapping (left-right).

As can be seen in Figure 3 the Fe was increasingly evenly dispersed on the catalyst surface with the increase of Si content (x < 0.1) in the catalyst. The possible reasons for this phenomenon are as follows. When a certain amount of TEOS is added to ferric nitrate solution, Si-OH compounds were produced by hydrolysis to different degrees, the corresponding hydrolysis reaction is presented in equation 6.

$$Si(OC_2H_5)_4 + 4H_2O \rightarrow Si(OH)_4 + 4C_2H_5OH \quad (6)$$

The Si-OH in the resulting compound acts as a bridge, connecting the Fe^{3+} in the solution to the support. When the Si content is low (x = 0.05, 0.1), a small amount of silicic acid preferentially reacts with the hydroxyl groups on the surface of AlO(OH) to form a Si-O-Al interface bonding structure; at the same time, silicic acid undergoes coordination interaction with Fe^{3+}, stabilizing and anchoring the Fe ions on the surface of the support, which led to a more uniform distribution of the active component Fe on the surface of the support, as shown in reaction equations 7 and 8.

$$Si(OH)_4 + Al\text{-}OH(surface) \rightarrow Al\text{-}O\text{-}Si(OH)_3 + H_2O \quad (7)$$

$$Fe^{3+} + Al\text{-}O\text{-}Si(OH)_3 \rightleftharpoons Al\text{-}O\text{-}Si(OH)_2\text{-}O\text{-}Fe^{2+} + H^+ \quad (8)$$

When the Si content is high (x = 0.2), silicic acid formed by excessive hydrolysis of TEOS undergoes intermolecular condensation on the Boehmite support surface, producing a continuous amorphous SiO_2 coating. This coating shields the hydroxyl groups on the support surface and weakens the strong metal–support interaction between Fe and the support, further leading to agglomeration of the active components on the catalyst surface, as shown in reaction equation 9.

$$nSi(OH)_4 \rightarrow (SiO_2)n + 2nH_2O \quad (9)$$

As a result, Fe was more evenly distributed on the surface of Si-Fe/γ-Al_2O_3 (x = 0.10) catalyst. Xiao et al [32] found that the volume percentages of blocky-shaped phases increased with increasing addition of Si (0.10 - 0.20 wt.% Si). This phenomenon is consistent with the results of this study.

Figure 4 shows a typical SEM image and EDS spectra of the Si-Fe/γ-Al_2O_3 (x = 0.10) catalyst sample in the specified region. The presence of C in the EDS spectra is due to the addition of TEOS in the catalyst preparation, and the peaks at 2.120 and 9.712 keV (Figure 4b) belong to Au, which is mentioned in the “EXPERIMENTAL SECTION”. The corresponding elemental compositions of the Si-Fe/γ-Al_2O_3 (x = 0.10) catalyst sample are depicted in Table 3. It can be seen that the mass ratio of Si to Fe in the specific portion of the catalyst is 1.25 : 12.40, which is approximately equal to the theoretical value of 0.1. This phenomenon indicates that Si and Fe are well distributed on the surface of the Si-Fe/γ-Al_2O_3 (x = 0.10) catalyst in the specific portion; i.e., the active component Fe is fully exposed on the catalyst surface, which is favorable to the catalytic reaction.

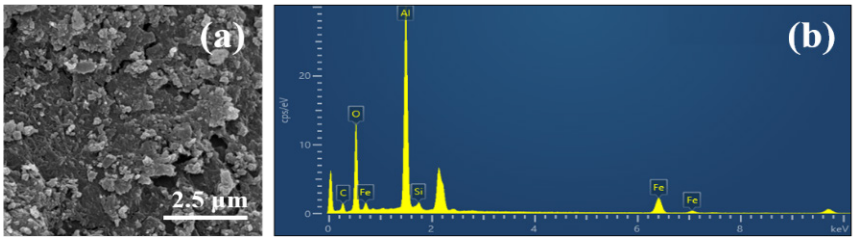

Figure 4. SEM image (a) and EDS spectra (b) of Si-Fe/γ-Al_2O_3 (x = 0.10) catalyst.

Table 3. Elemental composition of Si-Fe/γ-Al_2O_3 (x = 0.10) catalyst in the specified region.

Elements	wt.%
C	14.88
O	37.92
Al	33.54
Si	1.25
Fe	12.40
Total	100.00

The acid-base properties of heterogeneous catalysts are an important factor affecting the activity of catalysts [33]. Temperature programmed desorption (TPD) is an important method to characterize the acid-base properties of catalysts. CO_2-TPD analyses of the Si-Fe/γ-Al_2O_3 (x) catalysts were determined, and the results are shown in Figure 5. Accordingly, two peaks at 340 °C and 601 °C were observed in all samples, indicating the presence of two distinct types of alkaline sites in the catalysts. It can be seen that the Si-Fe/γ-Al_2O_3 (x = 0) catalyst exhibits a relatively high content of both types of alkaline sites. However, the introduction of a small amount of Si into the Fe/γ-Al_2O_3 catalyst (x = 0) resulted in a slight decrease in the content of these two alkaline sites in the resulting catalyst.

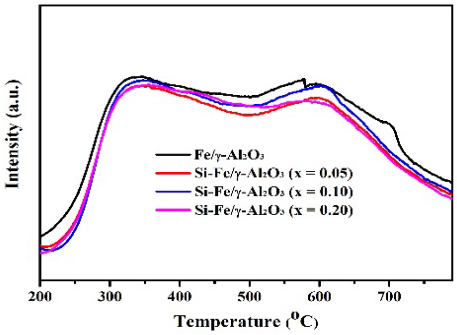

Figure 5. CO_2-TPD profiles of the Si-Fe/γ-Al_2O_3 (x) catalysts.

The reasons for this phenomenon are as follows: For the Fe/γ-Al_2O_3 catalyst, its basicity mainly originates from the interaction between coordinatively unsaturated Al^{3+} on the catalyst surface and O^{2-}, which gives rise to alkaline sites (Al-O^-). When a small amount of Si is introduced into the catalyst, Si-O-Al bonds are formed on the surface, which directly consume the Al-O^- basic sites and generate Si-O-Al bridges, thus further reducing the number of alkaline sites. The corresponding reaction is depicted in equation 10.

$$\equiv Al\text{-}O^- + \equiv Si\text{-}OH \rightarrow \equiv Al\text{-}O\text{-}Si\equiv + OH^- \quad (10)$$

Catalytic Performance

Phenol, being a type of organic pollutant that is the hard to degrade, how to completely decompose it into environmentally harmless small molecules has become a focus of research [24, 31, 34-36]. At the same time, as an important parameter to describe the content of organic pollutants in wastewater, Chemical Oxygen Demand (COD) is used as a key index to evaluate water pollution in many countries and regions. COD removal rate refers to the degree of oxidation of organic pollutants in wastewater, or more specifically, the process by which larger molecules are broken down into smaller fragments to the maximum extent (i.e., mineralization into CO_2 and H_2O) [24, 31, 35]. In this study, the COD removal rate was used as an evaluation index for catalyst activity.

The catalytic activities of the Si-Fe/γ-Al_2O_3 (x) catalysts were evaluated by the degradation of the 100 mg•L^{-1} phenol simulated wastewater under the optimal reaction conditions reported in our previous study [24]. Specifically, the reaction temperature was 30 ^oC, the initial pH of the wastewater was 3.5, the dosage of H_2O_2 was 1.5 mL, and the reaction time was 60 minutes.

Figure 6 shows the effects of different Si-Fe/γ-Al_2O_3 (x) catalysts on the COD removal rate of phenol simulated wastewater. It is observed that the COD removal rate of the phenol simulated wastewater was approximately 66% when the Fe/γ-Al_2O_3 (x = 0) catalyst was used. With the increase in Si content in the Si-Fe/γ-Al_2O_3 (x < 0.1) catalyst, the COD removal rate of the phenol simulated wastewater increased. For the Si-Fe/γ-Al_2O_3 (x = 0.10) catalyst, the highest COD removal rate (83%) was achieved under the given reaction conditions. Subsequently, with the further increase in Si content in the catalysts, the catalytic degradation for phenol simulated wastewater decreased. The possible reasons for this phenomenon are discussed in the “Catalytic Mechanism” section of this study.

Figure 6 demonstrates that the Si-Fe/γ-Al_2O_3 (x = 0.1) catalyst exhibits outstanding catalytic activity, and characterization of its physical and chemical properties further confirms its excellent intrinsic structural stability.

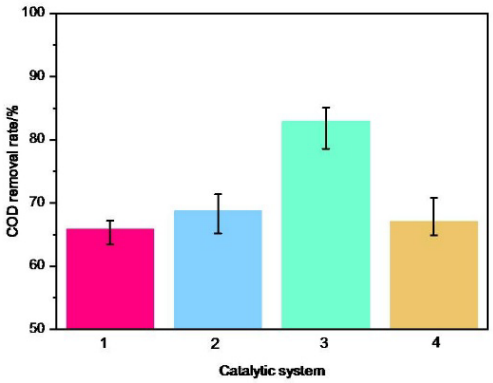

Figure 6. Influence of different catalysts on COD removal rate of phenol simulation wastewater. (1) Fe/γ-Al_2O_3 (x = 0); (2) Si-Fe/γ-Al_2O_3 (x = 0.05); (3) Si-Fe/γ-Al_2O_3 (x = 0.10); (4) Si-Fe/γ-Al_2O_3 (x = 0.20).

XRD results reveal a well-defined γ-Al_2O_3 crystal phase, indicating that trace Si doping does not damage the support lattice structure. SEM-EDS elemental mapping further verifies the uniform distribution of Fe elements within the catalyst. Additionally, BET results show that trace Si modification optimizes the catalyst's pore structure (including specific surface area, pore volume, and average pore size) while preserving good structural integrity. This intrinsic structural stability, attributed to trace Si doping, is a key advantage that facilitates maintaining the catalyst's structural and catalytic performance during the reaction process.

Catalytic Mechanism

To explore the correlation between the catalytic activity of catalysts in degrading the phenol simulated wastewater and their characterization results, this paper proposes a hypothetical catalytic reaction mechanism. In this study, the addition of the trace Si element during the catalyst preparation process may affect not only the physical properties of the prepared catalysts but also their chemical properties.

The following is a hypothetical catalytic reaction mechanism proposed based on the changes in physicochemical properties and reaction behaviors observed over Si-Fe/γ-Al_2O_3 (x) catalysts with the introduction of trace Si. The proposed mechanism is based on existing literature and has not yet been verified by direct experimental evidence such as radical scavenging experiments in this study.

On the one hand, the physical properties of catalysts may affect their catalytic activity. According to the XRD and XPS characterization results of the Si-Fe/γ-Al_2O_3 (x) catalysts, the Fe element in the catalysts exists in the form of α-Fe_2O_3. Meanwhile, the XRD, SEM, and EDS results showed that the addition of a small amount of Si in Si-Fe/γ-Al_2O_3 (x) promoted the distribution of Fe species, which further led to changes in the specific surface area, average pore size and pore volume of the catalysts (as shown by the N_2 adsorption-desorption results). These changes may be conducive to the catalytic degradation of phenol simulated wastewater. Firstly, the highly dispersed active component Fe in the catalyst is more favorable to react with H_2O_2 in the reaction system to produce highly oxidizing •OH (equations 1 and 2), thereby further promoting the degradation of phenol (equation 3). Secondly, the increase in the specific surface area of the catalyst expands the reaction region, thereby improving the phenol degradation efficiency. Thirdly, the increase in pore volume reduces reaction hindrance, which further enhances the degradation efficiency of phenol simulated wastewater. The effect of adding a trace amount of Si ($x < 0.10$) on the physical properties of the catalyst, as well as the subsequently inferred influence on its catalytic activity, are illustrated in Scheme 1.

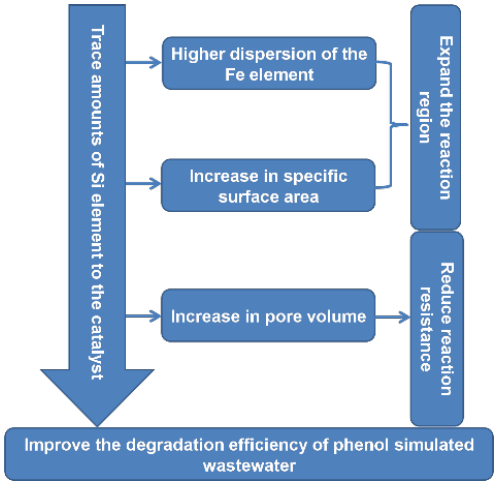

Scheme 1. The influence of trace Si doping on the physical properties and phenol wastewater degradation performance of the Si-Fe/γ-Al_2O_3 ($x < 0.10$) catalyst.

On the other hand, the chemical properties of catalysts may also influence their catalytic activity. In heterogeneous catalytic reactions, the adsorption of reactants on the catalyst surface is generally considered to be

the first step of heterogeneous catalysis [37, 38]. A non-linear relationship may exist between the number of alkaline sites on the catalyst surface and the catalytic activity, and surface alkaline sites may play a key role in balancing these factors. For instance, an excessive number of alkaline sites inhibit the Fe^{3+}/Fe^{2+} redox cycle in the Fenton reaction (which generates highly oxidative •OH, as shown in equations 1 and 2). Conversely, an insufficient number of alkaline sites will decrease the adsorption capacity toward phenolic pollutants, since phenolic compounds in wastewater are acidic. The competitive balance between these two effects may jointly determine the degradation efficiency.

Overall, the number of alkaline sites in the Si-Fe/γ-Al_2O_3 (x) catalysts may affect the COD removal rate of phenolic wastewater by regulating two key aspects: pollutant adsorption capacity and active species (•OH) generation efficiency. Only when the number of alkaline sites is within a suitable range can the synergistic effect between adsorption and the generation of •OH to achieve the optimal COD removal performance; otherwise, a decline in COD removal rate will occur.

It is speculated that the Si-Fe/γ-Al_2O_3 (x = 0.1) catalyst has an appropriate number of surface alkaline sites, which not only allows efficient adsorption of phenolic pollutants but also promotes the generation of strong oxidizing species such as •OH (equations 1 and 2), thus achieving the highest COD removal rate. In this study, Scheme 2 illustrates the effect of the number of alkaline sites on the degradation performance of Si-Fe/γ-Al_2O_3 (x) catalysts for phenol simulated wastewater.

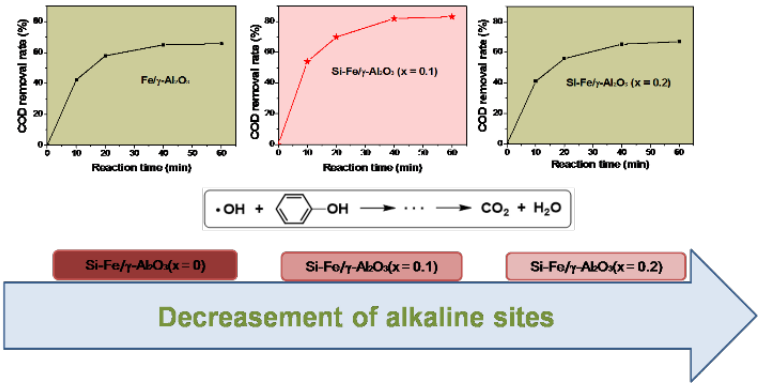

Scheme 2. Effect of surface alkaline sites of the Si-Fe/γ-Al_2O_3 (x) catalysts on degradation performance of phenol simulated wastewater.

The limitations of this study are as follows: it only focused on the influence of trace Si elements on the activity of iron-based catalysts. Specifically, the addition of trace Si elements in the catalyst was found to significantly enhance its catalytic activity. However, the changes in the service life of the catalyst before and after modification and the influencing factors still remain to be further explored. Meanwhile, the impact of Si on other active components (such as copper, manganese, etc.) also needs in-depth investigation, which will be one of the key focuses of subsequent research.

Looking ahead, this research not only offers a feasible strategy for the preparation of catalysts with highly dispersed active components, but also establishes a theoretical basis for the efficient application of such catalysts in the degradation of organic wastewater.

CONCLUSIONS

In the Si-Fe/γ-Al_2O_3 (x) catalysts prepared by the impregnation method, the mass ratio of Si to Fe enables us to gain a deep understanding of the influence of trace Si on the physical and chemical properties of the catalysts, and subsequently on the catalyst's activity in degrading phenolic wastewater. When a small amount of Si is added to a Fe/γ-Al_2O_3 catalyst, the dispersion of the active component Fe on the catalyst surface is enhanced, and the specific surface area, average pore size, and pore volume of the Si-Fe/γ-Al_2O_3 catalysts ($x < 0.1$) increase. Meanwhile, the introduction of a small amount of Si can also improve the alkaline sites on the catalyst surface, which is beneficial for enhancing the catalytic activity. As a result, the Si-Fe/γ-Al_2O_3 ($x = 0.1$) catalyst demonstrated outstanding catalytic activity in the degradation of phenolic wastewater. Under the given conditions, the COD removal rate of the phenolic wastewater by this catalyst reached 83%, which was superior to the activity of other catalysts. This study proposes a novel and effective strategy for preparing heterogeneous catalysts with highly dispersed active components, and also enables the improvement of the surface acid-base properties of such catalysts.

EXPERIMENTAL SECTION

Materials And Reagents

Analytical grade ferric nitrate ($Fe(NO_3)_3•9H_2O$), analytical grade phenol, sulfuric acid (H_2SO_4), potassium dichromate ($K_2Cr_2O_7$), silver sulfate (Ag_2SO_4), hydrogen peroxide (H_2O_2, 30%), and tetraethyl orthosilicate ($Si(OC_2H_5)_4$, TEOS,

>99%) were purchased from Sinopharm Chemical Reagent Co., Ltd. Analytical grade Boehmite was provided by Zibo Hengqi Powdered Advanced Material Co., Ltd, China. Above reagents were used as received without further purification.

Catalyst Preparation

A series of Si-Fe/γ-Al_2O_3 (x) catalysts were prepared by an impregnation method, where x represents the mass ratio of Si to Fe per gram of support.

First, an impregnation solution was prepared. 14.4284 g of $Fe(NO_3)_3$•$9H_2O$ was dissolved in 16 mL of deionized water under stirring until completely dissolved, and the resulting solution was equally divided into four portions. Then, 0, 0.2019, 0.4038, and 0.8076 mL of TEOS solution were added to these four solutions, respectively.

Next, 5.0 g of Boehmite with a particle size of 0.250-0.425 mm (40 - 60 mesh) was added into each solution, and the mixtures were stirred continuously at room temperature for 12 h.

Subsequently, the mixtures were dried in a constant temperature drying oven at 120 °C. The dried samples were transferred to a crucible and calcined in a Muffle oven at 500 °C for 4 h.

After cooling naturally to room temperature, in this paper, the final catalyst is labeled as Si-Fe/γ-Al_2O_3 (x), where x = 0, 0.05, 0.1, and 0.2, corresponding to the theoretical mass ratio of Si to Fe. The theoretical Fe content of all catalysts is 0.1 grams of Fe per gram of support.

Catalyst Characterization

Powder X-ray diffraction (XRD) patterns were collected on a Rigaku D/max-RA X-ray diffractometer with Cu Ka radiation, operating at a respective voltage of 40 kV and current of 40 mA. Diffractograms were recorded in the 2θ range of 20–80°.

X-ray photoelectron spectroscopy (XPS) data were collected on a Thermo Scientific K-Alpha instrument using monochromic Al Kα radiation. The binding energies were referenced to the C 1s line at 284.8 eV from adventitious carbon.

The surface area and the porous structure were characterized by N_2-physisorption at 77 K using a Micromeritics Tristar II 3020 surface analyzer. Prior to measurement, samples were degassed at 350 °C for 4 h. Specific surface areas were calculated using the Brunauer-Emmett-Teller (BET) equation at $P/P_0 < 0.3$. Pore size distributions were determined from the desorption branch of the N_2 adsorption isotherm using the Barrett-Joyner-Halenda (BJH) method.

The morphology and microstructure of the as-prepared catalysts were observed using a Zeiss Supra 40 scanning electron microscope (SEM, Germany). Prior to imaging, the samples were sprayed with gold to enhance conductivity, and then were examined under high vacuum at an accelerating voltage of 20 kV. Chemical composition and semi-quantitative elemental analysis were performed simultaneously using an Oxford Instruments X-Max energy dispersive spectrometer (EDS).

Carbon dioxide temperature programmed desorption (CO_2-TPD) was carried out on a laboratory-made apparatus to investigate the surface acid-base properties of Si-Fe/γ-Al_2O_3 (x) catalysts. 50 mg of sample were loaded in a quartz tubular reactor (i.d.: 6 mm) prior to the measurement, and then they were heated to 500 ^oC at the rate of 10 ^oC/min under a He flow, followed by being maintained at 500 ^oC for 1 h. After natural cooling to room temperature, pulse CO_2 gas into the catalyst until adsorption saturation. The physically adsorbed CO_2 was removed under a He flow at 100 ^oC for 1 h. Then, the sample was heated to 800 ^oC at a rate of 10 ^oC/min. The desorbed CO_2 was analyzed by an online gas chromatograph with a TCD detector.

Catalytic Activity Measurements

The catalytic activities of Si-Fe/γ-Al_2O_3 (x) samples were evaluated by the degradation of phenol simulated wastewater. The optimum experimental conditions were employed according to our previous work [24]. The catalytic degradation of phenol simulated wastewater was tested in a 150 mL three necked glass flasks at 30 ^oC. Firstly, the initial pH of phenol simulated wastewater with a concentration of 100 mg•L^{-1} was adjusted to 3.5 with a dilute H_2SO_4 solution, and its corresponding COD was about 238 mg•L^{-1}. Then, 50 mL phenol simulated wastewater, 150 mg catalyst, and 1.5 mL 30% (wt.%) aqueous H_2O_2 solution were added to a three necked glass flask, and the mixture was stirred constantly to ensure good dispersion of the catalyst in the reaction system at 30 °C. After a 60 min reaction, a 20 mL sample was extracted from the reaction system to determine its COD value, which was measured by the standard $Cr_2O_7^{2-}/Cr^{3+}$ method.

For each COD value, parallel experiments were conducted under identical experimental conditions, with a minimum of three repetitions. After the experiments are completed, the average value of the results from each experimental group shall be used as the final data.

The COD removal rate of the wastewater was calculated using equation 11:

$$\text{COD removal rate (\%)} = (COD_B - COD_A)/COD_B \times 100 \quad (11)$$

In the above equation, COD_B denotes the initial COD value of the wastewater, while COD_A represents its COD value after degradation.

ACKNOWLEDGMENTS

This research was funded by the Anhui Province Quality Engineering Project (2020kcszjxtd52); the National Natural Science Foundation of China (21978003); the National Natural Science Foundation of China (21503004); the Anhui Province Discipline (Specialty) Leader Cultivation Project (DTR2024050); the Guidance project of Science and Technology Innovation of Bengbu (20210349); Bengbu University Application-level Scientific Research Project (2024YYX30pj); the Bengbu University Student Innovation and Entrepreneurship Project (202511305007, S202511305015); the Cultivation Program for the Outstanding Young Teachers of Anhui Province (YQZD2023082) and the Bengbu University Research Team Fund (BBXYKYTDxj09).

REFERENCES

1. V. Vinayagam; K. N. Palani; S. Ganesh; S. Rajesh; V. V. Akula; R. Avoodaiappan; O. S. Kushwaha; A. Pugazhendhi; *Environ. Res.*, **2024**, 240, 117500.
2. K. M. AlAqad; M. M. Abdelnaby; A. Tanimu; I. Abdulazeez; A. M. Elsharif; *Environ. Pollut. Manag.*, **2025**, 2, 1-13.
3. T. Weng; H. Du; H. Luo; M. Jiang; Z. Chen; J. Wang; H. Chen; *Sep. Purif. Technol.*, **2025**, 355, 129573.
4. K. Haarstad; H. J. Bavor; T. Mæhlum; *Water Sci. Technol.,* **2012**, 65, 76–99.
5. B. Tunçsiper; *J. Clean. Prod.,* **2019**, 04, 211.
6. S. Yang; S. Yu; Y. Dong; J. Liu; P. Zhou; H. Zhang; Z. Xiong; C. S. He; B. Lai; *J. Hazard. Mater.*, **2025**, 490, 137752.
7. P. Koundle; N. Nirmalkar; G. Boczkaj; *J. Environ. Manage.*, **2025**, 374, 124107.
8. K. Tian; L. Hu; L. Li; Q. Zheng; Y. Xin; G. Zhang; *Chinese Chem. Lett.*, **2022**, 33, 4461-4477.
9. J. Nie; Z. Li; W. Liu; Z. Sang; D. A. Yang; L. Wang; F. Hou; J. Liang; *Adv. Mater.*, **2025**, 37, 2420236.
10. D. Ma; H. Yi; C. Lai; X. Liu; X. Huo; Z. An; L. Li; Y. Fu; B. Li; M. Zhang; L. Qin; S. Liu; L. Yang; *Chemosphere*, **2021**, 275, 130104.
11. X. Zou; Q. Shi; M. Cheng; D. Huang; G. Zhang; W. Wang; G. Wang; H. Liu; Y. Chen; A. Chen; S. Deng; *Adv. Energy Mater.*, **2025**, 15, 2501424.
12. R. Lin; Y. Li; T. Yong; W. Cao; J. Wu; Y. Shen; *J. Environ. Manage.*, **2022**, 306, 114460.
13. F. N. Chergui; S. Ounoki; M. Chebbi; T. Masmoudi; Y. Kadmi; *Int. J. Environ. Sci. Te.*, **2025**, 22, 13717–13730.
14. Y. Zhu; R. Zhu; Y. Xi; J. Zhu; G. Zhu; H. He; *Appl. Catal. B: Environ.*, **2019**, 255, 117739.

15. H. Liu; S. Tang; Z. Wang; Q. Zhang; D. Yuan; *Chemosphere*, **2024**, 353, 141581.
16. M. Zhang; H. Dong; L. Zhao; D. Wang; D. Meng; *Sci. Total Environ.*, **2019**, 670, 110-121.
17. J. Cai; J. Xiao; G. Du; Q. An; W. Tong; *J. Mater. Chem. B*, **2025**, 13, 4544-4569.
18. X. Wang; D. Zhang; Y. Cheng; B. Wu; L. Sun; *Molecules*, **2025**, 30, 4549.
19. J. Wang; C. Liu; J. Qi; J. Li; X. Sun; J. Shen; W. Han; L. Wang; *Environ. Pollu.*, **2018**, 243, 1068-1077.
20. L. Ma; Y. Wang; Y. Chen; D. Xu; R. Han; D. Jiao; H. Xing; D. Wang; X. Yang; *ACS Nano.,* **2025**, 19, 28410–28421.
21. P. Compton; N. R. Dehkordi; P. Larese Casanova; A. N. Alshawabkeh; *J. Chem. Eng. Catal.,* **2022**, 1: 203.
22. S. Guo; N. Yuan; G. Zhang; J. C. Yu; *Micropor. Mesopor. Mater.,* **2017**, 238, 62-68.
23. Q. U. Ain; U. Rasheed; Z. Chen; R. He; Z. Tong; *J. Ind. Eng. Chem.*, **2024**, 134, 327-342.
24. J. Zhao; K. Ding; B. Ding; *Water Air Soil Poll.*, **2017**, 228, 442.
25. N. K. Puthenveettil; G. Dražic; A. Pintar; N. N. Tušar; *Catalysts,* **2026**, 16, 34.
26. N. Farhadian; S. Liu; A. Asadi; M. Shahlaei; S. Moradi; *J. Mol. Liq.*, **2021**, 321, 114896.
27. J. Zeng; W. Wang; Y. Du; *Environ. Prog. Sustainable Energy,* **2026**, e70397.
28. S. T. Yang; W. Zhang; J. Xie; R. Liao; X. Zhang; B. Yu; R. Wu; X. Liu; H. Li; Z. Guo; *RSC Adv.,* **2014**, 5, 5337-5345.
29. Y. Chen; S. Zhang; Y. Chen; H. Ding; S. Yao; Y. Tang; Z. Qiu; K. Xu; Y. Hu; H. Pang; *Nano Res.,* **2025**, 18, 94907446.
30. B. Ma; Y. Zha; H. Shi; Y. Qin; M. Zhao; J. Li; S. Wang; B. Yan; B. Zhao; Y. Ma; H. Xie; *Sep. Purif. Technol.*, **2025**, 354, 129086.
31. B. Rezaei; M. Khamforoush; F. Rahmani; *J. Clean. Prod.*, **2025,** 513, 145744.
32. C. Xiao; Y. Han; *Mat. Sci. Eng. A*, **2002**, 323, 58-61.
33. V. Calvino-Casilda; R. Martin-Aranda; I. Sobczak; M. Ziolek; *Appl. Catal. A-Gen.*, **2006**, 303, 121-130.
34. A. Cheng; Y. He; X. Liu; C. He; *J. Environ. Sci.*, **2024**, 136, 390-399.
35. X. Wang; Z. Yang; Y. Jiang; P. Zhao; X. Meng; *Sep. Purif. Technol.*, **2024**, 330, 125267.
36. M. Tian; X. Ren; S. Ding; N. Fu; Y. Wei; Z. Yang; X. Yao; *Environ. Res.*, **2024**, 243, 117848.
37. B. W. Chen; M. Mavrikakis; *Nat. Chem. Eng.*, **2025**, 2, 181-197.
38. M. Yaghi; S. Chidiac; S. Awad; Y. El Rayess; N. Zgheib; *Clean Technol.*, **2025**, 7, 62.

STUDIA UBB CHEMIA, LXXI, 2, 2026 (p. 189-208)
(RECOMMENDED CITATION)
DOI:10.24193/subbchem.2026.2.10

BEYOND THE SALINITY GRADIENT ENERGY HARVESTING

Cristiana-Nicoleta FUICU[a], Nicolae VASZILCSIN[b,c], Mircea-Laurențiu DAN[a], Delia-Andrada DUCA[a,*]

ABSTRACT. Recently, salinity gradient energy – known as blue energy – has sparked the interest of researchers in identifying a new source of renewable energy, available at the contact between river water and seawater. In this paper, which is a mini-review of the salinity gradient energy harvesting, the appreciable potential of this energy source is emphasized by calculating the thermodynamic effect of mixing a water of high salinity, which simulates seawater, with water of low salinity, characteristic of rivers. Unfortunately, this potential of salinity gradient energy is difficult to exploit due to technical limitations. In such circumstances, the seawater-river water system was approached as an electrochemical thermodynamic system, at the interface of which an electric potential difference occurs. In the simplest case, this is a diffusion potential, evaluated based on Henderson equation. The value of the diffusion potential is low (about 20 mV) because the interface between these two media is crossed by both cations and anions. If, however, the two media of different salinity are separated by an ion exchange membrane, there is a much larger potential difference between them (about 100 mV), called membrane potential, which can be capitalized using a concentration cell. Moreover, the main methods applied so far for the recovery of the salinity gradient energy are highlighted: pressure retarded osmosis, reverse electrodialysis and capacitive mixing methods.

Keywords: *diffusion potential, Henderson relationship, membrane potential, reverse electrodialysis, pressure retarded osmosis, blue energy, capacitive mixing method.*

[a] *Faculty of Chemical Engineering, Biotechnologies and Environmental Protection, University Politehnica Timisoara, 300223 Timisoara, Romania.*
[b] *Technical Sciences Academy of Romania, Bd. Dacia 26, 010414 Bucuresti, Romania.*
[c] *Research Institute for Renewable Energies, University Politehnica Timisoara, Piata Victoriei 2, 300006 Timisoara, Romania.*
[*] *Corresponding author: delia.duca@upt.ro*

INTRODUCTION

Over the past decades, especially after the Paris Agreement in 2015, signed by 195 states, research on renewable energy resources has been enhanced to reduce greenhouse gas emissions and maintain the increase in the global average temperature up to +2°C compared to the pre-industrial period [1-3]. Moreover, the United Nations Climate Conference COP29 (Baku 2024) recommended increasing efforts to protect the environment and mitigate climate change by imposing a +1.5 C° limit on the average temperature increase [4]. The constant interest in hydro, solar, wind, biomass renewable sources, as well as thermal water energy, has been followed by recent research for the use of low energy density sources, difficult to capitalize at commercial level, such as salinity gradient energy (SGE) [5-9].

In principle, SGE is the energy obtained by mixing two saline aqueous solutions, which differ in the concentration of the components. The Gibbs free energy change of mixing ΔG_{mix} can be calculated using the relation (1) [10-12].

$$\Delta G_{mix} = \nu RT \sum x_i ln x_i \quad (1)$$

where n is the number of chemical species (ionic species, in the case of electrolyte solutions), R – the universal gas constant, T – the thermodynamic temperature, x_i – the molar fraction of the chemical species i.

The idea of capitalizing the SGE has been launched as early as the middle of the last century by R. E. Pattle, who stated: "*when a river mixes with the sea, free energy equal to that obtainable from a water fall 680 ft. high is lost*" [13]. This remark of R. E. Pattle sparked the imagination of researchers who were probably already seeing the waters of the Amazon, with a flow of 200,000 m^3 s^{-1}, passing through generators of electricity from a height equivalent to 207 m (680 ft.), before pouring into the Atlantic Ocean, thus ensuring the energy needs of all South America. Unfortunately, the possibilities offered by thermodynamics cannot always be fully exploited due to technical limitations.

In order to rigorously evaluate the energy available for the mixing of seawater and river water, equation (1) has been customized for the case of concentrated and diluted sodium chloride solutions (2) [14].

$$\Delta G_{mix} = 2RT[(n_c + n_d) ln x_{mix} - n_c ln x_c - n_d ln x_d] \quad (2)$$

where n_c and n_d are the number of moles of NaCl in the concentrated solution, respectively diluted, x_c, x_d and x_{mix} – the molar fractions of NaCl in the concentrated, diluted solution, respectively in the mixture of the two solutions. Factor 2 is due to the fact that NaCl is dissociated into the two ionic species Na^+ and Cl^-.

By replacing the molar fractions with the respective molar concentrations, the relationship (3) is obtained [14].

$$\Delta G_{mix} = -2RT\left[V_c c_c ln\frac{c_c}{c_{mix}} + V_d c_d ln\frac{c_d}{c_{mix}}\right] \quad (3)$$

where V_c and V_d are the volume of concentrated solution, respectively diluted, L; c_c, c_d and c_{mix} – the molar concentrations of NaCl in the concentrated, diluted and mixed solution, mol L^{-1}.

When mixing 1 L of 3.5% NaCl solution (0.6 mol L^{-1}), which simulates seawater, with 1 L of dilute NaCl solution (0.01 mol L^{-1}), which simulates river water, 2 L of 0.305 mol L^{-1} NaCl solution is obtained.

Under these conditions: $V_c = V_d = 1$ L; $c_c = 0.6$ mol L^{-1}; $c_d = 0.01$ mol L^{-1}; $c_{mix} = 0.305$ mol L^{-1}. The Gibbs free energy value will be:

$$\Delta G_{mix} = -2 \times 8.314 \times 298\left[1 \times 0.6ln\frac{0.6}{0.305} + 1 \times 0.01ln\frac{0.01}{0.305}\right] = -1842 \text{ J}$$

Therefore, for 1 L of seawater-river water mixture, an energy of 921 J is obtained, which means that the available energy is equivalent to the potential energy of a 1 L of mixture of the two solutions at a height of about 92 m. The value obtained is much lower than the one reported by R. E. Pattle (207 m), because in the evaluation of Gibbs free energy change the salinity of river water is taken into account and the obtained value is referred to 1 L of seawater – river water mixture.

The above evaluations of the SGE consider that the seawater-river water mixture is a thermodynamic system for which the available energy is given by ΔG_{mix}, without taking into account the fact that the interface between the two media is crossed by ionic species that have different mobilities. Under these circumstances, there is an electric potential difference between the two solutions, called diffusion potential, which can be harnessed from an energetic point of view.

DIFFUSION POTENTIAL

Let us consider two solutions 1 and 2 in contact, which contain the ionic species $X_1^{z_1}$, $X_2^{z_2}$ … $X_n^{z_n}$ at molar concentrations c_{11}, c_{21}, …, c_{n1}, in solution 1, respectively c_{12}, c_{22}, …, c_{n2}, in solution 2, z_i being the charge of X_i ion (Figure 1). When the solutions are in contact, both phases are electrically neutral, which means that $\sum_i z_i c_{i1} = 0$ şi $\sum_i z_i c_{i2} = 0$.

Since, the ionic species in the two solutions have different diffusion coefficients and implicit mobilities, under the influence of the concentration gradients between the two solutions, the ionic species will diffuse at different

rates, which will lead to the development of a potential difference, known as the diffusion potential Dϕ_d. It can be calculated using Henderson general equation (4) [15-17].

$$\Delta\phi_d = \phi_1 - \phi_2 = \frac{\sum_i \frac{u_i}{z_i}(c_{i2}-c_{i1})}{\sum_i u_i(c_{i2}-c_{i1})} \cdot \frac{RT}{F} ln \frac{\sum_i u_i \cdot c_{i2}}{\sum_i u_i \cdot c_{i1}} \quad (4)$$

where ϕ_1 is the potential of the solution 1, ϕ_2 – the potential of the solution 2, u_i – mobility of the ionic species *i*.

Diffusion potential $\Delta\phi_d$ is not a constant value, it decreases continuously as the concentrations in the solutions in contact are equalized, and when the equilibrium is reached $\Delta\phi_d = 0$.

For two solutions of the same electrolyte at different concentrations, in contact, the diffusion potential is given by the relationship (5).

$$\Delta\phi_d = \phi_1 - \phi_2 = \frac{\frac{u_1}{z_1}(c_{12}-c_{11})+\frac{u_2}{z_2}(c_{22}-c_{21})}{u_1(c_{12}-c_{11})+u_2(c_{22}-c_{21})} \cdot \frac{RT}{F} ln \frac{u_1 \cdot c_{12}+u_2 \cdot c_{22}}{u_1 \cdot c_{11}+u_2 \cdot c_{21}} \quad (5)$$

For a z–z valent electrolyte, completely dissociated into ions X_1^{z+} and X_2^{z-}, for which the concentrations of the two ionic species in the same solution are equal to each other ($c_{11} = c_{12} = c_1$ and $c_{21} = c_{22} = c_2$, the equation (5) is simplified in the form given to the relationship (6).

$$\Delta\phi_d = \phi_1 - \phi_2 = \frac{u_c - u_a}{u_c + u_a} \cdot \frac{RT}{zF} ln \frac{c_2}{c_1} \quad (6)$$

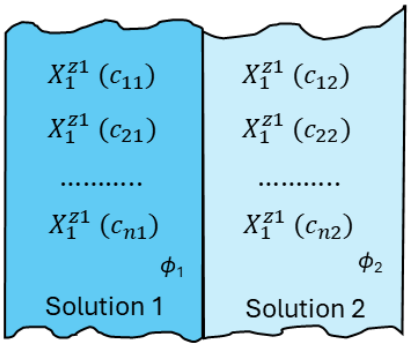

Figure 1. Diffusion potential at the interface between solutions 1 and 2.

Let us take as an example two sodium chloride solutions, one with a concentration of c_1 = 0.6 mol L^{-1} (phase 1), similar to the concentration of seawater, and one with a reduced salinity of c_2 = 0.01 mol L^{-1} sodium chloride (phase 2), which simulates river water.

The ionic mobility for Na^+ is u_{Na^+} = 5.19·10^{-8} m^2 V^{-1} s^{-1}, and the one for Cl^- is u_{Cl^-} = 7.92·10^{-8} m^2 V^{-1} s^{-1} [18]. Whereas $u_{Na^+} < u_{Cl^-}$, the diffusion of Cl^- ions from the concentrated solution to the diluted solution will be faster than that of Na^+ ions. Consequently, the diluted solution becomes enriched in negative charges, whereas the more concentrated solution exhibits an excess of positive charges. Using the relation (3), for the diffusion potential, the value $\Delta\phi_d = 22\ \mathrm{mV}$ is obtained.

More accurate values of diffusion potential can be obtained if the average activities of the ionic species $a = f_{\pm} \times c$ are involved instead of concentrations. For 0.6 mol L^{-1} NaCl solution, the average activity coefficient is $f_{\pm 1}$ = 0.675, and for 0.01 mol L^{-1} NaCl solution, $f_{\pm 2}$ = 0.902 [19]. Accordingly, for the diffusion potential, the value $\Delta\phi_d$ = 20 mV has been obtained.

Since the difference between the two values is insignificant, we will still use concentrations instead of activities and ionic mobilities at infinite dilution instead of real mobilities.

Certainly, both seawater and river water have a much more complicated composition. An approximate composition of seawater and the water of an arbitrary river is given in Table 1.

Table 1. Ionic mobilities [18,20] and the average composition of seawater [21] and river water

Ionic species	Ionic mobility $u^o \cdot 10^8$ [m^2 s^{-1} V^{-1}]	Molar mass [g mol^{-1}]	Concentration in seawater		Concentration in river water	
			[g L^{-1}]	[mol L^{-1}]	[g L^{-1}]	[mol L^{-1}]
Cl^-	7.92	35.45	19.162	c_{11}=0.5405	0.070	c_{12}=0.001975
Na^+	5.19	22.99	10.679	c_{21}=0.4645	0.070	c_{22}=0.003045
Mg^{2+}	4.18	24.31	1.278	c_{31}=0.0526	0.020	c_{32}=0.000823
SO_4^{2-}	8.29	96.06	2.680	c_{41}=0.0278	0.100	c_{42}=0.001041
Ca^{2+}	6.16	40.08	0.4096	c_{51}=0.0010	0.080	c_{52}=0.001996
K^+	7.62	39.10	0.3953	c_{61}=0.0101	0.005	c_{62}=0.000128
HCO_3^-	4.59	61.02	0.0276	c_{71}=.00045	0.150	c_{72}=0.002458
Br^-	8.10	79.90	0.0663	c_{81}=.00083	0	c_{82}=0
NO_3^-	7.40	62.00	0	c_{91}= 0	0.020	c_{92}=0.000323

It is easy to see that the diffusion potential is a non-equilibrium potential, since the ionic species in the more concentrated solution will continuously pass into the dilute solution until the concentrations are equalized, when the diffusion potential becomes zero. On the other hand, the

equalization of concentrations can be achieved not only as a result of a concentration gradient, but also by convection, because of a density, pressure or temperature gradient, a phenomenon that accelerates the uniformity of the ionic concentrations in the solutions in contact. To avoid convection phenomena, the two solutions can be separated by non-selective diaphragms, which allow the passage of all ionic species present in the electrolyte solutions.

An efficient exploitation of the energy potential at the saline/ freshwater interface can be achieved by using a selective separator of ionic species between in solutions in contact, e.g., a cation- or anion exchange membrane.

Consider the case where the two solutions of NaCl 0.6 mol L^{-1} (solution 1) and 0.01 mol L^{-1} (solution 2) are separated by a cation exchange membrane (CEM), e.g., Nafion (Figure 2) [22, 23].

Under the action of the concentration gradient between the two electrolyte solutions, only Na^+ ions can cross the membrane. The equilibrium state will be reached when the electrochemical potentials of the Na^+ ions in both solutions become equal (7).

$$\bar{\mu}_{Na^+(1)} = \bar{\mu}_{Na^+(2)} \tag{7}$$

where $\bar{\mu}_{Na^+(1)}$ şi $\bar{\mu}_{Na^+(2)}$ are the electrochemical potentials of Na^+ ions in solutions 1 and 2.

By explicitly expressing Na^+ ions electrochemical potentials, the relation (8) is obtained.

$$\mu^o_{Na^+} + RTlgc_{Na^+(1)} + F\phi_1 = \mu^o_{Na^+} + RTlgc_{Na^+(2)} + F\phi_2 \tag{8}$$

Therefore, the potential that arises between the two solutions separated by the cationic membrane, called the membrane potential $\Delta\phi_M$, will be given by the relation (9).

$$\Delta\phi_M = \phi_2 - \phi_1 = \frac{RT}{F} ln \frac{c_{Na^+(1)}}{c_{Na^+(2)}} \tag{9}$$

Numerical value for concentrations $c_{Na^+(1)}$= 0.6 mol L^{-1} and $c_{Na^+(2)}$ = 0.01 mol L^{-1}, is $\Delta\phi_M = 0.105$ V, significantly higher than the diffusion potential $\Delta\phi_d$.

If ionic mean activities are used instead of concentrations, the value of $\Delta\phi_M$ = 98 mV is obtained, close to that obtained using the concentrations of ionic species.

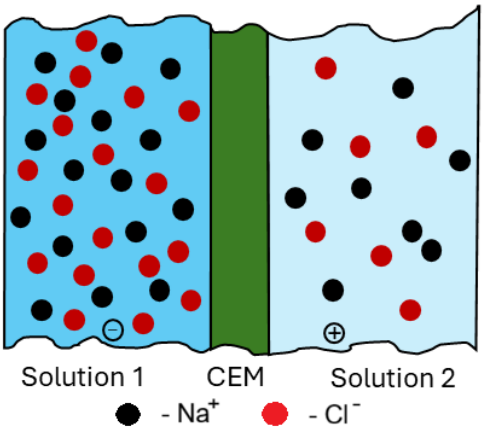

Figure 2. The emergence of the membrane potential across the two interfaces of the Nafion (CEM).

If an anion exchange membrane is used, only the Cl^- ions will diffuse through the membrane until electrochemical equilibrium is reached, when the electrochemical potential of the chloride ions in solution 1 will become equal to that in solution 2. Under these conditions, the expression of the membrane potential in this case is given by the relation (10) [22].

$$\Delta\phi_M = \phi_1 - \phi_2 = \frac{RT}{F} ln \frac{c_{Cl^-(1)}}{c_{Cl^-(2)}} \quad (10)$$

Measurement of the diffusion or membrane potential is possible by inserting two inert electrodes into the two electrolyte solutions. The electrochemical cell thus realized is known as the concentration cell.

CONCENTRATION CELLS

By introducing two inert metals into the two electrolyte solutions in contact, an electrochemical concentration cell is achieved. If the same electrochemical equilibrium is established at the two electrodes, then the electromotive force of the concentration cell will be equal to the diffusion potential or the membrane potential. Figure 3 shows a concentration cell with the electrochemical chain Pt (H_2)/H_2(g), H^+(aq), NaCl(c_1)//NaCl(c_2), H^+(aq), H_2(g)/Pt(H_2), in which the solutions are separated by a cation exchange membrane [23], and Figure 4 shows the profile of the Galvani potential (ϕ) along the electrochemical chain of the cell.

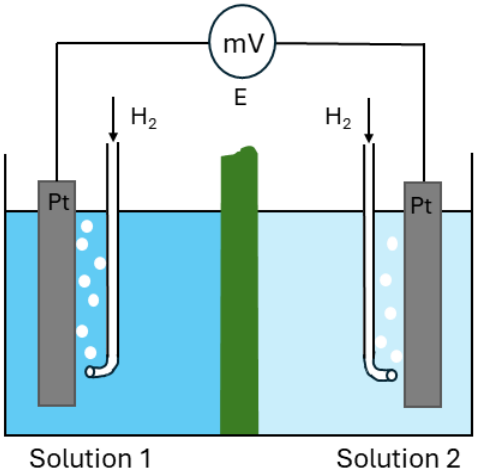

Figure 3. Concentration cell Pt (H_2)/H_2(g), H^+(aq), NaCl(c_1)//NaCl(c_2), H^+(aq), H_2(g)/Pt(H_2).

From the electrochemical chain of the concentration cell, it can be seen that the two electrodes are hydrogen electrodes whose absolute potential is given by the relation (11).

$$\Delta\phi_{eq} = \Delta\phi^{o}_{H_2/H^+} + \frac{RT}{F} ln \frac{a_{H^+}}{\sqrt{p_{H_2}}} \quad (11)$$

where $\Delta\phi^{o}_{H_2/H^+}$ is the absolute potential of the standard hydrogen electrode, p_{H_2}- hydrogen partial pressure, a_{H^+}- hydronium ion activity.

Since the hydrogen electrodes are identical, at the two Pt - electrolyte solution interfaces, the Galvani potential drops are identical (12) as shown in Figure 4.

$$\phi_{Pt1} - \phi_{S1} = \phi_{Pt2} - \phi_{S2} \quad (12)$$

According to Figure 4, the electromotive force, measured with an electronic voltmeter having high input impedance, in order do not allow a current during the measurement, is given the algebraic sum of the potential drops in the electrochemical chain (13).

$$E = \phi_{Pt1} - \phi_{S1} - \Delta\phi_M + \phi_{S2} - \phi_{Pt2} \quad (13)$$

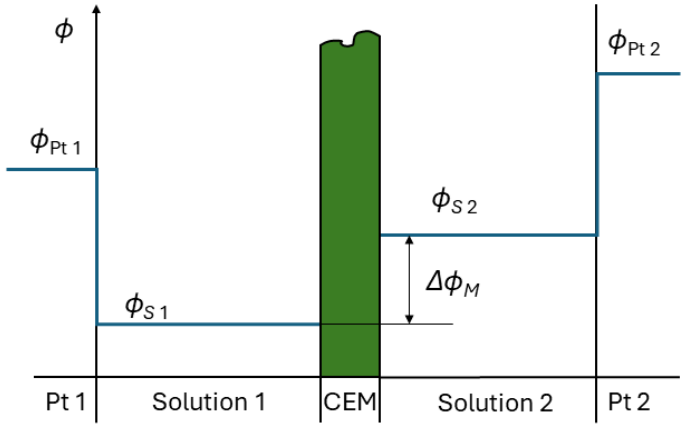

Figure 4. Potential Galvani profile along the electrochemical system.

Therefore, the membrane potential is numerically equal to the value of the cell electromotive force with opposite sign (14).

$$\Delta\phi_M = -E \tag{14}$$

As a rule, such concentration cells are not used as electrochemical power sources, owing to their low energy density and significant internal resistance. Their practical relevance lies primarily in potentiometric measurement for evaluating the electrolyte activity in solutions. The most well-known application is the glass electrode, a selective-ion electrode used to determine the activity of hydronium ions in electrolyte solutions. Ion-selective electrodes have also been developed for the quantitative determination of anionic or cationic species in aqueous solutions [24-28].

Modified concentration cells can be used to convert salinity gradient energy into electrical energy. In such systems, when current flows through the external circuit, reduction takes place at the cathode and oxidation at the anode. Equations (9) and (10), used to evaluate the membrane potential $\Delta\phi_d$, provide the maximum electromotive force *E*, corresponding to the thermodynamic equilibrium state. The value of *E* decreases over time as the concentration gradient between the two solutions diminishes. Under dynamic operating conditions, the actual cell voltage is lower than the *E* because of polarization effects.

BLUE ENERGY HARVESTING

The most important technical variants for the valorisation of SGE are pressure retarded osmosis (PRO), reverse electrodialysis (RED) and capacitive mixing (CapMix) [29-32].

Pressure retarded osmosis is a widely studied technology for capturing SGE, originating from pioneering research of S. Loeb et al. in 1976. They have used a semi-permeable membrane between seawater and river water [33]. This allows the passage of water molecules from river water (diluted) to seawater (concentrated), creating a pressure difference due to the osmosis phenomenon, which is converted into electricity by means of a turbine (Figure 5) [7,34,35]. At equilibrium, the pressure difference becomes equal to the osmotic pressure.

One of the most important components of the PRO system is the semi-permeable membrane, which must permit the passage of water molecules while effectively restricting the transfer of ionic species. Consequently, membranes employed in PRO technology are typically composite structures integrated into a rigid support in order to withstand the pressure difference between the seawater and river water compartments [36,37]. Successful semi-permeable membranes have proven to be those that have a polyamide or polyamide-polyethylene composites as a selective layer. Polydopamine is also a promising polymer, as it contains both nucleophilic and electrophilic groups in its structure [38].

For PRO technology, various values of power densities have been reported: 2.56 W m^{-2} [39], 0.7 – 1.2 W m^{-2} [40], but also exceedingly high values, difficult to achieve under normal conditions: 38 W m^{-2} [41].

Reverse electrodialysis is based on bringing seawater and river water into contact by means of two ion-selective membranes: an anion exchange membrane and a cation exchange one (Figure 6). Seawater flows between the two membranes, while river water circulates in the outer compartments. The anion exchange membrane will allow the passage of anions from seawater to river water in the left compartment, which will acquire an excess of negative charges. At the same time, the cation exchange membrane will allow cations to pass from seawater to river water, which will thus have an excess of positive electrical charges. Therefore, if inert electrodes are placed into the two extreme compartments, an electromotive force is generated between them, thus creating an electrochemical power source that converts SGE into electricity [42].

Basically, a cell stack is used to transform the SGE into electricity in which the anion exchange membranes alternate with the cation exchange ones, so that the potential difference at the ends of the cell is increased (Figure 7) [43,44]. J. Veermana et al. realized a stack of 50 elementary cells, supplied with solutions simulating seawater and river water, except for the electrode compartments fed with potassium hexacyanoferrate(II) and potassium hexacyanoferrate(III) solution. In these circumstances, electricity generation occurs via the oxidation of hexacyanoferrate(II) to hexacyanoferrate(III) at the anode, and the reverse reduction reaction at the cathode. Titanium

meshes coated with ruthenium and iridium oxides layers have been used as electrodes [45]. Other authors have reported the use of platinum or iridium films deposited on titanium mesh [12].

In general, the ion-exchange membranes employed in the RED technique are similar to commercially available membranes used in electrolyzers and fuel cells. P. Długołęcki et al. investigated Tokuyama Corporation Neosepta membranes and Asahi Glass Co. Selemion membranes in RED cells. The Neosepta CMX and Selemion CMV membranes are cation-exchange membranes based on a styrene–divinylbenzene copolymer reinforced with polyvinyl chloride, containing sulfonate groups $-SO_3^-$ as fixed ionic groups. In contrast, the Neosepta AMX and Selemion APS membranes are anion-exchange membranes containing quaternary ammonium groups $-NR_3^+$ as fixed ionic groups. In addition, membranes produced by FUMATECH (Fumasep) and MEGA (Ralex) have also been reported in the literature [42]. J. W. Post et al. established several requirements that membranes used in RED must satisfy in order to achieve acceptable energy efficiency: permselectivity > 95%; electrical resistance < 3 Ω cm²; chemical stability with a lifetime > 5 years; sufficient mechanical strength for stack construction; and a cost below 2 €/m² [11]. A rigorous comparison of the different types of cation- and anion exchange membranes used in RED was conducted by Jaewon Jang et al. [46].

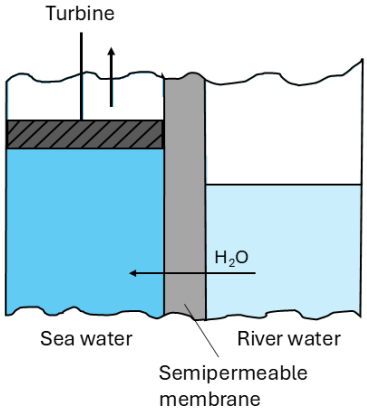

Figure 5. PRO principle.

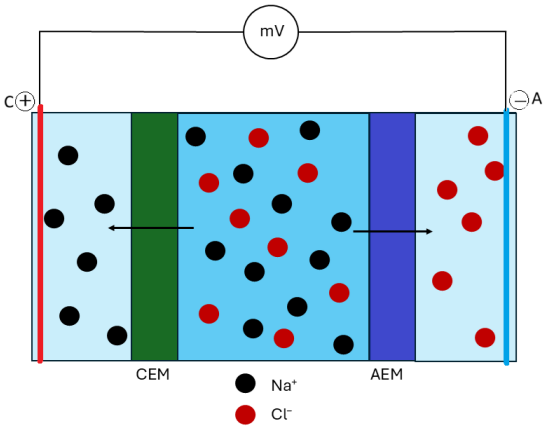

Figure 6. RED principle.

The maximum power density that can theoretically be achieved in RED technology is 6 W m^{-2}, but considering the limitations introduced by the selectivity of the membranes, as well as their specific conductivity, practical values of the power density of up to 2.4 W m^{-2} [47].

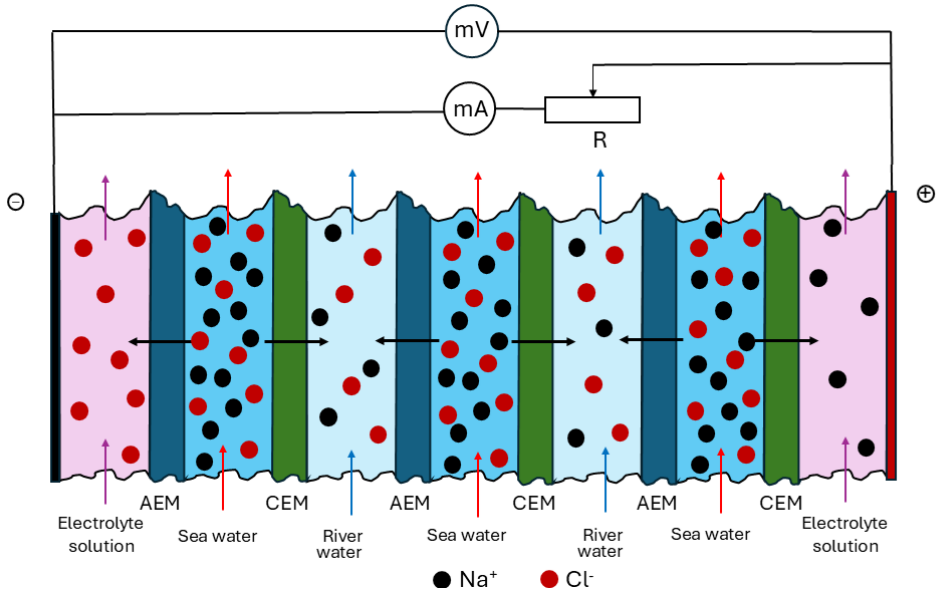

Figure 7. RED cell stack.

A simplified variant of RED is *nanopore power generation* (NPG), which employs a single separator between concentrated saline and diluted solution, thus reducing energy converter costs (Figure 8) [48]. As interphase separators, nanotubes with atoms or groups of atoms carrying electric charges are used, which reject selectively the diffusion of ions with electric charges of the same sign.

As an interphase separator, the use of boron nitride nanotubes has been proposed. Due to the partial hydration of boron nitride, according to the reaction (15), immobilized negative charges are generated into the nanotubes.

$$BN + 2H_2O \rightleftarrows HNBO^- + H_3O^+ \quad (15)$$

Consequently, an interphase separator based on boron nitride nanotubes allows the passage of cations but prevents the access of anions [49]. Recently, membranes have been made based on alumina nanotubes [50], molybdenum disulfide [51,52] or silicon nitride [53,54].

Capacitive mixing method (CapMix) is a reversible electrical energy storage system based on the electric double-layer capacitance at the interfaces between electronic and ionic conductors. In practice, a supercapacitor is used, consisting of an electrolytic cell equipped with inert electrodes possessing a very high specific surface area. Typically, the electrodes are made of activated

carbon, which provides high electrical capacitance through the specific adsorption of ionic species from the solution in contact with the electrode surface (Figure 9) [35,55,56].

In the first stage of capacitor charging, the electrochemical cell is filled with seawater. At the activated carbon–seawater interface A, connected to the positive terminal of the external power source, Cl^- ions are adsorbed, leading to an increase of the electric double-layer (EDL) capacitance at interface A. The extent of charge separation increases with the concentration of Cl^- ions in the solution. The negative plate of the EDL at interface A is located on the electrode surface, whereas the positive plate is situated in the electrolyte solution.

Similarly, at the activated carbon–seawater interface B, connected to the negative terminal of the power source, Na^+ ions are adsorbed, resulting in an increase in the EDL capacitance at interface B. In this case, the positive plate of the EDL is formed on the activated carbon surface, while the negative plate is located in the solution. Consequently, the electrochemical cell can be regarded as a system of two capacitors connected in series, where the terminal voltage is equal to the sum of the absolute values of the potential drops across the two EDLs.

In the second stage, during the discharge of the capacitor, the seawater in the cell is replaced with river water. In this manner, by replacing the concentrated solution with a dilute one, the EDL thickness at both interfaces (A and B) increases, leading to a rise in the voltage at the cell's terminals. In fact, the use of the dilute solution allows for an advanced discharge of the two EDLs, given that the electrical permittivity of the two solutions does not change significantly [54, 57].

An advanced configuration of CapMix separates the two activated carbon electrodes with a cation exchange membrane and an anion exchange membrane, respectively (Figure 10) [58–61].

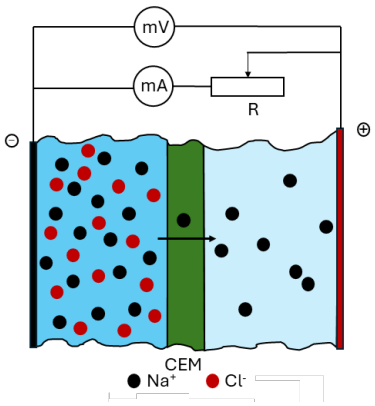

Figure 8. NPG principle.

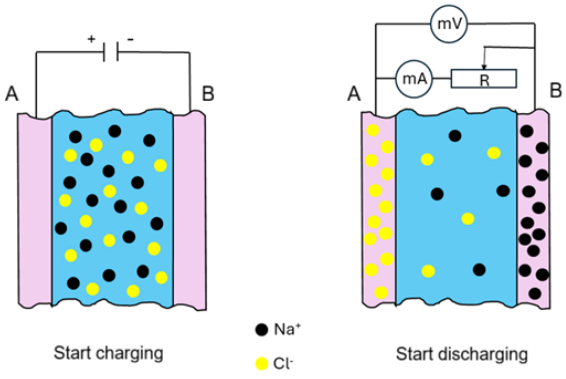

Figure 9. CapMix principle.

In this way, during the charging cycle, Na^+ ions spontaneously cross the cation exchange membrane and are adsorbed into the surface of the activated carbon, while Cl^- ions cross the anion exchange membrane and are adsorbed onto the surface of the opposite electrode. Since the two charging processes of the EDL at interfaces A and B are spontaneous, it is not necessary to polarize the electrodes using an external source. Equilibrium at the electronic conductor – ionic conductor interface A is established when the electrochemical potential of the adsorbed Na^+ ions becomes equal to their electrochemical potential in the seawater. Similarly, equilibrium at interface B is reached when the electrochemical potential of the adsorbed Cl^- ions equals that of the Cl^- ions in the seawater. As a result, a charge difference is generated between the two electrodes, which can subsequently be converted into electrical energy during the second discharge stage, when a dilute solution is passed between the electrodes.

Since the two charging processes of the EDL at interfaces A and B are spontaneous, it is not necessary to polarize the electrodes using an external source. Equilibrium at the electronic conductor – ionic conductor interface A is established when the electrochemical potential of the adsorbed Na^+ ions becomes equal to their electrochemical potential in the seawater. Similarly, equilibrium at interface B is reached when the electrochemical potential of the adsorbed Cl^- ions equals that of the Cl^- ions in the seawater. As a result, a charge difference is generated between the two electrodes, which can subsequently be converted into electrical energy during the second discharge stage, when a dilute solution is passed between the electrodes.

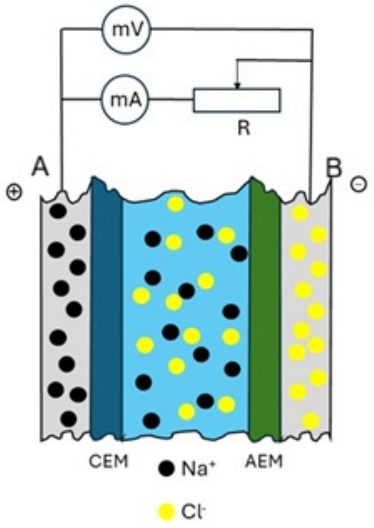

Figure 10. Advanced CapMix.

At the current level of research, the power density obtained by the CapMix technique is much lower than in the case of the PRO and RED methods. The most optimistic ratings for CapMix do not exceed 0.9 W m^{-2} [62,63]. On the other hand, the practical application of this technique has difficulties due to the membrane fouling and technical challenges of replacing seawater with river water in a short timeframe and without cross-dilution [35].

S. Sarp et al. have shown that PRO technology has some advantages over other SGE conversion methods, such as higher power density, as well as the possibility to use membranes from water desalination plants [64]. In 2009, the SINTEF research institute put into operation, in Tofte (Norway), an experimental facility to allow obtaining the necessary data for the application of PRO technology on a commercial scale [65]. Recently, in Japan, at Fukuoka, a PRO facility was put into operation, which is set to generate about 880,000 kWh per year [66]. Since the efficiency of the PRO method is dependent on the salinity difference between the two solutions, the Fukuoka facility was coupled with the desalination plant, using the resulting brine as a concentrated solution. As disadvantages of PRO, the following can be mentioned: the necessity of a large salinity gradient, the sensitivity of the membranes to impurities presents in the used solutions, as well as the use of moving equipment - the turbine that converts SGE into electrical energy. The RED technique, although it is not yet applied at a commercial level, has the advantage of the possibility to capitalize on small salinity differences between the two solutions, without the necessity of using a turbine. Unfortunately, this process also has a series of disadvantages: the sensitivity and high costs of the membranes, to which are added the construction difficulties due to the high internal electrical resistance of the solutions in the cell compartments. The CapMix method has the advantage of using a simple cell design, as well as inexpensive carbon-based electrodes, but their reduced mechanical resistance is a challenge for researchers. Constructive versions without ion-exchange membranes, although economically advantageous, are not efficient from an energetic point of view.

CONCLUSIONS

SGE, known within the scientific community as *blue energy*, remains a major challenge for researchers in the field of renewable energies. In principle, SGE represents the energy obtained by mixing two saline solutions that differ in their component concentrations, with the available energy being determined by the variation in the Gibbs free energy of mixing ΔG_{mix}. R. E. Pattle was the first to suggest the concept of harvesting the salinity gradient

between seawater and river water. The Gibbs free energy of mixing for 1 L of 0.6 mol L^{-1} NaCl solution (simulating seawater) with 1 L of 0.01 mol L^{-1} NaCl solution (simulating river water) is 1842 J. This implies that upon mixing the two solutions, the temperature increases by approximately 0.2 K, a variation that is difficult to exploit using a thermal engine.

Harvesting this Gibbs free energy variation ΔG_{mix} can be achieved by separating the two solutions with a selective membrane, which allows the passage of water molecules while rejecting the solutes. Driven by osmotic pressure, water molecules flow from the dilute solution to the concentrated one, thereby creating a hydraulic head that drives a turbine connected to an electrical generator. This constitutes the operating principle of PRO (Pressure-Retarded Osmosis) for converting SGE into electricity.

Furthermore, the electrochemical route represents another technique for harvesting the Gibbs free energy variation ΔG_{mix}. Due to the differences in mobility between Na^+ and Cl^- ionic species, a diffusion potential arises between the two solutions, which can be calculated using the Henderson equation. For the two solutions under consideration, the diffusion potential is approximately 20 mV. Naturally, as the two solutions mix, the diffusion potential decreases, reaching zero when the concentrations equalize. To prevent the mixing of the solutions, they can be separated by an ion-exchange membrane. By inserting two inert electrodes into the two solutions, a concentration cell is realized, whose electromotive force is numerically equal to the membrane potential $\Delta\phi_M$.

In the case of the 0.6 mol L^{-1} and 0.01 mol L^{-1} NaCl solutions separated by a cation-exchange membrane, the initial electromotive force was approximately 100 mV. In practice, however, a cell stack is realized, in which the compartments are alternately separated by cation- and anion-exchange membranes, thereby yielding a significantly higher electromotive force. Since the electrodes within the electrode compartments are identical, noble metals in a hexacyanoferrate(II) / hexacyanoferrate(III) solution, the electromotive force is determined by the sum of all absolute membrane potentials. Nanotubes functionalized with charged atoms or functional groups, which repel the diffusion of co-ions (ions bearing charges of the same sign), can also be utilized as separators between the two solutions.

Another electrochemical process for SGE conversion is the capacitive mixing method, which is based on the electric double-layer capacitance at the electronic conductor–ionic conductor interface. In practice, this is implemented as a carbon-based electrode supercapacitor. Charging of the supercapacitor is accomplished by passing seawater through the capacitor plates, whereas its discharging is carried out using river water. If the capacitor plates are isolated with a cation-exchange membrane and an

anion-exchange membrane, respectively, the charging of the electric double-layer occurs spontaneously, requiring no external energy input.

The analysis conducted by Shihong Lin et al. [35] demonstrated that, currently, SGE is not yet competitive due to the following reasons: the energy density of the seawater–river water system is low; the conversion efficiency of SGE into other energy forms is reduced due to technical difficulties that limit the advanced conversion of SGE into useful work; the membranes utilized in SGE conversion are expensive and sensitive to impurities present in the water; and the activity of the electrodes degrades over time. Among SGE conversion technologies, PRO is the most advanced, having reached a commercial level through the commissioning of a facility in Fukuoka, Japan; this plant utilizes the brine resulting from a desalination facility, which is significantly more concentrated than standard seawater.

Moreover, the European Commission has notified in 2014 that the exploitation of "Blue energy" currently involves excessive costs, and overcoming this bottleneck requires additional public support to render SGE conversion techniques economically viable [60]. Achieving this objective necessitates further experimental research into SGE conversion, targeting the following goals: the development of active electrodes to minimize their polarization during electricity generation in the external circuit; the identification of membranes with high selectivity and low electrical resistivity; the design of cells with ultra-narrow compartments to reduce the voltage drop within the solution; and the assurance of an optimal hydrodynamic flow regime to maintain high salinity gradients between the solutions in contact.

ACKNOWLEDGEMENTS

The authors gratefully acknowledge the support of the Doctoral School of the University Politehnica Timişoara in the preparation of this paper.

REFERENCES

1. N. Yilmaz; K. Looby; A. Atmanli; *Int. J. Hydrogen Energy*, **2025**, *150*, 150133.
2. F. P. Pinheiro; D. M. Gomes; F. L. Tofoli; R. F. Sampaio; L. S. Melo; R. C. F. Gregory; D. Sgro; R. P. S. Leao; *Int. J. Hydrogen Energy*, **2025**, *97*, 690–707.
3. M. Akhtaruzzaman; A. K. Banerjee; S. Boubaker; *Energy Econ.*, **2025**, *145*, 108185.
4. B. Su; W. Dong; T. Jiang; Z. W. Kundzewicz; *Innov.*, **2025**, *8*, 100888.
5. D. Jina; Y. Jinb; *Chem. Eng. Res. Des.*, **2023**, *198*, 69–80.

6. X. Y. Yuan; W. B. Zhang; A. Batol; X. Y. Liu; N. S. Zhou; J. Zhou; J. Feng; J. H. Liu; X. J. Ma; *Chem. Eng. J.*, **2025**, *519*, 165103.
7. Z. Jia; B. Wang; S. Song; Y. Fan; *Renew. Sustain. Energy Rev.*, **2014**, *31*, 91–100.
8. D. Suárez-Alfonso; A. Ruiz-García; M. Khayet; *Renew. Energy*, **2026**, *256*, 124344.
9. P. Wang; Y. Liu; Y. Li; T. Tang; Q. Ren; *Energy*, **2024**, *313*, 133729.
10. K. Touati; G. Nouri; C. N. Mulligan; *J. Environ. Chem. Eng.*, **2025**, *13*,118490.
11. J. W. Post; C. H. Goeting; J. Valk; S. Goinga; J. Veerman; H. V. M. Hamelers; P. J. F. M. Hack; *Desalin. Water Treat.*, **2010**, *16*, 182–193.
12. R. A. Tufa; S. Pawlowski; J. Veerman; K. Bouzek; E. Fontananova; G. di Profio; S. Velizarov; J. G. Crespo; K. Nijmeijer; E. Curcio; *Appl. Energy*, **2018**, *225*, 290–331.
13. R. E. Pattle; *Nature*, **1954**, *174*, 660.
14. K. Watanabe; Y. Akiba; H. Ishidaira; H. Shima; *Desalination*, **2025**, *605*, 118706.
15. N. Bonciocat; *Electrochimie şi aplicaţii*, Editura Dacia Europa Nova, Timişoara, România, **1996**, pp. 87.
16. K. J. Vetter; *Electrochemical Kinetics: Theoretical Aspects*, Academic Press, New York, **1967**, pp. 48.
17. O. A. Petrii; G. A. Tsirlina; *Electrode potentials*. In Encyclopedia of Electrochemistry, 1st ed.; E. Gileadi, M. Urbakh Eds.; Wiley-VCH, Weinheim, Germany, **2002**; Volume 1, pp. 9.
18. L. Oniciu; E. Constantinescu; *Electrochimie şi coroziune*, Editura Didactică şi Pedagogică, Bucureşti, România, **1982**.
19. D. Dobos; *Electrochemical Data*, Elsevier Scientific, Amsterdam, Olanda, **1975**.
20. Y. D. Raka; R. Bock; H. Karoliussen; Ø. Wilhelmsen; O. S. Burheim; *Membranes*, **2021**, *11*, 135.
21. https://www.britannica.com/science/seawater
22. C. Gui; B. Liao; X. Zhang; Y. Wang; G. Ding; H. Huang; T. Ren; P. Liu; X. Hu; L. Huang; *Chem. Eng. Sci.*, **2026**, *320*, 122605.
23. R. W. Baker; *Membrane Technology and Applications*, McGraw Hill, New York, USA, **2000**.
24. G. Wilczek-Vera; J. H. Vera; *Fluid Phase Equilib.*, **2005**, *236*, 96–110.
25. P. Ocon; M. D. Reboiras; *Bioelectrochem. Bioenerg.*, **1987**, *17*, 489-501.
26. R. Stepak; *Anal. Chim. Acta*, **1987**, *203*, 79-83.
27. G. Scatchard; W. H. Orttung; *J. Colloid Interface Sci.*, **1966**, *22*, 12-18.
28. S. B. B. Solberg; M. Hammer; Ø. Wilhelmsen; S. Burheim; *Fluid Phase Equilib.*, **2024**, *586*, 114173.
29. G. Tan; S. Lu; J. Fan; G. Li; X. Zhu; *Electrochim. Acta*, **2019**, *322*, 134724.
30. M. Essalhi; A. H. Avci; F. Lipnizki; N. Tavajohi; *Renew. Energy*, **2023**, *215*, 118984.
31. K. Touati; G. Nouri; C. N. Mulligan; *J. Environ. Chem. Eng.*, **2025**, *13*, 118490.
32. X. Zhou; W. – B. Zhang; J. – J. Li; X. Bao; X. – W. Han; M. M. Theint; X. – J. Ma; *Energy Convers. Manag.*, **2022**, *255*, 115315.

33. S. Loeb; F. Van Hessen; D. Shahaf; *J. Membr. Sci.*, **1976**, *1*, 249-269.
34. J. Pan; W. Xu; Y. Zhang; Y. Ke; J. Dong; W. Li; L. Wang; B. Wang; B. Meng; Q. Zhou; F. Xia; *Nano Energy*, **2024**, *132*, 110412.
35. S. Lin; Z. Wang; L. Wang; M. Elimelech; *Joule*, **2024**, *8*, 334–343.
36. M. Sharma; P. P. Das; A. Chakraborty; M. K. Purkait; *Sustain. Energy Technol. Assess.*, **2022**, *49*, 101687.
37. J. T. Arena; K. K. Reimund; J. R. McCutcheon; *Desalination*, **2021**, *498*, 114804.
38. M. Malankowska; Z. Su; K. Karlsen; M. F. Buhl; H. Guo; L. S. Pedersen; M. Pinelo; *Chem. Eng. J.*, **2024**, *297*, 120221.
39. D. Suárez-Alfonso; A. Ruiz-García; M. Khayet; *Renew. Energy*, **2026**, *256*, 124344.
40. M. Sharma; P. P. Das; A. Chakraborty; M. K. Purkait; *Sustain. Energy Technol. Assess.*, **2022**, *49*, 101687.
41. A. Altaee; A. Cipolina; *Renew. Energy*, **2019**, *141*, 139-147.
42. P. Długołecki; K. Nymeijer; S. Metz; M. Wessling; *J. Membr. Sci.*, **2008**, *319*, 214–222.
43. Z. Y. Guo; W. Z. Cui; Z. Y. Ji; K. Tumba; J. Wang; L. J. Fu; Z. X. Zhang; J. Liu; Y. Y. Zhao; Z. D. Zhang; J. S. Yuan; *Desalination*, **2023**, *566*, 116900.
44. J. Veerman; M. Saakes; S. J. Metz; G. J. Harmsen; *J. Membr. Sci.*, **2009**, *327*, 136–144.
45. R. A. Tufa; S. Pawlowski; J. Veerman; K. Bouzek; E. Fontananova; G. di Profio; S. Velizarov; J. G. Crespo; K. Nijmeijer; E. Curcio; *Appl. Energy*, **2018**, *225*, 290–331.
46. J. Janga; Y. Kanga; J. H. Hanb; K. Janga; C. M. Kima; I. S. Kima, *Desalination*, **2020**, *491*, 114540.
47. Z. Wang; L. Wang; M. Elimelech; *Engineering*, **2022**, *9*, 51–60.
48. A. Siria; P. Poncharal; A. L. Biance; R. Fulcrand; X. Blasé; S. T. Purcell; L. Bocquet; *Nature*, **2013**, *494*, 455–458.
49. J. Wang; C. S. Law; K. N. Vu; S. Gunenthiran; K. Nielsch; A. D. Abell; A. Santos; *Chem. Eng. J.*, **2025**, *515*, 163453.
50. L. Wang; Z. Wang; S. K. Patel; S. Lin; M. Elimelech; *ACS Nano*, **2021**, *15*, 4093–4107.
51. M. Macha; S. Marion; V. V. R. Nandigana; A. Radenovic; *Nat. Rev. Mater.*, **2019**, *4*, 588.
52. M. Tsutsui; K. Yokota; I. W. Leong; Y. He; T. Kawai; *Cell Rep. Phys. Sci.*, **2022**, *3*, 101065.
53. K. Yazda; K. Bleau; Y. Zhang; X. Capaldi; T. St-Denis; P. Grutter; W. W. Reisner; *Nano Lett.*, **2021**, *21*, 4152–4159.
54. D. Brogioli; R. Ziano; R. A. Rica; D. Salerno; F. Mantegazza; J*. Colloid Interface Sci.*, **2013**, *407*, 457–466.
55. G. R. Iglesias ; S. Ahualli ; M. M. Fernandez ; M. L. Jimenez ; A. V. Delgado *J. Power Sources*, **2016**, *318*, 283–290.
56. M. Marino; L. Misuri; M. L. Jiménez; S. Ahualli; O. Kozynchenko; S. Tennison; M. Bryjak; D. Brogioli; *J. Colloid Interface Sci.*, **2014**, 436,146–153.

57. B. E. Conway, *Electrochemical Supercapacitors*, Kluver Academic, New York, **1999**.
58. B. B. Sales; M. Saakes; J. W. Post; C. J. N. Buisman; P. M. Biesheuvel; H. V. M. Hamelers; *Environ. Sci. Technol.*, **2010**, *44*, 5661–5665.
59. D. Lee; J. Choi; U. Paik; T. Song; Y. G. Jung; S. Yang; *Chem. Eng. J.*, **2025**, *525*, 170452.
60. Z. Zou; L. Liu; S. Meng; X. Bian; *Energy Rep*., **2022**, *8*, 7325–7335.
61. K. Smolinska-Kempisty; A. Siekierka; M. Bryjak; *Desalination*, **2020**, *482*,114384.
62. H. Choi; D. Kim; D. G. Kim; Y. Kim; J. G. Park; M. G. Kim; Y. G. Jung; J. Yoo; J. Baek; S. Kang; B. Kim; J. H. Bang; D. Lee; B. G. Kim; S. Yang; *Desalination*, **2024**, *581*, 117591.
63. H. Zhu; W. Xu; G. Tan; E. Whiddon; Y. Wang; C. G. Arges; X. Zhu; *Electrochim. Acta*, **2019**, *294*, 240-248.
64. S. Sarp; Z. Li; J. Saththasivama; *Desalination*, **2016**, *389*, 2-14.
65. https://www.power-technology.com/projects/statkraft-osmotic/ (accesat 15.05.2026)
66. https://www.renewableinstitute.org/japans-first-osmotic-power-plant-what-it-means-for-clean-energy/ (accesat 15.05.2026)

STUDIA UBB CHEMIA, LXXI, 2, 2026 (p. 209-225)
(RECOMMENDED CITATION)
DOI:10.24193/subbchem.2026.2.11

COMPUTATIONAL AND WATER ELECTROLYSIS STUDY OF 5,10,15,20-TETRAKIS(3-HYDROXYPHENYL)-PORPHYRIN

Marina Alexandra TUDORAN[a], Bogdan-Ovidiu TARANU[a,*]

ABSTRACT. The free-base, symmetrically substituted 5,10,15,20-tetrakis(3-hydroxyphenyl)-porphyrin was the subject of a study combining computational and experimental analysis, with an emphasis on the molecule's water-splitting electrocatalytic characteristics. Ab initio and DFT methods were used to investigate the porphyrin's structural and electronic properties. The water-splitting experiments, performed in solutions with different pH values, were carried out with porphyrin-based electrodes that were modified using different strategies. The electrode manufactured by drop-casting a catalyst ink containing the porphyrin and carbon black on a graphite substrate displayed an overpotential value for the oxygen evolution reaction of 0.595 V *vs.* RHE and a Tafel slope of 0.337 V/dec in a neutral environment. Data acquired during the electrochemical experiments were used to perform statistical analysis. The correlation analysis indicated a significant association between pH and overpotential. The combined study improves the current scientific understanding of the porphyrin's properties and shows the effect of the electrode modification strategies on its water-splitting electrocatalytic activity.

Keywords: *quantum chemical calculations, electrocatalyst, aggregate, water-splitting, oxygen evolution reaction, correlation analysis.*

INTRODUCTION

High energy prices and environmental issues, such as air pollution, are pressing concerns that have led the scientific community to consider hydrogen as a clean energy alternative [1]. Out of several methods for

[a] *National Institute of Research and Development for Electrochemistry and Condensed Matter, Dr. Aurel Paunescu Podeanu Street No. 144, RO-300569, Timisoara, Romania*
* *Corresponding author: b.taranu84@gmail.com*

obtaining hydrogen, the most common ones are steam-methane reforming and electrochemical water-splitting (or water electrolysis) [2]. The latter, consisting of the splitting of the water molecule using electricity, is the method upon which green hydrogen production is primarily based [3].

During electrochemical water-splitting, O_2 is produced at the anode via the oxygen evolution half-cell reaction (OER), while H_2 is generated at the cathode through the hydrogen evolution half-cell reaction (HER). One of the main problems facing water electrolysis is the sluggish reaction kinetics of the specified reactions due to high overpotentials [4]. Many materials with electrocatalytic properties have been synthesized and tested in water electrolysis experiments in search of a solution to this issue [5]. The use of inexpensive and earth-abundant catalysts is important for transitioning from a small-scale H_2 production system to a large-scale one [6]. Platinum and IrO_2 are currently the benchmark electrocatalysts for evaluating the performance of other catalytic materials, but their scarcity and high cost prevent large-scale application. The organic tetrapyrrolic structures known as porphyrins are among the more accessible classes of compounds that have been found to possess water-splitting electrocatalytic properties. They exist naturally but can also be synthesized. They share a macrocyclic configuration and constitute extended aromatic systems with amphoteric properties that can be substituted with a wide variety of functional moieties [7]. The various ways in which the porphyrin macromolecule can be modified lead to structures with versatile properties and high applicative potential [8]. The current relevance of porphyrins as water-splitting electrocatalysts is outlined by studies reported in the past few years [9-11]. Porphyrins are also known for their stability in a wide pH range and ability to self-assemble through non-covalent interactions, resulting in aggregates with properties quite distinct from the ones possessed by the molecules comprising them [8].

The current paper presents an integrated investigation of the A_4 free-base 5,10,15,20-tetrakis(3-hydroxyphenyl)-porphyrin. The first part is relevant to the computational chemistry domain, while the second part focuses on the porphyrin's applicative potential in water electrolysis. The molecule was the focus of several studies reported in the literature [12-16], but these are not concerned with its electrochemical water-splitting activity. The results of the electrochemical experiments reveal the porphyrin's properties for water electrolysis in environments with different pH values, complement its current scientific understanding, and outline the effect of different electrode modification strategies on its OER and HER electrocatalytic activity.

RESULTS AND DISCUSSION

Part 1. Theoretical analysis

The optimized molecular structure of 5,10,15,20-tetrakis(3-hydroxyphenyl)-porphyrin is presented in Figure S1 (Supplementary Material file). Data regarding the structural parameters (bond lengths, bond angles, and dihedral angles) are presented in Table S1. These findings confirm the mild conjugative interaction observed between the porphyrin ring and the phenyl ring, which influence the electrochemical behavior of 5,10,15,20-tetrakis(3-hydroxyphenyl)-porphyrin [17,18]. Natural bond orbital analysis is based on the virtual and filled orbital spaces. It can be used to investigate bonding characteristics, charge transfer, and conjugative interaction phenomena in molecular systems [19-21]. The results obtained for the studied molecule are presented in Table S2.

Figure S2 depicts the molecular orbital diagrams for HOMO-1, HOMO, LUMO, and LUMO+1 calculated using the B3LYP functional method. Their corresponding energies are presented in Table S3. In case of 5,10,15,20-tetrakis(3-hydroxyphenyl)-porphyrin, the HOMO–1, HOMO, LUMO, and LUMO+1 electron density is primarily localized on the porphyrin macrocycle, indicating that the frontier molecular orbitals are largely π-conjugated over the core structure. Such delocalization is consistent with the redox behavior of porphyrins, in which a higher degree of conjugation facilitates electron transfer with limited structural reorganization upon oxidation or reduction [18]. Additional data regarding global reactivity descriptors are provided in Table S3.

The analysis of charge localization patterns was conducted using the electrostatic potential map for the molecule in the gas phase (Figure S3). The uneven charge distribution observed for the 5,10,15,20-tetrakis(3-hydroxyphenyl)-porphyrin is important in determining nonlinear optical (NLO) properties, as it shows the extent to which electrons are able to diffuse within the molecule [19]. The NLO properties were investigated, and the results are provided in Tables S4 and S5. Literature reports that a high value of the first hyperpolarizability, as observed for 5,10,15,20-tetrakis(3-hydroxyphenyl)-porphyrin, may indicate electron cloud delocalization within a conjugated framework, involving charge transfer from electron-donor to electron-acceptor groups [22].

Part 2. Water-splitting experiments

Study of the electrodes manufactured using the first modification strategy. The anodic and cathodic polarization curves recorded on the electrodes obtained with the first modification strategy described in the Experimental Section and tested in the acidic medium are shown in Figures S4 and S5 of the Supplementary Material file. Regarding the OER (Figure S4), the linear sweep voltammograms (LSVs) recorded on the modified electrodes and on an unmodified GC sample (GC_0) reveal that GC_0 was more electrocatalytically active. The only exception was the $GC_{P1\text{-}PhCN\text{-}1}$ electrode, in the sense that its activity was more similar to that of GC_0 (Figure S4a). Concerning the HER (Figure S5), all the porphyrin-based electrodes exhibited a lower electrocatalytic activity compared to GC_0. Furthermore, the increase in the number of drop-casted porphyrin layers did not improve the water-splitting properties of the modified samples. Figure S10 displays the heat maps of the calculated OER and HER overpotentials at current densities of 1 and -1 mA/cm², respectively, for the electrodes studied in the acidic medium.

Better results were obtained in the neutral medium, where the OER activity of some modified electrodes was higher than that of GC_0. Figure 1 shows the anodic polarization curves recorded on the electrodes manufactured using the first strategy detailed in the Experimental Section. The highest OER activity was exhibited by $GC_{P1\text{-}PhCN\text{-}1}$ (Figure 1a).

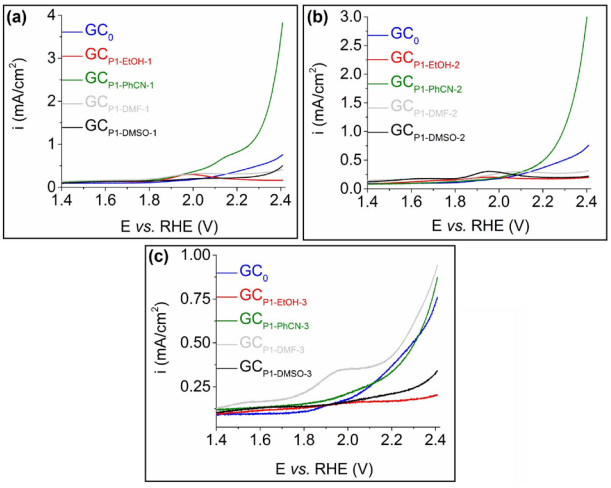

Figure 1. Anodic polarization curves recorded on GC_0 and on (a) $GC_{P1\text{-}EtOH\text{-}1}$, $GC_{P1\text{-}PhCN\text{-}1}$, $GC_{P1\text{-}DMF\text{-}1}$ and $GC_{P1\text{-}DMSO\text{-}1}$; (b) $GC_{P1\text{-}EtOH\text{-}2}$, $GC_{P1\text{-}PhCN\text{-}2}$, $GC_{P1\text{-}DMF\text{-}2}$ and $GC_{P1\text{-}DMSO\text{-}2}$ and (c) $GC_{P1\text{-}EtOH\text{-}3}$, $GC_{P1\text{-}PhCN\text{-}3}$, $GC_{P1\text{-}DMF\text{-}3}$ and $GC_{P1\text{-}DMSO\text{-}3}$. Electrolyte solution: 0.1 M KCl. v = 5 mV/s.

Regarding the HER catalytic activity of the electrodes immersed in the same medium (Figure S6), it was lower than that of GC_0, with the exception of $GC_{P1\text{-}PhCN\text{-}1}$. As shown in Figure S6a, the specified electrode exhibited similar activity to GC_0.

Figure S11 displays the heat maps of the calculated OER and HER overpotentials at current densities of 1 and -1 mA/cm², respectively, for the electrodes studied in the neutral electrolyte solution.

Statistical analysis. The relationship between the overpotential and the experimental factors was further investigated using correlation analysis. In the case of OER (Table S6), a moderate positive correlation was observed between overpotential (η_{OER}) and the pH of the electrolyte solution (r = 0.628, p < 0.05, r^2 = 0.394). No significant correlation was observed between η_{OER} and solvent polarity. The findings indicate that increases in pH are associated with higher overpotential, while solvent polarity exerts no measurable influence on the same parameter, given the selected experimental conditions. In the case of HER (Table S7), correlation analysis revealed a moderate negative association between overpotential (η_{HER}) and pH (r = -0.620, p < 0.05, r^2 = 0.384). A moderate correlation was also identified between η_{HER} and solvent polarity, but in the positive direction (r = 0.602, p < 0.05, r^2 = 0.484). These findings imply that pH and solvent polarity exert opposing, yet significant influences: higher pH is associated with lower overpotential, while increased solvent polarity is associated with higher overpotential. The results are consistent with those reported in the literature on multi-step proton-electron transfer reactions, which demonstrate a clear dependence of the overall reaction rate on the pH value. Furthermore, research has shown that changes in pH affect the electrode|electrolyte interface, as well as the kinetics of electrochemical reactions. From a thermodynamic perspective, in specific electrochemical reactions, modifying the pH level can induce a shift in the electrode's thermodynamic equilibrium potential [23,24].

Study of the electrodes manufactured using the second modification strategy. The results obtained during the experiments performed on the porphyrin-based electrodes modified with the second strategy presented in the Experimental Section are shown in Figure S7 and Figure 2a.

The heat maps of the η_{OER} values calculated at the current densities of 5 and 10 mA/cm^2, as well as the η_{HER} values determined at the current densities of -5 and -10 mA/cm^2, for the electrodes studied in the acidic and neutral electrolyte solutions are presented in Figure S12 and Figure S13, respectively.

Data acquired in the acidic medium (Figures S7a and S7b) indicate that the OER and HER electrocatalytic activity of the porphyrin-containing electrodes was lower than that of the GC_{CB} electrode, manufactured using a GC pellet and a catalyst ink containing 10 mg Carbon Black, 50 µL Nafion solution, and 450 µL double-distilled water. The same situation is observed in the case of the HER results obtained for the neutral medium (Figure S7c). However, the OER data acquired for the same electrolyte solution (Figure 2a) show that O_2 evolved on the $GC_{P1\text{-}CB}$ sample at lower potential values than on the other studied electrodes. To improve the OER activity, the substrate was replaced with spectroscopic graphite [25,26]. Graphite pellets were modified with the second strategy presented in the Experimental Section, and Figure 3b shows the LSVs recorded on the obtained electrodes and on an unmodified graphite pellet (Gr_0). At i = 10 mA/cm^2, the current density value at which η_{OER} is usually determined in water electrolysis studies [27], a η_{OER} value of 0.595 V was found for the $Gr_{P1\text{-}CB}$ electrode. Because of its higher electrocatalytic activity, GrP1-CB was selected for further electrochemical evaluation.

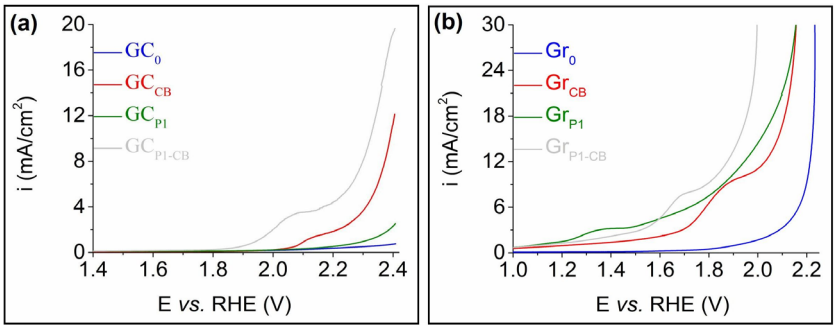

Figure 2. Anodic polarization curves recorded on (a) GC_0, GC_{CB}, GC_{P1} and $GC_{P1\text{-}CB}$ and (b) Gr_0, Gr_{CB}, Gr_{P1} and $Gr_{P1\text{-}CB}$. Electrolyte solution: 0.1 M KCl. *v* = 5 mV/s.

Figure 3 shows the results obtained on $Gr_{P1\text{-}CB}$ by performing additional experiments aimed at revealing more of the electrode's electrochemical properties.

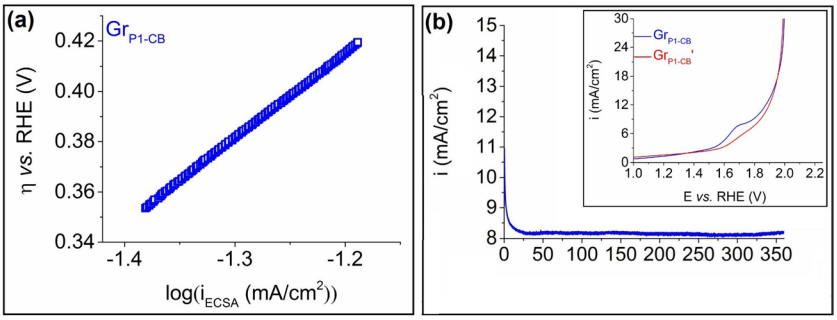

Figure 3. (a) The Tafel plot for $Gr_{P1\text{-}CB}$ in 0.1 M KCl solution. The current density (i_{ECSA}) values from the plot are ECSA-normalized. (b) Amperogram obtained on $Gr_{P1\text{-}CB}$ in 0.1 M KCl solution and inset with the LSVs obtained on the same electrode before ($Gr_{P1\text{-}CB}$) and after ($Gr_{P1\text{-}CB}$') the electrochemical stability test (0.1 M KCl solution, v = 5 mV/s).

The OER kinetics at the electrode:electrolyte solution interface were studied using the Tafel plot shown in Figure 3a. The current density values were obtained by considering the electrode's electrochemically active surface area (ECSA). The value of this parameter, of 27.67 cm^2, was estimated using the method described in the Supplementary Material file, Figure S8, and Equations (S8) and (S9). The Tafel slope of 0.337 V/dec (R^2 = 0.9998) was determined using the Tafel equation, specified as Equation (S10).

Lastly, the $Gr_{P1\text{-}CB}$ electrode was tested in terms of its electrochemical stability over time. The chronoamperogram in Figure 3b was recorded at a constant potential value of 0.595 V *vs.* RHE. The current density reached a value of ~ 8.1 mA/cm^2 after 30 min and remained almost constant throughout the rest of the experiment. The polarization curves obtained before and after the test can be seen in the inset of Figure 3b. The η_{OER} value at i = 10 mA cm^{-2} increased by 35 mV, but no change in the OER overpotential was found in the higher current density region. Raman analysis was performed to verify if the experiment led to structural modifications, and the recorded Raman spectra are shown in Figure S9. The signals visible on the spectrum obtained before the electrochemical stability test are also visible on the one recorded after the test. This indicates the absence of any significant modifications in the chemical structure of the materials at the surface of the modified electrode.

Observations about the water-splitting properties of $Gr_{P1\text{-}CB}$. Out of the carbon-based electrodes modified with the free-base porphyrin, $Gr_{P1\text{-}CB}$ exhibits the highest OER activity. It catalyzes this electrochemical water-splitting half-cell reaction in a neutral electrolyte solution, and its electrocatalytic

properties are probably the result of its surface structural characteristics, charge transport effects, and enhanced π-resonance [28]. Several observations regarding this electrode and the electrocatalyst used to obtain it are appropriate.

According to reported studies, the catalytic center of free-base porphyrins is the N_4 site located in the center of their macrocycle [29,30]. Since the investigated molecule is also a free-base porphyrin, it is probable that its N_4 site serves as the catalytic center. It has also been reported that the value of the ECSA parameter is directly proportional to the number of active sites involved in electrochemical processes [31]. The ECSA value estimated for $Gr_{P1\text{-}CB}$ (27.67 cm^2) is significantly higher than its geometric surface (0.28 cm^2), indicating a relatively high number of catalytically active sites. Charge transfer is also an important factor in electrocatalysis, and it unfolds between neighboring porphyrin molecules through non-covalent π-π interactions. However, when the electrode is immersed in an aqueous electrolyte solution, hydrogen bonds may also become involved. Intermolecular H-bonds can form between the functional moieties of adjacent porphyrin molecules through H_2O molecules [29]. The porphyrin's hydroxyl groups have the potential to form such bonds. Furthermore, charge transfer also occurs between the porphyrins and the carbon substrate. The nitrogen atoms of the N_4 site are more electronegative than the carbon atoms of the electrode's substrate, and this leads to the electropositive doping of that substrate [29]. The electronic effects of the substituents that porphyrins are functionalized with influence their water-splitting electrocatalytic activity as well [30]. The OH^- groups located at the porphyrin's *meta*-positions are electron-withdrawing, which means they decrease the macrocycle's electron density [30]. Lastly, catalytic activity is affected by the pH of the electrolyte solution. Out of the three types of environments used in water-splitting studies – acidic, alkaline, and neutral – investigations performed in neutral electrolyte solutions are more challenging, primarily because of the need to improve the sluggish kinetics of water dissociation in neutral pH [32]. In the case of $Gr_{P1\text{-}CB}$, despite the features that improve its catalytic activity - such as a large number of active sites - the neutral pH of the electrolyte solution, and the electron-withdrawing effect of the OH^- functional moieties are probably responsible for the relatively low OER activity.

The OER electrocatalytic activity of $Gr_{P1\text{-}CB}$ was compared with that of various electrodes reported in the scientific literature, especially with porphyrin-modified electrodes. The electrolyte solutions used to investigate them cover a wide pH range: acidic, neutral, near-neutral, and alkaline. The comparison was performed using the values shown in Table 1. Regarding the OER overpotential, of the 46 values reported in the literature, 12 are higher than

the value found for the $Gr_{P1\text{-}CB}$ electrode, and 8 are smaller but comparable (values > 500 V *vs.* RHE). Regarding the Tafel slope, of the 31 values reported in other studies, 7 are > 337 V/dec, and one is smaller but comparable (0.313 V/dec). These results show that $Gr_{P1\text{-}CB}$ has a place among the electrodes documented in the scientific literature.

Table 1. The OER activity of $Gr_{P1\text{-}CB}$, and of other electrodes reported in the scientific literature. The η_{OER} values are read at i = 10 mA/cm^2.

Electrode or electrocatalyst	Environment	η_{OER} (V *vs.* RHE)	OER Tafel slope (V/dec)	Ref.
Fe-porphyrin polymer@carbon paper	1 M KOH	0.506	0.196	[9]
Co-porphyrin polymer@carbon paper	1 M KOH	0.435	0.069	
Ni-porphyrin polymer@carbon paper	1 M KOH	0.424	0.096	
$G_{P1\text{-}DMF\text{-}3}$	1 M KOH	0.780	0.343	[28]
$G_{P2\text{-}BN\text{-}1}$	1 M KOH	0.780	0.350	
$G_{P3\text{-}DCM\text{-}1}$	1 M KOH	0.850	0.340	
ZnTAPP-NA@GC	1 M KOH	-	0.313	[33]
CoTAPP-NA@GC	1 M KOH	0.416	0.068	
CoTcPP/ZrP@GCRDE	0.1 M KOH	0.467	0.076	[34]
$(Co–P)_{0.5}(Fe–P)_{0.5}$/CNT @GCRDE	0.1 M KOH	0.420	-	[35]
3,4,5-OMe-CoP/CNT@GC	1 M KOH	0.482	0.081	[36]
2,4,6-OMe-CoP/CNT@GC	1 M KOH	0.500	0.090	
CoTPP-SD@CFP	1 M KOH	0.670	-	[37]
CoCOP@CFP	1 M KOH	0.350	0.151	
PIZA-1-400@FTO	1 M KOH	0.430	0.052	[38]
CeO_2/PIZA-1-400@FTO	1 M KOH	0.370	0.048	
Co-MPPy-1@RDE	1 M NaOH	0.420	0.058	[39]
rGO/$(Ni^{2+}–THPP/Co^{2+}–THPP)_8$@RDE	1 M KOH	0.330	0.050	[40]
CoP-2ph-CMP-800@GC	1 M KOH	0.370	0.086	[41]
CoP-3ph-CMP-800@GC	1 M KOH	0.410	-	
CoP-4ph-CMP-800@GC	1 M KOH	0.430	-	
$(CoP)_n$-MWCNTs@GC	1 M KOH	0.290 [a]	0.055	[42]
CoP-TIPS/MWCNTs@GC	1 M KOH	0.440 [a]	-	
$G_{CoP\text{-}DMSO\text{-}1}$	0.5 M H_2SO_4	0.510	0.270	[43]
$G_{CoP\text{-}CH3CN\text{-}1}$	0.1 M KCl	0.630 [b]	-	
$G_{ZnP\text{-}PhCN\text{-}1}$	0.1 M KCl	0.620 [b]	-	
$G_{ZnP\text{-}PhCN\text{-}1}$	1 M KOH	0.560	-	
Porphvlar-based ink @carbon paper	0.1 M PBS	0.670 [c]	0.485	[44]
$G_{CB\text{-}PZn}$	0.1 M KCl	0.780	0.390	[45]
$G_{P1\text{-}BN}$	1 M KOH	0.730	-	[46]

Electrode or electrocatalyst	Environment	η_{OER} (V *vs.* RHE)	OER Tafel slope (V/dec)	Ref.
$G_{P1\text{-}DMF}$	0.5 M H_2SO_4	0.340	-	
$G_{P2\text{-}DMF}$	0.5 M H_2SO_4	0.470	-	
$V_{0.1}Co_{2.9}O_4$	1 M KOH	0.453	-	[47]
C_{60}-SWCNTs	0.5 M H_2SO_4	0.430	-	[48]
TDA-Trz-POP	0.5 M H_2SO_4	0.410	-	[49]
P-CC	1 M KOH	0.450	-	[50]
NH_4@COF-SO_3	1 M KOH	0.543	0.267	[51]
Pristine-COF	1 M KOH	0.652	0.235	[52]
$Fe_{0.5}Ni_{0.5}O_x$	0.1 M KOH	0.584	0.072	[53]
$(FeCoNiCuZn)Al_2O_4$	1 M KOH	0.430	-	[54]
Co-Sn-Mo-Sb oxides	1 M KOH	0.440	-	[55]
CoSAs-MoS2/TiN NRs	1 M PBS	0.508	0.172	[56]
TiN NRs	1 M PBS	-	0.376	
CoSAs-MoS_2 NSs	1 M PBS	-	0.348	
MoS_2/TiN NRs	1 M PBS	-	0.246	
1/MWCNT@GC	0.1 M PBS	0.790	-	[57]
1/MWCNT/Py-Py@GC	0.1 M PBS	0.650	-	
Cr-doped WSe_2/graphene heterojunction	1 M PBS	0.520	0.113	[58]
Co_9S_8/Ni_3S_2/NF	1 M PBS	0.495	0.226	[59]
CoO domains on $CoSe_2$ nanobelts/Ti mesh	0.5 M PBS	0.510	0.198	[60]
$Gr_{P1\text{-}CB}$	0.1 M KCl	0.595	0.337	This work

[a] at 1 mA/cm^2; [b] at 5 mA/cm^2; [c] at 2.5 mA cm^{-2}

CONCLUSIONS

A metal-free symmetrically substituted A_4 porphyrin was investigated in terms of its water-splitting electrocatalytic properties. Computational methods were used to explore the molecule's structure and behavior. Overall, the results suggest that the molecular conformation favors electron-withdrawing behavior. Porphyrin-based electrodes were manufactured using different modification strategies, and their OER and HER catalytic activities were studied in neutral and acidic electrolyte solutions. The experimental data reveal that the most active electrode is the one obtained by drop-casting the catalyst ink containing the porphyrin and carbon black on the surface of a graphite support. This sample exhibits an OER overpotential of 0.595 V *vs.* RHE (at i = 10 mA/cm^2) and a Tafel slope of 0.337 V/dec, in 0.1 M KCl electrolyte solution. While the electrode is relatively stable in the specified

environment, the high overpotential and Tafel slope values indicate that the simple substrate modification strategy should be replaced with more sophisticated ones. Future studies will consider the use of Pulsed Laser Deposition and MAPLE-based protocols for electrode manufacturing.

The relationship between the OER and HER overpotential, on the one hand, and electrolyte pH and solvent polarity, on the other, was investigated as a first step towards improving the design of future experiments aimed at further revealing the water-splitting electrocatalytic properties of the studied porphyrin.

COMPUTATIONAL AND EXPERIMENTAL SECTION

Computational details. Quantum chemical calculations for 5,10,15,20-tetrakis(3-hydroxyphenyl)-porphyrin were performed with Gaussian 03 [61] and visualized with GaussView 6.0 [62]. Geometry optimization in the gas phase was achieved without symmetry constraints by using the Hartree–Fock (HF) method, and the stationary points were identified as minima by performing a vibrational analysis at the same level of theory. The optimized Hartree-Fock (HF) geometry was used to determine the bond lengths and bond angles, in addition to performing natural bond orbital (NBO) analysis. Single-point calculations were conducted on fully optimized geometries with two different hybrid DFT functionals. B3LYP, which combines the Becke three-parameter exchange functional (B3) with the Lee-Yang-Parr (LYP) generalized gradient correlation functional [63,64], and B3PW91, which combines the Becke three-parameter exchange functional (B3) with the Perdew-Wang 91 (PW91) gradient-corrected correlation functional [65,66]. The two approaches yielded analogous results.

Materials and reagents. The 5,10,15,20-tetrakis(3-hydroxyphenyl)-porphyrin was synthesized using a literature-based method [14]. Briefly, propionic anhydride and *m*-hydroxybenzaldehyde were mixed and dissolved in propionic acid under vigorous stirring and heating to reflux. A solution of pyrrole (four times exceeding the molar amount of aldehyde) in propionic acid was slowly added within 45 min. The vigorous stirring and refluxing continued for two more hours and were followed by cooling the reaction mixture to 23 ± 2 °C. Ethanol (95 %) was added, and the precipitation stage was completed in the presence of hexane. A dark purple powder resulted after filtering and repeated hot water washing. The drying and purification of the powder were the final stages of the porphyrin synthesis. The characterization of the compound by ^{1}H-NMR, UV-Vis, TLC, HPLC, MS, FT-IR, and fluorescence spectroscopy was previously reported by Fagadar-Cosma *et al.* [12,14,15]. The chemical structure of the porphyrin derivative is presented in Scheme 1.

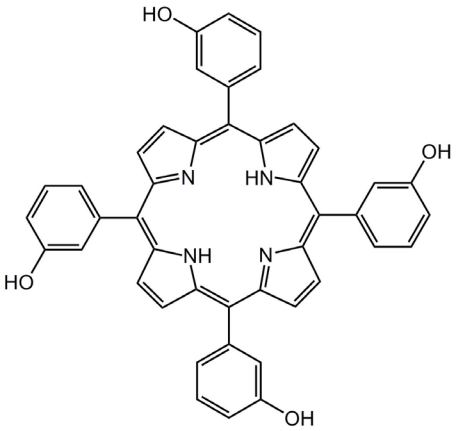

Scheme 1. Chemical structure of 5,10,15,20-tetrakis(3-hydroxyphenyl)-porphyrin.

Benzonitrile (PhCN), dimethylsulfoxide (DMSO), potassium chloride, and sulfuric acid (98 %) were purchased from Merck (Darmstadt, Germany). Ethanol of 99.5 % purity (EtOH) was procured from Honeywell (Charlotte, NC, USA), N,N-dimethylformamide (DMF), and Nafion® 117 solution were acquired from Sigma Aldrich (Saint Louis, MO, USA). The materials used in the study are glassy carbon (GC) pellets purchased from Andreescu Labor & Soft SRL (Bucharest, Romania), SW.114 spectroscopic graphite rods produced at “Kablo Bratislava” (National Corporation “Electrocarbon Topolcany” Factory, Bratislava, Slovakia) and carbon black - Vulcan XC 72 (Fuell Cell Store, Bryan, TX, USA). All aqueous solutions were prepared with double-distilled water from a water distiller (Fistreem, Cambridge, UK). All reagents were used as received without further purification.

Electrode modification strategies. The first protocol for manufacturing porphyrin-based electrodes involved modifying the GC pellets by applying porphyrin solutions of 5 mM concentration to their surface. These solutions were obtained by dissolving the compound in different organic solvents during a 30-minute ultrasonication treatment. The order in which the polarity of the utilized solvents increases is the following: EtOH < PhCN < DMF < DMSO [67]. The procedure for obtaining the modified electrodes consisted in drop-casting a 10 µL volume of porphyrin solution on the surface of the electrically conductive carbon substrate, followed by solvent evaporation at 40 °C. This strategy can be repeated for additional porphyrin layers. Samples with up to three layers were investigated in terms of their OER and HER electrocatalytic activity. The labels used to identify the electrodes are shown in Table 2.

Table 2. Porphyrin-modified electrodes manufactured with the first strategy.

Electrode label	Solvent	Porphyrin layers
$GC_{P1\text{-}EtOH\text{-}1}$	EtOH	1
$GC_{P1\text{-}EtOH\text{-}2}$		2
$GC_{P1\text{-}EtOH\text{-}3}$		3
$GC_{P1\text{-}PhCN\text{-}1}$	PhCN	1
$GC_{P1\text{-}PhCN\text{-}2}$		2
$GC_{P1\text{-}PhCN\text{-}3}$		3
$GC_{P1\text{-}DMF\text{-}1}$	DMF	1
$GC_{P1\text{-}DMF\text{-}2}$		2
$GC_{P1\text{-}DMF\text{-}3}$		3
$GC_{P1\text{-}DMSO\text{-}1}$	DMSO	1
$GC_{P1\text{-}DMSO\text{-}2}$		2
$GC_{P1\text{-}DMSO\text{-}3}$		3

The second protocol for obtaining porphyrin-based electrodes is based on a previously published procedure and involves the deposition of porphyrin-containing catalyst inks on the carbon substrate [68]. Table 3 presents the labeling of the modified electrodes, as well as the compositions of the inks used to manufacture them. These inks were ultrasonicated for 30 min before being drop-casted onto the surface of the pellets (a volume of 10 µL was utilized for each pellet). The electrodes resulted after a drying stage at 40 °C.

Table 3. Porphyrin-modified electrodes manufactured with the second strategy.

Electrode label	Porphyrin amount (mg)	Carbon black (mg)	Nafion solution (µL)	Double-distilled water (µL)
GC_{P1}	10	-	50	450
$GC_{P1\text{-}CB}$	5	5	50	450

Electrochemical investigation. A standard electrolysis setup comprised of a glass cell together with three electrodes connected to a potentiostat (Voltalab PGZ 402 from Radiometer Analytical, Lyon, France) was used throughout the electrochemical study. Each GC-based electrode served as working electrode after insertion into a polyamide support that limited its geometric surface (S_{geom}) to 0.28 cm^2. A Pt plate (S_{geom} = 0.8 cm^2) and the Ag/AgCl(sat. KCl) electrode were utilized as auxiliary and reference electrodes. Since the porphyrin is soluble in alkaline media, the electrolyte

solutions for the experiments were acidic (0.1 M H_2SO_4) and neutral (0.1 M KCl). For the HER investigations, high purity N_2 was used to deaerate the specified solutions. All OER and HER polarization curves were IR-corrected and recorded at the scan rate (*v*) of 5 mV/s [44].

Apart from the mentioned exceptions, the specified current density (i) values refer to the geometric current density. The E values are represented *vs.* RHE (the Reversible Hydrogen Electrode) using Equation (1) [69]. The O_2 and H_2 evolution overpotentials were determined with Equations (2) and (3) [70].

$$E_{RHE} = E_{Ag/AgCl(sat.\ KCl)} + 0.059 \times pH + E°_{Ag/AgCl(sat.\ KCl)} \quad (1)$$

$$\eta_{OER} = E_{RHE} - 1.23 \quad (2)$$

$$\eta_{HER} = |E_{RHE}| - 0 \quad (3)$$

Where E_{RHE} is the converted potential *vs.* RHE (V); $E_{Ag/AgCl(sat.\ KCl)}$ is the measured potential *vs.* the Ag/AgCl(sat. KCl) reference electrode (V); $E°_{Ag/AgCl(sat.\ KCl)}$ = 0.197 V; η_{OER} and η_{HER} are the O_2 and H_2 evolution overpotentials (V).

Statistical analysis. Some of the data obtained during the electrochemical experiments were analyzed using statistical methods. A quantitative evaluation of the overpotential's distribution was carried out using heat maps. Correlation analysis was conducted to assess the relationship between the overpotential and some experimental factors. All statistical calculations were performed using Minitab 22 [71].

Physical-chemical characterization. Raman spectra were acquired with a MultiView-2000 system (Nanonics Imaging Ltd., Jerusalem, Israel) equipped with a Shamrock 500i spectrograph (Andor, Essex, UK).

SUPPLEMENTARY MATERIAL

The Supplementary Material file can be downloaded at:
https://doi.org/10.5281/zenodo.20571954

ACKNOWLEDGMENTS

The authors would like to thank Dr. Eugenia Fagadar-Cosma for providing the porphyrin and Dr. Florina Stefania Rus from INCEMC Timisoara (Romania) for recording the Raman spectra.

REFERENCES

1. A. Dev; V. Kumar; A. S. L. V. Tummala; V. K. Verma; R. Gajjar; A. K. Chaudhary; G. Sarvaiya; B. Parmar; *Discov. Appl. Sci.*, **2025**, *7*, 1336.
2. I. Ali; G. Imanova; O. M. L. Alharbi; A. M. Hameed; M. N. Siddiqui; *J. Umm Al-Qura Univ. Appl. Sci.*, **2023**, *10*, 567-578.
3. H. A. Dhahri; M. Hussain; M. A. A. Ghani; A. Inayat; A. H. Al-Muhtaseb; L. Al-Haj; F. Jamil; *Renew. Sust. Energ. Rev.*, **2026**, *229*, 116617.
4. K.-H. Lin; K.-H. Lee; A. Mukundan; R. Karmakar; E. Rahmawati; K. N. Abdullah; C.-C. Wang; H.-C. Wang; *Energy Rep.*, **2025**, *14*, 5112-5127.
5. Y. Wu; P. Chen; *Green Chem.*, **2026**, *28*, 3043-3072.
6. J. Guo; Y. Haghshenas; Y. Jiao; P. Kumar; B. I. Yakobson; A. Roy; Y. Jiao; K. Regenauer-Lieb; D. Nguyen; Z. Xia; *Adv. Mater.*, **2024**, *36*, 2407102.
7. E. Fagadar-Cosma; D. Vlascici; G. Fagadar-Cosma; *Porfirinele de la Sinteză la Aplicații*; Eurostampa, Timisoara, Romania, **2008**, pp. 10-94.
8. M. Birdeanu; E. Fagadar-Cosma; The self-assembly of porphyrin derivatives into 2D and 3D architectures, in *Quantum nanosystems: Structure, properties and interactions*, M.V. Putz, Ed.; Apple Academic Press, Toronto, Canada, **2014**, Chapter 5, pp. 173-206.
9. N. Ocuane; Y. Ge; C. Sandocal-Pauker; D. Villagran; *Dalton T.*, **2024**, *53*, 2306-2317.
10. I. A. Lane; R. Kumar; *Inorg. Chim. Acta,* **2025**, *576*, 122453.
11. N. Wang; Y. Wang; X. Liu; J. Liu; C. Guo; X. Deng; J. Liang; M. Cao; N. Wang; *Int. J. Hydrogen Energ.*, **2025**, *177*, 151412.
12. E. Fagadar-Cosma; L. Cseh; V. Badea; G. Fagadar-Cosma; D. Vlascici; *Comb. Chem. High T. Scr.*, **2007**, *10*, 466-472.
13. D. Vlascici; E. F. Cosma; E. M. Pica; V. Cosma; O. Bizerea; G. Mihailescu; L. Olenic; *Sensors*, **2008**, *8*, 4995-5004.
14. C. Cretu; C. Bucovicean; I. Armeanu; A. M. Lacrama; E. Fagadar-Cosma; *Rev. Chim.-Bucharest*, **2008**, *59*, 979-981.
15. E. Fagadar-Cosma; M. C. Mirica; I. Balcu; C. Bucovicean; C. Cretu; I. Armeanu; G. Fagadar-Cosma; *Molecules*, **2009**, *14*, 1370-1388.
16. L. Salageanu; D. Muntean; M. Licker; A. Lascu; D. Anghel; E. Fagadar-Cosma; *Farmacia*, **2020**, *68*, 288-298.
17. J. Wang; *J. Phys.: Conf. Ser.*, **2025**, *3008*, 012058.
18. T. T. Tran; M. R. Gan; Y. P. Tzeng; H. Shaw; T. K. Hoang; M. Y. Kuo; Y. O. Su; *J. Electroanal. Chem.*, **2018**, *815*, 40-46.
19. M. Hasnain; S. Urrehman; A. Yousuf; M. A. Ali; T. Fatima; S. Bibi; F. Q. Bai; *Chem. Pap.*, **2025**, *79*, 6809-6824.
20. C. B. Yildiz; Z. O. Sagir; T. Kilic; A. Azizoglu; *Studia UBB Chemia*, **2014**, *59*, 17-32.
21. S. Dhifaoui; A. Azaid; M. Bourass; L. Ben Haj Hassen; H. Nasri; M. Bouachrine; *Phys. Chem. Res.*, **2021**, *9*, 701-713.

22. M. Karabacak; E. Yilan; *Spectrochim. Acta A Mol. Biomol. Spectrosc.*, **2012**, *87*, 273-285.
23. M. T. M. Koper; *Chem. Sci.*, **2013**, *4*, 2710–2723.
24. S. Liu; Z. Wang; S. Qiu; F. Deng; *Carbon Lett.*, **2024**, *34*, 1269-1286.
25. B. O. Taranu; M. G. Ivanovici; P. Svera; P. Vlazan; P. Sfirloaga; M. Poienar; *J. Alloy. Compd.*, **2020**, *848*, 156595.
26. M. Poienar; P. Svera; B.-O. Taranu; C. Ianasi; P. Sfirloaga; G. Buse; P. Veber; P. Vlazan; *Crystals*, **2022**, *12*, 1803.
27. P. W. Menezes; C. Panda; S. Loos; F. Bunschei-Bruns; C. Walter; M. Schwarze; X. Deng; H. Dau; M. Driess; *Energy Environ. Sci.*, **2018**, *11*, 1287-1298.
28. B. O. Taranu; E. Fagadar-Cosma; *Processes*, **2022**, *10*, 611.
29. S. Seo; K. Lee; M. Min; Y. Cho; M. Kim; H. Lee; *Nanoscale*, **2017**, *9*, 3969-3979.
30. W. Zhang; W. Lai; R. Cao; *Chem. Rev.*, **2017**, *117*, 3717-3797.
31. Z. Zhou; W. Q. Zaman; W. Sun; L. M. Cao; M. Tariq; J. Yang; *Chem. Commun.*, **2018**, *54*, 4959-4962.
32. Y. Xu; C. Wang; Y. Huang; J. Fu; *Nano Energ.*, **2021**, *80*, 105545.
33. G. Cai; L. Zeng; L. He; S. Sun; Y. Tong; J. Zhang; *Chem-Asian J.*, **2020**, *15*, 1963-1969.
34. I. B. Alvarez; Y. Wu, J. Sanchez; Y. Ge; M. V. Ramos-Garces; T. Chu; T. F. Jaramillo; J. L. Colon; D. Villagran; *Sustain. Energy Fuels*, **2021**, *5*, 430-437.
35. H. Lei; Q. Zhang; Y. Wang; Y. Gao; Y. Wang; Z. Liang; W. Zhang; R. Cao; *Dalton T.*, **2021**, *50*, 5120-5123.
36. H. Lv; H. Guo; K. Guo; H. Lei; W. Zhang; H. Zheng; Z. Liang; R. Cao; *Chinese Chem. Lett.*, **2021**, *32*, 2841-2845.
37. A. Wang; L. Cheng; W. Zhao; X. Shen; W. Zhu; *J. Colloid Interf. Sci.*, **2020**, *579*, 598-606.
38. D.-J. Li; Z.-G. Gu; W. Zhang; Y. Kang; J. Zhang; *J. Mater. Chem. A*, **2017**, *5*, 20126-20130.
39. S. Bhunia; K. Bhunia; B. C. Patra; S. K. Das; D. Pradhan; A. Bhaumik; A. Pradhan; S. Bhattacharya, *ACS Appl. Mater. Inter.*, **2019**, *11*, 1520-1528.
40. J. Sun; H. Yin; P. Liu; Y. Wang; X. Yao; Z. Tang; H. Zhao; *Chem. Sci.*, **2016**, *7*, 5640-5646.
41. H. Jia; Y. Yao; Y. Gao; D. Lu; P. Du; *Chem. Commun.*, **2016**, *52*, 13483-13486.
42. H. Jia; Z. Sun; D. Jiang; P. Du; *Chem. Mater.*, **2015**, *27*, 4586-4593.
43. B.-O. Taranu, E. Fagadar-Cosma, *Nanomaterials*, **2022**, *12*, 3788.
44. Y. Ge, Z. Lyu, M. Marcos-Hernandez, D. Villagran, *Chem. Sci.,* **2022**, *13* 8597.
45. B.-O. Taranu, F. S. Rus, E. Fagadar-Cosma, *Coatings*, **2024**, *14*, 1048.
46. I. Fratilescu; A. Lascu; B. O. Taranu; C. Epuran; M. Birdeanu; A.-M. Macsim; E. Tanasa; E. Vasile; E. Fagadar-Cosma; *Nanomaterials*, **2022**, *12*, 1930.
47. C. Placke-Yan; G. Bendt; S. Salamon; J. Landers; H. Wende; U. Hagemann; S. Schulz; *Mater. Adv.*, **2024**, *5*, 3482–3489.

48. R. Gao; Q. Dai; F. Du; D. Yan; L. Dai; *J. Am. Chem. Soc.*, **2019**, *141*, 11658-11666.
49. A. Ghosh; M. Mondal; R. N. Manna; A. Bhaumik; *J. Colloid Interface Sci.*, **2024**, *658*, 415-424.
50. Z. Liu; Z. Zhao; Y. Wang; S. Dou; D. Yan; D. Liu; Z. Xia; S. Wang; *Adv. Mater.*, **2017**, *29*, 1606207.
51. Z. Gao; L. L. Gong; X. Q. He; X. M. Su; L. H. Xiao; F. Luo; *Inorg. Chem.*, **2020**, *59*, 4995–5003.
52. Y. Zheng; H. Song; S. Chen; X. Yu; J. Zhu; J. Xu; K. A. I. Zhang; C. Zhang; T. Liu; *Small*, **2020**, *16*, 2004342.
53. J. Jiang; C. Zhang; L. Ai; *Electrochim. Acta*, **2016**, *208*, 17–24.
54. R. R. Katzbaer; F. M. S. Vieira; I. Dabo; Z. Mao; R. E. Schaak; *J. Am. Chem. Soc.*, **2023**, *145*, 6753–6761.
55. A. Pineiro-Garcia; X. Wu; E. J. Canto-Aguilar; A. Kuzhikandathil; M. Rafei; E. Gracia-Espino; *ACS Appl. Mater. Interfaces*, **2024**, *16*, 70429–70441.
56. T. L. L. Doan; D. C. Nguyen; S. Prabhakaran; D. H. Kim; D. T. Tran; N. H. Kim; J. H. Lee; *Adv. Funct. Mater.*, **2021**, *31*, 2100233.
57. I. K. Attatsi; W. Zhu; X. Liang; *New J. Chem.*, **2020**, *44*, 4340-4345.
58. C. H. Chiang; Y. C. Yang; J. W. Lin; Y. C. Lin; P. T. Chen; C. L. Dong; H. M. Lin; K. M. Chan; Y. T. Kao; Suenaga, K.; P.-W. Chiu; C.-W. Chen; *ACS Nano*, **2022**, *16*, 18274–18283.
59. Y. Yang; H. Yao; Z. Yu; S.M. Islam; H. He; M. Yuan; Y. Yue; K. Xu; W. Hao; G. Sun; H. Li; S. Ma; P. Zapol; M. G. Kanatzidis; *J. Am. Chem. Soc.*, **2019**, *141*, 10417–10430.
60. K. Li; J. Zhang; R. Wu; Y. Yu; B. Zhang; *Adv. Sci.*, **2015**, *3*, 1500426.
61. M. J. Frisch; G. W. Trucks; H. B. Schlegel; G. E. Scuseria; M. A. Robb et al.; Gaussian 03, Revision C.02, **2004**, Gaussian, Inc., Wallingford CT.
62. R. Dennington; T. A. Keith; J. M. Millam; GaussView, Version 6.1, **2016**, Semichem Inc., Shawnee Mission, KS.
63. A. D. Becke; *J. Chem. Phys.*, **1993**, *98*, 5648-5652.
64. C. Lee; W. Yang; R. G. Parr; *Phys. Rev. B.*, **1988**, *37*, 785-789.
65. A. D. Becke; *Phys. Rev. A.*, **1993**, *48*, 3098–3100.
66. J. P. Perdew; Y. Wang; *Phys. Rev. B.*, **1992**, *45*, 13244–13249.
67. L. R. Snyder; J. J. Kirkland; J. L. Glajch; Practical HPLC Method Development; John Wiley & Sons, New Jersey, USA, **1997**; pp. 721-728.
68. J. Chang; Q. Lv; G. Li; J. Ge; C. Liu; W. Xing; *Appl. Catal. B-Environmental*, **2017**, *204*, 486-496.
69. B. C. M. Martindale; E. Reisner; *Adv. Energy Mater.*, **2016**, *6*, 1502095.
70. K. Zh. Bekmyrza; K. A. Kuterbekov; A. M. Kabyshev; M. M. Kubenova; A. A. Baratova; N. Aidarbekov; M. D. Chaka; N. E. Benti; *Sci. Rep.*, **2025**, *15*, 28418.
71. Minitab, LLC, **2022**. Minitab (Version 22.x). [Software]. State College, PA, USA: Minitab, LLC.

STUDIA UBB CHEMIA, LXXI, 2, 2026 (p. 227-242)
(RECOMMENDED CITATION)
DOI:10.24193/subbchem.2026.2.12

VALIDATED UAE-GC-MS-SIM ANALYSIS OF PCBs IN SOILS: FROM METHOD PERFORMANCE TO HOMOLOGUE AND CONGENER PATTERNS

Diana Klara GAIA[a,b], Irina CIOTLĂUȘ[b,*], Mihaela Cecilia VLASSA[b], Iulia AJTAI[a], Călin BACIU[a]

ABSTRACT. Polychlorinated biphenyls (PCBs) are persistent organic pollutants that accumulate in soils, making their reliable determination in this complex matrix analytically challenging. This study presents the validation of a method based on ultrasound-assisted extraction (UAE) coupled with gas chromatography–mass spectrometry operating in selected ion monitoring mode (GC-MS-SIM) for the determination of 19 PCB congeners in soil samples. Method performance was evaluated in terms of selectivity, linearity, limits of detection and quantification, precision, and accuracy, demonstrating robust analytical performance for trace-level PCB determination. The obtained LODs ranged from 0.05 to 0.78 ng•g^{-1}. The validated method was applied to 92 soil samples collected from the Copșa Mică area (Romania) at two depth intervals (0–5 cm and 5–20 cm). Comparable ΣPCB concentrations were observed between the two soil layers, indicating a relatively uniform vertical distribution. Congener-specific analysis revealed the predominance of PCB 118 and PCB 187, while homologue distribution patterns were dominated by penta- and hepta-CBs. These results confirm the suitability of the validated method for PCB determination in soils and provide insight into congener- and homologue-level compositional patterns in real environmental samples.

Keywords: *polychlorinated biphenyls, soil, ultrasound-assisted extraction, GC-MS-SIM, method validation, homologue distribution, congener profile*

[a] *Babeș-Bolyai University, Faculty of Environmental Sciences and Engineering, 30 Fântânele str., RO-400294, Cluj-Napoca, Romania.*
[b] *Babeș-Bolyai University, Raluca Ripan Institute for Research in Chemistry, 30 Fântânele str., RO-400294, Cluj-Napoca, Romania*
* *Corresponding author: irina.ciotlaus@ubbcluj.ro*

INTRODUCTION

Polychlorinated biphenyls (PCBs) are a class of persistent organic pollutants characterised by high chemical stability, a hydrophobic nature, and resistance to degradation. These characteristics have contributed to their widespread accumulation in the environment, even after most countries banned their production and use [1,2]. Although their industrial applications were progressively phased out since the 1970s and 1980s, PCBs continue to be detectable in environmental matrices due to their long-lasting persistence and their ability to redistribute through atmospheric and pedological processes [1]. Consequently, soils serve as important environmental reservoirs and potential secondary sources of PCB contamination [3], where these chemicals may occur across a wide range of concentrations and degrees of chlorination. The complexity of the soil matrices, along with the presence of PCB congeners with varying physicochemical characteristics and the typically low concentrations at which these compounds occur, presents considerable analytical challenges. That's why efficient extraction procedures combined with advanced and sensitive instrumental techniques that ensure reliable quantification in intricate solid matrices are necessary.

The precise identification of PCBs in soils depends on efficient extraction and purification techniques, as well as rigorously validated experimental methods that guarantee adequate sensitivity, linearity, precision, and selectivity over wide concentration ranges. Gas chromatography coupled with mass spectrometry in selected ion monitoring mode (GC–MS–SIM) represents one of the most widely applied techniques for PCB determination in environmental samples due to its high selectivity and sensitivity [4-6]. Nevertheless, thorough method validation is crucial, especially when addressing several congeners with varying degrees of chlorination and inconsistent instrumental responses. In addition, ultrasound-assisted extraction (UAE) has been increasingly employed for the extraction of organic contaminants from solid matrices, offering advantages such as reduced solvent consumption, shorter times, and good extraction efficiency [7,8].

Although numerous studies have investigated the occurrence and distribution of PCBs in soils, most research has focused primarily on concentration levels or spatial contamination patterns [9,10]. However, relatively few studies combine a thoroughly validated UAE–GC–MS–SIM analytical approach for the simultaneous determination of multiple PCB congeners with a detailed evaluation of PCB compositional patterns at both the congener and homologue levels in real soil samples. In addition, information regarding PCB compositional profiles in soils from Copșa Mică area remains limited. Such an integrated approach is important because the distribution of individual

congeners and homologue groups can provide additional information regarding contamination characteristics, environmental behaviour, and potential transformation processes of PCBs. The Copșa Mică area (Romania) represents a historically industrialised region affected by long-term metallurgical activities, making it a relevant site for investigating the occurrence and distribution of persistent organic contaminants in soils.

In this context the aim of this study was to validate and apply an ultrasound-assisted extraction combined with gas chromatography-mass spectrometry operating in selected ion monitoring mode (UAE–GC–MS–SIM) method for the simultaneous determination of 19 PCB congeners in complex soil matrices. The validated method was subsequently applied to soil samples collected from the Copsa Mica area, specifically from two depth intervals (0-5 cm and 5-20 cm). This application aimed to evaluate PCB concentrations and assess their compositional patterns based on congener and homologue distributions in accordance with the degree of chlorination. The selected congeners include indicator PCBs and compounds representative of several homologue groups (di-deca PCBs). This selection facilitates the characterisation of PCB profiles in soils while ensuring a focused analytical approach that is suitable for routine environmental analysis.

RESULTS AND DISCUSSION

Validation of GC-MS-SIM method parameters

The analytical method for quantifying polychlorinated biphenyls (PCBs) in soil samples was validated in accordance with international guidelines for persistent organic pollutant analysis (US EPA Method 8082A, US EPA Method 3550C, and US EPA Method 3630C) and involved a specific PCB standard mixture. The parameters evaluated included detection limits (LOD), quantification limits (LOQ), linearity, precision, selectivity and recovery.

Our study utilised selected ion monitoring (SIM) mode, using one target ion and two or three qualifier ions for confirmation alongside the retention times relative to calibration standards, thereby ensuring the *selectivity* of the method. These ions were identified using mass spectrometry analysis, and the validation of PCBs relied on retention times, qualifier ions, and target ions based on qualifier/target ion ratio. For increased reliability, this ratio must be within ±20% [11] in accordance with established GC-MS identification criteria (Table 1).

Table 1. Selected ion monitoring method parameters for PCB congeners

Analyte	t_R (min)	TI	QI^1	QI^2	QI^1/TI (%)	QI^2/TI (%)
PCB 8	16.383	222	152	186	7.3	8.6
PCB18	18.645	186	256	221	68.5	35.5
PCB 28	20.907	256	186	150	63.9	23.6
PCB 44	22.773	292	220	255	91.8	27.5
PCB 52	24.243	220	292	257	91.9	38.8
PCB 66	26.011	292	220	150	54	15.8
PCB 101	26.816	326	254	184	69.4	26.5
PCB 77	28.844	292	220	110	46.2	17.9
PCB 118	29.617	326	254	184	38	16.3
PCB 153	30.285	360	290	145	65	28.1
PCB 126	31.155	326	254	184	41.1	18.3
PCB 138	31.829	360	290	145	70.6	32.5
PCB 170	32.074	326	394	254	45.3	42.6
PCB 128	33.307	360	290	145, 218	90	35.5, 35.5
PCB 180	34.048	396	324	162	73.2	29.2
PCB 187	35.552	394	324	162	80.2	38.9
PCB 195	37.089	430	358	179	74.6	45.5
PCB 206	38.666	464	392	207	61.2	40.9
PCB 209	39.868	498	428	207	43.7	40
Standards						
IS	36.827	486	207	163	41	37.5
PCB 155	26.243	360	290	145	51	23.5
PCB 198	35.165	430	358	179	75.9	38.7

t^R – retention time; TI – target ion; QI^1, QI^2 – qualifier ions; IS – internal standard

The method *selectivity* is illustrated in Figure 1, which compares the chromatogram of the PCB standard mixture with the chromatograms of real soil samples. The chromatographic separation demonstrates good selectivity, with the target PCB congeners being efficiently separated and with no significant interferences observed at the retention times of the target congeners. A slight asymmetry was observed for the chromatographic signal at RT 20.91 min, which may be attributed to minor matrix-related co-elution effects without significantly affecting the identification and quantification of the target PCB congener.

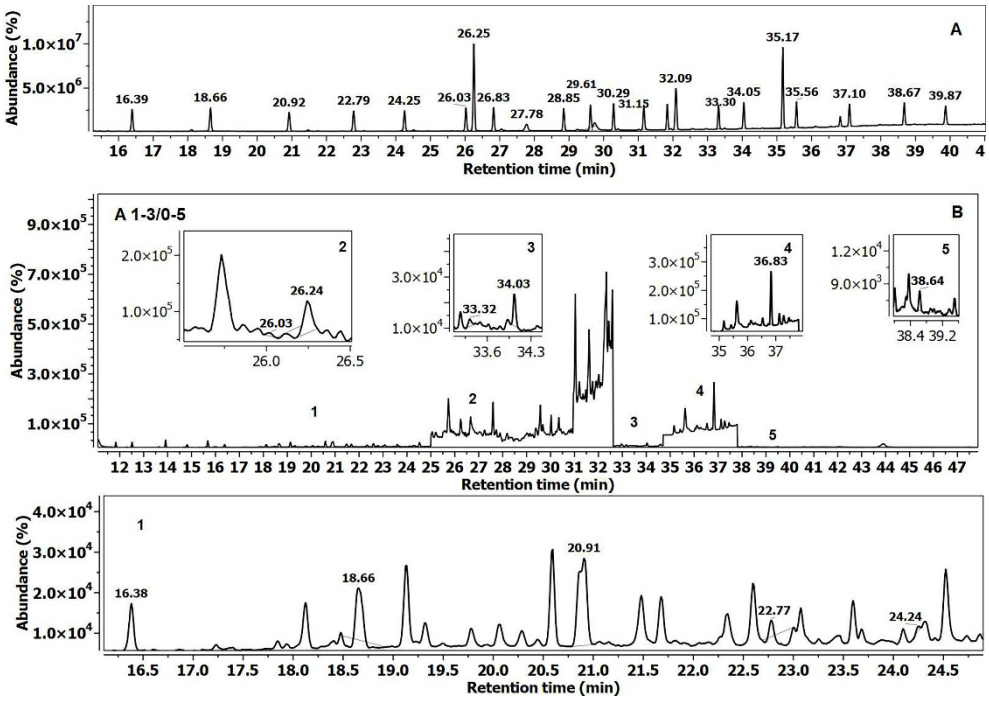

Figure 1. Selectivity assessment for PCB congeners by GC-MS (SIM mode): **(A)** chromatogram of PCB standard mixture; **(B)** soil sample extract with enlarged chromatographic zones (1-5), including a detailed view of zone 1

Given the significant differences in instrumental response and the extensive variation of PCB concentrations documented in Romanian soils [12,13], the *linearity* of the method was assessed by constructing calibration curves across two separate concentration ranges (0.125–12.5 and 12.5–1000 ng·mL^{-1}) (Table 2) to guarantee precise quantification at both low and high concentration levels. Calibration curves were constructed using the mean peak area ratio ($A_{analyte}/A_{IS}$) of multiple injections at each calibration level. A PCB stock solution mixture was utilised to create each calibration curve at six concentration levels. The correlation coefficients (R^2) exceeded 0.99 for all investigated congeners across both calibration ranges, indicating good linear relationships throughout the operating range.

Table 2. Calibration curves and linearity parameters (R^2) for PCB congeners between two concentration ranges

Analyte	Low Range		High Range	
	Equation of calibration	**R^2**	**Equation of calibration**	**R^2**
PCB 8	y = 0.0171x + 0.0054	0.9964	y = 0.0136x + 0.0929	0.9983
PCB18	y = 0.0195x + 0.0017	0.9965	y = 0.0152x + 0.0532	0.9993
PCB 28	y = 0.0198x + 0.0028	0.9936	y = 0.0165x + 0.0635	0.9994
PCB 44	y = 0.0197x + 0.0026	0.9973	y = 0.0158x + 0.1047	0.9993
PCB 52	y = 0.0189x + 0.002	0.9986	y = 0.0144x + 0.1304	0.9994
PCB 66	y = 0.0171x + 0.0019	0.9988	y = 0.0137x + 0.1267	0.999
PCB 101	y = 0.0144x + 0.0023	0.9951	y = 0.0117x + 0.0057	0.9991
PCB 77	y = 0.0098x + 0.0009	0.9989	y = 0.0089x + 0.0631	0.9994
PCB 118	y = 0.0129x + 0.0016	0.9979	y = 0.0112x + 0.0106	0.9995
PCB 153	y = 0.0109x + 0.0017	0.9978	y = 0.0087x + 0.0866	0.998
PCB 126	y = 0.0128x + 0.0027	0.9975	y = 0.0111x + 0.0394	0.9985
PCB 138	y = 0.0079x + 0.0008	0.9977	y = 0.0065x + 0.0346	0.9994
PCB 170	y = 0.0158x - 0.0006	0.9989	y = 0.0137x + 0.0548	0.9997
PCB 128	y = 0.0105x + 0.0013	0.9991	y = 0.0089x + 0.0078	0.9994
PCB 180	y = 0.0106x + 0.0051	0.9985	y = 0.0083x + 0.086	0.9995
PCB 187	y = 0.0025x - 0.0028	0.9995	y = 0.0018x + 0.0113	0.9996
PCB 195	y = 0.0064x + 0.0004	0.9956	y = 0.0054x + 0.0297	0.9995
PCB 206	y = 0.0064x - 0.0003	1	y = 0.0055x + 0.0276	0.9994
PCB 209	y = 0.0071x + 0.0001	0.9987	y = 0.0057x + 0.0463	0.9993
Standards	**Range 0.0125-0.2 µg·mL^{-1}**			
PCB 155	y = 12.088x + 0.0436		R^2 = 0.994	
PCB 198	y = 4.7607x + 0.0211		R^2 = 0.9942	

R^2 - regression coefficient of calibration curve

Method *sensitivity* was expressed by the limits of detection (*LOD*) and quantification *(LOQ*), using the formulas LOD = 3.3 × σ/S and LOQ = 10 × σ/S (where σ is the standard error of the intercept from linear regression and *S* represents the slope of the calibration curve), calculated in accordance with IUPAC guidelines [14]. These limits correspond to signal-to-noise ratios of approximately 3 and 10, respectively, demonstrating the high detection capacity of the PCB congeners. Therefore, the limit of detection and quantification were calculated only for the lower calibration range (0.125–12.5 ng·mL^{-1}), as they reflect the method sensitivity at low concentrations. The obtained LOD and LOQ values are summarised in Table 3 and indicate a high sensitivity of the analytical method for PCB determination. The high-range calibration curve was used for quantification of higher levels.

Precision was evaluated in terms of repeatability and expressed as relative standard deviation (*RSD, %),* calculated using back-calculated concentrations obtained through repeated measurements. For some analytes, RSD was evaluated across the full low range (0.125–12.5 ng·mL^{-1}), whereas for others it was evaluated over reduced ranges (0.25–12.5 ng·mL^{-1}, 0.5–12.5 ng·mL^{-1}, and 2.5–12.5 ng·mL^{-1}). When the lowest levels (0.125 and/or 0.25, 0.5 ng·mL^{-1}) yielded negative back-calculated concentrations (below the quantifiable range), these values were excluded from RSD calculations (Table 3).

Table 3. Analytical performance for the determination of PCBs in soil samples using GC-MS-SIM

Analyte	Range 0.125–12.5 ng·ml^{-1}			Range 25–1000 ng·ml^{-1}
	LOD	LOQ	RSD_{mean} (min-max) (%)	RSD_{mean} (min-max) (%)
PCB 8[a]	0.46	1.40	5.64 (2.46-9.90)	4.84 (0.68-15.19)
PCB18[a]	0.46	1.39	15.14 (0.42-73.05)	4.54 (0.8-13.47)
PCB 28[a]	0.62	1.87	5.31 (3.72-6.5)	8.04 (1.78-23.10)
PCB 44[a]	0.40	1.21	5.03 (3.32-6.83)	3.09 (0.08-5.92)
PCB 52[a]	0.29	0.87	5.80 (1.46-9.83)	3.67 (0.49-9.16)
PCB 66[a]	0.27	0.82	6.17 (2.43-12.74)	5.63 (0.18-13.89)
PCB 101[a]	0.54	1.62	11.61 (2.82-27.34)	5.44 (0.59-12.40)
PCB 77[a]	0.25	0.76	5.46(1.56-13.28)	3.86 (1.03-7.59)
PCB 118[a]	0.35	1.06	5.65 (1.01-14.80)	4.54 (1.07-8.69)
PCB 153[a]	0.36	1.08	5.30 (2.16-10.78)	4.95 (0.28-15.06)
PCB 126[a]	0.38	1.17	8.50 (1.35-21.36)	8.69 (0.09-39.35)
PCB 138[a]	0.37	1.11	10.92 (2.40-19.23)	5.83 (2.03-12.27)
PCB 170[a]	0.25	0.76	6.47 (2.81-8.58)	4.08 (0.29-8.12)
PCB 128[a]	0.24	0.71	4.61 (1.44-9.05)	5.13 (0.41-12.87)
PCB 180[b]	0.35	1.07	7.89 (3.87-12.35)	5.01 (0.08-11.66)
PCB 187[d]	0.57	1.73	12.53 (4.13-18.75)	3.87 (1.08-7.50)
PCB 195[c]	0.78	2.36	16.37 (0.22-51.89)	4.24 (1.64-7.50)
PCB 206[a]	0.05	0.15	16.94 (1.53-55.11)	4.56 (0.36-10.49)
PCB 209[b]	0.34	1.03	7.06 (2.28-14.83)	5.14 (0.51-12.78)

Standards	Range 0.0125–0.2 µg·ml^{-1}	
	LOD	LOQ
PCB 155	0.02	0.02
PCB 198	0.05	0.05

12.5 ng·mL^{-1} was used as an overlap point in both calibration ranges; for precision, it was included only in the low range; mean - average of multiple determinations

a–d indicate the low-range concentration intervals used for RSD calculation (ng·mL^{-1}), depending on the analyte quantifiability (**a**: 0.125–12.5 ng·mL^{-1}; **b**: 0.25–12.5 ng·mL^{-1}; **c**: 0.5–12.5 ng·mL^{-1}; **d**: 2.5–12.5 ng·mL^{-1})

The method's *accuracy* was assessed by determining the recovery rates for procedural recovery standards (PCB 155 and 198) and PCB congeners in the certified reference material (CRM) and is summarised in Table 4. The recovery control compounds were added prior to extraction to assess procedural performance; they were not included as target analytes and were not used for quantification. The recovery rates ranged from 78.7% to 129.1%, and all measured PCB concentrations fell within the recommended acceptance windows of the CRM, confirming the accuracy and reliability of the method used.

Table 4. Accuracy of the GC-MS(SIM) method based on recoveries of PCB congeners determined in a CRM

Analyte	Certified value ($ng \cdot g^{-1}$)	Suggested Acceptance Windows ($ng \cdot g^{-1}$)	Recovery (%)
PCB 28	58.8 ± 4.9	17.6 to 100.0	97.6
PCB 52	107.0 ± 8.2	32.1 to 181.9	78.7
PCB 101	58.3 ± 4.4	17.5 to 99.1	127.4
PCB 118	40.1 ± 3.3	12.0 to 68.2	83.5
PCB 138	38.5 ± 1.8	11.6 to 65.5	107.1
PCB 153	52.9 ± 2.7	15.9 to 89.9	115.8
PCB 180	59.6 ± 3.2	17.9 to 101.3	103.1
Recovery standards			
PCB 155	80	na	103.9
PCB198	80	na	129.1

na - not assessed
"Suggested acceptance windows" – represent the acceptance ranges provided in the certificate of the CRM and were used as reference criteria for method performance evaluation.

Application of the validated method to soil samples

To assess the level of PCB contamination in real soil samples collected from Copșa Mică, we investigated the ∑PCB concentrations in two soil depth layers (0–5 cm and 5–20 cm). The selected congeners include indicator PCBs and compounds representative of several homologue groups commonly monitored in environmental studies. This selection facilitates the characterisation of PCB profiles in soils while ensuring a targeted analytical approach that is suitable for routine environmental analysis. The total PCB concentrations (∑PCB) obtained for the analysed samples are presented in Table 5. The results indicate comparable concentration levels between the two investigated depth intervals with a mean value slightly higher in the 5–20 cm intervals, compared to the 0-5 cm layer. Both layers exhibited moderate variability.

Table 5. Concentrations of total PCB (∑PCB) in soil samples from Copșa Mică area, from two depth intervals (ng·g^{-1} dw)

Depth (cm)	∑PCB (ng·g^{-1} dw)		
	min-max	mean ± SD	median
0-5	2.98-35.64	15.36 ± 8.31	14.39
5-20	2.08-46.15	16.94 ± 10.01	15.49

Congener distribution

The distribution of $\sum_{17}$PCB concentrations across the two investigated soil layers is presented in Figure 2 as a boxplot, providing a graphical representation of the variability of concentrations of individual values. Slightly higher median and mean values were observed in the 5-20 cm layer compared to the surface horizon (0–5 cm). However, the Mann-Whitney U test indicated no statistically significant differences between the two depth intervals (U = 994, p = 0.62). These results suggest a relatively uniform vertical distribution of total PCBs within the investigated soil profile.

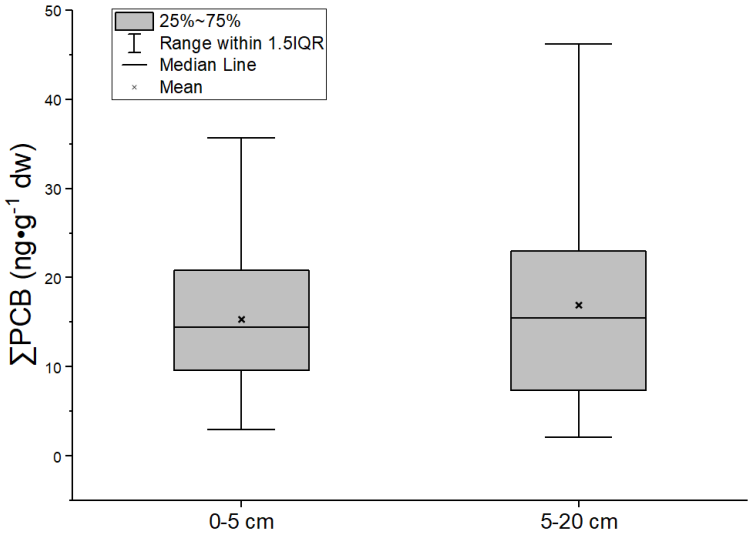

Figure 2. Distribution of $\sum_{17}$PCB concentrations (ng·g^{-1}) in soils from Copșa Mică at two depth intervals (0–5 cm and 5–20 cm). Boxes represent the interquartile range (25–75%); whiskers indicate values within 1.5 IQR; the horizontal line denotes the median; and the symbol (x) represents the mean

To determine the individual contributions of congeners to the PCB concentration shown in Figure 2, Table 6 provides the mean values (± SD) for each congener identified in two analysed depth intervals.

The distribution of the PCB congeners revealed that PCB 118 and PCB 187 were the most prevalent in both soil depth intervals, exhibiting the highest concentrations among the analysed congeners. In the 0-5 cm layer, PCB 118 accounted for 30% of ∑PCB (216 out of 706 $ng \cdot g^{-1}$ dw) and displayed similar mean concentrations across both soil depths, while PCB 187 represented 20% of the total concentration. In contrast, in the 5-20 cm layer, PCB 187 became the dominant congener, accounting for 28% of ∑PCB (215 out of 780 $ng \cdot g^{-1}$ dw), whereas PCB 118 represented 24% of total concentration. The predominance of PCB 118 observed in the analysed samples is consistent with previous studies on PCB distribution in soils. PCB 118, a dioxin-like congener known for its toxicological properties, is commonly detected in environmental matrices due to its persistence and occurrence in technical mixtures utilised in electrical devices (capacitors, transformers) [15,16]. Higher chlorinated congeners, such as PCB 187, exhibit strong hydrophobicity and high affinity for soil organic matter, leading to their accumulation and persistence in soils [16,17].

Table 6. Distribution of PCB congeners in soil samples at two depth intervals ($ng \cdot g^{-1}$ dw)

Congener	0-5 cm (mean ± SD)	5-20 cm (mean ± SD)
PCB 8	0.9 ± 0.65	0.84 ± 0.42
PCB18	1.68 ± 1.27	1.80 ± 1.92
PCB 28	2.57 ± 1.94	3.09 ± 3.66
PCB 44	0.4 ± 0.47	0.37 ± 0.29
PCB 52	0.16 ± 0.49	0.16 ± 0.17
PCB 66	0.25 ± 0.23	0.31 ± 0.30
PCB 101	0.47 ± 0.88	0.56 ± 0.79
PCB 77	0.14 ± 0.14	0.14 ± 0.09
PCB 118	6.97 ± 3.81	6.87 ± 3.27
PCB 153	0.58 ± 0.89	0.49 ± 0.51
PCB 126	nd	nd
PCB 138	nd	nd
PCB 170	0.03 ± 0	0.16 ± 0.14
PCB 128	0.17 ± 0.22	0.17 ± 0.35
PCB 180	1.24 ± 1.04	1.07 ± 0.64
PCB 187	5.99 ± 4.60	7.96 ± 6.09
PCB 195	2.78 ± 0	1.93 ± 1.77
PCB 206	0.13 ± 0.07	0.51 ± 0.50
PCB 209	0.07 ± 0	0.11 ± 0.06

nd - not detected

The congeners PCB 28 and PCB 180 also presented relatively elevated mean concentrations compared to most other congeners, while PCB 195 showed higher values in the surface layer. The remaining congeners were characterised by lower mean concentrations (< 1 $ng \cdot g^{-1}$ dw) and a moderate distribution across the two investigated soil depth intervals.

Neither PCB 126 nor PCB 138 was detected in the analysed soil samples. Overall, the PCB congener profile is similar across the two soil layers with specific differences for certain compounds, without indicating a major change in the contamination structure based on depth.

Homologue distribution

To better understand the compositional characteristics of PCB contamination in the investigated soils, the analysed congeners were grouped according to their degree of chlorination into homologue groups: PCB 8 (di-CB); PCB 18 and PCB 28 (tri-CBs); PCB 44, PCB 52, PCB 66, and PCB 77 (tetra-CBs); PCB 101 and PCB 118 (penta-CBs); PCB 128 and PCB 153 (hexa-CBs); PCB 170, PCB 180 and PCB 187 (hepta-CBs); PCB 195 (octa-CB); PCB 206 (nona-CB); and PCB 209 (deca-CB). The relative contribution of each homologue group to the total PCB concentration is illustrated in Figure 3. The results showed that *penta-CBs* were the dominant group in the surface layer, accounting for the largest proportion of ∑PCB. In contrast, in the 5-20 cm layer, the contribution of hepta-chlorinated biphenyls increased, while tri-CBs also represented an important fraction of the total PCB burden in both soil depth intervals.

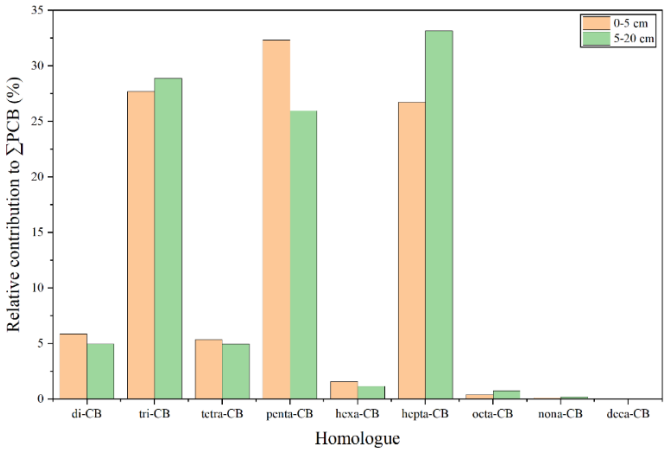

Figure 3. Homologue distribution of PCBs in soils from Copsa Mica at two depth intervals (0-5 cm and 5-20 cm), expressed as the relative contribution (%) to ∑PCB.

These results contrast with previous studies where penta-CBs were recorded among dominant homologues in soils from Midway Atoll (North Pacific Ocean) [18], as well as in pine needle samples and soil samples from an industrial area in Ulsan, South Korea [19]. Similar homologue patterns, dominated by penta- and hepta-CBs, have been reported in other regions as well [20,21].

The remaining homologue groups occurred in a comparatively lower proportion in both investigated soil intervals.

CONCLUSIONS

A robust analytical method based on ultrasound-assisted extraction coupled with gas chromatography–mass spectrometry operating in selected ion monitoring mode (UAE–GC–MS–SIM) was successfully validated for the determination of 19 PCB congeners in soil samples. The validation results demonstrated satisfactory selectivity, linearity over the investigated calibration ranges, low limits of detection and quantification, as well as good precision and accuracy, confirming the suitability of the method for trace-level PCB determination in complex soil matrices. The validated procedure was subsequently applied to 92 soil samples collected from the Copșa Mică area (Romania), from two depth layers (0–5 cm and 5–20 cm), enabling the evaluation of both concentration levels and compositional patterns of PCBs in real soils. The obtained results showed comparable ΣPCB concentrations between the two soil layers, and statistical analysis using the Mann–Whitney U test indicated no significant differences between the investigated depth intervals, suggesting a relatively uniform vertical distribution within the analysed soil profile. At the congener level, PCB 118 and PCB 187 were identified as the dominant compounds in both soil layers, while the remaining congeners generally occurred at lower concentrations. Evaluation of the homologue distribution revealed the predominance of penta- and hepta-chlorinated biphenyls, highlighting characteristic compositional patterns of PCBs in the studied soils. Overall, the validated UAE–GC–MS–SIM approach proved to be a reliable analytical tool for PCB determination in soils and for supporting detailed compositional assessment based on congener and homologue distributions in real environmental samples. By combining method validation with the compositional evaluation of PCB congeners and homologues in real soil samples, the present study provides a reliable analytical framework for the characterisation of PCB occurrence and distribution in soil matrices.

EXPERIMENTAL SECTION

The study area and sample collection

Copșa Mică is located along a lowland corridor of the Târnava Mare River in northern Sibiu County, Transylvania, Romania. Historically, this town was recognised as one of Europe's most polluted cities [22], primarily due to its persistent industrial emissions. The pollutants originated from two major industrial facilities in the area: Carbosin, which produced carbon black from 1936 to 1993, and Sometra, which specialised in non-ferrous metallurgy.

Soil samples were obtained from two depth levels (0-5 cm and 5-20 cm) across 46 locations, yielding a total of 92 samples. Figure 4 illustrates the study area around Copșa Mică industrial platform; samples were collected from locations at different distances from the former Sometra and Carbosin industrial sites, which were historically the primary sources of pollution in the region. Prior to extraction, the samples were homogenised, air-dried, ground and sieved (≈ 1-2 mm) and subsequently stored in a dark and dry environment.

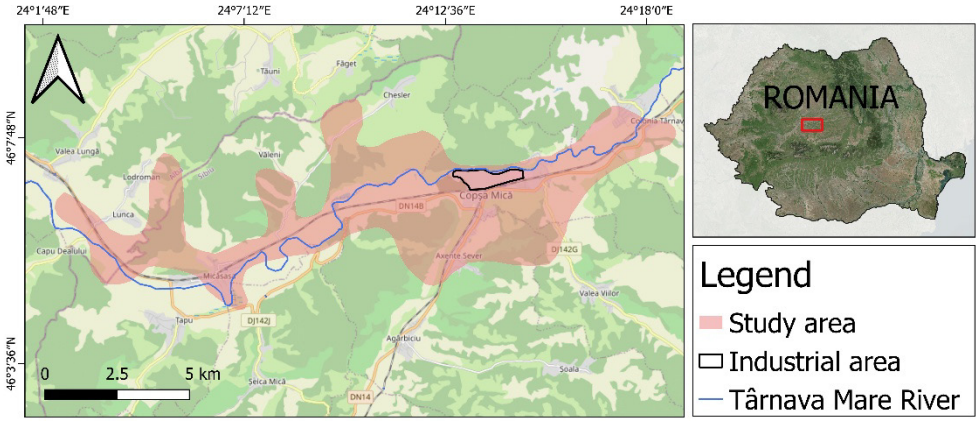

Figure 4. Location of the study area in the Copșa Mică region, Romania, including the industrial platform and the sampling zone along the Târnava Mare River

Chemicals and reagents

A standard stock solution mixture containing 19 PCBs (8, 18, 28, 44, 52, 66, 77, 101, 118, 126, 128, 138, 153, 170, 180, 187, 195, 206, 209, each at 100 $\mu g \cdot mL^{-1}$ in isooctane), was purchased from Restek (USA). The polychlorinated biphenyl-rich certified reference material (CRM) was purchased

from Sigma-Aldrich, USA. PCB 155 (97% purity) and PCB 198 (97% purity) were used as recovery standards and purchased from LGC Labor GmbH (Germany), and as an internal standard, 3,3′,4,4′-tetrabromodiphenyl ether (BDE 77) (10 μg·mL^{-1} in isooctane) was used and purchased from CPAchem Ltd. (Bulgaria). Acetone, n-hexane, and dichloromethane (DCM) were purchased from Honeywell (Germany) and isooctane from VWR (France), all at HPLC grade. Anhydrous sodium sulfate (12-60 mesh) was purchased from J.T. Baker (Mexico), and silica gel was purchased from Merck (Germany); all of them were analytical grade and were baked at 420℃ for 4 h before use. The copper (< 425 μm, 99.5%, Sigma-Aldrich, USA) was activated using a 1N HCl solution, subsequently rinsed with water until a pH of 5 was attained, and finally washed with acetone and DCM. All the glassware was thoroughly washed and soaked in alkaline bath solution for 12 hours and oven-dried at 120℃ for 12 hours before use.

Extraction and purification of PCBs

The ultrasound extraction (UAE) method was used to extract PCBs from soil samples. Subsequently, the extract solutions underwent a cleanup protocol. UAE was performed using an ultrasonic water bath (Elma Transsonic T660/H) equipped with a generator operating at a frequency of 35 kHz and a nominal power output of 320 W. Ultrasonication was carried out in continuous mode. The extraction temperature was monitored and maintained approximately constant at room temperature by cooling the water bath during sonication. These procedures were conducted based on previous studies reported by Barhoumi [23], Adesina [24] and Güzel [25] with minor modifications. Prior to extraction, approximately 9 g of soil sample was spiked with 200 μL (0.08 μg·mL^{-1}) recovery standard mixture to ensure the integrity of the extraction process. Then, 30 mL solvent mixture of hexane and acetone (v/v, 1:1) was added. The sample was placed in an ultrasonic bath and sonicated for 20 minutes. After the extraction process, the extract was centrifuged for 15 minutes at 4000 rpm and 10°C. These procedures were repeated two additional times using fresh solvent mixtures. The resulting extract was concentrated using a rotary evaporator to 2–3 ml and allowed to stand overnight on 0.5 g of activated copper for sulphur elimination. An additional 10 mL n-hexane was added to the flask and evaporated to 1 mL. This concentrated fraction was purified using thin-layer chromatography consisting of 4 g silica gel and 1 g sodium sulphate and eluted with a 40 mL mixture of n-hexane and dichloromethane (v/v, 4:1). Finally, the sample was concentrated to approximately 0.5 ml and spiked with 0.5 ml (1 μg·ml^{-1}) of internal standard prior to GC analysis.

Instrument analysis

The analysis of PCBs was performed using an Agilent 7890 gas chromatograph, equipped with a mass spectrometer (MSD) model 5975. The Zebron ZB-PAH-EU capillary column measuring 30 m x 0.25 mm x 0.2 µm was provided by Phenomenex (USA). Helium (99.99%) is used as the carrier gas at a flow rate of 1 mL/min, and the injector temperature is set at 280°C. The analytical method used a column heating gradient that went from the column temperature being held at 70°C for 2 minutes, increasing to 150°C at a rate of 25°C/min, subsequently rising to 200°C at a rate of 3°C/min, and finally ramping up to 280°C at a rate of 5°C/min, maintained for 10 minutes. The mass spectrometer detector (MSD) operated in electron impact ionisation at an ionising energy of 70 eV, with the ion source temperature set at 300°C and a quadrupole temperature of 180°C. The study was conducted by selected ion monitoring (SIM) utilising one target ion and two or three qualifier ions. The identification of these ions was conducted using mass spectrometry analysis. The confirmation of PCBs relied on retention times (which should be ± 0.2-0.3 min), qualifier ions, and target ions according to the qualifier/target ion ratio; for enhanced reliability, this ratio must be at least 20%. The data acquisition was performed using ChemStation software No. 2.

Data handling

Data processing was performed using Microsoft Excel and OriginPro 2025 software. For statistical evaluation, descriptive parameters including mean, median, minimum, maximum and standard deviation were calculated for each depth interval. The distribution of ∑PCB concentrations was illustrated by boxplot representations. Differences between the two soil depth intervals were assessed using the Mann-Whitney U test, and statistical significance was considered $p < 0.05$.

ACKNOWLEDGMENTS

This work was supported by a fellowship offered to the first author by the Romanian Ministry of Education, and by the Project PN-III-P1-1.2-PCCDI-2017-0721 – INTERASPA, funded by UEFISCDI.

REFERENCES

1. K. Breivik, A. Sweetman, J. M. Pacyna, K. C. Jones; *Sci. Total Environ.,* **2007***, 377*, 296–307
2. A. A. Bhat; M. Ahmed; N. Elboughdiri; J. Singh; K. Kriaa; C.Maatki; B. Hadrich; A.K. Wani; *Microchem J.*, **2026**, 117041

3. J. M. Armitage; M. Hanson; J. Axelman; I. T. Cousins; *Sci. Total Environ.*, **2006**, *371(1–3)*, 344–352
4. K. Jia; X. Feng; K. Liu; Y. Han; Y. Xue; C. Xue; *J. Chromatogr. B*, **2013**, *923–924*, 37–42
5. T. Nenin; T. Mitrović; A. Petković; J. Čolić; *Microchem. J.*, **2024**, *207*, 111761
6. F. Ben Salem; O. Ben Said; R. Duran; M. Monperrus; *Bull. Environ. Contam. Toxicol.*, **2016**, *96(5)*, 678–684
7. V. A. Pănescu; V. Bocoș-Binținținș; M. C. Herghelegiu; R.T. Coman; V. Berg; J. L. Lyche; M. S. Beldean-Galea; *Sustainability*, **2023**, *16(1)*, 232
8. G. Bianco; G. Novario; D. Bochicchio; G. Anzilotta; A. Palma; T. R. I. Cataldi; *Chemosphere*, **2008**, *73(1)*, 104–112
9. S. N. Meijer; W. A. Ockenden; E. Steinnes; B. P. Corrigan; K. C. Jones; *Environ. Sci. Technol.*, **2003**, *37(3)*, 454–461
10. S. A. Debela; I. Sheriff; J. Wu; Q. Hua; Y. Zhang; A. K. Dibaba; *Sci. Afr.*, **2020** *8*, e00329
11. C. Sánchez-Brunete; B. Albero; J. L. Tadeo; *J. Agric. Food Chem.*, **2004**, *52(6)*, 1445–1451
12. D. Dragan; S. Cucu-Man; A. C. Dirtu; R. Mocanu; L. V. Vaeck; A. Covaci; *Int. J. Environ. Anal. Chem.*, **2006**, *86(11)*, 833–842
13. A. Covaci; C. Hura; P. Schepens; *Sci. Total Environ.*, **2001**, *280(1–3)*, 143–152
14. M. Thompson; S. L. R. Ellison; R. Wood; *Pure Appl. Chem.*, **2002**, *74(5)*, 835–855
15. V. C. Eze; T. O. Maduka; C. I. Iheme; A.C. Chiedozie; H. O. Abugu; J. C. Egbueri; S. I. Ogbuefi; M. O. Muogbo; S. I. Abba; *Int. J. Environ. Anal. Chem.*, **2025**, *105(17)*, 5551–5577
16. https://www.atsdr.cdc.gov/toxprofiles/tp17.pdf, **2000**, Accession date: 02.02.2026-12:30
17. J. J. Nam; O. Gustafsson; P. Kurt-Karakus; K. Breivik; E. Steinnes; K. C. Jones; *Environ. Pollut.*, **2008**, *156(3)*, 809–817
18. J. Ge; L. A. Woodward; Q. X. Li; J. Wang; *PLoS ONE*, **2013**, *8(8)*, e71521
19. H.-K. Cho; S. N. Khuman; I.-G. Cho; M.-K. Park; S.-D. Choi; *Chemosphere*, **2024**, *369*, 143821
20. S. N. Meijer; W. A. Ockenden; E. Steinnes; B. P. Corrigan; K. C. Jones; *Environ. Sci. Technol.*, **2003**, *37(3)*, 454–461
21. B. Aichner; B. Bussian; P. Lehnik-Habrink; S. Hein; *Environ. Sci. Technol.*, **2013**, *47(22)*, 12703–12714
22. I. Rusu; *Eur. J. Sci. Theol.*, **2008**, *4(4)*, 33–40
23. B. Barhoumi; M. S. Beldean-Galea; A. M. Al-Rawabdeh; C. Roba; I. M. Martonos; R. Bălc; M. Kahlaoui; S. Touil; M. Tedetti; M. R. Driss; C. Baciu; *Sci. Total Environ.*, **2019**, *660*, 660–676
24. O. A. Adesina; I. Ezengwa; K. A. Abdulraheem; A. J. Adewole; O. B. Oyetunji; *Chem. Environ. Eng.*, **2023**, *7*, 100343
25. B. Güzel; O. Canlı; E. Aslan; *Mar. Pollut. Bull.*, **2022**, *175*, 113172

STUDIA UBB CHEMIA, LXXI, 2, 2026 (p. 243-263)
(RECOMMENDED CITATION)
DOI:10.24193/subbchem.2026.2.13

VISUALIZATION OF LATENT FINGERPRINTS BY COMBINED TETRA-*N*-BUTYLAMMONIUM IODIDE DUSTING AND NITROGEN DIOXIDE TREATMENT: MECHANISTIC INSIGHTS

Varinder SINGH[a], Metodija NAJDOSKI[b], Om Prakash JASUJA[a], Slobodan OKLEVSKI[c], Sasho STOJKOVIKJ[d,*]

ABSTRACT. The development of methods for latent fingerprints visualization is still attractive considering that there is no approach that is universal for all types of fingerprints and substrates. A thorough understanding of the visualization mechanism is crucial for expanding methods application and making them practical for real case scenarios. In this research, nitrogen dioxide (NO_2) treatment, previously limited to thermal paper substrates, is expanded towards visualization of latent fingerprints on various non-porous and porous substrates by introduction of pre-treatment with tetra-*n*-butylammonium iodide (TBAI). The visualization processes were studied using Raman, UV-Visible, FTIR and ^{1}H NMR spectroscopy, combined with various validation experiments. The results show that formation of molecular iodine (I_2), generated by reactions between NO_2 and TBAI, plays a key role in the visualization mechanism. The as-generated I_2 further reacts with excess TBAI, producing tetra-*n*-butylammonium triiodide ($TBAI_3$). $TBAI_3$ is a dark colored compound that provides the dominating contrast of the visualized fingerprint. Besides reactant, TBAI resembles a role of a phase-transfer catalyst that enables NO_2 to penetrate deeper into fingerprint's residue and to react with the fatty acid esters producing intrinsically colored nitro-compounds that additionally contribute towards fingerprints visualization effect.

Keywords: *Latent fingerprints visualization, Tetra-n-butylammonium iodide, Nitrogen dioxide*

[a] *RIMT University, Punjab, India.*
[b] *Institute of Chemistry, Faculty of Natural Sciences and Mathematics, Ss. Cyril and Methodius University - Skopje, Arhimedova 5, 1000, Skopje, Republic of North Macedonia.*
[c] *Ministry of Interior, Republic of North Macedonia.*
[d] *MIT University Skopje, Boris Trajkovski 62, 1000 Skopje, Republic of North Macedonia.*
* *Corresponding author: sasho.stojkovikj@dm.mit.edu.mk*

INTRODUCTION

Latent fingerprint visualization has long served as an essential aspect of forensic identification due to the uniqueness and persistence of friction ridge patterns. Various traditional methods such as dusting, ninhydrin treatment, cyanoacrylate fuming etc. have been widely used to visualize latent prints on variety of surfaces in terms of composition and surface morphology. These techniques often offer good efficacy, yet in many cases they suffer from limitations related to substrate specificity or destructive nature of the process during the print development. For example, ninhydrin/solvent-based reagents can have issues related to the solvent itself. Namely, if a paper on which fingerprints are to be developed has ink writings, the ink may bleed in contact with the solvent used for preparation of the ninhydrin solutions [1] hence important evidence might be lost. To address such problems, many researchers have looked for an alternative method where either modified application method is used [2] or intermediate and alternative solvents are used to apply the ninhydrin [3]. Researchers reported visualization based on UV light induced luminescence of latent fingerprints after treating the sample with electric discharge in nitrogen gas and subsequent exposure to vapors formed by heating ammonium hydrogen carbonate [4]. Recent research appeared in literature where efforts have been made to develop latent fingerprints with solvent- free chemicals. Kelly et al. [5] reported the use of sulfur nitrides and Shah [6] used selenium dioxide, phosphorus sulfides and hexachlorophosphazene in vapor phase to develop latent fingerprints on various surfaces. Clarke et al. [7] reviewed the status of solvent free methods to visualize latent fingerprints and claims that dry transfer method for porous surfaces was found to be most promising among all existing solvent-free methods. Regarding the solvent-free, among physical and chemical methods, iodine fuming, as one of the oldest methods, is safe and non-destructive visualization approach, suitable for both aged and freshly impressed latent prints on porous and semi-porous surfaces [8]. However, the temporary nature of iodine-developed prints due to iodine sublimation and lack of fixation has posed a significant challenge to its long-term forensic application. Researchers have attempted to stabilize iodine-developed prints using starch, paraffin wax, or post-treatment with chemical fixatives, but these often introduce complications such as color interference or surface alteration [9-10]. The fingerprint development methods can be significantly improved if the visualization mechanism is well understood. The spectroscopic characterization techniques such as Raman and FTIR can play a pivotal role [11-12]. Namely, in one of our previous studies, tetra-*n*-butylammonium iodide - $(C_4H_9)_4NI$ (abbreviated as TBAI), a quaternary ammonium salt with phase-transfer catalytic (PTC) properties, was used for

sample dusting prior to iodine fuming thus achieving successful and irreversible iodine fixation and the chemical reaction mechanism during the course of fingerprint development was characterized using FTIR, Raman and UV–Visible spectroscopy [11]. Another previous study was focused on developing latent fingerprints using nitrogen dioxide (NO_2) treatment [13]. However, the NO_2 method is only limited to visualization of latent fingerprints on thermal paper samples and showed poor performance when visualizing prints impressed on other materials. Introducing TBAI powdering and subsequent NO_2 gas treatment expands both the application of the NO_2 method [13] and further application of the phase-transfer catalyst TBAI, that was successfully combined with the iodine fumes treatment [11]. The overall evaluation of the visualization performance from such combination of both methods (abbreviated as TBAI/NO_2 method in the following text) and the possibility to visualize fingerprints on various substrate types, showed valuable results, simplicity of the method and perspective for its application in forensic scenarios. This opened an opportunity for deeper understanding of the chemical background leading to fingerprint visualization effects, thus studying the reaction mechanisms represents the main focus of this research. For that purpose, we utilized several spectroscopic characterization techniques in combination with various validation experiments.

RESULTS AND DISCUSSION

Forensic evaluation of the TBAI/NO_2 method

The forensic examination of visualized fingerprints impressed on various substrate types significantly highlights how surface characteristics apply on the quality and clarity of papillary ridge detail, which is crucial for identification purposes. Therefore, the fingerprints visualization capacity of the TBAI/NO_2 method proposed in this research is evaluated on sebaceous latent fingerprints impressed on various porous and non-porous surfaces such as standard office paper, laminated wooden chipboard, glass and glazed ceramics. The as-visualized fingerprints are presented in Figure 1, while the results from qualitative and quantitative evaluation of the method, in Table 1 and Table 2, respectively.

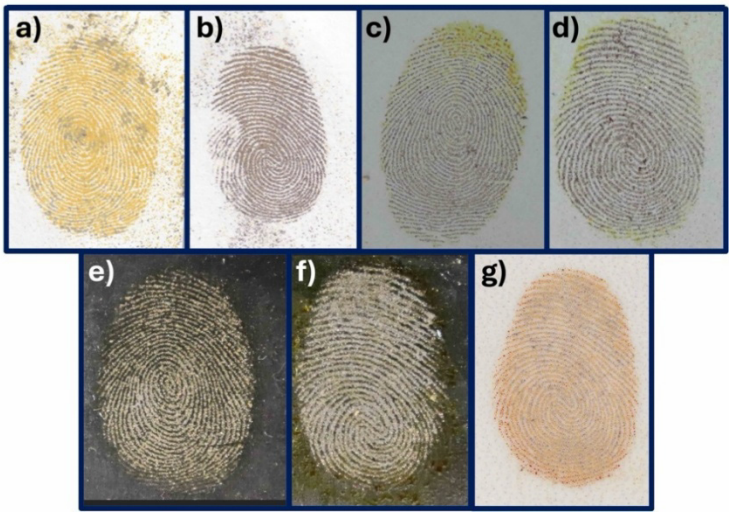

Figure 1. Visualized sebaceous fingerprints on various porous and non-porous surfaces: **(a, b)** Standard 80 gsm paper; **(c, d)** Laminated chipboard; **(e, f)** Glass and **(g)** Glazed ceramic.

Table 1. Comparative qualitative analysis of latent fingerprints visualized on various types of substrates, presented in Figure 1.

Substrate type	Surface	Pattern type	Ridge clarity
(a) Standard 80 gsm paper – Fingerprint 1	Porous	Whorl	Good
(b) Standard 80 gsm paper – Fingerprint 2	Porous	Whorl	Good
(c) Laminated chipboard – Fingerprint 1	Non-porous, smooth	Whorl	Excellent
(d) Laminated chipboard – Fingerprint 2	Non-porous, smooth	Whorl	Excellent
(e) Glass – Fingerprint 1	Non-porous, smooth	Whorl	Excellent
(f) Glass – Fingerprint 2	Non-porous, smooth	Whorl	Moderate
(g) Glazed ceramic	Non-porous, glazed	Whorl	Good

Table 2. Identification of 2nd level minutiae and 3rd level features and evaluation of the forensic suitability for the latent fingerprints visualized on various types of substrates, presented in Figure 1.

Substrate type	2nd level minutiae	3rd level features visibility	Forensic suitability
(a) Standard 80 gsm paper – Fingerprint 1	50	Not visible	High
(b) Standard 80 gsm paper – Fingerprint 2	45	Not visible	Moderate
(c) Laminated chipboard – Fingerprint 1	59	Partially visible	High
(d) Laminated chipboard – Fingerprint 2	59	Partially visible	High
(e) Glass – Fingerprint 1	45	Partially visible	High
(f) Glass – Fingerprint 2	30	Not visible	Moderate
(g) Glazed ceramic	41	Not visible	Sufficient

Porous substrates, such as standard office paper, generally enable visualization of continuous ridge patterns with acceptable contrast. However, the partially absorbent nature of the substrate prevents the clear manifestation of 3rd level features, such as ridge edge contours and pore structures. Despite this limitation, the quantification of 45–50 identifiable 2nd level minutiae ensure the possibility of conducting reliable comparative analyses, consistent with the international forensic guidelines [14-15].

On the other hand, surfaces with non-porous and smooth finish, such as laminated chipboards, provide highly suitable conditions for detection and visualization of latent fingerprints. These materials enable formation of outlined ridge patterns with very significant contrast versus the background surface. Therefore, the TBAI/NO_2 method provides extensive number of 2nd level features (up to 59 minutiae), also observing 3rd level details, including pores and edge features. Glazed ceramic materials, due to their smoothness enable satisfactory development of papillary ridge patterns, ensuring clear separation between ridges and furrow spaces. In the examined cases, up to 41 – 2nd level minutiae are identified, much higher than the thresholds for comparative purposes [14-15]. Nevertheless, 3rd level features cannot be identified. Finally, glass surfaces which encompass very smooth texture offer favorable conditions for latent fingerprint visualization. Hence, the visualized fingerprints exhibit strong contrast and clear ridge contours, leading to quantification of up to 45 – 2nd level minutiae, again higher than the reported minutiae thresholds [14-15]. Partial visibility of 3rd level features is further enhancing the value of the TBAI/NO_2 method for forensic applications in real case scenarios.

In summary, the TBAI/NO_2 method is simple, fast, reliable and practical for utilization in forensic laboratories. The forensic evaluation shows that smooth and non-porous surfaces offer optimal conditions for detecting 2nd level fingerprint features and, in certain areas, elements of 3rd level detail, collectively enhance the reliability of forensic identification, while the porous substrates enable identification processes that rely predominantly on 2nd level fingerprint features.

Furthermore, it is obvious from the images on Figure 1 that the color of the visualized fingerprints can differ even when impressed on the same type of substrate, especially noticeable in the case of the fingerprints impressed on paper's surface i.e., the fingerprint on Figure 1a is mostly orange in color, while the one on Figure 1b is brown when visualized via the TBAI/NO_2 method. The fingerprints impressed on laminated chipboard are predominately brownish, but significant orange color area can be observed on Figure 1c. This could possibly imply to differences in the visualization mechanism related to the chemical processes between TBAI, NO_2 and fingerprint's sebaceous residue, which is found to be worth studying in the scope of this research.

Study of fingerprint visualization mechanism

Characterization with Raman spectroscopy

The characterization started with Raman spectroscopy analysis of the fingerprints impressed on glass as non-porous and paper as porous substrate, visualized under 5- and 20 s exposures to NO_2, after being dusted with TBAI. The sample preparation procedures are given in Table S1 in SI and the Raman spectra results are presented in Figure 2a and Figure S1 in SI (full range Raman spectra).

The Raman spectra of the fingerprints impressed on glass and paper surfaces, exposed to NO_2 for 5 s show features that are typical for vibrational modes in I_3^- ion [16-17]: strong band attributed to symmetric stretching vibration at ~112 cm^{-1} with a shoulder at ~145 cm^{-1}, that can be recognized as asymmetric stretching vibration. This is suggesting that the visualization mechanism follows identical pathways, as presented in our previous research [11], that is formation of tetra-*n*-butylammonium triiodide - $TBAI_3$, according to Eq. 1. Moreover, the visualized fingerprints with 5 s NO_2 treatment appear very similar in color - dark yellow on both glass and paper surfaces, as described in Table S1 in SI, albeit pure $TBAI_3$ is a very dark-colored compound [11].

$$TBAI + I_2 \rightarrow TBAI_3 \qquad \text{Equation 1}$$

The second set of spectra in Figure 2a are recorded on fingerprints impressed on paper surfaces, from which one is immediately visualized, and one was visualized 2 months prior to characterization, both with 20 seconds NO_2 treatment. The immediately visualized fingerprint appeared orange in color, while the one developed after 2 months - dark brown (Table S1 in SI). Besides the distinctive bands characteristic for the fundamental vibrational modes of the I_3^- anion [11, 16-17] at ~112 and ~110 cm^{-1} for the immediately visualized- and the fingerprint visualized after 2 months, respectively, additional distinctive bands can be observed at higher wavenumbers for both samples. Namely, one band appears at ~167 cm^{-1} with a small shoulder at ~148 cm^{-1} in the case of the immediately visualized fingerprint, whilst a strong band is observable at ~220 cm^{-1} for the fingerprint visualized 2 months prior to the characterization with Raman spectroscopy. According to some literature data [18-19], the band at ~167 cm^{-1} including the shoulder at ~148 cm^{-1}, observable in the spectrum of the immediately visualized fingerprint, could be attributed to vibrations in polyiodide ions [18] and vibrations in perturbed I_2 molecule together with symmetric/asymmetric vibrations in the I_3^- anion [19]. The band at ~220 cm^{-1} in the spectrum of the fingerprint visualized 2 months prior to

the characterization could possibly be attributed to overtone of the fundamental bending vibration in the I_3^- ion [17] appearing at ~110 cm^{-1}. However, the absence of such distinctive overtone bands in the spectra of the other visualized fingerprints on glass and paper remains an open question. A very weak feature is observable at ~1100 cm^{-1} in the spectrum of immediately visualized fingerprint on paper with 20 s NO_2 treatment which can be possibly attributed to aliphatic stretching vibrations in the butyl groups [11, 20]. Additional very weak features can be observed in the Raman spectra of the visualized fingerprints in Figure 2 and Figure S1 in SI (full range Raman spectra), yet their interpretation can be neglected at this point. The identification of I_3^- anion in the fingerprint that is characterized 2 months after being visualized, shows that the as formed $TBAI_3$ remains stable and no additional post-treatment or fixation is required. This is very suitable for preservation of important forensic evidence.

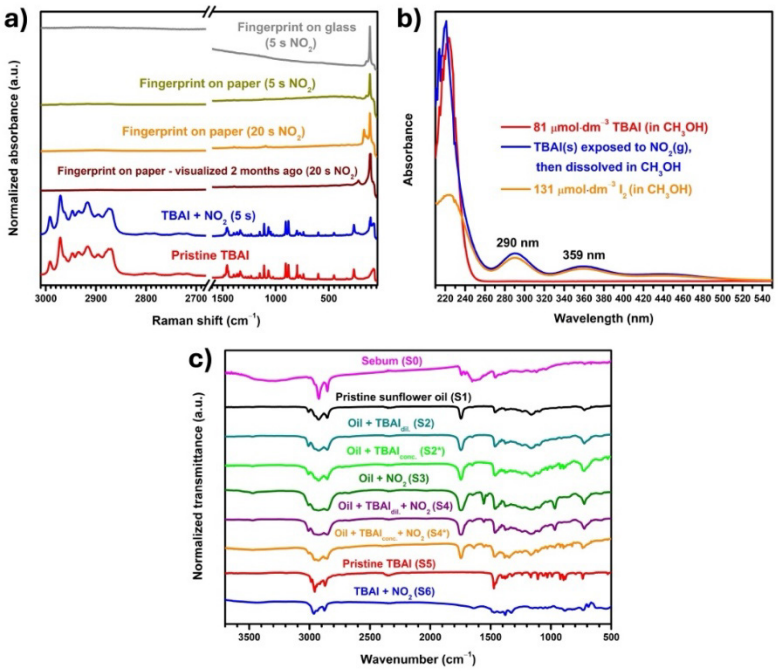

Figure 2. (a) Raman spectra of visualized fingerprints on glass and paper surfaces under various conditions and Raman spectra of pristine TBAI and TBAI treated with NO_2 gas: **(b)** UV-Vis spectra of TBAI, TBAI exposed to NO_2 and of iodine, recorded in methanol as solvent; **(c)** FTIR spectra of various samples including human sebum residue (Sample 0), pristine sunflower oil (Sample 1), sunflower oil treated under different conditions (Sample 2–Sample 4*), pristine TBAI as a reference material (Sample 5) and TBAI exposed to NO_2 (Sample 6).

Up to now it is quite certain that the latent fingerprint coloration mechanism is most possibly based on the formation of $TBAI_3$ via reaction between TBAI and I_2 (Eq. 1), as in the case of our previous research [11], and according to the previous discussion, even polyiodide ions [18] can be formed. Nevertheless, the question that arises at this point is what is the origin of the molecular iodine that reacts with TBAI? In order to tackle this question, Raman spectra are recorded on pristine TBAI and TBAI exposed to NO_2 gas for 5 seconds. The sample preparation is described in Table S1 in SI. According to the results presented in Figure 2 and Figure S1 in SI (full range Raman spectra), the NO_2 treated TBAI resembles all spectral features as in the case of pristine TBAI with an exception in the region below 200 cm^{-1}. The bands typical from C–C and C–H stretching and C–H bending vibrational modes can be typically assigned in the region 3000–1000 cm^{-1} region [11, 20-21], originating from the four n-butyl groups. Moreover, the region between 1000 and 300 cm^{-1}, is typical for various vibrations involving the $–CH_2–$, $–CH_3$ groups, C–C skeleton and C–N bonds in the case of TBA^+ cation [21], but also for other aliphatic quaternary ammonium compounds [22], while the bands at ~262 cm^{-1} in both spectra are possibly related to TBA^+ cation lattice vibrations and the position of this band is influenced by the anion's chemical identity and presence of crystalline water [11, 20, 23]. Similar anion-cation interaction affected modes in the TBA^+ group are the most probable reason for observation of the broad feature at ~75 cm^{-1}. Though, a band at ~108 cm^{-1} is clearly visible only in the spectrum of NO_2 treated TBAI, which also appears in the spectra of all visualized fingerprints on various surfaces, and which is assigned to fundamental vibrational modes of the I_3^- anion [11, 16-17], as discussed in the text above. This is suggesting that few seconds of NO_2 exposure is transforming TBAI into $TBAI_3$ via oxidation of the I^- anion into molecular I_2. Subsequently, I_2 reacts with excess TBAI to form $TBAI_3$, as described with Eq. 1. Regarding the oxidation of the I^- anion with gaseous NO_2, there are several possible reactions (Eq. 2–7), from which some are reported in the literature [24]. Eq. 2 represents the simplest case describing net oxidation of I^- anion directly with NO_2. The gaseous NO_2 can also dimerize and establish an equilibrium with N_2O_4, according to Eq. 3, whereas N_2O_4 is reported to be more reactive than NO_2, thus oxidizing the I^- anion into molecular I_2 [24] according to Eq. 4.

$$2I^- + 2NO_2 \rightarrow I_2 + 2NO_2^- \qquad \text{Equation 2}$$

$$2NO_2 \rightleftarrows N_2O_4 \qquad \text{Equation 3}$$

$$2I^- + N_2O_4 \rightarrow I_2 + 2NO_2^- \qquad \text{Equation 4}$$

However, the presence of moisture (water vapor) in the reaction vessel for treating the latent fingerprints with NO_2, based on exothermic reaction between Zn and HNO_3 [13], cannot be neglected. The water vapor

can react with both NO_2 and N_2O_4 and form HNO_3 and HNO_2 according to Eq. 5 and 6, respectively.

$$2NO_2 + H_2O \rightarrow HNO_3 + HNO_2 \quad \text{Equation 5}$$
$$N_2O_4 + H_2O \rightarrow HNO_3 + HNO_2 \quad \text{Equation 6}$$

HNO_3 can subsequently oxidize the I^- anion into molecular I_2, according to Eq. 7:

$$6I^- + 8H^+ + 2NO_3^- \rightarrow 3I_2 + 2NO + 4H_2O \quad \text{Equation 7}$$

Other side reactions between the I^- anion, NO_2 and their products are also possible to occur, yet the main point of this discussion is that when nitrogen resembles oxidation states of +4 and +5, such compounds are strong oxidizers that can easily transform the I^- anion into I_2 which can further react with excess TBAI to form the colored compound $TBAI_3$ (Eq. 1), achieving visualization of the latent fingerprints.

Characterization with UV-Vis spectroscopy

To further clarify that molecular I_2 is formed via oxidation of the I^- anion when exposed to NO_2, pristine TBAI, TBAI exposed to NO_2 for 5 seconds and pristine I_2 crystals are dissolved in polar organic solvents and characterized with UV-Visible spectroscopy. The first attempt was to use *tert*-butanol as a solvent for this purpose, yet however it was observed that when pristine TBAI is dissolved in this solvent in various concentrations, the UV-Vis spectra show identical absorption maximums, as in the case of TBAI exposed to NO_2 (Figure S3 in SI), and moreover the solution turned pale yellow in color suggesting per se formation of molecular I_2 from TBAI (Figure S4 in SI). Nonetheless, the main discussion of this phenomenon and its possible explanations are presented in Subsection S2.2 in SI. Therefore, another attempt was made, and methanol was used as a solvent instead, as in the case of our previous research [11]. The preparations of the samples for characterization with UV-Vis spectroscopy are presented in Table S2 in SI and the recorded spectra in Figure 2b. The spectrum of TBAI in CH_3OH shows distinctive absorption only in the UV region with sharp peak at ~227 nm. When TBAI is exposed to NO_2 for 5 minutes and dissolved in CH_3OH, besides the absorption in the UV region that shifts towards lower wavelength (~221 nm), two more broad peaks at 290 and 359 nm, appear. These results are in agreement with the UV-Vis spectra of TBAI and $TBAI_3$ in our previous publication [11], and they are generally attributed to absorption from I_3^- anion [25-26]. Furthermore, the broad peaks at 290 and 359 nm are also observable in the spectrum of I_2 in CH_3OH. This is suggesting that these

peaks are likely not originating only from a single specie but rather from several species in equilibrium. Namely, the $TBAI_3$ formed when TBAI is exposed to NO_2 (via the molecular I_2 mechanism discussed above) undergo dissociation in the solution according to Eq. 8.

$$TBAI_3\,(solution) \rightarrow TBA^+\,(solution) + I_3^-\,(solution) \qquad \text{Equation 8}$$

The I_3^- forms an equilibrium with the I^- anion and molecular I_2, according to Eq. 9, which is the reason for the characteristic peaks (at 290 and 359 nm) overlapping in the UV-Vis spectra of both I_2 and TBAI exposed to NO_2 (Figure 2b).

$$I_3^-\,(solution) \rightleftarrows I^-\,(solution) + I_2\,(solution) \qquad \text{Equation 9}$$

The results from the UV-Vis- strongly support the Raman spectroscopy findings and from both discussions can be concluded that molecular I_2 is indeed formed via oxidation of the I^- anion from TBAI, subsequently reacting with excess TBAI to form $TBAI_3$ (Eq. 1), achieving visualization of the latent fingerprints.

Regarding the utilization of *tert*-butanol as solvent for characterization with UV-Vis spectroscopy, the UV-Vis spectrum of pristine TBAI dissolved in this solvent shows the characteristic peaks at 292 and 360 nm that can be attributed to the $I_3^-/I^-/I_2$ equilibrium (Figure S2 in SI) and the solution turns pale yellow (Figure S3 in SI) over the course of few hours regardless whether the solution is kept in dark or exposed to sunlight. This means that the I^- anion from TBAI is undergoing per se oxidation into I^- when dissolved in tert-butanol but the actual reason for such behavior is not very clear, though the possibility of photochemical processes is excluded. Subsection S2.2 in SI is dedicated to discussion of such empirical observations.

The fingerprints visualization mechanism appears to be rather clear when exclusively interactions between TBAI and NO_2 leading to formation of the colored compound $TBAI_3$ are observed, and the key process in the pathways is the formation of I_2 via oxidation of the I^- anion from TBAI. The question that subsequently follows up is: What is the role of the sebaceous residue from which latent fingerprints are composed of, in the overall visualization process? Observing all Raman spectra presented in Figure 2a, bands associated to vibrations typical for lipidic compounds that are present in the human sebum from which fingerprints are naturally composed of, are not identified. Furthermore, utilizing Raman spectroscopy to probe the surface of freshly impressed latent fingerprint prior to visualization (labelled as human sebum - Sample 0 in Table S1 in SI) has somewhat expectedly led to obtaining an ill-shaped spectrum, presented in Figure S4 in the SI. The absence of distinctive features originating from lipids in the human sebum spectrum is possibly

caused by the amorphous nature of the sebaceous residue, showing that utilizing only Raman and UV-Vis spectroscopy in the available configurations that are used in this research, are not sufficient to fully resolve the visualization mechanism. Therefore, additional characterization methodologies and experimental approaches are required.

Characterization with FTIR spectroscopy

The following discussion is mainly focused on the results obtained from characterization using FTIR and ^{1}H NMR spectroscopy. Starting with FTIR spectroscopy, the general sample preparation for characterization is presented in the Supplementary Information – SI, while the specific sample preparation/abbreviations are presented in Table S4 in SI. All recorded FTIR spectra are presented in Figure 2c. The FTIR characterization of latent fingerprint, when freshly impressed on KBr tablet, is significantly more successful compared to the Raman spectroscopy, that is, the spectrum of Sample 0 indeed shows features originating from vibrations associated with various functional groups characteristic for triglycerides and fatty acids, that are typically present in the human sebum residue. Namely, the strong bands at ~2924 cm^{-1} and ~2841 cm^{-1} are attributed to the asymmetric and symmetric stretching of aliphatic C–H bonds in $–CH_2–$ groups [27]. The broad band above 3100 cm^{-1} can be attributed to O–H group stretching vibrations due to presence of moisture [27], possibly excreted from the human sweat glands. The bands at ~1746 and ~1712 cm^{-1} are attributed to C=O group stretching vibrations, originating from esters and free fatty acids, respectively [27-28]. The broad band peaking at ~1645 cm^{-1} can possibly arise from C=C stretching vibrations in unsaturated fatty acids and their esters [27], while the bands at ~1460 cm^{-1} correspond to $–CH_2–$ groups bending modes [27-28] and the weak feature at ~1120 cm^{-1} is generally attributed to stretching C–O vibrations in ester groups [27]. However, the broad band at ~1645 cm^{-1} can also be identified for H–O–H bending vibrations in water molecules [29], which together with the broad band above 3100 cm^{-1} arising from O–H group stretching vibrations are indeed identifying presence of water. Additionally, the weak band at ~712 cm^{-1} arises from rocking-bending vibrations in CH_2 groups [27], indicating the presence of hydrocarbon chains. The band at ~1745 cm^{-1} in the spectrum of Sample 0 is significantly more prominent (lower absolute transmittance) compared to the one at ~1712 cm^{-1}, suggesting that the ester forms, that is, glycerides, are rather more abundant in the human sebum compared to free fatty acids [28]. The composition of human sebum can be variable, and such variations generally originate from body part, age, diet, ethnicity, climate etc. [28,

30-31], but also from other factors such as substrate types used for impressing (deposition of) the fingerprint, timescale between deposition and analysis, deposition conditions etc. [30]. Subjecting the latent fingerprints impressed on KBr tablets to TBAI dusting and NO_2 gas treatment for the purpose of characterizing the visualized fingerprints with FTIR spectroscopy and studying the visualization mechanism is rather challenging due to the fact that bromide anion from KBr is prone to reaction with NO_2. On the other hand, the FTIR-, in the configuration utilized for this research is typically bulk sensitive compared to the Raman spectroscopy, limiting the possibility for experimenting with very small quantities of sebaceous material in terms of characterizing the products obtained from possible interactions of the human sebum with TBAI and NO_2 and moreover collecting large amount of sebaceous residue, and later treating it with TBAI and NO_2 in a laboratory vessel, was found not to be very feasible approach. Therefore, we decided to use refined cooking sunflower oil as a reasonable substitute for the human sebum residue and proceed with the experiments and characterization.

The FTIR spectrum of pristine sunflower oil (Sample 1) in Figure 2c resembles all key features as in the case of the human sebum residue including significantly higher abundance of ester forms (glycerides) compared to free fatty acids, as mentioned above, since the band at ~1745 cm^{-1}, typical for C=O stretching vibrations in ester groups [32], is clearly observable. Therefore, if other lipidic substances such as squalene, cholesterol and wax esters, typical for the human sebum residue [30] are excluded, the sunflower oil appears to be an adequate substitute expected to show very similar chemical reactivity when performing various experiments based on interaction of this material with TBAI and NO_2 intended for study of the fingerprint's visualization mechanism.

In the first step TBAI-sunflower oil mixtures are prepared with low and high TBAI concentrations, labeled as Sample 2 (diluted) and Sample 2* (concentrated). The FTIR spectrum of the diluted sample is practically identical as the one of pristine sunflower oil, however, the sample with higher concentration of TBAI, besides the typical features originating from the oil, shows additional features. These features resemble group of medium and weak bands in 880-1035 cm^{-1} that are characteristic for C–N+ stretching vibrations in the quaternary alkylammonium cation [33-34], that are also observable in the spectrum of pristine TBAI (Sample 5), recorded as a reference for comparison.

The next experiment encompasses treatment of pristine sunflower oil with NO_2 gas (Sample 3). A medium to strong band at ~1557 cm^{-1} appears in the FTIR spectrum of this sample, attributed to asymmetric stretching vibrational modes in nitro ($–NO_2$) group [35-37]. However, the weak to medium band attributed to symmetric stretching in the $–NO_2$ group, expected to appear at

1389–1259 cm^{-1} [35], in the FTIR spectrum of Sample 3, is hardly resolvable due to interference with the bands arising from twisting and wagging $–CH_2–$ groups in long hydrocarbon chains in a similar wavenumber range [35]. Such bands from twisting and wagging $–CH_2–$ groups also appear in all spectra of Samples 0-2*, yet they are very weak in the case of human sebum residue (Sample 0). The identification of nitro groups in the spectrum of Sample 3 is suggesting that NO_2 gas is reacting with the sunflower oil (nitration). Similar chemical behavior is expected between NO_2 and the fingerprint sebaceous residue, possibly via complex mechanisms including addition of nitro group on a double bond in unsaturated fatty acids and their esters, and processes of hydrogen abstraction, alongside with double bond position rearrangements [37-40]. The band at ~1649 cm^{-1} in the spectrum of Sample 3 could be associated to C=C double bonds vibrations [27], presuming that either the nitration is not complete or processes of double bond position rearrangements indeed occur. However, as discussed above, this band can also be attributed to H–O–H bending vibrations in water molecules [29], and since a weak band, possibly arising from O–H stretching modes is observable at ~3470 cm^{-1}, this claim is reasonably strong. At this point the deconvolution between the bands originating from C=C double bond stretching and H–O–H bending vibrations is hardly possible, however vegetable oils, such as the sunflower oil, indeed contain significant amounts of unsaturated fatty acids, such as oleic and linoleic acid, and their esters [32], thus the presence of C=C double bonds cannot be simply excluded. Regardless of the possible water presence in Sample 3, the nitration reactions can be considered as concurrent with the set of reactions between NO_2 and the I^- anion from TBAI (Eq. 2–7) forming I_2 that further reacts with excess TBAI to form $TBAI_3$ (Eq. 1), as discussed above in this research, thus leading to varieties in the color of the visualized fingerprints (see Figure 1).

In the final experiment, low and high amount of TBAI was mixed with sunflower oil, and these mixtures were exposed to NO_2 gas. The samples are abbreviated as Sample 4 for lower- and Sample 4* for higher TBAI concentration, respectively (see Table S4 in the SI). The spectrum of Sample 4 resembles all features as the case of Sample 3 - spectrum, however the band attributed to the asymmetric stretching vibrations in nitro group at ~1556 cm^{-1} [35-37] is significantly weaker. Similar weaker nitro group band compared to the spectrum of Sample 3, can be observed in the case of Sample 4* with higher concentration of TBAI, however in the spectrum of the latter sample, besides the typical for Sample 3, additional features associated to the TBA^+ cation can be also observed, when compared to the reference spectrum of pristine TBAI (Sample 5). The diminishing of the nitro group bands in Samples 4 and 4* compared to Sample 3 is suggesting that the nitration processes

are less favorable than the reaction between TBAI and NO_2 (described with Eq. 2–7) leading to formation of $TBAI_3$ (Eq. 1) which, again, could be related to the yellow to brown color variations of the fingerprints during the visualization process, as presented in Figure S5. It appears that shorter exposure of the TBAI dusted latent fingerprint to NO_2 gas leads to development of light color (yellow or dark yellow), while longer NO_2 treatment (20 s or more), but this is not always the case. Namely, the NO_2 treatment duration in the case of the visualized fingerprints on paper, presented in Figure 1a, b, is equal (5 seconds) but the fingerprint on Figure 1b is dark brown, while on Figure 1a - orange with some dark brown spots. From this it can be actually assumed that it is not the NO_2 exposure duration that defines the color outcome during the visualization process, but rather the TBAI powder coverage during the dusting pre-treatment. It is important to note that, if latent fingerprint, is treated with NO_2 gas from 5 s up to 10 minutes, without pre-dusting with TBAI, no visualization occurs, as presented in Figure S6 in SI, and this is the justification why the NO_2 method, originally developed for visualization of latent fingerprints on thermal paper [13], was modified by introducing TBAI pre-treatment. This is suggesting that TBAI most probably plays additional role and that is phase-transfer catalyst that facilitates the delivery of NO_2 from the gaseous phase into the sebaceous residue. The nitration of sunflower oil in the absence of TBAI (Sample 3 – see Table S4 in SI) is possible but it requires vigorous and repetitive mixing of the oil with NO_2. Anyhow, recalling the results from the Raman spectroscopy characterization (Figure 2a) discussed above, the I_3^- anion from $TBAI_3$ is identified on the surface of all visualized fingerprints, regardless of the color appearance and the type of surface on which the fingerprints were impressed (Table S1 in SI), yet this technique is not sensitive enough in the configuration we used to identify the lipidic compounds (including nitro- fatty acids and their esters), possibly because of their amorphous nature. On the other hand, Raman spectroscopy appears to be significantly more useful to identify the formation of $TBAI_3$ from reaction between TBAI and NO_2, while the FTIR spectrum of the reaction product between TBAI and NO_2 (Sample 6) does not provide very significant identification information in terms of the stretching vibrational modes of triiodide anion which are low frequency and expected to appear at wavenumbers in the far-infrared region ~200 cm^{-1} [29]. Though, the typical features originating from the TBA^+ cation, that also appear in the spectrum of pristine TBAI, are identifiable: C–H stretching from butyl groups at 3000–2850 cm^{-1} [35]; weak band at ~1465 cm^{-1} that correspond to CH_2 groups scissoring modes [35]; very weak bands from twisting and wagging $–CH_2–$ groups (1330 and 1152 cm^{-1}) and medium band associated to symmetrical C–H bending modes in CH_3 groups at ~1379 cm^{-1} [35]; bending weak broad bands at 1035–880 cm^{-1} that are characteristic for quaternary

alkylammonium cation C–N+ stretching- [33-34] and rocking-bending vibrations in $–CH_2–$ groups at ~730 cm^{-1} [35]. The band at ~1635 cm^{-1} is suggesting H–O–H bending vibrations in water molecules [29], even though the expected bands above 3000 cm^{-1} for O–H stretching vibrational modes [29], are not identifiable, possibly due to presence of only trace amounts of water.

Characterization with ^{1}H NMR spectroscopy

The last discussion in this research is dedicated to the results from characterization with ^{1}H NMR spectroscopy. The ^{1}H NMR instrumental setup and parameters are presented in the Supplementary Information - SI (sample preparation is described in Table S5). The characteristic features as chemical shift positions are presented in Table S6 and the spectra for all samples, in Figures S7–S12 in SI. Starting with assignation of the features in ^{1}H NMR spectrum of pristine sunflower oil Sample 1 - (Table 2 in the main text and Figure S7a–c in SI), aliphatic peaks (0.75–1.51 ppm) confirm the presence of long hydrocarbon chains involving protons from $–CH_2–$ and terminal $–CH_3$ groups in fatty acids and their esters [32, 41]. The peaks at 1.89–2.73 ppm can be assigned to $–CH_2–$ protons from allyl and double allyl groups typical for oleic and linoleic acids and their esters in sunflower oil, and $–CH_2–$ protons bound to ester groups [32, 41]. Protons originating from glycerol backbone in the fatty acid esters typically appear at 3.96–5.24 ppm, while the peaks at 5.29–5.34 ppm can be assigned to protons in –CH=CH– groups [32, 41] again typical for unsaturated fatty acids and their esters, even though, as discussed in the previous subsection dedicated to FTIR characterization, it was difficult to deconvolute the band associated with C=C stretching from the one originating from H–O–H bending vibrational modes.

When TBAI is mixed with sunflower oil (Sample 2), besides the ^{1}H NMR features associated to the sunflower oil itself, discussed above, the spectra (Table S6 and Figure S8a–d in SI) show additional features originating from TBAI that are also identifiable in the spectra of pristine dry TBAI reference sample (Sample 5, Figure S11a, b in SI). Namely, the $–CH_3$ and $–CH_2–$ protons from the *n*-butyl groups in TBAI appear significantly downfield compared to the protons from the hydrocarbon chains in various fatty acids and their esters present in the sunflower oil, likely caused by strong de-shielding effect from the positively charged nitrogen atom and iodide anion. The chemical shift intervals 0.92–0.95 ppm, 1.28–1.36 ppm, 1.54–1.58 ppm and 3.15–3.18 ppm can, most probably, be assigned to protons from terminal $–CH_3$ group, from $–CH_2–$ group bound to terminal $–CH_3$, internal $–CH_2–$ group and $–CH_2–$ group bound to the positively charged nitrogen atom in TBA^+ cation, respectively [21].

The strong singlet peak at 3.31 ppm, also observable in Sample 4 and Sample 5, is possibly originating from water impurities [42].

Treating pristine sunflower oil with NO_2 gas, without- (Sample 3) and in the presence of TBAI (Sample 4), leads to formation of compounds that generally show de-shielding effect in the peak positions compared to the pristine oil as presented in Table S6 in SI and in Figure S9a–c and Figure S10a–d in SI, for Sample 3 and 4, respectively. Namely, it can be observed from the spectra and the values in Table S6 in SI that the protons from $–CH_3$, $–CH_2–$, the glycerol backbone and from –CH=CH– groups indeed show downfield chemical shift values in Sample 3 and 4 compared to Sample 1. According to some literature data [37], features from strongly de-shielded protons originating from $–CH=C–NO_2$, $–CH_2–CH=CH–$ and –CH=CH–CH= groups, at ~7.52, ~6.32 and ~6.19 ppm, respectively, as product from nitration of linoleic acid, are also expected to appear at in the spectrum, however they are not observable in Figure S9a–9c and S10a–d in SI. The identification of nitro group using FTIR characterization as band at ~1557 cm^{-1} arising from asymmetric stretching vibrations, discussed in the previous subsection, undoubtedly refers that nitro-fatty acids and their esters are being synthesized. Hence, the probable explanation for not observing the abovementioned ^1H NMR features (6.2–7.5 ppm) associated to highly de-shielded protons, could be lack of conjugations between the C=C double bonds and/or between C=C double bonds and nitro group in the reaction products. This is possibly suggesting that the nitration mechanism is either based on synthesis of unsaturated- but non-conjugated compounds via hydrogen abstraction that could also involve double-bond rearrangement mechanism, or saturated nitro-fatty acids and their esters via nitro group addition mechanism [37-40].

Finally, when pristine TBAI is treated with NO_2 gas (Sample 6), slight shielding effect of the protons in the *n*-butyl groups can be observed in the ^1H NMR spectra compared to pristine TBAI (Table S6 and Figure S12a, b vs. S11a, b in SI). The explanation for the upfield shift possibly is a consequence to formation of the I_3^- anion, i.e. $TBAI_3$, when the I^- anion from TBAI and I_2 react (Eq. 1). The I_3^- represents a linear anion with delocalized electronic structure, showing less tendency for electron attraction compared to the I^- anion, hence causing shielding effect in the four *n*-butyl groups protons. Furthermore, an interesting observation is present in the ^1H NMR spectra of Sample 6, that is a weak broad feature at 7.52 ppm. Features around that position are characteristic for strongly de-shielded aromatic protons [35], but in this case, such feature is possibly attributed to a proton that is directly interacting with the electronically delocalized I_3^- anion.

The process of latent fingerprints visualization and the most important findings from the systematic spectroscopic characterization combined with various control and validation experiments are depicted in Scheme 1.

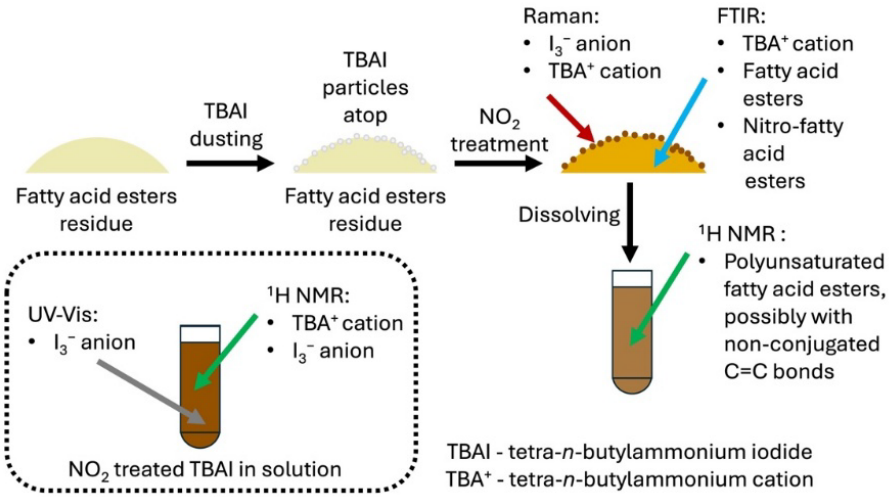

Scheme 1. Visualization of sebaceous latent fingerprints, characterization approach and results.

CONCLUSIONS

A two-step method intended for visualization of sebaceous latent fingerprints, on various porous and non-porous surfaces, is proposed in this research, based on tetra-*n*-butylammonium iodide (TBAI) dusting, followed by treatment with NO_2 gas (TBAI/NO_2 method).

The proposed method is simple, fast and reliable. It shows very significant identification capacity by reaching high number of second-level characteristics and additionally third-level features can be revealed.

The characterization with Raman spectroscopy identified I_3^- anion when TBAI pre-dusted fingerprints are treated with NO_2 gas and moreover identified both I_3^- anion and features associated to TBA^+ cation when TBAI powder is treated with NO_2 gas, suggesting formation of tetra-*n*-butylammonium triiodide – $TBAI_3$.

The UV-Vis spectroscopy characterization of the product, obtained from NO_2 treatment of TBAI, shows features that are characteristic for both I_3^- anion and molecular I_2, suggesting that both species are in equilibrium and the latter specie is formed via NO_2 caused oxidation of the I^- anion from

TBAI. I_2 further reacts with excess TBAI leading to formation of I_3^- anion i.e. $TBAI_3$. The molecular I_2 and the processes leading to its formation play the key role in the fingerprint's visualization mechanism, while $TBAI_3$ that resembles dark color, is providing the dominating contrast in the fingerprint's visualization process versus the substrates background surface.

The I_3^- is also identified on a fingerprint that was visualized two months prior to characterization, showing that the visualized fingerprints are composition-wise stable, making the proposed $TBAI/NO_2$ method very suitable for preserving forensic evidence.

FTIR and ^1H NMR spectroscopy characterization revealed that, even though the reaction between I_2 and excess TBAI, obtaining dark colored $TBAI_3$, is the main process leading to latent fingerprints visualization, the formation of nitro fatty acid esters, possibly with non-conjugated C=C bonds, caused by nitration of the lipidic residues, is also contributing towards the coloration effect considering that such nitro compounds appear orange-yellowish to brown in color.

The color outcome of the visualized fingerprints is mostly dependent on the TBAI coverage during the process of surface dusting and finally, besides a reactant, TBAI plays a role as a phase-transfer catalyst that allows NO_2 to penetrate into the bulk of fingerprint's sebaceous residue, thus subjecting this material to nitration reactions.

EXPERIMENTAL SECTION

The latent sebaceous fingerprints are deposited on various porous and non-porous surfaces (Table 1 and Table 2) using right hand forefinger after rubbing the forefinger near the nose. The visualization procedure encompasses two steps: Brush dusting of the latent fingerprints with powdered TBAI, followed by 5 seconds exposure to NO_2 gas (Figure 1 – visualized fingerprints). The NO_2 gas is generated by reaction between Zn pellets and 1:1 diluted HNO_3 [13]. After the visualization process, the fingerprints are subjected to forensic evaluation. The fingerprints, as well as the validation samples are characterized using spectroscopic methods (Raman, UV-Vis, FTIR and ^1H NMR spectroscopy). All details regarding the utilized reagents, methodology, validation experiments and characterization procedures can be found in the Supplementary Information – SI file.

Supplementary Information:

SI file is uploaded on zenodo.org and available at:
https://doi.org/10.5281/zenodo.19711846

ACKNOWLEDGMENTS

The authors are thankful to Mr. Manish Kumar of Sophisticated Analytical Instrumentation Facility (SAIF) Center, Panjab University, Chandigarh, India, for extending the facilities for NMR analysis.

REFERENCES

1. D. A. Crown, *J. Crim. L. & Criminology* **1969**, *60*, 258-264 https://scholarlycommons.law.northwestern.edu/jclc/vol60/iss2/17
2. O. P. J. M. I. U. A. Singla, *Identification Evidence* **2003** https://www.researchgate.net/profile/O-P-Jasuja/publication/372941076
3. W. J. Watling; K. O. Smith; *J. Forensic Identif.*, **1993**, *43*, 131-134 https://www.ojp.gov/ncjrs/virtual-library/abstracts/heptane-alternative-freonninhydrin-mixture
4. N. Meylan; C. J. Lennard; P. A. Margot; *Forensic Sci. Int.*, **1990**, *45*, 73-83 https://doi.org/10.1016/0379-0738(90)90223-L
5. P. F. Kelly; R. S. P. King; B. Shah; R. J. Mortimer; presented at *SPIE Security + Defence*, Berlin, Germany **2009** https://doi.org/10.1117/12.833980
6. B. C. Shah; *Doctor of Philosophy Doctoral Thesis*, *Loughborough University*, Loughborough, **2013** https://hdl.handle.net/2134/12533
7. K. T. Clarke; S. L. Cresswell; W. J. Gee; *Analyst* **2023**, *148*, 5547-5563 http://dx.doi.org/10.1039/D3AN01112G
8. S. M. Bleay; M. J. Bailey; R. S. Croxton; S. Francese; *WIREs Forensic Science*, **2021**, *3*, e1403 https://doi.org/10.1002/wfs2.1403
9. O. P. Jasuja; A. Kaur; P. Kumar; *Forensic Sci. Int.*, **2012**, *223*, e47-e52 https://doi.org/10.1016/j.forsciint.2012.09.013
10. K. Kumari Sharma; G. H. Kannikanti; T. R. R. Baggi; J. R. Vaidya; *J. Forensic Sci.*, **2019**, *64*, 1859-1866 https://doi.org/10.1111/1556-4029.14139
11. V. Singh; P. Mandal; S. Stojkovikj; M. Najdoski; O. Slobodan; O. P. Jasuja; *J. Indian Chem. Soc*.,**2025**, *102*, 101694 https://doi.org/10.1016/j.jics.2025.101694
12. M. J. Baker; J. Trevisan; P. Bassan; R. Bhargava; H. J. Butler; K. M. Dorling; P. R. Fielden; S. W. Fogarty; N. J. Fullwood; K. A. Heys; C. Hughes; P. Lasch; P. L. Martin-Hirsch; B. Obinaju; G. D. Sockalingum; J. Sulé-Suso; R. J. Strong; M. J. Walsh; B. R. Wood; P. Gardner; F. L. Martin; *Nat. Protoc*., **2014**, *9*, 1771-1791 https://doi.org/10.1038/nprot.2014.110
13. S. Stojkovikj; S. Oklevski; O. P. Jasuja; M. Najdoski; *Forensic Chem*., **2020**, *17*, 100196 https://doi.org/10.1016/j.forc.2019.100196
14. B. T. Ulery; R. A. Hicklin; G. I. Kiebuzinski; M. A. Roberts; J. Buscaglia; *Forensic Sci. Int*., **2013**, *230*, 99-106 https://doi.org/10.1016/j.forsciint.2013.01.012
15. M. K. Thakar; T. Sharma; *Egypt. J. Forensic Sci*., **2016**, *6*, 194-201 https://doi.org/10.1016/j.ejfs.2016.05.008

16. L. Andrews; E. S. Prochaska; A. Loewenschuss; *Inorg. Chem.*, **1980**, *19*, 463-465 https://doi.org/10.1021/ic50204a036
17. J. C. Rubim; O. Sala; *J. Raman Spectrosc.*, **1981**, *11*, 320-321 https://doi.org/10.1002/jrs.1250110505
18. P. H. Svensson; L. Kloo; *J. Chem. Soc., Dalton Trans.*, **2000**, 2449–2455 https://doi.org/10.1039/B002492I
19. A. J. Blake; C. Castellano; V. Lippolis; E. Podda; M. Schröder; *Acta Crystallogr. C*., **2024**, *80*, 311-318 https://doi.org/10.1107/S2053229624004194
20. Y. Jin; M. Kida; J. Nagao; *J. Chem. Eng. Data*, **2016**, *61*, 679-685 https://doi.org/10.1021/acs.jced.5b00842
21. R. Chromá; M. Vilková; I. Shepa; P. Makoś-Chełstowska; V. Andruch; *J. Mol. Liq*., **2021**, *330*, 115617 https://doi.org/10.1016/j.molliq.2021.115617
22. N. Hattori; M. Hara; H. Okabayashi; C. J. O'Connor; *Colloid Polym. Sci*., **1999**, *277*, 306-317 https://doi.org/10.1007/s003960050386
23. Y. Miwa; T. Nagahama; H. Sato; A. Tani; K. Takeya; *Molecules* **2022**, *27*. https://doi.org/10.3390/molecules27154743
24. E. O'Neill; R. Z. Hinrichs; Journal of Geophysical Research: *Atmospheres* **2011**, *116* https://doi.org/10.1029/2010JD014880
25. R. Xian; G. Corthey; D. M. Rogers; C. A. Morrison; V. I. Prokhorenko; S. A. Hayes; R. J. D. Miller; *Nat. Chem*., **2017**, *9*, 516-522 https://doi.org/10.1038/nchem.2751
26. J. M. Gardner; M. Abrahamsson; B. H. Farnum; G. J. Meyer; *J. Am. Chem. Soc*., **2009**, *131*, 16206-16214 https://doi.org/10.1021/ja905021c
27. K. D. Mekonnen; Heliyon **2023**, *9* https://doi.org/10.1016/j.heliyon.2023.e14699
28. A. S. Anderson; J. E. Fulton; *J. Investig. Dermatol*., **1973**, *60*, 115-120 https://doi.org/10.1111/1523-1747.ep12682018
29. K. Nakamoto, Infrared and raman Spectra of inorganic and coordination compounds. In *Handbook of Vibrational Spectroscopy*, E. J. M. Chalmers., P. R. Griffiths Eds.; John Wiley & Sons, Ltd., New York, **2006**. https://doi.org/10.1002/0470027320.s4104
30. A. Girod; R. Ramotowski; C. Weyermann; *Forensic Sci. Int*., **2012**, *223*, 10-24 https://doi.org/10.1016/j.forsciint.2012.05.018
31. A. Pappas; J. Fantasia; T. Chen; *Dermatoendocrinol.*, **2013**, *5*, 319-324 https://doi.org/10.4161/derm.25366
32. P. P. Chiplunkar; A. P. Pratap; *Prog. Org. Coat*., **2016**, *93*, 61-67 https://doi.org/10.1016/j.porgcoat.2016.01.002
33. A. S. Hume; W. C. Holland; F. Fry; *Spectrochim. Acta A Mol. Biomol. Spectrosc*., **1968**, *24*, 786-788 https://doi.org/10.1016/0584-8539(68)80109-6
34. N. Zaltsman; D. Kesler-Shvero; E. I. Weiss; N. Beyth; *J. Appl. Biomater. Funct. Mater.*, **2016**, *14*, 205-211 https://doi.org/10.5301/jabfm.5000269
35. R. M. Silverstein; F. X. Webster; D. Kiemle; *Spectrometric Identification of Organic Compounds*, 7th Edition, John Wiley & Sons, New York, **2005**
36. M. Hassan; S.-C. Krieg; C. Ndefo Nde; J. Roos; T. J. Maier; E. A. El Rady; M. A. Raslan; K. U. Sadek; G. Manolikakes; *Eur. J. Org. Chem.*, **2021**, *2021*, 2239-2252 https://doi.org/10.1002/ejoc.202100247

37. M. Fazzari; S. R. Woodcock; P. Rowart; K. Ricart; J. R. Lancaster; R. Patel; D. A. Vitturi; B. A. Freeman; F. J. Schopfer; *Redox Biol.*, **2021**, *41*, 101913 https://doi.org/10.1016/j.redox.2021.101913
38. S. R. Woodcock; G. Bonacci; S. L. Gelhaus; F. J. Schopfer; *Free Radic. Biol. Med.*, **2013**, *59*, 14-26 https://doi.org/10.1016/j.freeradbiomed.2012.11.015
39. V. B. O'Donnell; J. P. Eiserich; P. H. Chumley; M. J. Jablonsky; N. R. Krishna; M. Kirk; S. Barnes; V. M. Darley-Usmar; B. A. Freeman; *Chem. Res. Toxicol.*, **1999**, *12*, 83-92. https://doi.org/10.1021/tx980207u
40. W. A. Pryor; J. W. Lightsey; D. F. Church; *J. Am. Chem. Soc.*, **1982**, *104*, 6685-6692 https://doi.org/10.1021/ja00388a035
41. S. D. Caño-Ochoa; A. Ruiz-Aracama; M. D. Guillén; *Antioxidants*, **2022**, *11*, 722 https://doi.org/10.3390/antiox11040722
42. G. R. Fulmer; A. J. M. Miller; N. H. Sherden; H. E. Gottlieb; A. Nudelman; B. M. Stoltz; J. E. Bercaw; K. I. Goldberg; *Organometallics*, **2010**, *29*, 2176-2179 https://doi.org/10.1021/om100106e

STUDIA UBB CHEMIA, LXXI, 2, 2026 (p. 265-288)
(RECOMMENDED CITATION)
DOI:10.24193/subbchem.2026.2.14

EVIDENCE OF ABNORMAL HIGH SILVER CONTENT IN A POLISH POLOTRAK COIN ISSUED IN 1624 AS CONSEQUENCE OF ADVANCED COPPER CORROSION

Nicoleta IGNAT[a], Emanoil PRIPON[b], Simona Elena AVRAM[c], Lucian Barbu TUDORAN[d,e], Gheorghe BORODI[e], Ioan PETEAN[a*], Marzena GROCHOWSKA-JASNOS[f*]

ABSTRACT. Long ground resting of coins small denomination might affect their microstructure due to advanced corrosion. It is well known that cleaning of silver-copper alloy artifacts leads to a surface enrichment of the silver amount due to the partial removal of the copper grains which are more corroded. We found a półtorak issued in 1624 with abnormal characteristics like lower weight and dull sound when it is thrown on the solid surfaces. It resulted to be made of very high silver content about 97 wt. % according SEM-EDX correlated with XRD in great discordance with the common półtoraks from 1624 having about 70 wt.% silver. Advanced investigation of the abnormal półtorak reveals a porous internal structure indicating complete dissolution of β grains and copper sheets within the eutectic. All observation pleads for a progressive corrosion involving partial leaching of product through the wet resting ground which might ensure the dissipation of the corrosion-product and affecting deeper layers. Such dynamic-corrosion for

[a] *Faculty of Chemistry and Chemical Engineering, Babes-Bolyai University, 11 Arany Janos Street, 400028 Cluj-Napoca, Romania.*
[b] *Zalau County Museum of History and Art, 9 Unirii Street, 450042, Zalau, Romania.*
[c] *Faculty of Materials and Environmental Engineering, Technical University of Cluj-Napoca, 103-105 Muncii Bd., RO-400641, Cluj-Napoca, Romania.*
[d] *Faculty of Biology and Geology, Babes-Bolyai University, 44 Gheorghe Bilascu Street, 400015 Cluj-Napoca, Romania.*
[e] *National Institute for Research and Development of Isotopic and Molecular Technologies, 65-103 Donath Street, 400293 Cluj-Napoca, Romania.*
[f] *Museum of Archaeology and History in Głogów, Brama Brzostowska 1, 67-200 Głogów, Poland.*
[*] *Corresponding authors: ioan.petean@ubbcluj.ro; marzena.grochowska@gmail.com*

300 years might explain this intragranular corrosion which transforms an Ag-Cu hypereutectic alloy into almost pure silver. This preliminary hypothesis must be further investigated on larger półtoraks hoards which might have such abnormally corroded coins and on suspicious random finds.

Keywords: *półtorak, microstructure, corrosion, copper loss*

INTRODUCTION

Półtorak coins issued by King Sigismund III of Poland had a great impact in the monetary circulation during 17th century with real impact in early 18th century supplying demand of small trustful silver coins. Their relative steady quality makes them desirable for daily commerce and is found in many hoards discovered in whole Central and Eastern Europe [1, 2].

Półtoraks, silver coins worth one-and-half groschen (pol. *grosz*) are among the most distinctive types of small money minted in the Polish-Lithuanian Commonwealth during the reign of Sigismund III Vasa (1587–1632). The introduction of this denomination in 1614 was a response to the shortage of small coins in the west border areas of the Polish Kingdom, which had been ongoing since the late 16th century, and to the growing influx of weaker German coins, including the so-called "apple" groschen from Brandenburg. In this way, the półtoraks became not only a means of payment within the country but also a component of Poland's monetary and economic expansion into neighbouring European markets.

Circulating alongside Hungarian denars, Imperial groschen and Czech groschen, they met the need for small change in everyday trade, whilst also serving as a tool for speculation and manipulation by experienced traders, who exploited the general monetary confusion to inflate the value of individual currency units [3]. This is evidenced by the fact that one-and-a-half-groschen (półtorak) coins are found alongside other small denominations minted at that time in Central European countries. The situation in the money market of Central and Eastern Europe was brought under control to some extent following a series of reforms implemented in 1659 by Emperor Leopold I in the Roman-German Empire, and in the early 1660s and 1670s in the Polish-Lithuanian Commonwealth, as well as through the imperial ordinances of Zinna (1667) and Leipzig (1690) [4, 5]. Półtoraks, even more than Polish half-groschen (pol. *półgrosz)* and 3-groschen (pol. *trojak*) coins, were the most common Polish coins in the first half of the 17th century in Austria, Bohemia,

Moravia and Silesia, but also to the east and south-east of Poland – in Ukraine, Slovakia, Hungary and Romania, as well as other Balkan countries within the sphere of Turkish influence (Ottoman Empire) [3, 5, 6, 7].

The moment of the Polish półtorak entering Transylvania has long been disputed in Romanian numismatics. In 1964, Costin C. Kirițescu, referring to the monetary circulation in the period 1620-1625, stated that Polish półtoraks are present in large quantities [8]. Eugen Chirilă also advanced the idea of the półtoraks entering immediately after 1620, with the subsequent clarification that, since they needed four to six years to reach Transylvania, the maximum flow of coins occurred in the years 1627-1629 [9]. Judita Winkler rejected the idea of the massive penetration of Polish półtorak in the second half of the third decade of the 17th century [10], and the Hungarian numismatist János Buza also supported the idea of the massive penetration of półtorak into monetary circulation in Transylvania, since the first years of Gabriel Bethlen's reign, but demonstrates that these issues were not to blame for triggering the monetary crisis in the first half of the third decade, as was long believed [11].

In 2016, Corina Toma published the results of an analysis carried out on a batch of 38 monetary hoards (with over 19,900 coins, of which półtoraks represented 77%, present in 32 hoards), belonging to the chronological group 1625/1626-1668 [11]. According to this analysis, it places the penetration of Polish coins with a value of one and a half groschen, only after the death of Gabriel Bethlen, when a new wave of Polish currency, to which is added, in overwhelmingly smaller percentages, półtoraks issued in Elbing, Riga, Brandenburg-Prussia (Königsberg), in the second and third decade of the 17th century, still in circulation in Poland [11]. Although the first early attestation of półtoraks in hoards was made with the discovery of a hoard from Zalău with eight półtoraks issued during 1622-1625, we subscribe to the opinion that this monetary type entered Transylvania towards the end of the third decade-beginning of the fourth decade of the 17th century [7]. In the hoards of Transylvania, the issue of 1624 counts 2869 pieces [11].

A study conducted on a batch of medieval coins, part of a hoard of about 1400 coins discovered in Iași, highlighted the fact that some of the coins showed advanced intragranular corrosion, which led to their disintegration. Also, due to the long period of lying in the soil, the surface of the coins was affected by the selective corrosion process, resulting in an increase in the concentration of silver on the surface, in relation to the coin as a whole. The surface silver enrichment process is responsible for the apparent silvering appearance, observed in cross-section, by optical microscopy

[12]. Of course, the cross section metallographic investigation of a coin reveals valuable information of the surface and bulk microstructure but very often consists of complete damage of the investigated coin. However, the enriched silver outermost layer can be gently removed from a small, targeted area allowing a proper investigation of the coin's bulk without sectioning it.

The półtoraks conservation state strongly depends on the long resting in the ground and its physicochemical parameters such soil composition and moistening degree. A minor mishandling of a półtorak issued in 1624 reveals abnormal characteristics like increased brittleness and fragile structure associated with reduced weight and dull sound when it is ringed on the solid surface. This behavior is completely different than well preserved półtoraks issued in the same year. Therefore, the aim of the present study is to effectuate a comparative physicochemical investigation between a regular półtorak issued in 1624 and the abnormal one. The microstructural investigations assisted by high resolution SEM coupled with EDX elemental analysis can provide useful clues for proposing a corrosion mechanism. Thus, an advanced intra granular corrosion of the coins facilitated by the long resting in a specific soil might involve with some hydro soluble product. Its repeated contact with pluvial water infiltration might leak copper from the microstructure altering the coins characteristics, a fact which will be further discussed.

RESULTS AND DISCUSSION

Most of the półtoraks were issued in the Bydgoszcz mint, having a constant design pattern. Photographs of the investigated coins are presented in Figure 1. The obverse feature Poland kingdom shield with Wasa family arms in the middle covered with the kingdom crown. The surrounding legend text feature SIGIS 3 D G REX PMDL divided by a small shield with numeral 3 (meaning equivalent to 3 half groschen) meaning Sigismund the III-rd by God's mercy King of Poland and Grand Duke of Lithuania. The reverse features an orb with a cross with inscription 24 below the cross meaning that 24 of such coins are equal to one thaler. The year is marked by numerals divided by the cross respectively 2 and 4 (1624). The surrounding legend feature MONE NO REG POLO meaning new coin issued by the king of Poland, divided by the grand treasurer's arms, a vertical arrow flanked by two stars with a moon crescent on the base, these symbols are surrounded by square brackets making the appearance of a smiley face.

Figure 1. Investigated samples: a) well preserved półtorak issued in 1624 and b) abnormally corroded półtorak from 1624.

Figure 1a, feature the general aspect of the good coin reference having the striken details very well preserved with a sharp detail. The abnormal półtorak is presented in Figure 1b revealing partly swelled details of the text and cross arms. There were found significant metrological differences between them, Table 1. Literature data reveal that pure silver density is about 10.49 g/cm^3 and copper density is 8.96 g/cm^3 [13, 14].

Table 1. Metrological characteristics of the investigated coins

Sample	Diameter, mm	Thickness, mm	Weight, g		Temp., °C	ρ_{water}, g/cm^3	ρ_{sample}, g/cm^3	Alloy, wt. %	
			air	water				Ag	Cu
a	19	0.56	0.9219	0.8298	22.1	0.9877	9.98	70.07	29.93
b	19	0.71	0.7414	0.6361	22.1	0.9978	7.02	-	-

Thus, the well preserved półtorak is situated in the hypereutectic domain closely after the eutectic position [15]. Copper amount increase causes a the alloy denisity decreasing. It would have been espected that the abnormally corroded półtorak to have too much copper but its density is far below than pure copper, Table 1. Since the abnormally corroded coin has a fine silvery aspect, we wonder what it might happened there to affect the density. Microstructural observations are required.

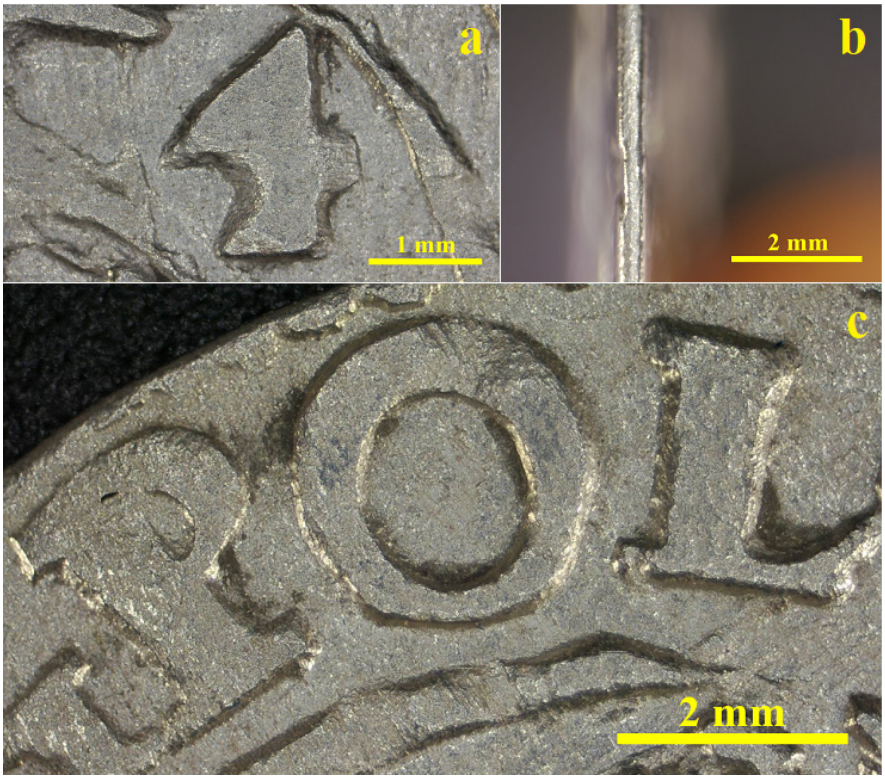

Figure 2. Macrostructural details observed at low magnification (x10) in reflected light of the well preserved półtorak issued in 1624: a) detail on year distinctive number 4, b) coin's edge aspect and c) aspect of the coin's text.

Figure 2 reveal the low magnification aspect of the well preserved półtorak surface. The date numeral 4 has a sharp edged shape well imprinted into the alloy and has heavy worn marks on the top as consequence of intensive circulation, Figure 2a. Since the coins were cleaned without aggressive chemicals the silver enriched areas are found only on the lower areas of the surface while the top of inscription are heavily worn and thus it makes them less prone to the silver enrichment [1]. Moreover, choosing a proper microstructural area like the numeral 4 or the character L for a micro polishing with 8000 grains sand paper followed by gentle felt brushing with colloidal alumina ensures a proper removal of the silver enriched layer and optimally prepares the targeted micro area for metallographic observation. The coin's edge, Figure 2b, is well defined without microstructural flaws.

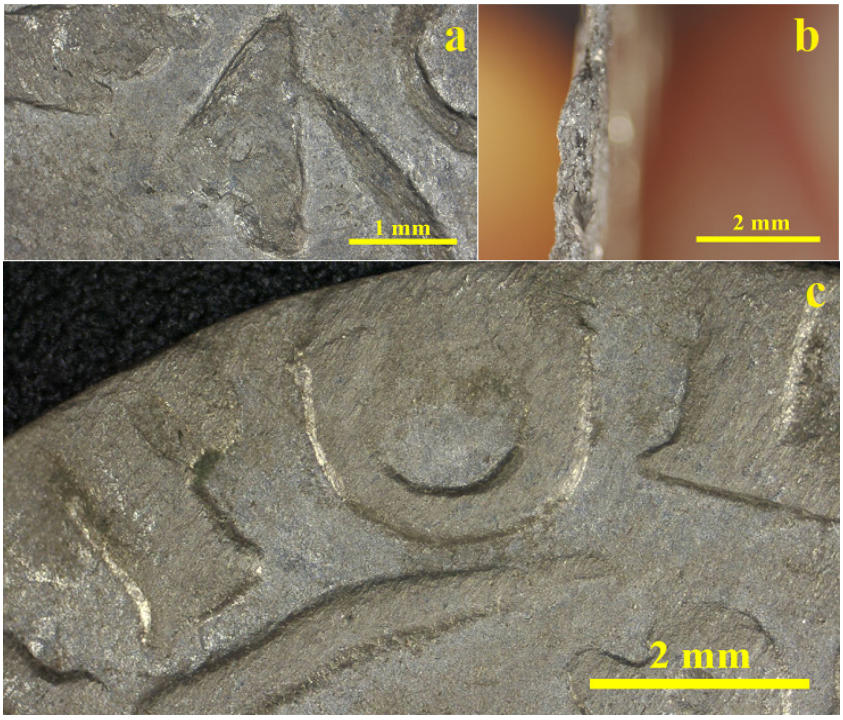

Figure 3. Macrostructural details observed at low magnification (x10) in reflected light of the abnormally corroded półtorak from 1624: a) detail on year distinctive number 4, b) coin's edge aspect and c) aspect of the coin's text.

Circular text of the coin is also well stricken into the coin blank with well defined characters, minor oxidation marks appear as dark spots on the O character from inscription. The abnormally coroded coin has a deeply worn year numeral, Figure 3a, with fuzzy edges partly generated by the intensive worn from caused by prolonged circulation, fact sustained by the faded inscription of POL in Figure 3c. The lower areas of the surface are well preserved showing a extremly good looking enriched silver layer (caused by the removal of the corrosion products) but top areas of inscription being heavily worn resemble better the bulk characteristics. The biggest surprise occurs on the coin's edge examination, Figure 3b. It is blunted featuring deeper internal fissures which causes the increase of the edge thickness which almost become double than the one of the well preserved coin. It is the first phisical proof that something abnormal issue affects the coin integrity. X ray diffraction (XRD) effectuated on the coin's reverse which was gently brushed with felt disc reveal the overall phase composition of the alloy, Figure 4.

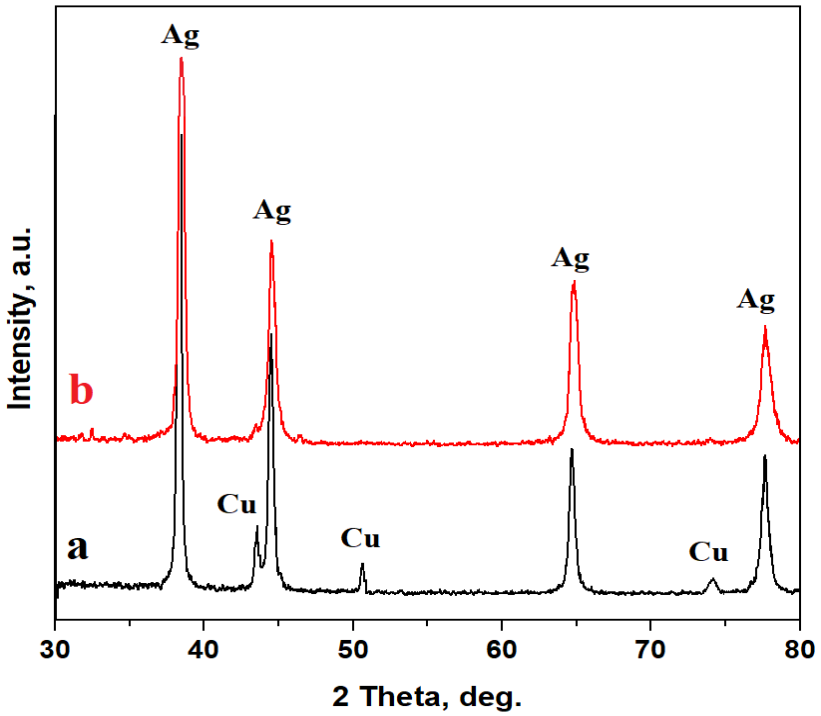

Figure 4. XRD patterns of the investigated samples: a) well preserved półtorak issued in 1624 and b) abnormally corroded półtorak from 1624. Peaks assignment according PDF 89-3722 for Ag and PDF 89-2838 for Cu.

The well preserved półtorak reveal an XRD pattern with well developed peaks belonging to Ag and Cu. Relative Intensity Ratio (RIR) method allow to calculate the mass participation of each identified phase corelating the relative intensity of the specific peaks with the corrundum factor of the identified phases [16, 17]. It results that the well preserved poltorak has a silver content of 69 wt. % and 31 wt. % copper which is in good accordance with the composition determined from the coin's density and agrees our previous observations on the poltoraks issued in 1624 [1].

On the other hand the abnormally corroded półtorak has an astonishing composition made of pure silver without copper. It is in a fragrant disagreement with the observations made uppon the density variation. Thus, the metallographic investigation of the bulk microstructure is mandatory, Figure 5.

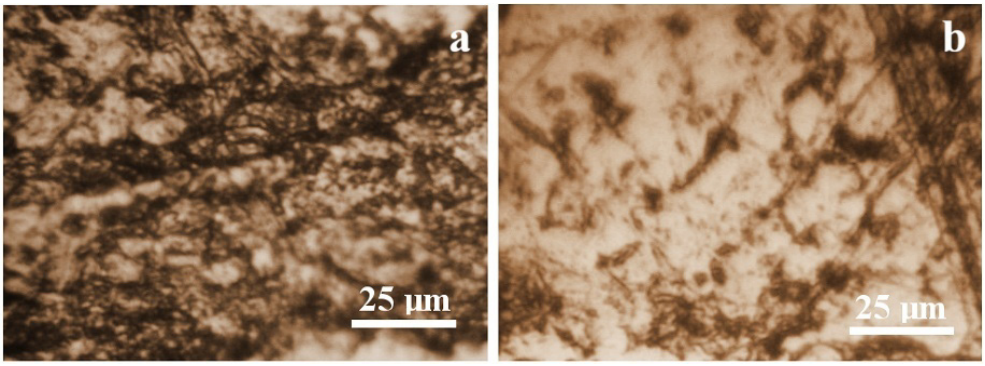

Figure 5. Metallographic microscopy images of: a) well preserved półtorak issued in 1624 and b) abnormally corroded półtorak from 1624.

The metallographic aspect of well preserved półtorak, Figure 1a, reveal a dense matrix of eutectic grains having white appearance with darken lamellas within alternating with compact dark grains of β phase. Both of the grains are elongated under the rolling dirrection and have a length of about 20 – 25 µm and a width of 8 – 12 µm. It confirm a normal microstructure of a hypereutectic Ag-Cu alloy which was subjected to rolling lamination and subsequent stricking.

On the opposite, the abnormal półtorak reveal a predominant α grains matrix spoted with corroded eutectic grain remains. The copper loss from the microstructure is evident, however the grain texturing clearly indicate elongation under the rolling dirrection but it is difficult to establish a precise size because of removal of the advanced intergranular corrosion product which let the grain boundaries fuzzy. The α grains can be estimated with a length of 20 µm and width of about 10 µm while the eutectic grains remains are about 25 µm length and width is difficult to be established. High resolution SEM images are required to elucidate better these microstructural aspects.

SEM investigation sustains the optical microscopy observation regarding the overview of the microstructural aspects of the well preserved półtorak, Figure 6a. It is clearly observed that the mild felt brushing let the lower areas untouched while the enriched silver outermost layer on the top worn areas was successfully removed revealing the true bulk microstructure as observed in the detail cached in Figure 6b.

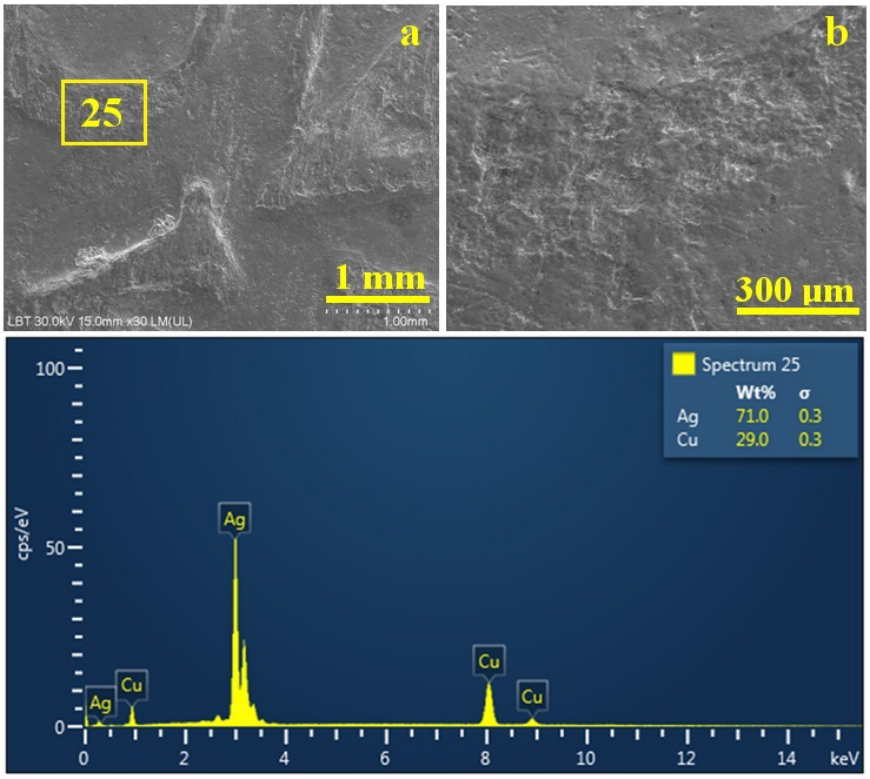

Figure 6. Overall aspect of the well preserved półtorak observed by SEM:
a) macrostructure view, b) overall microstructure and
c) EDS spectrum of overall elemental composition.

EDS spectrum was taken on these worn areas, spectrum 25 in Figure 6c. It reveals the elemental composition of the alloy resulting in 71 wt.% Ag and 29 wt.% Cu being in great agreement with the XRD and density related measurements. Since the density based calculation of the alloy composition is certainly related to the bulk composition, the confirmation of the surface based measurements like XRD and SEM-EDX prove the efficiency of mild felt brushing in removal of the cleaning silver enriched outer most layer within the worn areas. Moreover, the targeted metallographic preparation of such certain areas allows an optimal view of the grain's microstructure through SEM – EDS investigation, Figure 7.

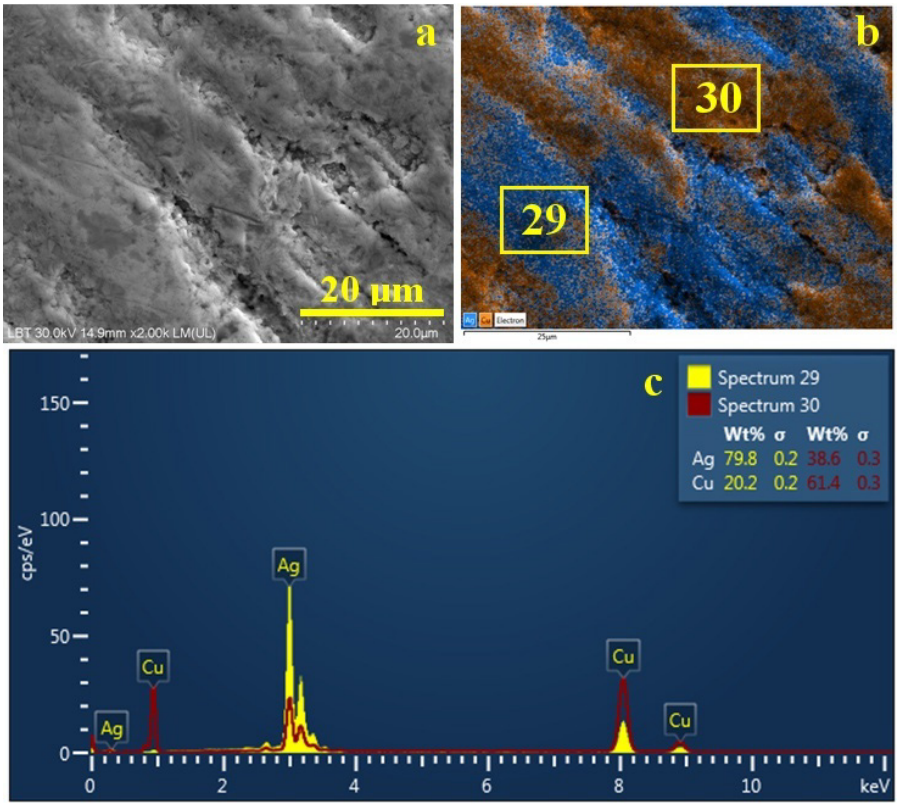

Figure 7. Microstructural constituents of the well preserved półtorak observed by SEM: a) SEI image, b) BSE image with superimposed elemental map, and c) EDS spectra comparison between eutectic grains (blue – spectrum 29) and β phase grains (orange – spectrum 30).

Secondary electron image (SEI) of the micro polished and lustred area of the well reserved półtorak reveal a smooth surface making rather difficult observing grains, some eroded eutectic grains are obvious in the central and lower right area of the image indicating partly breaking of the thin lamellas as consequence of intensive circulation worn as reported in our previous study [1]. Backscattered electron image (BSE) overlapped with the elemental distribution, Figure 7b, reveals better the grains microstructure. Eutectic grains have a blue appearance spotted with fine orange points while pure copper β has an orange aspect. They are elongated in the rolling direction proving the mechanical processing of silver alloy sheet prior striking. Grains

elemental composition was investigated with targeted EDS spectra. Spectrum 29 was taken on the blue grains revealing an amount of 79.8 wt.% Ag and 20.2 wt.% Cu very close to the eutectic composition. Spectrum 30 was taken on a orange grain revealing dominance of copper as 61.4 wt.% within the β phase while the silver remains of 38.6 wt.% belongs to the eutectic grains boundaries that were partly caught in the EDS sampling spot.

Overall, the well preserved półtorak issued in 1624 has a good cohesion of the internal microstructure explaining the metallic sound when it is thrown on the solid surfaces (e.g. table, floor, and pavement). Such testing method was very popular when these coins were in circulation to distinguish them from the lead and thin forgeries which have dull sound when they are throw on solid surfaces [18, 19]. Despite the dull sound, our abnormal półtorak is made almost pure silver having an abnormal density. It clearly indicates severe microstructural flaws which require advanced investigations.

Its surface is well preserved as a consequence of the striking dies punching alloy ensuring a smooth and uniform lower areas, Figure 8a. The inscriptions are relatively swelled having a large curvature connection with the lower areas instead of the sharp connection implying a small curvature radius observed on the normal półtorak, in good agreement with optical microscopy. SEM imagining confirms that the top of inscriptions is deeply worn. Figure 8b presents a microstructural detail of the worn areas. The grains are quite eroded due to the intensive circulation of the coin but have extra eroded patterns as scaly structure suggesting in depth erosion of the microstructure via intra-crystalline corrosion.

The internal microstructure of the abnormal półtorak is properly observed on the damaged margin observed by optical microscopy in Figure 3b. SEM investigations were conducted to catch both damaged margin and a small part from adjacent lower areas from the coin surface, Figure 8c. The lower right corner evidence of excoriation of the top surface layer revealing deeply corroded microstructure beneath.

The surface has a smoother appearance compared to the damaged margin which reveals a deeply corroded microstructure of the coin. BSE image with elemental distribution map in Figure 8c reveals a uniform distribution of silver both on the surface and in the bulk of the coin (uniform blue color). Small orange points represent copper distribution which is very scarce on the surface and slightly more present in the damaged margin. Thus, spectrum 19 taken on the coin surface reveals a composition of 98.6 wt.% silver and 1.4 wt.%, Figure 8e. Spectrum 20 reveals the slightly appreciation of the copper content to 2.6 wt.% in the damaged margin. It suggests that the initial state of this coin contained much more copper in the bulk most likely a similar content as observed in the normal półtorak.

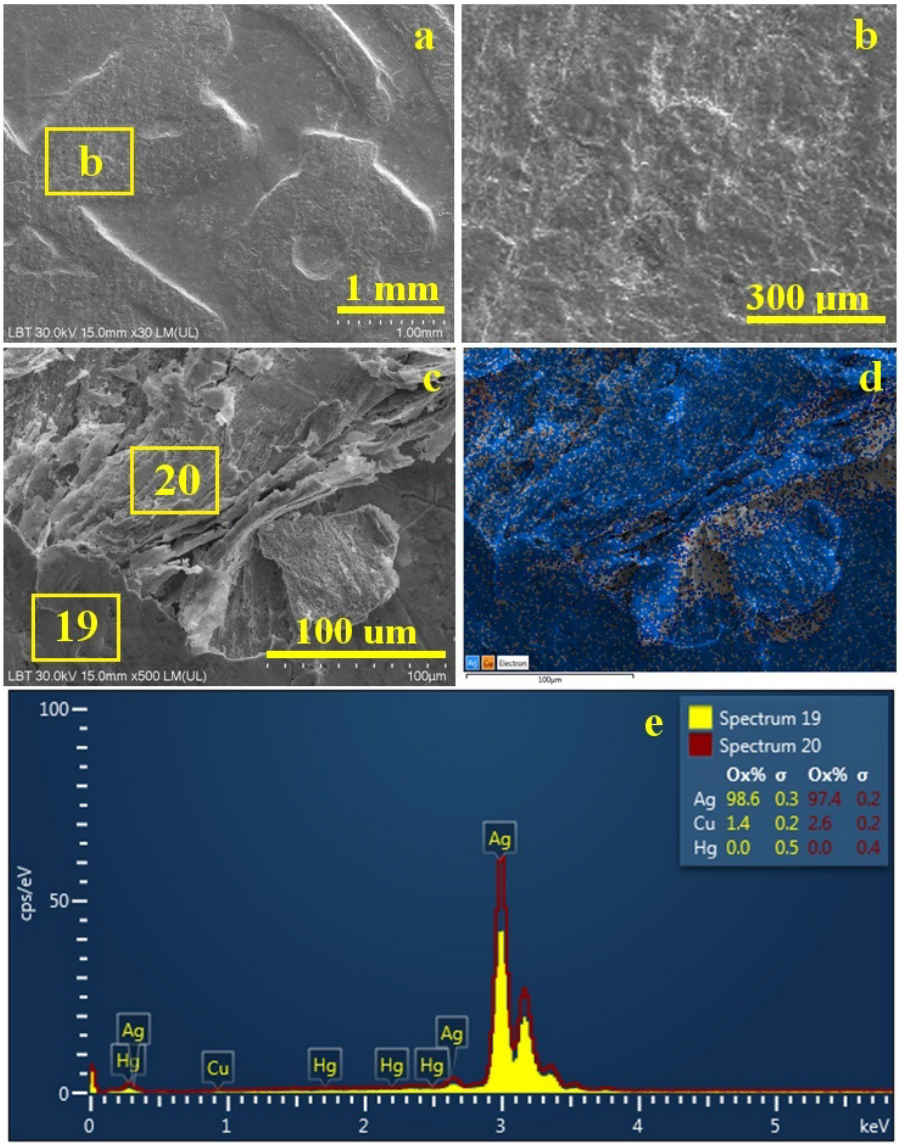

Figure 8. SEM images of the abnormally corroded półtorak: a) macrostructure view, b) overall microstructure and c) SEI image of microstructural detail of damaged margin of the coin, d) BSE image superimposed with the elemental map of the damaged margin of the coin, and e) EDS spectra taken on the coin surface and on the damaged margin.

Abnormal półtorak bulk microstructure, Figure 9a, is formed by grains elongated under the rolling direction respecting the pattern observed in the normal półtorak. Their length ranges from about 15 to 20 μm and their width ranges from about 3 – 8 μm. The abnormal aspect is given by the elongated pores resembling to the β grains within the normal alloy. The other grains are merely eroded into thin silver sheets, a fact better observed at high magnification in Figure 9b. Both abnormal situations are confirmed by spectrum 22 which reveal their composition as 97.8 wt.% Ag and only 2.2 wt.% Cu, Figure 9c.

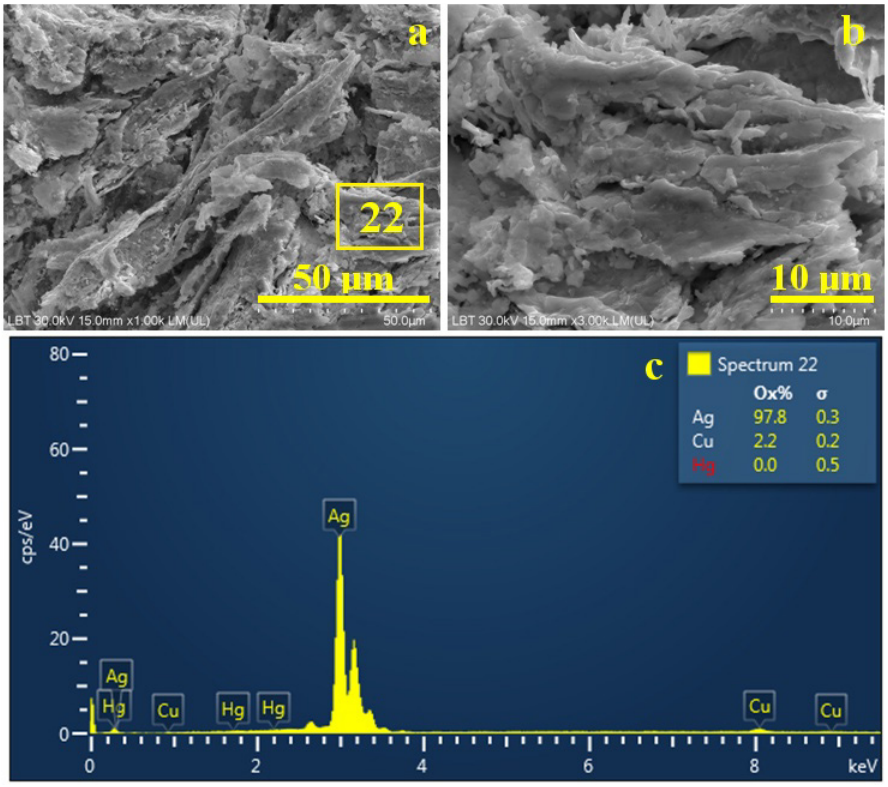

Figure 9. SEM images of the abnormally corroded półtorak broken side:
a) overall microstructure, b) microstructural detail, and
c) EDS spectrum of the microstructural detail.

SEM advanced microstructural investigations confirm that lower density of the coin is caused by large internal voids produced by an advanced corrosion which extract progressively copper from the microstructure. The

evidence is strongly sustained by all employed physicochemical investigation methods. Thus, we wonder how it was possible to extract selectively copper from the coin. It is well known that silver is more noble than copper and then is prone affected by corrosion [18]. Thus, a corrosion mechanism can be established based on literature.

Wet underground conditions induce the galvanic corrosion of the microstructure activating copper microstructural components as anode because of its higher reactivity while silver microstructural components play cathode role [19]. Thus, the microstructural decuprification occurs through the β grains and Cu lamellas within eutectic oxidization with formation of tenorite and cuprite:

$$2Cu + O_2 \rightarrow 2CuO \quad (1)$$

$$4Cu + O_2 \rightarrow 2Cu_2O \quad (2)$$

where CuO crystallizes as Tenorite having black color and Cu_2O crystallizes as cuprite having brown color [20, 21]. These further react with the salts dissolved in soil. The most aggressive enhancers of the underground corrosions are chlorides like sodium chloride which denaturizes copper oxides transforming them in sodium dichloro-cuprate:

$$Cu_2O + 4NaCl + H_2O \rightarrow 2Na[CuCl_2] + 2NaOH \quad (3)$$

The sodium dichloro-cuprate has a water solubility of 22.7 g/(100 mL) at 25 °C representing a high solubility that makes this corrosion product susceptible to dissolving in high moisture and prone to removal through the liquid dispersion through the ground particles. However, this reaction is very slow, taking a longer time to generate the soluble products [22, 23]. The laboratory reaction can be accelerated by acetic or hydrochloric acid.

Carbonate minerals from soil like calcite and aragonite $CaCO_3$ also interacts with copper oxides generating malachite as main corrosion product [19, 24]:

$$2Cu_2O + 2\ CaCO_3 + 4H_2O + O_2 \rightarrow 2Cu_2(CO_3)(OH)_2 + 2Ca(OH)_2 \quad (4)$$

where: $Cu_2(CO_3)(OH)_2$ is malachite which is insoluble in water but the other product $Ca(OH)_2$ slacked lime has a water solubility of 1.73 g/L at 20 °C and thus it might affect the natural balance of the corrosion products in high wet ground moisture facilitating corrosion products dissipation.

Literature reveals that sulfide that might occur in the resting ground does not directly react with copper or with copper oxides but however might affect the balance of the other reaction products [25].

Several corrosion products like tenorite, cuprite and malachite are practically insoluble in water than their tight deposits formed on the coins surface act as a shield preventing mineral loss. On the other hand, sodium dichloro-cuprate has a high solubility and slaked lime also has a limited water solubility facilitating the corrosion products evacuation through the moisture flow within the resting ground. Mineral diversity within resting ground could generate complex copper chlorides like atacamite $Cu_2Cl(OH)_3$ having a more complex chemical structure than sodium dichloro-cuprate and it is insoluble in water. However, its occurrence is strongly related to the arid conditions which imply moderate moisture. Considering the slow reaction rate of sodium dichloro-cuprate formation within high salted moisture soil facilitates slowly and progressive dissipation of this copper corrosion product into the adjacent environment. Continuing this process for several hundreds of years explains progressive decuprification of the półtorak microstructure preserving silver grains relatively untouched.

The corrosion products chemistry reveals that almost all copper-based compounds are practically insoluble in water excepting sodium dichloro-cuprate that forms into the aqueous state when halite crystals (sodium chloride crystallized in cubic system) are dissolved by pluvial water. Thus, the proposed mechanism explaining the abnormally corrosion pattern observed in 1624 półtorak works in sedimentary soil rich in calcium carbonate minerals like calcite and halides like sodium chloride.

Such soils are common in the Transylvanian basin due to the evaporitic deposits formed during Badenian age as consequence of intensive evaporation of water from Tethys Sea (covering actual areas of Transylvanian Basin and Pannonian Field) generating large deposits on the Praid – Sovata – Dej line up to Salaj County [26, 27, 28]. These salty soils are common in the półtorak discoveries areas and thus we might assume that some of the random finds might be affected by intensive corrosion.

Malachite belonging to carbonate minerals is situated in the noble patina components while atacamite is generate by resting grounds rich in halides altering the noble patina [29]. However, the patina stratification depends on the subsequent interactions and the coexistence of malachite and atacamite is reported as bronze disease where chlorides transform the compact noble patina in a green powdery corrosion product [30].

Pluvial water infiltration within such soils dissolves halite crystals generating sodium chloride aqueous solution which reacts directly with the copper oxide formed on the coins surface and generate sodium dichloro-

cuprate in aqueous solution which is dissipated away along with the water flux reducing the copper content. Considering this progressive corrosion pattern over few hundreds of years the decuprification affects deeply the alloy microstructure which losses the copper content enriching in silver, a fact in good agreement with literature data regarding intra-crystalline corrosion [12]. Moreover, it is confirmed by the oxygen presence in the elemental analysis of the broken side of abnormal półtorak but the content was subtracted from the analysis quantification to reveal only the alloy composition (the fact is properly displayed as Ox wt.% in the label of spectra 19, 20 and 22 in Figures 8e and 9c.

The lack of corrosion products associated with the abnormal półtorak and unknown resting ground consists of a main limitation of the present study. The proposed in deep progressive corrosion mediated by chlorides present in the resting ground consist in a good start point for advanced research implying fresh archeological discoveries of such coins, case in which soil samples and corrosion product samples can be collected properly and investigated prior to the complete cleaning of the coin.

Certainly the proposed corrosion mechanism is only a hypothesis that requires more advanced investigation on larger representative samples number preferably with the discovery place known. The lack of knowledge about the abnormally corroded poltorak makes difficult searching for soluble corrosion products that might explain more precise the leakage of copper from the microstructure. A fresh archeological discovery from scientifically investigated sites would be of great importance compared to random finds because the resting ground sampling will be possible as well as targeted collection of corrosion products from the coins surface prior cleaning. All these samples subjected to physicochemical investigations like the one performed in the present research will give important data for refining the advanced corrosion mechanism.

NUMISMATIC SIGNIFICANCE

Of course, large silver numismatic pieces such as thalers are more impressive from a numismatic point of view and on the other hand are less exposed to corrosion of the deeper layers. But, the everyday monetary circulation of ordinary people, such as buying and selling at the market, was mainly ensured by small coins, the basis being provided by półtoraks. This brings them to the forefront as the basis of monetary circulation. Data from the literature show that półtoraks issued by King Sigismund III of Poland were

considered reliable coins, surpassing local circulation and being recognized and appreciated throughout Central and Eastern Europe.

Numerous 17th-century hoards and coin accumulations contain significant quantities of półtoraks. Many of these are discovered in what is now Poland, but the literature reports significant hoards and coin accumulations of this type in Transylvania.

Polish mint implication under grand treasurer Nikolai Daniłowicz had ensured a good standard of półtoraks production in large quantities. King's Sigismund III półtoraks emissions ceased after 1627 three years after Nikolai Daniłowicz death under new grand treasurer Hermolaus Ligęza. The 1614 Crown półtorak coins weighed 1.576 g and, with a fineness of 0.469, contained 0.739 g of silver. In 1619, their mint rate raised from 128 to 164 minted coins from the Kraków mark (201.802 g). From 1619 onwards, the półtoraki had the following specifications: weight 1.230 g, fineness 0.406, and 0.500 g content of Ag. Finally, mint regulation of 1623 devalued półtorak more, so that they weighed 1.201 g and, with a fineness of 0.375, contained 0.450 g of pure silver, and from then on, 168 one-and-a-half-groschen coins were minted from the same Krakow fine. Półtoraks minted from 1619, were almost equal to the two Austrian kreuzers of 1625 (weight 0.567 g), and the youngest półtoraks, minted from 1623, were approximately equal to 1.5 kreuzer (half of Imperial groschen) minted after the monetary reform of 1623–1624 [5]. This relation meant that they became readily exchangeable currency on the Central European market and effectively supplemented the supply of small change in circulation. This is confirmed by numerous finds of one-and-a-half-groschen coins in Central European hoards dating from the 1620s to the 1660s.

The findings show that the oldest, i.e. better, emissions are favoured and occur more often and in greater quantity. Although, mass issues of the półtoraks, particularly from the 1620s, which account for such a large proportion of coin finds from the Polish state and Hungary, including Transylvania, in the 17th century, did not reach the Austria, Bohemia, Moravia or Silesia market in the same quantities. The first one and half groschen coins in the Kingdom of Bohemia are recorded in hoards dating back to the 1620s. In 1623, Czech and Moravian sources show a break in the influx of coins from Poland. At that time, a coinage reform introduced by Ferdinand II (great kalada) was carried out in the Bohemia (Czechia, Moravia, Silesia, Lusatia), successfully overcoming a severe monetary crisis. At the same time, a new coinage regulation in the Polish state introduced a coin of lower quality, which could no longer play an active role in the finally stabilized Czech market. This contrasts with Hungary and Transylvania, where, despite access to silver deposits, there was still a deficit in the production of medium and small denominations, and the demand for this type of coin was met by imports from

Polish-Lithuanian Commonwelth and the Roman-German Empire. Their proportion in hoards in those territories, likewise in Poland, declined markedly after 1663, when new denominations were introduced as part of reforms in the Holy Roman Empire and the Polish-Lithuanian Commonwealth [7, 31].

In hoards from the territory of the Kingdom of Poland, one-and-a-half-grosch coins have been found as early as 1614. At least nine hoards containing this denomination, dating from immediately after its introduction, have been recorded. Such an early and relatively frequent presence of półtoraks in hoards may indicate that users recognised their more favourable metal composition — the silver content was approximately 11% higher than that of the groschen coins in circulation at the time. These groschen coins were struck from silver of a fineness of V 3/4 lute (lute is a medieval and pre-modern way to express the silver fineness where 16 lutes correspond to pure silver, in consequence V 3/4 lute corresponds to 75% silver and 25 % copper), weighing approx. 1.580 g and containing approx. 0.571 g of pure silver, which corresponds to a fineness of 359 3/8‰ (i.e. 36.139%) [5].

The large scale of the issue of one-and-a-half groschen coins, their novelty and their relative ‘overvaluation’ compared to the grosch may have encouraged their withdrawal from circulation and hoarding, a trend reflected in the composition of the earliest hoards. Between 1615 and 1623, there was a decline in the number of hoards containing półtoraks, as well as a reduction in their proportion within individual hoards. This phenomenon may be linked to the outflow of this coin beyond the borders of the Polish-Lithuanian Commonwealth, a fact confirmed by finds from neighbouring regions. A renewed increase in the frequency of półtoraks in hoards occurred from 1624 and—despite some annual fluctuations—persisted until the 1660s. In the following decades (the 1670s and 1680s), these coins continue to appear in hoards, though their significance gradually declined. In the 1690s, there was a marked decline in the presence of one and half groschen coins in hoards, although isolated examples still appeared sporadically at the beginning of the 18th century [32, 33]. The evidence gathered suggests that Polish coins—particularly the półtorak—served a supplementary role to the local monetary system in Silesia, especially in the case of small denominations. Their presence was constant, though usually limited in quantity. Exceptional accumulations from the years 1656–1667, however, should be interpreted as the result of extraordinary factors linked to population migrations and political instability in the region [32, 33].

An analysis of the Głogów hoard indicates that the półtoraki coins originated from numerous mints, which clearly illustrates the wide scope of their circulation. Hoard primarily issues from crown mint represented by circ 2300 pieces from Bydgoszcz (1618–1627), several hundred exemplars from:

the Duchy of Prussia in Königsberg (1621–1633), from the municipal mint in Riga (1620; 1623–1626; 1644–1649), including issues from Livonia (1648), as well as municipal issues from Elbląg during the Swedish occupation (1628–1633) and Swedish issues minted in that city between 1632 and 1637. Such a diverse minting structure confirms that the półtorak functioned as a supra-regional coin, easily crossing political borders. Particularly noteworthy is the fact that this hoard — alongside regular issues — also contains imitations of półtoraks, which constitutes significant evidence of their international influence. Noted here are both a Transylvanian poltur from 1638 (minted at an unknown mint, other Transylvanian sources mention the same coin issued in Koloszvar – actually Cluj –Napoca mint having CV mark inscribed on a small circle below the cross orb on the obverse) and six so-called dreipölker minted in Koszalin in 1621–1622by Prince-Bishop Ulrich of Pomerania and Cammin (pol. Kamień). These imitations form part of a wider trend of adapting the półtorak in Central and South-Eastern Europe. Particularly in Transylvania, the półtorak served as a model for local issues (poltura) minted between 1636 and 1638, which were adapted to the local monetary system whilst retaining the form and function of a small silver coin useful in regional and international trade. Similarly, in the area of Western Pomerania and the Kamień Bishopric, issues of the dreipölker type constituted a deliberate imitation of the Polish półtorak, often with reduced specifications, intended for circulation in neighbouring markets, mainly within the Polish-Lithuanian Commonwealth. The presence of both original issues and their imitations in a single hoard indicates that the półtorak functioned not only as part of the Polish monetary system, but also as an important monetary standard in the region. Its popularity encouraged the creation of numerous imitation issues, which — often with a lower silver content — circulated beyond the region and were used in cross-border transactions [34, 35].

Such a large spread of półtoraks from the issuing place to all over Central and Eastern Europe in numerous hoards and random finds imply their exposure to various resting grounds with different humidity degrees and pluvial water infiltration. It normally leads to different conservation state and slightly variation of patina compounds subscribed to the triangle formed by oxides – carbonates and halides. Such advanced intragranular corrosion like observed in our abnormal półtorak most likely was previously observed by the archaeologists and numismatists investigating the previously mentioned hoards. Thus, the advanced corrosion hypothesis discussed in the current article should be further investigated on the larger number of affected coins from different sources consisting in a future research work.

CONCLUSIONS

The abnormal density and extremely high silver content of the unusual półtorak issued in 1624 is caused by a progressive intra-crystalline corrosion which implies the decuprification through complete dissolution of β phase grains and copper lamellas from the eutectic grains leaving behind a porous microstructure of almost pure silver grains as observed by SEM-EDX in agreement with optical microscopy and XRD observations.

Sodium dichloro-cuprate is the single corrosion product having high water solubility while copper oxides, malachite and atacamite are practically insoluble in water. Thus, all aspects plead for a progressive corrosion in a high moistened soil containing evaporitic deposits of sodium chloride crystallized as halite. Moisture water circulation can ensure a progressive removal of sodium dichloro-cuprate during few hundreds of resting years causing deeply decuprification of the coin generating a porous microstructure explaining the dull sound when it is ringed on solid surfaces.

The proposed corrosion mechanism needs further investigations regarding the resting ground soil composition and a precise investigation of the patina layer formed on the coin surface prior to its complete cleaning. Such investigation should be further conducted on the fresh archeological discoveries of random finds and monetary accumulations. Also, it would be interesting to effectuate a search for such abnormally corroded półtoraks if they occur in large hoards.

EXPERIMENTAL SECTION

Numismatic examination of some półtoraks issued by Sigismund III King of Poland in early XVII century reveal one coin from 1624 having abnormal properties line relative low weight and a dull sound when it was ringed on the table. A manipulation accident occurs chipping its edge revealing deep internal structural flaws which were further investigated by physicochemical methods. The normal etalon was considered in a similar coin issued in the same year 1624 at the same place in Bydgoszcz mint.

Coins density was measured using an AX120 Shimadzu hydro-balance with a measuring range from a minimum of 10 mg to a maximum of 120g. Each coin's mass was measured in atmosphere and in water. The density is given by following equation:

$$\rho_{solid} = \frac{m_{air}}{m_{air}-m_{water}} \cdot \rho_{water} \quad (5)$$

where: ρ_{solid} is the coin's density, m_{air} is the coin's mass measured in atmosphere and m_{water} is the coin's mass measured in water, ρ_{water} is water density at the measurement temperature which was 21 °C respectively 0.9978 g/cm^3. Knowing the coin density and assuming its standard composition within Ag-Cu binary system the weight percents of silver ω_{Ag} and of copper $\omega_{Cu} = 1 - \omega_{Ag}$ can be calculated with the following equation:

$$\frac{1}{\rho_{solid}} = \frac{\omega_{Ag}}{\rho_{Ag}} + \frac{1-\omega_{Ag}}{\rho_{Cu}} \quad (6)$$

where: ρ_{Ag} = 10.49 g/cm^3 and ρ_{Cu} = 8.96 g/cm^3.

Both coins are well cleaned under the museum's standard procedures, being free of corrosion products at visual inspection. According to the literature, such cleaning procedures might enrich the silver content of the outermost layer. Therefore, their reverse featuring the orb with cross was subjected to a gentle brushing with felt disc to remove the enriched silver layer from the heavily worn areas from the top of inscriptions and representations while the lower areas on the surface remaining undisturbed.

Furthermore, there were identified certain spots on the worn areas at the top of inscriptions that were further mild micro-polished with very high granulation sandpaper i.e 8000 grains and micro-lustred with colloidal alumina using felt pointers. The chemical etching was effectuated at the room temperature (20 °C) by swabbing method using a reagent containing ferric chloride and sodium thiosulfate applied with a small cotton cloth for 5 seconds followed by rinsing with deionized water. The procedure was gently effectuated to avoid damaging the coin surface but enough precise to allow metallographic analysis and SEM investigations.

Reflected light microscopy was effectuated using a Bresser WiFi 1080P 2L microscope equipped with an integrated computer aided image acquiring system working on the Windows platform using png high resolution output format 720 x 1080 pixels.

Metallographic microscopy was effectuated with an IOR MC8 metallographic microscope (IOR, Bucharest, Romania) equipped with a digital image capture camera Sony 14 MPx (Sony Co., Minato, Japan).

X ray diffraction (XRD) was performed with a Bruker D8 Advance diffractometer with Cu kα monochromatic radiation having a wavelength of 1.540562 Å. The patterns were registered at a speed of 1°/min. in the range of 10 – 80°. Crystal phase identification was made upon the XRD peaks using Match 1.0 software (Crystal Impact Company, Bonn, Germany).

Scanning Electron Microscopy (SEM) was done with the Hitachi SU8230 operated in high vacuum mode at an acceleration voltage of 30 kV. The samples were coated with a thin layer of Pt to ensure proper electrical conductivity. The elemental analysis was effectuated with the Energy Dispersive Spectroscopy (EDS) detector X-Max 1160 EDX (Oxford Instruments, Oxford, UK). The Pt component was subtracted from the EDS results.

REFERENCES

1. I. Petean; G.A. Paltinean; E. Pripon; G. Borodi; L. Barbu Tudoran; *Materials,* **2022**, *15*, 7514. https://doi.org/10.3390/ma15217514
2. I. Petean; G.A. Paltinean; A.C. Taut; S.E. Avram; E. Pripon; L. Barbu Tudoran; G. Borodi; *Materials*, **2023**, *16*, 5809. https://doi.org/10.3390/ma16175809
3. B. Koch; *Wiadomości Numizmatyczne*, **1985**, *29 (3-4)*, 217-220.
4. Z. Żabiński, *The Development of Monetary Systems in Western and Northern Europe*, Ossoliński National Institute Publishing House, Wroclaw, Poland, **1989**, p. 51.
5. Z. Żabiński; *Monetary systems in Poland*, Ossoliński National Institute Publishing House, Wroclaw, Poland, 1981, pp. 116 -119.
6. A. Mikołajczyk; *Wiadomości Numizmatyczne*, **1985**, *29 (1-2)*, 87-100.
7. E. Pripon; *Tezaure monetare medievale şi premoderne descoperite pe teritoriul oraşului Zalău (I)*, Ed. Mega Zalau, Romania, **2018**, pp. 100.
8. C. C. Kirițescu; *Sistemul bănesc al leului și precursorii lui, vol. I*, București, Romania, **1964**.
9. E. Chirilă; V. Lucăcel; *Studia Universitatis Babeș-Bolyai, Series Historia*, **1965**, *2*, 33-55.
10. I. Winkler; *Buletinul Societății Numismatice Române*, **1976-1980**, *70-74*, 369-397.
11. C. Toma; Tezaure monetare și tezaurizare în Transilvania secolelor XV/XVI-XVII, Editura Muzeului Țării Crișurilor, Oradea, Romania, **2016**.
12. A.M. Vlad; Gh. Niculescu; Metode instrumentale de analiză în artă și arheologie, Editura Performantica, Iași, Romania, **2013**. pp. 246.
13. J.C. Kraut; W.B. Stern; *Gold Bulletin*, **2000**, *33(2)*, 52-55.
14. L.B. Moller; J. Aaseth; *Chapter 10 - Copper*, Editor(s): Gunnar F. Nordberg, Max Costa, Handbook on the Toxicology of Metals (Fifth Edition), Academic Press, **2022**, pp.243-266. https://doi.org/10.1016/B978-0-12-822946-0.00009-X
15. S.M. Northover; J.P. Northover; *Materials Characterization*, **2014**, *90*, 173-184. https://doi.org/10.1016/j.matchar.2014.01.028
16. S.E. Avram; L.B. Tudoran; G. Borodi; I. Petean; *Appl. Sci.,* **2025**, *15*, 6445. https://doi.org/10.3390/app15126445
17. S.E. Avram; L.B. Tudoran; G. Borodi; M.R. Filip; I. Ciotlaus; I. Petean; *Sustainability,* **2025**, *17*, 2906. https://doi.org/10.3390/su17072906

18. M. Orlik; *Chemistry and Electrochemistry of Silver*, Editor(s): Jürgen Garche, Encyclopedia of Electrochemical Power Sources (Second Edition), Elsevier, **2025**, pp. 826-837. https://doi.org/10.1016/B978-0-323-96022-9.00089-X
19. F. Boccaccini; C, Riccucci; E. Messina; M. Pascucci; F. Bosi; L. Aldega; A. Ciccola; P. Postorino; G. Favero; G.M. Ingo; G. Di Carlo; *Materials*, **2024**, *17*, 442. https://doi.org/10.3390/ma17020442
20. V. Graziani; L. Tortora; *Corrosion mechanisms in copper-based artifacts investigated by secondary ion mass spectrometry*, Editor(s): Klaus Wandelt, Gianlorenzo Bussetti, Encyclopedia of Solid-Liquid Interfaces (First Edition), Elsevier, **2024**, pp. 486-504, https://doi.org/10.1016/B978-0-323-85669-0.00085-4
21. B.S. van der Meulen-van der Veen; *Journal of Archaeological Science: Reports*, 2023, 48, 103839. https://doi.org/10.1016/j.jasrep.2023.103839
22. D.C.M. Whynot; C.R. Corbeil; D.J.W. Mercer; C.C. Pye; *Molecules,* **2025**, *30*, 3147. https://doi.org/10.3390/molecules30153147
23. B. González; S. Díaz-Quezada; M. Bravo-Gutiérrez; A. Muñoz-Sepúlveda; S. Montserrat; P. Hernández; W. Liu; T. Vargas; H. Estay; *Hydrometallurgy*, **2026**, *243*, 106722. https://doi.org/10.1016/j.hydromet.2026.106722
24. O. Oudbashi; R. Wanhill; *Heritage*, **2021**, *4*, 2287-2319. https://doi.org/10.3390/heritage4030130
25. M. Habibzadeh; O. Oudbashi; R. Naseri; S. Bahadori; *Journal of Archaeological Science: Reports*, **2025**, *65*, 105186. https://doi.org/10.1016/j.jasrep.2025.105186
26. S.E. Avram; L. Rus; V. Micle; S.S. Hola; *Water*, **2022**, *14(15)*, 2366. https://doi.org/10.3390/w14152366
27. S.E. Avram; M.R. Filip; L. Barbu Tudoran; G. Borodi; I.Petean; *Stud. UBB Chem.,* **2023**, *68*, 57–70. https://doi.org/10.24193/subbchem.2023.4.05
28. S.E. Avram; C. Mandiuc; I.Petean; L. Barbu Tudoran; G. Borodi; *Stud. UBB Chem.*, **2025**, *70*, 35-53. https://doi.org/10.24193/subbchem.2025.3.03
29. E. Tartaglia; F. Abate; M. Galeotti; A. Cagnini; S. Porcinai; E. Verlato; M. A. Baldo; C. Zanardi; A. Traviglia; *Journal of Cultural Heritage*, **2026**, *79*, 296-307. https://doi.org/10.1016/j.culher.2026.04.004
30. Y. Zhao; W. Liu; B. Wang; K. Chen; X. Cheng; X. Li; *Corrosion Science*, **2026**, *258*, 113403. https://doi.org/10.1016/j.corsci.2025.113403
31. A. Mikołajczyk; *Numismatický Sborník*, **1993**, *19 (1)*, 213- 230.
32. M. Męclewska; A. Mikołajczyk; *Coin hoards from 1500–1649 in the Polish People's Republic Inventory*, PTAiN Komisja Numizmatyczna, Warszawa, Poland, **1983**.
33. M. Męclewska; A. Mikołajczyk; *Wiadomości Numizmatyczne*, **1992**, *36*, 141-142.
34. M. Grochowska-Jasnos; *The Glow of Gold, Silver, and Money in the Baroque*, Archaeological and Historical Museum in Głogów, Głogów, **2023**. pp. 299.
35. M. Grochowska-Jasnos; *Acta Musei Porolisensis*, **2025**, *47*, 409-416.

STUDIA UBB CHEMIA, LXXI, 2, 2026 (p. 289-306)
(RECOMMENDED CITATION)
DOI:10.24193/subbchem.2026.2.15

EFFECT OF MEDIUM-RANGE TEMPERATURES ON THE CONVECTIVE DRYING KINETICS OF CELERY LEAVES AND STEMS

Alexandra Ana CSAVDARI[a,b], Andrea BOGYOR[a], Graziella-Liana TURDEAN[a,*]

ABSTRACT. This work focuses on the comparative description of convective thin-layer drying of celery leaves and stalks at 40, 50 and 60°C, respectively. Close to 100% moisture loss was recorded, yet total process time shortens at elevated temperatures. The adjusted determination coefficient, the root mean square error and the hybrid fractional error deviation, respectively, were simultaneously employed as selection criteria for the most suitable kinetic model. The empirical parabolic model was chosen to describe drying kinetics of both plant parts. Its parameters and their temperature dependence were quantified. Calculated drying parameters reflect the results of ANOVA testing. Effective water diffusivity coefficients are 3 orders of magnitude higher for stem and its drying activation energy is 34% lower. Specific energy consumption values prove that drying of stems is more energy efficient than that of leaves.

Keywords: *Apium graveolens, Convective drying, Kinetic modeling, Leaf and stem*

INTRODUCTION

Apium graveolens, commonly known as celery, is a widely grown and consumed biennial plant of the *Apiaceae* family [1-4]**.** Because of its unique flavor, well-documented biologic proprieties, and low caloric content [2,5-7],

[a] *Babeş-Bolyai University, Faculty of Chemistry and Chemical Engineering, Department of Chemical Engineering, 11 Arany János str., RO-400028, Cluj-Napoca, Romania.*
[b] *Al-Farabi Kazakh National University, Department of Analytical, Colloidal Chemistry and Technology of Rare Elements, 71 Al-Farabi Avenue, 050040 Almaty, Kazakhstan*
* *Corresponding author: graziella.turdean@ubbcluj.ro*

all parts of it (leaf, stem, root, seeds) are of economic importance. Thus, market demand and supply are high, either in its fresh, dried, or other commercial form.

Besides the fresh plant, the Romanian celery market is characterized by two major product groups. The first targets its direct use as a spice and consists of 0.1¸ 1 Kg packages of dehydrated celery leaves, roots and/or seeds, either as such or as a powder, sometimes also in salty mixtures. The second refers to phytopharmaceutical products, for example hydroalcoholic extracts. In either case, appropriately dried celery parts serve as raw material. Hence, there is a clear industrial need for rapid, cost-effective, and highly efficient drying methods, capable of reducing the plant's moisture content below 10%, yet also ensuring the retention of its phytochemical characteristics.

The most common procedures are: the conventional hot-air (forced convective) drying, open-air drying at room temperature, freeze-drying (lyophilization), vacuum drying, sublimation drying, and microwave drying [3,5,7], respectively.

Research in the field focuses on two directions. One targets the retention of phytochemical composition, by investigating antioxidant activity, total phenolic and/or flavonoid content, as well as antibacterial activity of various dried celery parts [7,8]. Some studies also evaluate organoleptic properties and mechanical changes, such as grindability [7]. Ultimately, the retention of these attributes depends on the drying procedure and its specific operational parameters (e.g., drying time, temperature, microwave power, etc.) [9]. Another research direction targets the understanding of the moisture removal process itself, by explaining experimental data with various theoretical, semi-theoretical and/or empirical drying kinetic models [1,10,11]. It describes drying rates and mechanisms as a function of the specific procedure and its parameters [1,6,11,12].

Despite the multitude of investigated techniques, convective drying remains the most commonly used [13]. Its wide industrial practicality relies on commercially available and affordable equipment, designed for high quantity throughput. The overall temperature range reported in the literature spans from 25 °C to 120 °C, yet existing studies focus either on its lower or higher values end [8,13]. Low temperature convective drying is less energy consuming, but more time demanding. On the other hand, the use of elevated temperature might save time, but compromises phytochemical characteristics, such as antioxidant activity or chlorophyll content [3,7]. Therefore, operation at medium-range temperature might offer a solution to affordable energy / time costs, while retaining the plant's desired bioactive proprieties. However, no thorough and systematic such study has been reported yet.

Furthermore, while drying various celery parts (leaf, stem, root, or seeds) is well described, research typically focuses strictly on either of these. No comparative data can be found in the literature, detailing the distinct drying behaviours of various morphological celery components under identical experimental conditions. This is a significant gap since simultaneous drying of various plant parts, such as leaves and stalks for instance, makes sense from an economic point of view. On the Romanian market for example, both the commercially available dehydrated spices and hydro-alcoholic extracts are based on mixtures of all parts [14,15,16,17].

The present study aims a comparative kinetic study between *Apium graveolens* leaves and stalks, under the same mid-range temperature, forced convective drying conditions. As such, it tries to bridge both data gaps described above.

RESULTS AND DISCUSSION

General characteristics of the drying process

Samples of 10 g celery leaf and stem were subjected to forced convective drying, under identical experimental conditions, at 40, 50 and 60°C, respectively. Each sample's residual mass was recorded against the total drying time, leading to the kinetic curves presented in Figure 1 and Figure 2 for leaves and stalks, respectively.

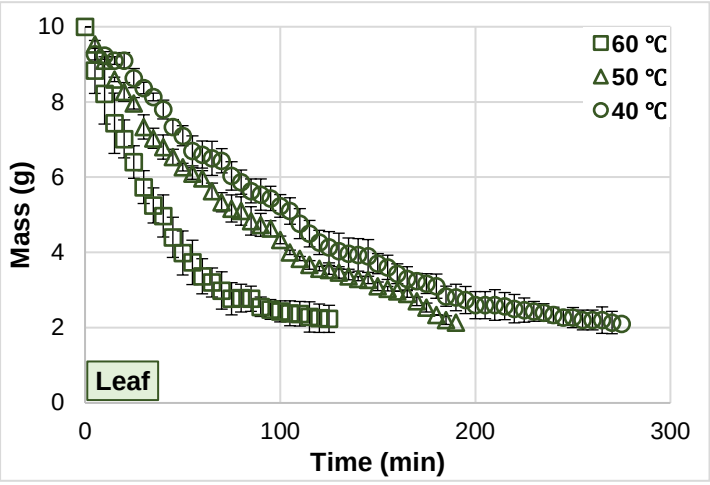

Figure 1. Leaf sample retained mass versus total drying time.

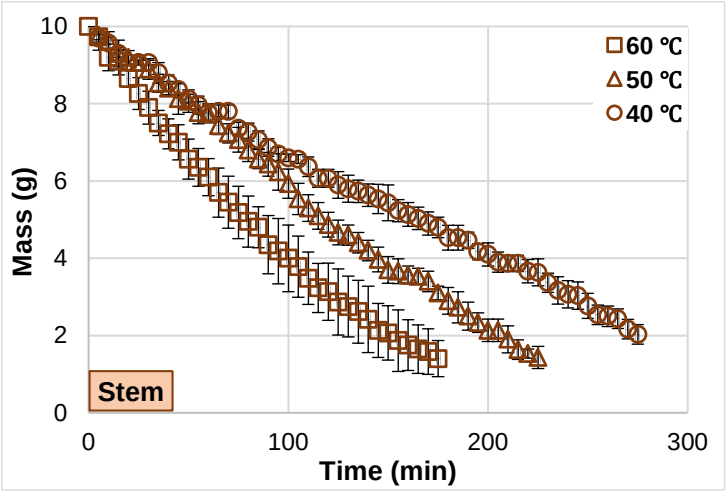

Figure 2. Stem sample retained mass versus total drying time.

These present mean values and their respective error bars for 3 distinct measurements at 40 and 50°C, whereas the 60°C data correspond to sets of 6 repetitions. The error bar values prove that data variability decreases with temperature.

Data in Figures 1 and 2 were subjected to mono- and bi-factorial statistical ANOVA testing, to determine whether the two independent variables (temperature and type of plant material) affect the drying kinetic behavior in a statistically significant manner, or whether they interact in determining its shape. The results, translated into probability p-values, are presented in Table 1. Lower than 0.05 values mean statistically significant effect and are correlated with the H_1 hypothesis, whereas the opposite is true for higher than 0.05 values, for which hypothesis H_0 is accepted [18].

All mono-factorial tests prove that both parameters affect significantly drying kinetics, but more so the temperature. The bi-factorial test proves the same yet demonstrates that there is no interaction (or at least at the threshold of statistically significance) between the 2 independent variables in shaping the kinetics of this particular drying process (p of 0.083 very close to the threshold of 0.05).

Table 1. Results of ANOVA testing for data given in Figures 1 and 2; probability p-values and their corresponding accepted hypotheses.

Type of ANOVA test	p-value *	Accepted hypothesis
Mono-factorial testing of either the effect of temperature or of plant material type		
Effect of temperature – *Leaf*	3.69×10^{-5}	H_1
Effect of temperature – *Stem*	9.59×10^{-4}	H_1
Effect of plant material type – *40°C*	1.77×10^{-2}	H_1
Effect of plant material type – *50°C*	6.32×10^{-4}	H_1
Effect of plant material type – *60°C*	2.87×10^{-4}	H_1
Bi-factorial testing of combined effects of temperature and plant material type		
Effect of temperature	2.98×10^{-8}	H_1
Effect of plant material type	1.72×10^{-7}	H_1
Interaction between the 2 above factors	8.29×10^{-2}	H_0

* Statistically significant threshold fixed at probability p-value 0.05.

The shapes of curves in Figures 1 and 2 lead to the following conclusions:

1) Leaves dry faster than stems at all temperatures (more visible at 60°C). This is probably due to their 20 to 30-fold lower thickness (see data in Table 7).
2) Drying rates decrease and total drying times increase with lowering temperatures, for both celery parts (see also Table 2). This is most probably caused by the higher diffusivity of water at elevated temperatures [19,12] (see Figure 5).
3) Drying rates decrease during time, together with the loss of moisture. Explanation relies on the fact that the fast surface water removal is predominant at process beginning, whereas towards equilibrium it is replaced by the more slower core moisture removal [11].

Findings 2) and 3) above agree with previous reports for celery leaves [19,12], slices [20] and stems [7].

The efficacy of each drying process can be assessed not only by the length of the total drying time necessary to reach constant sample masses (equilibrium), but also by the values of final humidities (translates into moisture loss). Both are presented comparatively in Table 2 for all employed conditions. It can be observed that fresh celery stalks contain more water than leaves and that their drying leads to less dry mass (see also the corresponding experimental section). This means that more water is eliminated during the exact same drying procedure, making the drying of celery stems more energetically effective (see Figure 6).

Table 2. Total drying time and humidity of fresh and dried celery leaves and stalks.

Drying q (°C)	Total drying time (min)	Humidity (% m/m)	
		Leaf	*Stem*
40	180	4.69 ± 0.16	1.52 ± 0.34
50	235	4.74 ± 0.54	1.93 ± 0.18
60	285	5.62 ± 0.31	2.49 ± 0.66
105	-	4.89 ± 0.28	1.92 ± 0.28
Fresh plant	-	87.15 ± 0.80	91.66 ± 0.74

Data in Table 2 prove that a slower, low temperature convective drying results in a 100% moisture loss, since retained humidity values at 40 and 50°C are comparable with those at 105°C (where the absolute dry mass was determined) for both leaf and stem. On the other hand, the rather forced process at 60°C retained 14.9% more water in leaves and 29.7% more in stalks. This is undesirable because higher retained humidity can lead to plant putrefaction during storage. Table 2 also underlines the well-known fact that elevated drying temperatures shorten significantly process duration: in this case with 36.8% when going from 40 to 60°C.

Kinetic modeling of the drying process

Various kinetic models have been put forward in the literature for the thin-layer drying of agricultural products [7,11,12,19,20]. The theoretical ones are based on analytical solutions of various heat transfer or diffusion describing equations for some simple geometries, but under simplifying assumptions of an ideal drying process. Because these are rarely met, the most suitable models have proved to be either semi-theoretical or empirical [11,12].

Regardless of the equation they use to describe the time-resolved process evolution, all models rely on moisture ratio MR data *versus* total drying time t. Hence, raw kinetic information of Figures 1 and 2 was translated into such curves, by means of equation (1) to (3) (see the Experimental section). An example of MR mean values is presented in Figure 3, for data collected at 60°C for both leaf and stem.

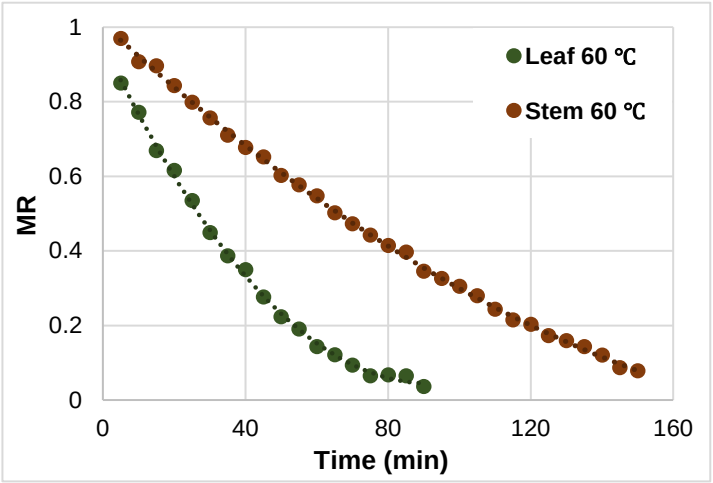

Figure 3. Moisture ratio profiles for celery leaf and stem convective drying at 60°C.

Table 3. Tested kinetic models, their equations and number of parameters n_{mp}.

Nb.	Model *	Equation	n_{mp}
		Semi-theoretical models	
1	Page	$MR = \exp(-kt^n)$	2
2	Midilli & Kucuk	$MR = a\exp(-kt^n) + bt$	4
3	Two terms	$MR = a\exp(-kt) + b\exp(-k_1 t)$	4
		Empirical models	
4	Sledz	$MR = b\exp(-kt) / (1 + a\exp(k_1 t))$	4
5	Parabolic	$MR = a + bt + ct^2$	3
6	Wang & Singh	$MR = 1 + at + bt^2$	2

* Parameters k, k_1 and k_2 stand for drying coefficients (expressed in min^{-1} if drying time is expressed in min); a, b and c stand for equation coefficients (with dimensions depending on the model); n is a dimensionless exponent with values usually higher than 1, respectively.

Table 3 contains the list of 3 semi-theoretical and 3 empirical kinetic models chosen for testing on all MR *vs* time curves. The first 4 models were chosen because they have been previously found to describe drying kinetics of celery and parsley leaves, celery stalks, slices, and roots [7,12,19,20] or various other fruits, vegetables, and seeds [11]. The last 2 were selected because of their simplicity and universal application in various physical and/or chemical parameter descriptions.

The Page model derives from the Newton's law of cooling and assumes that the moisture loss in air for agricultural products is similar to the heat loss of a body immersed in cold fluid [11]. On the other hand, both the Midilli & Kucuk and the two-term model derive from the analytical solution of the Fick's second law of diffusion [11]. The Sledz model is a more recently introduced empirical model [21,22], the parabolic one is a simple quadratic equation, whereas the Wang & Singh simplifies the latter by considering the free term equal to 1 [12].

Table 4. Values of statistical parameters indicating kinetic model predicting quality.

Model *	θ (°C)	n_{obs}	R^2_{adj}	RMSE	HYBRID
			Leaf		
Midilli & Kucuk	40	40	0.9962	0.0166	0.0731
	50	36	0.9969	0.0144	0.1720
	60	18	0.9982	0.0113	0.0797
Sledz	40	40	0.9954	0.0182	0.1015
	50	36	0.9969	0.0144	6.1039
	60	18	0.9985	0.0103	0.0719
Parabolic	40	40	0.9957	0.0177	0.0793
	50	36	0.9941	0.0198	0.3797
	60	18	0.9985	0.0102	0.0724
			Stem		
Midilli & Kucuk	40	54	0.9973	0.0140	0.1505
	50	40	0.9955	0.0185	0.1212
	60	30	0.9992	0.0076	0.0175
Sledz	40	54	0.9974	0.0139	0.1831
	50	40	0.9977	0.0133	0.0867
	60	30	0.9991	0.088	0.0230
Parabolic	40	54	0.9972	0.0144	0.1596
	50	40	0.9968	0.0155	0.0591
	60	30	0.9992	0.0077	0.0169

* Only best fits are presented.

The suitability of each tested model to describe drying kinetics was decided upon the simultaneous satisfaction of 3 statistical model quality criteria: adjusted determination coefficient (R^2_{adj}) closest to 1 and both root mean

square error (RMSE), and hybrid fractional error deviation (HYBRID) closest to zero – see equations (7) to (9). All consider the number of observations of individual kinetic curves (n_{obs}), as well as the number of parameters of each model (n_{mp}). As such, results based on different n_{obs} and n_{mp} are normalized and the 6 models in Table 3 have a uniform base of comparison.

Three out of 6 tested models presented both best, and comparable results: the Midilli & Kucuk, the Sledz and the parabolic models, respectively. Table 4 summarizes the values of statistical parameters which prove the good prediction quality of these. The differences among model performances are practically insignificant and each could serve as drying kinetics behaviour predictor. These results agree with previous reports indicating the Midilli & Kucuk equation as best for celery [19] and coriander leaves [23]. The Sledz equation is also mentioned for celery leaves [19]. On the other hand, drying of celery roots [1], stem [7] and slices [20] was previously best fitted by the Page model. Yet, in this case the Midilli & Kucuk one proves to be the best fit.

However, the authors have decided for the empirical parabolic model as the best drying kinetics descriptor of both celery leaves and stalks. The reasoning is based on the simplicity of the quadratic equation as well as on the very good values of its quality indicators in Table 4. Hence, the corresponding kinetic parameters are presented in Table 5 for all employed experimental conditions.

Table 5. Drying kinetic parameter values of the parabolic model.

θ (°C)	**a**	**(-1x10^3) x b (min^{-1})**	**10^5 x c (min^{-2})**
		Leaf	
40	0.987 ± 0.009	7.57 ± 0.20	1.49 ± 0.09
50	0.947 ± 0.010	9.20 ± 0.26	2.41 ± 0.14
60	0.954 ± 0.008	19.89 ± 0.39	10.87 ± 0.40
		Stem	
40	0.974 ± 0.006	4.07 ± 0.10	0.23 ± 0.04
50	1.018 ± 0.008	5.30 ± 0.17	0.31 ± 0.08
60	1.009 ± 0.004	8.88 ± 0.13	1.78 ± 0.08

It can be observed from Table 5 that all free term values are very close to 1, hence the Wang & Singh equation would also have been a very good fit. Parameter b values are all negative and decreasing at higher temperatures, whereas parameter c values are positive and increase in direct relation with temperature. This measurable temperature dependence is sustained by the findings of the ANOVA tests (see Table 1). Moreover, it follows a typical exponential relationship of Arrhenius type and permits the calculus of some "apparent activation energies" with correlation coefficients from 0.8828 to 0.9075. These have no physical meaning; they simply express a temperature effect. The values are presented in Table 6 and prove a stronger temperature dependence of equation coefficient b as compared to a in the parabolic model.

Table 6. Apparent activation energies for equation coefficients a and b of the parabolic kinetic model.

Type of plant material	Apparent activation energy * (KJ/mole)	
	Parameter a	Parameter b
Leaf	41.58	82.67
Stem	33.68	87.51

* Has no physical meaning; it is a way to estimate the temperature dependence of parabolic model coefficients a and b.

Drying parameters

According to equation (4), the slopes of ln(MR) *versus* drying time plots are used to estimate effective water diffusion coefficient D_{eff} values. An example is presented for both leaf and stem at 60^{o}C, in Figure 4, for data in Figure 3. Only linear portions are presented, but they cover for all employed temperatures 3 successive half-times for leaves and 2 for stalks, respectively. In other words, the linear dependence described by equation (4) is valid for at least 87.5% of process advance in the case of leaves, and for at least 75% for stem.

Towards the equilibrium (end of drying process at high times), the plots tend to curve down, more so in the case of stem. This curvature was also reported in the literature [19] and explained by the variations in the thickness of pieces subjected to drying. This reasoning agrees with the present observations since the strong variations in the stem's thickness are obvious from Figure 7 and Table 7.

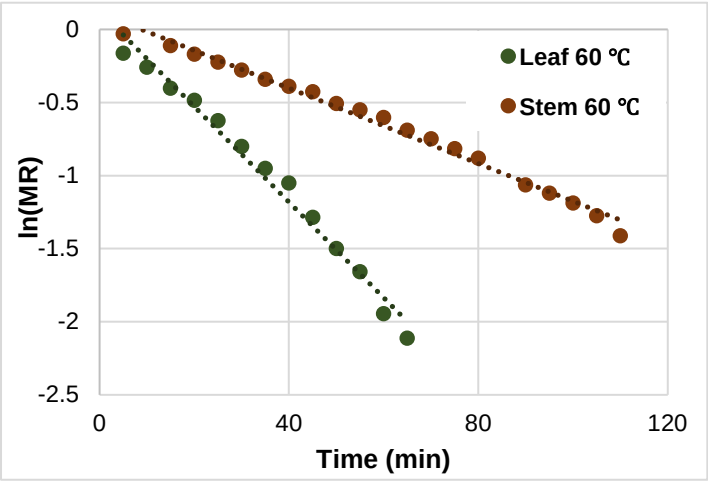

Figure 4. ln(MR) *versus* drying time plots corresponding to data in Figure 3.

Figure 5 presents the calculated D_{eff} values for celery leaf and stem as a function of drying temperature. Watter diffusivity proves to be 3 orders of magnitude higher for stem (values of 10^{-9} order of magnitude as compared to 10^{-12} for leaf), probably due to its different microstructure. Similar orders of magnitude have been reported in the literature in the case of convective drying: 10^{-12} [12] to 10^{-10} [19] for celery leaves, and 10^{-10} for basil [22], respectively.

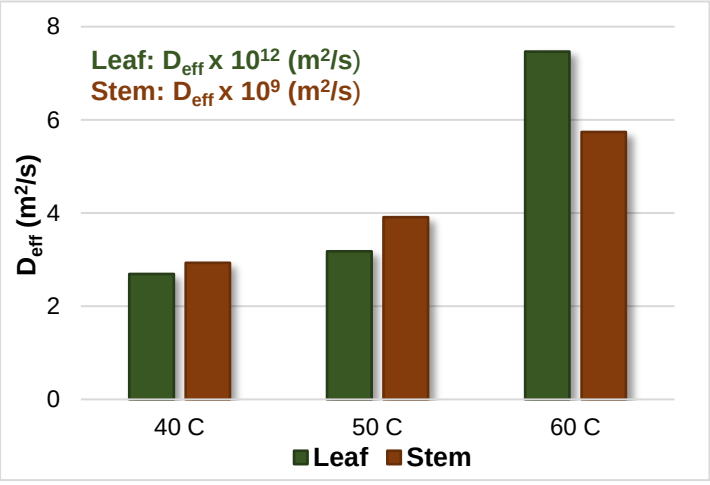

Figure 5. Values of effective water diffusivity (D_{eff} values are of 10^{-12} and 10^{-9} order of magnitude for leaf and stem, respectively).

Water diffusivity increases with temperature and D_{eff} values in Figure 5 served for the determination of drying activation energy, by means of equation (5). An average value of 44.01 KJ/mole of removed water was obtained for leaves, and of 29.02 KJ/mole for stalks (with corresponding correlation coefficients of 0.8575 and 0.9902), respectively. These values show that the moisture loss occurs more easily and is less temperature dependent for celery stem than for leaf. They agree with previous findings, for example 36.09 [12] and 31.72 KJ/mole [19], respectively, for celery leaves [12]. Convective drying of many other fruits and vegetables, although carried out under different conditions, also exhibits comparable values [12].

The specific energy consumption SEC was computed, for both leaves and stalks, by dividing the total amount of consumed energy during drying with the mass of removed water – see equation (6). Its values are illustrated in Figure 6 and agree with previous reports for the convective drying of celery [12].

Results indicate that drying of celery leaves is approximately twice as energy demanding than that of stalks, even under identical process conditions. This finding agrees with their 3 orders of magnitude lower water diffusivity coefficient, as well as with their 34% higher drying activation energy (see Figure 5). The use of an elevated temperature leads to a more energetically efficient process, due to a significantly shorter drying time (see Table 2) and better water diffusivity (see Figure 5).

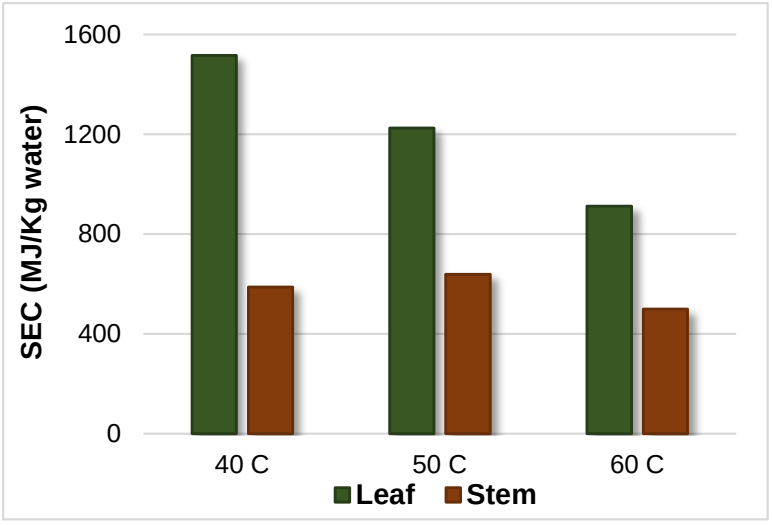

Figure 6. Values of specific energy consumption.

CONCLUSIONS

Despite the wide use of forced convective drying for various fruits and vegetables, there is a lack of systematic studies at mid-range temperature, as well as process comparison for various useful parts of the same plant when dried under identical conditions. Hence, this work focused on the comparative description of thin-layer drying of celery leaves and stalks (industrially often dried together) at 40, 50 and 60°C, respectively.

Gravimetric measurements were used to obtain time-resolved data under all employed conditions. The procedure resulted in almost 100% moisture loss for both celery leaf and stem, regardless of employed temperature. However, drying of leaves is somewhat faster. A total of 6 semi-theoretical and empirical models were tested for their best suitability with kinetic behavior, by means of 3 statistical parameters as indicators of model prediction quality. The Midilli & Kucuk, Sledz and parabolic equations showed best but comparable performances. Yet, because of its simplicity, the empirical parabolic model was chosen to describe the drying kinetics of both celery leaves and stalks.

Mono- and bi-factorial ANOVA tests were used to prove that both independent operating parameters (temperature and type of plant material) affect the evolution of the process in a statistically significant manner, but that they do not interact. Hence, the calculated drying parameters were consistent with these observations. For example, 2 out of 3 equation coefficients of the chosen kinetic model are temperature affected and permit quantification of the respective dependence.

Effective water diffusivity coefficients were also temperature dependent for both employed plant parts, but 3 orders of magnitude higher for stalks. Hence, their drying activation energy was 34% lower. These values correlate with the calculated specific energy consumption and drying of stems proved to be more energy efficient than that of leaves.

EXPERIMENTAL SECTION

Preparation of characterization of celery samples

Fresh and leaf rich celery stalks with no roots were purchased from a local market. The ones lacking visible defects and with a uniform appearance were kept for experimental use. Leaves and stems were separated, washed under tap water, and air-dried for 30 min on paper towels at room temperature. Further, the vegetal material was cut in approximately 1x1 cm pieces, as shown in Figure 6.

Figure 6. Example of celery leaf and stalk pieces prepared for drying.

Leaf and stalk *thickness* measurements were performed in 3 different regions (A, B and C, respectively), as depicted in Figure 7, and according to the morphological particularities of the plant parts. A calliper (YATO, TOYA S.A., Wroclaw, Poland) was used for this purpose. The results are presented in Table 7.

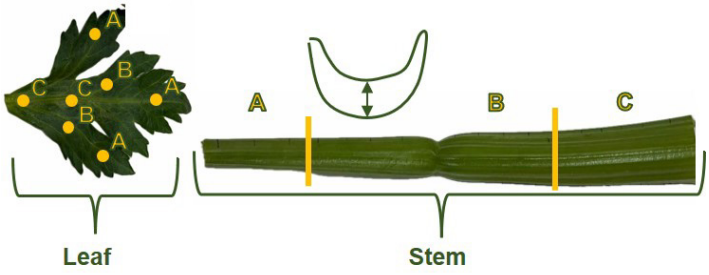

Figure 7. Thickness measurement points/regions for celery leaves and stalks.

The *humidity* (% m/m) of fresh and dried celery was determined with an infrared moisture analyser (Model MA 50.X2.IC.A., Radwag, Poland); 1 g samples were heated by means of IR radiation at 105°C until reaching constant mass.

Table 7. Thickness values of celery leaves and stalks.

Thickness (mm)	Point A	Point B	Point C	Mean value*
Leaf	0.245 ± 0.053	0.383 ± 0.041	0.475 ± 0.050	0.368 ± 0.116
Stem	6.125 ± 0.427	7.950 ± 1.476	10.600 ± 0.126	8.225 ± 2.250

***** Refers to the average of the measurements in points A, B and C, respectively.

Drying procedure

Samples of 10 g of either leaf or stalk pieces were placed in parchment paper trays and subjected to drying on the middle grid of an electrical oven (HB-8053NG, Hausberg, Ergene, Turkey) with ventilation. Temperatures of 40, 50, 60, and 105°C, respectively, were employed.

The process' evolution at 40, 50 and 60°C was monitored gravimetrically, every 5 min, until the mass of each individual sample remained constant for at least 3 successive determinations. Mass measurements were carried out with a 0.01 g accuracy digital analytical balance (Model AXE, KERN & SOHN GmbH, Balingen, Germany).

Besides the electronic setting of temperature, its actual value inside the oven was monitored with a laboratory thermometer ranged 0 to 150°C. The air flow hit the samples vertically, from both above and below, at a velocity of (4.16 ± 0.22) m/s. The latter was measured in 12 points, with a digital hand anemometer (Model JV796255, NJTY, Guangdong, China).

All kinetic measurements were carried out in triplicate, except the ones at 60°C, which had 6 repetitions, for both leaves and stem. Drying time at 105°C took 24 hours (triplicate) and finalized with one mass measurement each.

Calculus of drying parameters

The *moisture ratio* MR [1,7,12,19] was calculated from each mass *versus* drying time individual measurement by means of equation (1),

$$MR = \frac{X - X_e}{X_0 - X_e} \tag{1}$$

in which X, X_i and X_e stand for the dry base moisture content of the sample at a certain time t, at the start of the process and at its equilibrium, respectively. X values are expressed in g water / g dry base and calculated as

$$X = \frac{Sample\ mass - Dry\ mass}{Dry\ mass} (g / g) \tag{2}$$

for each mass measurement. The plant dry mass was determined after drying 10 g at 105°C for 24 hours, to be equal to (1.97 ± 0.06) g and (0.75 ± 0.09) g, for leaf and stem samples, respectively. Because of constant 10 g initial mass samples, the values of X_0 are constant and equal to 4.085 g/g and 12.333 g/g, for leaf and stem, respectively. On the other hand, the values of X_e differ for each set of kinetic measurements, in agreement with the final stable sample mass recorded at process equilibrium.

A combination of equations (1) and (2) leads to an MR value expressed simply as a function of mass measurements, as follows:

$$MR = \frac{Momentary\ mass - Equilibrium\ mass}{Initial\ mass - Equilibrium\ mass} \quad (3)$$

The *effective water diffusion coefficient* D_{eff} (m^2/s) was determined from the slope of ln(MR) *versus* drying time graphs [12,19,21,22], according to:

$$\ln(MR) = \ln\left(\frac{8}{p^2}\right) - \frac{p^2 D_{eff} t}{4L^2} \quad (4)$$

where L stands for the half-thickness of the material subjected to drying (m). Its value was considered equal to the half of the last column values in Table 7 (since moisture loss occurs from all sides of the plant pieces).

The *activation energy* E_a (KJ/mole evaporated water) was calculated from the temperature dependence of D_{eff} values, described as:

$$D_{eff} = D_0 \exp\left(-\frac{E_a}{RT}\right) \quad (5)$$

where D_0 (m^2/s) stands for a pre-exponential factor, T (K) for temperature and R for the universal gas constant, respectively.

The *specific energy consumption* SEC (J/Kg removed water) [12,22] was computed by:

$$SEC = \frac{TT}{m_s(X_0 - X_e)}E \quad (6)$$

where TT stands for the total drying time (s), E (equalling 2225 W) is an oven characteristic, and m_s (Kg) represents the dried solid matter at equilibrium, respectively. Variables m_s and X_i have individual values for each kinetic curve, whereas X_0 is constant (see above).

Calculus of statistical parameters

The following statistical indicators were calculated for each kinetic curve: the *adjusted determination coefficient* R^2_{adj}, the *root mean square error* RMSE, and the *hybrid fractional error deviation* HYBRID, respectively [12,19,24,25]. Their respective formulas are given in equations (7) to (9).

$$R^2_{adj} = 1 - (1 - R^2)\frac{(n_{obs} - 1)}{(n_{obs} - n_{mp} - 1)} \quad (7)$$

$$RMSE = \sqrt{\frac{\sum_{i=1}^{n_{obs}} (MR_{exp} - MR_{calc})_i^2}{n_{obs}}} \quad (8)$$

$$HYBRID = \frac{100}{n_{obs} - n_{mp}} \sum_{i=1}^{n_{obs}} \left[\frac{(MR_{exp} - MR_{calc})^2}{MR_{exp}} \right]_i \quad (9)$$

In equation (7), R^2 stands for the correlation coefficient of the model. In equations (8) and (9), MR_{exp} and MR_{calc} stand for the experimental and model calculated moisture ratios, respectively. The variable n_{obs} equals the number of experimental observations in a kinetic curve, whereas n_{mp} the parameter number of a tested model. The values of R^2_{adj} and RMSE were generated automatically during model fitting, while the HYBRID value was calculated by hand for each tested model.

Employed software

Statistical mono- and bi-factorial ANOVA analysis was carried out with the "*Data Analysis"* tool of Microsoft Excel for Microsoft 365 (Microsoft Corporation, Redmond, WA, USA).

Kinetic curve fittings and model parameter calculus were performed with the "*Nonlinear Curve Fit*" module of Origin 2018, Version 95E (OriginLab Corporation, Northampton, MA, USA).

ACKNOWLEDGMENTS

The authors kindly acknowledge the support of the *Sapientia Hungariae Foundation* (Budapest, Hungary) by means of its *Collegium Talentum* Scholarship Program 2025-2026.

REFERENCES

1. M. Kręcisz; J. Kolniak-Ostek; J. Łyczko; B. Stępień; *Food Chem.*, **2023**, *413*, 135490.
2. W. Kooti; N. Daraei; *J. Evid. Based Complementary Altern. Med.*, **2017**, *22*, 1029-1034.
3. S. Latinovi´c; L Vasilišin; L. Pezo; N. Laki´c-Karali´c; D. Cvetkovi´c; A. Ranitovi´c; S. Brunet; T. Cvani´c; J. Vuli´c; *Foods*, **2024**, *13*, 3355.
4. G. Daoud; F. Ahsan; T. Mahmood; S. Bano; V. A. Ansari; S. M. H. Zaidi; J. A. Ansari; *Pharmacol. Res. Rep.*, **2025**, *3*, 100039.

5. S. Lal; M. K. Mahatma; S. N. Saxena; C. K. Jangir; O. P. Aishwath; V. Bhardwaj; M. Choudhary; *Appl. Food Res.*, **2026**, *6*, 101694.
6. K. Mouhoubi; L. Boulekbache-Makhlouf; N. Guendouze-Bouchefa; M. L. Freidja; A. Romero; K. Madani; *Ann. UDJG Food Technol.*, **2020**, *44*, 48-69.
7. S. Rudy; D. Dziki; B. Biernacka; R. Polak; A. Krzykowski; A. Krajewska; R. Stanisławczyk; M. Rudy; J. Zurek; G. Rudzk; *Foods*, **2024**, *13*, 2585.
8. M. A. Sorour; N. H. M. Hassanen; M. H. M. Ahmed; *Am. J. Energy Eng.*, **2015**, *3*, 12-16.
9. K. Ramachandraiah; K. B. Chin; *J Sci Food Agric*, **2017**, *97*, 4539–4547.
10. A. A. Csavdari; C. Racz; D. M. Sabou; S. A. Tonk; I. D. Spiridon, *Rev. Chim. (Bucharest)*, **2016**, *67*, 1906-1913.
11. C. Ertekin; M. Z. Firat; *Crit. Rev. Food Sci. Nutr.*, **2017**, *57*, 701–717.
12. K. Mouhoubi; L. Boulekbache-Makhlouf; K. Madani; A. Palatzidi; J. Perez-Jimenez; I. Mateos-Aparicio; A. Garcia-Alonso; *Int. J. of Food Sci. Tech.*, **2022**, *57*, 3467–3476.
13. Y. Chen; C. Song; Z. Li; H. Chen; G. Jin; *J. Food Process Preserv.*, **2019**, *44*, 00:e14310.
14. https://topingrediente.com/telina-frunze-deshidratate/ (Retrieved: 05.06.2026)
15. https://www.ft-shop.ro/sare-cu-telina-celery-salt-1kg.html (Retrieved:05.06.2026).
16. https://www.daciaplant.ro/telina-tinctura.html (Retrieved: 05.06.2026).
17. https://www.sanavita.ro/tinctura-telina.html (Retrieved: 05.06.2026)
18. S.L.R. Ellison; V.J. Barwick; T.J.D. Farrant; *Practical Statistics for the Analytical Scientist: A Bench Guide*, 2nd ed., The Royal Society of Chemistry, Cambridge, UK, 2009, pp. 59-91.
19. N. Nasfi; M. Romdhane; *Eng. Technol. Appl. Sci. Res.*, **2025**, *15*, 19068–19072.
20. A.Ö. Karabacak; S. Suna; C.E. Tamer; Ö.U. Çopur; *Qual. Assur. Saf. Crop. Foods.,* **2018***, 10,* 193-205.
21. M. Sledz; A. Wiktor; K. Rybak; M. Nowacka; D. Witrowa-Rajchert; *Appl. Acoust.,* **2016***,103*, 148-156.
22. M. Sledz; A. Wiktor, M. Nowacka; D. Witrowa-Rajchert; *J. Food Process Eng*., **2017**, *40*, e12271.
23. A. Sarimeseli; *Energy Convers. Manag.*, **2011**, *52*, 1449-1453.
24. A. Bogyor; A. A. Csavdari; T. Lovász; E. Bitay; *Int. J. Mol. Sci.*, **2025**, *26*, 516.
25. M. M. Rahman; M. Muttakin; A. Pal; A. Z, Shafiullah; B. B. Saha; *Energies*, **2019**, *12*, 4565.

STUDIA UBB CHEMIA, LXXI, 2, 2026 (p. 307-334)
(RECOMMENDED CITATION)
DOI:10.24193/subbchem.2026.2.16

PLA - ZnO COMPOSITE WITH BACTERICIDAL AND FUNGICIDAL ACTIVITY

Raluca-Elena DRAGOMIR[a], Cristina-Maria DUȘESCU-VASILE[a], Andra-Ioana STĂNICĂ[b], Marian BĂJAN[a], Daniel BOMBOȘ[c], Ioan SAROSI[d], Andrei MOLDOVAN[d], Gabriel VASILIEVICI[e*]

ABSTRACT. A plasticized polylactic acid (PLA) composite incorporating zinc oxide (ZnO) was synthesized via melt mixing and hot pressing. The physicochemical and preliminary microbiological properties of the composite were systematically evaluated. ZnO powder, produced through precipitation and calcination, was characterized using dynamic light scattering and nitrogen sorption analysis. The PLA composite, comprising PLA, Proviplast 2624, Span 60, and ZnO, was subjected to tensile and flexural testing, oxygen and water vapor barrier measurements, water uptake analysis, contact angle assessment, and Atenuated Total Reflectance – Fourier Transform Infrared spectroscopy (ATR-FTIR). The ZnO powder exhibited a broad, aggregate-dominated particle-size distribution and a moderate specific surface area. The composite displayed reduced stiffness and strength relative to neat PLA, indicating effective plasticization. Preliminary microbiological assays indicated decreased recovery of the tested microorganisms under the specified conditions.

Keywords: *PLA composite, Proviplast 2624, ZnO, Bacillus subtilis, Aspergillus mold*

[a] *Department of Petroleum Refining Engineering and Environmental Protection, Petroleum-Gas University of Ploiesti, 39 Bucharest Blvd., 100680 Ploiesti, Romania.*
[b] *Technological Highschool "Toma Socolescu", Gheorghe Grigore Cantacuzino St., 328, 100466 Ploiești, Romania.*
[c] *S.C. Medacril S.R.L, 8 Carpați Street, Mediaş, Sibiu County, Romania.*
[d] *Department Environmental Engineering and Sustainable Development Entrepreneurship, Technical University of Cluj-Napoca, 400641 Cluj-Napoca, Romania.*
[e] *National Institute for Research Development for Chemistry and Petrochemistry-ICECHIM-București, 202 Spl. Independenței, 060021, Bucharest, Romania.*
[*] *Corresponding author : gvasilievici@icechim.ro*

INTRODUCTION

The most widely used thermoplastics globally are polyethylene (PE) and polypropylene (PP) but they share a common challenge: because they degrade slowly, they contribute to long-term ecological damage [1]. The degradable alternatives are (bio)polymers such as PBS (polybutylene succinate) and PLA obtained from renewable resources such as corn starch and sugarcane [2-3] and poly(hydroxyalkanote)s (PHAs) produced by bacterial fermentation. Yu et al. have investigated the potential antimicrobial ZnO's properties through the PLA integration. Their results demonstrated improved degradability, antibacterial activity and enhanced air filtration performance, framing PLA/P(3HB-co-4HB)/ZnO melt-blown nonwovens as well-suited options for next-generation sustainable air filters, medical masks, and protective healthcare textiles. PLA has also garnered considerable attention from food packaging industry experts due to its high transparency, good biological compatibility and high tensile plasticity. Considerable scientific inquiry has concentrated on adapting PLA structure to enhance its functional performance and increase its versatility. Li et al. obtained an electrospun PLA composite by incorporating different concentrations of ZnO nanoparticles and evaluated their mechanical, thermal, hydrophobic, and antibacterial properties. Moreover, they studied the effectiveness of these materials in preserving fresh chicken meat, establishing a foundation for degradable antibacterial food packaging [4].

Torche et al. have recently explored the alternative of using deep eutectic solvents (DESs) obtained by complexation between hydrogen-bond donors and quaternary ammonium salts. The obtained PLA-based composite plasticized with DESs and reinforced with green-synthesized ZnO particles derived from date palm seed extracts exhibited robust antibacterial efficacy, most notably at a 3 wt% ZnO concentration, demonstrating substantial reductions in *Staphylococcus aureus* and *Escherichia coli*, alongside complete inhibition of the spore-forming pathogen *Bacillus cereus* [5].

Significantly valued since the days of antiquity for its extensive economic importance and medicinal properties, *mesquite* or *algarroba*, belonging to the *Prosopis* family, continues to be utilized globally. Scientific research reveals that pastes, gums, and leaf smoke derived from the plant contain bioactive compounds that fight cancer, diabetes, inflammation, and microbial infections. Raja Thandavamoorthy et al. aimed to select the optimal materials for developing a composite made of epoxy resin matrix reinforced with *Prosopis juliflora* fibers (PJFR) and zinc oxide particles, to be fabricated via the conventional hand layup method. They evaluated the mechanical, thermal, and morphological characteristics of an innovative PJ composite,

showing that the addition of zinc oxide as a filler material significantly enhanced the thermal performance of the PJ fiber composite, yielding an average improvement of 26.7% [6].

A novel approach was introduced by Chen et al. by using 3-aminopropyltriethoxysilane (APTES) to form capped ZnO quantum dots. The study investigates the structure–property relationships of AC-ZnQDs/PLA composites, highlighting that the end-group modulation fundamentally transforms polymer performance by tailoring chain-end chemistry. This targeted structural tuning drives simultaneous optimization across three critical areas: interfacial compatibility, mechanical integrity and hydrolytic degradation [7].

Detecting microorganisms contaminating membrane surfaces is essential across fields such as biotechnology, environmental engineering, the food industry, pharmaceuticals, and medical applications. Membrane surfaces are used in separation processes, coarse particle filtration, and biological treatment plants to purify water containing persistent pollutants [8-13]. Microbial colonization of these surfaces can cause biofouling, structural degradation, and reduced performance.

Membrane surfaces serve as effective substrates for microorganisms, including bacteria, fungi, and microalgae. Once attached, these organisms may form biofilms, complex communities embedded in a polymeric extracellular matrix. Biofilm formation reduces membrane permeability, increases hydraulic resistance, and impacts separation selectivity. Microbiological testing identifies colonizing species and assesses their ability to adhere to and grow on membrane surfaces [14].

Assessing microorganisms is crucial for ensuring the safety and stability of membrane-based systems. In medical and pharmaceutical settings, microbiological contamination can compromise product or equipment sterility and pose serious health risks. In water treatment, ultrafiltration, and microfiltration, microbial communities on membranes can decrease purification efficiency and contaminate the final product. Studying how microorganisms interact with membrane surfaces helps identify surface properties, such as roughness, hydrophobicity, electrical charge, and chemical composition, that influence microbial adhesion. These insights guide the development of antimicrobial membranes, which can extend the operational lifespan of filtration systems [15].

Microbiological testing guides the development of effective strategies for preventing and controlling contamination. Identifying dominant microbial species and their adhesion and proliferation mechanisms enables the selection of appropriate cleaning, disinfection, or sterilization procedures for membranes. Microbiological monitoring is therefore essential for operational

management in membrane-based systems. Testing for microorganisms that can contaminate membrane surfaces helps clarify colonization mechanisms, maintain membrane performance, and ensure process safety [16-20]. This approach also helps prevent premature material degradation and supports the development of new technologies to reduce microbiological contamination.

The goal of our study is to help design versatile, environmentally friendly PLA materials with high bactericidal activity that are both sustainable and biodegradable.

RESULTS AND DISCUSSION

Characterization of ZnO powder

Determination of particle size distribution. For this study, 0.03 g of the sample was dispersed in 25 mL of distilled water. Further, the resulting dispersion was ultrasonicated in a water bath for approximately 3 minutes to separate aggregated particles. The results of Dynamic Light Scattering (DLS) are presented in Table 1 and Figures 1 and 2.

Table 1. Evaluation of particle size by DLS

Sample	Dm (nm)	PdI	Peak position by intensity (nm)
ZnO	840± 56	0.697	P_1 = 873 P_2 = 216

The relatively high average hydrodynamic particle size (Dm) can be attributed to the elevated NaOH dosing flow rate of 0.5 mL/min, which results in less controlled nucleation and the formation of larger particles. A 30-minute post-reaction at 60°C can facilitate the dissolution of smaller particles and the growth of larger ones, thereby narrowing the size distribution and increasing the average size. Calcination at 300°C for 4 hours, with a heating rate of 10°C/min, achieves complete conversion of $Zn(OH)_2$ to ZnO and promotes moderate particle growth via incipient sintering. Ethanol washing decreases particle agglomeration, although it does not entirely prevent it.

The Polydispersity Index (PdI) highlights the inhomogeneity of the particle population size. Thus, the polydispersity index value of 0.697 suggests a multimodal population distribution. Also, the relatively high PDI value indicates that particle populations with very different sizes coexist, the nucleation process was uncontrolled, and there are probably agglomerates alongside primary particles.

Figure 1 shows a bimodal particle size distribution, with populations averaging 873 nm and 216 nm, as the average of five determinations. Larger aggregates are also present, as indicated by the correlation curve in Figure 2.

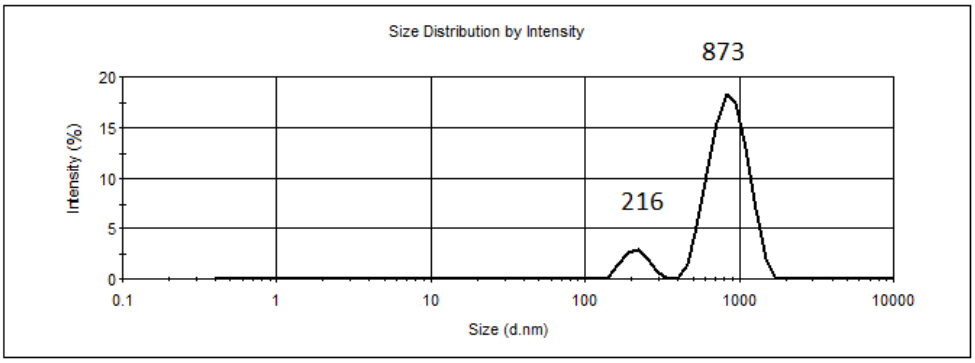

Figure 1. Size distribution for ZnO powder

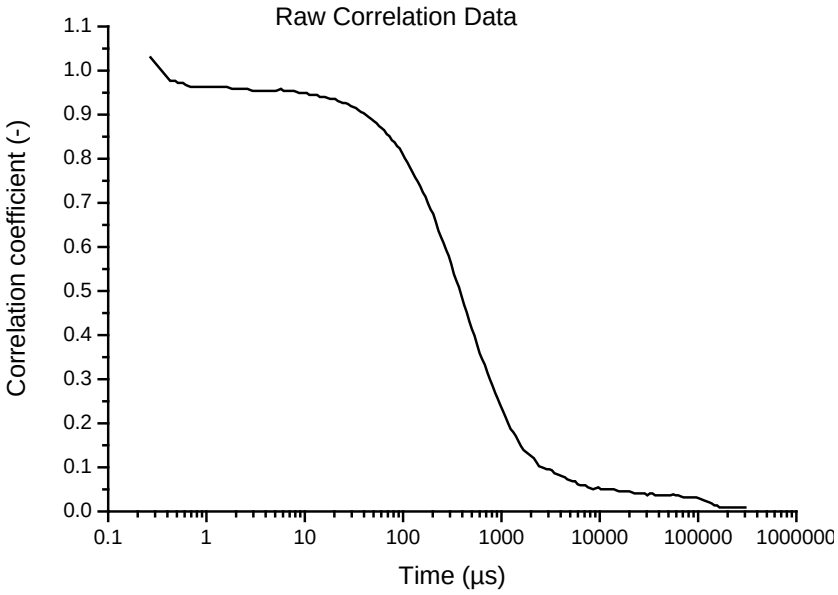

Figure 2. Correlation curve

Determination of textural characteristics. The specific surface area, total pore volume, and average pore diameter were determined by nitrogen adsorption (Figures 3-4, Table 2).

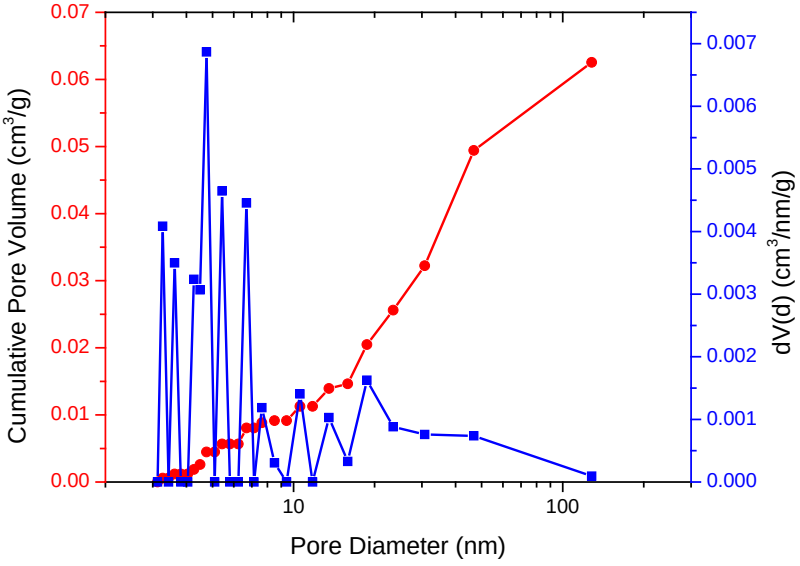

Figure 3. The pore size distribution of ZnO powder

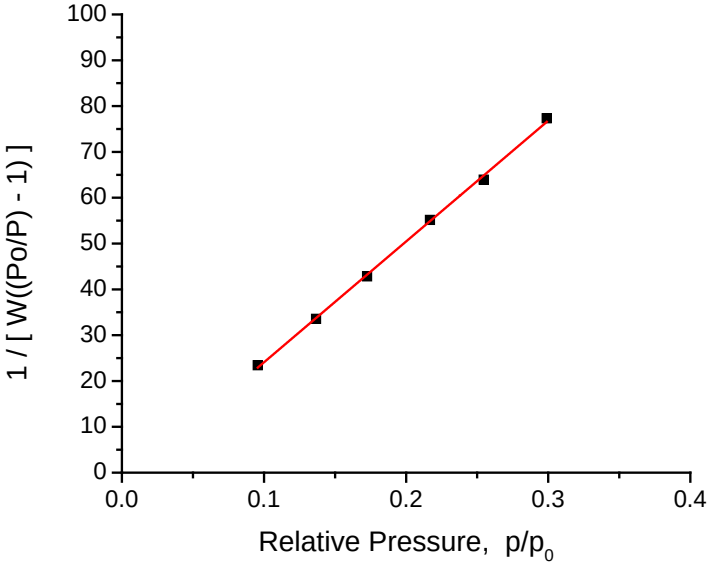

Figure 4. Multi-Point BET (Brunauer–Emmett–Teller) Plot

Table 2. Textural characteristics of ZnO powder particles

Sample	Specific surface area (m^2/g)	Total pore volume (cm^3/g)	Mean pore diameter (nm)
ZnO	13.744	0.063	4.750

The BET-specific surface area is relatively low for ZnO powder, indicating particles that are small-sized but partially agglomerated or sintered. Thus, the specific surface area indicates the formation of ZnO particles in the submicron range, but also significant agglomeration after calcination at 300°C. Therefore, the value of 13.7 m^2/g indicates a reduction in surface area due to a slight sintering during calcination.

The total pore volume indicates low to moderate porosity, reflecting interparticle spaces and pores formed upon removal of water and hydroxide. The relatively low total pore volume suggests particle compaction or aggregation and possible densification during heat treatment. This value demonstrates the existence of accessible, predominantly interparticle porosity. In systems produced by NaOH precipitation, gel or hydroxide drying, and calcination, pores typically form through water removal, decomposition of $Zn(OH)_2$ or basic intermediates, and aggregate reorganization.

The average pore diameter falls within the mesoporous range (2–50 nm, as defined by IUPAC), indicating a relatively uniform structure with free spaces between nanoparticles or aggregates. Such porosity is advantageous for antimicrobial activity and promotes effective dispersion in polymer matrices, such as PLA.

From the multipoint BET graph (Figure 4), it can be seen that the points are well aligned, confirming good linearity of the experimental values in the analyzed relative pressure range, with a correlation coefficient very close to 1. Thus, the BET specific surface area, obtained from automatic sample processing, indicates a relatively moderate value, consistent with an oxide with relatively agglomerated or partially sintered particles.

SEM analysis of ZnO powder. Scanning electron microscopy (SEM) analysis of ZnO powder at a 4 µm scale (Figure 5) reveals that the smallest visually distinguishable particles measure approximately 80–150 nm. Significant agglomeration obscures individual particle boundaries, resulting in poorly defined edges. The SEM image predominantly displays micrometric aggregates composed of smaller primary particles, with the smallest visible formations estimated at 50–150 nm.

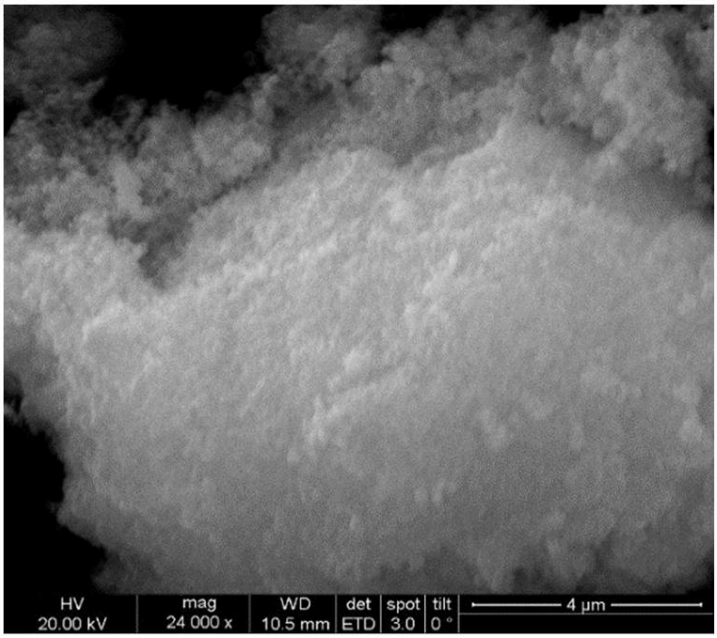

Figure 5. SEM image of ZnO

The SEM image supports the results obtained from DLS analysis, indicating that ZnO particles are strongly agglomerated and do not appear as well-separated individual particles.

In summary, the SEM image of ZnO powder demonstrates an agglomerated morphology, with fine particles forming irregular micrometric aggregates. This observation indicates substantial agglomeration of primary particles into larger clusters. The non-uniform size distribution and observed surface roughness suggest the presence of interparticle spaces, which may contribute to porosity, as confirmed by BET analysis.

Mechanical Properties of the ZnO-reinforced PLA composite

Bending test interpretation. The mechanical performance of the ZnO-reinforced PLA composite, plasticized with Proviplast 2624 and Span 60, reveals a significant behavior change compared to pure PLA. Thus, as shown in Tables 3 and 4, the material's mechanical behavior changes radically, especially at low temperatures (4°C and -18°C). Normally, pure PLA (from Ingeo) is a rigid and brittle polymer, especially at temperatures below its glass transition temperature (approx. 55−60ºC). Both at 4ºC and especially at -18ºC, pure PLA becomes extremely brittle, with a very high Young's Modulus (often between 2000 and 3500 MPa) and a very low elongation at break.

Although ZnO acts as a stiffener and nucleating agent, in the presence of a large amount of plasticizers such as Proviplast 2624 and Span 60 (17% in total), the flexibilization effect of the plasticizers dominates the matrix, increasing the free volume and molecular mobility. This dramatically decreases the Young's Modulus (stiffness) and increases flexibility, even at freezing temperatures. Thus, the Young's Modulus (approx. 437 MPa) is very low compared to pure PLA (which at 4ºC is over 3000 MPa). This demonstrates the efficiency of the Proviplast 2624 plasticizer, the composite becoming extremely flexible and elastic at a temperature close to that of a food refrigerator. Also, the maximum bending stress (approx. 28 MPa) is lower than in pure PLA (which can exceed 60-80 MPa).

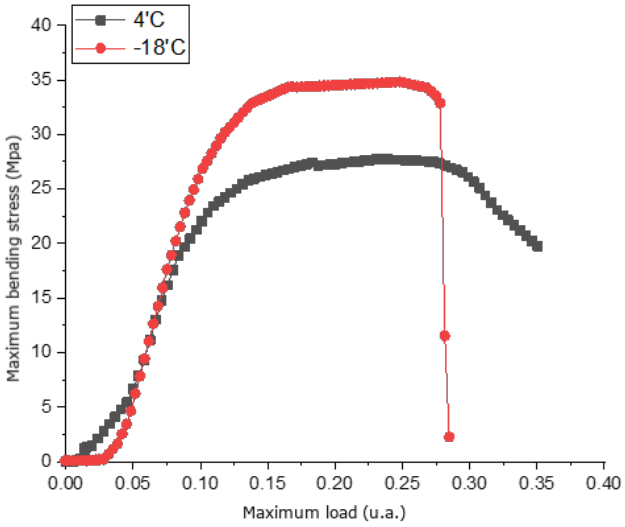

Figure 6. Variation of maximum bending stress with load, at 4ºC and -18ºC

The material yields at much lower forces because plasticization has reduced the polymer's internal cohesion. Although the material is flexible (low modulus), the capacity for plastic deformation at this temperature, as evidenced by the elongation value, remains relatively limited before a crack initiates. Normally, as the temperature decreases from 4ºC to -18ºC, polymers become stiffer and more brittle. Thus, an increase in the Young's modulus (to 517 MPa) and the maximum bending stress at maximum load (35 MPa) is normal. At -18ºC, the movement of the PLA and plasticizer chain segments is further reduced, making the material stiffer and capable of supporting a higher maximum load (83 N versus 63 N). The fact that the elongation increased by more than 3 times suggests a synergistic toughening

mechanism at extremely low temperatures, probably due to controlled phase separation. Thus, at -18ºC, Proviplast 2624 or Span 60 could form distinct micro-domains that deflect microcracks and allow the composite to deform further before complete failure. Therefore, Figure 6 highlights the superior behavior of the sample at -18ºC, as evidenced by the maximum load supported, stiffness, and maximum bending stress.

Table 3. Results obtained from the bending test at 4ºC

Maximum load (N)	**Young's modulus** in bending **(MPa)**	Bending stiffness **(Nm²)**	Maximum bending stress at maximum load **(MPa)**	Elongation **(mm)**
63.194 ± 2.13	436.667 ± 9.14	0.011 ± 0.002	27.750± 0.95	1.265± 0.23

Table 4. Results obtained from the bending test at a temperature of -18ºC

Maximum load (N)	Young's modulus in bending **(MPa)**	Bending stiffness **(Nm²)**	Maximum bending stress at maximum load **(MPa)**	Elongation **(mm)**
83.000 ± 2.61	517.094 ± 11.25	0.014± 0.003	34.824± 1.28	4.054± 0.71

Table 5 presents the tensile test results, and Figure 7 shows the tensile deformation curve.

Table 5. Results obtained from the tensile test

Tensile strength (MPa)	**Maximum load (N)**	**Breaking load (N)**	**Elongation at break (mm)**	**Young's modulus (MPa)**	**Tensile strength at break (MPa)**
13.650± 0.72	143.609 ± 3.97	142.628± 3.47	5.246± 0.82	512.298 ± 10.41	13.557 ± 0.63

Flexural Properties. The flexural properties of the ZnO-reinforced PLA composite plasticized with Proviplast 2624 and Span 60 are presented in Tables 3 and 4. The results indicate that storage temperature significantly influenced the mechanical response of the material. At 4 ºC, the composite exhibited a flexural modulus of 436.67 MPa, a maximum bending stress of 27.75 MPa, and a maximum load of 63.19 N. After storage at −18 ºC, these values increased to 517.09 MPa, 34.82 MPa, and 83.00 N, respectively.

The increase in flexural modulus and maximum bending stress at −18 ºC indicates a stiffer and stronger material under bending conditions. This behavior is consistent with the reduced mobility of polymer chains at lower temperatures, which generally leads to increased rigidity. Despite the presence of ZnO, which may contribute to reinforcement of the PLA matrix, the relatively low modulus values compared with those typically reported for neat PLA suggest that the plasticizing effect of Proviplast 2624 and Span 60 plays a dominant role in determining the overall mechanical behaviour of the composite.

The elongation value increased from 1.27 mm at 4 ºC to 4.05 mm at −18 ºC. Although this result suggests an improved deformation capacity before failure, additional microstructural investigations would be required to identify the mechanisms responsible for this behaviour. Overall, the composite maintained its structural integrity at both storage temperatures while exhibiting higher stiffness and load-bearing capacity at −18 ºC.

Tensile Properties. The tensile properties of the ZnO-reinforced PLA composite are presented in Table 5. The material exhibited a tensile strength of 13.65 MPa, a maximum load of 143.61 N, a breaking load of 142.63 N, and a Young's modulus of 512.30 MPa. The small difference between the maximum load and breaking load indicates that failure occurred shortly after the maximum stress was reached.

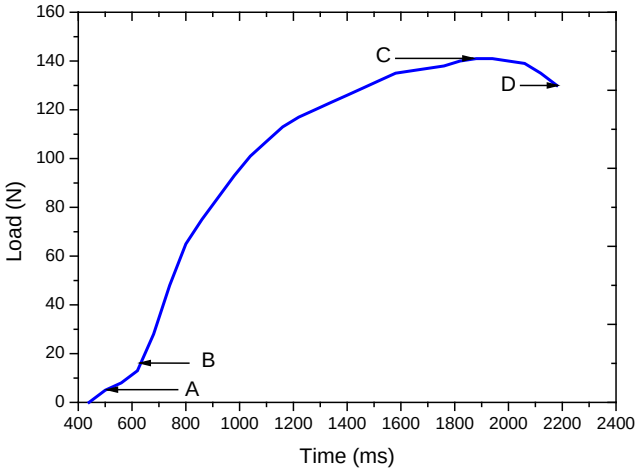

Figure 7. Tensile strain curve of PLA-ZnO composite

The measured Young's modulus was substantially lower than values commonly reported for neat PLA, confirming the effectiveness of the plasticizers in reducing matrix stiffness. The elongation at break of 5.25 mm indicates a moderate capacity for deformation before failure. These results

demonstrate that incorporating Proviplast 2624 and Span 60 modifies the mechanical response of PLA, producing a material with reduced stiffness and moderate flexibility while maintaining sufficient mechanical strength for handling and packaging applications.

Overall, the combination of ZnO and plasticizers resulted in a composite characterized by lower rigidity than conventional PLA and satisfactory mechanical performance over the investigated temperature range.

SEM analysis of the ZnO-reinforced PLA composite. The SEM image demonstrates that the PLA ZnO composite exhibits a uniform morphology. The polymer displays a homogeneous microstructure without evidence of phase separation (Figure 8). Furthermore, the incorporation of ZnO particles into PLA does not alter the composite surface, resulting in a smooth, non-porous foil that does not promote biological activity such as adhesion, migration, or proliferation of cultured cells.

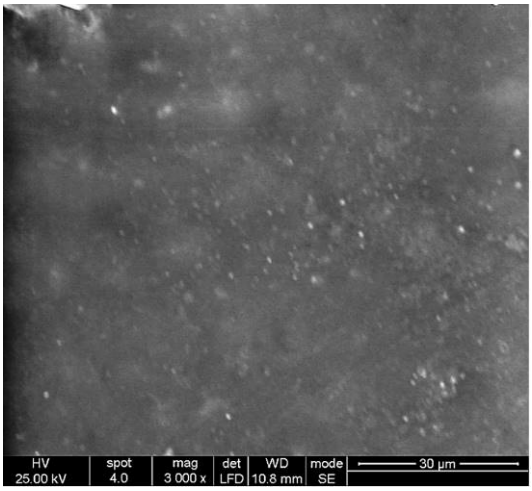

Figure 8. SEM micrograph of the ZnO-reinforced PLA composite

The SEM micrograph (Figure 8) reveals a relatively homogeneous and continuous surface morphology of the ZnO-reinforced PLA composite. Numerous fine bright spots are distributed throughout the polymer matrix that can be attributed to ZnO particles dispersed within the PLA. Although small-localized agglomerates are visible, no large clusters, cracks, or significant voids were observed, indicating a satisfactory distribution of the inorganic phase in the plasticized PLA matrix.

The absence of major structural defects suggests adequate compatibility between the matrix and the filler, which may contribute to the overall mechanical integrity of the PLA composite. The relatively uniform morphology is consistent with the mechanical results, where the material exhibited sufficient strength while maintaining moderate flexibility due to the plasticizing effect of Proviplast 2624 Span 60.

Barrier properties of the ZnO-reinforced PLA composite

Determination of oxygen permeability. Permeability was measured at 1 atm pressure, temperature 23ºC, and 0% relative humidity for 5 specimens of PLA composite containing ZnO. Table 6 presents the thickness and the average oxygen permeability and normalized oxygen permeability values of the PLA-ZnO composite, both normalized to a layer thickness of 1 mm.

Table 6. Oxygen Permeability Test (OTR) Results

Sample	Sample thickness (mm)	OTR, (mL/m^2 x day)	OTR, $mL/m^2 \cdot day$ (relative to a thickness of 1 mm)
PLA-ZnO	0.97	106.53± 0.83	109.82± 0.86

Table 6 indicates that the tested PLA formulation exhibits more than five times higher oxygen permeability compared to pure PLA [21]. This increase is attributed to relaxation of the polymer structure and enhanced PLA chain mobility resulting from the high concentration (15% wt.) of Proviplast 2624 plasticizer. The barrier effect of ZnO is substantially diminished due to this increased chain mobility. Furthermore, Span 60 acts as an interfacial lubricant, thereby facilitating oxygen diffusion through the PLA membrane.

Oxygen permeability in the PLA formulation is mainly determined by the plasticizer content and polarity, rather than by the powder content. The addition of non-polar plasticizers increases the formulation's oxygen permeability. When the polarity of the plasticizer matches that of the polymer, swelling increases free volume and oxygen permeability. Materials that block pores can partially offset this increase in oxygen diffusion. Consequently, adjusting the concentration of inorganic powders enables control over oxygen permeability in PLA-based composites, even when high levels of polar plasticizers such as Proviplast 2624 are present.

Water absorption. Figure 9 presents the results obtained. The absorption rate at both temperatures is initially higher, as indicated by the steeper slope of the curve, and subsequently decreases, approaching

equilibrium (saturation) around days 6 to 7. On day 7, both samples reach an identical absorption value of 0.47%. This finding suggests that the maximum absorption capacity of the polymer network in 10% saline solution is determined by the chemical structure of PLA and the presence of salt, rather than by temperature. The higher initial diffusion rate observed at elevated temperature is attributed to increased kinetic energy of water molecules and greater mobility of the polymer chains. At 23ºC, the free volume between PLA chains forms and changes more rapidly, enabling the saline solution to penetrate the matrix more efficiently during the initial phase of the experiment.

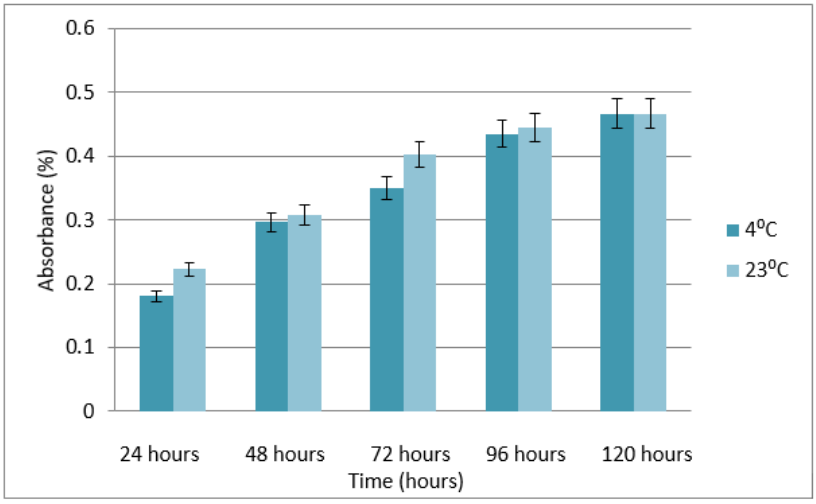

Figure 9. Absorption in saline solution of the PLA sample at temperatures of 4 and 23 ºC, for a storage period of 120 hours

The maximum absorption value of 0.47% is relatively low. In pure water, PLA typically absorbs slightly more water, typically between 0.5% and 1%, depending on its degree of crystallinity. The presence of 10% NaCl in the external solution induces an osmotic effect. The high external salt concentration retains water, reducing its chemical potential and, consequently, the driving force for water ingress into the hydrophobic PLA sample. Therefore, temperature (23ºC versus 4ºC) influences only the rate of equilibrium attainment during the initial days, accelerating the process. The maximum absorption capacity at saturation remains independent of temperature over the 4–23ºC range, limited to 0.47% by the polymer's structural properties and the osmotic pressure exerted by the 10% saline solution.

Goniometric study of a PLA-based sample. Figure 10 shows the sample image together with the contact angle report for the distilled water drop.

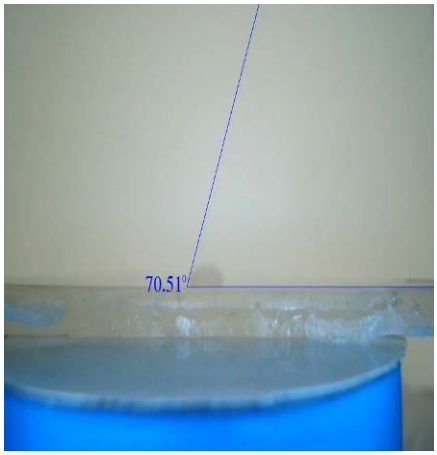

Figure 10. Image of a drop of distilled water deposited on the PLA-ZnO composite

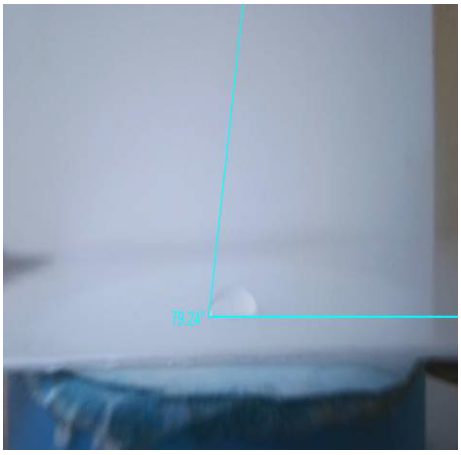

Figure 11. Image of a drop of distilled water deposited on the PLA sample

The PLA-ZnO composite exhibits moderate hydrophilicity, as evidenced by a contact angle of 70.51° between a distilled water droplet and the substrate. This measurement reflects strong water affinity and partial wetting, in contrast to the near-spherical droplets observed on highly hydrophobic materials such as Teflon or wax. In comparison, pure PLA displays a contact angle of 79.24°, which positions it at the threshold between weakly hydrophilic and hydrophobic behavior due to its aliphatic chain structure (Figure 11). The enhanced hydrophilicity of the PLA-ZnO composite, as indicated by its lower contact angle, is attributed to the characteristics of the primary plasticizer (Proviplast 2624) and the specific composite preparation method. During melt processing, Proviplast molecules are likely to orient their polar sides toward the sample surface, particularly when the composite melt remains in extended contact with highly polar metal pressing plates.

The 70.51° contact angle measured for the PLA-ZnO formulation is consistent with the behavior observed in the preceding saline solution test. Although the surface permits water adhesion and wetting, which initiates diffusion, the overall mass absorption remains low at 0.47%.

The incorporation of 3% ZnO into the PLA matrix can alter the contact angle; however, the resulting change in hydrophilicity is not necessarily

linear. This effect depends on the dispersion state of the particles and modifications to surface topography. Zinc oxide is inherently hydrophilic, with numerous polar hydroxyl (−OH) groups present on the particle surfaces. When well dispersed and exposed at the composite surface, these particles increase the material's surface energy, attracting water to the polar centers and reducing the contact angle below 70°. Nevertheless, at a 3% concentration, which represents a critical threshold in composite rheology, ZnO submicron particles tend to agglomerate, unlike the uniform dispersion observed at lower concentrations (0.5 %...1 %). These findings indicate that surface properties differ from bulk properties. While the surface readily interacts with water (contact angle of 70.51°), the compact, predominantly polyester internal structure of PLA restricts deeper water penetration, particularly under the osmotic influence of salt.

Water vapor permeability. The calculation of water vapor permeability was carried out with the relationship (1):

$$WVP = \frac{\Delta M \cdot d}{\Delta t \cdot \Delta P \cdot A}, \quad g \times mm / m^2 \times h \times kPa \tag{1}$$

where:

- ΔM - the difference in weight of the Petri dish before and after the determination, (g)
- Δt – time unit (h),
- d - probe thickness (mm),
- A - the area of the probe exposed to moisture (m^2),
- Δp - the difference in water vapor pressure between the inside and outside of the Petri dish (3.1671 kPa at 25 °C).

The average value of water vapor permeability after three determinations was: WVP = 0.54 $g \times mm / m^2 \times h \times kPa$

FTIR analysis. Figure 12 shows the ATR - FTIR spectrum of the PLA, Proviplast 2624, and ZnO composite. Absorption bands were detected at wavenumbers of 2992, 1747, 1454, 1361, 1267, 1180, 1079, 1043, 956, 865, and 754 cm^{-1}. The peaks at 1747, 1180, and 1079 cm^{-1} exhibit the highest intensities. These last peaks correspond to C–O or C=O stretching, functional groups originated from PLA or plasticizer.

The ATR - FTIR spectrum reveals the predominant features of the polymer matrix (PLA), the effects of the plasticizer, and the specific interactions with the inorganic phase (ZnO). Most of the absorption bands are characteristic of PLA's chemical structure, like 2992 cm^{-1}, specific for C–H

stretching form PLA backbone, or 1454 cm^{-1}, specific for CH_3 asymmetric deformation. The most intense bands confirm the presence of ester groups. The absorption at 1747 cm^{-1} exhibits the highest intensity and corresponds to the stretching vibration of the carbonyl group in the ester bond of PLA, a position typical for amorphous or semi-crystalline PLA. The bands at 1180 cm^{-1} and 1079 cm^{-1} correspond to the asymmetric and symmetric stretching vibrations of the ester bond, respectively, and their high intensities are typical of polyesters. The absorption at 2992 cm^{-1} is attributed to the asymmetric stretching vibrations of methyl groups, while the bands at 1454 cm^{-1} and 1361 cm^{-1} correspond to the deformation vibrations of the $-CH_3$ and $-CH-$ groups. The band at 1267 cm^{-1} is assigned to the stretching vibration of the C−O bond in ether or ester groups [19].

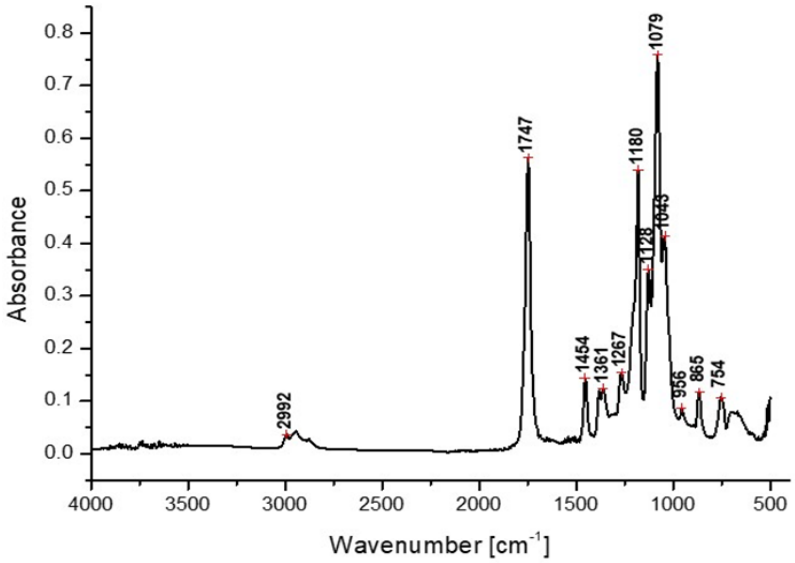

Figure 12. ATR - FTIR spectrum of the PLA – ZnO composite

Also, Proviplast 2624 is an ester-type plasticizer having a chemical structure similar to that of PLA (both contain ester groups), so that its bands overlap those of the polymer. Thus, the presence of the plasticizer can broaden the peak at 1747 cm^{-1}, since it also contains C=O groups, and the 1043 cm^{-1} and 956 cm^{-1} bands are more pronounced due to the specific structure of the plasticizer (vibrations of aliphatic or C−O chains specific to low molecular weight esters).

Zinc oxide, as an inorganic material, exhibits fundamental vibrations typically below 500 cm^{-1} (Zn−O bond), which are not detected in the IR range. Its presence in the composite is inferred from the formation of hydrogen bonds or electrostatic interactions between the ZnO particle surfaces and the polar groups of the polymer or plasticizer, as evidenced by the C=O band at 1747 cm^{-1} and the C−O bands at 1180 cm^{-1}. The high intensities of the bands at 1747, 1180, and 1079 cm^{-1} suggest a structure dominated by ester bonds, confirming effective homogenization of the plasticizer within the PLA matrix and the absence of significant chemical degradation of the polymer during processing. For example, hydrolysis would have produced a broad −OH peak above 3200 cm^{-1}. $^{-1}$. As Kim and co. shows that the presence of plasticizer may increase absorption in the area 1730–1750 cm^{-1}, adding ester carbonyls and slightly shifting the existing peaks [19].

Microbiological analysis

Preparation of Petri dishes and microbial inoculation procedure. For the testing procedure, 15 Petri dishes were used for each condition, containing 15 mL of a culture medium specific for bacterial growth, and an additional 15 Petri dishes containing 15 mL of a culture medium specific for fungal growth. The chemical composition of the culture media is presented in Table 7. The microbial strains *Bacillus subtilis* and *Aspergillus sp.* were obtained from the microorganism collection of the TPP laboratory within UPG. The culture media for bacterial and fungal growth were prepared in accordance with the protocol described in the USP and EU *Pharmacopoeia* [20,22,24].

The sterilized culture media, cooled to 30°C, were poured into labeled Petri dishes. In each Petri dish containing bacterial growth medium, 400 µL of pure *Bacillus subtilis* culture at a concentration of 10^5 cells/mL was added. The media were homogenized by gentle swirling of the plates and allowed to cool at room temperature until solidification.The same procedure was applied to 15 Petri dishes containing fungal growth medium. Each plate was inoculated with 400 µL of pure *Aspergillus* sp. culture at a cell concentration of 10^4 cells/mL.

Table 7. Composition of culture media used in microbiological analyses

Culture medium	Composition	Preparation method
Bacterial growth medium	Peptone 10 g Sodium chloride 5 g Agar 20 g Meat extract 10 g Water up to 1000 mL	The mixture was heated to boiling, the pH was adjusted to 7.4, then filtered and sterilized at 121 °C for 15 minutes
Fungal growth medium	Peptone 10 g Glucose monohydrate 20 g Agar 20 g Water up to 1000 mL	All components were mixed until dissolved, the pH was adjusted to 5.5, and the medium was sterilized at 121 °C for 15 minutes

Assessment of the inhibitory effect of the chemical composition of the tested samples. In each Petri dish, two specimens from Series A (PLA–ZnO CONTROL samples), Series B (inoculated PLA–ZnO samples), and Series C (agar-only film samples) were placed at equal distances from one another on the surface of the culture medium.The Petri dishes inoculated with *Bacillus subtilis* were incubated at 37°C for 48 hours, while those inoculated with *Aspergillus* sp. were incubated at 28 °C for 14 days. After incubation, the bacterial culture plates were examined microscopically. The obtained results were quantified by measuring the zone of microbial growth inhibition according to the protocol described in the USP and EU *Pharmacopoeia* [20,22,24].

Experimental results. The inhibition zones formed around the PLA–ZnO composite samples labeled CONTROL (A1 and A2), compared with the controlled-inoculated PLA–ZnO samples (B1 and B2) and the agar film samples (C1 and C2), were different. As shown in Figure 13, the control samples exhibited the largest inhibition zones. The samples previously contaminated with bacteria showed a smaller inhibition zone. However, it can still be observed that the chemical composition of the PLA exhibits bactericidal potential, considering that the samples were pre-inoculated with microorganisms. Regarding sample C, it was observed that its chemical composition does not exhibit antimicrobial activity, as no inhibition zone was detected. On the contrary, *Bacillus subtilis* was able to grow, since the culture medium was favorable for cellular development. Similar results were obtained in the case of incubation with the fungal strain *Aspergillus* sp.

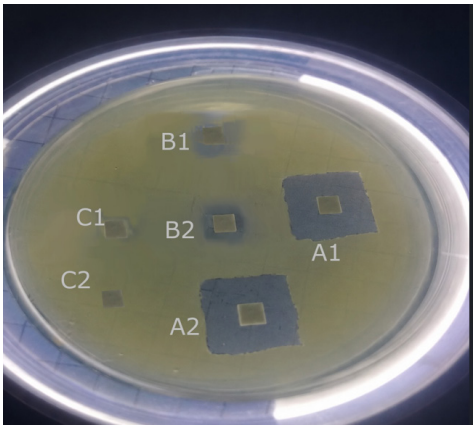

Figure 13. Microscope image of the Petri appearance of Petri dishes inoculated with *Bacillus subtilis* **i**n culture medium after 48 h incubation at 37 °C

Figure 13 illustrates the culture media after incubation, showing the visual appearance of the Petri dishes inoculated with *Bacillus subtilis* and the corresponding samples.

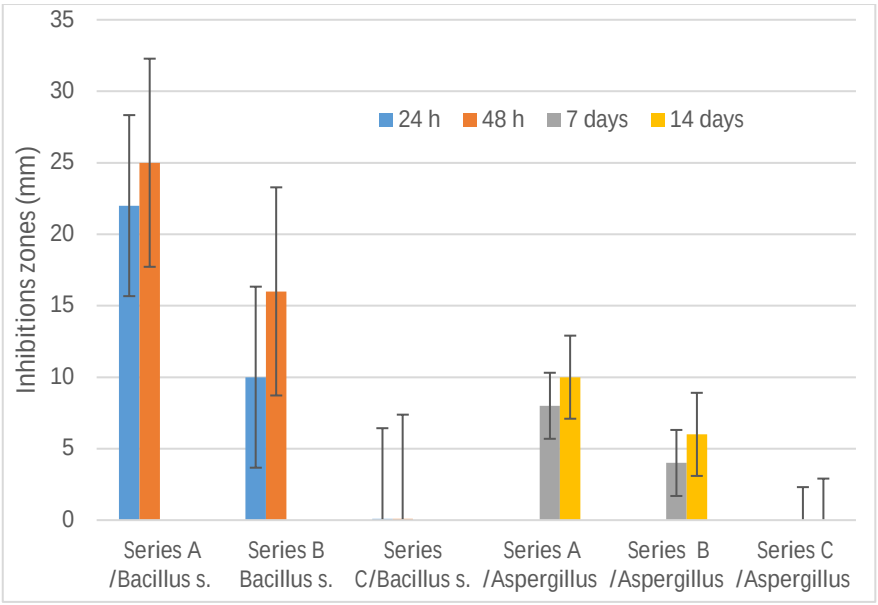

Figure 14. Graphical representation of the experimental results obtained from microbiological tests

Given the results obtained after 48 hours of incubation, which showed a significantly larger inhibition zone than the other samples, the experiment was extended to 72 hours to highlight the microbicidal effect of the ZnO powder within the composite's chemical composition. Thus, larger PLA–ZnO Control samples (50 mm × 50 mm) were transferred onto Petri dishes previously inoculated with *Bacillus subtilis* and containing a culture medium specific for bacterial growth. The results obtained after 72 hours of incubation clearly demonstrated that the inhibition zone generated by the ZnO particle pellets effectively suppressed bacterial growth, maintaining the microorganisms at a distance over time. Figure 14 shows the graphical representation of the experimental results from microbiological tests regarding the inhibition generated by the chemical composition of the analyzed samples. The values are presented as mean ± standard deviation, n = 4, performed in quintuplicate.

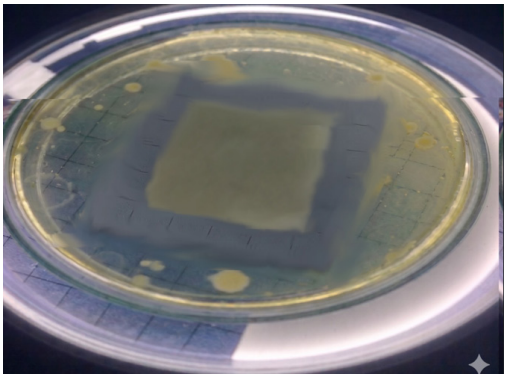

Figure 15. Visual appearance of Petri dishes inoculated with *Bacillus subtilis* in culture medium after 72 h incubation at 37 °C

In addition, the results obtained after 72 hours of incubation showed that bacterial colony-forming units (CFUs) appeared on the Petri dish outside the diffusion zone of ZnO, while inhibition of cellular growth was maintained around the CONTROL sample.

CONCLUSIONS

ZnO powder produced by the precipitation method features a mesoporous structure, partially agglomerated particles, moderate porosity, and a specific surface area suitable for antimicrobial applications. Conducting the precipitation process at a controlled flow rate with 2% wt Polysorbate 80,

followed by 30 minutes of maturation and calcination at 300°C, yields a ZnO powder with a narrow particle size distribution and aggregate-containing ZnO powder with a broad size distribution suitable for antimicrobial applications. The PLA composite containing ZnO demonstrates good mechanical performance, with adequate resistance to bending and tensile stresses. At -18°C, the material supports higher loads than at 4°C, indicating increased strength and stiffness at lower temperatures. However, its relatively low elongation suggests limited flexibility, making it more suitable for applications requiring mechanical stability and rigidity rather than high deformability. The addition of 15% by weight Proviplast 2624 increases PLA chain mobility, which partially reduces the barrier effect of ZnO and allows limited oxygen diffusion through the PLA-based membrane. The measured water vapor permeability indicates good particle dispersion, low porosity, a homogeneous interface, and a structure suitable for packaging or antimicrobial membrane applications. The contact angle of the water droplet with the surface of the PLA-ZnO composite of 70.51° shows a decrease in the hydrophobic character of the composite in the vicinity of the PLA-ZnO composite surface, probably due to the migration of ZnO particles to the composite surface or the orientation of the polar groups of Proviplast 2624 to its surface during the composite preparation process. This contact angle value is consistent with the variation of the absorption of saline water in the composite with the contact time with the saline solution. Microbiological tests have highlighted the important contribution of ZnO particles in inhibiting the growth of *Bacillus subtilis* and *Aspergillus sp*. cultures.

EXPERIMENTAL SECTION

Materials and Methods

For the preparation of ZnO powder, zinc acetate, sodium hydroxide, ethanol, and Polysorbate 80 (Sigma-Aldrich) were used. Zinc oxide was synthesized by precipitation of a 0.1M solution of zinc acetate with a 0.1M solution of NaOH at a flow rate of 0.5 mL/min, in the presence of Polysorbate 80 at a concentration of 2%wt. The reaction was carried out at 60°C in an Erlenmeyer flask equipped with magnetic stirring at 600 rpm to a final pH of 10. The precipitate obtained was washed with distilled water 3 times and then with ethanol, after which it was dried in an oven with air recirculation at 90°C for 3 hours, then calcined at 300°C for 4 hours with a heating rate of 10°C/min. The experimental program was developed in accordance with findings from previous research [22-28].

Biodegradable composite was prepared using PLA (Ingeo® brand, NatureWorks LLC, Tokyo, Japan), plasticizers Proviplast 2624 (Proviron, Hangzhou, China) and Span 60 (sorbitan monostearate, Sabo), and ZnO powder with submicron particles synthesized as described above. The material was produced by hot mixing of components in a Brabender plastograph at 180°C and 60 rpm for 30 minutes, followed by pressing the resulting mixture between hot plates at 170°C for 5 minutes at 100 bar pressure. The formulation consisted of 80% by weight PLA, 15% Proviplast 2624, 2% Span 60 and 3% ZnO powder with submicron particles.

Characterization methods

Characterization of ZnO powder

Characterization of ZnO powder involved determining particle size distribution, textural properties and SEM analysis. Particle size and distribution were measured using a Nano ZS (Red badge) device, calibrated for particle sizes ranging from 0.6 nm to 6 µm, employing the DLS method. The Zetasizer Nano device measures fluctuations in the intensity of scattered light to calculate particle size within the sample.

The textural properties of the samples were evaluated using a Quantachrome NOVA 2200e gas sorption analyzer. Nitrogen adsorption/desorption isotherms were recorded at 77.35 K over a relative pressure (p/p_0) range from 0.005 to 1.0. The total pore volume was estimated from the desorbed volume at a relative pressure close to unity using the BJH (Barrett–Joyner–Halenda) method and the specific surface area was calculated using the BET method.

The structure and morphology of the ZnO powder and the PLA-ZnO composite were analyzed using scanning electron microscopy (SEM-Inspect S, FEI Company) operated at 15 kV.

Characterization of PLA composite

The PLA composite was characterized by measuring flexural and tensile strengths, assessing oxygen and moisture barrier properties, SEM and conducting FTIR analysis.

Mechanical Properties. Mechanical properties were evaluated using a Lloyd LR5k Plus universal testing machine (Lloyd Instruments, AMETEK Inc., West Sussex, UK; 5 kN load capacity) equipped with Nexygen software (version 4.0). All tests were performed at a crosshead speed of 1 mm/min, and each measurement was carried out on ten specimens (n = 10). Results

are reported as mean ± standard deviation. Statistical differences between samples stored at 4 °C and −18 °C were assessed using Student's t-test, with significance set at $p < 0.05$.

Tensile properties were determined according to ISO 527-3:2018 [24,28] using rectangular specimens (40 × 4 × 3 mm). Tensile strength, elongation at break, maximum load, breaking load, and Young's modulus were calculated from the stress–strain curves.

Flexural properties were measured according to ASTM D790 using the three-point bending method [25,30-31] on rectangular specimens (30 × 2 × 2 mm) with a support span of 20 mm. Maximum load, flexural modulus, bending stiffness, maximum flexural stress, and elongation were determined from the load–displacement curves.

Barrier properties. The barrier properties of the PLA were evaluated by measuring oxygen permeability, water absorption, and hydrophobicity using goniometric analysis [32-36].

Oxygen permeability. The determination of oxygen permeability was performed using the manometric method adapted for plastics on a Gaze-LYSSY permeability measuring device, in accordance with ASTM D1434 and ISO 2556, at 1 atm, 23 °C, and 0% relative humidity.

Water absorption. The sample was maintained in a desiccator until a constant weight was achieved, which was recorded as the initial mass (M_initial). The sample was then immersed in 15 mL of 10% saline solution and stored at 4 °C for 24 hours. Prior to weighing, the sample was rinsed with distilled water cooled to 4 °C, blotted with absorbent paper, and weighed three times in quick succession. The resulting value was recorded as the final mass (M_final) for that day. After each weighing, the sample was returned to the bottle, maintained at room temperature (22–23 °C) for 4 hours. The aforementioned steps were then repeated. After each measurement, the sample was returned to the bottle and refrigerated for another 24 hours. This procedure was conducted daily for 7 days. An identical protocol was followed at 23 °C. Absorption was calculated using the formula (2):

$$Ab = \frac{M_{final} - M_{initial}}{M_{initial}} \cdot 100, \quad \% \tag{2}$$

where $M_{initial}$ and M_{final} represent the mass weighed daily at 4° and 23°C, respectively.

Wetting degree by goniometry. A goniometric analysis of the PLA-based sample was performed using a camera connected to a computer running

specialized software. The wetting properties were quantified by measuring the contact angle between a water droplet and the sample surface.

Study of barrier properties. Water vapor permeability was measured using the ASTM E96 gravimetric method. A total of 20 g of anhydrous calcium chloride was placed in a Petri dish, sealed with PLA-based foil, and the assembly was weighed. The assembly was subsequently placed in a desiccator containing 300 ml of distilled water and maintained in an oven at 25°C.

FTIR spectroscopy. The Fourier-transformed infrared (FT-IR) spectra were recorded with a Jasco FTIR spectrometer (Jasco Europe srl, Cremella, Italy), using the total attenuated reflectance (ATR) device equipped with a horizontal ZnSe crystal (Jasco PRO400S, Jasco Inc., Easton, USA). FTIR spectra were registered for all samples at a resolution of 4 cm^{-1} as the mean of 100 scans in the wavenumber range of 4000-500 cm^{-1}.

Microbiological analysis. To evaluate whether the PLA containing ZnO exhibits antibacterial and/or antifungal properties, tests were performed to assess the degree of inhibition generated by the chemical composition of the PLA–ZnO composite in comparison with a plain agar-based sample [10-16]. The analysis procedure was carried out according to the protocol described in the USP and EU *Pharmacopoeia* [20,22,24].

Preparation of test samples. Test specimens were cut into 5 × 5 mm squares from three type materials, as follows: A) PLA–ZnO composite samples labeled CONTROL (Series A); B) PLA–ZnO composite samples subjected to controlled microbial inoculation (Series B); and C) samples cut from an agar film that did not contain any active substances in its composition (Series C).

Procedure for contamination of samples (Series B). The inoculation procedure of the microbial flora onto the surface of the composite PLA–ZnO sample (50 × 50 mm) was performed through controlled contamination using a defined amount of test microorganisms prepared in tenfold serial dilutions in physiological saline. The inoculum was applied onto the sample surface using a micropipette (400 µL of pure culture prepared in serial dilutions: *Bacillus subtilis* at concentrations of 10^5 cells/mL and 10^4 cells/mL, as well as *Aspergillus* sp.). After inoculation, the samples were kept in contact for 10 minutes, during which the inoculated suspension was evenly distributed by gently rotating and spreading it over the sample surface until complete drying at room temperature [25, 27, 29, 37, 38].

ACKNOWLEDGMENTS

Development of innovative food packaging without negative impact on the environment (AMBAL-INOV)", My SMIS: 120994, contract: 375/ 390051/ 30.09.2021, Competition: 63/POC/163/1/3/LDR.

G.V. acknowledges the support of the PN 23.06 Core Program – ChemNewDeal, within the National Plan for Research, Development and Innovation 2022–2027, developed with the support of the Ministry of Research, Innovation and Digitalization, Project No. PN 23.06.02.01, InteGral.

REFERENCES

1. J. Yu; H. Tian; Y. Zhao; L. Li; H. Pan; H. Yang; J. Bian; Z. Tan; H. Zhang. Development of antibacterial PLA-based melt-blown nonwovens via incorporation of P(3HB-co-4HB) and ZnO nanoparticles: Processing and property evaluation. *ACS Appl. Polym. Mater.* **2025**, *7* (18), 12269-12282.
2. C. A. Avila-Orta; C. A. Covarrubias-Gordillo; H. A. Fonseca-Florido; L. Melo-Lopez; R. Radillo-Ruiz; E. Gutierrez-Montiel. PLA/modified-starch blends and their application for the fabrication of non-woven fabrics by melt-blowing. *Carbohydr. Polym.* **2023**, *316*, 120975.
3. Q. Ren; M. Wu; L. Wang; W. Zheng; Y. Hikima; T. Semba; M. Ohshima. Cellulose nanofiber reinforced poly(lactic acid) with enhanced rheology, crystallization and foaming ability. *Carbohydr. Polym.* **2022**, *286*, 119320.
4. D. Li; F. Chen; Z. Dong; F. Jia; R. Wen; C. Sun; Q. Yu. Electrospun PLA/ZnO composite films: Enhanced antibacterial properties and application in fresh chicken meat preservation. *Food Packag. Shelf Life* **2025**, *49*, 101536.
5. A. Torche; T. Chouana; S. A. Uzun; C. A. Isik; M. E. Parlak; M. D'Elia; L. Rastrelli; F. T. Saricaoglu. Biodegradable PLA films plasticized with hydrophobic deep eutectic solvents and enriched with green-synthesized ZnO nanoparticles from date palm pits for antimicrobial food packaging. *LWT* **2026**, *241*, 119105. https://doi.org/10.1016/j.lwt.2026.119105
6. R. Thandavamoorthy; V. Mohanavel; A. Sivapragasam; V. Vekariya; D. Paul; P. Velmurugan; S. Al Obaid; S. A. Alharbi; N. Basavegowda. Environmental sustainability and waste conversion of Prosopis juliflora fibre-reinforced ZnO nanofiller particulates PLA composite - mechanical and thermal analysis. *Heliyon* **2024**, *10* (19), e38327. https://doi.org/10.1016/j.heliyon.2024.e38327
7. J. Chen; R. Tan; J. Ren; M. Huang; L. Wang; Q. Zhang. Polylactic acid (PLA) composites reinforced by end-capped ZnO quantum dots for enhanced mechanical, thermal, and degradation properties. *Polymer* **2025**, *337*, 129007.
8. X. Feng; Y. Guo; N. Zhao; Q. Dong; Z. Li. Bioinspired medical indwelling catheters with hierarchically structured coatings exhibiting specific wettability and antibacterial property. *Colloids Surf. B Biointerfaces* **2023**, *227*, 113388.

9. K. Yang; J. Shi; L. Wang; Y. Chen; C. Liang; L. Yang; L.-N. Wang. Bacterial anti-adhesion surface design: surface patterning, roughness and wettability: a review. *J. Mater. Sci. Technol.* **2022**, *99*, 82-100.
10. M. Carbureanu; C. G. Gheorghe. A machine learning-based data-driven model for predicting wastewater quality parameters in the industrial domain. *Appl. Sci.* **2026**, *16* (2), 694. https://doi.org/10.3390/app16020694
11. R. M. Goulter; I. R. Gentle; G. A. Dykes. Issues in determining factors influencing bacterial attachment: a review using the attachment of Escherichia coli to abiotic surfaces as an example. *Lett. Appl. Microbiol.* **2009**, *49*, 1-7.
12. C. G. Gheorghe; O. Pantea; V. Matei; D. Bombos; A.-F. Borcea. The efficiency of flocculants in biological treatment with activated sludge. *Rev. Chim.* **2011**, *62* (10), 1023-1026.
13. M. Morgelin. *Bacterial Pathogenesis: Methods and Protocols*; P. Nordenfelt; M. Collin, Eds.; Springer: New York, NY, **2017**; pp. 211-217.
14. S. V. Oopath; A. Baji; M. Abtahi; T. Q. Luu; K. Vasilev; V. K. Truong. Nature-inspired biomimetic surfaces for controlling bacterial attachment and biofilm development. *Adv. Mater. Interfaces* **2022**, *10* (4), 2201425.
15. C. McGoverin; C. Steed; A. Esan; J. Robertson; S. Swift; F. Vanholsbeeck. Optical methods for bacterial detection and characterization. *APL Photon.* **2021**, *6*, 080903. https://doi.org/10.1063/5.0057787
16. C. G. Gheorghe; O. Pantea; V. Matei; D. Bombos; A.-F. Borcea. Testing the behavior of pure bacterial suspension (*Bacillus subtilis, Pseudomonas aeruginosa* and *Micrococcus luteus*) in case of hydrocarbons contaminators. *Rev. Chim.* **2011**, *62* (9), 926-929. ISSN 0034-7752.
17. F. Pantanella; P. Valenti; T. Natalizi; D. Passeri; F. Berlutti. Analytical techniques to study microbial biofilm on abiotic surfaces: pros and cons of the main techniques currently in use. *Ann. Ig.* **2013**, *25*, 31-42.
18. T. R. Putri; A. Adhitasari; V. Paramita; M. E. Yulianto; H. D. Ariyanto. Effect of different starch on the characteristics of edible film as functional packaging in fresh meat or meat products: A review. *Mater. Today Proc.* **2023**, *87*, 192-199.
19. K. Tyagi; A. Malik. Antimicrobial action of essential oil vapours and negative air ions against Pseudomonas fluorescens. *Int. J. Food Microbiol.* **2010**, *143* (3), 205-210. https://doi.org/10.1016/j.ijfoodmicro.2010.08.023
20. Chapter 2.6.12, 2.6.13. Microbiological Examination of Non-sterile Products-Microbial Enumeration Tests, *European Pharmacopoeia*, **2013** Edition. Available online: https://ehpm.org/wp-content/uploads/2022/04/QG22_2-6-12_Microbiological_examination_of_non-sterile_products-microbial_enumeration_tests_ep10-2.pdf
21. J. K. Nayak, L. Behera, B. R. Jali. TiO_2 strengthened PLA nanocomposites: A prospective material for packaging application, *J. Mol. Struct.,* **2024**, *1316*, 138892, https://doi.org/10.1016/j.molstruc.2024.138892
22. NCCLS Performance Standards for Antimicrobial Disk and Dilution Susceptibility Tests for Bacteria Isolated from Animals, Approved Standard. 2nd Edition, NCCLS Document M31-A2 22(6), *Clinical and Laboratory Standards Institute,* Wayne, **2002** Available online: https://www.dbt.univr.it/documenti/OccorrenzaIns/matdid/matdid485539.pdf

23. C. G. Gheorghe; C. Dusescu; M. Carbureanu. *Asphaltenes biodegradation in biosystems adapted on selective media*. Rev. Chim. **2016**, *67* (10), 2106-2110.
24. Microbiological Examination of Non-Sterile Products: Microbial Enumeration Tests <61>; USP 39-NF 34; *United States Pharmacopeial Convention*: Rockville, MD, USA, **2016**; Available online: https://www.usp.org/sites/default/files/usp/document/harmonization/gen-method/q05b_pf_ira_34_6_2008.pdf
25. D. R. Popovici; C. G. Gheorghe; C. M. Dusescu-Vasile. Assessment of the active sludge microorganisms population during wastewater treatment in a micro-pilot plant. *Bioengineering* **2024**, *11* (12), 1306.
26. Japanese Industrial Standards Association. *JIS Z 2801:2010 Antibacterial Products - Test for Antibacterial Activity and Efficacy*; Japanese Industrial Standards Committee: Tokyo, Japan, **2010**.
27. C. G. Gheorghe; O. Pantea; V. Matei; D. Bombos; A.-F. Borcea. Testing of bacterial and fungal selection in the pollution of water with cationic detergents. *Rev. Chim.* **2011**, *62* (7), 707-711.
28. A. L. Koch. Growth Measurement. In *Methods for General and Molecular Bacteriology*; P. Gerhardt et al., Eds.; American Society for Microbiology: Washington, DC, **1994**; pp. 248-277.
29. F. Lupu; C. G. Gheorghe; C. Calin; O. Pantea. Biotreatment of the oil pollutants. *Rev. Chim.* **2013**, *64* (2), 210-212. ISSN 0034-7752.
30. C. Wiegand; A. Volpel; A. Ewald; M. Remesch; J. Kuever; J. Bauer; et al. Critical physiological factors influencing the outcome of antimicrobial testing according to ISO 22196/JIS Z 2801. *PLoS One* **2018**, *13*, e0194339.
31. P. Gilbert; et al. Inocula for antimicrobial sensitivity testing: a critical review. *J. Antimicrob. Chemother.* **1987**, *20*, 147-154.
32. General Chapter <62> Microbiological Enumeration of Non-Sterile Products - Tests for Specified Microorganisms. *USP 35-NF 30*; United States Pharmacopeial Convention, Inc.: Rockville, MD.
33. R. H. Katzenberger; A. Rosel; R. P. Vonberg. Bacterial survival on inanimate surfaces: a field study. *BMC Res. Notes* **2021**, *14*, 97.
34. S. Maitz; S. Polzl; D. Dreisiebner; C. Kittinger. Antimicrobial non-porous surfaces: a comparison of the standards ISO 22196:2011 and the recently published ISO 7581:2023. *Front. Microbiol.* **2024**.
35. EP. 5.1.3 Efficacy of Antimicrobial Preservation. *Pharm. Eur.* **2006**, *5.0*, 447-449.
36. Validation of Alternative Microbiological Method <1223>. *USP 39-NF 34*; United States Pharmacopeial Convention: Rockville, MD.
37. M. D. Campos; P. C. Zucchi; A. Phung; S. N. Leonard; E. B. Hirsch. The activity of antimicrobial surfaces varies by testing protocol utilized. *PLoS One* **2016**, *11*, e0160728. https://doi.org/10.1371/journal.pone.0160728
38. C. G. Gheorghe; C. M. Dusescu-Vasile; D. R. Popovici; D. Bombos; R.-E. Dragomir; F. M. Dima; M. Bajan; G. I. Vasilievici. Monitoring the biodegradation progress of naphthenic acids in the presence of *Spirulina platensis* algae. *Toxics* **2025**, *13* (5), 368.

STUDIA UBB CHEMIA, LXXI, 2, 2026 (p. 335-350)
(RECOMMENDED CITATION)
DOI:10.24193/subbchem.2026.2.17

PHYTOCHEMICAL PROFILE, ANTIOXIDANT ACTIVITY AND HPTLC FINGERPRINTING OF *GERANIUM ROBERTIANUM* L. EXTRACTS

Anamaria HOSU[a,*], Andreea HÎRB[a]

ABSTRACT. The present study evaluated the phytochemical composition and antioxidant activity of some hydroalcoholic extracts of *Geranium robertianum*. Total polyphenol content (TPC) and total flavonoid content (TFC) were estimated using colorimetric methods, while antioxidant activity was evaluated by DPPH and ABTS assays. High performance thin layer chromatography (HPTLC) was performed to obtain the fingerprints of samples and for preliminary investigation of the presence of isoflavonoids in their composition. The leaf extract exhibited the highest TPC (9.47 ± 0.66 mg gallic acid equivalents/mL), TFC (736.66 ± 9.38 mg rutin equivalents/mL), and showed the strongest antioxidant activity in both DPPH (12.55 ± 1.01 mg vitamin C equivalents/mL) and ABTS (5.63 ± 0.34 µmol Trolox equivalents/mL) assays. Flowers extract demonstrated considerable levels of phenolic compounds and antioxidant activity. The chromatographic fingerprints are characteristic of each analyzed part of the plant. The extracts purchased from the market have fingerprints different from those prepared in the laboratory. Also, the obtained fingerprints highlight the possible presence of isoflavonoids in the composition of the analyzed extracts. These findings demonstrate that leaves and flowers of *Geranium robertianum* represent valuable source of natural antioxidants and provide new information regarding the phytochemical characteristics of commercial Romanian preparations.

Keywords: *polyphenolic compounds, flavonoid, antioxidant activity, HPTLC fingerprinting, isoflavonoid*

[a] *Faculty of Chemistry and Chemical Engineering, Babeş-Bolyai University, Cluj-Napoca, Romania*
** Corresponding author: anamaria.hosu@ubbcluj.ro*

INTRODUCTION

Plants are the main tool used in traditional medicine for the treatment of diseases [1], this being reported since antiquity, until the 19th century when they were replaced in medical treatments by the synthetic compounds [2]. Recently, plants regain attention due to their phytochemistry based on compounds with biological activity and their medical effects [3]; in 2010 the World Health Organization (WHO) estimated that approximately 80% of the world's population uses traditional herbal products in primary health care [4].

The *Geraniaceae* family comprises six genera of medicinal and ornamental plants, including *Geranium, Pelargonium, California, Monsonia, Hypseocharis,* and *Erodium*, which are cultivated or grow naturally in the wild flora [5]. Species belonging to the *Geraniaceae* are recognized for their biological activities such as antioxidant (*Geranium robertianum*) [2], antiviral, antiasthmatic (*Pelargonium sidoides, Geranium sanguineum*) [6], antiallergic *(Pelargonium graveolens*) [7], antitumor (*Geranium thunbergii*, *Geranium robertianum*) [5].

Geranium robertianum L. (*G. robertianum*), commonly known as herb-Robert or “năpraznic”, is a herbaceous species native to Europe, where it occurs spontaneously in forest ecosystems, forest edges, rocky slopes, and other shaded or semi-shaded habitats [8, 9]. Due to its wide ecological adaptability, the species is well distributed across temperate regions [2, 10].

From a botanical point of view, *G. robertianum* is a plant characterized by a fibrous rooting system. The stems branched in many directions from the base, being long, thin and fragile [8]. Their colour varies from all green to a mixture between red and green [2]. The leaves are usually greener with a triangular shape divided into three segments [2, 11]. At the time of flowering, the plant can have two to four flowers of five rounded petals arranged radially around the superior ovary and colored in various shades of pink and purple [11].

Traditionally, *G. robertianum* has been used in folk medicine for the treatment of inflammatory conditions, skin disorders, gastrointestinal complaints, and wound healing [2, 12]. These ethnopharmacological uses are supported by its rich phytochemical composition, which includes hydrolysable tannins (notably ellagitannins such as geraniin), flavonoids (rutin, quercetin and kaempferol derivatives) [13], and phenolic acids (ellagic acid, caffeic acid, gallic acid, and ferulic acid) [13, 14], considered to be responsible for its biological activities [2, 7].

Different products based on *G. robertianum* therapeutic effects could be purchased from market as food supplements [9]. The method of administration can be internal or external, depending on the form of the preparation and the purpose of use [10], but once administered, every kind of product can serve in a different way depending on the part of the plant used in preparation [2]. For example, *G. robertianum* leaves exert anti-inflammatory, antioxidant, antidiabetic and antirheumatic effects [9], the aerial parts are recommended in cancer, diabetes and for stopping nosebleeds [2]. It is worth mentioning that, most often, extracts from the leaves and aerial parts of *G. robertianum*, but not from the flowers, have been characterized in terms of their constituents and biological activity.

Although *G. robertianum* is recommended to be used in hormonal deficiencies, in male and female sterility, frigidity, impotence, uterine bleeding of various etiologies, dysmenorrhea, etc. [15], no scientifically documented studies to support these actions have been published yet. Similar effects were also described for red clover (*Trifolium pratense*) and kudzu (*Pueraria lobada*) and they were associated with their isoflavonoid constituents which extert estrogenic activity [16].

This study aimed to provide a comparative phytochemical and antioxidant characterization of extracts obtained from different parts of plant of *G. robertianum* and also of some commercialy available extracts from Romanian market. In addition, HPTLC fingerprinting was performed to compare their chromatographic profiles and to preliminary investigate the presence of izoflavonoid constituents.

RESULTS AND DISCUSSION

Hydroalcoholic extracts prepared from flowers, leaves, stems and aerial parts of *G. robertianum* were comparatively evaluated in terms of total polyphenol (TPC) and flavonoid (TFC) content and antioxidant activity (AA), as well as chromatographic fingerprints, with extracts of aerial parts of the plants commercially available on the Romanian market, from four different manufacturers (A-D).

Therefore, TPC, TFC and AA of extracts were determined spectrophotometrically, and the results obtained are presented in **Table 1**. AA was evaluated *in vitro* using two free radicals, namely DPPH and $ABTS^{+\bullet}$.

Table 1. TPC, TFC and AA of *G. robertianum* extracts

Extract	TPC (mg GAE/mL)	TFC (µg RE/mL)	AA_{DPPH} (mg vit CE/mL)	AA_{ABTS} (µmol TroloxE/mL)
Flowers	8.91 ± 0.62	517.54 ± 8.15	10.97 ± 0.81	5.16 ± 0.25
Leaves	9.47 ± 0.66	736.66 ± 9.38	12.55 ± 1.01	5.63 ± 0.34
Stems	6.08 ± 0.34	358.02 ± 6.49	5.32 ± 0.30	2.39 ± 0.09
Aerial parts	9.33 ± 0.71	533.16 ± 8.74	11.24 ± 0.95	5.24 ± 0.33
A	8.76 ± 0.55	411.59 ± 7.21	10.57 ± 0.75	4.75 ± 0.29
B	7.14 ± 0.40	333.81 ± 6.75	8.65 ± 0.66	3.98 ± 0.15
C	6.22 ± 0.41	211.71 ± 5.34	7.94 ± 0.47	3.38 ± 0.11
D	5.31 ± 0.29	191.95 ± 5.11	6.78 ± 0.45	2.45 ± 0.08

The results are presented as mean ± standard deviations of three replicates
GAE-gallic acid equivalents, RE- rutin equivalents, vit CE- vitamin C equivalents

Total phenolic content

The TPC values of the analyzed samples ranged from 5.31 ± 0.29 to 9.47 ± 0.66 mg GAE/mL extract. Among the laboratory-prepared extracts, the leaf extract had the highest polyphenol content (9.47 ± 0.66 mg GAE/mL), followed by the aerial parts extract (9.33 ± 0.71 mg GAE/mL) The stem extract showed the lowest TPC value (6.08 ± 0.34 mg GAE/mL). Flowers also contain high amounts of phenolic compounds (8.91 ± 0.62 mg GAE/mL), contributing together with leaves to the high TPC level of extract of aerial parts of geranium. The commercial extracts exhibited lower and more variable values, ranging between 5.31 ± 0.29 and 8.76 ± 0.55 mg GAE/mL, which may be attributed to differences in raw material quality and extraction procedures, including solvent.

Total flavonoid content

A similar trend was observed for TFC, which varied between 191.95 ± 5.11 and 736.66 ± 9.38 mg RE/mL extract. The highest flavonoid content was determined in the leaf extract (736.66 ± 9.38 mg RE/mL), followed by the aerial parts extract (533.16 ± 8.74 mg RE/mL) and the flower extract (517.54 ± 8.15 mg RE/mL). The stem extract contained considerably lower flavonoid levels (358.02 ± 6.49 mg RE/mL), while commercial products showed the lowest and most variable values of TFC.

Antioxidant activity evaluation

The antioxidant activity measured by DPPH and ABTS assays followed the same general pattern as that observed for TPC and TFC. The leaf extract exhibited the highest antioxidant activity, reaching 12.55 ± 1.01 mg vit CE/mL (DPPH) and 5.63 ± 0.34 µmol TroloxE/mL (ABTS), respectively. Flower and aerial parts extracts also showed strong antioxidant activity, whereas stem extracts and several commercial products exhibited lower values. These results suggest that phenolic compounds, particularly flavonoids, are major contributors to the antioxidant capacity of *G. robertianum* extracts.

Pearson's correlation coefficients (r) were also calculated to evaluate relationships between TPC, TFC and AA determined by both methods. Statistical significance was set at $p < 0.05$. Pearson correlation analysis revealed strong positive relationships between TPC and AA_{DPPH} ($r = 0.942$, $p < 0.001$) and AA_{ABTS} ($r = 0.974$, $p < 0.001$), while TFC was also significantly correlated with AA_{DPPH} ($r = 0.814$, $p = 0.014$) and AA_{ABTS} ($r = 0.841$, $p = 0.009$). In addition, a strong correlation was observed between TPC and TFC ($r = 0.884$, $p = 0.004$), confirming the contribution of flavonoids to the total phenolic content and to the antioxidant activity of extracts.

The present findings are consistent with previous studies reporting *G. robertianum* as a rich source of phenolic compounds with strong antioxidant properties [2, 11, 17]. Literature data indicate that leaves generally contain higher levels of phenolic compounds than stems, which agrees with the trends observed in the present study [13, 17, 18]. The higher accumulation of bioactive compounds in leaves can be explained by their metabolic role and exposure to environmental stress factors such as UV radiation and oxidative stress. Also, the lower values of TPC, TFC and antioxidant activity of stem extracts agree with previous observations, showing reduced accumulation of phenolic compounds in supporting tissues [19].

In addition, extraction solvent and methodology are known to significantly influence phenolic yield and antioxidant activity. This may explain the variability observed among commercial products, which likely reflects differences in extraction procedures, solvent composition, plant material quality, and storage conditions [2].

An important contribution of this study is the evaluation of the flower extract of *G. robertianum*. To our knowledge, no previous study has reported the TPC, TFC and AA of extracts prepared exclusively from the flowers of this species, although the literature has mentioned that the infusion of flowers or leaves obtained from *G. robertianum* has been used for infertility problems [20]. In this regard, the label of each analyzed extract mentions that the

product is also recommended for use as an adjuvant in sterility and sexual dynamics disorders in both sexes, in ovarian cyst cancer, polycystic ovaries, etc. These recommendations, as well as the high content of polyphenols (8.91 ± 0.62 mg GAE/mL) and flavonoids (517.54 ± 8.15 µg RE/mL) and the antioxidant activity determined in the analyzed extract, demonstrate that *G. robertianum* flowers could be a valuable source of bioactive compounds.

Also, this study provides the first comparative characterization of some commercially available *G. robertianum* hydroalcoholic extracts marketed in Romania. The considerable variability observed among products highlights the need for standardization and importance of quality control in herbal preparations.

HPTLC fingerprinting

High-performance thin layer chromatography (HPTLC) was used to obtain the phytochemical fingerprints of the investigated extracts of *G. robertianum*. Plants of the genus *Geranium*, including *G. robertianum*, have been frequently studied for the identification and determination of their bioactive constituents, but to our knowledge, the HPTLC fingerprinting of flowers, leaves, stems and hydroalcoholic extracts available on the Romanian market has not been reported. However, a study in which the chromatographic fingerprinting of polyphenols from alcoholic extracts obtained from aerial parts of four wild-grown *Geranium* species (*G. dissectum*, *G. lucidum*, *G. pusillum*, and *G. robertianum*) from Romania was reported [12]. Therefore, hydroalcoholic extracts from flowers, leaves, stems and aerial parts of the plant, as well as four extracts from aerial parts of the plant obtained from four different producers in Romania, were fingerprinted by HPTLC.

The proposed method considered not only the fingerprinting of *G. robertianum* extracts in terms of separation of polyphenols, but also the attempt to identify some of the most common compounds from the isoflavone class (genistin, daidzin, genistein and daidzein), as they are known to act as phytoestrogens. The idea that *G. robertianum* might contain polyphenols from the phytoestrogen class came from the recommendations for the use of plant extracts, mentioned by manufacturers on the products analyzed (Table 3), but not yet scientifically supported.

Seven mobile phase systems (Table 2) were tested to obtain a good chromatographic separation of the compounds of interest. The best separation was obtained with mobile phase 4, chloroform-ethyl acetate-methanol-water, 4:2:2.2:1 (*v/v*). This was then optimized to ensure the good separation of the constituents from the *G. robertianum* extracts, so that the chromatographic separations were further performed with the solvent mixture consisting of chloroform-ethyl acetate-methanol-water, 1:2:1.2:0.4 (*v/v*).

Table 2. The composition of the tested mobile phases

No.	Mobile phase composition	Ref.
1	Chloroform-methanol, 19:1 (*v/v*)	[21]
2	Chloroform-methanol-water, 9:1:0.1 (*v/v*)	[22]
3	Chloroform-methanol-water-acetic acid, 60:30:10:0.5 (*v/v*)	[22]
4	Chloroform-ethyl acetate-methanol-water, 4:2:2.2:1 (*v/v*)	[23]
5	Ethyl acetate-butanone-formic acid-water, 5:3:1:1 (*v/v*)	[24]
6	Ethyl acetate-methanol-acetic acid-water, 60:30:3:0.5 (*v/v*)	[25]
7	Benzene-ethyl acetate-formic acid, 10:3:1 (*v/v*)	[26]

The image of the plate under UV light at 245 nm (Figure 1a) shows that the extracts prepared in the laboratory from the leaves and aerial parts of the plant have similar chromatographic fingerprints, the intensity of the bands characteristic of the separated compounds being higher in the aerial parts extract. Moreover, the fingerprint of the aerial parts extract highlights two compounds contained only in the flower and stem extracts, separated in the lower half of the plate. The chromatographic fingerprint of the flower extract differs greatly from that of the leaf and stem extracts, but seems to be very similar to that of the extract from producer A, highlighting in both samples the presence of a compound in high concentration that appears separately in the middle area of the plate and which could be contained in lower concentration in the extracts from leaves and aerial parts, as well as in the extract from producer C. Also, the fingerprint of extract of the aerial parts prepared in the laboratory is very different from those of the samples from producers A, B and D.

Seven mobile phase systems (Table 2) were tested to obtain a good chromatographic separation of the compounds of interest. The best separation was obtained with mobile phase 4, chloroform-ethyl acetate-methanol-water, 4:2:2.2:1 (*v/v*). This was then optimized to ensure the good separation of the constituents from the *G. robertianum* extracts, so that the chromatographic separations were further performed with the solvent mixture consisting of chloroform-ethyl acetate-methanol-water, 1:2:1.2:0.4 (*v/v*).

The fluorescence detection (366 nm) before derivatization (Figure 1b) provided additional important information about some constituents useful for evaluation and authentication of closely related samples. Thus, the images obtained at 366 nm confirm that the chromatographic fingerprints of the leaf and aerial part extracts are very similar, also highlighting in the middle of the plate a succession of three light orange and orange-pink zones characteristic of compounds found in both samples, but also in the stem extract in a much lower concentration. The flower extract has a different fingerprint from all the other samples, highlighting separate characteristic compounds in the

lower half of the plate. It can also be clearly seen that in the middle part of the plate there is a blue zone characteristic of a compound contained in high concentration in both the flower extract and the extract from producer A. This is not found in the leaf extract nor in the aerial parts extract prepared in the laboratory. The print of the extract from the stems is different from that of the leaves and stems, highlighting the presence of characteristic light blue bands separated in the lower third of the plate. Extracts from producers B, C and D have very similar fingerprints, showing few separated constituents, the difference between them being mainly given by the intensity of the separated bands. This justifies the lower TPC, TFC and AA values of these samples compared to those prepared in the laboratory and that from producer A.

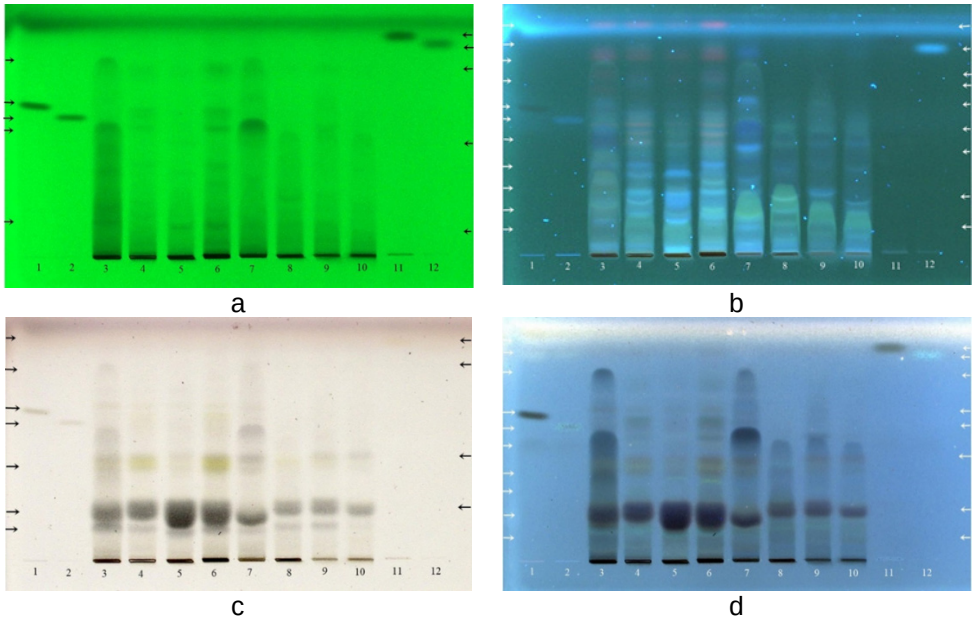

Figure 1. HPTLC fingerprints of samples on silica gel $60F_{254}$ with chloroform-ethyl acetate-methanol-water,1:2:1.2:0.4(*v/v*) as mobile phase. a-UV 254nm, b-UV 366nm, c-Derivatization with 10% H_2SO_4 in ethanol, white light, d-Derivatization with 10% H_2SO_4 in ethanol UV 366nm. Tracks: 1-genistin, 2-daidzin, 3-flowers, 4-leaves, 5-stem, 6-aerial parts, 7-A, 8-B, 9-C, 10-D, 11-genistein, 12-daidzein

The images of the plate in white light and at 366 nm after derivatization support the information provided in the other detection modes. It can also be seen that there are two zones, one at the bottom of the plate (gray in

white light and light green at 366 nm) and another in the middle (colored in gray-yellow in white light and light brown at 366 nm) that are found in the chromatographic fingerprints of all the analyzed samples.

Another aim of HPTLC fingerprinting was to check if the analyzed samples contain isoflavone. Therefore, some standards of isoflavone were analyzed together with *G. roberianum* extracts. The image of the plate under UV light at 254 nm before derivatization (Figure 1a), highlights the separation of the isoflavonoid standards at values of $R_{f\ daidzin}$ = 0.54, $R_{f\ genistin}$= 0.58, $R_{f\ daidzein}$ = 0.82 $R_{f\ genistein}$ = 0.86. Comparing the chromatographic fingerprints of the analyzed samples, it can be seen that the leaf extract and the aerial part extract show a compound separated at R_f = 0.54 which could be daidzin, the intensity of its characteristic band being higher in the aerial part extract. Also, in the fingerprint of extract A, a band at R_f = 0.58 can be observed that could be attributed to genistin. Moreover, the compound separated at R_f = 0.54 appears as light blue zones in leaf and aerial extracts when the plates were documented at 366 nm, similar to the characteristic band of the daidzin (Figure 1b). Derivatization with 10% H_2SO_4 solution in ethanol allows genistin to be visualized in white light (Figure 1c) as a yellow-brown colored zone, the characteristic shade of isoflavones with a -OH group in position 5. Daidzin appears as a gray-yellow zone, less intensely colored than genistin, due to the absence of the -OH group in position 5 from its structure. Thus, the fingerprints of the extracts from flowers, leaves, stems and aerial parts of the plant, as well as the extract from producer A, obtained in white light after derivatization, show the presence of zones at R_f =0.58, like that characteristic of genistin. Also, the images of the plates at 366 nm after derivatization (Figure 1d), confirm the presence of this compound in all the mentioned samples, but also in the extract from producer C. The image of the plate under white light after derivatization shows the presence of gray-yellow zones in the extracts from leaves and aerial parts, at R_f = 0.54, similar to daidzin. On the other hand, the image of the plate under UV light at 366 nm, after derivatization, does not clearly highlight the presence of this compound.

Regardless of how the chromatographic plate was documented, daidzein and genistein could not be identified in any of the analyzed samples. This may be because most isoflavones are present as glycosides in plants and also in hydroalcoholic extracts. Therefore, for the separation and identification of aglycones, the literature has described the need to perform an acidic hydrolysis step, followed by extraction in ethyl acetate [23].

The plate image at 254 nm (Figure 2a) obtained after the chromatographic separation of hydrolyzed extracts shows that in the fingerprints of hydrolyzed extracts of leaves and aerial parts of the plant the presence of a band at

R_f = 0.86, of weak intensity in the case of the aerial parts extract, which could be attributed to genistein. This observation is supported by the fact that in the fingerprints of the hydrolyzed extracts of flowers, leaves and aerial parts, after derivatization with 10% ethanolic solution of H_2SO_4, characteristic zones are observed at the same R_f, both in white light and at 366 nm. Also, in the chromatographic fingerprint of the hydrolyzed flower extract, at 366 nm after derivatization, the presence of a light blue zone at R_f = 0.54 which appears to be similar with daidzin can be observed. Furthermore, in the hydrolyzed extract from producer D, the presence of a light blue band at R_f = 0.82, similar to the characteristic band of daidzein, can be highlighted.

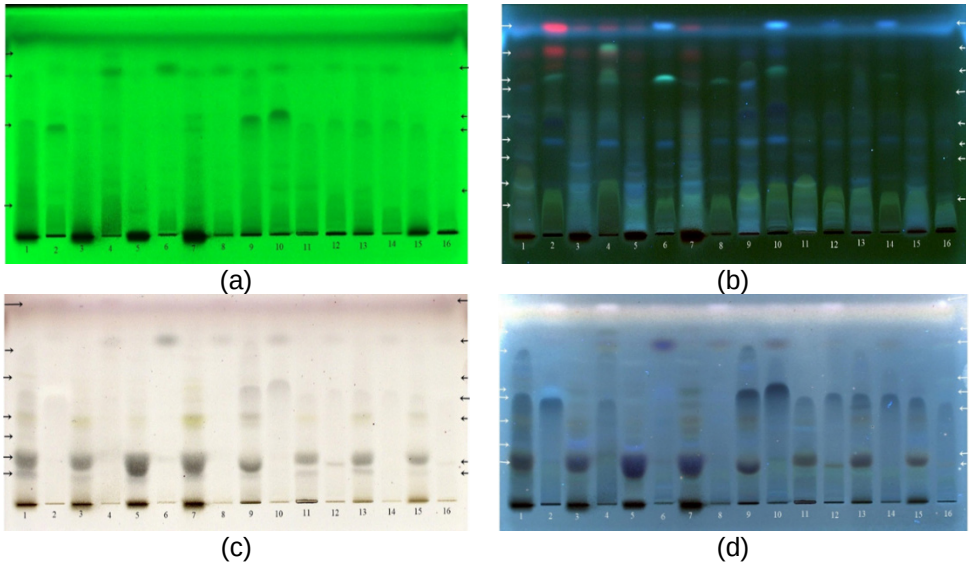

Figure 2. HPTLC fingerprints of samples on silica gel 60F254 with chloroform-ethyl acetate-methanol-water,1:2:1.2:0.4(v/v) as mobile phase. a-UV 254nm, b-UV 366nm, c-Derivatization with 10% H_2SO_4 in ethanol, white light, d-Derivatization with 10% H_2SO_4 in ethanol UV 366nm. Tracks: 1-flowers, 2-hydrolyzed flowers, 3-leaves, 4- hydrolyzed leaves, 5-stem, 6-hydrolyzed stem, 7-aerial parts, 8- hydrolyzed aerial parts, 9-A, 10- hydrolyzed A, 11-B, 12- hydrolyzed B, 13-C, 14- hydrolyzed C, 15-D, 16-hydrolyzed D.

The results obtained suggest the possible presence of the investigated isoflavones in the analyzed *G. robertianum* extracts. However, further analysis using more selective techniques would be required for clear identification and quantification of these compounds.

CONCLUSIONS

G. robertianum extracts showed high levels of phenolic compounds and significant antioxidant activity, particularly in leaves and flowers. Strong positive correlations between phenolic content and antioxidant activity confirmed the important contribution of polyphenols and flavonoids to the antioxidant potential of the investigated extracts. Considerable differences were observed among the commercial hydroalcoholic preparations, highlighting the influence of extraction and processing conditions on phytochemical composition and emphasizing the need for quality control and standardization.

HPTLC fingerprinting of extracts revealed distinct phytochemical profiles and suggested the possible occurrence of isoflavonoid compounds. However, further studies using more selective analytical techniques are required for definitive identification. The results provide new information regarding flower extracts and commercial Romanian preparations, contributing to a better understanding of the phytochemical variability of *G. robertianum* and supporting its potential use as a natural source of bioactive compounds.

EXPERIMENTAL SECTION

Chemicals

All reagents used in the study were of analytical grade. Ethanol 96%, 1,1-diphenyl-2-picrylhydrazyl radical, (DPPH•), potassium persulfate ($K_2S_2O_8$), 2,2 ′-azino-bis(3-ethylbenzothiazoline-6- sulfonic acid) ($ABTS^+$), 6-hydroxy2,5,7,8-tetramethylchroman-2-carboxylic acid (Trolox), ascorbic acid (vitamin C), gallic acid (GA), rutin, aluminum chloride ($AlCl_3$), Folin-Ciocalteau reagent 2N, sodium acetate (CH_3COONa), sodium carbonate (Na_2CO_3), sulfuric acid 95-98%, hydrochloric acid were purchased from Merck (Darmstadt, Germany). The solvents used for the chromatographic analysis were ethyl acetate, acetic acid, formic acid, butanone, benzene and methanol, and were purchased from Millipore (Bedford, USA).

Materials and sample preparation

The plant material used in this investigation was collected in June 2021, from Strâmtura (47.778890N, 24.144720E), Maramureş County, Romania. The aerial parts of the plants were collected during the flowering period, and after drying in a dark, well-ventilated space at room temperature, samples of entire aerial parts, flowers, leaves and stems were separated and grounded.

Also, four *G. robertianum* food supplements available on the market in Romania, produced by Faunus Plant (A), Farmanat Poieni (B), Aroma plant Bonchiş (C) and Dorel Plant (D) were purchased. These are hydroalcoholic extracts from aerial parts of plant, and their characteristics, according to the manufacturers' labels, are presented in Table 3.

Although the Romanian Pharmacopoeia recommends the extraction of polyphenolic compounds in ethanol-water 7:3 (v/v), in this study an extraction system consisting of ethanol-water, 1:2.5 (v/v), similar to those used by the producers of extracts A-D (Table 3) was chosen. The extraction of bioactive compounds was done by maceration, using 1 g of dried grounded plant material and 10 mL of ethanol-water, 1:2.5 (*v/v*). After maceration at room temperature, in the dark for 10 days, the extracts were decanted and centrifuged for 15 min at 6000 rpm using a C2006 centrifuge (Centurion Scientific Limited, Bosham, UK). The resulting supernatants were collected and stored in dark bottles, at 4◦C until further analysis.

Table 3. Characteristics of analyzed *Geranium robertianum* food supplements

Extract	Ingredients	Administration	Recommendation
A	aerial parts of plant 20%, ethanol min. 30% *v/v*	internal use: 5 mL in 50ml water or tea, 3-4 times/day, on an empty stomach	male and female sterility, frigidity, impotence, uterine bleeding of various etiologies, dysmenorrhea, benign tumors of various locations, cancer (uterine, lung, intestinal, breast or other locations), diarrhea, intestinal inflammation, irradiation, sequelae after irradiation
B	whole plant, hydroalcoholic solution 34°	5 mL as it is or diluted in water or tea, 3-5 times/day	male and female sterility, frigidity, impotence, low immunity, menstrual cycle disorders, cysts and uterine bleeding of various etiologies, dysmenorrhea, benign tumors of various locations, cancer (uterine, lung, intestinal, breast or other locations), diarrhea, intestinal inflammation, chronic fatigue
C	aerial part plant 26%, water 50%, grain alcohol (96%)-24%.	5 mL, 3 times/day, 30 min before main meals, on an empty stomach	male and female sterility, frigidity impotence, uterine bleeding of various causes, benign tumors of various locations, dysmenorrhea intestinal inflammation, diarrhea, uterine fibroids, ovarian cysts, supporting the body after irradiation
D	aerial parts of plant – 20%; hydroalcoholic solution (96° alcohol: water 1:2)– 80%	5 mL diluted in tea, 3 times/day, 30 min before main meals	breast, lung, ovarian, intestinal, gastric cancer, ovarian cysts, polycystic ovaries, hematuria, irradiation, sterility and sexual dynamics disorders in both sexes, low spermatogenesis and sperm motility, hemorrhagic, leukorrhea, chronic diarrhea, gastroenteritis, hemorrhagic enteritis, cystitis

Spectrophotometric Measurements

Spectrophotometric measurements were performed at room temperature, in triplicate using a T80+ UV-Vis spectrophotometer (PG Instruments, Lutterworth, UK).

Total Phenolic Content (TPC)

TPC was determined according to the Folin–Ciocalteu assay with slight modification [27]. Thus, 0.3 mL of each extract properly diluted were mixed with 1.5 mL Folin–Ciocalteu's reagent (0.2 N). After 5 min, 1.2 mL sodium carbonate (0.7 M) were added, and then all the mixtures were incubated for 2 h, at room temperature in dark conditions. The absorbance was measured at 760 nm and the TPC was calculated from the calibration curve ($y = 0.009x + 0.1247$, $R^2 = 0.9996$) obtained in the same conditions, using solutions of gallic acid with concentrations between 0 and 100 µg/mL. The results were expressed as mg gallic acid equivalents/mL of extract (mg GAE/mL).

Total flavonoids content (TFC)

TFC of was determined by a colorimetric method described in the Romanian Pharmacopoeia [28], using $AlCl_3$. Aliquots of 0.5 mL of each extract optimally diluted were mixed with 0.4 mL of 25 g/L $AlCl_3$ solution, 0.5 mL of 100 g/L CH_3COONa solution and 4 mL distilled water. After 15 min, the absorbance was measured at 430 nm and TFC was determined from the calibration curve of rutin ($y = 0.0063x + 0.0084$, $R^2 = 0.9995$) obtained in a range of concentration of 0-120 µg/mL. TFC of extracts were expressed as µg rutin equivalents/mL (µg RE /mL).

Antioxidant activity (AA)

Antioxidant activity of geranium extracts was determined by DPPH assay [29] and ABTS assay [30], with some modifications.

DPPH assay

Aliquots of 0.25 mL of each extract properly diluted were added to 3.0 mL of 0.09 mg/mL solution of DPPH prepared in ethanol. After 20 min, the absorbance was measured at 517 nm. Also, for each analyzed sample, the absorbance of a mixture obtained from 0.25 mL of sample solvent and 3.0 mL of DPPH solution was measured in parallel, in the same conditions.

Both measured absorbance values were considered in the calculation of the antioxidant activity. The antioxidant activities of extracts were determined based on the calibration curve (y = 1.4714x, R^2 = 0.9996) obtained in the same conditions, using solutions of vitamin C with different concentrations between 0.150 and 0.275 mg/mL. The antioxidant activities (AA_{DPPH}) of samples were expressed as mg vitamin C equivalents/mL (mg vit CE/mL).

ABTS assay

First, the cationic radical $ABTS^{\bullet+}$ was generated from the reaction of 7 mmol/L ABTS diammonium salt solution with 2.45 mmol/L $K_2S_2O_8$. These solutions were mixed in a ratio of 1:1 (*v/v*) and incubated for 24 h at room temperature, in the dark. Then, $ABTS^{\bullet+}$ solution was freshly diluted so that their absorbance measured at 734 nm to be between 0.800 and 0.900. Mixtures obtained from 0.5 mL of each extract properly diluted and 3.0 mL $ABTS^{\bullet+}$ solution were incubated at room temperature in dark for 15 min and then the absorbance was measured at 734 nm. Also, for each analyzed sample, the absorbance of a mixture obtained from 0.3 mL of sample solvent and 3.0 mL of $ABTS^{\bullet+}$ solution was measured in parallel, in the same conditions. In the calculation of the antioxidant activity, both measured absorbance values were considered. The antioxidant activities were using the calibration curve (y = 3.8759x + 0.1191, R^2 = 0.9998) obtained with Trolox solutions in a range of 1.10-1.35 µmol/mL. The results (AA_{ABTS}) were expressed as Trolox equivalents (µmol TroloxE/mL).

Hydrolysis of extracts

Acidic hydrolysis of extracts was performed according to Chen et al. [23], with some modifications. Thus, aliquots of 1.0 mL of 0.1 M hydrochloric acid were added to 1.0 mL of each extract and the obtained mixtures were incubated for 2h at 96°C, using a water bath. The hydrolyzed extracts were then extracted twice with 1.0 mL portions ethyl acetate. The resulting ethyl acetate fractions were pooled and made up to 2.0 mL in a volumetric flask.

HPTLC analysis

Aliquots of 16 µL of each extract and 5 µL of each standard 0.1 mg/mL solutions of genistin, daidzin, genistein and daidzein were applied as 8 mm bands at 15 mm from the low edge of the plate with a flow rate of 40 nL/s using a semi-automatic application device Linomat 5 (CAMAG, Basel, Switzerland). The chromatographic analysis was performed on silica

gel $60F_{254}$ HPTLC plates 20 cm × 10 cm, Merck (Darmstadt, Germany), using a mixture of chloroform-ethyl acetate-methanol-water, 2:4:2.4:0.8 (v/v) as the mobile phase. The plates were developed to a distance of 80 mm at room temperature in normal chromatographic twin trough chamber (CAMAG, Basel, Switzerland), pre-saturated for 30 min with the mobile phase. After development, the dried plates were sprayed with 10% sulphuric acid ethanolic solution, using an electro-pneumatic device TLC Sprayer (CAMAG, Basel, Switzerland). The plates were then heated at 105°C for 10 min using the TLC Plate Heater 3 (CAMAG, Basel, Switzerland). The detection was done in UV light at 254 and 366 nm before and after derivatization and in white light after derivatization. The documentation of the plates was performed using a TLC visualizer device Digistore 2 (CAMAG, Basel, Switzerland). All CAMAG devices were controlled by winCATs 1.4.3 software.

REFERENCES

1.S. Amaral; L. Mira; J. M. Nogueira; A. P. Silva; M. Helena Florencio; *Bioorg. Med. Chem.*, **2009**, *17(5)*, 1876-1883
2.V. C. Graça; I. C. F. R. Ferreira; P. F. Santos; *Ind. Crops Prod.*, **2016**, *87*, 363-378
3.E. Neagu; G. Paun; D. Constantin; G. L. Radu; *Arab. J. Chem.*, **2017**, *10*, S2547-S2553
4.World Health Organization (WHO). Guidelines for registration of traditional medicines in the WHO African Region. Geneva: World Health Organization; **2010**
5.V. C. Graça; I.C.F.R. Ferreira; P.F., Santos; *Curr. Pharm. Des*., **2020**, 26, 1838–1865
6.E. Neagu; G. Paun; V. Moreanu; G. L. Radu; *Rev. Roum. Chim.*, **2010**, *55*, 321-325
7.D. I. Cocoș; K. Earar; M. Dinu; I. Lungu; C. Bazbanela; C. Galea; *Rom. J. Med. Dent. Educ.,* **2023**, *12*, 23-34
8.O. Bas; A. T. Kandili; N. Comlekcioglu; *Int. J. Chem. Technol.*, **2025**, *9*, 185-198
9.J. R. Tofts; *J. Ecol.*, **2004**, *92*, 537-555.
10. M. Wierzbicka; H. Galera; B. Sudnik-Wojcikowska; B. Wilkomirski; *Plant Syst. Evol.*, **2014**, *30*, 973-985.
11. D. Haj Ali; A. M. Dărăban; D. Ungureanu; A. Căta; I. M. C. Ienașcu; Ș. Dinu; C. A. Dehelean; C. Danciu; *Plants*, **2025**,*14*, 918
12. C. Bejenaru; A. E. Segneanu; A. Bită; L. E. Bejenaru; M. V. Hovane; M. V. Ciocîlteu; A. C. Tîrnă; A. Blendea; G. D. Mogoșanu, *Plants*, **2025**, *14*, 3190
13. V. C. Graça; L. Barros; R. C. Calhelha; M. I. Dias; I. C Ferreira; I. C. Santos, *Ind. Crops Prod.*, **2017**,*108*, 543–552.
14. C. S. Fodorea; L. Vlase; S. Suciu; M. Tămaş; S. E. Leucuţa; *Rev. Med. Chir. Soc. Med. Nat.*, **2005**,*109,* 174–178.

15. D. C. Vitale; C. Piazza; B. Melilli; F. Drago; S. Salomone; *Eur. J. Drug Metab. Pharmacokinet.*, **2013**, *38*, 15-25
16. P. Gaya; Á. Peirotén; J. M. Landete; *J. Funct. Foods.*, **2017**, *39*, 198-205
17. M. D. Catarino; A. M. S. Silva; M. T. Cruzb; S. M. Cardoso; *Food Funct.*, **2017***, 8*, 3355-3365
18. V. C. Graça; L. Barros; R. C. Calhelha; M. I. Dias; A. M. Carvalho; C. Santos-Buelga; P. F. Santos; I. C. Ferreira; *Food Funct*, **2016**, *7*, 3807-3814
19. P. Pant; S. Pandey; S. Dall'Acqua; *Chem. Biodiv.*, **2021**, *18*, e2100345, DOI: 10.1002/cbdv.202100345
20. J. Petelka; B. Plagg; I. Säumel; S. Zerbe; *J. Ethnobiol. Ethnomed.*, **2020**, *16*, 1–15
21. B. Thiem, A. Krawczyk, *Herba Pol.*, **2010**, 56(1), 48-56.
22. S.C. Mun; G. S. Mun; *J. Food and Drug Anal.*, **2015**, 23, 538-544.
23. S. B. Chen; H. P. Liu; R. T. Tian; D. J. Yang; S. L. Chen; H. X. Xu; A. S. C. Chan; P. S. Xie; J. Chromatogr. A, **2006**, *1121*, 114–119
24. M. A. Berhow; Modern Analytical Tehniques for Flavonoids Determination, *Flavonoids in Cell Function*, B. Buslig, J. Manthey, *Kluwer Academic/Plenum Publishers*, *New York*, **2002**, pp. 61-76.
25. A. Puri; B. P. Panda; *J.Chromatogr.Sci.,* **2015**, *53*, 338–344.
26. E. Reich; A. Schibli; *High-performance Thin-Layer Chromatography for the Analysis of Medicinal Plants*, First Edition, *Thieme*, New York, **2006**, pp. 130-132.
27. V. L.Singleton; R. Orthofer; R. M. Lamuela-Raventos; *Methods Enzymol*. **1999**, *299*, 152–178
28. Farmacopeea Română, Editia X, Editura Medicala, Bucuresti, Romania, **2021**, pp. 1060-1063
29. C. Sánchez-Moreno; J. A. Larrauri; F. Saura-Calixto; *J. Sci. Food Agric.*, **1998**, *76*, 270-276
30. R. R. Pellegrini; N. Proteggente; A. Pannala; A. Yang; M. Rice-Evans; *Free Radic. Biol. Med.*, **1999**, *26*, 1231–1237